

テーマ2 細胞モデルを用いた細胞機能の自在操作技術

(1) 概要

テーマ2では、物理・化学的な点から細胞機能に着目し、その自在操作のための細胞モデルの構築と、それを用いた解析システムの構築を目的として研究を行った。多様な内包物を有し、運動性をもち互いに集合する細胞において、分子機能に影響する因子として、分子集団、集合体スケールでの物理的効果が分子ダイナミクスに及ぼす影響が重要である。この中で、細胞の運動性、集団形成、膜に関わる輸送現象、内包物のクラウディング効果、を取り上げ、これらの機能を有するモデル系を構築し、ここでの分子ツールの物理化学的な挙動を解明することを目指し、さらに、これらモデル細胞系を対象とした顕微レーザー分光系の構築を行い、機能性分子の溶存状態や機能の解明を分光学的観点からも進めた。

(2) 構成員

テーマ責任者:塩井章久

学内(同志社大学)研究員:

理工学部:塩井章久, 木村佳文, 松本道明, 八坂能郎(2017年まで), 遠藤太佳嗣(2017年から), 山本大吾(2016年から), 田原義朗(2019年から)

生命医科学部:吉川研一, 剣持貴弘, 貞包浩一郎

学外研究員:柳澤実穂(東京大), 熊崎茂一(京都大)

(3) 成果報告

「細胞モデルを用いた細胞機能の自在操作技術」をテーマとして、細胞やそのモデル系が示す①自己運動性、非平衡パターン形成、②細胞集団形成、③2分子膜環境での輸送現象、④分子クラウディング効果、⑤分子ダイナミクスの研究に分類して研究を進めた。小テーマのそれぞれが、必ずしも特定の研究者と対応しているわけではなく、各研究者が①～⑤の複数に関与しているものも多い。

テーマ2では、5年間のプロジェクトにおいてこれまでに、計148報の査読付き学術論文誌に論文が掲載されており、今後も順次論文投稿を継続する。下記に、①～⑤の主だった成果(学術論文22編)についての概要を示す。

①について、塩井、山本らは、イオン感知性(文献1)やpH感知性(文献2)を備えた液滴、両親媒性分子集合体を作製し、また、単一パルスしか示さないような時計反応からでも、物質移動過程とのシステム化によって連続運動を生成するモデル系を作製した(文献3)。山本、塩井、吉川らは、酸素による酸化をエネルギー源として、生物と似た運動を示す粒子系を見出した(文献4)。また、貞包、剣持、吉川らは、デザインしたマイクロ流路を用い、液体の相分離臨界点近傍の組成の溶液の一点にレーザーを照射することにより、マイクロポンプができることを見出し、理論的にもメカニズムを解明した(文献5)。山本、塩井、吉川らは、微小空間にかかる直流電場という細胞類似の環境で働くモーター粒子を得ることに成功した(文

献6)。

②について、細胞モデル作製のため、吉川らは DNA など生体高分子を取り込んだ細胞サイズの液滴の生成に成功した(文献7)。また、剣持、吉川らは、病理組織切片を機械的に伸展することにより生じたひび割れのパターンを解析することにより、癌の信頼性の高い診断が可能になることを見出し、臨床応用に向けて研究を更に進めている(文献8)。

③について、松本らは、分子がモデル細胞膜に与える影響を解明するため、大腸菌と似た組成のリン脂質からなるベシクルへのイオン液体の分配を明らかにし、分配とイオン液体の毒性との関連を示した。さらに、イオン液体と類似の両親媒性の水溶性薬剤分子のリン脂質ベシクルへの分配機構を明らかにし、分配と分子の疎水性、モル液体体積や極性表面積との関連を示した。これらの基礎となるイオン液体への様々な物質の抽出挙動に関する成果も得ている(文献9, 10)。田原らは、これらの成果が、抗がん剤の水への溶解性向上によるがん細胞への抗がん剤送達方法につながることを見出している。

②と④について、剣持、貞包、吉川らはレーザートラップの活用により、3次元の細胞集団を形成できることを明らかにした(文献11)。柳澤らは、リポソームやマイクロ液滴内部に、高分子溶液や高分子ゲルからなる細胞質や細胞骨格のモデルを付与し、膜変形や構造形成を、その力学特性や分子拡散と相関付けて解明した(文献12)。

⑤について、八坂、木村らは過渡回折格子レーザー分光法により、CO が非極性部位の構造を反映して運動することを明らかにし(文献13)、光受容タンパク質の反応における場の効果を検討し、特異な環境に置かれた生体分子のふるまいを明らかにした。木村、八坂らは、アルキル鎖長(疎水性)の異なるイオン液体を合成し、それらの中でのCO やLi⁺等の回転・並進ダイナミクスを明らかにした(文献14)。熊崎らは、細胞中の分子ダイナミクスについて、蛍光寿命画像化顕微鏡、蛍光スペクトル画像化顕微鏡、吸収スペクトル画像化顕微鏡を発展させ、シアノバクテリアへの応用方法を確立し、976nm 励起ラマン散乱スペクトル顕微鏡についても運用できるようにした(文献15)。また、八坂、木村らは不均一環境における電荷移動反応やプロトン移動反応などの素反応過程の速度定数と、環境を特徴づけるパラメーターとの関連を明らかにした(文献16)。さらに、遠藤、木村らは、不均一環境のモデル場として、イオン液体そのものの構造・ダイナミクスを調べるとともに(文献17)、CO 分子をプローブとして、局所的な構造・ダイナミクスを、NMR 及び分子動力学計算から明らかにした。熊崎らは、実際の細胞について、細胞内分子ダイナミクスを観測する 976nm および 1064nm 励起ラマン散乱スペクトル顕微イメージング装置の開発・改良を行い、。シアノバクテリア単一細胞の分化診断に成功し、ライン状励起光による画像取得の高速化も達成した。(文献18)。

上記以外にも多数の学術論文が発表された。これらの研究成果の一部として、自ら物質を捕獲し生成物を排出して動く分子集合体(文献19)、自律的な動的集団パターンを示すフッ素油滴群(文献20)を見出し、それぞれ ChemistryWorld(RSC)ならびに Nature Publishing Group の web サ

トで紹介された。また、沸騰点近傍でも生命活動を維持している好熱菌に関して、この菌に特異的なポリアミンが DNA の高次構造を安定化していることを一分子観察により明らかにし、ChemPhysChem 誌の Best Paper として Front Cover に採用された(文献21)。高分子混雑環境下で、DNA や Actin が自発的に細胞サイズ液滴に取り込まれ、細胞様の構造—例えば、細胞分裂期の構造—を自発的に作り出すことを見出し、ChemBioChem 誌に Very Important Paper として掲載されるなどしている(文献22)。

本報告書の末尾に、上に示した研究概要に関する図と、下記リストに挙げた主要論文を添付する。

(4) 参考文献

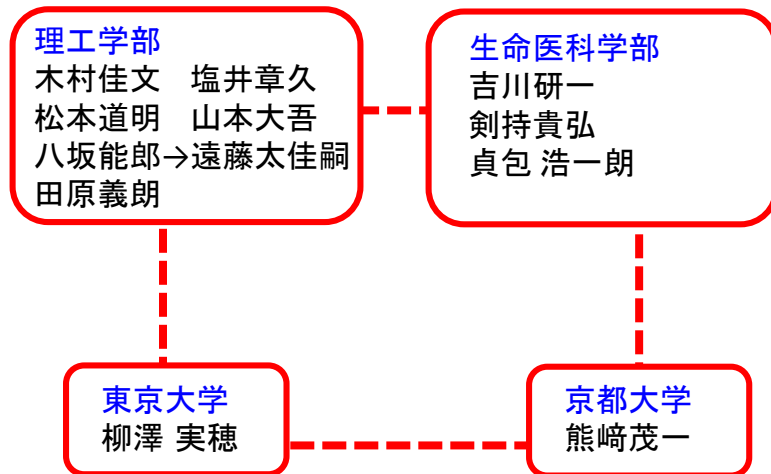
1. “Ionic Tuning of Droplet Motion on Water Surface”
Yudai Mikuchi, Hirofumi Yamashita, Daigo Yamamoto, Erika Nawa-Okita, Akihisa Shioi, *Frontiers in Chemistry*, 7, 788 (2019).
2. “A molecular assembly machine working under a quasi-steady state pH gradient”,
Nawa-Okita, Erika; Nakao, Yuki; Yamamoto, Daigo; Shioi, Akihisa, *The Bulletin of the Chemical Society of Japan*, **93**, 604-610 (2020)
3. “Autonomous Movement System Induced by Synergy between pH Oscillation and a pH-Responsive Oil Droplet”
Yasunao Okamoto, Yoko Sasaki, Erika Nawa-Okita, Daigo Yamamoto, and Akihisa Shioi, *Langmuir*, **35**, 14266–14271 (2019)
4. “Micromotors working in water through artificial aerobic metabolism”
D. Yamamoto, T. Takada, M. Tachibana, Y. Iijima, A. Shioi and K. Yoshikawa, *Nanoscale*, **7**, 13186-13190 (2015).

5. "Optical Fluid Pump: Generation of Directional Flow via Microphase Segregation/Homogenization"
H.Sakuta, S.Seo, Shuto .Kimura, M.Hörning, K.Sadakane, T.Kenmotsu, M.Tanaka, K.Yoshikawa, *The Journal of Physical Chemistry Letters*, **9**, 5792-5796 (2018).
6. "Helical micromotor operating under stationary DC electrostatic field"
Daigo Yamamoto, Kento Kosugi, Kazuya Hiramatsu, Wenyu Zhang, Akihisa Shioi, Kaori Kamata, Tomokazu Iyoda, and Kenichi Yoshikawa, *J. Chem. Phys.*, **150**, 014901 (2019)
7. "Aqueous/Aqueous Micro Phase Separation: Construction of an Artificial Model of Cellular Assembly"
H.Sakuta, T.Fujimoto, Y.Yamana, Y.Hoda, K.Tsumoto, K.Yoshikawa, *Frontiers in Chemistry*, **7**, 1-7 (2019)
8. "Cracking pattern of tissue slices induced by external extension provides useful diagnostic information"
K. Danno, T. Nakamura, N. Okoso, N. Nakamura, K. Iguchi, Y. Iwadate, T. Kenmotsu, M. Ikegawa, S. Uemoto, K. Yoshikawa, *Scientific Reports*, **8**, 12167-12173 (2018)
9. "In situ extractive fermentation of lactic acid by *Rhizopus oryzae* in an air-lift bioreactor"
M. Matsumoto, H. Furuta, *Chem. Biochem. Eng. Q.*, **32**, 275-280 (2018)
10. "Durability of chitosan/cellulose hydrogel beads regenerated from ionic liquid in acidic and basic media and their metal adsorptive characteristics"
M. Matsumoto, S. Ishikawa, T. Kamigaki, *Prog. Chem. Appl. Chitin Deriv.*, **24**, 145-150 (2019)
11. "Manipulating Living Cells to Construct a 3D Single-Cell Assembly without an Artificial Scaffold"
A.Yoshida, S.Tsuji, H.Taniguchi, T.Kenmotsu, K.Sadakane, K.Yoshikawa, *Polymers*, **9**, (2017)
12. "Sol-gel coexisting phase of polymer microgels triggers spontaneous buckling"
K. Koyanagi, K. Kudo, M. Yanagisawa, *Langmuir*, **35**, 2283-2288 (2019).
13. "Polarity and Nonpolarity of Ionic Liquids Viewed from the Rotational Dynamics of Carbon Monoxide"
Y. Yasaka, Y. Kimura, *J. Phys. Chem. B*, **119**(50), 15493–15501 (2015).
14. "Universality of Viscosity Dependence of Translational Diffusion Coefficients of Carbon Monoxide, Diphenylacetylene, and Diphenylcyclopropanone in Ionic Liquids under Various Conditions"
Y. Kimura, Y. Kida, Y. Matsushita, Y. Yasaka, M. Ueno, K. Takahashi, *J. Phys. Chem. B*, **119**, 8096-8103 (2015).
15. "Spectral microscopic imaging of heterocysts and vegetative cells in two filamentous cyanobacteria based on spontaneous Raman scattering and photoluminescence by 976 nm excitation."

- K. Tamamizu; S. Kumazaki. *Biochimica et Biophysica Acta, Bioenergetics*, **1860**, 78 - 88 (2019).
16. "Excited-State Proton Transfer of Cyanonaphthols in Protic Ionic Liquids: Appearance of a New Fluorescent Species"
K. Fujii, Y. Yasaka, M. Ueno, Y. Koyanagi, S. Kasuga, Y. Matano, Y. Kimura, *J. Phys. Chem. B*, **121**, 6042–6049 (2017).
17. "Structure-property Relationship for 1-Isopropyl-3-methylimidazolium and 1-tert-Butyl-3-methylimidazolium-based Ionic Liquids: Thermal properties, density, viscosity, and quantum chemical calculations"
T. Endo, K. Sakaguchi, K. Higashihara, Y. Kimura, *J. Chem. Eng. Data*, **64**, 5857 (2019)
18. "Characterization of thylakoid membrane in a heterocystous cyanobacterium and green alga with dual-detector fluorescence lifetime imaging microscopy with a systematic change of incident laser power"
S. Nozue, A. Mukuno, Y. Tsuda, T. Shiina, M. Terazima, and S. Kumazaki, *Biochimica et Biophysica Acta, Bioenergetics*, **1857**, 46–59 (2016).
19. "A molecular assembly that crawls on a solid substrate with a metabolic-like process"
M. Nakada, Y. Fujikami, M. Kawaguchi, D. Yamamoto, A. Shioi, *Molecular Systems Design & Engineering*, **1**, 208 – 215 (2016).
20. "The evolution of spatial ordering of oil drops fast spreading on water surface",
D. Yamamoto, C. Nakajima, A. Shioi, M. P. Krafft, K. Yoshikawa, *Nature Communications*, **6**, 7189, (2015).
21. "Branched-Chain Polyamine Found in Hyperthermophiles Induces Unique Temperature-Dependent Structural Changes in Genome-Size DNA"
T.Nishio, Y.Yoshikawa, W.Fukuda, N.Umezawa, T.Higuchi, S.Fujiwara, T.Imanaka K.Yoshikawa, *ChemPhysChem*, **19**, 2299-2304 (2018)
22. "Specific Spatial Localization of Actin and DNA in a Water/Water Microdroplet: Self-Emergence of a Cell-Like structure"
N.Nakatani, H.Sakuta, M.Hayashi, S.Tanaka, K.Takiguchi, K. Tsumoto . K.Yoshikawa, *ChemBioChem*, **19**, 1370-1374 (2018)

グループ2

細胞モデルを用いた細胞機能の自在操作技術



- ・細胞的環境が現れる物理的機構
- ・それが分子機能へ及ぼす影響



細胞に加えてモデル細胞に着目
(多様な要因による現象の複雑化を回避)

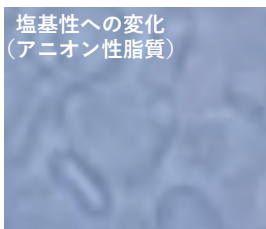


- ・自己運動機能, 分子クラウディング機能, 膜輸送, 分配
- ・レーザーによる操作
- ・特異な環境(細胞, 細胞モデル)での分子ダイナミクス

目的

1. モデル細胞を構築して
細胞的環境が現れる物理的機構を研究
2. モデル細胞, 細胞系での分子分光系を構築し
分子機能に及ぼす場の特徴を解明
⇒第1グループで開発した分子など
機能性分子に与える細胞的な場の影響を
物理的, 物理化学的側面に注目して研究

自己運動機能を示すモデル系 (両親媒性分子集合体, 触媒粒子)



水中の溶存酸素による
有機物の酸化で
運動する粒子集団
(講演 2)

chemistryworld | SOCIETY OF CHEMISTRY

Crawling chemical system acts as if it's alive

24 May 2016 | Kathryn Geipel

They crawl. They eat. They excrete. So you'd be forgiven for thinking these globules created by a team at Osaka University – but they're not.

Discovering life-like motion in non-living systems fascinates Akihisa Saito, from Osaka University. He and his team are currently combining new chemicals to investigate the idea.

They already knew that droplets of dicationic diethylammonium bromide (DDAB), a cheap surfactant, react with iodide ions, then scoot around and break chemical bonds. The molecule turns vesicle. Unlike cells, though, these vesicles shrink, and collapse after a few seconds. They needed feeding. Their acid and calcium ions proved the missing link.

Together, DDAB, glucose and calcium, form globules, called vesicles, with intriguing life-like movement. The result

size 2

**“捕食”によってエネルギーを得て,
“排泄”しながら運動する分子集合体**

nature COMMUNICATIONS

出版リスト | 研究分野ナビゲート | My Naturelinks | サイトマップ

水面上を急速に拡がる油滴の空間秩序の発展

The evolution of spatial ordering of oil drops fast spreading on a water surface

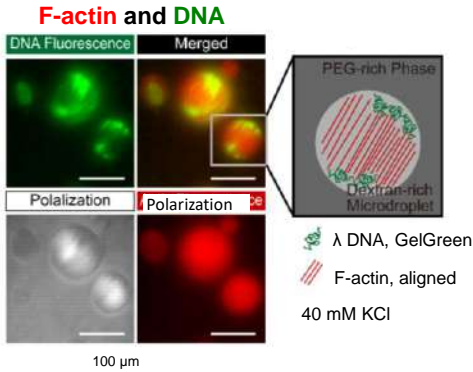
2016年5月22日 | Nature Communications 6: 7189 doi: 10.1038/ncomms1591 (2015)

研究機関から自ら空間パターンを形成するといった、特異な集団についての論文。第一着で面での認めれられた。液体の集団が自己集約性、それが動的に費なれいかに集約することを示した。この動的な現象は、お互いに安定性のフラクタル(perfluorooctyl bromide, PFDB)の電離性分子を面へと輸送することによって、その動的な現象を形成

自発的集団運動を示す液滴

細胞的構造が出現するモデル系

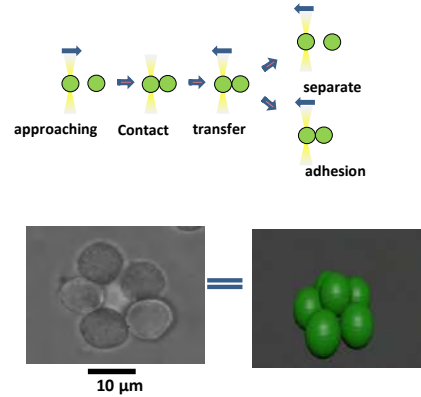
Self-Emergent Cell-Like Structure



Tsumoto & Yoshikawa, *MRS Adv.*, 2017.

レーザー操作によるモデル多細胞 (講演4)

Construction of Stable Cellular Assembly through Remote Control by Laser



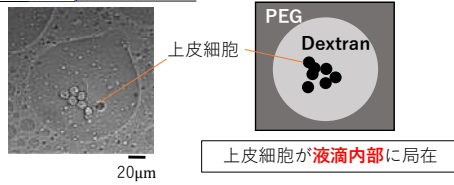
Yoshida, et al., *Polymers*, 2017.

細胞の局在構造が現れるモデル系

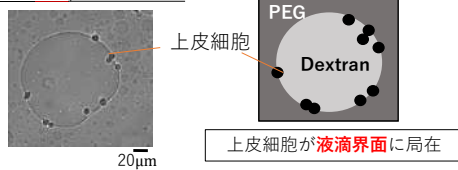
■これまでの研究成果 (水・水相分離系)

水・水相分離系における、細胞サイズのDextran液滴内の上皮細胞分布の濃度依存性を明らかにした。

PEG10%, Dextran 5%



PEG5%, Dextran5%

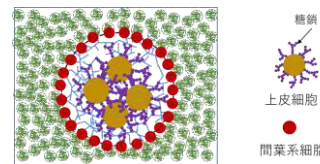


特許申請中：「細胞の配置方法」、特願2017-219854

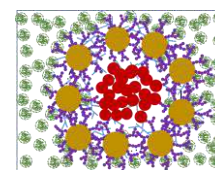
■今後の研究計画

水・水相分離現象を利用し、上皮、間葉、実質系からなる、多様な細胞組織体を形成する。

PEG 10%, Dextran 5%



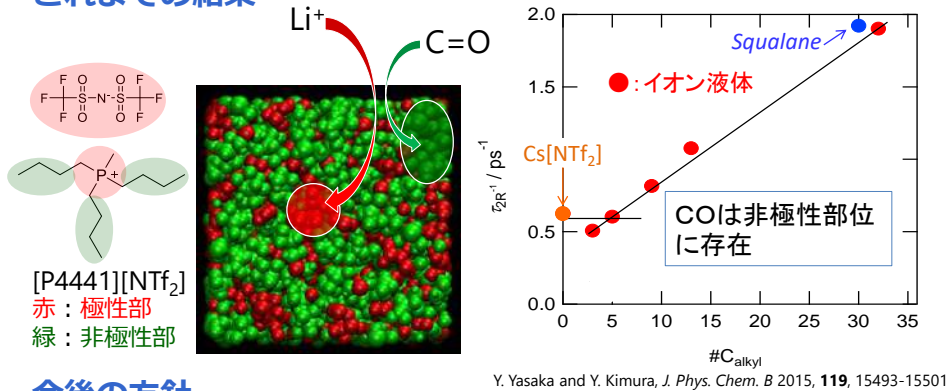
PEG 5%, Dextran 5%



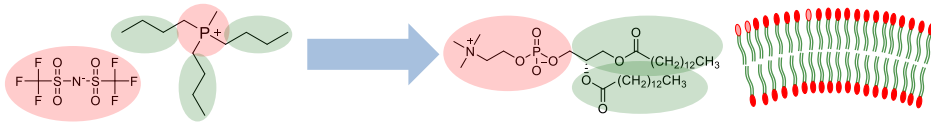
糖鎖
上皮細胞
間葉系細胞
PEG
Dextran

NMRを用いたモデル細胞膜と溶質分子の 分子レベルでの観察

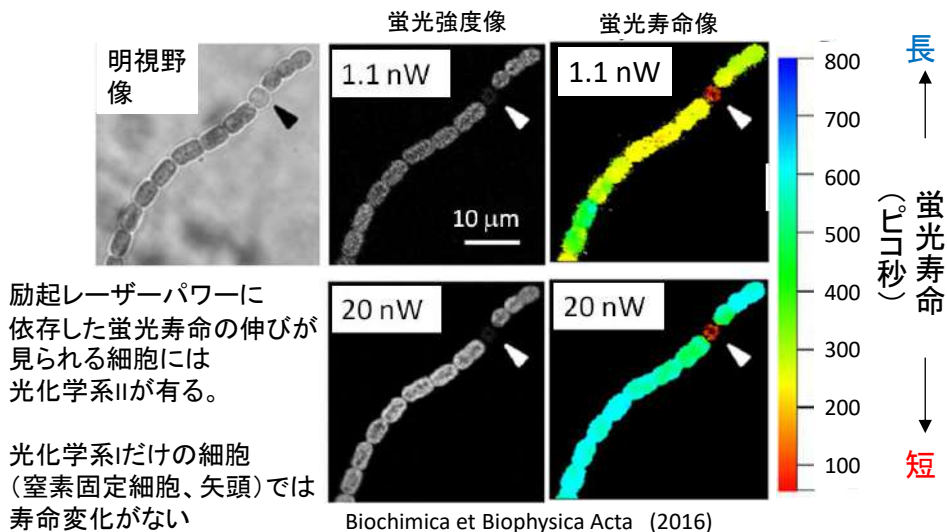
これまでの結果



今後の方針



植物、藻類、シアノバクテリアの細胞における分子イメージングを進展させる基盤として、自家蛍光の情報を細胞レベルで最大限引き出す方法論の開発



今後は、遺伝子発現プローブ、人工的染色なども利用して、細胞全体の生理活動と光合成反応の関係性を画像化する。

発展のために

- ・モデル系と細胞との化学的な距離(を近づけ、の意味を考察し)細胞モデルとしての特徴を明らかとする
- ・ツインレーザー等を活用した細胞操作の効率化
- ・分光実験において検討した不均一場の対象範囲を広げ、モデル系を拡張

これからの方向

- ・遺伝子発現や自発運動性をもった、より細胞的な液滴やリボソームなどを形成
- ・3次元組織体の生成手法を発展させミニ臓器の創製に挑戦
- ・細胞モデルの構造と力学特性との関係を検討し細胞の形や構造の生成原理を導く
- ・モデル細胞膜と物質との相互作用についての生理活性物質を用いた検討
- ・種々の低分子の運動ならびに生体分子の構造変化、プロトン移動や電荷移動などに対する細胞モデルの場の効果を検討
- ・細胞に対する顕微分光イメージングの技法を発展させ、非蛍光性分子の分析、動物細胞における様々な染色法等を検討



波及効果, 副次的効果

- ・化学環境に自律応答した動的性質を示す化学系が有する最小の構成要素を解明
- ・分子膜と生体関連物質との相互作用に関する、熱力学的、量子論的な包括的知見
- ・レーザートラップによる再生医療に活用可能なミニ臓器の生成
- ・細胞や細胞的環境でのタンパク質の揺らぎや素反応のダイナミクスを解明



Ionic Tuning of Droplet Motion on Water Surface

Yudai Mikuchi, Hirofumi Yamashita, Daigo Yamamoto, Erika Nawa-Okita and Akihisa Shioi*

Department of Chemical Engineering and Materials Science, Doshisha University, Kyoto, Japan

Herein, the oscillation of an oil droplet on the surface of water is studied. The droplet contains an anionic surfactant that can react with the cations present in water. The oscillation starts after a random motion, and the oscillation pattern apparently depends on the cation species in the water phase. However, a common pattern is included. The cation species only affects the amplitude and frequency and sometimes perturbs the regular pattern owing to the instability at the oil/water interface. This common pattern is explained by a simple model that incorporates the surfactant transport from the droplet to the surrounding water surface. The dependency of the amplitude and frequency on cation species is expressed quantitatively by a single parameter, the product of the amplitude and square of frequency. This parameter depends on the cationic species and can be understood in terms of the spreading coefficient. The simple model successfully explains this dependency.

OPEN ACCESS

Edited by:

Hideki Seto,

High Energy Accelerator Research
Organization, Japan

Reviewed by:

Hiroyuki Kitahata,
Chiba University, Japan
Nobuhiko J. Suematsu,
Meiji University, Japan

*Correspondence:

Akihisa Shioi
ashioi@mail.doshisha.ac.jp

Specialty section:

This article was submitted to
Physical Chemistry and Chemical
Physics,
a section of the journal
Frontiers in Chemistry

Received: 16 July 2019

Accepted: 01 November 2019

Published: 19 November 2019

Citation:

Mikuchi Y, Yamashita H, Yamamoto D,
Nawa-Okita E and Shioi A (2019) Ionic
Tuning of Droplet Motion on Water
Surface. *Front. Chem.* 7:788.
doi: 10.3389/fchem.2019.00788

Keywords: droplet oscillation, oil/water interface, di(2ethylhexyl)phosphate, spatiotemporal pattern, ionic tuning

INTRODUCTION

A droplet on a liquid surface often shows various spatiotemporal pattern formations. Recently, the number of studies focusing on droplet dynamics under a non-equilibrium state has increased, where the non-equilibrium is caused by mass transport and/or chemical reactions (Ye et al., 1994; Shioi et al., 2003; Sumino et al., 2005; Lagzi et al., 2010; Pimienta et al., 2011; Ban et al., 2013; Hermans et al., 2013; Banno and Toyota, 2015; Seemann et al., 2016; Zwicker et al., 2016; Seyboldt and Jülicher, 2018). This is one of the simplest pattern formations in non-equilibrium open systems. The studies in this field may be associated with the physicochemical understanding of the spatiotemporal patterns in living systems (Zwicker et al., 2016; Seyboldt and Jülicher, 2018) and application of non-linear dynamics to chemical processes such as wetting (Wang et al., 2015; Zhang et al., 2015), drying (Ok et al., 2016; Janssens et al., 2017), and active transport (Bottier et al., 2009; Goto et al., 2015). Furthermore, these studies potentially lead to the design of abiotic chemical where evaporation produces the non-equilibrium state (Stocker and Bush, 2003; Pimienta et al., 2011; Antoine and Pimienta, 2013). However, the chemical control of such droplet dynamics is an attractive topic because it can yield its chemo-responsive nature. Only a few studies have been reported for the chemical control of droplet dynamics on a liquid surface (Lagzi et al., 2010; Ban et al., 2013), and how the droplet dynamics under evaporation is affected by chemistry is not fully elucidated. In general, the interplay between the mass transport and chemical reactions is a key topic in the design of biomimetic systems. However, this is not fully studied for droplet dynamics on a liquid surface despite it being the simplest system.

An oil/water interface containing bis(2-ethylhexyl) phosphate (DEHPA) shows chemo-sensitive instability (Hosohama et al., 2011; Miyaoka et al., 2012). Some types of cations cause a spontaneous convection by chemical reactions with DEHPA, whereas other types of cations do not. Even among

the cations causing instability, the characteristics of the convection depend on the cation species. When a float is placed at an oil/water interface, its motion can be regulated by the cation species in water (Yasui et al., 2015). Such an oil/water system is very much suitable to study the chemical control of droplet dynamics. In the present study, the dynamics of an oil droplet containing DEHPA on a water dissolving electrolyte is investigated: The oil droplet with DEHPA spontaneously moves on the water surface. It shows a regular oscillation with some types of cations, whereas it is perturbed or violated by other types of cations. The frequencies and amplitudes of the regular oscillations depend on the cation species. This dependency can be explained by a simple model, in which the cation effect is considered in terms of the effects on the surface and interfacial tension.

MATERIALS AND METHODS

DEHPA (> 97%) was purchased from Sigma-Aldrich Co. LLC. Silicone oil was purchased from Shin-Etsu Chemical Co., Ltd. Other chemicals were reagent grade and purchased from Wako Pure Chemical Industries, Ltd. $\text{CaCl}_2 \cdot 2\text{H}_2\text{O}$, $\text{FeCl}_2 \cdot 4\text{H}_2\text{O}$, $\text{FeCl}_3 \cdot 6\text{H}_2\text{O}$, $\text{SrCl}_2 \cdot 6\text{H}_2\text{O}$, $\text{MgCl}_2 \cdot 6\text{H}_2\text{O}$, $\text{MnCl}_2 \cdot 4\text{H}_2\text{O}$, and $\text{CoCl}_2 \cdot 6\text{H}_2\text{O}$ were used as electrolytes. Decane was used as the oil phase (Silicone oil was also used for a control experiment). DEHPA and each electrolyte were dissolved in the oil and water phases, respectively. The concentrations of DEHPA and electrolyte were 100 and 10 mM, respectively. Subsequently, 10 mL of water phase was poured into a petri-dish of 48 mm diameter, after which an oil droplet of 3 μL was placed on the water surface. The droplet motions were monitored by a single-lens reflex camera (Canon EOS Kiss X9) with 30 fps frame rate. Digital microscope VW-6000 (Keyence corporation) with a frame rate ranging from 30 to 250 fps was also used when a higher time resolution was required. The movie was analyzed by image analysis software Ulead Video Studio (Corel Corporation) and TEMA (Photron Limited).

We also measured the droplet diameter under equilibrium. Then, 10 mL of the water phase was poured in another petri-dish of 48 mm diameter. Just after an oil droplet of 3 μL was placed on the water, this petri-dish was covered to avoid evaporation to outside environment. The petri-dish fogged owing to the evaporation of the oil in the petri-dish. Thus, we used the shadow graph technique to measure the droplet diameter. The diameter after 300 s was measured. The single-lens reflex camera (Canon EOS Kiss X9) with 30 fps frame rate was also used for this experiment.

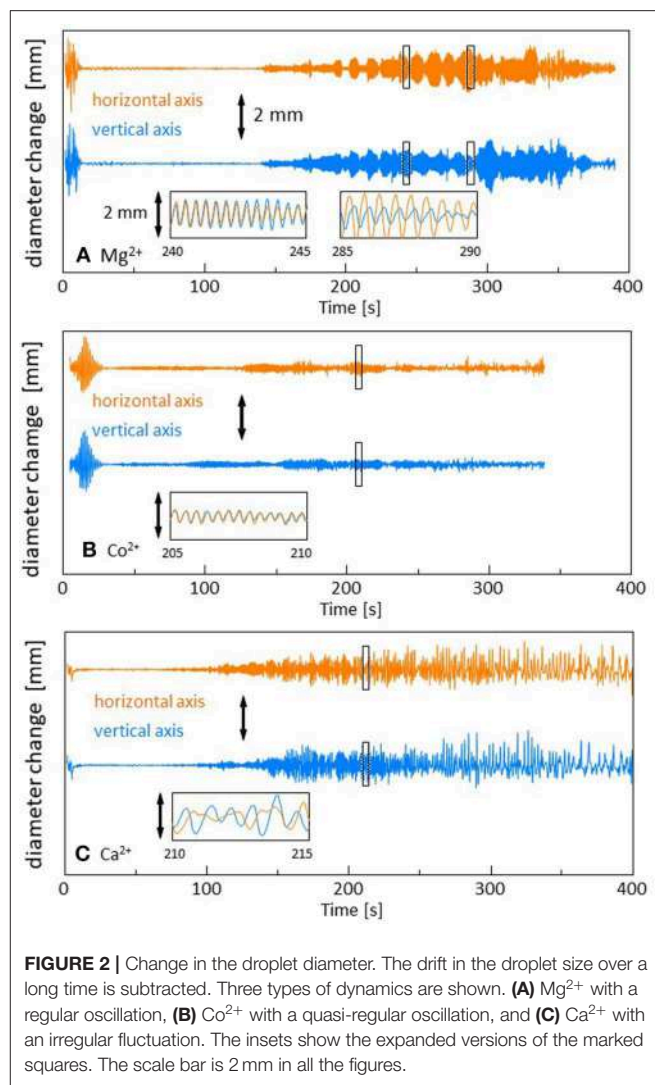
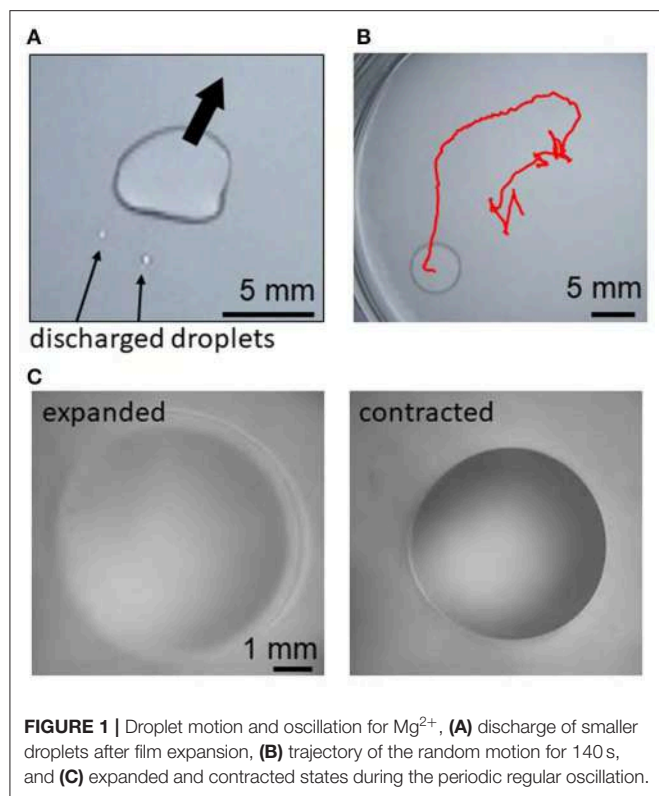
The surface and interfacial tensions were also measured. In these experiments, the oil and water phases, the volume of which were 10 mL, were equilibrated. After the equilibration, the surface and interfacial tensions were measured by a pendant drop technique with one attention (Biolin Scientific Holding AB). A drop of a higher density fluid was formed in a lower density fluid. Spreading coefficient S was calculated from these surface and interfacial tensions.

The evaporation rate of oil was also measured from the weight loss of the oil phase. Then, 5 mL oil (decane or silicone oil) was poured in a petri-dish of 48 mm diameter. The petri-dish was set on an electronic balance to measure its weight every 5 min. We also observed the convection pattern in the water phase on which an oil droplet was placed. Separately, carbon powder (~ 3 mg) was dispersed in 10 mL of water phase as tracer particles. This water phase was poured in a petri-dish of 48 mm diameter. A core of a mechanical pencil (Mitsubishi Pencil Co., Ltd. uni.3-202ND) was inserted vertically across the water surface. An oil droplet of 3 μL was placed on the water surface around this inserted pillar. The droplet migration was restricted so that a stable convection pattern was observed. The motion of the tracers was monitored by the single-lens reflex camera (Canon EOS Kiss X9) at a frame rate of 30 fps. Particle image velocimetry analysis was performed (LaVision, DaVis 8). All the experiments were performed at room temperature (20–25°C).

RESULTS

Figure 1 shows examples of droplets motions. Just after a decane droplet is placed, a thin film begins to expand from the droplet periphery. This is observed for the cations except Fe^{3+} . Smaller droplets are sometimes discharged from a part of the film edge (**Figure 1A**). Then, the original droplet moves toward the opposite direction of this discharge. This motion is repeated, resulting in a random motion (**Figure 1B**) and deformation (**Figure 1A**) of the droplet. When Fe^{2+} or Ca^{2+} are dissolved in water, this random motion continues until the droplet disappears by transformation into a film and/or smaller droplets, evaporation, and dissolution. When Mg^{2+} , Sr^{2+} , Mn^{2+} , or Co^{2+} is dissolved, the random motion gradually weakens. After it stops, the droplet starts to exhibit an oscillatory shape change between expanded and contracted shapes (**Figure 1C**). (See **Supplementary Video 1** for all the cations and **Supplementary Video 2** for Mg^{2+} for the regular oscillation regime.) When Fe^{3+} is dissolved in water, the oil droplet only expands on water and disappears by transforming into a film, evaporation, and dissolution.

The time course of the droplet diameter is shown in **Supplementary Figure 1**, in which we see weak drifts and discontinuous changes in the droplet diameter. These weak drifts and discontinuous changes are subtracted in **Figure 2** because they are caused by an error in the treatment of the video files in the software. The diameters are measured along the two orthogonal directions in the video frame. For Mg^{2+} (and Sr^{2+} and Mn^{2+}), one can see the time range within which the droplet shape oscillates quite regularly (140 s–390 s in **Figure 2A**). The oscillation amplitude changes over a long time, during which the envelopes oscillate with a long period (beat). Though a similar oscillation is observed for Co^{2+} (90 s–280 s in **Figure 2B**), the regularity of the pattern, as shown in the inset, is slightly perturbed. Here, we refer it as a quasi-regular oscillation. For Ca^{2+} (and Fe^{2+}), the diameter changes irregularly throughout the experiment (90 s–400 s in **Figure 2C**). This irregular diameter change is similar to that reported by

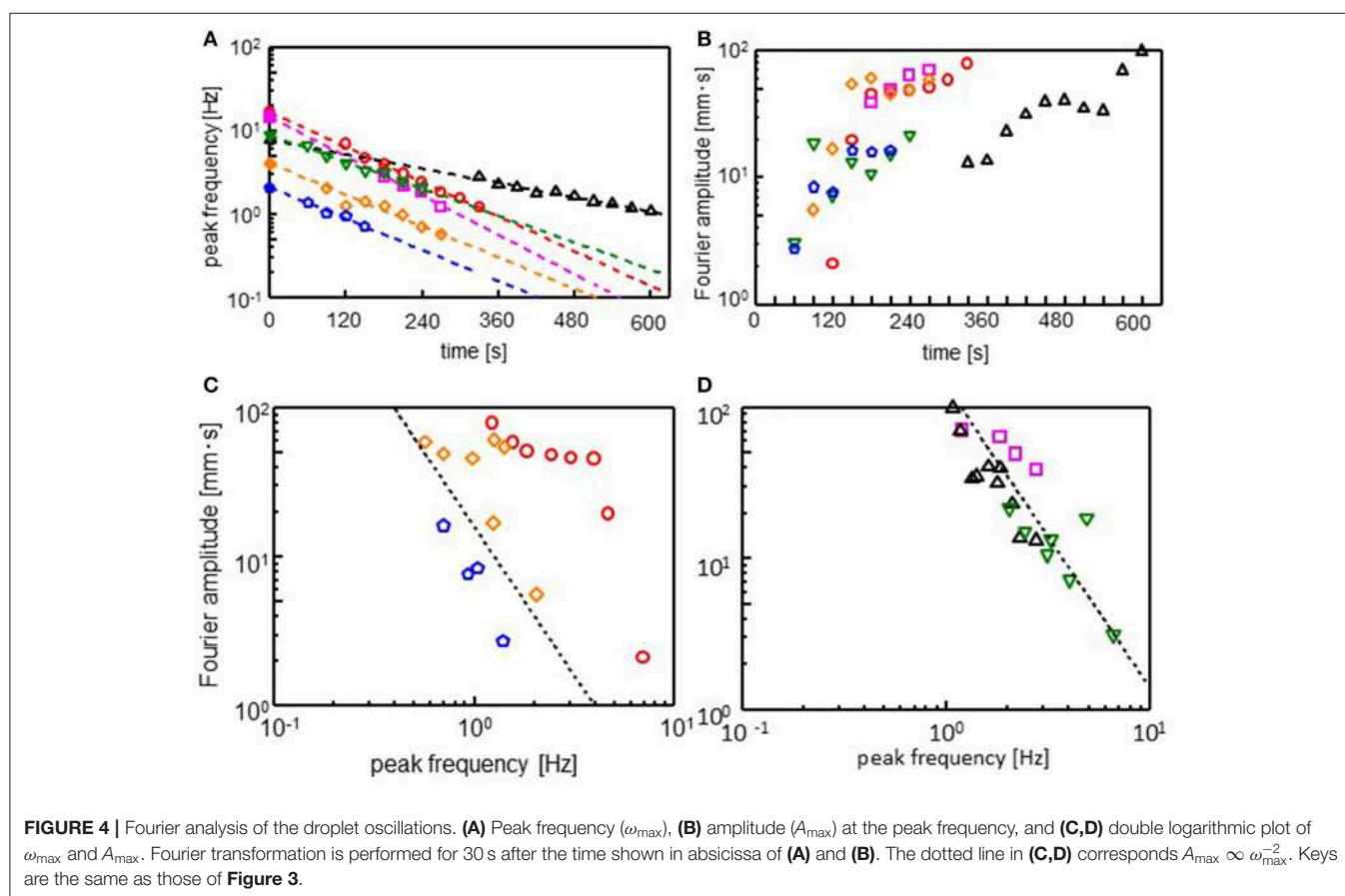
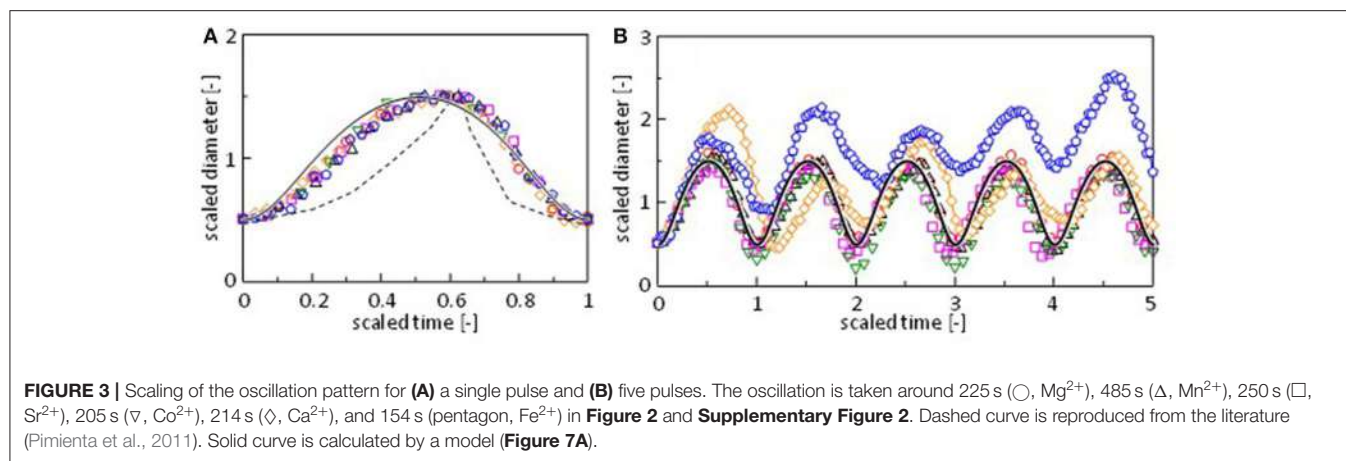


Stocker and Bush (2003). A regular oscillation of a floating droplet was also reported by Antoine and Pimienta (2013). The droplet oscillations reported until now have been caused by the evaporation of the oil (Stocker and Bush, 2003; Antoine and Pimienta, 2013), and the patterns were dependent on the oil species and evaporation rate. In the present system, the different types of droplet dynamics are generated by an appropriate selection of cations (The results for the cations that are not presented in Figure 2 are shown in Supplementary Figure 2).

One period of the diameter change, i.e., the period between two neighboring local minima, is scaled appropriately and superposed in Figure 3A. For Mg^{2+} , Sr^{2+} , and Mn^{2+} , a pulse in the regular oscillation regime is selected. A pulse in the quasi-regular regime is selected for Co^{2+} . For Fe^{2+} and Ca^{2+} , a pulse is randomly selected from the fluctuation pattern. The result shows that the diameter change has a common pattern independent of the cation species. Figure 3B shows the scaling for five periods. Figures 3A,B indicate that even irregular shape changes in case of Ca^{2+} and Fe^{2+} exhibit a common pattern. For these cations, fluctuations in the amplitude and periodicity produce randomness. This common pattern is different from the oscillation pattern reported by Antoine and Pimienta, which is superposed in Figure 3A (Antoine and Pimienta, 2013).

The similarity in the droplet dynamics with film formation and droplet discharge reported until now is discussed in terms of hydrodynamics, in which the evaporation of oil plays a crucial role (Karapetsas et al., 2011). Here, the surface flow to maintain the film is associated with the droplet motions: The surface flow

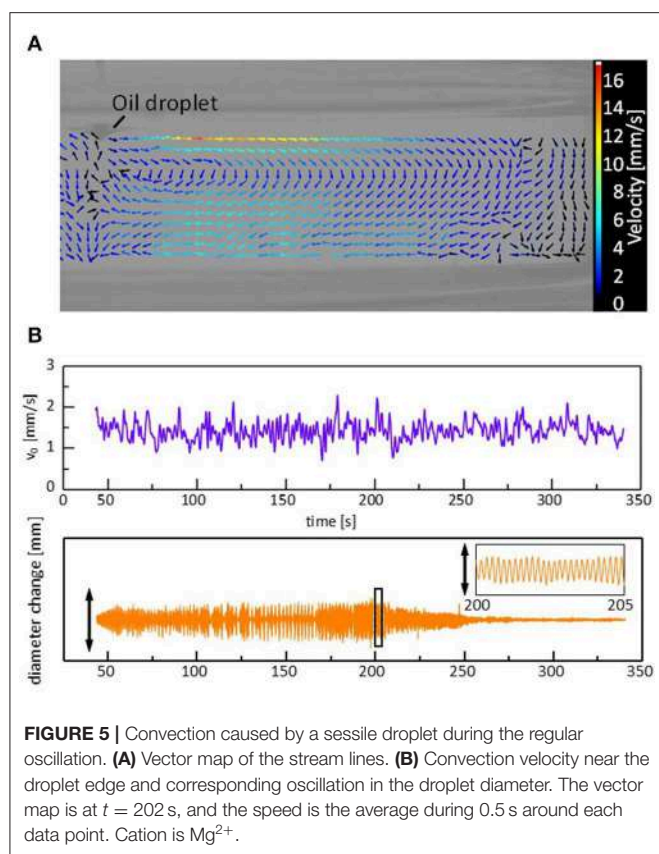
transports the surfactant molecules and modulates the interfacial (surface) tension and contact angle of a sessile lens (Antoine and Pimienta, 2013). In the present study, the measurement of the weight loss of decane reveals that the evaporation flux of decane is $\sim 1.74 \times 10^{-6} \text{ g/mm}^2$, resulting in 0.3% weight loss in petri-dish during 1 h (Supplementary Figure 3). This evaporation rate appears to be very much smaller than for the dichloromethane droplet reported previously. Despite its low volatile nature, the decane droplet can exhibit the oscillatory shape change. To examine the effects of evaporation further, silicone oil was used. We confirmed that silicone oil does not evaporate during the experimental time range (Supplementary Figure 3). For all the cations used in this study, outstanding motion and shape change was not observed. We also performed experiments with a decane droplet and Mg^{2+} in a closed container. Even in these experiments, no remarkable and sustainable shape change and motion were observed. These results demonstrated that evaporation was required for droplet motion, and a low evaporation rate was



sufficient to maintain the motion. The common pattern shown in Figure 3A is obtained probably when the evaporation rate is sufficiently low.

The oil/water interface with DEHPA and cations shows instability (spontaneous interfacial flow) when Ca²⁺, Mn²⁺, Fe²⁺, Fe³⁺, and Co²⁺ were dissolved in water (Miyaoaka et al., 2012; Yasui et al., 2015). Contrastingly, this instability is not observed for Mg²⁺ and Sr²⁺. This indicates that an oil droplet without instability (Mg²⁺ and Sr²⁺) can show the regular

oscillations in the droplet shape. The common pattern in Figure 3A is also observed with Co²⁺, Ca²⁺, and Fe²⁺. When the spontaneous interfacial flow is generated, this common pattern is probably perturbed. This may be responsible for the less-regular pattern for Co²⁺, Ca²⁺, and Fe²⁺. The droplet with Mn²⁺ shows a regular oscillation although it causes instability. The instability is observed under restricted experimental conditions. Further studies are necessary for the elucidation of the effects of instability on droplet dynamics.



The Fourier spectra of the oscillations were calculated (see **Supplementary Figure 4** for Fourier spectra). **Figures 4A,B** show the peak frequency (ω_{max}) and its Fourier amplitude (A_{max}). After an induction period, the droplet starts to oscillate. The range of ω_{max} is not large enough. However, the peak frequency appears to decay exponentially with time during the oscillation, as shown in **Figure 4A**. Thus, we obtain

$$\omega_{max} = \omega_0 e^{-\frac{t}{\tau}} \quad (1)$$

Here, ω_0 is the frequency extrapolated to $t = 0$ and τ denotes the characteristic time for the frequency decay. The τ value is insensitive to the cations species, whereas it affects ω_0 . The amplitude increases to reach its maximum, as shown in **Figure 4B**: At the beginning of the oscillation, an oscillation with a high frequency and small amplitude governs the droplet dynamics. Subsequently, the amplitude increases, whereas the frequency decreases. This trend is observed irrespective of the cation species. The relationship between ω_{max} and A_{max} is shown in **Figures 4C,D**, which show that A_{max} is proportional to ω_{max}^{-n} . Exponent n is approximately equal to 2 for all the cations. This result indicates

$$A_{max} \omega_{max}^2 = p \quad (2)$$

Constant p depends on the cation species.

When a droplet shows the regular oscillations, a steady convection is observed in the water phase. **Supplementary Video 3, Figure 5A** shows a vector map of the stream lines drawn by particle image velocimetry (PIV) analysis. The surface flow starts from the droplet edge and shows a circular pattern. The time course of a tracer speed in the vicinity of the droplet edge is shown in **Figure 5B**. A similar surface flow has already been pointed out (Stocker and Bush, 2003; Antoine and Pimienta, 2013), where an oil that spread over a surface was evaporated, followed by an oil supply from the droplet. In the present system, two types of explanations are possible for the origin of the flow. One is that the flow compensates for the oil evaporation from the film spread over the water surface. The other is the Marangoni effect due to the gradient in the adsorption density of DEHPA at the surface. The density may be higher near the droplet edge than that far from the droplet as the droplet contains a large amount of the surfactant, DEHPA. The droplet oscillation is caused by the force balance at the droplet edge, as discussed later. Therefore, the change in the surface (interfacial) tension should be synchronized with the droplet oscillation, as shown in the next calculation. In this case, if the Marangoni effect is the main reason for the surface flow, its velocity must be synchronized with the droplet oscillation. Considering that the velocity appears to fluctuate randomly, the surface flow is considered to be caused by the solvent evaporation from the film spread on the water surface, though the surface flow may be enhanced by the Marangoni effect.

MODEL FOR REGULAR OSCILLATION

Here, we focus on the regular oscillation of the droplet, typically observed for Mg^{2+} , Sr^{2+} , and Mn^{2+} . The scaling shown in **Figure 3** indicates that the oscillation in case of the Ca^{2+} , Co^{2+} , and Fe^{2+} systems can be understood based on essentially the same mechanism.

The surface flow, as shown in **Figure 5**, carries the DEHPA molecules from the droplet to the water surface. Thus, the local adsorption density of DEHPA on the water surface in the vicinity of the droplet periphery, $\Gamma(t)$, depends on time. This may be expressed by

$$\frac{d\Gamma(t)}{dt} = \frac{j(v(t) - v_0)^2}{\delta} - \frac{v_0 - v(t)}{\delta} \Gamma(t) \quad (3)$$

Here, v_0 and $v(t)$ denote the velocity of the surface flow and moving edge of the droplet, respectively (see **Figure 6A**.) We assume a constant v_0 because the time change in the surface flow does not show a systematic change as shown in **Figure 5B**. $v(t)$ reflects the droplet oscillation. The second term in the right hand side represents the flux of the DEHPA molecules from the droplet edge to outward. Here, a one-dimensional surface flow is considered as the simplest case. The flux of the molecules carried by the one-dimensional flow with velocity v is expressed by $v\Gamma(x)$, where x denotes the one-dimensional coordinate. Then, $\partial\Gamma(x)/\partial t = -v\partial\Gamma(x)/\partial x$. When the surface density is constant at $x > 0$ and zero at $x < 0$, $\partial\Gamma(x)/\partial t$ at $x \sim 0$ may be approximated as $-v(\Gamma - 0)/\delta$, where Γ is the uniform density at $x > 0$. δ is the

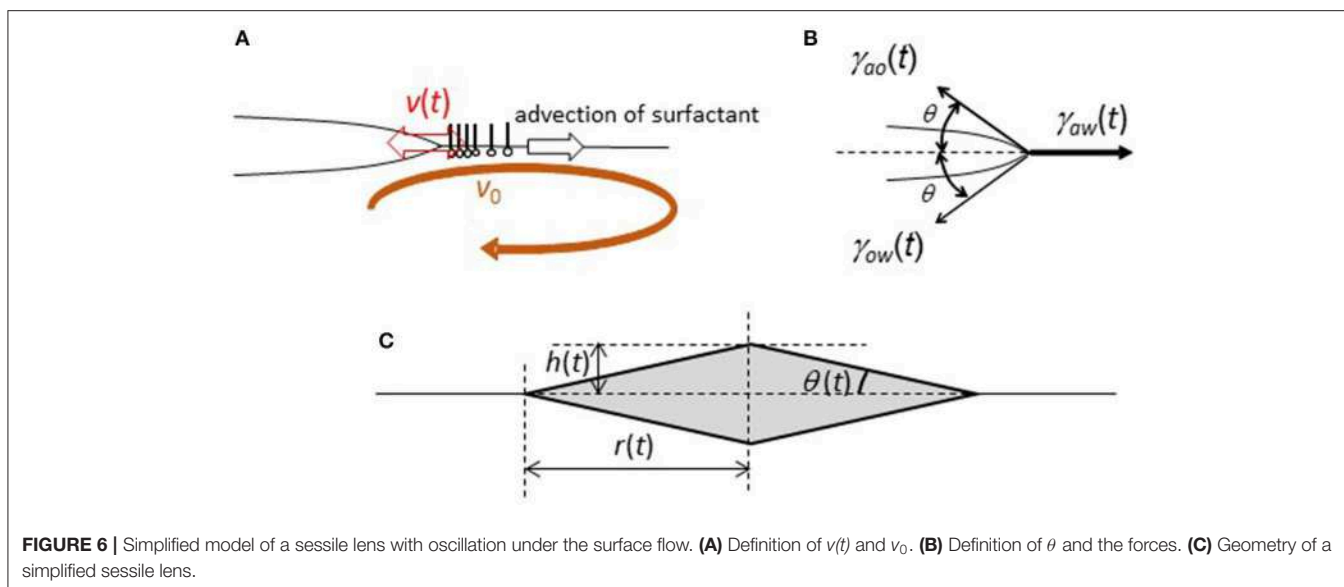


FIGURE 6 | Simplified model of a sessile lens with oscillation under the surface flow. **(A)** Definition of $v(t)$ and v_0 . **(B)** Definition of θ and the forces. **(C)** Geometry of a simplified sessile lens.

characteristic length of a range, which may be regarded as the edge. Considering the droplet edge as $x=0$, the second term can be derived, where the relative velocity of v_0 against $v(t)$ determines this flux. On the other hand, the DEHPA molecules are supplied from the droplet to the water surface near the edge. The first term corresponds to this flux. We assume that the molecules supplied from the droplet are spread over the water surface with length δ . Then, $\partial\Gamma(t)/\partial t$ is given by flux/δ . When the droplet edge moves with a faster or slower speed than that of the surface flow, an agitation effect enhances this mass transport. Thus, the larger the absolute value of $v(t)-v_0$, the higher must be the flux. The mass transport coefficient enhanced by convection is usually expressed by the power of Reynolds number for the convection (Bird et al., 2006). This Reynolds number should be calculated with the relative velocity, $v(t)-v_0$. Thus, we may consider that the mass transport coefficient is proportional to the power of the relative velocity. The exponent depends on the actual situation, and it is not easy to evaluate it in the present droplet oscillation. In the present case, however, the enhanced effect should be symmetry with respect to $v(t)-v_0 = 0$, because the agitation effect is probably the same regardless of its sign. The simplest expression satisfying this is that the mass transport coefficient is proportional to $(v(t)-v_0)^2$. The j in Equation 3 is the proportional constant. The result of calculation is insensitive to the exponent value, if the flux is an even function of $v(t)-v_0$. In Equation 3, the effect of diffusion on the DEHPA transport is ignored.

The droplet oscillates with the contact angle change, the schematic representation of which is shown in **Figure 6B**. Here, angle $\theta(t)$ is defined. The geometry is simplified such that the angles to the air side and water side are the same. When a droplet oscillates with angle $\theta(t)$, force $F(t)$ that pulls the droplet edge outward is given by

$$F(t) = \gamma_{aw}(t) - (\gamma_{ao}(t) + \gamma_{ow}(t)) \cos \theta(t) \quad (4)$$

Here, $\gamma_{ij}(t)$ denotes the interfacial tension, which is shown in **Figure 6B**.

The equation of motion may be expressed by

$$\frac{d^2 r(t)}{dt^2} = F(t) - \mu (v(t) - v_0) \quad (5)$$

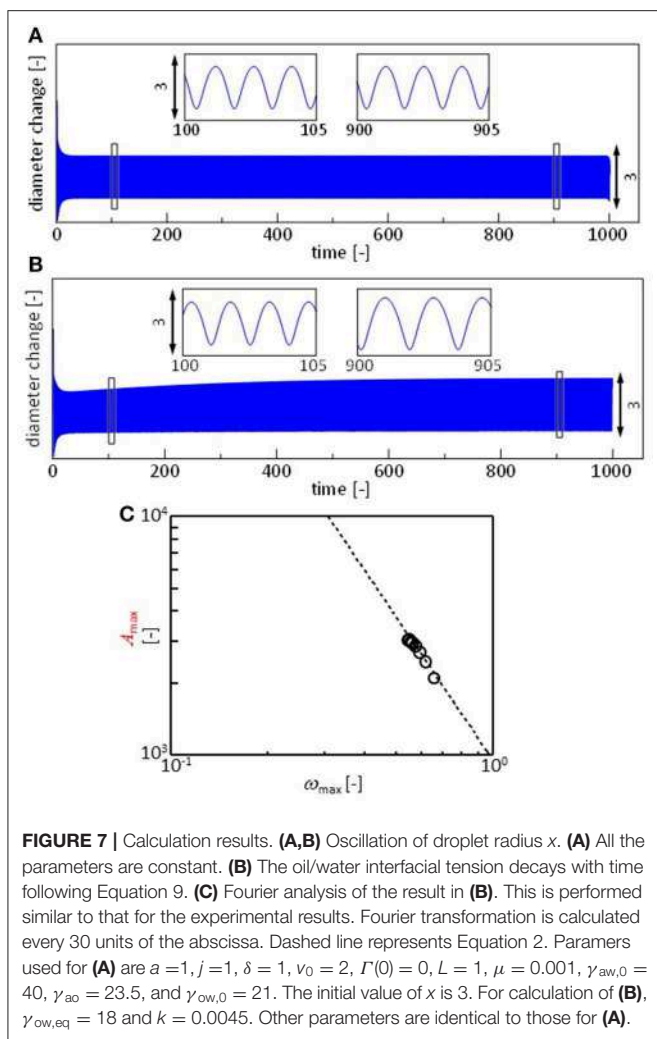
Here, we calculate the one-dimensional motion of a unit mass at the edge. The last term represents the viscous drag. $r(t)$ is defined in **Figure 6C**. In the present experiments, Reynolds number of a droplet oscillation is approximately 10^0 - 10^1 in the order of magnitude (The density/viscosity is $\sim 10^5$ s/m² in air and 10^6 s/m² in water). The diameter of a droplet and velocity of droplet edge are ~ 5 mm and 5 mm/s. Thus, the inertia term (the left hand side of Equation 5) cannot be neglected. The inertia plays an important role in for droplet oscillation in the present model, which is different from the model for contact line oscillation in camphor disk (Kitahata et al., 2008). The external force $F(t)$ and dissipation term (the second term of the right hand side of Equation 5) are necessary for the oscillation caused by inertia effect.

For further calculation, one-dimensional coordinate x must be related to angle $\theta(t)$. Here, we consider a simple geometry, which is shown in **Figure 6C** (rhombus of revolution). This is only for simplicity. Assuming the conservation of the droplet volume, $L^3 = r(t)^2 h(t)$ is a constant. Noting that $v(t) = \frac{dr(t)}{dt}$, one obtains

$$\frac{1}{\cos \theta(t)} = \sqrt{1 + \left(\frac{L}{r(t)}\right)^6} \quad (6)$$

Equations 4, 5, and 6 yield

$$\frac{d^2 r(t)}{dt^2} = \gamma_{aw}(t) - \frac{\gamma_{ao}(t) + \gamma_{ow}(t)}{\sqrt{1 + \left(\frac{L}{r(t)}\right)^6}} - \mu \left(\frac{dr(t)}{dt} - v_0\right) \quad (7)$$

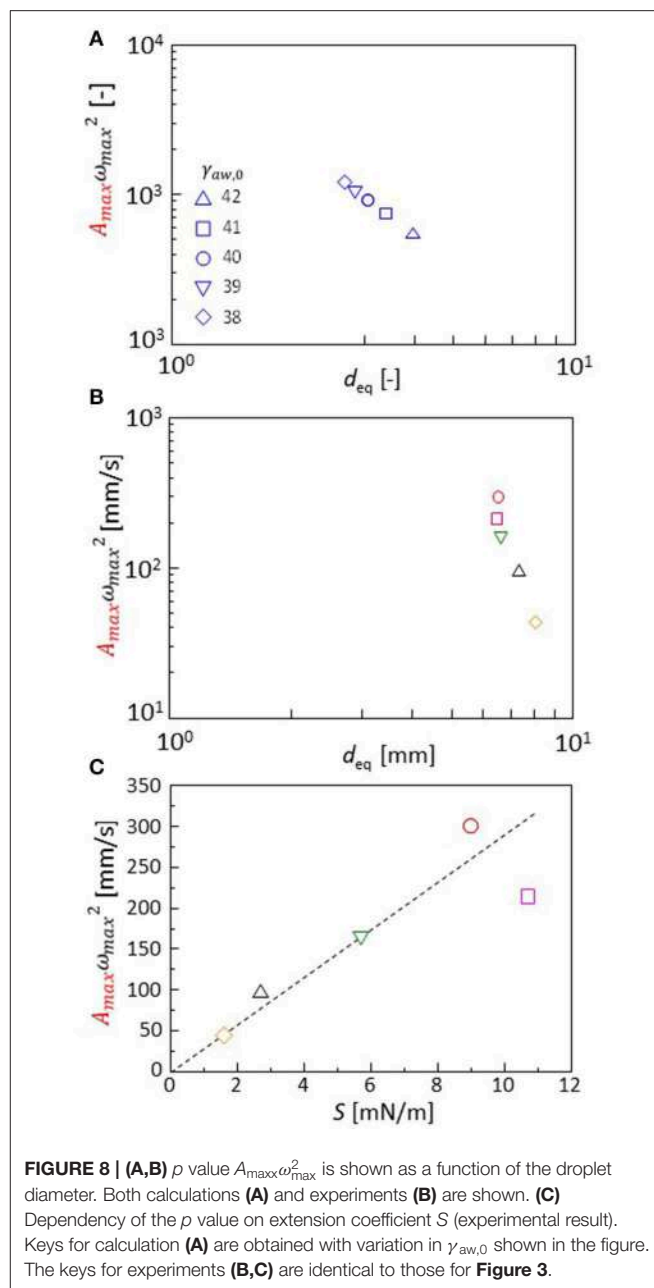


We assume a linear dependency of $\gamma_{aw}(t)$ on $\Gamma(t)$:

$$\gamma_{aw}(t) = \gamma_{aw,0} - a\Gamma(t) \quad (8)$$

where $\gamma_{aw,0}$ denotes the air/water surface tension without DEHPA. $r(t)$ can be calculated from Equations 3, 7, and 8 with an appropriate initial condition.

Figure 7A shows the $r(t)$ calculated with Equations 3, 7, and 8, assuming that all the parameters are independent of time. The parameters for the surface and interfacial tension are adjustable, though they are determined such that their ratios become approximately equal to those in the experiments. The pattern is similar to the experimental results shown in **Figure 3**, in which the result of the calculation is also shown. In the experiments, the frequency and amplitude of the oscillations vary as shown in **Figure 4**. This may be reproduced by considering the time dependency of the parameters. The oil/water interface is free from the surfactant immediately after the droplet is placed on the surface. However, the DEHPA molecules are adsorbed at the interface, and hence, $\gamma_{ow}(t)$ must decrease in time to approach



equilibrium value $\gamma_{ow,eq}$. This effect may simply be expressed by

$$\gamma_{ow}(t) = \gamma_{ow,eq} + (\gamma_{ow,0} - \gamma_{ow,eq}) \times \exp(-kt) \quad (9)$$

Here, $\gamma_{ow,0}$ and k denote the interfacial tension immediately after the droplet is placed and the rate constant, respectively. Note that the dependency of γ_{aw} on the DEHPA adsorption density is already considered with Equation 8, and γ_{ao} is practically independent of the DEHPA concentration. The exponential form of the dynamic interfacial tension has been reported in many systems (Dukhin et al., 1995). In present system, adsorbed DEHPA molecules react with cations. The products tend to aggregate at the interface. This aggregation retards the desorption. The degree of aggregation depends on cation species

(Hosohama et al., 2011; Miyaoka et al., 2012). As a result of these, the interfacial tension shows the very slow dynamics (Shioi et al., 2000), which agrees with Equation 9. The result is shown in **Figure 7B**. The amplitude increases with time, and the frequency decreases. Fourier transformation is calculated every 30 units of the abscissa, and ω_{\max} and $f(\omega_{\max})$ are plotted in **Figure 7C** using Equation 2.

The Fourier transformation of the oscillation in the experiments approximately follows Equation 2. Though the range ω_{\max} is narrow, this range is almost the same as that of experimental result of one type of cation shown in **Figures 4C,D**. The effects of the cation species on the droplet oscillation is expressed as a value of p using Equation 2. The cations affect the surface and interfacial tension. They must affect the droplet diameter after the oscillation has stopped. Equations 3, 7, 8, and 9 are calculated with $\gamma_{\text{aw},0}$ (Equation 8) ranging from 38 to 42. The droplet diameter after sufficient time steps is shown as a function of the p value in **Figure 8A**. In the experiments, the droplet diameter (d_{eq}) is measured after the droplet is dropped on the water phase in a closed container. At 300 s after the dropping, the diameter is measured. It is shown as a function of the p value in **Figure 8B**. The droplet diameter and p values are dimensionless in the calculation. Thus, a double logarithmic plot is used for the comparison between calculation and experiment. In both the cases, the p value decreases with an increase in the droplet diameter. The present model well-captures the oscillation dynamics that are observed in the experiments depending on the cation species.

Spreading coefficient $S(= \gamma_{\text{aw,eq}} - \gamma_{\text{ao,eq}} - \gamma_{\text{ow,eq}})$ is a typical parameter that is associated with the droplet diameter. The S value is measured from the interfacial and surface tension under equilibrium of the oil and water phases. The p value obtained by the experiments is shown with S in **Figure 8C**. The p value is well-correlated with S . The cation species changes the spreading coefficient, which determines the characteristics in the droplet oscillation. When comparing the calculation and experiment, the droplet diameter may be used as a common parameter that may be related to the spreading coefficient: An estimation of the S value in calculation is not easy because the oscillation can be maintained only under a non-equilibrium state. Thus, the parameter values of the surface and interfacial tensions [$\gamma_{\text{aw},0}$, $\gamma_{\text{ow,eq}}$, and γ_{ao} (time-independent)] do not correspond to the equilibrium surface and interfacial tensions observed in the experiment.

For Ca^{2+} , Fe^{2+} , and Co^{2+} , the randomness is contained in the common pattern shown in **Figure 3**. In these cases, the spontaneous interfacial flow is generated at the oil/water interface (Hosohama et al., 2011). Therefore, the random fluctuation in $\gamma_{\text{aw}}(t)$ and $\gamma_{\text{ow}}(t)$ should be considered. The less-regular pattern for these cations can be explained on the basis of the present model containing the randomness.

When a flat oil/water interface is formed with DEHPA and Fe^{3+} , a spontaneous interfacial flow appears intermittently. Once it is generated, it propagates over a long distance (Yasui et al., 2015). This dynamics may enhance the wetting caused by the positive spreading coefficient. Subsequently, the oil droplet is rapidly transformed into a thin film and disappears.

CONCLUSION

The tuning of a droplet motion on a water surface by cations is studied. After a random motion, the droplet shows an oscillation between an expanded and a contracted state. This oscillation is driven by the evaporation of the droplet. A common pattern is shown in the oscillation. For a type of cation that does not cause instability, this common pattern is clearly observed. The frequency and amplitude in the common pattern depend on the cation species. This dependency is explained by the effect of the cation on the spreading coefficient and droplet size at equilibrium. The oscillation pattern and cation dependency are well-captured by a simple model. This study may be a basis for the chemical control of droplet dynamics on a liquid surface.

DATA AVAILABILITY STATEMENT

All datasets generated for this study are included in the article/**Supplementary Material**.

AUTHOR CONTRIBUTIONS

YM and HY found the oscillation phenomenon and performed all experiments. All calculations have been performed by YM. DY, EN-O, and AS conceived this research. YM and AS considered mathematical model. All authors discussed for this research.

ACKNOWLEDGMENTS

AS gratefully acknowledges the financial support from JSPS KAKENHI Grant Number 16H04189. AS and DY also acknowledge the MEXT-Supported Program for the Strategic Research Foundation at Private Universities. The authors would like to thank Prof. Katsumi Tsuchiya (Doshisha University) for particle image velocimetry analysis. We would like to thank Editage (www.editage.jp) for English language editing.

SUPPLEMENTARY MATERIAL

The Supplementary Material for this article can be found online at: <https://www.frontiersin.org/articles/10.3389/fchem.2019.00788/full#supplementary-material>

Supplementary Figure 1 | Change in the droplet diameter.

Supplementary Figure 2 | Change in droplet diameter. The drift in the droplet size over a long time is subtracted. The insets show the expanded versions of the marked squares. The scale bar is 2 mm in all the figures.

Supplementary Figure 3 | Decrease in the weight of the oil. The initial volume of oil was 5 mL, which was poured in a petri-dish with diameter of 48 mm. The total weight of the dish and oil was measured every 5 min. The weight of the dish was subtracted to obtain the weight of the oil as a function of time. The petri-dish was not covered. The oil weight was scaled by its initial value.

Supplementary Figure 4 | Examples of the Fourier spectra of the diameter change. Time range and cation species are shown in the graphs.

Supplementary Video 1 | Droplet oscillations for six types of cations.

Supplementary Video 2 | Regular oscillation of a droplet with Mg^{2+} .

Supplementary Video 3 | Convection in water with a droplet pinned by a pillar.

REFERENCES

- Antoine, C., and Pimienta, V. (2013). Mass-spring model of a self-pulsating drop. *Langmuir* 29, 14935–14946. doi: 10.1021/la403678r
- Ban, T., Yamagami, T., Nakata, H., and Okano, Y. (2013). pH-Dependent motion of self-propelled droplets due to marangoni effect at neutral pH. *Langmuir* 29, 2554–2561. doi: 10.1021/la3047164
- Banno, T., and Toyota, T. (2015). Design of reactive surfactants that control the locomotion mode of cell-sized oil droplets along oriented microtubules by kinesin molecular motors. *Curr. Phys. Chem.* 5, 37–51. doi: 10.2174/1877946805666150729231330
- Bird, R. B., Stewart, W. E., and Lightfoot, E. N. (2006). *Transport Phenomena*, 2nd Edn, New York, NY; London; Sydney: Wiley.
- Bottier, C., Fattaccioli, J., Tarhan, M. C., Yokokawa, R., Morin, F. O., Kim, B., et al. (2009). Active transport of oil droplets along oriented microtubules by kinesin molecular motors. *Lab Chip* 9, 1694–1700. doi: 10.1039/b822519b
- Dukhin, S. S., Kretschmar, G., and Miller, R. (1995). *Dynamics of Adsorption at Liquid Interfaces, 1st Edn, Theory, Experiment, Application*. Amsterdam; Lausanne; New York, NY; Oxford, UK; Shannon; Tokyo: Elsevier Science.
- Goto, Y., Kanda, M., Yamamoto, D., and Shioi, A. (2015). An abiotic glass-bead collector exhibiting active transport. *Sci. Rep.* 5:14348. doi: 10.1038/srep14348
- Hermans, T. M., Frauenrath, H., and Stellacci, F. (2013). Droplets out of equilibrium. *Science* 341, 243–244. doi: 10.1126/science.1241793
- Hosohama, T., Megumi, K., Terakawa, S., Nishimura, J., Iida, Y., Ban, T., et al. (2011). Ion-Selective marangoni instability coupled with the nonlinear adsorption/desorption rate. *Langmuir* 27, 14131–14142. doi: 10.1021/la203145f
- Janssens, S. D., Koizumi, S., and Fried, E. (2017). Behavior of self-propelled acetone droplets in a Leidenfrost state on liquid substrates. *Phys. Fluids* 29:032103. doi: 10.1063/1.4977442
- Karapetsas, G., Craster, R. V., and Matar, O. K. (2011). Surfactant-driven dynamics of liquid lenses. *Phys. Fluids* 23:122106. doi: 10.1063/1.3670009
- Kitahata, H., Kawata, K., Sumino, Y., and Nakata, S. (2008). Oscillation of a water surface in contact with a fixed camphor disk. *Chem. Phys. Lett.* 457, 254–258. doi: 10.1016/j.cplett.2008.03.075
- Lagzi, I., Soh, S., Wesson, P. J., Browne, K. P., and Grzybowski, B. A. (2010). Maze solving by chemotactic droplets. *J. Am. Chem. Soc.* 132, 1198–1199. doi: 10.1021/ja9076793
- Miyaoka, T., Nishimura, J., Iida, Y., Maki, S., and Shioi, A. (2012). Ion-selective Marangoni instability—Chemical sensing of specific cation for macroscopic movement. *Chaos* 22:037111. doi: 10.1063/1.4729142
- Ok, J. T., Choi, J., Brown, E., and Park, S. (2016). Effect of different fluids on rectified motion of Leidenfrost droplets on micro/sub-micron ratchets. *Microelectr. Eng.* 158, 130–134. doi: 10.1016/j.mee.2016.04.018
- Pimienta, V., Brost, M., Kovalchuk, N., Bresch, S., and Steinbock, O. (2011). Complex shapes and dynamics of dissolving drops of dichloromethane. *Angew. Chem. Int. Edn.* 50, 10728–10731. doi: 10.1002/anie.201104261
- Seemann, R., Fleury, J. B., and Maass, C. C. (2016). Self-propelled droplets. *Eur. Phys. J. Spl. Top.* 225, 2227–2240. doi: 10.1140/epjst/e2016-60061-7
- Seyboldt, R., and Jülicher, F. (2018). Role of hydrodynamic flows in chemically driven droplet division. *N. J. Phys.* 20 105010. doi: 10.1088/1367-2630/aae735
- Shioi, A., Katano, K., and Onodera, Y. (2003). Effect of solid walls on spontaneous wave formation at water/oil interfaces. *J. Colloid Interface Sci.* 266, 415–421. doi: 10.1016/S0021-9797(03)00672-6
- Shioi, A., Sugiura, Y., and Nagaoka, R. (2000). Oscillation of interfacial tension at a liquid/liquid interface composed of Di(2-ethylhexyl) phosphoric acid and calcium chloride. *Langmuir* 16, 8383–8389. doi: 10.1021/la000431v
- Stocker, R., and Bush, J. (2003). Spontaneous oscillations of a sessile lens. *J. Fluid Mech.* (2007) 583, 465–475. doi: 10.1017/S0022112007005940
- Sumino, Y., Magome, N., Hamada, T., and Yoshikawa, K. (2005). Self-running droplet: emergence of regular motion from nonequilibrium noise. *Phys. Rev. Lett.* 94:068301. doi: 10.1103/PhysRevLett.94.068301
- Wang, T., Li, W., Liu, L., Chen, H., Wang, Y., Zhang, J., et al. (2015). The mechanism for the motion of nanoscale water droplet induced by wetting gradient: a molecular dynamic study. *Comput. Mater. Sci.* 105, 39–46. doi: 10.1016/j.commatsci.2015.04.025
- Yasui, D., Yamashita, H., Yamamoto, D., and Shioi, A. (2015). Cation-dependent emergence of regular motion of a float. *Langmuir* 31, 11005–11011. doi: 10.1021/acs.langmuir.5b03049
- Ye, R. A., Ryazantsev, Y. S., and Velarde, M., G. (1994). Active drops and drop motions due to Nonequilibrium Phenomena. *J. Non-Equilib. Thermodyn.* 19, 95–113. doi: 10.1515/jnet.1994.19.1.95
- Zhang, Z. Q., Dong, X. H., Ye, F., Cheng, G., J. Ding, N., and Wetting, Z., et al. (2015). Motion behaviors of water droplet on graphene under thermal-electric coupling field. *J. Appl. Phys.* 117:074304. doi: 10.1063/1.4913207
- Zwicker, D., Seyboldt, R., Weber, C. A., Hyman, A. A., and Jülicher, F. (2016). Growth and division of active droplets provides a model for protocells. *Nat. Phys.* 13, 408–413. doi: 10.1038/nphys3984

Conflict of Interest: The authors declare that the research was conducted in the absence of any commercial or financial relationships that could be construed as a potential conflict of interest.

Copyright © 2019 Mikuchi, Yamashita, Yamamoto, Nawa-Okita and Shioi. This is an open-access article distributed under the terms of the Creative Commons Attribution License (CC BY). The use, distribution or reproduction in other forums is permitted, provided the original author(s) and the copyright owner(s) are credited and that the original publication in this journal is cited, in accordance with accepted academic practice. No use, distribution or reproduction is permitted which does not comply with these terms.

Advance Publication Cover Page



A molecular assembly machine working under a quasi-steady state pH gradient

Erika Nawa-Okita,* Yuki Nakao, Daigo Yamamoto, Akihisa Shioi*

Advance Publication on the web February 18, 2020

doi:10.1246/bcsj.20190348

© 2020 The Chemical Society of Japan

Advance Publication is a service for online publication of manuscripts prior to releasing fully edited, printed versions. Entire manuscripts and a portion of the graphical abstract can be released on the web as soon as the submission is accepted. Note that the Chemical Society of Japan bears no responsibility for issues resulting from the use of information taken from unedited, Advance Publication manuscripts.

A molecular assembly machine working under a quasi-steady state pH gradient

Erika Nawa-Okita*¹, Yuki Nakao², Daigo Yamamoto², Akihisa Shioi*²

¹Organization for Research Initiatives and Development, Faculty of Science and Engineering, Doshisha University, 1-3 Tatara Miyakodani, Kyotanabe, Kyoto 610-0321

²Department of Chemical Engineering & Materials Science, Doshisha University, 1-3 Tatara Miyakodani, Kyotanabe, Kyoto 610-0321

E-mail: < ashioi@mail.doshisha.ac.jp >



Akihisa Shioi

Akihisa Shioi graduated from Kyoto University (Chemical Engineering) at 1981. He joined Institute of Atomic Energy (Advanced Energy), Kyoto University as a research associate from 1981. From 1999 to 2006, he worked as assistant professor of Yamagata university. From 2006, he worked for Doshisha university and was promoted to professor in 2008. He has been focusing his research on the dynamics, and pattern formation of non-equilibrium chemical systems. His research interests are the development of chemical systems that mimic the behavior of living matter, and the determination of characteristics that impart a semblance of life to chemical systems.



Erika Nawa-Okita

Erika Nawa-Okita graduated from Doshisha University (Chemical Engineering) at 2016. She worked as Research Fellowship for Young Scientists of Japan Society for the Promotion of Science from 2015 to 2017. From 2017, she worked for Doshisha university as Research Associate. She has been studying the dynamics and periodic formation of various vesicles. Her research interests are the development of biomimetic chemical systems and the understanding of universal characteristics included in common for chemical systems of artificial active matter in relation to living matter.

Abstract

Biological functions are maintained by various types of molecular motors driven at several pico-Newton, where the driving force is obtained from a chemical potential difference within the microscale. Here, we show in detail artificial vesicles that generate mechanical work from a local pH gradient. This study demonstrates that they can be regarded as a molecular assembly machine. We have previously reported that the vesicles are composed of oleate and oleic acid and exhibit rhythmic shape changes. This cyclic motion involves both rotation of the entire vesicle and its inside-out inversion, which constitute relaxation and excitation processes, respectively, that sustain the cycle. These motions were observed under a quasi-steady state pH gradient, and the driving force of rotation was determined to be of the order of 10^{-2} – 10^{-1} pN, which is consistent with the membrane elasticity driving the deformation (vesicle inversion).

Keywords: Vesicle, pH gradient, rhythmic motion

1. Introduction

Biological systems are capable of generating mechanical work from chemical potential differences at the microscale. This chemical potential difference is induced by active transport involving chemical reactions. For instance, ATPase is a molecular machine that rotates^{1,2} under a pH gradient across the inner mitochondrial membrane to synthesize adenosine triphosphate (ATP) from adenosine diphosphate (ADP). In contrast, ATPase operates as a proton pump driven by the hydrolysis of ATP in the absence of a pH gradient. Both energy transformations, from a chemical potential to mechanical work and active transport, are required to maintain the living system³. The design of abiotic chemical systems with similar characteristics remains a great challenge. Such studies may prove to be useful in the development of the simplest biomimetic chemical systems that mimic energy transformations and active

transport in the micro space. They may also lead to the development of chemical technology for smart actuators and mass transport for application in microfluidic networks and Micro-Total Analysis Systems.

Recently, the autonomous motion of a solid particle and a liquid drop driven by chemical reactions has been studied in detail^{4–18}. In most of these studies, Marangoni convection induces the motion^{9–18}. On the other hand, the autonomous motion of amphiphilic molecular assemblies such as vesicles remains less studied. Vesicles are composed of amphiphilic molecules, and their structure is similar to that of biological cells. Until now, several research groups have reported vesicles that exhibit periodic structural change between opening and closing pore in the membrane^{19–23} caused by physical and/or chemical stimuli. These motions appear accompanied by a vesicle size reduction^{19–22}. These results suggest that such vesicle motions are relaxation due to dissolution of the membrane ingredient. As another example, a vesicle that imitates translation by actin polymerization has been reported, constituting a model of *Listeria monocytogenes* motion^{24–30}. In this case, the vesicle exhibits self-motion without size reduction. In a further example, the migration of phospholipid vesicles toward a higher-pH region has been reported³¹, where the vesicle size was not reduced, as could be deduced from the results in the paper.

We have previously reported rhythmic changes in the shape of vesicles under a pH gradient³². The vesicles were composed of oleate and oleic acid (acid/soap) with a similar structure to that of stomatocytes at pH 8–9³³. The shape changes comprised both rotation of the entire vesicle and inversion, in which the vesicle structure was turned inside out. Such vesicle motion must involve both excitation and relaxation processes, since just a relaxation process would not be able to maintain periodic changes. Therefore, this system seems rather similar to molecular motor motion involving excitation (proton pump) and relaxation (ATP synthesis) events. From this point of view, such periodic shape changes warrant their further study.

In our previous work, vesicle motion was observed under

an unsteady pH gradient generated by diffusion of a base solution. This study clearly showed that oleate/oleic acid vesicles exhibit various motions under a pH gradient^{31, 32}. However, quantitative aspects such as the driving force strength were unclear. In this paper, we observed periodic shape changes under a quasi-steady state pH gradient, meaning that the pH gradient can be regarded as constant throughout the observation period. For this purpose, a device able to maintain a quasi-steady state pH gradient over a sufficient period of time was built. With this setup, the pH and pH gradient around a vesicle undergoing shape changes could be estimated. From the motion analysis of the vesicle, the driving force for vesicle motion was evaluated as a function of the pH and pH gradient. As a result, a quantitative discussion of the self-excitation and relaxation processes is provided. The present results demonstrate that this vesicle can be regarded as a molecular assembly machine working under a pH gradient.

2. Experimental

2.1. Chemicals

Sodium oleate was purchased from Tokyo Chemical Industry Co., Ltd. (>97.0%). Bicine (>99.0%) and a NaOH aqueous solution (1 M) were purchased from Sigma-Aldrich Co. LLC. New Coccine (Wako, 1st grade) was purchased from Wako Pure Chemical Industries, Ltd. The bicine buffer was prepared as follows: bicine (570 mg) was dissolved in pure water (50 mL), and the pH of the resulting solution was adjusted to 8.4 with a NaOH solution. Sodium oleate (37.5 mg) was dissolved in bicine buffer (5 mL). Next, a sodium oleate solution (24.6 mM) was prepared and the pH of the resulting solution was 8.6. For visualization of the diffusion, New Coccine (red dye, 302 mg) was dissolved in the NaOH solution (10 mL).

2.2. Formation of a quasi-steady state pH gradient in the vesicle solution

Figure 1 shows the device employed for the experiments under a quasi-steady state pH gradient. A channel (length, 10 mm; width, 6 mm; depth, 0.5 mm) with adits (length, 1 mm; width, 6 mm) at both ends was placed in the center of the device. Reservoirs (length, 40 mm; width, 40 mm; height, 20 mm) were placed at both sides of the channel, such that the liquids in the reservoirs would penetrate the channel.

A sodium oleate solution (30 μ L) was injected in the channel, and vesicles were formed by letting the sodium oleate

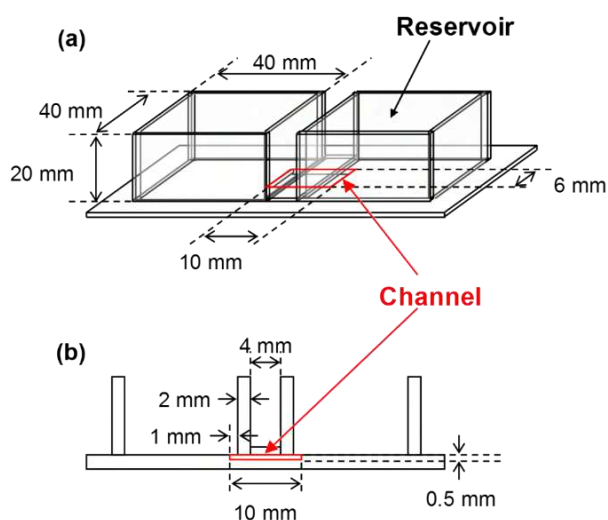


Figure 1. Schematic representation of the device providing a quasi-steady state pH gradient: (a) bird's-eye and (b) cross-sectional views.

solution set for 24 h. Then, bicine buffer (15 mL) was injected in each reservoir. Next, further bicine buffer (0.89 mL) was added to one of the reservoir, while the same volume of NaOH solution containing the red dye was added to the other reservoir (see Fig. S1). As a result, the pH of one of the reservoirs became 12.4 (higher-pH solution), while the other was maintained at 8.4 (lower-pH solution). The diffusion coefficient of New Coccine is considered to be smaller than that of NaOH. When the New Coccine color gradient reaches a steady state, the gradients of NaOH concentration and pH also reach such steady state. Just after NaOH was injected in the reservoir, convection was observed in the channel. This may shorten the time taken for the pH and New Coccine concentration gradients to reach the steady state. After the conditions in the channel presented a quasi-steady state pH gradient, vesicle motion in the channel was observed with an optical microscope (IX73, Olympus Corporation). The pH distribution upon NaOH diffusion was evaluated from the gray scale image of the channel using calibration curves, as explained in the next section.

2.3. Determination of the local pH

The determination of the local pH around a vesicle exhibiting cyclic motion is necessary for a quantitative study such as this one. In this study, New Coccine and NaOH diffused at the same time. Thus, their scaled concentrations at a given position should be the same in the steady state when they are scaled between the maximum (higher-pH side) and minimum (lower-pH side) values. The New Coccine concentration can be estimated by the gray scale converted from the red-color and calibration curve (see SI 1 and Fig. S2). The gray scale was quantified using the image analysis software Image J. The scaled value of the New Coccine concentration was used to estimate the concentration of Na^+ (see SI 1 and Fig. S2(a)). We had already measured the pH of the solution containing the same concentration of NaOH in the vesicle solution with bicine buffer. Using these results, the local pH was determined (see SI 1 and Fig. S2(b)).

2.4. Deformation of the vesicle membrane by optical tweezer manipulation

A sodium oleate solution (100 μ L) containing small polyethylene beads (mean particle size = 10 μ m) was injected in the channel of a μ -slide cell (μ -slide I for Live Analysis, NIPPON Genetics). Stomatocyte vesicles were formed with the beads after 24 h. The beads were then manipulated with an optical tweezer (MMS-1064-5000/1E/1S, SIGMA KOKI Co., LTD.). The laser wavelength and power were 1064 nm and approximately 1 W, respectively. The motion of the beads and deformation of the vesicle membrane were observed using an optical microscope (IX73, Olympus Corporation).

3. Results and Discussion

3.1. A vesicle with rhythmic shape changes under a quasi-steady state pH gradient

In this study, we were able to maintain the pH gradient almost constant throughout the observation period of vesicle motion, as discussed in the next section. This pH distribution is thus referred to as a quasi-steady state pH gradient. Under this condition, the vesicles composed of oleate and oleic acid exhibit rhythmic shape changes away from the substrate in the channel. The position of the vesicles was ascertained by microscope observation with vertical movement of the mechanical stage. Figure 2 shows one period of vesicle motion (see also SI Movie 1). The location of observation is the same for the snapshots and movie. This vesicle motion is essentially the same as that under an unsteady-state pH gradient using a μ -slide cell (μ -slide I for

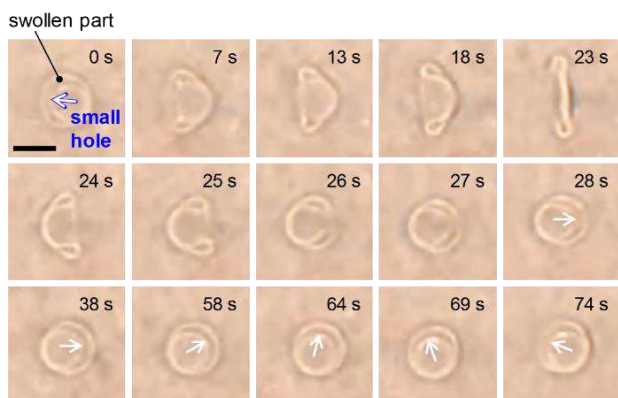


Figure 2. Rhythmic shape changes in a vesicle under a quasi-steady state pH gradient. NaOH diffuses from the left side in each image. The white arrow indicates a small hole in the swollen part and the orientation of the vesicle³². The scale bar is 20 μm .

Live Analysis, NIPPON Genetics)³², where the local pH and its gradient varied with the time because the μ -slide cell has 5 cm channel. Therefore, in this channel, forming the quasi-steady state pH gradient by diffusion requires exceedingly long time. Under such unsteady conditions, it was unclear what strength of pH gradients caused the vesicle motion. Therefore, the mechanics of this vesicle motion could not be discussed in detail. However, the present setup allows the quantitative discussion of the effects of both the pH and pH gradient on the observed vesicle motion using calibration curves (see SI 1 and Fig. S2) because the quasi-steady state pH gradient can be formed by the present device which has short channel and reservoirs with enough volume compared with volume of the channel.

The vesicle shape is not isotropic, and one can define the orientation of the vesicles based on their anisotropic shape, as indicated by the white arrows in Fig. 2. The shape changes are the same as those reported previously under unsteady diffusion conditions. The mechanisms and relationship with pH gradient have been reported about our previous study in detail³². However, the understanding of such shape changes is crucial in this work. The orientation of these vesicles is randomly distributed at homogeneous pH. A quasi-steady state pH gradient was generated after 1–2.5 h of NaOH diffusion. Then, the swollen part and small hole³² shown in Fig. 2 faces the higher-pH side via spontaneous rotation (0 s in Fig. 2). Here, we catch the orientation of swollen part from position of the small hole because the small hole exists at almost in the center of the swollen part. After this event, a small hole in the swollen part opens slowly until the vesicle shape is reversed via a flat state similar to that of a red blood cell (23 s in Fig. 2). Finally, it closes again, so that the orientation of the vesicle is opposite that of the initial state (28 s in Fig. 2). Then, the small hole indicated by the white arrow in Fig. 2 is formed again at the center of the swollen part. After this inversion motion, the swollen part faces the lower-pH side. The vesicle then begins to rotate so that it faces the higher-pH side again. Thus, the cyclic motion of the vesicle is constituted of inversion (0–28 s in Fig. 2) and rotation (38–74 s in Fig. 2). The period of this rhythmic shape variation is 1–10 min in the case of the vesicle in Fig. 2. This shape variation repeats itself for several times. In the longest case, the cyclic motion was maintained for over 50 min. Here, the pH gradient may be regarded as constant, at least throughout the observation period of vesicle motion (see SI 1 and Fig. S3). The determination of the local pH around the vesicle is explained in the Methods section (Determination of the local pH) and SI 1. In contrast, the cyclic motion under the unsteady state pH gradient

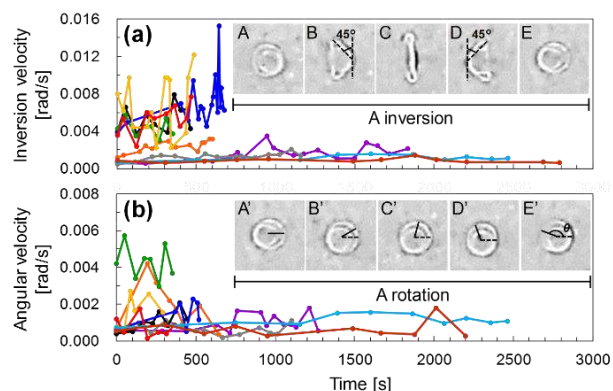


Figure 3. Time course of the transformation rate. (a) Time course of the velocity of inversion. The average inversion velocity was determined as $\pi/2$ (the angle between the two broken lines in B and D) divided by the time-lapse from B to D. (b) Angular velocity of rotation. The line connecting the small hole (center of the swollen part) and the center of the whole vesicle is drawn as a solid line in A'–E'. The angle variation from the line in A' was measured at each point (i.e., from B' to E'). The average angular velocity was determined from this angle divided by the duration of the rotation. The final angle (E') was chosen such that the angle is nearly or exactly equal to π . The experiments shown in (a) and (b) were performed for numerous vesicles under the same conditions. One cycle includes the transformations shown in (a) and (b). The abscissas in (a) and (b) denote the time at which the vesicle adopts the flat shape shown in Fig. 2(a), panel C.

continued for at most 10 min with a number of cycles of ~ 30 . Therefore, each single period and the overall duration of vesicle motion are longer under the present quasi-steady state pH gradient than under the previously reported unsteady state pH gradient.

Figure 3(a) and (b) shows the velocities of inversion and rotation during the cyclic motion. Vesicles with a number of repetitions of over seven times were chosen. The velocity of inversion was defined as the angle range shown in B and D (inset in Fig. 3) divided by the time elapsed from B to D. The velocity of rotational motion was defined as the angular velocity from A' to E' (inset in Fig. 3(b)).

The first plot (the most left-side plot) in Fig. 3(a) and (b) corresponds to the first cycle, meaning that no cyclic motion was observed before this point. The first cyclic motion started at 1–2.5 h from the beginning of NaOH diffusion. Figure 3(a) and (b) suggests that the velocities of inversion and rotation do not change systematically with time.

3.2. Driving forces for vesicle motion

In our previous study, acid/soap vesicles with disk-like structure exhibited the extrusion and contraction of pseudopods, similar to those in amoeba motion³⁴. Numerous pseudopods are typically extruded toward the higher-pH side. Thus, an attraction force toward the higher-pH side exists in acid/soap vesicles. The rotation may thus be discussed on the basis of this phoretic force³². Here, we assumed two types of phoretic forces, f_s and f_b , operating on the swollen and bound parts of the vesicle, respectively. These are shown in Fig. 4(a). In this work, the center of gravity is located near the geometric center of the vesicle because its inner part is filled with an aqueous phase of uniform density. Thus, the geometric center is taken as the origin of the coordinate system shown in Fig. 4(a). Force f_s pulls the vesicle membrane of the swollen part toward the higher-pH

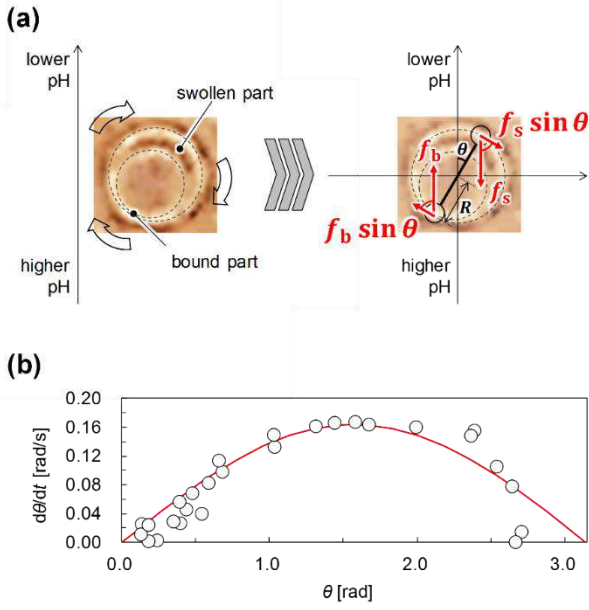


Figure 4. Analysis of vesicle rotation. (a) The two types of phoretic forces on a vesicle. The left image indicates the swollen part, bound part, and direction of rotation of the vesicle. The two spheres with broken lines indicate the boundaries of the structure. The right image shows how the phoretic forces f_s and f_b operate. The definition of θ is also shown. (b) Typical experimental result for the angular velocity and correlation curve based on eq. (1).

region. This corresponds to the above mentioned force toward the higher-pH side. On the other hand, a force f_b should exist pulling the vesicle membrane of the bound part toward the lower-pH region, since the vesicle is able to rotate around its center without translation toward the higher-pH side in spite of not being touching with the substrate in the channel.

Under a viscous liquid, the equation for rotational motion of a sphere with radius R is described by eq. (1).

$$Rf_s \sin \theta + Rf_b \sin \theta = 8\pi\eta R^3 \frac{d\theta}{dt} \quad (1)$$

The right hand side of eq. (1) represents the viscous drag force caused by rotation of a sphere in a fluid³⁵, where η is the viscosity of the solution around the vesicle. The diameter ($2R$) of a typical vesicle is around $20 \mu\text{m}$, and the Reynolds number of its rotation is approximately $\rho(\omega R)(2R)/\eta \approx 10^{-6}$, that is, much smaller than unity. Parameters ρ and η are the density and viscosity of water at $25 \text{ }^\circ\text{C}$, respectively, while ω is the angular velocity. Thus, the inertia term can be neglected. Here, we assume that these phoretic forces operate at the center of each section (swollen or bound), as shown in Fig. 4(a). Figure 4(b) shows the $d\theta/dt$ values throughout the time course for the rotation angle θ from insets A' to E' in Fig. 3(b). The red curve in Fig. 4(b) represents $d\theta/dt = A \sin \theta$, which correlates well with the experimental angular velocity. This demonstrates that the vesicle rotation is well described by eq. (1) and that $A = (f_s + f_b)/8\pi\eta R^2$. Therefore, the sum of the absolute value of the two phoretic forces, $F = f_s + f_b$, can be calculated.

In most of our experiments, vesicles exhibited translation toward the higher-pH side in addition to rotation. This translation of vesicles and other aggregates composed of oleate and oleic acid was not observed in lower-pH side (see SI movie 2). The distance between these two observed positions is 4 mm at most. If such migration was caused by convection, the vesicles would migrate in both sides. Thus, the vesicle translation toward the

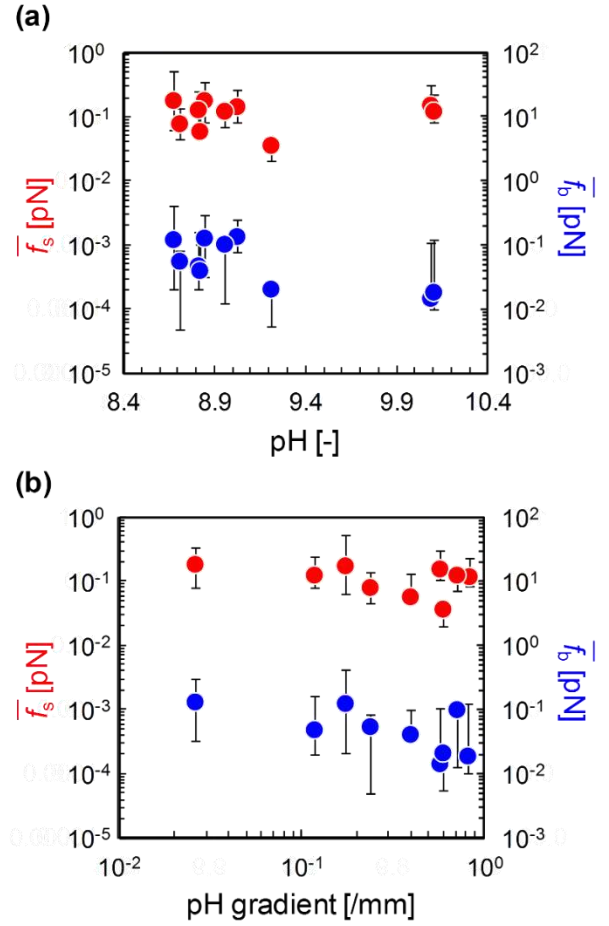


Figure 5. The phoretic forces evaluated for the vesicle rotation and translation are shown as a function of the pH and its gradient: (a) \bar{f}_s and \bar{f}_b vs pH, and (b) \bar{f}_s and \bar{f}_b vs pH gradient. The values of the phoretic forces are a little scattered because the velocity of the vesicle rotational motion may be affected by surrounding obstacles such as other vesicles. The error bars indicate the uncertainty due to this effect.

higher-pH side can be concluded not to be caused by convection. Therefore, the translation at the higher pH side may be occurred by the phoretic forces under the pH gradients. Then, the translation of vesicles and other aggregates composed of oleate and oleic acid in the lower pH side might be able to be observed with increasing the pH gradient after more time passes. This translation can be explained by $f_s - f_b \neq 0$, which drives the vesicle. Assuming Stokes' law for a viscous drag force, the net force for translation F' is given by eq. (2):

$$F' = 6\pi\eta Rv \quad (2)$$

where v is the average of the translation velocity that can be evaluated from the experimental results. Thus, both F and F' can be determined experimentally.

As such, f_s and f_b were determined from $F = f_s + f_b$ and $F' = f_s - f_b$. For one vesicle, the f_s and f_b values for each period were calculated in this way. We defined \bar{f}_s and \bar{f}_b as the average of f_s and f_b for all cycles following eq. (1), respectively. Figure 5(a) shows the \bar{f}_s and \bar{f}_b values including the result of the vesicle motion shown in Fig. 2 as a function of the pH, while Figure 5(b) shows them as a function of the pH gradient. The pH values and pH gradients were determined by the calibration curves of Fig. S2 after terminated the cyclic motion with translation of the vesicles. These phoretic forces are almost

independent of the pH and pH gradient. In this system, it is hard to observe vesicle motions under an extremely small pH gradient because the vesicles are metastable object and collapse before the quasi-steady state pH gradients forms in our experience when the difference of the pH values between two reservoirs and diffusing power was slight. However, if the pH gradient is 0/mm, \bar{f}_s and \bar{f}_b disappear because the vesicle does not show any systematic motion. In lower pH side, both f_s and f_b is close to zero since pH gradient may be exceedingly small. Therefore, both F and F' is close to zero, too. As the result, the rotation and translation of the vesicles could not be observed near the reservoir of lower pH side. Therefore, the vesicle shows rhythmic shape changes only when the pH gradient reaches a threshold value. The f_s and f_b likely originate from the different physicochemical properties of the vesicle membrane and its surrounding medium, since the properties of the inner aqueous solution are the same as those of the surrounding medium. Similar phoretic forces have already been proposed for the migration of phospholipid vesicles³¹, which moved toward the higher-pH region by a pulling force generated by micro-injections of NaOH. This motion occurs due to dissolution of the oleic acid generated by hydrolysis of the phospholipid molecules in the vesicle membrane located at the higher-pH region. In our previous study on disk-shaped acid/soap vesicles, the formation of pseudopods in oleate/oleic acid vesicles toward a higher-pH region under a pulling force was reported³⁴. The phoretic force \bar{f}_s was considered to be a thermodynamic force originating from simple neutralization of oleic acid with NaOH. On the other hand, \bar{f}_b would be the phoretic force attracting the bound part toward the lower-pH side. In actually, it is unclear why f_s balanced with f_b when the translation was not observation in this paper since the origin of these forces have not been sufficiently understood. However, the attractive force toward the acid side is interesting from the application point of view, such as in drug delivery (e.g., the pH is lower at sites of inflammation). Further studies are required on the underlying mechanism of this force.

In this study, the vesicles were found to rotate with 10^{-2} – 10^{-1} pN order of driving force, while the deformation of phospholipid vesicles is driven by 5 pN^{31, 36–38}. Moreover, the molecular motors in biological cells are driven at 1–10 pN^{39–43}. The driving force for the present vesicles is thus quite small. It is surprising that a vesicle can exhibit stable motion under such weak forces.

3.3. Estimation of membrane elasticity

The vesicle rotation is driven by the phoretic forces caused by a pH gradient, whereby both f_s and f_b rotate the vesicle. Then, the potential energy of the vesicle against the pH gradient is lost since the point of action of each force moves toward the ‘lower-potential’ side upon rotation. In other words, this rotation is a relaxation process against an external field (pH gradient). The vesicle must be excited to a higher potential energy state to maintain the cycle. The inversion event corresponds to this self-excitation process against the external field. As the simplest assumption, we neglected the effect of migration and considered that the mechanical work performed by membrane elasticity during the inversion is partly compensated for the loss of potential energy. Thus, we may consider

$$\kappa(1/R)^2 \times 4\pi R^2 < (f_s + f_b) \times 2R \quad (3)$$

We may assume that the curvature of the bound part changes from $1/R$ to 0 by membrane elasticity (spontaneous curvature at the flat state of vesicles). After this inversion, the vesicles are closed to form the small hole³². The left hand side of eq. (3) represents a change in the membrane elastic energy with

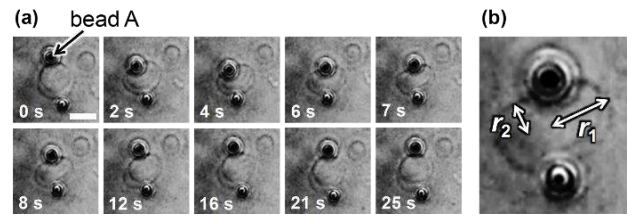


Figure 6. Time course of the vesicle shape during the optical tweezer experiment: (a) deformation of a vesicle by optical tweezer manipulation and its recovery by membrane elasticity, and (b) enlarged view of the image in (a) at 7 s. The scale bar is 10 μm .

elastic coefficient κ . The κ of right hand side of eq. (3) was estimated to be less than $4\text{--}80 k_B T$ with $R = 10 \mu\text{m}$, $F = 10^{-2}$ – 10^{-1} pN and $T = 300 \text{K}$.

For a quantitative estimation of the membrane elasticity, we observed the deformation of the vesicle caused by a physical force. For this purpose, vesicles were prepared in the presence of polyethylene beads. Two beads were moved by means of an optical tweezer such that a stomatocyte vesicle was placed between two beads. Figure 6(a) shows the vesicle deformation by those two beads. One bead (bead A in Fig. 6(a)) was further manipulated by the optical tweezer. As a result, the vesicle was deformed from spherical to oblate shape (0–7 s in Fig. 6(a)). After the laser was turned off, the vesicle returned to the spherical shape owing to its membrane elasticity, displacing bead A (7–25 s in Fig. 6(a)). Since the vesicle maintained its volume and membrane area, the loss of membrane elastic energy from oblate to spherical shape was converted into mechanical work to push said bead A. Thus, we obtain eq. (4):

$$-(\kappa H_s^2 - \kappa H_b^2) \times 4\pi R^2 = \int_{x_1}^{x_2} F_\eta(x) dx \quad (4)$$

where $H_s = 1/R$ is the curvature of a spherical vesicle and $H_b = (H_1 + H_2)/2$ is the average curvature of the oblate shape vesicle. For evaluation of its mean curvature, the vesicle was regarded as a disk with $H_1 = 1/r_1$ and $H_2 = 1/r_2$, as shown in Fig. 6(b). F_η is approximately equal to the viscous drag force acting on bead A, which was evaluated from the translation velocity of bead A and Stokes' law. The x_1 and x_2 are the distances between the two beads for the initial and final shape, respectively. The evaluated κ was approximately $5\text{--}20 k_B T$. This value does not contradict to the κ estimated from eq. (3). The elastic coefficient of bilayer membranes composed of phospholipids is approximately several tens $k_B T$ ^{44–46}. Therefore, these κ of acid/soap membrane calculated by two methods were equivalent to or less than phospholipid membrane. A membrane composed of oleate and oleic acid should be much more flexible and thus be able to adopt various shapes^{47–49}. This suggests that such a κ values for oleate vesicles is reasonable.

The present cyclic motion shown in Fig. 2 is maintained by alternating inversion (excitation process) and rotation (relaxation process). The inversion is likely completed before the start of rotation because the vesicle closes rapidly at the final stage of inversion (23–28 s in Fig. 2). In addition, the inversion cannot start until the rotation is finished, because the opening of the small hole requires an induction period (0–13 s in Fig. 2) in order to progress sufficiently for the degree of ionization of oleic acid around the small hole by diffusion of OH^- ³². The cyclic motion becomes possible by the remarked difference in the characteristic time scales for such inversion and rotation.

We have already reported that a vesicle can catch an object on the lower-pH side and carry it to the higher-pH side³². This

result indicates that mechanical work can be generated from the cyclic motion. This suggests that we may apply

$$\kappa(1/R)^2 \times 4\pi R^2 \approx F \times 2R + W \quad (5)$$

Here, W denotes the mechanical work performed by vesicle rotation. In the thermal cycle, $Q_H - Q_L = W$, where Q_H and Q_L denote the heat obtained from a hot reservoir and released to a cold reservoir, respectively. Considering an analogy to a thermal cycle, the vesicle can obtain energy from the higher-pH side and lose it on the lower-pH side.

4. Conclusion

A cyclic motion of vesicles which were consisted of oleate and oleic acid were observed under a quasi-steady state pH gradient. The cyclic motion involves both rotation and inversion. The pH and pH gradient around a vesicle exhibiting cyclic motion were evaluated quantitatively. The driving force for rotation was evaluated to be the order of 10^{-2} – 10^{-1} pN. The rotation is a relaxation process that loses the potential energy against the pH gradient, and the inversion is an excitation process. This cyclic motion was realized when characteristic time scales of these two types of motions were remarkably different. The present vesicles may be regarded as a molecular assembly machine that operates under a pH gradient.

Acknowledgement

A.S. and E.N.O. gratefully acknowledge the financial support from JSPS KAKENHI Grant Numbers 25630351 (A.S.) and 15J04606 (E.N.O.). A.S. and D.Y. acknowledge the financial support from the MEXT-Supported Program for the Strategic Research Foundation at Private Universities. E.N.O. gratefully acknowledges the financial support from the Scholarship Fund for Young/Women Researchers of the Promotion and Mutual Aid Corporation for Private Schools of Japan.

References

- H. Noji, R. Yasuda, M. Yoshida, K. Kinosita Jr, *Nature* **1997**, *386*, 299-302.
- T. Elston, H. Wang, G. Oster, *Nature* **1998**, *391*, 510-513.
- R. B. Phillips, J. Kondev, J. Theriot, *Physical Biology of the Cell*. 2nd ed., Garland Science, Abingdon-on-Thames, UK, **2009**.
- Y. Goto, M. Kanda, D. Yamamoto, A. Shioi, *Sci. Rep.* **2015**, *5*, 14348.
- Y. Wang, R. M. Hernandez, D. J. Bartlett, J. M. Bingham, T. R. Kline, A. Sen, T. E. Mallouk, *Langmuir* **2006**, *22*, 10451-10456.
- Y. Sumino, H. Kitahata, H. Seto, K. Yoshikawa, *Phys. Rev. E. Stat. Nonlin. Soft Matter Phys.* **2007**, *76*, 055202.
- W. F. Paxton, K. C. Kistler, C. C. Olmeda, A. Sen, S. K. St. Angelo, Y. Cao, T. E. Mallouk, P. E. Lammert, V. H. Crespi, *J. Am. Chem. Soc.* **2004**, *126*, 13424-13431.
- P. Lovass, M. Branicki, R. Toth, A. Braun, K. Suzuno, D. Ueyama, I. Lagzi, *RSC Adv.* **2015**, *5*, 48563-48568.
- K. Nagai, Y. Sumino, H. Kitahata, K. Yoshikawa, *Prog. Theor. Phys. Supp.* **2006**, *161*, 286-289.
- H. Kitahata, K. Yoshikawa, *Physica D: Nonlinear Phenomena* **2005**, *205*, 283-291.
- N. J. Suematsu, S. Nakata, A. Awazu, H. Nishimori, *Phys. Rev. E* **2010**, *81*, 056210.
- D. Yamamoto, C. Nakajima, A. Shioi, M. P. Krafft, K. Yoshikawa, *Nat. Commun.* **2015**, *6*, 7189.
- I. Lagzi, S. Soh, P. J. Wesson, K. P. Browne, B. A. Grzybowski, *J. Am. Chem. Soc.* **2010**, *132*, 1198-1199.
- K. Nagai, Y. Sumino, H. Kitahata, K. Yoshikawa, *Phys. Rev. E* **2005**, *71*, 065301.
- C. M. Bates, F. Stevens, S. C. Langford, J. T. Dickinson, *Langmuir* **2008**, *24*, 7193-7199.
- T. Toyota, N. Maru, M. M. Hanczyc, T. Ikegami, T. Sugawara, *J. Am. Chem. Soc.* **2009**, *131*, 5012-5013.
- F. Takabatake, N. Magome, M. Ichikawa, K. Yoshikawa, *J. Chem. Phys.* **2011**, *134*, 114704.
- H. Kitahata, K. Iida, M. Nagayama, *Phys. Rev. E* **2013**, *87*, 010901.
- F. Nomura, M. Nagata, T. Inaba, H. Hiramatsu, H. Hotani, K. Takiguchi, *Proc. Natl. Acad. Sci. U. S. A.* **2001**, *98*, 2340-2345.
- S. Takeda, A. Saitoh, M. Furuta, N. Satomi, A. Ishino, G. Nishida, H. Sudo, H. Hotani, K. Takiguchi, *J. Mol. Biol.* **2006**, *362*, 403-413.
- M. Kaga, T. Ohta, *J. Phys. Soc. Jpn.* **2007**, *76*, 094003.
- U. Tamiki, N. Fumimasa, I. Takehiko, T. Kingo, H. Hirokazu, *ChemPhysChem* **2005**, *6*, 1047-1050.
- F. Brochard-Wyart, P. G. de Gennes, O. Sandre, *Physica A: Statistical Mechanics and its Applications* **2000**, *278*, 32-51.
- A. Mogilner, G. Oster, *Biophys. J.* **1996**, *71*, 3030-3045.
- C. S. Peskin, G. M. Odell, G. F. Oster, *Biophys. J.* **1993**, *65*, 316-324.
- P. A. Giardini, D. A. Fletcher, J. A. Theriot, *Proc. Natl. Acad. Sci. U. S. A.* **2003**, *100*, 6493-6498.
- F. Gerbal, P. Chaikin, Y. Rabin, J. Prost, *Biophys. J.* **2000**, *79*, 2259-2275.
- A. Mogilner, G. Oster, *Biophys. J.* **2003**, *84*, 1591-1605.
- A. Upadhyaya, J. R. Chabot, A. Andreeva, A. Samadani, A. van Oudenaarden, *Proc. Natl. Acad. Sci. U. S. A.* **2003**, *100*, 4521-4526.
- J. Solon, P. Streicher, R. Richter, F. Brochard-Wyart, P. Bassereau, *Proc. Natl. Acad. Sci. U. S. A.* **2006**, *103*, 12382-12387.
- A. Kodama, Y. Sakuma, M. Imai, Y. Oya, T. Kawakatsu, N. Puff, M. I. Angelova, *Soft Matter* **2016**, *12*, 2877-2886.
- E. Nawa, Y. Nishigaki, D. Yamamoto, A. Shioi, *Soft Matter* **2013**, *9*, 7832-7842.
- U. Seifert, *Adv. Phys.* **1997**, *46*, 13-137.
- E. Nawa, D. Yamamoto, A. Shioi, *Bull. Chem. Soci. Jpn.* **2015**, *88*, 1536-1544.
- L. D. Landau, E. M. Lifshitz, *Fluid Mechanics*. 2th ed., Elsevier Science, Oxford, UK, **1987**.
- D. Cuvelier, I. Derényi, P. Bassereau, P. Nassoy, *Biophys. J.* **2005**, *88*, 2714-2726.
- I. Derényi, F. Jülicher, J. Prost, *Phys. Rev. Lett.* **2002**, *88*, 238101.
- A. Upadhyaya, M. P. Sheetz, *Biophys. J.* **2004**, *86*, 2923-2928.
- K. Svoboda, P. P. Mitra, S. M. Block, *Proc. Natl. Acad. Sci. U. S. A.* **1994**, *91*, 11782-11786.
- M. E. Fisher, A. B. Kolomeisky, *Proc. Natl. Acad. Sci. U. S. A.* **1999**, *96*, 6597-6602.
- H. Sakakibara, H. Kojima, Y. Sakai, E. Katayama, K. Oiwa, *Nature* **1999**, *400*, 586-590.
- H. Higuchi, E. Muto, Y. Inoue, T. Yanagida, *Proc. Natl. Acad. Sci. U. S. A.* **1997**, *94*, 4395-4400.
- E. Hirakawa, H. Higuchi, Y. Y. Toyoshima, *Proc. Natl. Acad. Sci. U. S. A.* **2000**, *97*, 2533-2537.
- J. R. Henriksen, J. H. Ipsen, *Eur. Phys. J. E* **2004**, *14*, 149-167.
- P. Méléard, C. Gerbeaud, P. Bardusco, N. Jeandaine, M. D. Mitov, L. Fernandez-Puente, *Biochimie* **1998**, *80*, 401-413.
- J. R. Henriksen, J. H. Ipsen, *Eur. Phys. J. E* **2002**, *9*, 365-

374.

47. K. Morigaki, P. Walde, *Langmuir* **2002**, *18*, 10509-10511.
48. I. Masako, T. Taro, T. Katsuto, S. Tadashi, S. Yoko, *Chem. Lett.* **2005**, *34*, 46-47.
49. I. Lagzi, D. Wang, B. Kowalczyk, B. A. Grzybowski, *Langmuir* **2010**, *26*, 13770-13772.

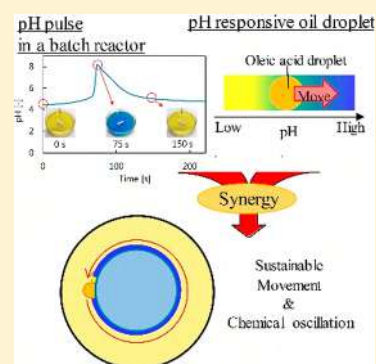
Autonomous Movement System Induced by Synergy between pH Oscillation and a pH-Responsive Oil Droplet

Yasunao Okamoto,[†] Yoko Sasaki,[†] Erika Nawa-Okita,[‡] Daigo Yamamoto,[†] and Akihisa Shioi^{*,†}

[†]Department of Chemical Engineering and Materials Science and [‡]Organization for Research Initiatives and Development, Faculty of Science and Engineering, Doshisha University, 1-3 Tatara Miyakodani, Kyoto 610-0321, Japan

Supporting Information

ABSTRACT: A sustainable droplet motion that is driven by pH oscillation was obtained. The pH oscillation is only of a single pulse in a batch reactor. However, it shows continuous oscillation around the moving droplet, as the motion itself controls the diffusion flux in an asymmetric manner. Various types of motions that are spontaneous in nature may be obtained by a single-pulse oscillation coupled with mass transport.

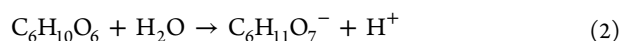
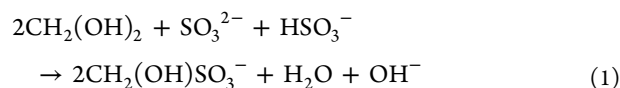


INTRODUCTION

Periodic chemical reactions, such as adenosine triphosphate (ATP) and tricarboxylic acid (TCA) cycles, occur in living cells and play crucial roles in maintaining life activities.^{1,2} These periodic reactions must be maintained in an open system with a reactant supply and waste discharge. In an abiotic system, the Belousov–Zhabotinsky (BZ) reaction is a typical chemical oscillation.^{3–6} The self-walking gel^{7–9} and self-propelled oil droplet^{10,11} have been studied with the BZ reaction. The reaction exhibits successive oscillations, even in a batch reactor, and this characteristic enables sustainable self-motions. In contrast, numerous abiotic chemical oscillations can be maintained by a continuous stirred-tank reactor (CSTR) or a semi-batch reactor with stirring. They exhibit only a single pulse in a batch reactor. pH oscillation also exhibits only a pulse in a batch reactor, and CSTR or semi-batch reactor is required for successive oscillation.^{12–17} The pH level drastically affects numerous chemical reactions in aqueous media, and its oscillation may be quite useful for actuator design.^{18–25} To the best of our knowledge, however, successive pH oscillation in a batch reactor has not been observed until now.²⁶ In this study, a self-moving oil droplet is designed with a single-pulse pH oscillation. Here, the mass transport enhanced by the droplet motion makes it continuous. Oleic acid is used as the pH-responsive oil droplet.²⁷ The oil/water interfacial tension strongly depends upon pH as well as the surface tension of water-containing oleate. The pH oscillation occurs just once in a batch reactor. However, the self-motion induces local convection. This agitation affects the mass-transfer rate of reactants. As a result, a semi-batch reaction is realized only in the vicinity of the moving droplet.

METHYLENE GLYCOL SULFITE GLUCONOLACTONE REACTION

We use the methylene glycol sulfite gluconolactone (MGSG) reaction¹⁴ as the pH oscillation. The reaction solution contains methylene glycol (or formaldehyde), sulfite buffer, and gluconolactone. The chemical reactions corresponding to pH increase and decrease, respectively, are as follows:



The pH increases by eq 1 in an autocatalytic manner and decreases by eq 2. The reaction rate is accelerated at the base condition represented by eq 1. The range of pH oscillation is approximately between 4.5 and 8.2 for the concentrations shown in Table 1. The pulse period is approximately 50 s.

Table 1. Chemical Compositions of Solutions

compound	solution A	solution B
Na ₂ SO ₃	2.50 mM	
NaHSO ₃	0.416 M	
HCHO		1.00 M
C ₆ H ₁₀ O ₆		6.80 mM

Received: July 7, 2019

Revised: September 27, 2019

Published: October 11, 2019

EXPERIMENTAL METHODS

Chemicals. Sodium sulfite (Na_2SO_3 , $\geq 98.0\%$), D-(+)-gluconic acid δ -lactone ($\text{C}_6\text{H}_{10}\text{O}_6$, $\geq 99.0\%$), and formaldehyde (HCHO , 37 wt %) were purchased from Sigma-Aldrich Co. LLC. Oleic acid (for biochemistry), sodium bisulfite (NaHSO_3 , Wako 1st grade), and agar powder (guaranteed reagent) were purchased from Wako Pure Chemical Industries, Ltd.

An agar gel containing Na_2SO_3 was set at the center of a Petri dish, as shown in Figure 1. The radius of the Petri dish is 9.1 cm, and the

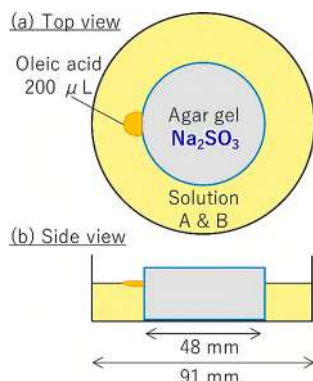


Figure 1. Experimental schematic.

volume of the gel is 25 mL. Solutions A and B in Table 1, each with a volume of 25 mL, were poured into a circular ring around the gel. Then, an oleic acid droplet of 200 μL was put on the surface of the mixed solution. The oil droplet made contact with the gel. Both solutions were stained by bromothymol blue (BTB) to observe their pH change.

RESULTS AND DISCUSSION

After contact with the gel, the oleic droplet moved along the gel, maintaining contact as shown in Figure 2a (see Video S1 of the Supporting Information). When the concentration of Na_2SO_3 in the gel was 0.1 M, the droplet exhibited a circular motion. The color of the water phase in the vicinity of the

droplet was blue, indicating that the local pH was above approximately 8. Figure 2c shows the variation in the azimuth of the center of the droplet (dotted lines) and the space–time plot around the gel. The angle θ is defined in Figure 2a. The space–time plot is a time series of circular photographs along the gel, where the circular shape is reshaped on a straight line. Figure 2c demonstrates that the solution color at a fixed position changed periodically in the order of yellow \rightarrow blue \rightarrow yellow and the droplet remained in the blue area. This indicates that a successive pH oscillation was induced by the droplet motion. The duration of the droplet motion exceeded approximately 50 min. The tangential velocity of the droplet is shown in Figure 3a. It gradually decreased over 15 min and approached a constant value of approximately 10 cm/min.

When ultrapure water was poured around the gel, it became blue with the droplet moving. The droplet exhibited a circular motion on the ultrapure water, as shown in Figure 2b; however, the duration was a maximum of 8 min, as shown in Figure 3a. These results indicate that pH oscillation increases the duration considerably. In this case, because pH oscillation does not occur, it is increased by Na_2SO_3 diffusion from the gel. pH may be decreased by the effect of the oleic acid droplet, and hence, the pH after the droplet passing may be decreased a little. Moreover, the pH increase as a result of Na_2SO_3 diffusion occurs gradually, and pH continues to increase for a while during the experiment. As a result of this, the droplet can move spontaneously for a while. However, this motion is not fully sustainable, because the pH does not decrease sufficiently. This decrease in pH oscillation is necessary for the sustainable motion with a much longer time.

The moving direction was selected occasionally. Both clockwise and anti-clockwise motions were observed.

For the pH oscillation system shown in Figure 3b, the color around the gel before the droplet appears is uniformly blue. As shown in Figure 3c, however, the color at the front of the moving droplet (red square) stays blue, but the color at the rear (black square) changes to yellow. The color change to yellow may be caused by pH oscillation or a pH decrease

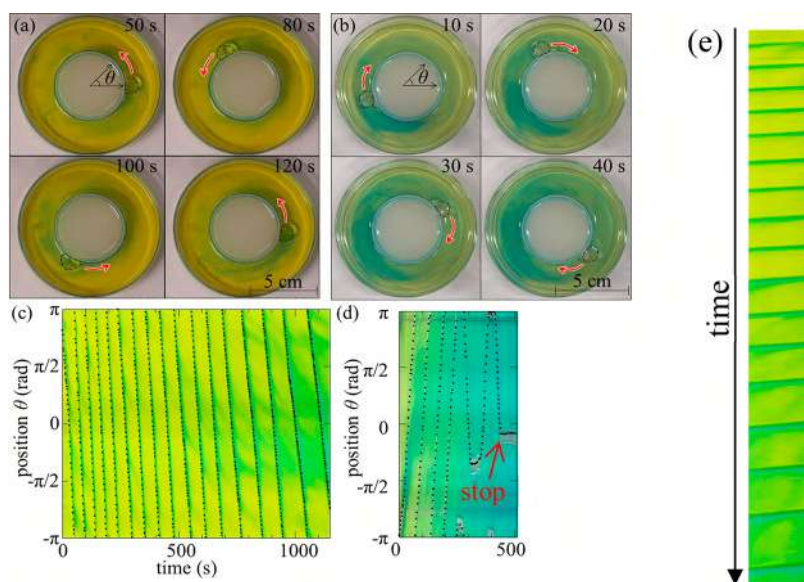


Figure 2. Circular motion of the droplet (a and c) with and (b and d) without pH oscillation. The solution was blue at $\text{pH} > 7.6$ and yellow at $\text{pH} < 6.0$. Broken lines, black arrows, and dots indicate oleic acid droplet peripheries, moving direction, and positions, respectively. (e) Space–time plot at $\theta = 0$ of panel c.

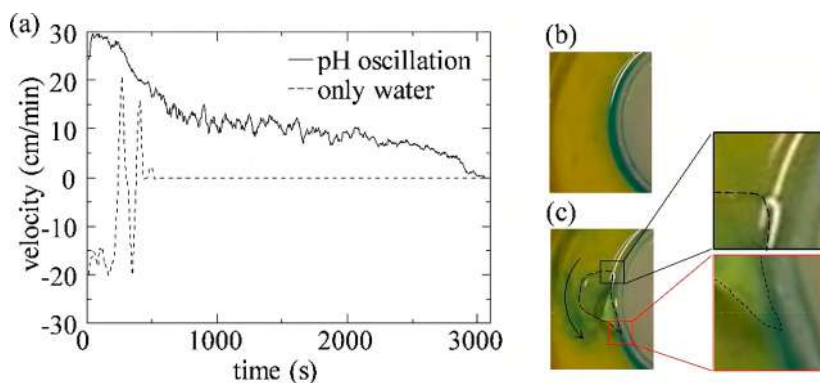


Figure 3. (a) Velocity of droplet motion. The running distance with/without pH oscillation is 594 and 103 cm, respectively. (b) Solution color after pouring solution through which no droplets have passed. (c) Solution color when a droplet passed through with pH oscillation. The arrow in panel c indicates the movement direction.

caused by oleic acid that has passed. However, no color change to yellow is shown in Figure 2b, and hence, this pH decrease is caused by pH oscillation. When the pH oscillation is coupled with the droplet motion, a pH difference between the front and rear of the droplet is maintained to a larger extent, as shown in Figures 2c and 3c. This is required for the sustainable droplet motion with much greater durations.

The convection inside the droplet was observed using carbon powder as tracer particles. The result is shown in Figure 4 (see Video S2 of the Supporting Information). Figure 4a

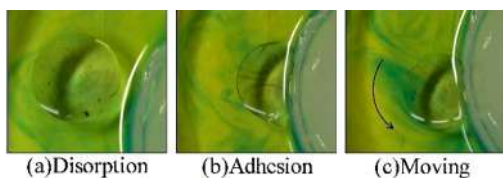


Figure 4. Internal convection of the droplet (a) before contact, (b) at active contact, and (c) during translation along the gel. The arrow indicates the moving direction.

shows a photograph before contact between the oil droplets and gel, where neither internal convection nor droplet motion was observed. Figure 4b shows the droplet just after contact with the gel, and Figure 4c shows the droplet during circular motion. The vector maps of the internal convections just after droplet and gel contact and that during motion are shown in Figure 5 (see also Video S3 of the Supporting Information). As shown in Figure 5a, the internal fluid flows toward the gel along the center line of the droplet, whereas the backward circular flows are observed along the periphery. The backward flow along the periphery causes water flow in the same direction, owing to the viscous drag. The droplet moves toward the opposite direction of this water flow for momentum conservation. Once this twin roll convection appears, the droplet actively maintains contact with the gel. This contact is referred to as active contact in this paper.

The symmetry of this twin roll may be perturbed by occasional droplet deformation. Then, one roll becomes larger than the other roll. This broken symmetry generates droplet translation along the gel, because the larger roll paddles water more strongly. The symmetric water flow along the droplet periphery at the adhesion state (black arrows in Figure 5a) cannot be maintained, and asymmetric water flow occurs, as shown by the thick and thin black arrows in Figure 5b. This

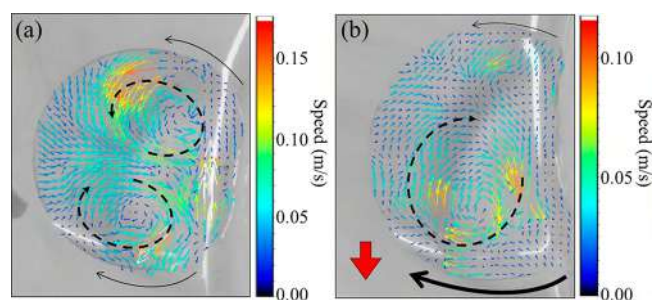


Figure 5. Particle image velocimetry (PIV) analysis of internal convection for (a) active contact and (b) translation. Red arrow, black arrows, and arrows in the droplet indicate the moving direction of a droplet, viscous flow, and internal convection, respectively. The color bar indicates the speed of internal convections. The flow pattern is emphasized by black dashed arrows.

asymmetry develops until the flow represented by the thick arrow dominates the whole flow pattern, as discussed later. As a result, the droplet starts to move. While the droplet moves in one direction, internal convection only forms in one roll. Figure 6 shows a schematic representation to discuss the reasons for the formation of these convections. Because diffusion of Na_2SO_3 from the gel initiates the pH increase reaction of eq 1, a pH gradient forms along the droplet, as shown in Figure 6a. The pH near the gel increases beyond that far away from the gel. As the oil/water interfacial tension increases with a decrease in pH, this pH gradient causes Marangoni flow at the oil/water interface, as shown in Figure 6a2. Its direction is from the higher to lower pH sides. Then, compensated flow develops for the conservation of the fluid volume. The flow pattern seen in Figure 5 is formed by this interfacial tension gradient. This interfacial flow drags the water near the interface. This convection forms a symmetric twin roll, as shown in Figure 6a1, and it causes contact between the droplet and gel. However, this twin roll must not have perfect symmetry for occasional fluctuations. For example, the droplet cannot be a perfect circle, because droplet motion distorts its shape, as illustrated in Figure 6b. In this case, asymmetric convections develop. Then, the agitation effect at point A is stronger than that at point B. As a result, the diffusion flux of Na_2SO_3 at point A becomes larger than that at point B. For this asymmetrical diffusion flux, the pH near point A becomes higher than that at point B. Thus, the roll generated near point A becomes larger and governs the convection

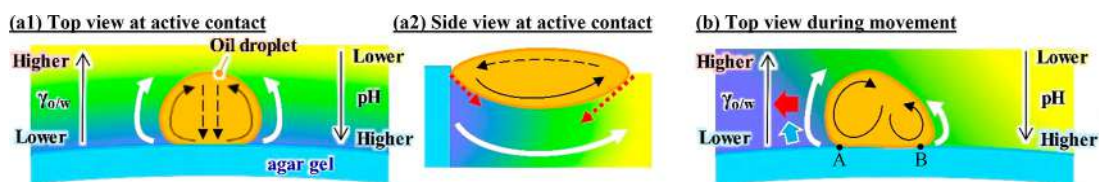


Figure 6. Mechanism of convection formed by diffusion of Na_2SO_3 . (a1) Top view at active contact. Black arrows, black broken arrows, and white arrows indicate interfacial flows, compensated flows, and viscous flows, respectively. (a2) Side view at active contact. Red arrows indicate oil–water interfacial tensions. The longer arrow indicates stronger tension. (b) Top view during movement of the oil droplet. The red arrow indicates the movement direction of the droplet. The blue arrow indicates stronger diffusion of Na_2SO_3 induced by bigger viscous flow.

pattern. The internal convection formed at point A dominates the whole convection pattern. This drives the droplet toward the red arrow in Figure 6b. Simultaneously, the droplet maintains contact with the gel for the water flow represented by the blue arrow in Figure 6b. The pH gradient causing the single roll inside the droplet is maintained, because the asymmetric diffusion flux is sustained by the droplet motion itself. A pH gradient is formed from the droplet front to rear by its motion. If there is no pH oscillation, this gradient cannot be maintained for longer durations (Figure 3a). The coupling between internal convection and the pH gradient with pH oscillation produces sustainable droplet motion.

A larger size (100–300 μL) generates higher velocity. This is probably because a larger size is capable of maintaining a larger difference in pH and interfacial tension.

We performed the experiment without formaldehyde, with other conditions remaining unchanged. Then, the droplet cannot maintain the contact to the gel. As mentioned, this contact is caused by an active motion of the droplet to the base side. This means that the autocatalytic increase in pH by formaldehyde is required for the propulsion. In the result of Figure 2, the experiment with ultrapure water (no gluconolactone), the droplet made an active contact and translation. The difference from the above-mentioned result is the effect of gluconolactone. It suppresses the increase in pH. The presence of gluconolactone makes the droplet motionless without formaldehyde. In addition, we performed a batch experiment, in which 0.1 M Na_2SO_3 solution was added little by little to the mixture without formaldehyde. In the experiment, pH simply increased after each addition. This result indicates that formaldehyde is needed for the pH pulse (oscillation). Therefore, formaldehyde is necessary for the droplet propulsion. As another control experiment, we use the silicon oil instead of oleic acid. Then, no motions, such as active contact to the gel and translational motion, were observed.

Three droplets were put on the surface to examine their cooperative motion (see Video S4 of the Supporting Information). As shown in Figure 7a, each mark (triangle, circle, and plus sign) shows the name of each droplet, where these droplets move in the same direction, indicated by the red arrow. In this experiment, the velocity of the droplet (plus sign) decreases occasionally at position P (1000 s). For this slowdown, the droplet (triangle) catches up with the droplet (plus sign) (1010 s). This corresponds to the flat sections, indicated by P, in Figure 7b. Figure 7b shows the variation in the azimuth of the center of the droplet and the space–time plot around the gel. Then, the droplet (triangle) stops to maintain its position (1025 s), while the droplet (plus sign) accelerates to reach a constant velocity. Because the droplet (triangle) does not move, the droplet (circle) reaches the

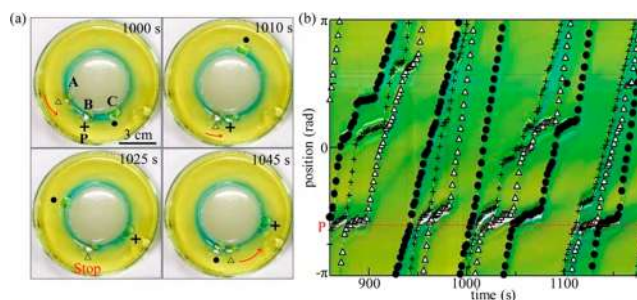


Figure 7. Billiards-like motion of three droplets (each droplet is shown as Δ , +, and \bullet): (a) snapshots of moving droplets and (b) space–time plots of three droplets.

position of the droplet (triangle) (1045 s). Then, the droplet (circle) stops to maintain its position, while the droplet (triangle) starts to move again. In this way, a billiards-like motion appears. This type of motion continues for approximately 20 min.

In addition to the circular rotation and billiards-like motion, the movement direction is reversed by a tip placed on the circumference of the gel, as shown in Figure 8 (see Video S5 of

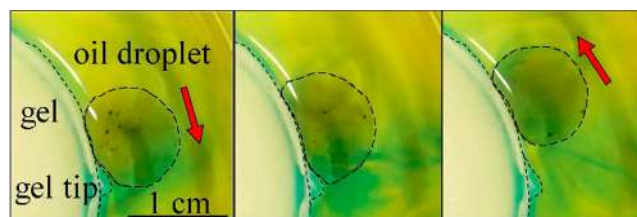


Figure 8. Back-and-forth motion of the droplet formed by a gel tip. Red arrows indicate the movement direction of the droplet.

the Supporting Information). The tip is made from Na_2SO_3 -free agar gel. The droplet does not pass through this tip position and shows back-and-forth motion along the circumference. This peripheral back-and-forth motion can be explained by internal and external convections, as discussed for the circular motion. Figure 9 shows the vector map of streamlines when the droplet changes its movement direction at the tip. As shown in Figure 9a, the internal convection is composed of a single roll until the droplet reaches the tip. When the droplet reaches the tip, the convection changes the pattern, as shown in Figure 9b. A new roll grows at the rear side of the droplet until a twin-roll pattern develops. The new roll replaces the original roll, and the direction of internal convection is reversed, as shown in Figure 9c. Then, the droplet moves in the opposite direction. The gel tip stops the droplet. However, the internal convection and the enhanced diffusion of Na_2SO_3 continue for a while. When the tip does

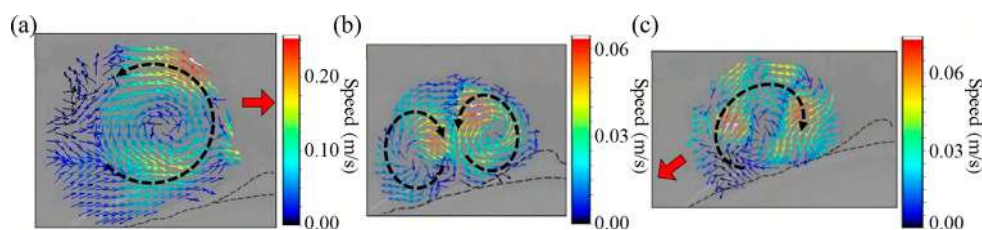


Figure 9. PIV analysis of internal convection during back-and-forth motion of a droplet with the gel tip. Droplet (a) approaching, (b) touching, and (c) departing from the gel tip. The red arrow and color bar indicate the movement direction and speed of internal convection, respectively. The broken line indicates the boundary of the circumference of the gel. The flow pattern is emphasized by black dashed arrows.

not contain Na_2SO_3 , the diffusion flux at the front (tip side) decreases. Contrary to this, the diffusion at the rear side proceeds. Then, the asymmetry of the pH distribution is reversed. In the billiards-like motion, observation of the internal convection was not easy. However, this can be explained by the same mechanism, which is essentially based on the convection pattern.

CONCLUSION

We achieved sustainable droplet motion driven by a pH oscillation. The reaction shows a single pulse in a well-stirred batch reactor; here, it is coupled with mass transport. The droplet motion itself controls the diffusion flux in an asymmetric manner to produce various types of motion. In living systems, various types of chemical oscillations play crucial roles in maintaining spontaneous motions; some of them may be sustained by a single-pulse chemical oscillation coupled with mass transport.

ASSOCIATED CONTENT

Supporting Information

The Supporting Information is available free of charge on the ACS Publications website at DOI: [10.1021/acs.langmuir.9b02072](https://doi.org/10.1021/acs.langmuir.9b02072).

Details about the methylene glycol sulfite gluconolactone reaction (PDF)

Circular motion of the droplet with pH oscillation, which is 100 times faster than real speed (Video S1) (MP4)

Internal convection visualized by carbon powder, which is a real-time video (Video S2) (MP4)

PIV of internal convection, which is a real-time video (Video S3) (AVI)

Billiards-like motion of three droplets, which is 30 times faster than real speed (Video S4) (MP4)

Back-and-forth motion of the droplet, which is 100 times faster than real speed (Video S5) (MP4)

AUTHOR INFORMATION

Corresponding Author

*E-mail: ashioi@mail.doshisha.ac.jp

ORCID

Yasunao Okamoto: [0000-0002-7964-3302](https://orcid.org/0000-0002-7964-3302)

Notes

The authors declare no competing financial interest.

ACKNOWLEDGMENTS

The authors express the deepest appreciation to Prof. Katsumi Tsuchiya (Doshisha University) for the particle image

velocimetry analysis. Akihisa Shioi gratefully acknowledges the financial support from Japan Society for the Promotion of Science (JSPS) Grant-in-Aid for Scientific Research (KAKEN-HI) Grant 16H04189. Akihisa Shioi and Daigo Yamamoto acknowledge the Ministry of Education, Culture, Sports, Science and Technology (MEXT)-Supported Program for the Strategic Research Foundation at Private Universities. The authors thank Editage (www.editage.jp) for English language editing.

REFERENCES

- (1) Liedl, T.; Olapinski, M.; Simmel, F. C. A surface-bound DNA switch driven by a chemical oscillator. *Angew. Chem., Int. Ed.* **2006**, *45* (30), 5007–10.
- (2) Howse, J. R.; Topham, P.; Crook, C. J.; Gleeson, A. J.; Bras, W.; Jones, R. A. L.; Ryan, A. J. Reciprocating Power Generation in a Chemically Driven Synthetic Muscle. *Nano Lett.* **2006**, *6* (1), 73–77.
- (3) Zaikin, A. N.; Zhabotinsky, A. M. Concentration Wave Propagation in Two-Dimensional Liquid-Phase Self-Oscillating System. *Nature* **1970**, *225* (5232), 535–537.
- (4) Field, R. J.; Noyes, R. M. Explanation of Spatial Band Propagation in the Belousov Reaction. *Nature* **1972**, *237* (5355), 390–392.
- (5) Busse, H. G. Spatial Periodic Homogeneous Chemical Reaction. *J. Phys. Chem.* **1969**, *73* (3), 750–750.
- (6) Steinbock, O.; Kettunen, P.; Showalter, K. Chemical Wave Logic Gates. *J. Phys. Chem.* **1996**, *100* (49), 18970–18975.
- (7) Maeda, S.; Hara, Y.; Sakai, T.; Yoshida, R.; Hashimoto, S. Self-Walking Gel. *Adv. Mater.* **2007**, *19* (21), 3480–3484.
- (8) Yoshida, R.; Sakai, T.; Hara, Y.; Maeda, S.; Hashimoto, S.; Suzuki, D.; Murase, Y. Self-Oscillating Gel as Novel Biomimetic Materials. *J. Controlled Release* **2009**, *140* (3), 186–93.
- (9) Yoshida, R. Self-Oscillating Gels and Application to Biomimetic Actuators. *Sensors* **2010**, *10* (3), 1810–22.
- (10) Liedl, T.; Simmel, F. C. Switching the Conformation of a DNA Molecule with a Chemical Oscillator. *Nano Lett.* **2005**, *5* (10), 1894–1898.
- (11) Suematsu, N. J.; Mori, Y.; Amemiya, T.; Nakata, S. Oscillation of Speed of a Self-Propelled Belousov-Zhabotinsky Droplet. *J. Phys. Chem. Lett.* **2016**, *7* (17), 3424–8.
- (12) Orban, M.; Kurin-Csörgei, K.; Epstein, I. R. pH-Regulated Chemical Oscillators. *Acc. Chem. Res.* **2015**, *48* (3), 593–601.
- (13) Zaknoun, F.; Al-Ghoul, M.; Sultan, R. pH Oscillations in the Bromate-Sulfite-Perchloric Acid Reaction. *Chaotic Modeling and Simulation (CMSIM)* **2012**, *2*, 387–394.
- (14) Kovacs, K.; McIlwaine, R. E.; Scott, S. K.; Taylor, A. F. pH Oscillations and Bistability in the Methylene Glycol-Sulfite-Gluconolactone Reaction. *Phys. Chem. Chem. Phys.* **2007**, *9* (28), 3711–6.
- (15) Szalai, I.; Kurin-Csörgei, K.; Orbán, M. Modelling pH Oscillators in Open, Semi-Batch and Batch Reactors. *React. Kinet., Mech. Catal.* **2012**, *106* (2), 257–266.
- (16) Vanag, V. K. Hydrogen Peroxide–Sulfite–Ferrocyanide–Horseradish Peroxidase pH Oscillator in a Continuous-Flow Stirred Tank Reactor. *J. Phys. Chem. A* **1998**, *102* (3), 601–605.

- (17) Okazaki, N.; Rábai, G.; Hanazaki, I. Discovery of Novel Bromate–Sulfite pH Oscillators with Mn^{2+} or MnO^+ as a Negative-Feedback Species. *J. Phys. Chem. A* **1999**, *103* (50), 10915–10920.
- (18) Yoshida, R. Self-Oscillating Gels Driven by the Belousov-Zhabotinsky Reaction as Novel Smart Materials. *Adv. Mater.* **2010**, *22* (31), 3463–83.
- (19) Maeda, S.; Hara, Y.; Yoshida, R.; Hashimoto, S. Self-Oscillating Gel Actuator for Chemical Robotics. *Adv. Robot.* **2008**, *22* (12), 1329–1342.
- (20) Varga, I.; Szalai, I.; Mészáros, R.; Gilányi, T. Pulsating pH-Responsive Nanogels. *J. Phys. Chem. B* **2006**, *110* (41), 20297–20301.
- (21) Nakata, S.; Iguchi, Y.; Ose, S.; Ishii, T. pH-Sensitive Self-Motion of a Solid Scraping on an Aqueous Phase. *J. Phys. Chem. B* **1998**, *102* (38), 7425–7427.
- (22) Ban, T.; Yamagami, T.; Nakata, H.; Okano, Y. pH-Dependent Motion of Self-Propelled Droplets Due to Marangoni Effect at Neutral pH. *Langmuir* **2013**, *29* (8), 2554–61.
- (23) Misra, G. P.; Siegel, R. A. New Mode of Drug Delivery: Long Term Autonomous Rhythmic Hormone Release across a Hydrogel Membrane. *J. Controlled Release* **2002**, *81* (1–2), 1–6.
- (24) Ramaswamy, S. The Mechanics and Statistics of Active Matter. *Annu. Rev. Condens. Matter Phys.* **2010**, *1* (1), 323–345.
- (25) Derenyi, I.; Lagzi, I. Fatty Acid Droplet Self-Division Driven by a Chemical Reaction. *Phys. Chem. Chem. Phys.* **2014**, *16* (10), 4639–41.
- (26) Poros, E.; Horvath, V.; Kurin-Csorgei, K.; Epstein, I. R.; Orban, M. Generation of pH-Oscillations in Closed Chemical Systems: Method and Applications. *J. Am. Chem. Soc.* **2011**, *133* (18), 7174–9.
- (27) Nagai, K. H.; Tachibana, K.; Tobe, Y.; Kazama, M.; Kitahata, H.; Omata, S.; Nagayama, M. Mathematical Model for Self-Propelled Droplets Driven by Interfacial Tension. *J. Chem. Phys.* **2016**, *144* (11), 114707.



Cite this: DOI: 10.1039/c5nr03300d

Received 19th May 2015,
Accepted 1st July 2015

DOI: 10.1039/c5nr03300d

www.rsc.org/nanoscale

Micromotors working in water through artificial aerobic metabolism†

D. Yamamoto,*^a T. Takada,^a M. Tachibana,^a Y. Iijima,^a A. Shioi^a and K. Yoshikawa^b

Most catalytic micro/nanomotors that have been developed so far use hydrogen peroxide as fuel, while some use hydrazine. These fuels are difficult to apply because they can cause skin irritation, and often form and store disruptive bubbles. In this paper, we demonstrate a novel catalytic Pt micromotor that does not produce bubbles, and is driven by the oxidation of stable, non-toxic primary alcohols and aldehydes with dissolved oxygen. This use of organic oxidation mirrors living systems, and lends this new motor essentially the same characteristics, including decreased motility in low oxygen environments and the direct isothermal conversion of chemical energy into mechanical energy. Interestingly, the motility direction is reversed by replacing the reducing fuels with hydrogen peroxide. Therefore, these micromotors not only provide a novel system in nanotechnology, but also help in further revealing the underlining mechanisms of motility of living organisms.

Introduction

The fabrication of minute, chemically propelled motors has been a popular yet challenging topic since Ismagilov *et al.* first demonstrated a centimeter-sized boat that travels on the surface of water. This initial structure was powered by hydrogen peroxide decomposition catalyzed by its Pt-covered stern,¹ a reaction that releases oxygen bubbles which serve to propel it. A primary goal since then has been the scaling down of these systems to the micrometer or even nanometer scale.^{2,3} The first type of catalytic motor relies on external reactants for fuel,⁴ and while many such systems have been developed, they generally use only hydrogen peroxide^{5–8} or hydrazine.^{9–11} Both the chemicals are undesirable in that they are irritants, and often form and store bubbles that can disrupt system oper-

ation. Likewise, the other type of catalytic motor, the self-reacted variant, generates bubbles or solid residue, and again often requires toxic materials.^{12–16} These limitations often make these devices unusable, especially in biomedicine and nanodevices.

Herein, we present a micromotor propelled by the oxidation of specific organic compounds using dissolved oxygen, a propulsion process very similar to that of minute organisms. While various types of micromotors have been proposed, we use a simpler micromotor that is composed of hundreds to thousands of primary Pt nanoparticles because the system is easily reproducible in any laboratories. The actual shape and structure of the Pt primary nanoparticles and their assemblies are shown in Fig. 1 and their SEM images are in ref. 17. This work relies on previous research that has demonstrated that catalytic Pt micromotors powered by hydrogen peroxide show different forms of propulsion (*i.e.*, active Brownian motion, translation, rotation, and spinning), depending on their shape.^{17–19} Furthermore, we have clarified that the dynamical mode can be predicted by quantitative analysis of the two-dimensional shape; we adapt these previously attested shapes to the tested reductant fuels.¹⁷

Results and discussion

Fig. 1A–D show the trajectory of these micromotors for various primary alcohol solutions at a concentration of 1 vol%. As with previous hydrogen peroxide systems, those motors exhibited two-dimensional regulated motion on the bottom of the employed containers, the type of which was dependent on their morphology.¹⁷ In addition based on the careful observations, it has been shown that the primary factor in determining the moving speed is the asymmetric morphology and that the change in the size of the Pt-particles exhibits minor effects. Although quantitative comparison of the speed of these motors was difficult due to a lack of one-to-one correspondence between the shapes in the previous and current experiments, the motors in the current experiment did seem

^aDepartment of Chemical Engineering and Materials Science, Doshisha University, Kyoto 610-0321, Japan. E-mail: dyamamoto@mail.doshisha.ac.jp

^bFaculty of Life and Medical Sciences, Doshisha University, Kyoto 610-0394, Japan

†Electronic supplementary information (ESI) available: Details of the experimental procedure, supplementary note S1, supplementary Fig. S1 to S5, and supplementary videos S1 to S4. See DOI: 10.1039/c5nr03300d

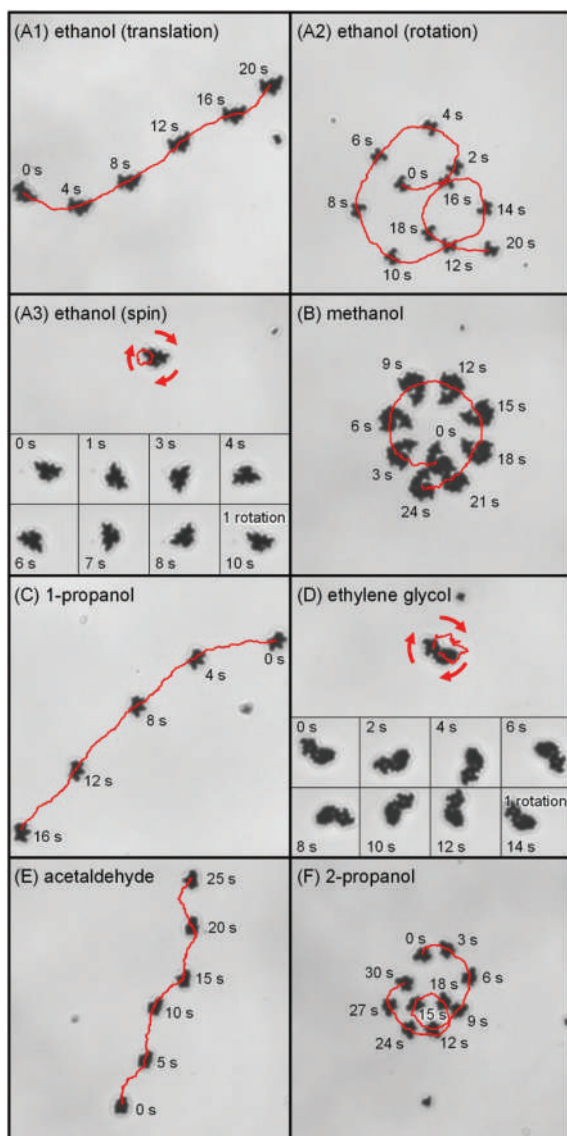


Fig. 1 Characteristic motions of Pt micromotors for various organic fuels. Trajectory and snapshots of Pt motor motion in various 1 vol% primary alcohols ((A) ethanol, (B) methanol, (C) 1-propanol, and (D) ethylene glycol), (E) 1 vol% acetaldehyde, and (F) 10 vol% 2-propanol aqueous solutions. The scale bar indicates a length of 20 μm .

to move somewhat more slowly. Overall, though, the speed seems to be primarily dependent on the morphology and not on the specific alcohol species (Video S1 and S2, ESI†). Acetaldehyde also gave regulated motion (Fig. 1E), though the secondary alcohol 2-propanol showed activity only for concentrations above 10 vol% (Fig. 1F). Likewise, the tertiary alcohol *tert*-butyl alcohol gave random, unregulated motion at any concentrations. We also confirmed that inert silica particles and their assemblies show random Brownian motion in these solutions, indicating that the observed activity is unique to the Pt structures.

While the designed motor generates regular motion, primary Pt nanoparticles simply seem to behave as “hot” colloids,²⁰ with an effective temperature markedly higher than the bare temperature (see Fig. S2, ESI†). In order to evaluate whether non-equilibrium random motion affects this seemingly random displacement, we analyzed the scaling behavior of deviation with respect to time by separating the diffusion constant from the apparent value for the primary Pt particles; in this case, $D_{\text{app}} = D_{\text{B}} + \Delta D$, where D_{B} and ΔD represent the ordinary Brownian diffusion constant and a constant describing excess diffusion. Fig. 2A shows these constants for various aqueous solutions of the employed fuels, having obtained them by calculating the trajectory of more than 10 particles according to the two-dimensional Einstein–Smoluchowski equation (see Fig. S3, ESI†). The apparent ethanol diffusion constant of $0.88 \mu\text{m}^2 \text{s}^{-1}$ was smaller than $0.93 \mu\text{m}^2 \text{s}^{-1}$ of hydrogen peroxide but larger than the ordinary Brownian diffusion constant in pure water $0.68 \mu\text{m}^2 \text{s}^{-1}$. Based

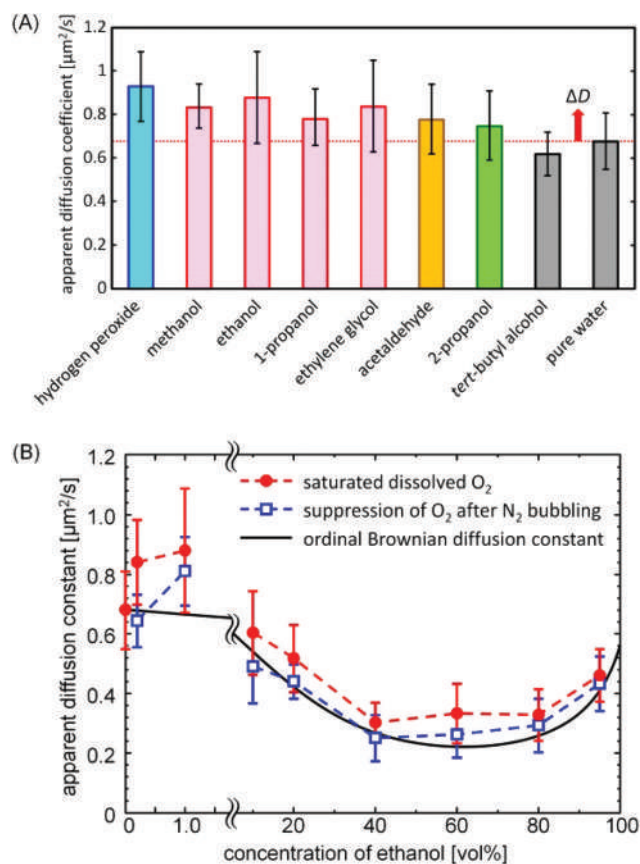
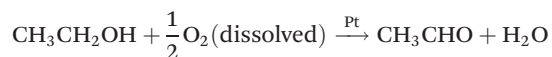


Fig. 2 Apparent diffusion constants for primary Pt particles. (A) The diffusion constants for various aqueous solutions of organic compounds (1 vol%) and hydrogen peroxide (1 wt%). (B) Apparent diffusion constants with respect to ethanol concentration for solutions with both saturated and minimally concentrated dissolved oxygen contents. D_{B} values with respect to ethanol concentration were calculated from the formula $(\mu_{\text{w}}/\mu_{\text{mix}}) \times D_{\text{w}}$, where μ represents the viscosity of the medium. The subscripts w and mix denote water and ethanol–water mixtures, respectively.

on the Einstein–Stokes relationship of $D \propto T^{-1}$, the reaction-induced random motion corresponds to the kind of thermal fluctuation that would occur at the effective temperature around 400 K (see eqn S1–4, ESI†).²⁰ Meanwhile, the non-equilibrium diffusion is transformed into directed motion for the Pt assembly; detailed discussion of the conversion efficiency is described in Note S1, ESI†. Likewise, the other primary alcohols and acetaldehyde increased apparent diffusion, while *tert*-butyl alcohol did not. Note that 2-propanol also increased apparent diffusion, though to a lesser extent.

To determine the chemical reaction responsible for propulsion, we used an enzymatic spectrophotometric assay to identify the reaction products for the ethanol and acetaldehyde trials (Fig. S4†). During the experiment, the solutions were vigorously stirred and were not permitted contact with the atmosphere, since oxygen can promote excess oxidation of the fuels. Fig. 3 shows that ethanol and acetaldehyde were oxidized to acetaldehyde and acetic acid, respectively. The final product concentrations of about 0.6 mM were almost twice as large as the initial concentration of dissolved oxygen. We additionally confirmed that the concentration of the fuels stays at a fairly constant value of about 2×10^2 mM throughout the course of the experiment, and furthermore that no product forms when the Pt particles are not present. This suggests the following reactions:

(i) in 1 vol% ethanol



(ii) in 1 vol% acetaldehyde



Additional oxidation hardly occurs because the initial concentration of the fuel is much larger than that of the dissolved oxygen. Likewise, secondary alcohols likely oxidize to the corresponding ketones; in this case, the decreased kinetics of this reaction would seem to account for the decreased propulsion observed.

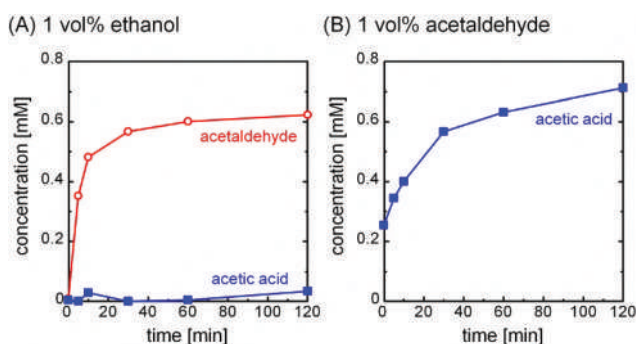
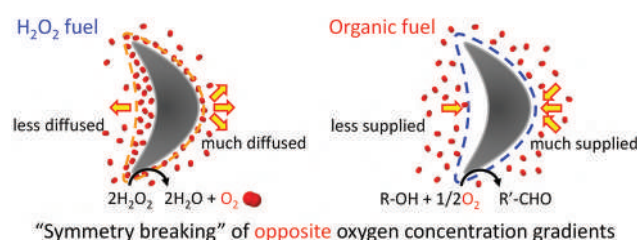


Fig. 3 Quantitative analysis of reaction products for the oxidation of primary alcohols and acetaldehyde. Ethanol, acetaldehyde, and acetic acid concentrations with respect to time for the oxidation of (A) 1 vol% ethanol and (B) acetaldehyde.

The ΔD values for the primary alcohols and acetaldehyde are very close to each other, implying that the provided propulsion is not significantly dependent on the individual reaction details, but rather on the commonality between all of them. Therefore, we propose that the generated oxygen concentration gradient resulting from oxygen consumption, and not bubble formation, is responsible for this motion. The concentration of dissolved oxygen in these experiments was on the order of 10^{-4} M, significantly lower than 10^{-1} M of the fuels. Therefore, as the fuel is oxidized, the surrounding oxygen concentration should drop rapidly, nearly completely disappearing in a short time. In other words, for the more rapid reaction observed with primary alcohols and acetaldehyde, the reaction rate is restricted by the diffusion limit of oxygen. On the other hand, the lower oxidation rate of secondary alcohols does not lead to the same diffusion-limited reaction. Overall, this suggests that the reaction rate depends strongly on the alcohol concentration.

Past studies with hydrogen peroxide have shown that the resulting oxygen concentration gradient is what propels Pt-containing Janus micromotors;^{21,22} this process is called self-diffusiophoresis.²³ The present micromotor propulsion may be caused by the self-diffusiophoresis because of the asymmetry of the morphology. Let us consider that a boomerang-like micromotor is propelled by self-diffusiophoresis (Scheme 1). For hydrogen peroxide as fuel, the morphology yields the difference in the diffusion flux of the resulting oxygen molecules: the oxygen molecules released from the concave surface concentrate near the surface. This higher oxygen concentration decreases the diffusion flux. On the other hand, the oxygen molecules released from the convex surface expand toward the wider area so that the oxygen concentration decreases. This results in a higher diffusion flux. The opposite driving force in this study, however, should propel the motors in the opposite direction, given the inverse spatial gradient formed by the reaction of the oxygen absorbing fuels when compared to oxygen producing hydrogen peroxide. In order to confirm the validity of this mechanism, we first measured the diffusion constant of a primary particle at different dissolved oxygen concentrations (Fig. 2B). The value dropped significantly for lower concentrations of oxygen, regardless of the ethanol concentration. Note that diffusion constants in all cases decreased between 40 and 80 vol% of ethanol because of the increased viscosity of the mixture.²⁴ In addition, we compared the performance of the identical micromotors in ethanol with that in



Scheme 1 Moving mechanism of a Pt-assembled micromotor propelled by hydrogen peroxide and organic fuels.

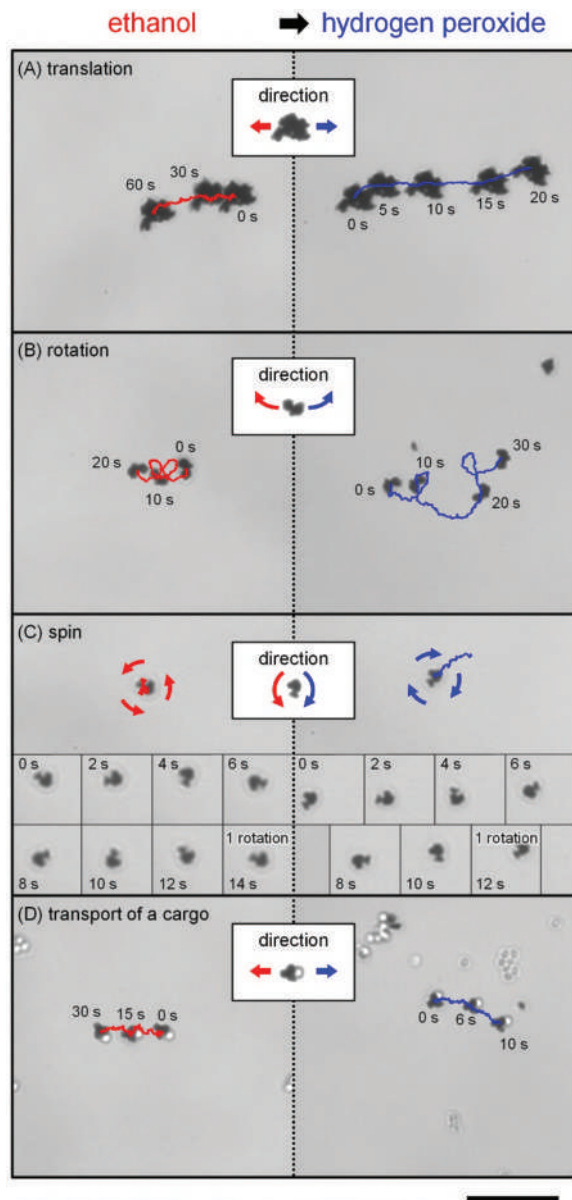


Fig. 4 Directional inversion on translational and rotational motions for Pt motors caused by switching of the fuels. Trajectory and snapshots of the (A) translational, (B) rotational, and (C) spin regulated motions for Pt micromotors and (D) accompanying silica cargo (diameter: 1.5 μm) before and after switching from 1 vol% ethanol to 1 wt% hydrogen peroxide. An identical micromotor was used throughout each experiment (Fig. S1, ESI \dagger). The scale bar indicates a length of 20 μm .

hydrogen peroxide (Fig. 4A–C and Video S3 and S4, ESI \dagger). As expected, all motion was perfectly reversed.

Conclusions

In conclusion, we have developed a micromotor system powered by a broad class of common, non-toxic fuels. A wide range of available chemicals and concentrations (Fig. S5, ESI \dagger) significantly increases the scope of application; for example,

because the minimal concentration of ethanol is comparable to that found in the blood when drinking alcohol, these motors should be able to operate *in vivo* without any additional modifications. In addition, the system does not produce any toxic compounds, nor does it generate bubbles or solids that could impede operation even after 10 h of continued operation. Furthermore, the new mechanism increases the available motilities by reversing those previously available with hydrogen peroxide. This functionality allows these motors to pull and push micro-sized silica cargo by alternating between ethanol and hydrogen peroxide (Fig. 4D and Video S4, ESI \dagger). Finally, this oxidative mechanism mirrors comparable biological systems, and the power of the system, on the order of 10^{-18} W, is roughly comparable to the power of around 10^{-17} W observed in a bacterium.²⁵ Both systems additionally become inactive at low oxygen concentrations. Given these characteristics, this new system, upon further development and improved motility, may not only be able to serve in new micro-devices and drug delivery systems, but also help to better understand the motility of microscopic organisms.

Experimental section

Chemicals

Spherical Pt particles (PT-354012, 99.00%) were purchased from Nilaco. Methanol (99.8%), ethanol (99.5%), 1-propanol (99.5%), ethylene glycol (99.0%), acetaldehyde (90%), and hydrogen peroxide (30%) were obtained from Wako Pure Chemical Industries. 2-Propanol (99.5%) and *tert*-butyl alcohol (99.0%) were purchased from Tokyo Chemical Industry.

Observation of Pt particle motion

The experimental setup was reported previously,¹⁷ and is briefly explained below. First, Pt powder was dispersed in de-ionized water by ultrasonication. The particle suspension was then mixed with organic solutes, typically to a concentration of 1 vol%. The resulting solutions were poured into μ -Slides (Nippon Genetics), and the motion of the Pt particles and assemblies were observed at room temperature by using an optical microscope (Olympus IX71, Olympus) and a high-speed CCD camera (30 frames per s). A separate device was used to obtain the results in Fig. 4 that replaced the solution around the Pt particles without convection, allowing for the observation of an identical particle in different solutions; this is explained in detail in Fig. S1, ESI \dagger

Acknowledgements

This work was supported in part by a Grant-in-Aid for Young Scientists (B) (Grant No. 26820341) from the Japan Society for the Promotion of Science (JSPS) and by MEXT Supported Program for the Strategic Research Foundation at Private Universities, 2015–2019. The Hosokawa Powder Technology Foundation also provided funding.

Notes and references

- 1 R. F. Ismagilov, A. Schwartz, N. Bowden and G. M. Whitesides, *Angew. Chem., Int. Ed.*, 2002, **41**, 652–654.
- 2 T.-C. Lee, M. Alarcón-Correa, C. Miksch, K. Hahn, J. G. Gibbs and P. Fischer, *Nano Lett.*, 2014, **14**, 2407–2412.
- 3 D. A. Wilson, R. J. M. Nolte and J. C. M. van Hest, *Nat. Chem.*, 2012, **4**, 268–274.
- 4 D. Yamamoto and A. Shioi, *KONA Powder Part. J.*, 2015, **32**, 2–22.
- 5 S. Fournier-Bidoz, A. C. Arsenault, I. Manners and G. A. Ozin, *Chem. Commun.*, 2005, 441–443.
- 6 J. G. Gibbs and Y.-P. Zhao, *Appl. Phys. Lett.*, 2009, **94**, 163104.
- 7 Y. He, J. Wu and Y. Zhao, *Nano Lett.*, 2007, **7**, 1369–1375.
- 8 W. F. Paxton, K. C. Kistler, C. C. Olmeda, A. Sen, S. K. St. Angelo, Y. Cao, T. E. Mallouk, P. E. Lammert and V. H. Crespi, *J. Am. Chem. Soc.*, 2004, **126**, 13424–13431.
- 9 W. Gao, A. Pei, R. Dong and J. Wang, *J. Am. Chem. Soc.*, 2014, **136**, 2276–2279.
- 10 W. Gao, S. Sattayasamitsathit, A. Uygun, A. Pei, A. Ponedal and J. Wang, *Nanoscale*, 2012, **4**, 2447–2453.
- 11 R. Laocharoensuk, J. Burdick and J. Wang, *ACS Nano*, 2008, **2**, 1069–1075.
- 12 W. Gao, X. Feng, A. Pei, Y. Gu, J. Li and J. Wang, *Nanoscale*, 2013, **5**, 4696–4700.
- 13 W. Gao, A. Pei and J. Wang, *ACS Nano*, 2012, **6**, 8432–8438.
- 14 W. Gao, A. Uygun and J. Wang, *J. Am. Chem. Soc.*, 2011, **134**, 897–900.
- 15 R. Liu and A. Sen, *J. Am. Chem. Soc.*, 2011, **133**, 20064–20067.
- 16 F. Mou, C. Chen, H. Ma, Y. Yin, Q. Wu and J. Guan, *Angew. Chem., Int. Ed.*, 2013, **52**, 7208–7212.
- 17 D. Yamamoto, A. Mukai, N. Okita, K. Yoshikawa and A. Shioi, *J. Chem. Phys.*, 2013, **139**, 034705.
- 18 B. Jingjing, Y. Zhan, M. Nakajima, S. Yajing, M. Takeuchi, H. Qiang and T. Fukuda, *IEEE Trans. Robot.*, 2014, **30**, 33–39.
- 19 N. I. Kovtyukhova, *J. Phys. Chem. C*, 2008, **112**, 6049–6056.
- 20 J. Palacci, C. Cottin-Bizonne, C. Ybert and L. Bocquet, *Phys. Rev. Lett.*, 2010, **105**, 088304.
- 21 S. J. Ebbens and J. R. Howse, *Langmuir*, 2011, **27**, 12293–12296.
- 22 J. R. Howse, R. A. L. Jones, A. J. Ryan, T. Gough, R. Vafabakhsh and R. Golestanian, *Phys. Rev. Lett.*, 2007, **99**, 048102.
- 23 R. Golestanian, T. B. Liverpool and A. Ajdari, *Phys. Rev. Lett.*, 2005, **94**, 220801.
- 24 I. Khattab, F. Bandarkar, M. Fakhree and A. Jouyban, *Korean J. Chem. Eng.*, 2012, **29**, 812–817.
- 25 S. Chattopadhyay, R. Moldovan, C. Yeung and X. L. Wu, *Proc. Natl. Acad. Sci. U. S. A.*, 2006, **103**, 13712–13717.

Optical Fluid Pump: Generation of Directional Flow via Microphase Segregation/Homogenization

Hiroki Sakuta,[†] Shunsuke Seo,[†] Shuto Kimura,[†] Marcel Hörning,^{‡,¶} Koichiro Sadakane,[†] Takahiro Kenmotsu,[†] Motomu Tanaka,^{§,¶,||} and Kenichi Yoshikawa^{*,†,||}

[†]Faculty of Life and Medical Sciences, Doshisha University, Kyotanabe 610-0394, Japan

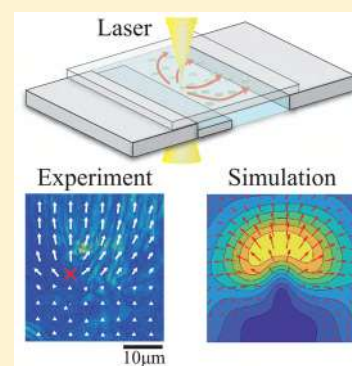
[‡]Institute of Biomaterials and Biomolecular Systems, University of Stuttgart, Stuttgart 70569, Germany

[¶]Institute for Integrated Cell-Material Sciences, Kyoto University, Kyoto 606-8501, Japan

[§]Institute of Physical Chemistry, University of Heidelberg, Heidelberg 69120, Germany

^{||}Center for Integrative Medicine and Physics Institute for Advanced Study, Kyoto University, Kyoto 606-8501, Japan

ABSTRACT: We report the successful generation of directional liquid-flow under stationary laser irradiation at a fixed position in a chamber. We adopt a homogeneous solution consisting of a mixture of water and triethylamine (TEA), with a composition near the critical point for phase segregation. When geometrical asymmetry is introduced around the laser focus in the chamber, continuous directional flow is generated, accompanied by the emergence of water-rich microdroplets at the laser focus. The emerging microdroplets tend to escape toward the surrounding bulk solution and then merge/annihilate into the homogeneous solution. The essential features of the directional flow are reproduced through a simple numerical simulation using fluid dynamic equations.



In general, oil/water systems exist as either a homogeneous solution or a macroscopically segregated solution,^{1–3} which can be interpreted in terms of a first-order phase transition. The phase coexistence on a microscopic scale is intrinsically unstable in the absence of a surfactant under equilibrium. This implies the possible occurrence of dynamic phenomena, including the emergence and annihilation of microscopic segregation under thermodynamically open conditions. Recently, it has been shown that a focused laser can generate microscopic phase-separation in a homogeneous solution composed of oil and water under a condition that is near the critical point for a phase transition.^{4–14} When the homogeneous solution is enriched with oil near the bimodal line in the phase diagram, water-rich microdroplets successively emerge from the laser focus under constant laser irradiation.^{15–19} The generated water-rich microdroplets tend to escape from the focus because of the lower dielectricity compared to that of the oil-rich medium. As they travel into the periphery, the microdroplets disappear by merging into the homogeneous bulk in the absence of a laser-induced dielectric potential. Here, it is expected that the emergence of several microdroplets at the laser focus will cause an increase in local pressure due to a transient increase in the total oil/water interfacial area, which is incommensurate with molecular packing. In this article, we propose a new methodology for producing an optically driven micropump by applying such kind of dynamical phenomenon with the emergence/annihilation of microdroplets caused by a focused laser.

There has been growing interest^{20–22} in the subject of micropumps below the millimeter scale in the medical and microengineering fields, such as in the use of micropumps in biosensors, small fuel cells, and drug-delivery equipment. However, micropumps smaller than a micrometer scale do not seem to be available for practical application. Trials that involve the downsizing of existing pump have encountered serious difficulties because of the relatively greater effects of viscosity and friction in a microscopic system. However, it is well-known that laser trapping is a useful tool for transporting objects smaller than the scale of several tens of micrometers.^{10,23–26} Several studies have shown that centimeter-sized objects at an interface can be transported by laser through a thermocapillary effect.^{27–32} Thus, methods for transporting objects on a scale between several millimeters and several tens of micrometers are needed.² Recently, Wang et al. reported that directional flow on the scale of several cm is generated by the use of a laser beam, through the photoacoustic effect.³³ The driving force is attributed to the generation of cavity caused by laser irradiation. Although this methodology seems to be interesting, we have to consider the possible effect of chemical damage induced by the breakage shock of the cavity.³⁴

Received: June 15, 2018

Accepted: September 17, 2018

Published: September 17, 2018

In this study, we examined a mixture of water and trimethylamine (TEA), in which we previously observed the formation of a flower-like dynamic pattern with radial symmetry as a result of the generation and annihilation of microdroplets under continuous irradiation by a focused laser.^{4,5} As shown in Figure 1a, an infrared laser (1064 nm

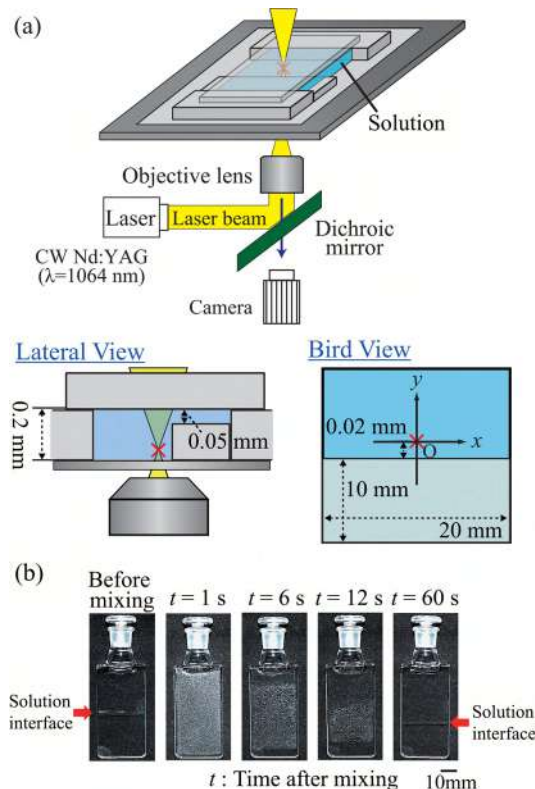


Figure 1. (a) Schematic illustration of the experimental setup. A Nd:YAG laser (1064 nm) was applied at a fixed power of 0.5 W. The laser light was passed through an oil-immersed objective lens with an inverted microscope, where the focus is denoted by a red “x”. The chamber was fully filled with TEA-rich solution and shielded from the outer environment. To introduce spatial-asymetry in the experimental system, a glass sheet with a width of 0.15 mm was situated on the right-hand side of the chamber. (b) Effect of mechanical agitation on the macroscopic phase-separated solution of water and TEA with a volume ratio of 1:1 at room temperature (291 K). Just after agitation, the solution becomes turbid and then tends to be transparent, accompanied by growth of the phase separation.

Nd:YAG laser, Millennia IR, Spectra-Physics; output power 0.5 W) was passed through an oil-immersion objective lens ($\times 100$, numerical apparatus; 1.3) with an inverted microscope (Nikon ECLIPSE TE300). The photointensity on the solution after passing through the objective lens was ca. 50 mW.¹¹ The images were recorded at a field of view of $45 \times 60 \mu\text{m}^2$ every 1/30 s using a high-sensitivity monochromatic digital video camera (Nikon WAT-120N). The temperature was set to 291 K to ensure that the solution was near criticality; see, e.g., refs 1 and 12. For preparation of the sample solution, triethylamine (TEA) and pure water were mixed in a volume ratio of 1:1. After vigorous mixing, the solution was allowed to stand for more than 1 h before the experiment. In Figure 1b, we have shown the visual images on the water and triethylamine solution, revealing the clear macroscopic phase separation when the solution has been standing still more than several

hours. By shaking the solution or mechanical agitation, the solution becomes turbid for the period of several tens of seconds, indicating the occurrence of microphase segregation. For the experiment of laser irradiation in the chamber, we transferred a part of TEA-rich phase (upper layer) from the well-separated solution (the panel of before mixing, Figure 1b) to the thin glass chamber in a fully occupied state with tight shielding from the outer environment (lateral view in Figure 1a). In the present study, we have examined the effect of spatial asymmetry on dynamic flow pattern. By adapting a very simple method to introduce spatial asymmetry, we placed a glass plate near the laser focus, as indicated in Figure 1a and the top picture of Figure 2.

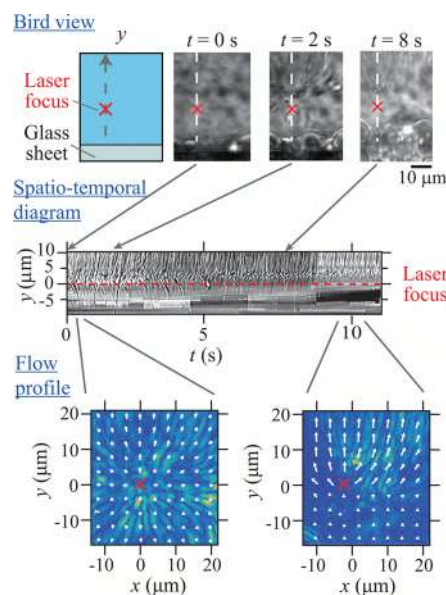


Figure 2. Spatiotemporal diagram for the water–TEA mixed solution (volume ratio, 1:1) from the start of laser irradiation, showing that microdroplets of water emerge continuously under situational laser irradiation. The images at the top show snapshots at $t = 0, 2,$ and 8 s. The emerging droplets tend to escape from the focus driven by the local increase in pressure near the region of droplet generation. The snapshots at the bottom exemplify flow patterns at different time-stages at 0.2 and 10 s, which were obtained by 2D FFT analysis. The flow velocity arrow was determined from the slopes of spatiotemporal diagrams with different geometrical directions.

Figure 2 shows the results of laser irradiation for a homogeneous solution that was allowed to equilibrate for more than 1 h, and the spatiotemporal diagram after the start of laser irradiation. The snapshots on the bottom of Figure 2 depict/illustrate the area around the laser focus at 0.2 and 10 s together with the corresponding flow profiles. Under laser irradiation, microdroplets successively emerge at the focus, and the generated droplets escape into the surrounding solution. Then, the droplets tend to merge into the solution and disappear. The driving force of the escaping motion around the laser focus is attributable to the gradient of dielectric potential together with scattering force, i.e., lower dielectricity, or refractivity, of emerging droplets with richer water content caused the repulsive effect from the laser focus as described in previous studies.^{4,5} The outgoing flow generally becomes asymmetric and transforms to directional flow after a few seconds (the bottom pictures in Figure 2). The flow profiles are depicted in 2D, which were obtained through a Fourier

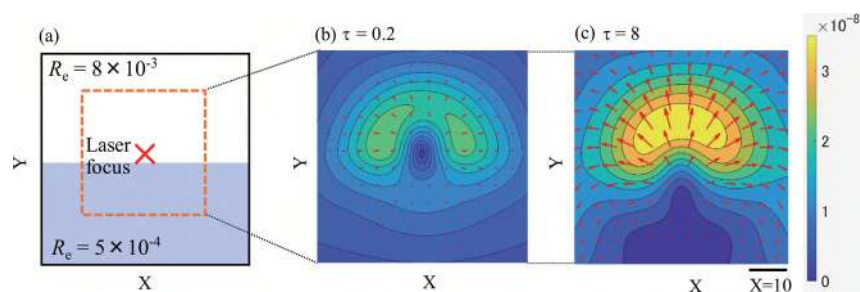


Figure 3. Numerical simulations on the flow pattern for a simplified 2D model. (a) The simulation was performed with a 2D square, $X = [-50, 50]$, $Y = [-50, 50]$, where the focus point is at $X = 0$, $Y = 5$, which are dimensionless values in calculations. To take into account the effect of geometrical asymmetry on depth, we adopted different Reynolds numbers, Re , as indicated in the figure: $Re = 8 \times 10^{-3}$ and $Re = 5 \times 10^{-4}$ for the upper and lower parts in the calculation region, respectively. (b) Snapshot of the flow pattern at $\tau = 0.2$. (c) Snapshot at $\tau = 8$. The region in orange corresponds to a square area around the laser spot with a width of 60.

image analysis. The time development of directional flow is found. The fluid velocity was evaluated on the basis of an analysis of the spatio-temporal dynamics by ImageJ/Matlab. For the initial radial symmetric flow ($t = 0-2$ s), the velocity in the positive direction along the y axis was $52 \pm 7 \mu\text{m/s}$ for the region around $5-10 \mu\text{m}$ from the focus and that in the negative direction was $47 \pm 14 \mu\text{m/s}$. For $t = 2-5$ s, the velocity in the positive direction along the y axis increased to ca. $100 \mu\text{m/s}$, whereas that between the boundary and laser focus, i.e., the negative direction, were not so different (positive directional flow $105 \pm 57 \mu\text{m/s}$ and negative directional flow $48 \pm 15 \mu\text{m/s}$). Interestingly, the flow velocity in the positive direction increased to ca. $180 \mu\text{m/s}$, for $t = 7-8$ s. Thus, we successfully constructed a micropump that increased the directed velocity of water droplets by more than 3-fold compared to the initial radial symmetric flow. In the present study, directional flow is induced by the combination of the photoinduced dielectric potential caused by the focused laser²⁹ and the geometrical asymmetry of the environment/boundary condition around the laser focus. On the basis of the results of past experimental studies concerning the effect of laser irradiation on to the mixed solution near critical condition of phase separation,^{4,11,19} it is expected that the dielectric potential caused by the focus laser is the main contributor to generate the microphase separation. For the homogeneous mixture between water and TEA under geometrically symmetric condition, it has been confirmed that essentially the same dynamical pattern of the droplets is observed with either H_2O and D_2O , or with a laser wavelength of either 800 and 1064 nm.¹⁸ Here, it is noted that the absorption of D_2O is less than 1/10 compared to H_2O at 1064 nm; i.e., the heating effect is significantly different between D_2O and H_2O , if one considers the microphase segregation as the main factor. It was also found that laser focusing on a microdroplet in a solution with lower critical solution temperature, LCST, causes disappearance or homogenization, i.e., the opposite effect against laser heating.¹⁹ In relation to the possible temperature effect, it was reported that a focused IR laser caused an apparent increase of the temperature on the laser spot, where the irradiation was performed for a homogeneous solution under negligible convective flow.³⁵ On the basis of these considerations, we conclude that the relatively fast fluid flow caused by the continuous emergence of droplets is attributable mainly to the dielectric effect by the focused laser.

To verify the experimental findings and pinpoint the essence of the underlying mechanisms, we examined the simple model shown in eq 1:

$$\frac{\partial \vec{u}}{\partial t} + (\vec{u} \cdot \nabla) \vec{u} = -\nabla p + \frac{1}{Re} \nabla^2 \vec{u} \quad (1)$$

where \vec{u} is the velocity of the fluid, p is the pressure, and Re is the Reynolds number. Here, we ignored the inertia term because of the low Reynolds number as mentioned below. To clarify the essential mechanism of directional flow in a simple manner, we reduce the dimensionality of the experimental system to two-dimensions by adapting the approximation that change in the effective Reynolds number for regions with different heights as in the lateral view in Figure 1a. Figure 3 exemplifies the numerical simulation with eq 1 under two-dimensional approximation. We adopted Reynolds numbers, Re , of 8×10^{-3} for the bulk solution in the fluid field and 5×10^{-4} for the local area, where the glass sheet was situated on the bottom of the glass chamber, as shown in the top view in Figure 1a. These values correspond to the experimental data determined from the observed viscosity of a water-triethylamine system.³⁶ We adapted a simple assumption that is the pressure at the laser focus linearly increases with reduced time from $\tau = 0$ to $\tau = 8$. The point with red "x" in Figure 3a was chosen as the laser focus on the simulation array of 100×100 in reduced length. The time step in calculations is set to 10^{-4} to ensure numerical stability, and the differential equation is solved by the cubic interpolated polynomial (CIP) method.³⁷ In Figure 3b,c are shown two snapshots of the flow dynamics at $\tau = 0.2$ and $\tau = 8$, respectively, close to the proximal area around the laser spot. These numerical results reproduce the essential aspect of the observed flow profiles in Figure 2 regardless the very simple approximation. Initially, isotropic flow escaping from the laser spot is observed, which gradually evolves into strongly anisotropic directed flow away from the boundary, as indicated by the vector-field. On the basis of the experiments and calculated results, we can conclude that the spatial asymmetry of viscosity is essential for creating strongly directed flow.

The present study has demonstrated the successful generation of directed flow by a continuous laser irradiation is achieved by introducing geometrical asymmetry in the experimental chamber. This self-establishing directional flow is regarded as a new type of light-driven micropump/motor, being difficult from the past studies.³⁸⁻⁴¹ The findings may also lead to the development of microsized pumps and motors that could not be engineered before on such a small scale. Further studies on the development of new optical pumps would be awaited to examine various liquidus system near criticality, which are composed of different kinds of chemical

species, together with the investigation toward more effective spatially asymmetric arrangements.^{42,43}

AUTHOR INFORMATION

Corresponding Author

*E-mail: keyoshik@mail.doshisha.ac.jp. Phone: +81-774-65-6243. Fax: +81-774-65-6243.

ORCID

Hiroki Sakuta: 0000-0001-8473-6370

Marcel Hörning: 0000-0001-8934-048X

Takahiro Kenmotsu: 0000-0002-6573-0974

Motomu Tanaka: 0000-0003-3663-9554

Kenichi Yoshikawa: 0000-0002-2751-7136

Notes

The authors declare no competing financial interest.

ACKNOWLEDGMENTS

The authors thank Dr. T. Kurimura for the advice on the numerical simulations. This work was supported by JSPS KAKENHI Grant Number 15H02121, 25103012 and 16K13655. H.S. received the support as Research Fellow of Japan Society for Promotion of Science.

REFERENCES

- (1) Cross, M. C.; Hohenberg, P. C. Pattern Formation Outside of Equilibrium. *Rev. Mod. Phys.* **1993**, *65*, 851–1112.
- (2) Safran, S. A. Statistical Thermodynamics of Surfaces, Interfaces, and Membranes; *Frontiers in Physics*; Addison-Wesley: Reading, MA, 1994; Vol. 90.
- (3) Onuki, A. *Phase Transition Dynamics*; Cambridge University Press: Cambridge, 2002.
- (4) Mukai, S.; Magome, N.; Kitahata, H.; Yoshikawa, K. Liquid/Liquid Dynamic Phase Separation Induced by a Focused Laser. *Appl. Phys. Lett.* **2003**, *83*, 2557–2559.
- (5) Mukai, S.; Kitahata, H.; Yoshikawa, K. Dynamical Phase Separation under Laser Scanning. *Chem. Phys. Lett.* **2005**, *402*, 529–534.
- (6) Schmidt, F.; Magazzu, A.; Callegari, A.; Biancofiore, L.; Cichos, F.; Volpe, G. Microscopic Engine Powered by Critical Demixing. *Phys. Rev. Lett.* **2018**, *120*, 068004.
- (7) Kitamura, N.; Yamada, M.; Ishizaka, S.; Konno, K. Laser-Induced Liquid-to-Droplet Extraction of Chlorophenol: Photothermal Phase Separation of Aqueous Triethylamine Solutions. *Anal. Chem.* **2005**, *77*, 6055–6061.
- (8) Yuyama, K.; Rungsimanon, T.; Sugiyama, T.; Masuhara, H. Formation, Dissolution, and Transfer Dynamics of a Millimeter-Scale Thin Liquid Droplet in Glycine Solution by Laser Trapping. *J. Phys. Chem. C* **2012**, *116*, 6809–6816.
- (9) Oana, H.; Kishimura, A.; Yonehara, K.; Yamasaki, Y.; Washizu, M.; Kataoka, K. Spontaneous Formation of Giant Unilamellar Vesicles from Microdroplets of a Polyion Complex by Thermally Induced Phase Separation. *Angew. Chem., Int. Ed.* **2009**, *48*, 4613–4618.
- (10) Buttinoni, I.; Volpe, G.; Kümmel, F.; Volpe, G.; Bechinger, C. Active Brownian Motion Tunable by Light. *J. Phys.: Condens. Matter* **2012**, *24*, 284129–284140.
- (11) Sadakane, K.; Kitahata, H.; Seto, H.; Yoshikawa, K. Rhythmic Oscillation and Dynamic Instability of Micrometer-Size Phase Separation under Continuous Photon Flux by a Focused Laser. *Phys. Rev. E* **2008**, *78*, 046214.
- (12) Bunkin, N. F.; Lobeyev, A. V. Light-Induced Phase Transitions in Stratifying Liquid Mixtures. *Colloids Surf., A* **1997**, *129–130*, 33–43.
- (13) Tsori, Y.; Tournilhac, F.; Leibler, L. Demixing in Simple Fluids Induced by Electric Field Gradients. *Nature* **2004**, *430*, 544–547.
- (14) Lalaude, C.; Delville, J. P.; Buil, S.; Ducasse, A. Kinetics of Crossover in Phase-Separating Liquid Mixtures Induced by Finite-Size Effects. *Phys. Rev. Lett.* **1997**, *78*, 2156–2159.
- (15) Ashkin, A. Acceleration and Trapping of Particles by Radiation Pressure. *Phys. Rev. Lett.* **1970**, *24*, 156–159.
- (16) Ashkin, A. Forces of a Single-Beam Gradient Laser Trap on a Dielectric Sphere in the Ray Optics Regime. *Biophys. J.* **1992**, *61*, 569–582.
- (17) Svoboda, K.; Block, S. M. Biological Applications of Optical Forces. *Annu. Rev. Biophys. Biomol. Struct.* **1994**, *23*, 247–285.
- (18) Delville, J. P.; Lalaude, C.; Ducasse, A. Kinetics of Laser-Driven Phase Separation Induced by a Tightly Focused Wave in Binary Liquid Mixtures. *Physica. A* **1999**, *262*, 40–68.
- (19) Toyama, H.; Yoshikawa, K.; Kitahata, H. Homogenization of a Phase-Separated Droplet in a Polymer Mixture Caused by the Dielectric Effect of a Laser. *Phys. Rev. E* **2008**, *78*, 068001.
- (20) Jun, I. K.; Hess, H. A Biomimetic, Self-Pumping Membrane. *Adv. Mater.* **2010**, *22*, 4823–4827.
- (21) Sengupta, S.; Patra, D.; Ortiz-Rivera, I.; Agrawal, A.; Shklyae, S.; Dey, K. K.; Córdova-Figueroa, U.; Mallouk, T. E.; Sen, A. Self-Powered Enzyme Micropumps. *Nat. Chem.* **2014**, *6*, 415–436.
- (22) Sengupta, S.; Spiering, M. M.; Dey, K. K.; Duan, W.; Patra, D.; Butler, P. J.; Astumian, R. D.; Benkovic, S. J.; Sen, A. DNA Polymerase as a Molecular Motor and Pump. *ACS Nano* **2014**, *8*, 2410–2418.
- (23) Magome, N.; Kitahata, H.; Ichikawa, M.; Nomura, S. M.; Yoshikawa, K. Rhythmic Bursting in a Cluster of Microbeads Driven by a Continuous-Wave Laser Beam. *Phys. Rev. E* **2002**, *65*, 045202.
- (24) Robert De Saint Vincent, M.; Chraïbi, H.; Delville, J. P. Optical Flow Focusing: Light-Induced Destabilization of Stable Liquid Threads. *Phys. Rev. Appl.* **2015**, *4*, 044005.
- (25) Wedershoven, H. M. J. M.; Berendsen, C. W. J.; Zeegers, J. C. H.; Darhuber, A. A. Infrared-Laser-Induced Thermocapillary Deformation and Destabilization of Thin Liquid Films on Moving Substrates. *Phys. Rev. Appl.* **2015**, *3*, 024005.
- (26) Song, C.; Moon, J. K.; Lee, K.; Kim, K.; Pak, H. K. Breathing, Crawling, Budding, and Splitting of a Liquid Droplet under Laser Heating. *Soft Matter* **2014**, *10*, 2679–2684.
- (27) Ivanova, N. A.; Starov, V. M.; Trybala, A.; Flyagin, V. M. Removal of Micrometer Size Particles from Surfaces Using Laser-Induced Thermocapillary Flow: Experimental Results. *J. Colloid Interface Sci.* **2016**, *473*, 120–124.
- (28) Lucchetta, D. E.; Simoni, F.; Nucara, L.; Castagna, R. Controlled-Motion of Floating Macro-Objects Induced by Light. *AIP Adv.* **2015**, *5*, 077147–077151.
- (29) Hanczyc, M. M. Droplets: Unconventional Protocell Model with Life-Like Dynamics and Room to Grow. *Life* **2014**, *4*, 1038–1049.
- (30) Yehoshua, S.; Pollari, R.; Milstein, J. N. Axial Optical Traps: A New Direction for Optical Tweezers. *Biophys. J.* **2015**, *108*, 2759–2766.
- (31) Takabatake, F.; Yoshikawa, K.; Ichikawa, M. Mode Bifurcation of Droplet Motion under Stationary Laser Irradiation. *J. Chem. Phys.* **2014**, *141*, 051103–051106.
- (32) Bergen, A.; Rudiuk, S.; Morel, M.; Le Saux, T.; Ihmels, H.; Baigl, D. Photodependent Melting of Unmodified DNA Using a Photosensitive Intercalator: A New and Generic Tool for Photo-reversible Assembly of DNA Nanostructures at Constant Temperature. *Nano Lett.* **2016**, *16*, 773–780.
- (33) Wang, Y.; Zhang, Q.; Zhu, Z.; Lin, F.; Deng, J.; Ku, G.; Dong, S.; Song, S.; Alam, M. K.; Liu, D. Laser Streaming: Turning a Laser Beam into a Flow of Liquid. *Sci. Adv.* **2017**, *3*, e1700555.
- (34) Kubota, R.; Yamashita, Y.; Kenmotsu, T.; Yoshikawa, Y.; Yoshida, K.; Watanabe, Y.; Imanaka, T.; Yoshikawa, K. Double-Strand Breaks in Genome-Sized DNA Caused by Ultrasound. *ChemPhysChem* **2017**, *18*, 959–964.
- (35) Ito, S.; Sugiyama, T.; Toitani, N.; Katayama, G.; Miyasaka, H. Application of Fluorescence Correlation Spectroscopy to the

Measurement of Local Temperature in Solutions Under Optical Trapping Condition. *J. Phys. Chem. B* **2007**, *111*, 2365–2371.

(36) Vitagliano, V.; Sartorio, R.; Chiaravalle, E.; Ortona, O. Diffusion and Viscosity in Water-Triethylamine Mixtures at 19 and 20 °C. *J. Chem. Eng. Data* **1980**, *25*, 121–124.

(37) Banijamali, B.; Bathe, K.-J. The CIP Method Embedded in Finite Element Discretizations of Incompressible Fluid Flows. *Int. J. Numer. Meth. Eng.* **2007**, *71*, 66–80.

(38) Mourran, A.; Zhang, H.; Vinokur, R.; Möller, M. Soft Microrobots Employing Nonequilibrium Actuation via Plasmonic Heating. *Adv. Mater.* **2017**, *29*, 1604825–1604832.

(39) Chen, H.; Zhao, Q.; Du, X. Light-Powered Micro/Nanomotors. *Micromachines* **2018**, *9*, 41–58.

(40) Xu, L.; Mou, F.; Gong, H.; Luo, M.; Guan, J. Light-Driven Micro/Nanomotors: From Fundamentals to Applications. *Chem. Soc. Rev.* **2017**, *46*, 6905–6926.

(41) ten Hagen, B.; Kümmel, F.; Wittkowski, R.; Takagi, D.; Löwen, H.; Bechinger, C. Gravitaxis of Asymmetric Self-Propelled Colloidal Particles. *Nat. Commun.* **2014**, *5*, 4829.

(42) Thomson, J. A.; Schurtenberger, P.; Thurston, G. M.; Benedek, G. B. Binary Liquid Phase Separation and Critical Phenomena in a Protein/Water Solution. *Proc. Natl. Acad. Sci. U. S. A.* **1987**, *84*, 7079–7083.

(43) Koningsveld, R.; Staverman, A. Liquid-Liquid Phase Separation in Multicomponent Polymer Solutions. II. The Critical State. *J. Polym. Sci., Part A* **1968**, *6*, 325–347.

Helical micromotor operating under stationary DC electrostatic field

Cite as: J. Chem. Phys. **150**, 014901 (2019); <https://doi.org/10.1063/1.5055830>

Submitted: 11 September 2018 . Accepted: 13 November 2018 . Published Online: 02 January 2019

Daigo Yamamoto, Kento Kosugi, Kazuya Hiramatsu, Wenyu Zhang, Akihisa Shioi, Kaori Kamata, Tomokazu Iyoda, and Kenichi Yoshikawa 



View Online



Export Citation



CrossMark

ARTICLES YOU MAY BE INTERESTED IN

[Activated micromotor propulsion by enzyme catalysis in a biofluid medium](#)

Applied Physics Letters **114**, 053701 (2019); <https://doi.org/10.1063/1.5081751>

[Tubular catalytic micromotors in transition from unidirectional bubble sequences to more complex bidirectional motion](#)

Applied Physics Letters **114**, 033701 (2019); <https://doi.org/10.1063/1.5059354>

[Hybrid BioMicromotors](#)

Applied Physics Reviews **4**, 031301 (2017); <https://doi.org/10.1063/1.4993441>

Lock-in Amplifiers
up to 600 MHz



Watch



Helical micromotor operating under stationary DC electrostatic field

Cite as: J. Chem. Phys. 150, 014901 (2019); doi: 10.1063/1.5055830

Submitted: 11 September 2018 • Accepted: 13 November 2018 •

Published Online: 2 January 2019



View Online



Export Citation



CrossMark

Daigo Yamamoto,^{1,a)} Kento Kosugi,¹ Kazuya Hiramatsu,¹ Wenyu Zhang,¹ Akihisa Shioi,¹ Kaori Kamata,² Tomokazu Iyoda,³ and Kenichi Yoshikawa⁴ 

AFFILIATIONS

¹Department of Chemical Engineering and Materials Science, Doshisha University, Kyoto 610-0321, Japan

²Division of Chemistry, School of Medicine, National Defense Medical College, Saitama 359-8513, Japan

³Harris Science Research Institute, Doshisha University, Kyoto 610-0321, Japan

⁴Faculty of Life and Medical Sciences, Doshisha University, Kyoto 610-0394, Japan

^{a)}Author to whom correspondence should be addressed: dyamamot@mail.doshisha.ac.jp

ABSTRACT

The direct current (DC) motor is a rotary device that converts DC electrical energy into mechanical energy. However, it is known that, in downsizing the currently available macromotor, rotary motion of DC micromotors cannot work well due to the larger viscous effect. Here, we report simple DC micromotors working under a new principle. We previously revealed that in an oil phase containing an ionic surfactant, non-spherical particles exhibit various types of regular motions such as spinning and circular orbital motions. In this study, we found that a microhelix exhibits a new type of periodic motion, namely, the cork-screw-type rotation, in a specific direction depending on the material of the helix, metal or non-metallic organics. The results show that a left-handed nickel helix rotates in the clockwise direction when viewed from the positive electrode, whereas an organic one rotates in the opposite direction (anti-clockwise) under the same electrode arrangement with stationary constant DC voltage. In addition, we demonstrate that the cork-screw rotation is switched to opposite direction by changing the handedness (chirality). It is to be noted that the micromotors reported here maintain their stable motion without any mechanical support such as rotational axes or electronic switching devices. The invented DC micromotor would be applicable for mechanical and fluidic devices, being useful as a smart device in microrobots and microfluidics.

Published under license by AIP Publishing. <https://doi.org/10.1063/1.5055830>

I. INTRODUCTION

Recent advancements in micro-electromechanical systems (MEMS) have led to increased attention toward microdevices such as microrobots and microfluidics, which have various applications in biotechnology and nanotechnology. In practice, submillimeter-sized motors or pumps working in a microspace can be used for propelling solid as well as liquid materials.¹⁻³ These micromotors must exhibit high performance in fluids with extremely low Reynolds number, wherein viscous forces dominate the motion instead of inertia ($Re \ll 1$).⁴ This is remarkably different from conditions under which currently available macroscopic electronic motors and other mechanical machines operate. The significant effects of viscosity and friction pose difficulties in downsizing currently available motors or pumps.

During the last decade, several studies have attempted to construct micromotors based on various types of mechanisms such as chemical,⁵⁻⁷ magnetic,⁸⁻¹¹ electric [under an alternating current (AC) field],¹²⁻¹⁴ optical,^{15,16} and ultrasound^{17,18} propulsion. However, stable and sustainable motions have not been demonstrated in most of the currently reported micromotor systems because of the fluctuating effect of the Brownian motion. This has prompted various groups to attempt strict directional control using a spatially confined field^{4,19} or with the help of a temporal external force.²⁰⁻²²

It has been reported that a water-in-oil microdroplet exhibits bouncing motion under a direct current (DC) electric field.²³⁻²⁵ Subsequently, several research groups have attempted to control the motion of a water droplet.²⁶ However, non-spherical, asymmetric particles, instead of

water, have exhibited unique rotations about the center of gravity. Recently, we found that an assembly with a small number of solid microspheres exhibits spin and rotation depending on their shape and applied voltage.²⁷ In this paper, we attempt to develop a micromotor system using geometrically chiral micro-objects. We report the successful construction of a stable rotating system with helical objects under a stationary DC voltage.

II. EXPERIMENTAL

Spiral blue-green algae, namely, *Spirulina*, were cultured in 500 ml of typical *Spirulina*-Ogawa-Terui (SOT) media³³ until a concentration of 10^5 *Spirulina* per 1 ml was reached. The preparation process of both right- and left-handed *Spirulina* and the control of the spiral pitch were carried out as previously reported.²⁸ The *Spirulina* in the SOT medium was filtered using a filter fabric with 355 mesh and was then dispersed into 100 ml of phosphate buffer solution (PBS, pH = 7.0). An 8 ml glutaraldehyde aqueous solution (50%) was added to fix the tissue of *Spirulina* with individual spiral features. The solvent was replaced by ethanol and later with *tert*-butyl alcohol (TBA) in repeated collection/dispersion cycles. The *Spirulina* solution was lyophilized in a TBA freeze dryer (VFD-21S, Vacuum Device Co., Ltd.). The resulting dried powder consisted of *Spirulina* with preserved original spiral features, which were used as the organic microhelices.

The fixed *Spirulina* was applied to the biotemplating process using nickel electroless plating. *Spirulina* (20 ml) fixed in a glutaraldehyde-PBS mixed solution with an average *Spirulina* concentration of 10^5 ml⁻¹ was used for one batch. Electroless plating of the nickel onto the *Spirulina* surface was performed using commercial products from Okuno Chemical Industries Co., Ltd.; OPC-370 Condiclean MA was used for the pre-dip treatment; OPC-50 series was used for the surface catalyzation; the Top Chem Alloy series was used for nickel deposition. Every plating bath was prepared for 1 liter to adjust the bath load as 200 cm²/l. The *Spirulina*-templated nickel microhelices were stored in distilled water overnight and collected using a membrane filter, yielding approximately two million microhelices (80 mg in weight, 80% yield).

The experimental setup was reported previously and is briefly described below. A sample of silicone oil (KF-56, Shinetsu Co.) containing microhelices was placed on a glass slide. Cone-shaped tungsten electrodes (Unique Medial Co., Ltd.) were inserted into the oil. The electrodes were placed at the same horizontal level but in a non-coaxial arrangement (see Fig. S1 in [supplementary material](#)). A constant voltage was applied across the particles between the electrodes. The particles were dispersed in the silicone oil by adding a surfactant, di-(2-ethylhexyl) phosphate (0.5M) (Aldrich Chemical Co.), followed by agitation using a vortex mixer for approximately 1 min. We observed the movement of the microhelices at room temperature (20–25 °C) using an optical microscope (Olympus IX71, Olympus Co.).

Figure S2 shows the experimental setup, wherein an acrylic tube is connected to a water pipe. A hand-made vinyl-coated wire helix was placed in the tube. To maintain the position of the helix, it was tied to a thread hanging from the water pipe (upper stream side). Water was then poured into the tube from the pipe.

III. RESULTS AND DISCUSSIONS

Figure 1 shows the four types of helical micromotors prepared using a biotemplating process.²⁸ We study the motions of the prepared materials, which exhibit chiral asymmetry, i.e., handedness [left-hand (LH) or right-hand (RH)]. Figure 2(a) shows the typical setup of the proposed helical micromotor system, wherein an LH nickel microhelix dispersed in silicon oil containing di-(2-ethylhexyl) phosphate rotates in a particular direction between two electrodes. This motion is termed “cork-screw rotation,” which is an inherent mode for helices. Interestingly, the microhelix maintains its position without any support from mechanical devices though a cork-screw rotation can often lead to translation in helical motile systems such as micro-organisms²⁹ and micromotors.^{9,30} In this article, the spinning direction is defined as the direction in which the shaft rotates when viewed from the electrode (mainly positive electrode) shown at the right corners of Fig. 2(b) and

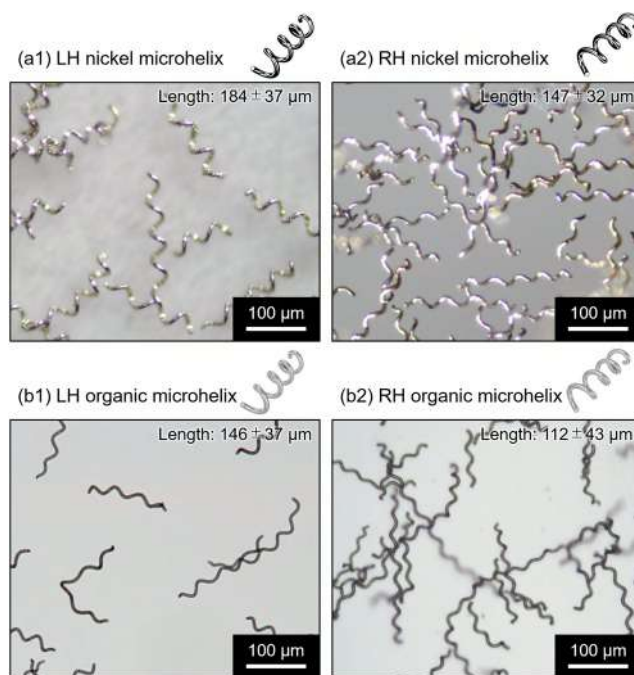


FIG. 1. Microscopic images of the prepared (a) nickel and (b) organic microhelices. They have chirality (handedness): (1) left-handed (LH) and (2) right-handed (RH). Each sample of helices is a little polydispersed as shown in upper right corner in each figures. We used helices with the length between 150 and 200 μm selectively in the experiment of a DC micromotor system because a smaller helix (length: $<100 \mu\text{m}$) tends to not cork-screw motion but revolution motion similar to a spherical particle.²⁷

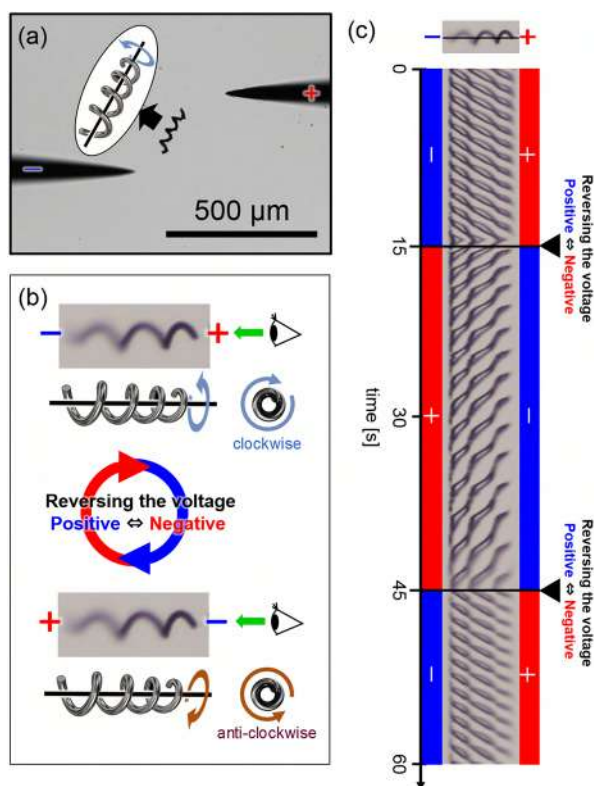


FIG. 2. Microhelices exhibiting cork-screw rotation. (a) Typical setup of the proposed helical micromotor system working under a DC field. When an LH nickel microhelix is placed between electrodes, it rotates in the clockwise direction when viewed from the positive electrode. (b) Scheme and (c) space-time plot of the rotation by reversing the applied voltage (140 V).

Fig. S1 in the [supplementary material](#) (or the lower part in Video S1).

According to this definition, the spinning direction of the helix, shown in Fig. S3, is anti-clockwise. The spinning direction can also be determined from the space-time plot, as shown in Fig. 2(c). The plot is prepared along the central axis of the helix [black line in the upper snapshot of Fig. 2(c)], showing a right-down stripe pattern during the time interval of 0–15 s. This demonstrates that the helix rotates in the clockwise direction. On the contrary, the helix can spin in the opposite direction (anti-clockwise) by reversing the voltage (positive ↔ negative). The plot for the time interval of 15–45 s exhibits a right-up stripe pattern. Furthermore, we can evaluate the spinning speed by measuring the intervals of the stripe. In this experiment, the speed is in the range of 20–50 rotations per minute (rpm).

To examine the influence of the applied voltage on the cork-screw motion, we observed the spinning motion as a function of the applied voltage. Figure 3(a) shows the space-time plot of the LH nickel helix under various applied voltages. When the voltage is above a certain threshold, the

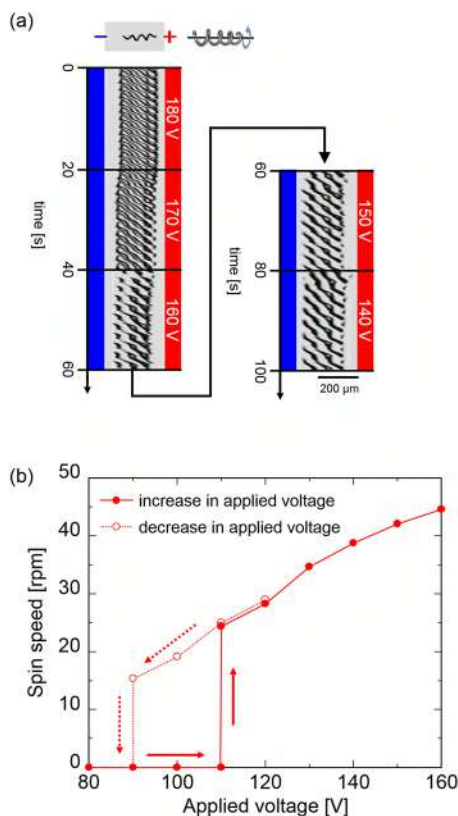


FIG. 3. Dependency of the applied voltage on cork-screw rotation of LH nickel helices. (a) Space-time plot of cork-screw motion, obtained by changing the applied voltage every 20 s and (b) variation in the spinning speed with respect to the applied voltage. Note that the results of (a) and (b) are obtained from different trials because of technical reasons. We observed the same helix at voltage intervals of 10 V.

speed of cork-screw rotation (frequency) is higher with an increase in the applied voltage; however, with a hysteresis, the threshold voltage (rest ↔ cork-screw motion) depends on the voltage between increasing and decreasing the applied voltage phases, as shown in Fig. 3(b). Existence of such kind of hysteresis suggests that the transition between the stationary state and rhythmic motion is attributable to “sub-critical bifurcation” on a nonlinear dynamical system. As for the essence of the occurrence of sub-critical bifurcation under DC field, we have discussed the underlying mechanism in our earlier articles.^{23,24} It is also noted that similar transition, or sub-critical bifurcation, also appears on the other types of motion, rotation and spinning, with assembly of microspheres.²⁷ We found that the speed and direction of the cork-screw motion can be easily controlled by tuning the voltage.

Another interesting characteristic of the proposed helical micromotors is that the spinning direction depends on the physical property of the materials. Figure 4 shows the cork-screw rotations of the conductive (nickel) and dielectric

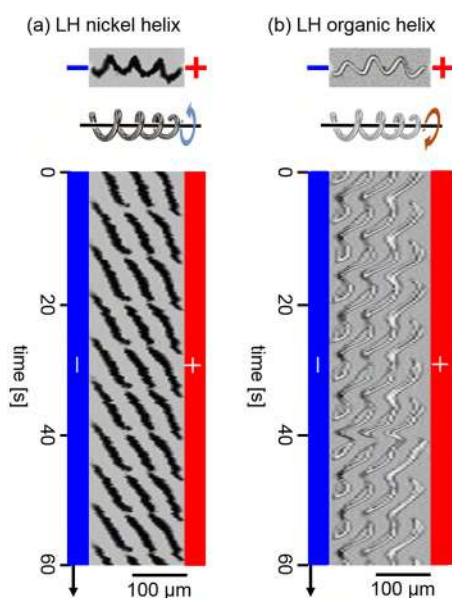


FIG. 4. Spinning direction of cork-screw rotation with respect to the type of microhelix material. The space-time plots of (a) nickel and (b) organic microhelices demonstrate that they rotate in opposite directions. Both samples are left-handed (LH).

(organic) microhelices. Although both the samples are left-handed and a positive electrode exists at the right-hand side, the spinning directions are opposite. The nickel helix rotates in the clockwise direction, whereas the organic one rotates in the opposite direction (anti-clockwise). In addition, we examined the relationship between the spinning direction and the properties of the helices by varying the handedness (LH or RH) of the nickel and organic helices. The experiment was carried out twenty times for each helix. As listed in Table I, the cork-screw directions of the helices depend on the material and handedness. In general, the LH nickel and organic helices spin in clockwise and anti-clockwise directions, respectively. However, the spinning directions of the corresponding RH helices are opposite to those of the corresponding LH helices.

The flow induced in the medium was visualized using carbon tracer powder under a DC voltage to investigate the mechanism of cork-screw rotation. Figure 5(a) shows the flow line maps obtained using particle image velocimetry (PIV) for the nickel and organic microhelices. The nickel helix induces flow from the positive electrode to the negative one, whereas the flow induced by the organic helix is opposite to this.

TABLE I. Relationship between helical properties (materials and handedness) and spinning direction.

Material/Handedness	LH (left-handed)	RH (right-handed)
Nickel	Clockwise	Anti-clockwise
Organic	Anti-clockwise	Clockwise

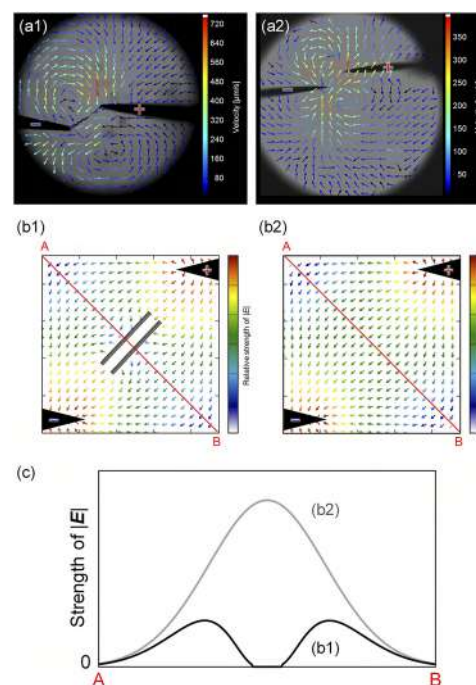


FIG. 5. Experimental and theoretical analysis of the flow around the microhelices. (a) Flow line maps (experimental) and (b) electric force diagram (calculation) between electrodes under DC voltage. Experiment and calculation were carried out (1) with a nickel microhelix and (2) with an organic microhelix (or without any helix). For the electric field calculation, the conductive helix is simplified with a cylindrical object. The color and direction of the vector represent the relative strength of $|E|$ and the direction of the electrical flux line φ , respectively. (c) Electric field strength along the red diagonal line from A to B in (b).

We also confirm that the flow direction does not depend on the handedness of the helices. These results show that the electrical property and handedness of micromotors have a definite influence on the flow pattern, which drives the micromotor.

The electrophoresis of ionic surfactants in bulk may have caused the flow. We confirmed that di-(2-ethylhexyl) phosphate, which is an anionic surfactant, causes flow from the negative electrode to the positive one without any helices. We had previously observed an opposite flow when an anionic surfactant was replaced by a cationic one (bis-2-ethylhexyl amine).³¹ This raises a question as to why the nickel helix system induces a flow from the positive electrode to the negative one, especially when the solvent contains an anionic surfactant. This may be a result of the perturbation of the electric lines of force induced by the conductive material between the electrodes. From the electric field calculation using Laplace's equation ($\Delta\varphi = 0$; see Calculation Procedure in the supplementary material), the electric field is distorted and is low in and around the nickel helix [Figs. 5(b) and 5(c)]. On the other hand, the electric field strength along the axis between the electrode tips is the highest when the organic helix is employed. This strength is largely the same as that without the

helixes if the electric permittivity of the microhelix is largely the same as that of silicon oil. Thus, for the organic helix, the main flow caused by the anionic surfactants develops simply from the negative electrode to the positive one. By contrast, for the nickel helix, the main flow line is in the form of an arc outside the helix, from the negative to the positive electrode, leading to an opposite, compensation flow in and around the helix.

One of the authors had demonstrated that the external force causes a torque to act on the chiral object, which determines the spinning direction.³² To confirm the relationship between the flow direction and the direction of cork-screw rotation, we used hand-made centimeter-sized wire helixes and observed the cork-screw direction under water flow (Fig. S4 and Video S2 in the [supplementary material](#)). The conditions of (a) left and (b) right panels correspond to a nickel helix system and an organic helix system, respectively. We found that the flow and cork-screw directions of the helixes are strongly correlated. This correlation is identical to the results of microhelixes.

IV. CONCLUSION

The proposed, novel helical micromotor exhibits inherent cork-screw rotation under a constant DC field. The motion is propelled by characteristic directional flows. Interestingly, the direction of the flow depends on materials, conductive or dielectric, of the helixes between electrodes, which is attributable to distortion of electric fields. We conclude that the switching of the flow direction causes the inversion of cork-screw rotation.

Currently, the required voltage is high (>100 V). However, downsizing the system may lower this value because the electric field strength depends on the distance between the electrodes. We previously reported that the periodic motion of a water droplet can be generated at a DC voltage below 10 V when the distance between the electrodes is reduced to the order of 10 μm .²⁴ Thus, our micromotor can be applied to microdevices, such as microrobots and microfluidics, because the direction and speed of the cork-screw motion can be easily tuned by adjusting the chirality and materials of the micromotors as well as the applied voltage.

SUPPLEMENTARY MATERIAL

See [supplementary material](#) for the procedure for calculating the electric force diagram (4 figures and 2 videos).

ACKNOWLEDGMENTS

We thank Professor S. Fujii for collaborating on previous studies. We also thank S. Mori and J. Sakuda (Doshisha University) for their cooperation in performing the experiments. We also thank Professor K. Tsuchiya and N. Umemura (Doshisha University) for the PIV analysis. We also thank I.

Kakimoto (Doshisha University) for the particle size measurement. This work was supported in part by a Grant-in-Aid for Young Scientists (A) (Grant No. 16H06125), Scientific Research (A) (Grant No. 15H02121), Scientific Research (B) (Grant No. 16H04189), Scientific Research (C) (Grant No. 25420751), Scientific Research on Innovative Areas (Grant No. 25103012), and Coordination Asymmetry (Grant No. JP16H06515) from the Japan Society for the Promotion of Science (JSPS). This work was also supported by the MEXT-Supported Program for the Strategic Research Foundation at Private Universities (2015-2019).

REFERENCES

- 1Z. Insepov, D. Wolf, and H. Ahmed, *Nano Lett.* **6**, 1893 (2006).
- 2R. E. Tuzun, D. W. Noid, and B. G. Sumpter, *Nanotechnology* **6**, 52 (1995).
- 3J. Wang and W. Gao, *ACS Nano* **6**, 5745 (2012).
- 4D. Yamamoto and A. Shioi, *KONA Powder and Part. J.* **32**, 2 (2015).
- 5W. F. Paxton, K. C. Kistler, C. C. Olmeda, A. Sen, S. K. St. Angelo, Y. Cao, T. E. Mallouk, P. E. Lammert, and V. H. Crespi, *J. Am. Chem. Soc.* **126**, 13424 (2004).
- 6D. Yamamoto, A. Mukai, N. Okita, K. Yoshikawa, and A. Shioi, *J. Chem. Phys.* **139**, 034705 (2013).
- 7D. Yamamoto, T. Takada, M. Tachibana, Y. Iijima, A. Shioi, and K. Yoshikawa, *Nanoscale* **7**, 13186 (2015).
- 8W. Gao, S. Sattayasamitsathit, K. Manian Manesh, D. Weihs, and J. Wang, *J. Am. Chem. Soc.* **132**, 14403 (2010).
- 9S. Tottori, L. Zhang, F. Qiu, K. K. Krawczyk, A. Franco-Obregón, and B. J. Nelson, *Adv. Mater.* **24**, 811 (2012).
- 10L. Zhang, T. Petit, Y. Lu, B. E. Kratochvil, K. E. Peyer, R. Pei, J. Lou, and B. J. Nelson, *ACS Nano* **4**, 6228 (2010).
- 11J. Vialletto, M. Hayakawa, N. Kavokine, M. Takinoue, S. N. Varanakkottu, S. Rudiuk, M. Anyfantakis, M. Morel, and D. Baigl, *Angew. Chem., Int. Ed.* **56**, 16565 (2017).
- 12P. Calvo-Marzal, S. Sattayasamitsathit, S. Balasubramanian, J. R. Windmiller, C. Dao, and J. Wang, *Chem. Commun.* **46**, 1623 (2010).
- 13S. T. Chang, V. N. Paunov, D. N. Petsev, and O. D. Velev, *Nat. Mater.* **6**, 235 (2007).
- 14S. Gangwal, O. J. Cayre, M. Z. Bazant, and O. D. Velev, *Phys. Rev. Lett.* **100**, 058302 (2008).
- 15Z. P. Luo, Yu L. Sun, and K. N. An, *Appl. Phys. Lett.* **76**, 1779 (2000).
- 16N. K. Metzger, M. Mazilu, L. Kelemen, P. Ormos, and K. Dholakia, *J. Opt.* **13**, 044018 (2011).
- 17D. Kagan, M. J. Benchimol, J. C. Claussen, E. Chuluun-Erdene, S. Esener, and J. Wang, *Angew. Chem., Int. Ed.* **51**, 7519 (2012).
- 18W. Wang, L. A. Castro, M. Hoyos, and T. E. Mallouk, *ACS Nano* **6**, 6122 (2012).
- 19Y. Sumino, N. Magome, T. Hamada, and K. Yoshikawa, *Phys. Rev. Lett.* **94**, 068301 (2005).
- 20J. Burdick, R. Laocharoensuk, P. M. Wheat, J. D. Posner, and J. Wang, *J. Am. Chem. Soc.* **130**, 8164 (2008).
- 21T. R. Kline, W. F. Paxton, T. E. Mallouk, and A. Sen, *Angew. Chem., Int. Ed.* **44**, 744 (2005).
- 22G. Zhao and M. Pumera, *Langmuir* **29**, 7411 (2013).
- 23M. Hase, S. N. Watanabe, and K. Yoshikawa, *Phys. Rev. E* **74**, 046301 (2006).
- 24T. Kurimura, M. Ichikawa, M. Takinoue, and K. Yoshikawa, *Phys. Rev. E* **88**, 042918 (2013).
- 25M. Takinoue, Y. Atsumi, and K. Yoshikawa, *Appl. Phys. Lett.* **96**, 104105 (2010).
- 26DoJ. Im, *Korean J. Chem. Eng.* **32**, 1001 (2015).
- 27D. Yamamoto, R. Yamamoto, T. Kozaki, A. Shioi, S. Fujii, and K. Yoshikawa, *Chem. Lett.* **46**, 1470 (2017).

²⁸K. Kamata, Z. Piao, S. Suzuki, T. Fujimori, W. Tajiri, K. Nagai, T. Iyoda, A. Yamada, T. Hayakawa, M. Ishiwara, S. Horaguchi, A. Belay, T. Tanaka, K. Takano, and M. Hangyo, *Sci. Rep.* **4**, 4919 (2014).

²⁹H. C. Berg and R. A. Anderson, *Nature* **245**, 380 (1973).

³⁰W. Gao, X. Feng, A. Pei, C. R. Kane, R. Tam, C. Hennessy, and J. Wang, *Nano Lett.* **14**, 305 (2014).

³¹T. Kurimura, S. Mori, M. Miki, and K. Yoshikawa, *J. Chem. Phys.* **145**, 034902 (2016).

³²T. Harada and K. Yoshikawa, *Appl. Phys. Lett.* **81**, 4850 (2002).

³³T. Ogawa and G. Terui, in *Proceedings of the 4th International Fermentation Symposium on Fermentation Technology Today* (Society of Fermentation Technology, Osaka, 1972), p. 543.



Aqueous/Aqueous Micro Phase Separation: Construction of an Artificial Model of Cellular Assembly

Hiroki Sakuta¹, Tadashi Fujimoto¹, Yusuke Yamana¹, Yusuke Hoda¹, Kanta Tsumoto^{2*} and Kenichi Yoshikawa¹

¹ Graduate School of Life and Medical Sciences, Doshisha University, Kyoto, Japan, ² Division of Chemistry for Materials, Graduate School of Engineering, Mie University, Tsu, Japan

OPEN ACCESS

Edited by:

John Paul Frampton,
Dalhousie University, Canada

Reviewed by:

Li Liu,
Osaka University, Japan
Xin Huang,
Harbin Institute of Technology, China
Ryugo Tero,
Toyohashi University of Technology,
Japan

*Correspondence:

Kanta Tsumoto
tsumoto@chem.mie-u.ac.jp

Specialty section:

This article was submitted to
Chemical Engineering,
a section of the journal
Frontiers in Chemistry

Received: 10 August 2018

Accepted: 16 January 2019

Published: 01 February 2019

Citation:

Sakuta H, Fujimoto T, Yamana Y,
Hoda Y, Tsumoto K and Yoshikawa K
(2019) Aqueous/Aqueous Micro
Phase Separation: Construction of an
Artificial Model of Cellular Assembly.
Front. Chem. 7:44.
doi: 10.3389/fchem.2019.00044

To artificially construct a three-dimensional cell assembly, we investigated the availability of long-duration microdroplets that emerged near a critical point in an aqueous two-phase system (ATPS) with the hydrophilic binary polymers, polyethylene glycol (PEG), and dextran (DEX), as host containers. We found that erythrocytes (horse red blood cells; RBCs) and NAMRU mouse mammary gland epithelial cells (NMuMG cells) were completely and spontaneously entrapped inside DEX-rich microdroplets. RBCs and NMuMG cells were located in the interior and at the periphery of the droplets at PEG/DEX = 5%:5%. In contrast, the cells exhibited opposite localizations at PEG/DEX = 10%:5%, where, interestingly, NMuMG cells apparently assembled to achieve cell adhesion. We simply interpreted such specific localizations by considering the alternative responses of these cells to the properties of the PEG/DEX interfaces with different gradients in polymer concentrations.

Keywords: aqueous two-phase system, microdroplet, phase separation, cell assembly, red blood cell, epithelial cell, polyethylene glycol, dextran

INTRODUCTION

Living organisms exhibit the self-organization of cells and intracellular organelles in a self-consistent manner. For decades, biochemical studies have unveiled the mechanisms that underlie such regulatory systems at the molecular level. Many macromolecules including nucleic acids and proteins are considered to act in a well-orchestrated manner to express biological functions, by building sophisticated structures under the specific interaction of gene products. On the other hand, it is also considered that even a single-cell system cannot be completely controlled through specific key-lock interactions. In these situations, the self-organization, or self-assembly, of biomolecules is indispensable for the development of various ordered structures, like phospholipid bilayers for cell membranes. Recently, it has been reported that membraneless organelles may arise from the micro phase separation of cytosols, which generates submicron-scale liquid droplets containing proteins and RNAs (Brangwynne, 2013; Courchaine et al., 2016). Since intracellular environments are highly crowded by such macromolecules, the emergence of liquid/liquid phase separation (LLPS) on a microscopic scale is a ubiquitous phenomenon inside living cells (Walter and Brooks, 1995; Spitzer and Poolman, 2013; Rivas and Minton, 2016; Uversky, 2017).

Along these lines, many pioneering researchers have tried to model cellular and intracellular microcompartments by simply using an aqueous two-phase system (ATPS) consisting of solutions with hydrophilic polymers that exhibit LLPS on a micro-scale (Aumiller and Keating, 2017). There are both some similarities and differences in

the properties of micro phase separation between *in vitro* ATPS droplets and actual protein/nucleic acid-based droplets (Zaslavsky et al., 2018). Polyethylene glycol (PEG), a flexible polymer, and dextran (DEX), a semi-flexible polymer, are popularly selected for the preparation of a typical ATPS (Esquena, 2016). Upon the vigorous mixing of a PEG/DEX solution, aqueous/aqueous (water-in-water) microdroplets are transiently formed, and various biomolecules and even inorganic materials can be partitioned into, or excluded from, these droplets, due to the chemical and morphological characteristics of the substances partitioned (Akbulut et al., 2012; Jia et al., 2014; Vis et al., 2015). Generally, this behavior of LLPS droplets is sharp (Nott et al., 2016), and could be associated with the origin of life and prebiotic functions (Poudyal et al., 2018). Originally, ATPSs with various hydrophilic polymers, in addition to the above PEG/DEX, have been developed to extract molecules and supramolecules from biological materials (Albertsson, 1971). Their simplicity makes them suitable for harboring functional proteins and living cells. For example, these microdroplets have been used to promote interaction between entrapped proteins to achieve their alignment (Monterroso et al., 2016; Song et al., 2018). Previously, we have reported DNA entrapment (Tsumoto et al., 2015), the formation of microparticles by crosslinking proteins (Tsumoto and Yoshikawa, 2017), and the selective entrapment of filamentous actin (F-actin) and subdomain formation with dsDNAs and F-actin proteins, inside PEG/DEX microdroplets (Nakatani et al., 2018).

ATPS is known as a useful system to get selective partition on various biomacromolecules, DNAs, proteins, etc., under certain compositions of polymers. As has been indicated by Albertsson (1971), previous literatures reveal a large number of phase diagrams for the phase separation of binary or more-component polymer solutions. The ATPS with PEG/DEX is popular in biochemical and biophysical research, and we previously used this system to investigate the dynamics (time-course development) of phase segregation of micro-scale regions (Toyama et al., 2008), as well as the specific localization of DNAs and proteins, such as the cytoskeletal protein actin (Tsumoto et al., 2015; Nakatani et al., 2018). In these studies, we observed aqueous/aqueous (water-in-water) microdroplets with an average diameter of $\sim 10\text{--}100\ \mu\text{m}$. Importantly, the droplets are stably generated and remain after vigorous mixing using a vortex mixer, etc., near the critical point in a phase diagram, because there is only a very small difference in density between the phases containing the two polymers in addition to the weak surface tension, which are unique characteristics of a polymer solution.

Compared to bulk ATPS, the above mentioned aqueous/aqueous microdroplet is suitable for microscopic observation; therefore, we can frequently observe intriguing phenomena with biological macromolecules only when these molecules are encapsulated within such microcompartments. For example, interestingly, actin proteins apparently change their preferred location (distributed evenly, encapsulated within the interior, and adhered to the inner surface) in droplets in PEG/DEX ATPS as their higher-ordered structure changes from monomeric (G-actin) through polymeric (F-actin) to bundled

actin (Nakatani et al., 2018). DNAs and F-actin entrapped simultaneously exclude each other to form subdomains inside the droplets. Thus, generally, biopolymers with semi-flexible and rigid chains are usually excluded from the PEG-rich exterior environment to the interior of DEX-rich microdroplets. In addition, further transformation of their structures as well as coexistence with other polymers possessing different properties could cause a change in their own positions.

Considering the unique characteristics to entrap certain biomolecules, it would also be expected that in even simple systems, living cells can find preferred locations in microdroplets and their localization can change with a change in the composition of the ATPS. Cells are much larger than the biomacromolecules, and cellular systems are more complicated. However, even though the model artificial system is quite simple, we would expect it to mimic the migration and arrangement of cells in an aqueous environment inside living bodies in a most basic manner, i.e., without any specific molecular interactions among genetic products.

Recently, Han et al. reported the formation and manipulation of cell spheroids (Han et al., 2015), clearly indicating that ATPS could be a powerful tool for controlling cell position without causing important damage. In the present study, we used two different kinds of cells, erythrocytes (horse red blood cells; RBCs) and NAMRU mouse mammary gland epithelial cells (NMuMG cells) as models, and investigated how these cells are localized when entrapped inside ATPS microdroplets. Interestingly, we found that RBCs and NMuMG cells alternatively preferred to localize either in the interior or at the periphery of microdroplets, and this preference could be switched by changing the PEG/DEX ratio. We considered that the PEG/DEX interface property could change with a change in the interface composition, and this could affect how the interface interacts with different types of cells to cause this switching.

MATERIALS AND METHODS

Reagents

We used polyethylene glycol (PEG) and dextran (DEX) to form an aqueous/aqueous two-phase system (ATPS): PEG 6,000 (molecular weight (M_w) 7,300–9,300 Da) and DEX 200,000 (M_w 180,000–210,000 Da) were purchased from FUJIFILM Wako Pure Chemical Industries (Osaka, Japan). PEG and DEX were stocked as solutions of 20 wt% dissolved in isotonic sodium chloride solution (0.9 wt% solution of NaCl) to regulate the osmotic pressure similar to that of cell membranes. The isotonic sodium chloride solution was prepared with nuclease-free water (Milli-Q, 18.2 $M\Omega\cdot\text{cm}$). Other reagents used were of analytical grade.

Microdroplets

A PEG/DEX solution shows the micro phase segregation at the conditions near to the bimodal line, i.e., the boundary of the homogeneous phase (mono-phase region) to the separated phase (two-phase region) of the solution. Due to the micro phase segregation of polymers, the microdroplets whose diameters range from ~ 10 to $100\ \mu\text{m}$ could be stable for around several

hours after mechanical agitation. In this study, we used the two types of conditions of PEG and DEX concentrations, PEG/DEX = 10%:5%, 5%:5%. Details of experimental solutions used here are described separately in the **Supplementary Material**.

Cells

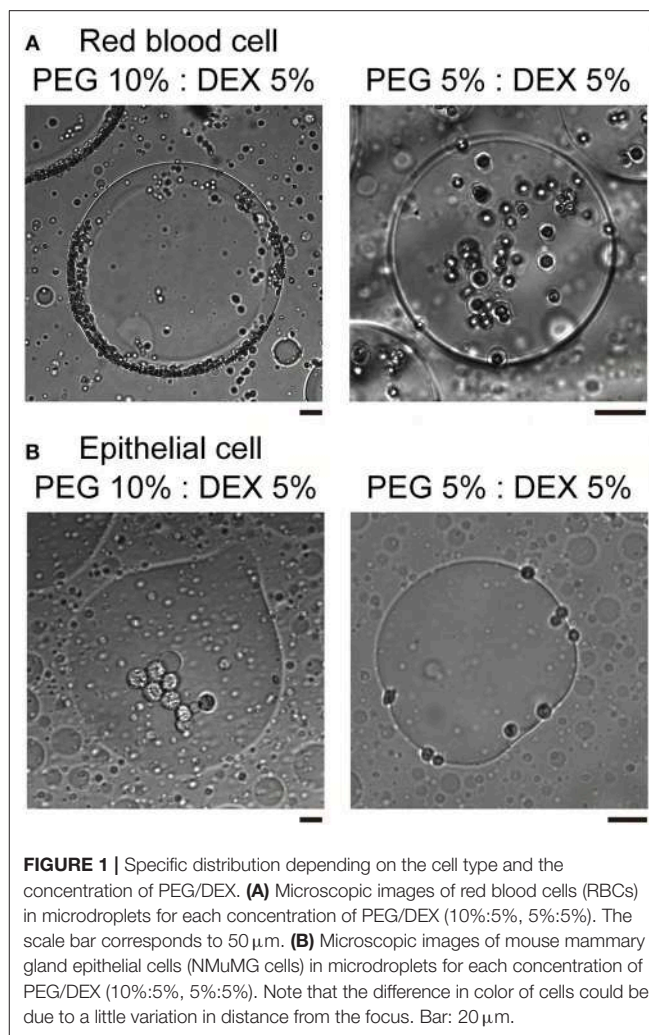
For observations of red blood cells (RBCs), we used the preserved blood of horse purchased from Nippon Bio-test Laboratories, Inc. (Saitama, Japan) and gently added a small aliquot of the blood to the PEG/DEX system without any washing. As model epithelial cells, we used NAMRU mouse mammary gland epithelial cells (NMuMG cells), which were cultivated from cultured cells at regular intervals as previously reported (Yoshida et al., 2017). For mixing in the PEG/DEX system, the epithelial cells were separated in advance from the culture medium by centrifuge.

Microscopy

We observed ATPS microdroplets using bright field microscopy or confocal laser scanning microscopy (CLSM). Bright field microscopy images were obtained with an Axio Observer.A1 (Carl Zeiss, Germany) equipped with a 40 \times objective and a CCD digital camera (C11440, Hamamatsu Photonics). CLSM images were acquired with an FV-1000 laser scanning microscope (Olympus, Japan) and the images were analyzed using FV10-ASW software (Olympus). The images acquired with the bright field microscope were analyzed using ImageJ software (Rasband, W.S., ImageJ, US National Institutes of Health, Bethesda, Maryland, USA, <http://imagej.nih.gov/ij/>, 1997–2016). In the CLSM observation, we used fluorescein isothiocyanate (FITC)-dextran (average M_w 250,000, Sigma-Aldrich; Ex. 488 nm) and the lipophilic dye Nile red (Thermo Fisher Scientific; Ex. 543 nm) to fluorescently visualize DEX-rich domains and RBCs, respectively. The details of experimental solutions subjected to the aforesaid observations are described in the **Supplementary Material**.

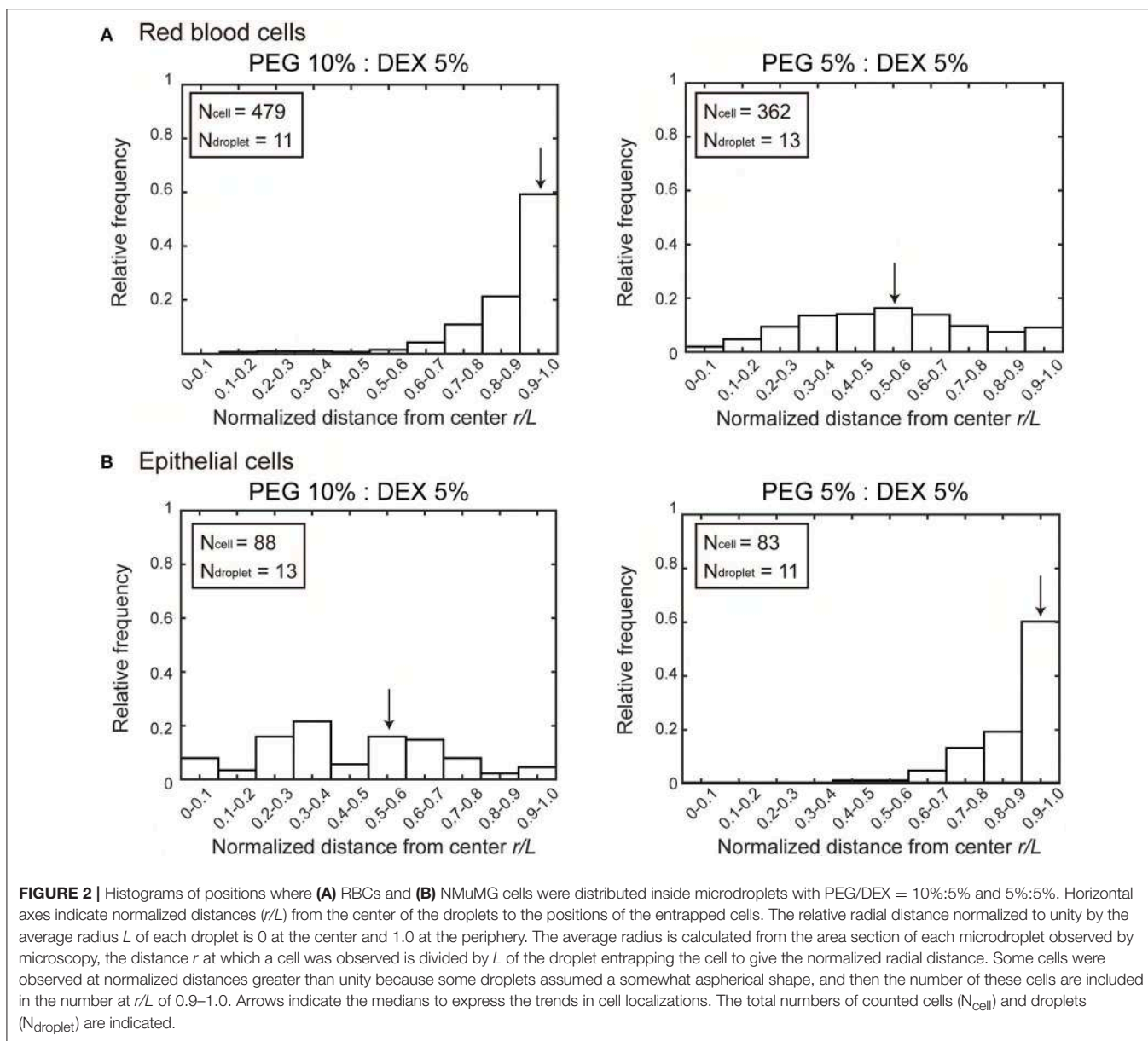
RESULTS AND DISCUSSION

In the present study, we used two kinds of mammal cells: red blood cells (RBCs) and NMuMG cells, which are a type of epithelial cell. As shown in typical microscopic images in **Figure 1**, both RBCs and NMuMG cells were entrapped inside DEX-rich microdroplets when they were mixed in the ATPS with PEG/DEX = 10%:5% and 5%:5%. However, a close look at their distribution revealed that their location switched between the center and the periphery of the droplet with a change in the PEG/DEX ratio. In both cases, DEX-rich microdroplets were located on the bottom of the chamber due to their a little bit larger density as observed in the bulk experiment. Interestingly, these cells showed an opposite preferred distribution inside the droplets (**Figure 1**); at PEG/DEX 10%:5%, RBCs gathered near the interface, while NMuMG cells gathered inside the droplets rather than the interface. In contrast, at PEG/DEX 5%:5%, these preferences were reversed; i.e., RBCs were situated inner part of the droplets, and NMuMG cells were localized at their periphery. RBCs tended not to contact each other when they



were trapped inside the droplets at either concentration of the coexisting polymers, whereas NMuMG cells positioned inside the droplets adhered more strongly to each other. Since NMuMG cells are adherent in their intrinsic property, encapsulation within DEX-rich droplets could enhance their attachment propensities (Yoshida et al., 2017).

Figure 2 shows histograms of the cell population vs. the position of microdroplets. Along the radial distance (r/L) normalized to unity by the average radius L of each droplet, entrapped cells were counted and the numbers were converted into a cell frequency. In both types of cells, the median location, which is indicated by arrow, of entrapped cells shifted from around the center (relative radial distance $r/L \sim 0.5$) to the periphery (relative radial distance r/L 1.0). But the preference is opposite; i.e., RBCs and NMuMG cells (epithelial cells) were observed adsorbed to the interfaces at PEG/DEX = 10%:5% and 5%:5%, respectively. It should be noted that if cells were included inside a droplet without any attraction but with some repulsion to the interface, a peak of the population may appear around $r/L \sim 0.5$ because of the larger area compared to the region near the center.



To further examine how cells switched their distribution inside the droplets, we conducted CLSM observation of the PEG/DEX ATPS containing RBCs labeled fluorescently by Nile red (Figure 3). FITC-DEX illuminated the microdroplets and RBCs emitting red fluorescence were fully entrapped, but their distribution was apparently different at PEG/DEX = 10%:5% and 5%:5%, as in Figure 1. Under the former condition, RBCs were visualized on the inner interface of the DEX-rich droplet emitting green fluorescence, and in the latter, RBCs were relatively dispersed into the DEX-rich droplets. Fewer cells were observed at the top than the middle of the droplet, indicating that entrapped cells could fall under the present conditions. A number of RBCs were here also found at the interface of the microdroplet at PEG/DEX = 5%/5% (Figure 3B), and this trend is consistent with the localization shown in Figure 2A.

We here observed the simple switching of cell localization inside DEX-rich droplets. Both cell types, RBCs and NMuMG cells, preferred the interior, but they exhibited opposite trends when settling in different compartments. The preference in cell localization may be caused by various factors related to difference in cell properties, including their sizes, morphologies, surface structures, adhesive (non-adhesive) behaviors, number density, etc., so it is too complicated to permit us to give a detailed precise explanation for the mechanism. Therefore, the present condition we investigated is considered to be moderately suitable for simple demonstration of switchable behavior of cell localization inside ATPS droplets. For speculation, instead, we try to simply discuss this different preference by imagining cells with different dimensions under a crowded environment with PEG/DEX schematically illustrated in Figure 4 as follows.

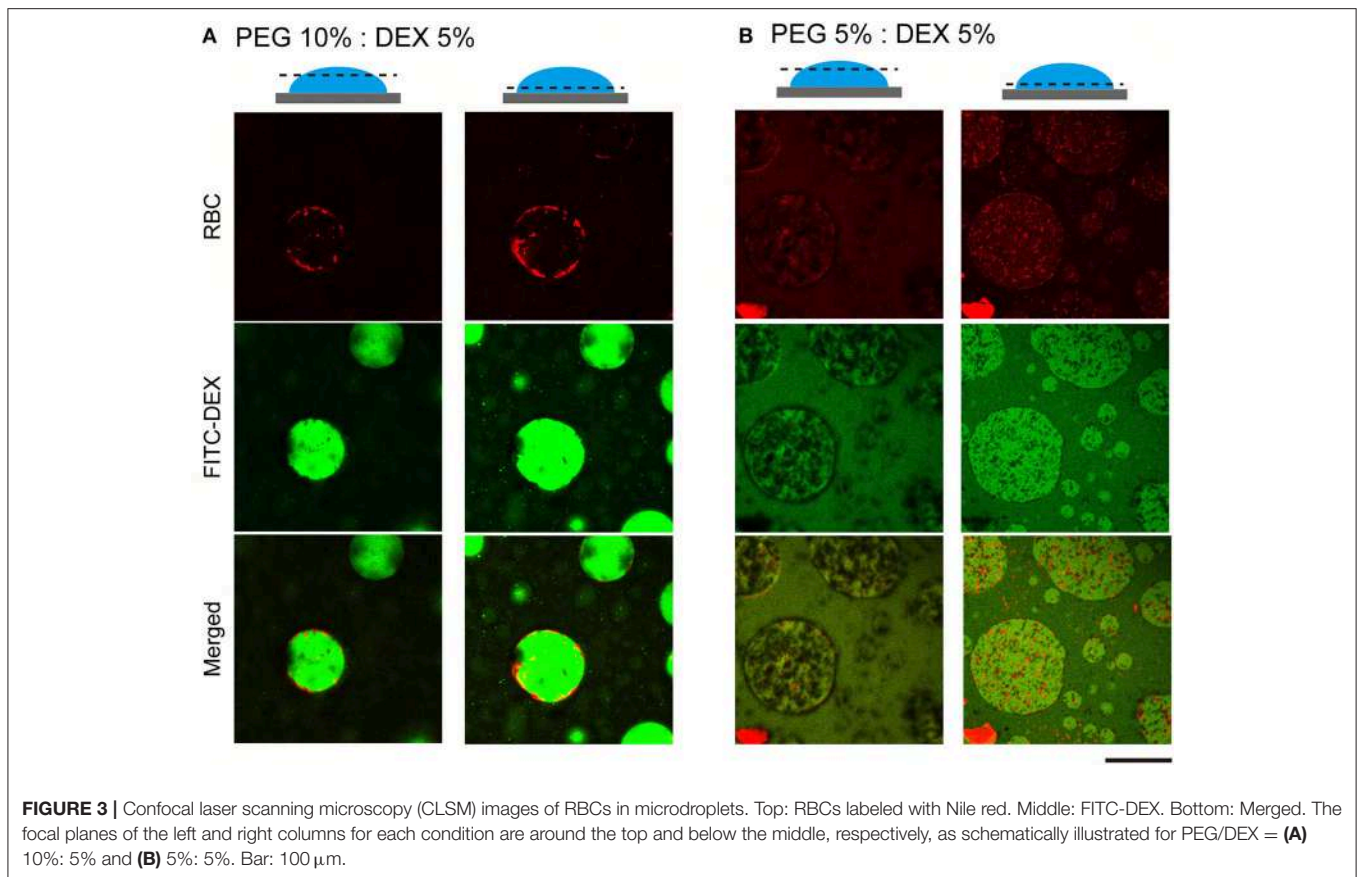


FIGURE 3 | Confocal laser scanning microscopy (CLSM) images of RBCs in microdroplets. Top: RBCs labeled with Nile red. Middle: FITC-DEX. Bottom: Merged. The focal planes of the left and right columns for each condition are around the top and below the middle, respectively, as schematically illustrated for PEG/DEX = **(A)** 10%: 5% and **(B)** 5%: 5%. Bar: 100 μm .

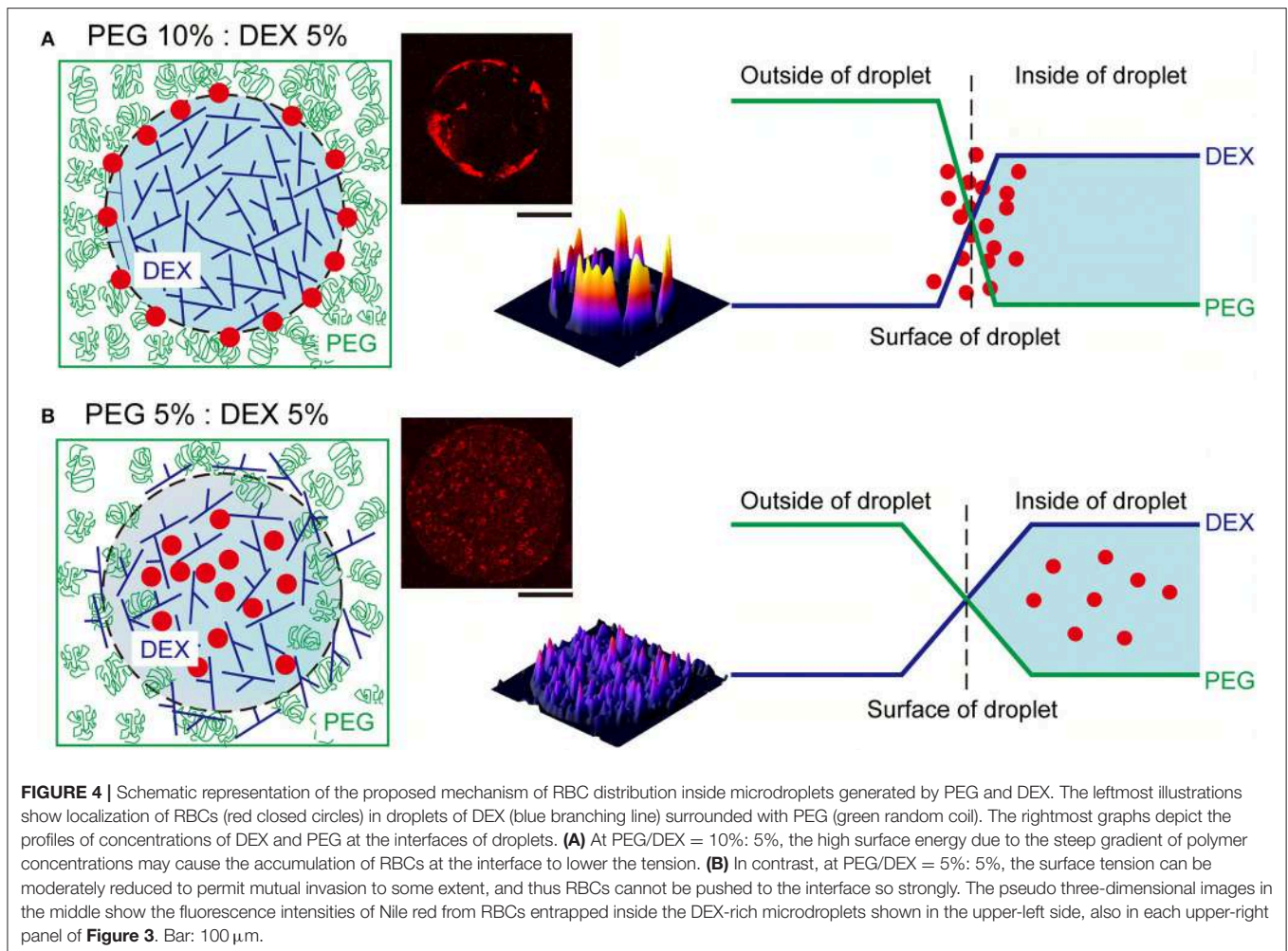
Generally, DEX molecules have branched structures with some room for harboring other biomacromolecules, and PEG molecules have linear flexible structures with a high excluded volume under concentrated conditions. Since these polymers provide different aqueous environments, not only large biomolecules but also cells prefer the DEX-rich phase, which is less crowded than the PEG-rich phase. In the present study, we used two PEG/DEX ATPSs with different conditions; one is near the critical point in the phase diagram (5%:5%); the other is somewhat far from that point, and accordingly, the binodal line (10%:5%).

The surface tension with such aqueous/aqueous interfaces is not so strong compared to oil/water interfaces (Atefi et al., 2014). Therefore, it can be finely modulated by changing the PEG/DEX ratio. In the present case, at PEG/DEX = 10%:5%, the interface has a higher tension (surface energy) with a steeper gradient of polymer concentrations, and thus RBCs, which are relatively smaller than NMuMG cells, could keep located on the surface, leading to reduction of the surface energy (**Figure 4A**). On the other hand, at PEG/DEX = 5%:5%, the surface free energy, or surface tension, is so low due to a small gradient of polymer concentrations that small RBCs with weaker effects on stabilization of the interface alternatively tend to leave and enter the interior of DEX-rich droplets, which can accommodate these cells (**Figure 4B**).

To interpret the opposite preference of NMuMG cells along the same scenario as the case of RBCs, their larger size can be taken into account in relation to depletion effects by PEG.

NMuMG cells appear to move to the interior of DEX-rich droplets, avoiding the interface where PEG exists more densely at PEG/DEX = 10%:5%. In other words, PEG could effectively induce depletion effect on NMuMG cells due to their larger sizes (surface areas), so these cells can be located not near a PEG-rich surrounding but in a DEX-rich inner space, where they might be associated with each other by moderate depletion force with DEX polymers (Atefi et al., 2015). At PEG/DEX = 5%:5%, where most RBCs are located inside the droplets, NMuMG cells can stand adhering to the interface, leading to the efficient stabilization due to their greater dimension. Note that the surface free energy of the interface through the phase segregation of polymer solutions is generally much smaller than those for interfaces with small molecules, because of the small contribution of the mixing entropy for polymer systems (Nakatani et al., 2018).

It has been shown that interface properties are in general strongly correlated to the positioning and qualities of cells with various origins (Atefi et al., 2015; Han et al., 2015) with some changes in genetic activities (Yu et al., 2018). To achieve assembly of highly organized compartments including cells in microfluidics, interfacial environments where cells and biopolymers are accumulated should be well-regulated (Yamada et al., 2016). We here simply chose physiological saline for suspending cells, but it is not suitable for cell proliferation, but, along this line, when some conditions that facilitate micro phase separation and cell growth are available, our results would be expected to aid development of such techniques for constituting assembled cell systems.



In conclusion, it was found that living cells exhibit specific localization in an aqueous solution with water/water microdroplets generated through phase separation in the presence of hydrophilic binary polymers. It was revealed that two type of cells are situated either in the interior or at the periphery of the droplets. By changing the relative ratio of the polymer content, switching of the cell localization was observed. The mechanism of such observations were interpreted in terms of polymer depletion effect on the micro phase separation. It is highly expected that the simple mixing procedure with micro water/water droplets provides novel methodology to construct 3D cellular assembly composed with difference cell species.

AUTHOR CONTRIBUTIONS

HS and TF conducted the experiments with the help of KT under direction by KY. HS, TF, and KT wrote the manuscript with the help of YY and YH under supervision by KY.

FUNDING

This work was supported, in part, by JSPS KAKENHI Grant Numbers JP15H02121, JP16K07293, JP18J12947, and JP16K13655 and by MEXT KAKENHI Grant Number JP18H04976.

ACKNOWLEDGMENTS

We thank Dr. Hiroaki Taniguchi (The Institute of Genetics and Animal Breeding, Polish Academy of Sciences) for help on the experiments with NMuMG cells.

SUPPLEMENTARY MATERIAL

The Supplementary Material for this article can be found online at: <https://www.frontiersin.org/articles/10.3389/fchem.2019.00044/full#supplementary-material>

REFERENCES

- Akbulut, O., Mace, C. R., Martinez, R. V., Kumar, A. A., Nie, Z., Patton, M. R., et al. (2012). Separation of nanoparticles in aqueous multiphase systems through centrifugation. *Nano Lett.* 12, 4060–4064. doi: 10.1021/nl301452x
- Albertsson, P.-Å. (1971). *Partition of Cell Particles and Macromolecules, 2nd Ed.* New York, NY: Wiley.
- Atefi, E., Joshi, R., Mann, J. A. Jr., and Tavana, H. (2015). Interfacial tension effect on cell partition in aqueous two-phase systems. *ACS Appl. Mater. Interfaces* 7, 21305–21314. doi: 10.1021/acsami.5b05757
- Atefi, E., Mann, J. A. Jr., and Tavana, H. (2014). Ultralow interfacial tensions of aqueous two-phase systems measured using drop shape. *Langmuir* 30, 9691–9699. doi: 10.1021/la500930x
- Aumiller, W. M. Jr., and Keating, C. D. (2017). Experimental models for dynamic compartmentalization of biomolecules in liquid organelles: reversible formation and partitioning in aqueous biphasic systems. *Adv. Colloid Interface Sci.* 239, 75–87. doi: 10.1016/j.cis.2016.06.011
- Brangwynne, C. P. (2013). Phase transitions and size scaling of membrane-less organelles. *J. Cell Biol.* 203, 875–881. doi: 10.1083/jcb.201308087
- Courchaine, E. M., Lu, A., and Neugebauer, K. M. (2016). Droplet organelles? *EMBO J.* 35, 1603–1612. doi: 10.15252/embj.201593517
- Esquena, J. (2016). Water-in-water (W/W) emulsions. *Curr. Opin. Colloid Interface Sci.* 25, 109–119. doi: 10.1016/j.cocis.2016.09.010
- Han, C., Takayama, S., and Park, J. (2015). Formation and manipulation of cell spheroids using a density adjusted PEG/DEX aqueous two phase system. *Sci. Rep.* 5:11891. doi: 10.1038/srep11891
- Jia, T. Z., Hentrich, C., and Szostak, J. W. (2014). Rapid RNA exchange in aqueous two-phase system and coacervate droplets. *Orig. Life Evol. Biosph.* 44, 1–12. doi: 10.1007/s11084-014-9355-8
- Monterroso, B., Zorrilla, S., Sobrinos-Sanguino, M., Keating, C. D., and Rivas, G. (2016). Microenvironments created by liquid-liquid phase transition control the dynamic distribution of bacterial division FtsZ protein. *Sci. Rep.* 6, 35140. doi: 10.1038/srep35140
- Nakatani, N., Sakuta, H., Hayashi, M., Tanaka, S., Takiguchi, K., Tsumoto, K., et al. (2018). Specific spatial localization of actin and DNA in a water/water microdroplet: Self-emergence of a cell-like structure. *Chem. Bio. Chem.* 19, 1370–1374. doi: 10.1002/cbic.201800066
- Nott, T. J., Craggs, T. D., and Baldwin, A. J. (2016). Membraneless organelles can melt nucleic acid duplexes and act as biomolecular filters. *Nat. Chem.* 8, 569–575. doi: 10.1038/nchem.2519
- Poudyal, R. R., Pir Cakmak, F., Keating, C. D., and Bevilacqua, P. C. (2018). Physical principles and extant biology reveal roles for RNA-containing membraneless compartments in origins of life chemistry. *Biochemistry* 57, 2509–2519. doi: 10.1021/acs.biochem.8b00081
- Rivas, G., and Minton, A. P. (2016). Macromolecular crowding *in vitro*, *in vivo*, and in between. *Trends Biochem. Sci.* 41, 970–981. doi: 10.1016/j.tibs.2016.08.013
- Song, Y., Michaels, T. C. T., Ma, Q., Liu, Z., Yuan, H., Takayama, S., et al. (2018). Budding-like division of all-aqueous emulsion droplets modulated by networks of protein nanofibrils. *Nat. Commun.* 9:2110. doi: 10.1038/s41467-018-04510-3
- Spitzer, J., and Poolman, B. (2013). How crowded is the prokaryotic cytoplasm? *FEBS Lett.* 587, 2094–2098. doi: 10.1016/j.febslet.2013.05.051
- Toyama, H., Yoshikawa, K., and Kitahata, H. (2008). Homogenization of a phase-separated droplet in a polymer mixture caused by the dielectric effect of a laser. *Phys. Rev. E Stat. Nonlin. Soft Matter Phys.* 78:060801. doi: 10.1103/PhysRevE.78.060801
- Tsumoto, K., Arai, M., Nakatani, N., Watanabe, S. N., and Yoshikawa, K. (2015). Does DNA exert an active role in generating cell-sized spheres in an aqueous solution with a crowding binary polymer? *Life* 5, 459–466. doi: 10.3390/life5010459
- Tsumoto, K., and Yoshikawa, K. (2017). The aqueous two phase system (ATPS) deserves plausible real-world modeling for the structure and function of living cells. *MRS Adv.* 2, 2407–2413. doi: 10.1557/adv.2017.358
- Uversky, V. N. (2017). Intrinsically disordered proteins in overcrowded milieu: Membrane-less organelles, phase separation, and intrinsic disorder. *Curr. Opin. Struct. Biol.* 44, 18–30. doi: 10.1016/j.sbi.2016.10.015
- Vis, M., Opdam, J., van't Oor, I. S. J., Soligno, G., van Roij, R., Tromp, R. H., et al. (2015). Water-in-water emulsions stabilized by nanoplates. *ACS Macro Lett.* 4, 965–968. doi: 10.1021/acsmacrolett.5b00480
- Walter, H., and Brooks, D. E. (1995). Phase separation in cytoplasm, due to macromolecular crowding, is the basis for microcompartmentation. *FEBS Lett.* 361, 135–139. doi: 10.1016/0014-5793(95)00159-7
- Yamada, A., Renault, R., Chikina, A., Venzac, B., Pereiro, I., Coscoy, S., et al. (2016). Transient microfluidic compartmentalization using actionable microfilaments for biochemical assays, cell culture and organs-on-chip. *Lab Chip* 16, 4691–4701. doi: 10.1039/C6LC01143H
- Yoshida, A., Tsuji, S., Taniguchi, H., Kenmotsu, T., Sadakane, K., and Yoshikawa, K. (2017). Manipulating living cells to construct a 3D single-cell assembly without an artificial scaffold. *Polymers* 9:319. doi: 10.3390/polym9080319
- Yu, L., Li, J., Hong, J., Takashima, Y., Fujimoto, N., Nakajima, M., et al. (2018). Low cell-matrix adhesion reveals two subtypes of human pluripotent stem cells. *Stem Cell Rep.* 11, 142–156. doi: 10.1016/j.stemcr.2018.06.003
- Zaslavsky, B. Y., Ferreira, L. A., Darling, A. L., and Uversky, V. N. (2018). The solvent side of proteinaceous membrane-less organelles in light of aqueous two-phase systems. *Int. J. Biol. Macromol.* 117, 1224–1251. doi: 10.1016/j.ijbiomac.2018.06.030

Conflict of Interest Statement: The authors declare that the research was conducted in the absence of any commercial or financial relationships that could be construed as a potential conflict of interest.

Copyright © 2019 Sakuta, Fujimoto, Yamana, Hoda, Tsumoto and Yoshikawa. This is an open-access article distributed under the terms of the Creative Commons Attribution License (CC BY). The use, distribution or reproduction in other forums is permitted, provided the original author(s) and the copyright owner(s) are credited and that the original publication in this journal is cited, in accordance with accepted academic practice. No use, distribution or reproduction is permitted which does not comply with these terms.

SCIENTIFIC REPORTS



OPEN

Cracking pattern of tissue slices induced by external extension provides useful diagnostic information

Keisuke Danno¹, Takuto Nakamura¹, Natsumi Okoso¹, Naohiko Nakamura², Kohta Iguchi², Yoshiaki Iwadate³, Takahiro Kenmotsu¹, Masaya Ikegawa¹, Shinji Uemoto² & Kenichi Yoshikawa¹

Although biopsy is one of the most important methods for diagnosis in diseases, there is ambiguity based on the information obtained from the visual inspection of tissue slices. Here, we studied the effect of external extension on tissue slices from mouse liver with different stages of disease: Healthy normal state, Simple steatosis, Non-alcoholic steatohepatitis and Hepatocellular carcinoma. We found that the cracking pattern of a tissue slice caused by extension can provide useful information for distinguishing among the disease states. Interestingly, slices with Hepatocellular carcinoma showed a fine roughening on the cracking pattern with a characteristic length of the size of cells, which is much different than the cracking pattern for slices with non-cancerous steatosis, for which the cracks were relatively straight. The significant difference in the cracking pattern depending on the disease state is attributable to a difference in the strength of cell-cell adhesion, which would be very weak under carcinosis. As it is well known that the manner of cell-cell adhesion neatly concerns with the symptoms in many diseases, it may be promising to apply the proposed methodology to the diagnosis of other diseases.

Biopsy, or the inspection of tissue samples, is one of the most important methods for making a precise diagnosis in human disease, especially for evaluating the stage of malignant cancer. Various techniques for preparing tissue samples have been developed and pathologists describe the features of a specimen in terms of cell type, cellular arrangement, abnormality, morphology of the cell nucleus, etc.^{1–10}. However, there is still some ambiguity in a diagnosis based on information obtained from the inspection of tissue slices. In addition, a great deal of skill is needed to give a precise pathological diagnosis. To realize quantitative pathological diagnosis, several attempts have been made to analyze images of pathological samples obtained by optical microscopy. These attempts have been based on pattern recognition or topology algorithms^{11–15}, and also on information processing by so-called AI algorithms using “big data”¹⁶. In the present study, we tried to obtain additional information from sliced tissue sections for samples obtained from mice with disease in different pathological stages. We prepared sections of mouse liver. These mice were sacrificed to obtain whole liver samples at 36 weeks after 12 h of fasting from the last feeding under general anesthesia by inhalation of 1–2% isoflurane. Small pieces of the liver were cut from the whole liver and then snap-frozen in liquid nitrogen immediately. These sliced tissues were placed on an elastic sheet of polyurethane, instead of a glass slide, which is usually used in microscopic observation. Slices were then stretched under observation by optical microscopy. Interestingly, characteristic fine-cracking pattern was generated for the slice with Hepatocellular carcinoma, which is markedly different from those for the slices with non-cancerous steatosis. It has been shown that the analysis of cracking patterns can be used to derive index parameters^{17–24}, which are quantitative parameters that are useful for obtaining a precise diagnosis.

¹Faculty of Life and Medical Sciences, Doshisha University, Kyotanabe, Kyoto, Japan. ²Department of Surgery, Graduate School of Medicine, Kyoto University, Kyoto, Japan. ³Faculty of Science, Yamaguchi University, Yamaguchi, Yamaguchi, Japan. Correspondence and requests for materials should be addressed to T.K. (email: tkenmots@mail.doshisha.ac.jp) or K.Y. (email: keyoshik@mail.doshisha.ac.jp)

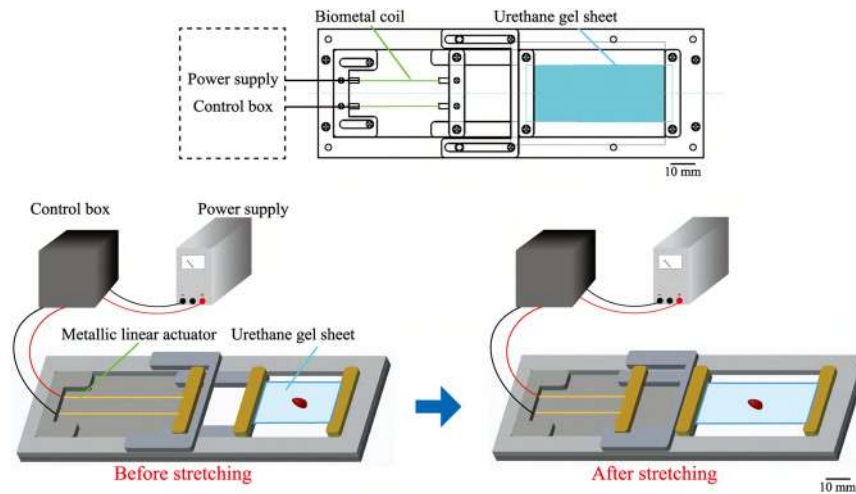


Figure 1. Schematic representation of the experimental set-up used to stretch a tissue slice attached to a gel sheet on the stage of an optical microscope.

Materials and Methods

Animal. Male 4 to 5 weeks old C57BL/6 mice were purchased from Japan SLC, Inc. (Shizuoka, Japan). All protocols were approved by the Ethics Committee of Animal Care and Experimentation at Kyoto University (MedKyo14250).

Mouse NAFLD-HCC models. We examined liver tissues of mice that reflected different disease states: Healthy normal (Normal), Simple steatosis, Non-alcoholic steatohepatitis (NASH) and Hepatocellular carcinoma (HCC). Mice of the old C57BL/6 were induced to develop different disease states through a well-established procedure involving chemical additives in feed and other dietary interventions^{25,26}. Mice were maintained at $24 \pm 3^\circ\text{C}$ under a 12-h light/dark cycle with free access to water. Mice were fed a control diet or high fat diet (D12331, Research Diets, New Brunswick, NJ, USA) combining with intraperitoneal administration of diethylnitrosamine. The physical conditions and body weight of the animals were checked every week. If general fatigue, decreased activity, respiratory distress, or weight loss were observed, the mice were euthanized before the predetermined day. Through the above mentioned treatment, mice develop simple steatosis, NASH, and HCC in a definite manner under the condition that they were fed for the period of 36 weeks. We count on conventional histopathological findings such as steatosis, lobular inflammation, and ballooning as a common set of diagnostic criteria to confirm the actual types of pathology. During the experiments, mice may sometimes deteriorate their health states because of liver dysfunction. We prepared sections of mouse liver. These mice were sacrificed to obtain whole liver samples at 36 weeks after 12 h of fasting from the last feeding under general anesthesia by inhalation of 1–2% isoflurane. Small pieces of the liver were cut from the whole liver and then snap-frozen in liquid nitrogen immediately. After the sampling, animals were killed by cutting the inferior vena cava under deep anesthesia using isoflurane.

Tissue slice preparation method. To obtain a tissue sample of mouse liver, we applied the following treatment. First, we embedded a mouse liver in Optimal Cutting Temperature (OCT) compound immediately after the liver was removed from the mouse body and frozen in liquid nitrogen at -80°C . The frozen sample was then sliced at a thickness of $20\ \mu\text{m}$ using a Cryostat (Leica, Germany), which maintains samples at -20°C for 15 minutes. Sample slices were then placed on a transparent urethane gel sheet (EXSEAL Corporation, Japan) in a careful manner so as to diminish any physical stress. It is known that polyurethane serves as tissue adhesive, and polyurethane-based sheets/scaffolds have been adopted to obtain tissue adhesive for application in tissue engineering²⁷. Thus, in the present study we used urethane gel sheet as the adhesive material for the tissue slices. After treatment with Nile Blue (NB), the tissue slice was stood still for ca. 30 min at room temperature, and then we observed the tissue slice by optical microscopy. During such waiting period, the moisture contained in the sample slices is absorbed on the gel sheet, and as the result, the slices stick to the sheet in a strict manner. The tissue slices with the $10 \times 10\ \text{mm}$ size prepared were stretched with the experimental set-up as shown in Fig. 1. The urethane gel sheet measured $40\ \text{mm}$ in length, $22\ \text{mm}$ in width and $1\ \text{mm}$ in thickness, and was fixed between a pair of bars, one fixed and one movable^{28,29}. Extension was carried out through the use of metallic linear actuator (Toki Corporation, Japan), which shrink under the application of an electric current. In the experiments reported here, the gel sheet was stretched to 150%, from $40\ \text{mm}$ to $60\ \text{mm}$. As for such degree of stretch, most of the stretch stress was forced on the urethane gel sheet. The tissue slices were monitored by optical microscopy using a $40\times$ objective lens.

Results

The upper rows in Fig. 2 show images of tissue samples of mouse liver on glass slides stained by Hematoxylin-Eosin (HE) (Norm-1, Steat-1, NASH-1, HCC-1) and Nile blue (NB) (Norm-2, Steat-2, NASH-2, HCC-2). These images indicate that there are rather significant differences between normal tissues and tissues with various stages of disease. However, it is not easy to clearly differentiate HCC (HCC-2) from simple steatosis (Steat-2) or NASH (NASH-2). The lower rows in Fig. 2 show images of tissue samples on a urethane gel sheet before (Norm-3, Steat-3, NASH-3,

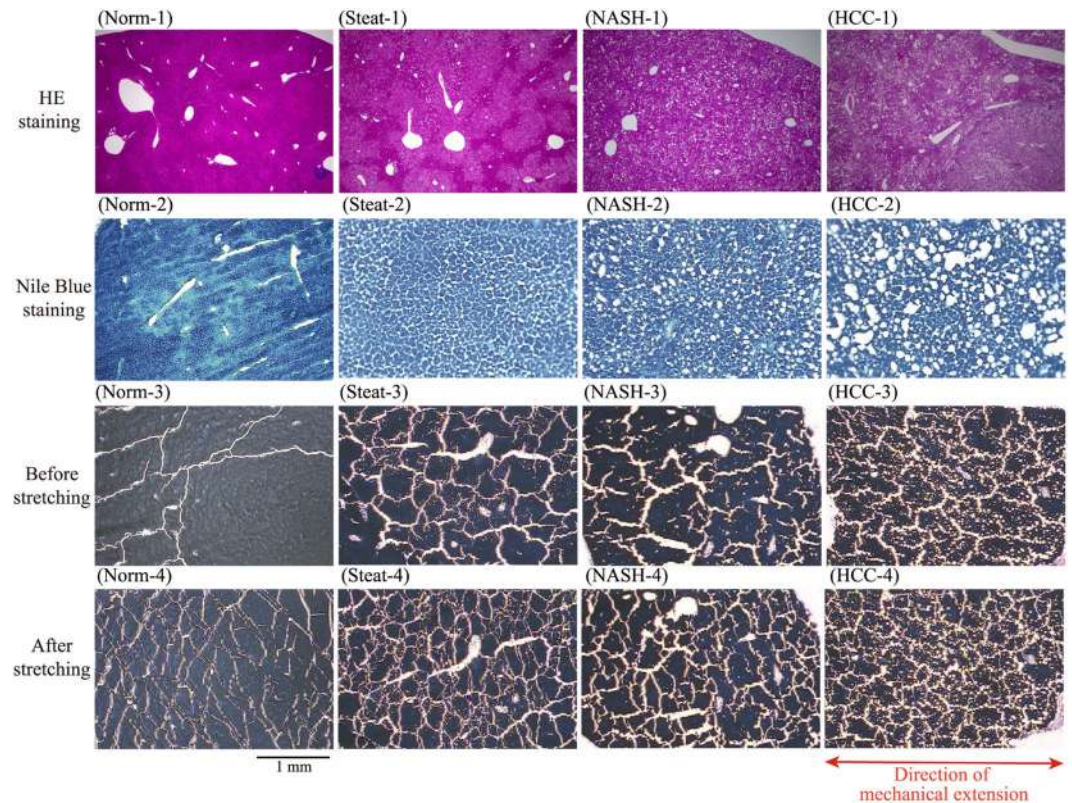


Figure 2. Optical microscopic images of tissue slices. (Norm-) healthy normal, (Steat-) simple steatosis, (NASH-) non-alcoholic steatohepatitis, (HCC-) hepatocellular carcinoma. From top to bottom: (1) HE staining on a glass slide, (2) NB staining on a glass slide, (3) Before stretching on a urethane gel sheet, (4) Stretched state with mechanical extension.

HCC-3) and after (Norm-4, Steat-4, NASH-4, HCC-4) stretching, under staining with NB. In this experimental set-up, the gel sheet to which tissue samples were attached was stretched to 150% (Norm-4, Steat-4, NASH-4, HCC-4). Comparison of the images obtained before and after stretching indicates a marked increase in tissue cracking under extension of the gel sheet. Here, it is noted that cracking appears even for the samples before the stretching. This is attributable to the dehydration effect caused through the hygroscopic nature of the gel sheet adhesive to the tissue slice. With the addition of the mechanical stress, cracking of the tissue is significantly enhanced as shown in Fig. 2(4). We have confirmed that the tissue slices kept to tightly stick to the gel sheet under stretch up to 150%. Interestingly, for the tissue with carcinoma (HCC-4), a fine cracking pattern is noted, whereas for the other tissues (Norm-4, Steat-4, NASH-4), the cracks appear as relatively straight lines without a fine pattern. Thus, stretching of the slices provides additional useful information specific to carcinoma; i.e., the appearance of a fine cracking pattern.

Discussion

The cracking patterns of the different tissues shown in Fig. 2 (Norm-4, Steat-4, NASH-4, HCC-4) varied according to the disease state, especially that of the cancerous tissue (HCC-4). Next, we will explore methods for the quantitative analysis of tissue cracking patterns toward future application for the diagnosis of disease states. We will adopt two different methodologies: i) evaluation of the degree of cracking in terms of the total length of cracks, and ii) evaluation of the degree of cracking in terms of the relative surface areas of cracks and uncracked tissues. We have applied Tukey-Kramer procedure to the statistical analysis on the experimental data, which is known as the standard procedure of analysis for multiple comparison^{30–34}. Figure 3 shows the procedure used for image-analysis of the cracking pattern through the application of a Gaussian filter, with the different values of the standard deviation (StDev; i.e., 1 or 6 pixels) to smooth the lines in the cracking patterns, where the number of head count of the mouse $N=4$. After the images were smoothed by Gaussian filtering, we binarized the images to sharpen the boundaries of the cracking patterns. The parts in white correspond to the cracking area of the samples after binarization. Next, we tried to evaluate the degree of the fineness in the cracking pattern based on the images with binarization where the distance between the neighboring pixels is 4.6 μm . By considering the characteristic size of individual cells on the order of 10 μm , we imposed Gaussian filter with the length scale of 27.6 μm (6 times larger than the distance between the neighboring pixels); in order words, the images were course grained above the size of individual cell. Then, we have evaluated the total lengths of the outlines of the cracking before and after the coursing and we have denoted these lengths as L and L' . The lower panel (Fig. 3) shows the ratio of the length L (StDev = 1 pixel) to L' (StDev = 6 pixels) for each disease state. The ratio L/L' for HCC is significantly greater (about 0.5-fold greater) than those for the

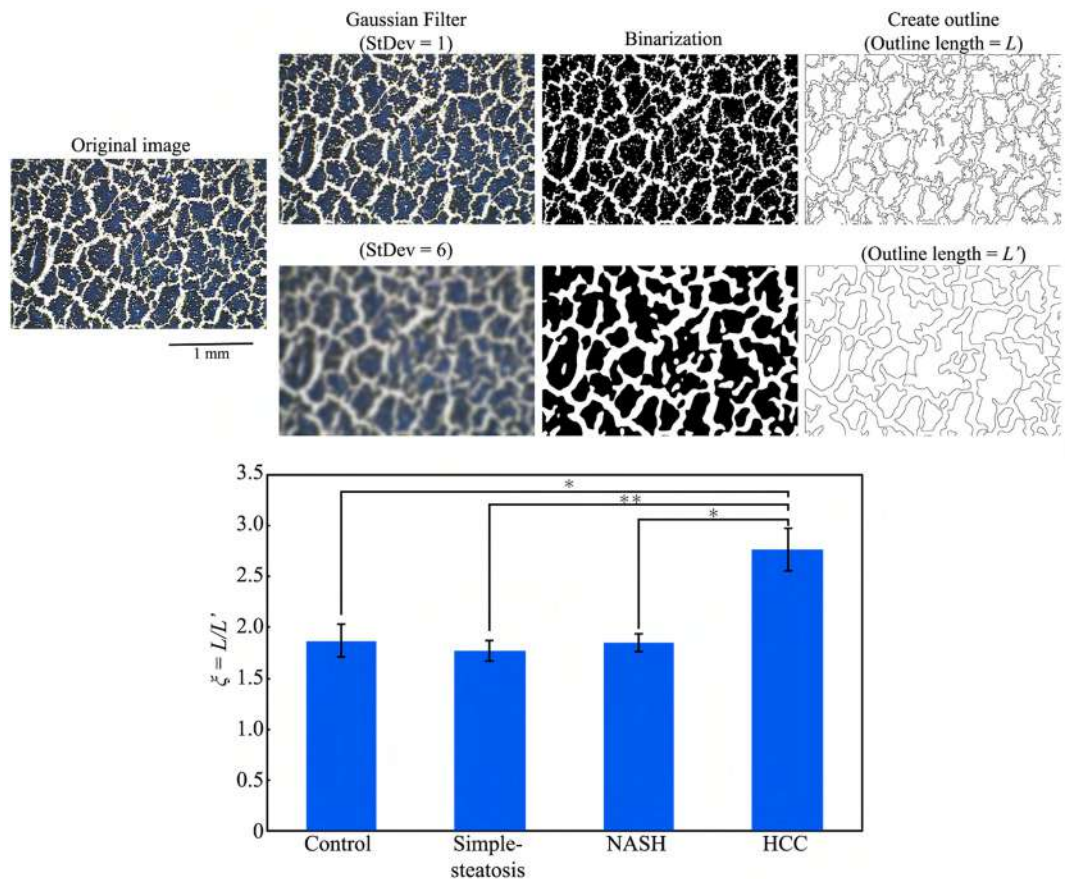


Figure 3. Schematic illustrations of the evaluation of uneven degrees of cracking lines. The total lengths of the outlines in binarized images before (L) and after (L') Gaussian filtering for a length scale of $27.6 \mu\text{m}$ (corresponding to 6 pixels), where the distance between neighboring pixels in the original image is $4.6 \mu\text{m}$. The bar graph shows the difference in L/L' for tissues with different disease states. (Mean \pm SE, * $p < 0.05$, ** $p < 0.01$, head count of the mouse $N = 4$).

other states. In other words, the roughening of the cracking pattern becomes significant in HCC; cancerous tissue. The micro-roughening on the cracking patterns as in Fig. 2 (HCC-3) and (HCC-4) are on the order of $10 \mu\text{m}$, corresponding to the usual cell-size in organs. In other words, the effect of couring with the Gaussian filter is marked in HCC; cancerous tissue. As mentioned above, the length scale ($27.6 \mu\text{m}$) of the adapted Gaussian filter is larger than the cell-size in organs. Thus, the larger ratio of L/L' implies the character of the cracking with the greater unevenness on the scale of individual cells. We may expect that the appearance of the fine unevenness on the cracking with the scale of the order of $10 \mu\text{m}$ is attributable to the decrease of cell-cell contact interaction^{35,36}.

Figure 4 shows another method of analysis different from that in Fig. 3 that is based on an evaluation of the area in the cracking pattern, where the number of head count of the mouse $N = 4$. We applied this method to images that had been binarized. In the binarized image in Fig. 4, the black and white parts correspond to the urethane sheet without tissue and to remaining tissue respectively. To evaluate the relative area of cracking, we counted the numbers of white and black pixels after binarization; i.e., N_w for white pixels and N_b for black pixels, and then used these values to calculate the ratio of N_b to $N_w + N_b$. This parameter increases gradually to the state of NASH. For tissue with HCC, this ratio is 0.5-fold greater than those for the other disease states. The increase of crack area in the stretched tissues is attributable to the weakening of adhesion strength between cells. These results show that it is possible to evaluate the state of a disease in a quantitative manner by using the parameters shown in Figs 3 and 4. The increase of the crack area in the stretched tissue of HCC is again attributable to the weakening of the cell-cell attractive interaction, as well as in the marked increase of L/L' as in Fig. 3. Such weakening effect of the cell-cell adhesion on the other disease states beside HCC and, thus, cracking patterns did not reveal large differences among them.

Conclusions

We have proposed a novel methodology for the pathological diagnosis of cancer, which involves making cracking patterns in tissue samples by stretching. We have shown experimental results together with the quantitative analysis on tissue samples of mouse liver in different disease states: Healthy normal state, Simple steatosis, Non-alcoholic steatohepatitis (NASH) and Hepatocellular carcinoma (HCC). It was revealed that the difference between NASH and HCC becomes significant for the tissues after mechanical stretching. The appearance of fine cracking on the order of cell-size in HCC implies the decrease of the strength of cell-cell attraction. Thus,

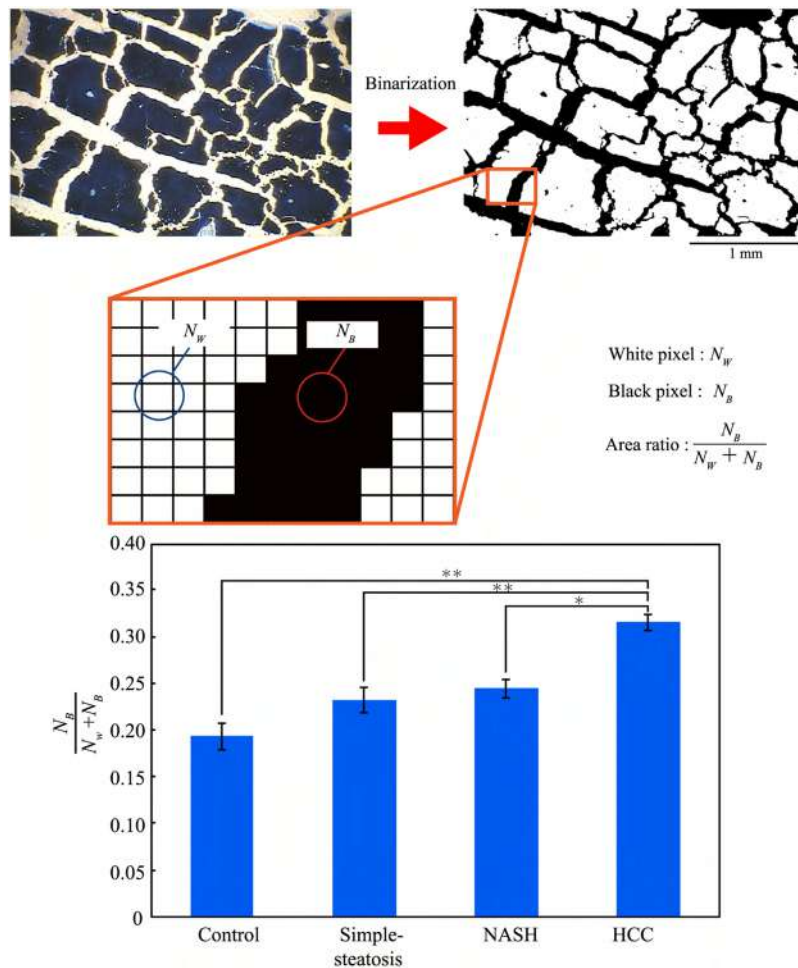


Figure 4. Schematic illustration of the evaluation of the cracking area. White and black pixels in the binarized image represent remaining tissue and cracks respectively. The bar graph shows the difference in the areas of cracks in tissues with different disease states. (Mean ± SE, * $p < 0.05$, ** $p < 0.01$, head count of the mouse $N = 4$).

the proposed methodology involving quantitative image-analysis on the cracking pattern is expected to serve as a useful diagnostic tool. In conclusion, cracking information with tissue stretching will be promising for the development of precise diagnosis, including malignancy in other tissues. Further studies on the cracking pattern formation by changing the experimental conditions, such as speed and magnitude of stretching, and method of freezing before tissue slicing, are awaited.

References

- Zucman-Rossi, J., Villanueva, A., Nault, J. C. & Llovet, J. M. Genetic landscape and biomarkers of hepatocellular carcinoma. *Gastroenterology* **149**, 1226–1239.e4 (2015).
- Yersiz, H. *et al.* Assessment of hepatic steatosis by transplant surgeon and expert pathologist: a prospective, double-blind evaluation of 201 donor livers. *Liver Transpl.* **19**, 437–449 (2013).
- Tiniakos, D. G., Vos, M. B. & Brunt, E. M. Nonalcoholic fatty liver disease: pathology and pathogenesis. *Annu. Rev. Pathol.* **5**, 145–171 (2010).
- Schwenzer, N. F. *et al.* Non-invasive assessment and quantification of liver steatosis by ultrasound, computed tomography and magnetic resonance. *J. Hepatol.* **51**, 433–445 (2009).
- Kudo, M. Multistep human hepatocarcinogenesis: correlation of imaging with pathology. *J. Gastroenterol.* **44**(Suppl 19), 112–118 (2009).
- Takayama, T. *et al.* Early hepatocellular carcinoma: pathology, imaging, and therapy. *Ann. Surg. Oncol.* **15**, 972–978 (2008).
- Yeh, M. M. & Brunt, E. M. Pathology of nonalcoholic fatty liver disease. *Am. J. Clin. Pathol.* **128**, 837–847 (2007).
- Cormier, J. N., Thomas, K. T., Chari, R. S. & Pinson, C. W. Management of hepatocellular carcinoma. *J. Gastrointest Surg.* **10**, 761–780 (2006).
- Llovet, J. M. & Bruix, J. Systematic review of randomized trials for unresectable hepatocellular carcinoma: Chemoembolization improves survival. *Hepatology* **37**, 429–442 (2003).
- Shimada, M. *et al.* Hepatocellular carcinoma in patients with non-alcoholic steatohepatitis. *J. Hepatol.* **37**, 154–160 (2002).
- Jang, H. J., Kim, T. K., Burns, P. N. & Wilson, S. R. CEUS: An essential component in a multimodality approach to small nodules in patients at high-risk for hepatocellular carcinoma. *Eur. J. Radiol.* **84**, 1623–1635 (2015).
- Wilson, S. R. & Burns, P. N. An algorithm for the diagnosis of focal liver masses using microbubble contrast-enhanced pulse-inversion sonography. *Am. J. Roentgenol.* **186**, 1401–1412 (2006).
- Futterer, J. J. *et al.* Prostate cancer localization with dynamic contrast-enhanced MR imaging and proton MR spectroscopic imaging. *Radiology* **241**, 449–458 (2006).

14. Quaia, E. *et al.* Characterization of focal liver lesions with contrast-specific US modes and a sulfur hexafluoride-filled microbubble contrast agent: diagnostic performance and confidence. *Radiology* **232**, 420–430 (2004).
15. Koda, M. *et al.* Qualitative assessment of tumor vascularity in hepatocellular carcinoma by contrast-enhanced coded ultrasound: comparison with arterial phase of dynamic CT and conventional color/power Doppler ultrasound. *Eur. Radiol.* **14**, 1100–1108 (2004).
16. Yoshida, H. *et al.* Automated histological classification of whole-slide images of gastric biopsy specimens. *Gastric Cancer* **21**, 249–257 (2018).
17. Segarra, M., Shimada, Y., Sadr, A., Sumi, Y. & Tagami, J. Three-dimensional analysis of enamel crack behavior using optical coherence tomography. *J. Dent. Res.* **96**, 308–314 (2017).
18. Fochesatto, N. S., Buezas, F. S., Rosales, M. B. & Tuckart, W. R. Effect of crack patterns on the stress distribution of hard chromium coatings under sliding contact: stochastic modeling approach. *J. Tribology* **139**, 061401 (2017).
19. Vida, L. M., Ostra, M., Imaz, N., García-Lecina, E. & Ubide, C. Analysis of SEM digital images to quantify crack network pattern area in chromium electrodeposits. *Surface Coatings Tech.* **285**, 289–297 (2016).
20. Nandakishore, P. & Goehring, L. Crack patterns over uneven substrates. *Soft Matter* **12**, 2253–2263 (2016).
21. Ghabache, E., Jossierand, C. & Seon, T. Frozen impacted drop: from fragmentation to hierarchical crack patterns. *Phys. Rev. Lett.* **117**, 074501 (2016).
22. Goehring, L. & Morris, S. W. Cracking mud, freezing dirt, and breaking rocks. *Phys. Today* **67**, 39–44 (2014).
23. Hofacker, M. & Miehe, C. A phase field model of dynamic fracture: Robust field updates for the analysis of complex crack patterns. *Int. J. Numerical Methods. Engineer* **93**, 276–301 (2013).
24. Nakahara, A. & Matsuo, Y. Imprinting memory into paste to control crack formation in drying process. *J. Statistical Mechanics: Theory and Experiment*. P07016 (2006).
25. Eek, J. *et al.* Dietary and genetic obesity promote liver inflammation and tumorigenesis by enhancing IL-6 and TNF expression. *Cell* **140**, 197–208 (2009).
26. Santhekadur, P. K., Kumar, D. P. & Sanya, A. J. Preclinical models of non-alcoholic fatty liver disease. *J. Hepatol.* **68**, 230–237 (2018).
27. Bhagat, V. & Becker, M. L. Degradable Adhesives for Surgery and Tissue Engineering. *Biomacromolecules* **18**, 3009–3039 (2017).
28. Iwadate, Y. *et al.* Myosin-II-mediated directional migration of Dictyostelium cells in response to cyclic stretching of substratum. *Biophys. J.* **104**, 748–758 (2013).
29. Iwadate, Y. & Yumura, S. Cyclic stretch of the substratum using a shape-memory alloy induces directional migration in dictyostelium cells. *Biotechniques* **47**, 757–767 (2009).
30. Tukey, C. W. Comparing individual means in the analysis of variance. *Biometrics* **5**, 99–114 (1949).
31. Kramer, C. Y. Extension of multiple range tests to group means with unequal numbers of replications. *Biometrics*. **12**, 307–310 (1956).
32. Driscoll, W. C. Robustness of the ANOVA and Tukey-Kramer statistical test. *Computers ind. Engng.* **31**, 265–268 (1996).
33. Rafter, J. A., Abell, M. L. & Braselton, J. P. Multiple comparison methods for means. *SIAM Review* **44**, 259–278 (2002).
34. Richter, S. J. & McCann, M. H. Using the Tukey-Kramer omnibus test in the Hayter-Fisher procedure. *Br. J. Math. Stat. Psychol.* **65**, 499–510 (2012).
35. Wright, T. C., Ukena, T. E., Campbell, R. & Karnovsky, M. J. Rates of aggregation, loss of anchorage dependence, and tumorigenicity of cultured cells. *Proc. Natl. Acad. Sci USA* **74**, 258–262 (1977).
36. Urushihara, H., Takeichi, M., Hakura, A. & Okada, T. S. Different cation requirements for aggregation of BHK cells and their transformed derivatives. *J. Cell Sci.* **22**, 685–695 (1976).

Acknowledgements

K.Y. is grateful for partial support from KAKENHI (Nos 15H02121, 25103012, 16K13655). T.K. is grateful for partial support from KAKENHI (No. 17K05615). We thank Prof. S. Kidoaki, Kyushu Univ., to the useful suggestion on the usage of urethane gel sheet and Prof. T. Tsumugiwa, Doshisha Univ., to the fruitful discussion on statistical analyses.

Author Contributions

T.K. and K.Y. conceived this research. T.N., K.D. and N.O. performed the main experiments. N.N. and K.I. prepared developed mice in different disease states for the research. T.N. and Y.I. developed the experimental setup. K.D. and N.O. analyzed the experimental data and performed image analyses. K.Y. and T.K. wrote the paper. K.D., T.K., N.N., K.I., Y.I. and K.Y. edited the paper. M.I., S.U. and K.Y. supervise over the research. All authors discussed the results and commented on the manuscript. N.O. contributed equally as a corresponding author to this work.

Additional Information

Competing Interests: The authors declare no competing interests.

Publisher's note: Springer Nature remains neutral with regard to jurisdictional claims in published maps and institutional affiliations.



Open Access This article is licensed under a Creative Commons Attribution 4.0 International License, which permits use, sharing, adaptation, distribution and reproduction in any medium or format, as long as you give appropriate credit to the original author(s) and the source, provide a link to the Creative Commons license, and indicate if changes were made. The images or other third party material in this article are included in the article's Creative Commons license, unless indicated otherwise in a credit line to the material. If material is not included in the article's Creative Commons license and your intended use is not permitted by statutory regulation or exceeds the permitted use, you will need to obtain permission directly from the copyright holder. To view a copy of this license, visit <http://creativecommons.org/licenses/by/4.0/>.

© The Author(s) 2018

In situ Extractive Fermentation of Lactic Acid by *Rhizopus oryzae* in an Air-lift Bioreactor



This work is licensed under a Creative Commons Attribution 4.0 International License

M. Matsumoto* and H. Furuta

Department of Chemical Engineering and Materials Science,
Doshisha University, Kyotanabe,
Kyoto 610-0321, Japan

doi: 10.15255/CABEQ.2017.1208

Original scientific paper
Received: September 1, 2017
Accepted: May 28, 2018

In this paper, the *in situ* extractive fermentation of lactic acid was developed with *Rhizopus oryzae* that grew in a medium without costly nutrients such as peptone or yeast extract. Tri-*n*-octylamine as an extractant and isotridecanol as a diluent were selected in an optimum extraction system from the viewpoint of the tolerance of organic solvents to *R. oryzae* and extraction capacity. Using this extraction system, batch fermentations were carried out in a stirred tank in the presence of an organic solution. It was found that a higher aeration rate was needed to enhance the production rate of the lactic acid and the extent of its extraction became relatively high due to the absence of extraction inhibitors, peptone and yeast extract. Finally, *in situ* extractive fermentation was carried out using pelleted *R. oryzae* in a fed-batch mode in an air-lift reactor. Lactic acid was successfully fermented and extracted from the broth to organic phase for 25 days.

Keywords:

in situ extractive fermentation, L-lactic acid, *Rhizopus oryzae*, trioctylamine, air-lift reactor

Introduction

Lactic acid, which plays an important role as a bulk chemical in the food, pharmaceutical, and cosmetic industries, is drawing great interest as the monomer of biodegradable poly-lactides¹. Demand is increasing for optically pure lactic acid for the production of poly-lactides because its optical purity significantly affects the physical properties of poly-lactides². Therefore, interest in the fermentative production of lactic acid is growing because the lactic acid produced by chemical synthesis routes is a racemic mixture. In addition, the biotechnological route has advantages for environmentally friendly production processes, such as low reaction temperature, low energy consumption, and the ability of using renewable resources instead of petrochemicals. The main biotechnological producers of lactic acid are bacteria and some filamentous fungi^{3,4}.

The fungus *Rhizopus oryzae* is widely studied as an L(+)-lactic acid producer^{3,4}. In the fermentative production of lactic acid using fungal cells, fungi possess better resistance to high concentrations of lactic acid and low pH of the medium than commonly used bacteria, and use media with much lower auxotrophic levels compared to those required by bacteria⁵, which simplifies the downstream product separation process. Studies on the fermentative production of lactic acid have been

conducted with pelleted and immobilized *R. oryzae*^{5–12} because free mycelia results in a highly viscous broth. The accumulation of lactic acid in the broth and the pH decrease in the medium associated with it negatively affect productivity¹⁰, although the fungi have better tolerance to the accumulation of lactic acid and low pH than bacteria. *In situ* extractive fermentation is a promising alternative to the conventional process because the accumulated lactic acid can be removed from the broth during fermentation. However, only one study¹⁰ has addressed the extractive fermentation of lactic acid with *R. oryzae*. In a previous paper¹⁰, trialkylphosphine oxide was used as the extractant of lactic acid. The reactive extraction of organic acids has already been heavily investigated^{13,14}. Such tertiary amines like tri-*n*-octylamine (TOA), diluted in a higher alcohol like 1-octanol, effectively extracted lactic acid¹⁵. Some studies have been conducted on the *in situ* extractive fermentation of lactic acid with bacteria and tertiary amines^{14,16}. One problem is the high toxicity of the extractant to bacteria. In our previous paper¹⁶, an *in situ* extractive fermentation process of lactic acid with TOA was constructed by co-immobilizing decanol-tolerant *Lactobacillus fructivorans* NRIC0224 cells and calcium carbonate into Ca-alginate capsules without pH control. The toxicity was considerably alleviated, but a slightly negative effect remained. As medium components, peptone and yeast extracts were found to be inhibitory compounds in the reactive extraction with TOA.

*To whom correspondence should be addressed.

Tel/Fax +81-774-65-6655; E-mail: mmatsumo@mail.doshisha.ac.jp

This paper developed the *in situ* extractive fermentation of lactic acid with *R. oryzae* in the growth medium which did not contain peptone or yeast extract. Firstly, the toxicity of extractants and diluents to *R. oryzae* was examined. Although some studies can be found on the solvent toxicity to lactic acid producing bacteria¹⁷, our previous study is the only report that is concerned with the toxicity of diluents to lactic acid producing fungi¹⁸. The toxicity of the extractant diluted in the organic solvent was studied in this paper. In the next section, we describe our extractive fermentation experiments conducted *in situ* with pelleted *R. oryzae* using our selected extraction system.

Materials and methods

Chemicals

Tri-*n*-butyl phosphate (TBP), tri-*n*-hexylamine (THA), and tri-*n*-octylamine (TOA) were used as extractants of lactic acid. The diluents for the extractant were 1-octanol, 1-decanol, isotridecanol and oleyl alcohol. All the chemicals of GR grade having purity of > 99 % were used as received from the suppliers.

Organisms and cultivation

We used a lactic acid producing mold: *Rhizopus oryzae* IAM 6022. The microorganisms were maintained on potato dextrose agar (PDA, Nissui) slants. The production medium consisted of glucose 20 g L⁻¹, (NH₄)₂SO₄ 1.35 g L⁻¹, K₂HPO₄ 0.3 g L⁻¹, MgSO₄·7H₂O 0.25 g L⁻¹ and ZnSO₄·7H₂O 0.04 g L⁻¹^{6,9}. Cultivations were performed at 30 °C.

Production in the presence of organic solvents

Lactate production in the presence of a second phase was determined based on a previous method¹⁶. A spore suspension from a PDA slant was transferred to a 100 mL production medium in a 250-mL culture bottle. The culture bottle was shaking-incubated for 24 h at 30 °C and 100 rpm (BW201, Yamato, Tokyo Japan). After pH of the medium was adjusted to 6 by adding a 5 mol L⁻¹ NaOH aqueous solution, we added 30 mL of each organic solvent listed in Table 1 to form the second phase. The culture bottles were sealed with Teflon valves to prevent evaporation and incubated for 48 h at 30 °C. The glucose concentration was then measured.

Batch fermentation in a stirred tank

Batch fermentations were performed with a working volume of 600 mL at 30 °C in 1-L stirred tank (MBF, EYELA, Tokyo Japan). A spore suspen-

Table 1 – Toxicity of organic solvents to *Rhizopus oryzae* IAM 6022

Solvent	Log $P_{o/w}$	Relative activity
1-Octanol	2.9	≈0
1-Decanol	3.8	0.21
Isotridecanol	5.2	0.70
Oleyl alcohol	7.5	1.09
Trioctylamine (TOA)	10.3	0.056
Trihexylamine	7.4	0.005
Tributyl phosphate	3.8	≈0
0.5 mol L ⁻¹ TOA in isotridecanol	–	0.99
0.5 mol L ⁻¹ TOA in 1-decanol	–	0.35

Relative activity is defined as ratio of glucose consumption of sample to that of control.

sion from a PDA slant was transferred to a 600 mL production medium. The aeration rate and agitation speed were 1.0 L min⁻¹ and 70 rpm. In the anaerobic condition, air was not bubbled. Samples were withdrawn periodically during the fermentation, analysed for glucose and lactic acid and measured pH value. In the absence of an organic phase, the pH of the broth was manually kept at the initial pH by adding a 5 mol L⁻¹ NaOH solution. In the case of extractive fermentation, 200 mL of organic solution, which consisted of 0.5 mol L⁻¹ TOA in isotridecanol, was added to the broth. Extractive fermentation was conducted without pH control.

Pellet formation

A spore suspension from a PDA slant was transferred to a 100 mL production medium in a 250-mL culture bottle, which was shaking-incubated for 72 h at 28 °C and 100 rpm (BW201, Yamato, Tokyo Japan). During the incubation, the pH was kept at the initial pH level of the culture by adding calcium carbonate to prompt a morphology change from dispersed filamentous to a pellet form 3 to 4 mm in diameter. Pellet formation was confirmed visually.

Extractive fermentation of lactic acid with pelleted *R. oryzae* in air-lift reactor

We also carried out lactic acid production using pelleted *R. oryzae* in an air-lift reactor (diameter 120 mm, length 250 mm) in a batch mode as illustrated in Fig. 1. The volumes of culture including 5 mL of antifoaming agent (Tween 80) and extraction phase were initially 2 L and 500 mL, respectively. The broth in the tank was held at 28 °C and the aeration rate from annular air tube was 6.0 L min⁻¹. In extractive fermentation, 500 mL of isotridecanol solution containing 0.5 mol L⁻¹ TOA was placed on

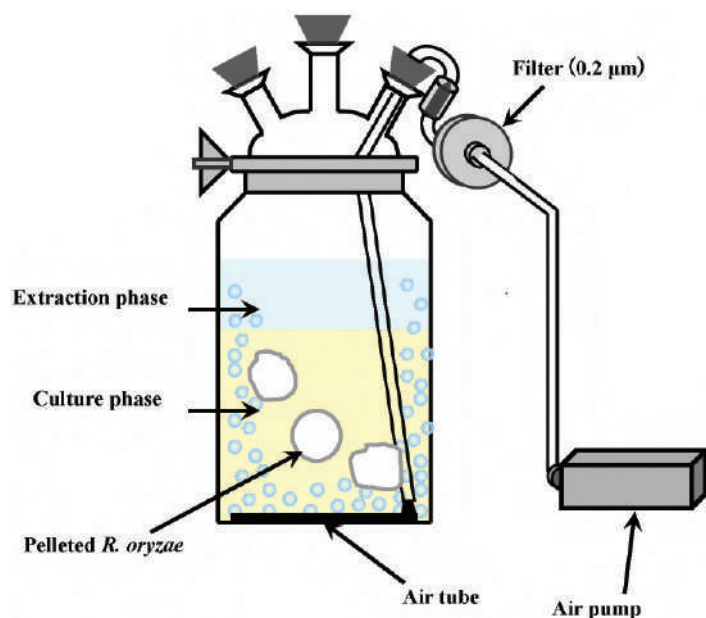


Fig. 1 – Schematic diagram of extractive fermentation with air-lift reactor

top of the medium solution. Samples were withdrawn periodically from the medium and the organic phase during fermentation, and analysed for pH, glucose and lactic acid. When the pH of the broth decreased to 3, the extraction phase was exchanged with a fresh one. When the glucose was depleted, an enriched 100 mL glucose solution was added to become an initial glucose concentration.

Analysis

The lactic acid in the organic phase was stripped with a 1 mol L⁻¹ NaOH solution. The concentrations of the lactic acid, glucose and ethanol in the resultant aqueous solutions were determined by HPLC (Shimadzu LC-10ADvp) with a Shodex SH-1011 column and a 5 mmol L⁻¹ H₂SO₄ solution as a mobile phase. Lactic acid, glucose and ethanol were detected with an RI detector (Shimadzu RID10A).

Results and discussion

Tolerance of *R. oryzae* to organic solvent

We previously¹⁸ investigated the tolerance of lactic acid-producing fungi *R. oryzae* JCM 5568 to organic solvents. A solvent with a high log $P_{o/w}$ exhibited the highest metabolic activities and solvents with a lower log $P_{o/w}$ ($P_{o/w}$ is the partition coefficient of a molecule between 1-octanol and water) were toxic to *R. oryzae* JCM 5568, which showed higher tolerance to aliphatic alcohols than to aliphatic hydrocarbons. Furthermore, long-chain aliphatic alcohols, such as octanol and decanol, were reported to

be active diluents for lactic acid extraction¹⁹. We examined the tolerance of *R. oryzae* IAM 6022 to long-chain aliphatic alcohols as diluents and extractants such as TBP, THA and TOA. Table 1 shows the relationship between the relative activity retained by cells exposed to long-chain aliphatic alcohols and extractants, and their log $P_{o/w}$ values. Relative activity in the presence of organic solvents was determined on the basis of the concentration of the glucose consumed after adding an organic solvent, where the relative activity was defined as the ratio of the glucose concentration of the sample to that of the control. Aliphatic alcohols with higher log $P_{o/w}$ were less toxic to *R. oryzae* IAM 6022¹⁸. All the extractants used in this study showed high toxicity to *R. oryzae* IAM 6022. Although oleyl alcohol produced the highest activity, one of its disadvantages is its relatively high viscosity of 28.32 mPa s at 25 °C²⁰. Therefore, we examined the tolerance of a mixture of TOA and isotridecanol or 1-decanol. In the case of TOA (0.5 mol L⁻¹) and isotridecanol, its relative activity is comparable to that of control. In the following experiment, this extraction system was employed.

Extractive fermentation in a stirred tank

Based on the above results, batch fermentations were carried out in a stirred tank to examine the effect of the addition of an organic solution on fermentation. Figs. 2 and 3 show the time courses of the concentrations of glucose, lactic acid and ethanol, and pH during fermentation in the absence and presence of an organic solution, respectively. In pH-controlled fermentation without an organic solution, the glucose was completely depleted at 68.5 h, and lactic acid and ethanol were produced ($Y_{p/s}$ = lactic acid produced/glucose consumed = 0.492 g-lactic acid g⁻¹-glucose). For the extractive fermentation, pH was uncontrolled because the condition of the lower pH was preferable for the extraction¹⁶. Lactic acid was successfully produced by fermentation in the presence of an organic solution. However, the fermentation rate was slower than that of the control, and the time required to deplete the glucose was extended to 120 h, although the presence of 0.5 mol L⁻¹ TOA in the isotridecanol had little effect on the lactic acid production as described above. This suggests that air supply for *R. oryzae* was insufficient because the layered organic phase cut off the air contact. Fig. 4 shows extractive fermentation under anaerobic conditions. As is evident from Figs. 2 and 4, the anaerobic fermentation is slower than the aerobic fermentation. Therefore, a higher aeration rate is needed to enhance the fermentation rate. After 120 h, 55 % of lactic acid produced was extracted to the organic phase at pH 4. In our previous paper¹⁶, it was reported that yeast ex-

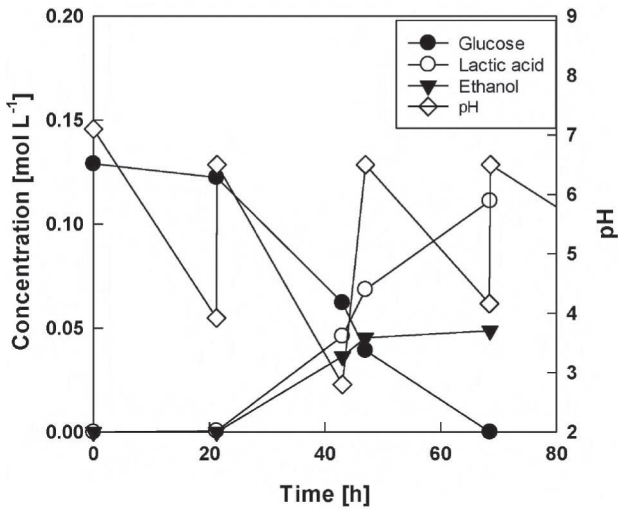


Fig. 2 – Lactic acid fermentation by *Rhizopus oryzae* IAM 6022 in stirred tank under aerobic conditions

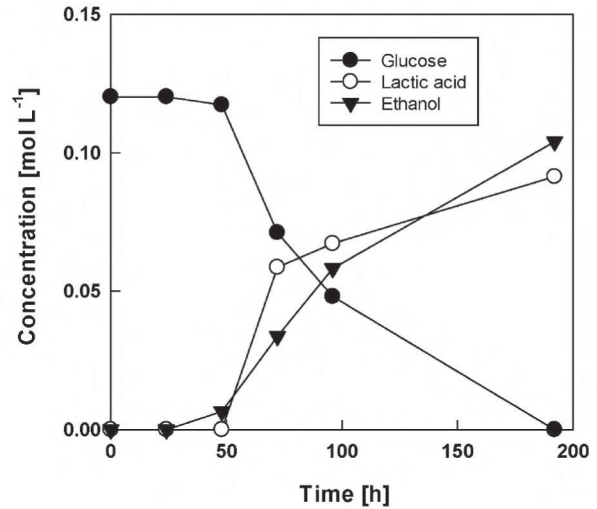


Fig. 4 – Lactic acid fermentation by *Rhizopus oryzae* IAM 6022 in stirred tank under anaerobic conditions

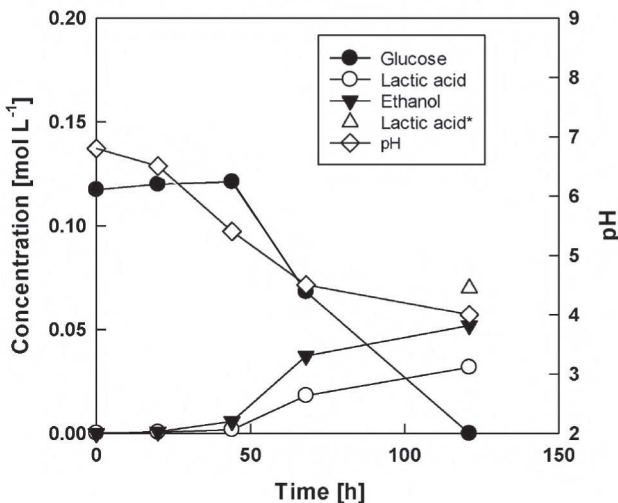


Fig. 3 – Extractive fermentation of lactic acid by *Rhizopus oryzae* IAM 6022 in stirred tank under aerobic conditions (*lactic acid produced considering lactic acid extracted in the organic phase)

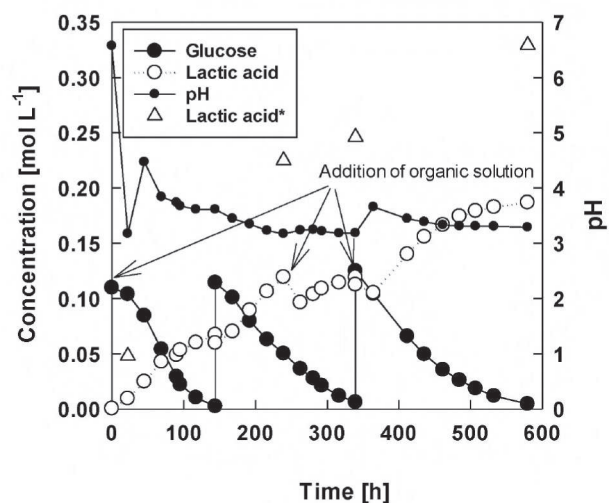


Fig. 5 – Extractive fermentation of lactic acid by *Rhizopus oryzae* IAM 6022 in air-lift reactor (*lactic acid produced considering lactic acid extracted in organic phase)

tract and peptone in the broth considerably interfered with the extraction of lactic acid and extractability in the broth decreased to 1/10 compared to that of the model solution in the absence of yeast extract and peptone. In this experiment, relatively high extractability was obtained, because the medium did not contain yeast extract or peptone.

Extractive fermentation in an air-lift reactor

The application of fungi such as *Rhizopus* for the commercial production of lactic acid was considered using air-lift reactors because of their low energy consumption⁴. As described above, a high aeration rate is needed to enhance the fermentation

rate. In this study, *in situ* extractive fermentation was carried out using pellets of *R. oryzae* in a fed-batch mode in air-lift reactor shown in Fig. 1.

Fig. 5 shows the time courses of the glucose and lactic acid concentrations in the extractive fermentation of lactic acid in an air-lift bioreactor without pH control. When the glucose was depleted in the broth, 100 mL enriched glucose solution was added so that it became an initial glucose concentration. We continued the fermentation until the glucose was depleted in the third cycle. Yield, $Y_{p/S}$, glucose consumption rate, v_{glu} , fermentation time (FT), and efficiency of extraction, E , in each cycle are listed in Table 2. These constants were defined by the following equations.

$$Y_{P/S} = \text{lactic acid produced/glucose consumed} \cdot 100 \text{ [g-lactic acid g}^{-1}\text{-glucose]}$$

$$v_{\text{glu}} = \text{concentration change of glucose/FT [mmol-glucose L}^{-1}\text{ h}^{-1}\text{]}$$

$$\text{FT} = \text{time from glucose addition to glucose consumption [h]}$$

From Fig. 5, the lactic acid was successfully fermented during each cycle and extracted to the organic phase for 600 h. The yield in an air-lift bioreactor exceeded that (= 98 %) in an aerobic batch reactor shown in Fig. 2. In an air-lift bioreactor, the pH gradually decreased after the initial stage, and when it fell to 3.3, the organic phase was replaced with a fresh one, because an extraction equilibrium was achieved. As is evident from Table 2, however, after repeated cycles, the yield and glucose consumption rate slightly decreased, and the fermentation time was prolonged, probably due to the slight toxicity of the organic phase. The extractability of lactic acid from the broth remained unchanged from the model solution described in the previous paper¹⁶.

Future work will introduce a circulation system of an organic solution combined with a stripping process to continuously recover lactic acid from the fermentation broth.

Conclusion

This paper developed the *in situ* extractive fermentation of lactic acid with *Rhizopus oryzae* that grew in a medium without costly nutrients, such as peptone and yeast extract. Firstly, we examined a suitable organic solution for this fermentation system, and selected tri-*n*-octylamine as an extractant and isotridecanol as a diluent based on the tolerance of organic solvents to *R. oryzae* and extraction capacity. Using this extraction system, batch fermentations were carried out in a stirred tank to examine the effect of the addition of an organic solution on the fermentation. We found that a higher aeration rate was needed to enhance the production rate of the lactic acid and the extent of lactic acid extracted became relatively high due to the absence of extraction inhibitors such as peptone and yeast extract. Finally, *in situ* extractive fermentation was carried out using pellets of *R. oryzae* in a fed-batch mode in an air-lift reactor. Lactic acid was successfully fermented and extracted to an organic phase for 600 h.

Table 2 – Constants of extractive fermentation in air-lift reactor

Cycle	$Y_{P/S}$ (%)	v_{glu} (mmol L ⁻¹ h ⁻¹)	FT (h)	E (%)
1st	66	7.46	144	46.9*
2nd	57	5.53	196	52.9
3rd	48	5.01	240	43.2

*This value was measured at 239 h.

Having developed optimal fungi for lactic acid production, this paper demonstrates that extractive fermentation is a promising method.

ACKNOWLEDGMENTS

This work was supported by JSPS KAKENHI Grant Number 16H04556 and the MEXT-Supported Program for the Strategic Research Foundation at Private Universities.

References

- Nampoothiri, K. M., Nair, N. R., John, R. P., An overview of the recent developments in polylactide (PLA) research, *Bioresource Technol.* **101** (2010) 8493. doi: <https://doi.org/10.1016/j.biortech.2010.05.092>
- Inkinen, S., Hakkarainen, Albertson, A.-C., Södergård, A., From lactic acid to poly(lactic acid) (PLA): Characterization and analysis of PLA and its precursors, *Biomacromolecules* **12** (2011) 523. doi: <https://doi.org/10.1021/bm101302t>
- Ghaffar, T., Irshad, M., Anwar, Z., Aqil, T., Zulifqar, Z., Tariq, A., Kamran, M., Ehsan, N., Mehmood, S., Recent trends in lactic acid biotechnology: A brief review on production to purification, *J. Radiation Res. Appl. Sci.* **7** (2014) 222. doi: <https://doi.org/10.1016/j.jrras.2014.03.002>
- Juturu, V., Wu, J. C., Microbial production of lactic acid: The latest development, *Crit. Rev. Biotechnol.* **36** (2016) 967. doi: <https://doi.org/10.3109/07388551.2015.1066305>
- Ranjit, C., Srividya, S., Lactic acid production from free and polyurethane immobilized cells of *Rhizopus oryzae* MTCC 8784 by direct hydrolysis of starch and agro-industrial waste, *Int. Food Res. J.* **23** (2016) 2646.
- Miura, S., Arimura, T., Hoshino, M., Kojima, M., Dwiarti, L., Okabe, M., Optimization and scale-up of L-lactic acid fermentation by mutant strain *Rhizopus* sp. MK-96-1196 in airlift bioreactors, *J. Biosci. Bioeng.* **96** (2003) 65. doi: [https://doi.org/10.1016/S1389-1723\(03\)90098-3](https://doi.org/10.1016/S1389-1723(03)90098-3)
- Bai, D., Jia, M., Zhao, X., Ban, R., Shen, F., Li, X., Xu, S., L(+)-Lactic acid production by pellet-form *Rhizopus oryzae* R1021 in a stirred tank fermentor, *Chem. Eng. Sci.* **58** (2003) 785. doi: [https://doi.org/10.1016/S0009-2509\(02\)00608-5](https://doi.org/10.1016/S0009-2509(02)00608-5)
- Koide, M., Hirata, M., Gao, M., Takashi H., Hano, T., Continuous fermentation of L-lactic acid by the mold *Rhizopus oryzae*, *Kagaku Kogaku Ronbunshu* **30** (2004) 432. doi: <https://doi.org/10.1252/kakoronbunshu.30.432>
- Miura, S., Dwiarti, L., Okabe, M., Enhanced production of L-lactic acid by ammonia-tolerant mutant strain *Rhizopus* sp. MK-96-119, *J. Biosci. Bioeng.* **97** (2004) 19. doi: [https://doi.org/10.1016/S1389-1723\(04\)70159-0](https://doi.org/10.1016/S1389-1723(04)70159-0)
- Lin, J., Zhou, M., Zhao, X., Luo, S., Lu, Y., Extractive fermentation of L-lactic acid with immobilized *Rhizopus oryzae* in a three-phase fluidized bed, *Chem. Eng. Process.* **46** (2007) 369. doi: <https://doi.org/10.1016/j.cep.2006.06.015>

11. Wu, X., Jiang, S., Liu, M., Pan, L., Zheng, Z., Luo, S., Production of L-lactic acid by *Rhizopus oryzae* using semicontinuous fermentation in bioreactor, *J. Ind. Microbiol. Biotechnol.* **38** (2011) 565.
doi: <https://doi.org/10.1007/s10295-010-0804-8>
12. Vodnar, D. C., Dulf, F. V., Pop, O. L., Socaciu, C., L(+)-Lactic acid production by pellet-form *Rhizopus oryzae* NRRL 395 on biodiesel crude glycerol, *Microbial Cell Factories* **12** (2013) 92.
doi: <https://doi.org/10.1186/1475-2859-12-92>
13. Li, Q. Z., Jiang, X. L., Feng, X. J., Wang, J. M., Sun, C., Zhang, H. B., Xian, M., Liu, H. Z., Recovery processes of organic acids from fermentation broths in the biomass-based industry, *J. Microbiol. Biotechnol.* **26** (2016) 1.
doi: <https://doi.org/10.4014/jmb.1505.05049>
14. Komesu, A., de Oliveria, J. A. R., Martins, L. H. da S., Maciel, M. R. W., Filho, R. M., Lactic acid production to purification: A review, *BioResources* **12** (2017) 1.
doi: <https://doi.org/10.15376/biores.12.2.Komesu>
15. Krzyżaniak, A., Leeman, M., Vossebeld, F., Visser, T. J., Schuur, S., de Haan, A. B., Novel extractants for the recovery of fermentation derived lactic acid, *Sep. Purif. Technol.* **111** (2013) 82.
doi: <https://doi.org/10.1016/j.seppur.2013.03.031>
16. Matsumoto, M., Nishimura, M., Kobayashi, H., Kondo, K., Extractive fermentation of lactic acid with Hiochi bacteria in a two-liquid phase system, *Ferment. Technol.* **5** (2016) 1000129.
doi: <https://doi.org/10.4172/2167-7972.1000129>
17. Matsumoto, M., Mochizuki, K., Kondo, K., Toxicity of ionic liquids and organic solvents to lactic acid-producing bacteria, *J. Biosci. Bioeng.* **98** (2004) 344.
doi: [https://doi.org/10.1016/S1389-1723\(04\)00293-2](https://doi.org/10.1016/S1389-1723(04)00293-2)
18. Matsumoto, M., Aoki, K., Kondo, K., Toxicity of organic solvents to *Rhizopus oryzae* JCM 5568, *Solv. Extr. Res. Develop. Japan* **15** (2008) 127.
19. Tik, N., Bayraktar, E., Mehmetoglu, Ü., In situ reactive extraction of lactic acid from fermentation media, *J. Chem. Tech. Biotechnol.* **76** (2001) 764.
doi: <https://doi.org/10.1002/jctb.449>
20. Blahušiak, M., Marták, J., Miranda, F., Schlosser, S., Teixeira, J. S., Effect of viscosity of a liquid membrane containing oleyl alcohol on the pertraction of butyric acid, *Chem. Paper* **67** (2013) 1560.
doi: <https://doi.org/10.2478/s11696-013-0370-4>

DURABILITY OF CHITOSAN/CELLULOSE HYDROGEL BEADS REGENERATED FROM AN IONIC LIQUID IN ACIDIC AND BASIC MEDIA AND THEIR METAL ADSORPTIVE CHARACTERISTICS

Michiaki Matsumoto*, Sayumi Ishikawa, Tatsuya Kamigaki

*Department of Chemical Engineering and Materials Science,
Doshisha University
Kyotanabe, 610-0321 Kyoto, Japan
e-mail: mmatsumo@mail.doshisha.ac.jp*

Abstract

Chitosan–cellulose gel beads were regenerated from an ionic liquid, and their application to a metal adsorbent was examined. The chitosan–cellulose gel beads, which were prepared from 1-ethyl-3-methylimidazolium acetate, were more stable in the acidic and basic aqueous solutions than cellulose or chitosan. The adsorption of copper on chitosan–cellulose gel beads was examined, and the adsorption amount of copper ion increased with pH, suggesting that amino groups on chitosan were related to adsorption. The adsorption isotherm of copper, zinc, and nickel ions was well described by the Langmuir model, and the adsorption ability of these metal ions obeyed the Irving-Williams series. Fe^{3+} , Mn^{2+} , and Co^{2+} from a buffer solution and Pt^{4+} , Au^{3+} , and Pd^{2+} from a hydrochloric acid solution were not adsorbed on the chitosan–cellulose gel beads.

Keywords: *Chitin, cellulose, ionic liquid, Emim, adsorption, copper, zinc, nickel*

Received: 25.02.2019

Accepted: 15.04.2019

1. Introduction

Chitosan, which consists of D-glucosamine with β -(1,4) bonds, is a superior metal adsorbent and is expected to be used in the removal of metallic ions in wastewater. Its adsorption capacity and selectivity can be enhanced by chemical modification [1]. However, chitosan is easily soluble in dilute acidic solutions because of the protonation of the amino group. In most cases, crosslinking among amino groups of chitosan is carried out for insolubilization. The metal adsorption capacity generally decreases with an increase in the extent of crosslinking because amino groups on chitosan bind the metal ions. Recently, the preparation of chitosan–cellulose hydrogel beads enhanced the mechanical and chemical strength. Li and Bai mechanically prepared chitosan–cellulose hydrogel beads [2]. The prepared gel beads were also soluble in the acidic solution, and crosslinking of the gels was needed as an adsorbent. Because an ionic liquid can dissolve polysaccharides such as cellulose and chitosan, Sun *et al.* prepared chitosan–cellulose beads by regeneration from the ionic liquid 1-butyl-3-methyl imidazolium chloride ([Bmim][Cl]) [3]. Their gel beads were stable in a 0.1 mol/dm³ HCl solution and were applied to Ni adsorption. Chitosan–cellulose gel beads, regenerated from [Bmim][Cl], were also applied to microcystin adsorption [4]. Moreover, to easily recover the gel beads, magnetic cellulose–chitosan hydrogels were prepared as a metal adsorbent [5,6]. Chitosan–cellulose gel beads that were regenerated from 1-ethyl-3-methyl imidazolium acetate ([Emim][Ac]) were prepared and applied to dye adsorption [7]. The preparation condition of the chitosan–cellulose gel beads regenerated from [Emim][Ac] was milder than those of [Bmim][Cl].

In this study, we prepared chitosan–cellulose gel beads regenerated from [Emim][Ac] and examined their durability in acidic and basic solutions and the adsorptive characteristics of the metal ions.

2. Materials and Methods

2.1. Chemicals

Cellulose powder (type C; Advantec, Japan) and chitosan (low molecular weight, 75–85% deacetylated, Sigma-Aldrich, USA) were used. The ionic liquid used in this study was 1-ethyl-3-methyl imidazolium acetate ([Emim][Ac]) (IOLITEC Ionic Liquid Technology, Germany). All the remaining reagents were of analytical grade and were used without further purification.

2.2. Preparation of Chitosan–Cellulose Hydrogel Beads

Chitosan–cellulose hydrogel beads were prepared by modifying a previously reported procedure [7]. Cellulose and chitosan were added to [Emim][Ac] and stirred at 80°C to form a homogeneous solution with a total concentration of 5–10% (w/w). Using a Terumo 1-mL syringe, the obtained solution was extruded dropwise into water and left to stand for 1 h for the beads to harden. Then, the hydrogel beads were collected and thoroughly rinsed with deionized water. The obtained hydrogel beads were stored in the deionized water and filtered just before use. Although cellulose hydrogel beads were prepared in a similar procedure, chitosan gel beads could not be prepared.

2.3. Characteristic of Chitosan–Cellulose Hydrogel Beads

Both the specific surface area and the pore size of the hydrogel beads were measured by micromeritics automatic surface area and a porosimetry analyser (Tristar 3000, Shimadzu, Japan). The surface of the adsorbent was observed by electron microscopy (JSM7500 FD, JEOL, Japan). The hydration rates of the hydrogel beads were measured by a moisture analyser (MOC63u, Shimadzu, Japan). The durability tests of the

hydrogel beads were conducted in 0.1 mol/dm³ acetic acid, 0.1 mol/dm³ HCl, 0.1 mol/dm³ H₂SO₄, and 0.1 mol/dm³ NaOH solutions.

2.4. Adsorption of Metals on Hydrogel Beads

The adsorption tests of various metal ions, including Fe(III), Cu(II), Co(II), Ni(II), Zn(II), Mn(II), Pt(IV), Au(III), and Pd(II), on hydrogel beads were measured to evaluate the adsorption ability by shaking 250 mg of gel beads in 20 mL of the test solution that contained 1.0 mmol/dm³ of the individual metal ions at 100 rpm for 24 h at 30°C. It was confirmed that an adsorption equilibrium was attained within 12 h. The pH values and acidities were adjusted using the following solution: 0.1 mol/dm³ HCl/CH₃COOH/CH₃COONa for Fe(III), Cu(II), Co(II), Ni(II), Zn(II), and Mn(II) and 1–5 mol/dm³ HC for Pt(IV), Au(III), and Pd(II). After attaining equilibrium, the mixtures were filtered to separate the gel beads.

The adsorption isotherms were measured to evaluate the maximum adsorption capacity of both adsorbents by shaking 250 mg of the adsorbents with 10 mL of the test solutions containing individual metals that ranged from 0.5 to 40 mmol/dm³. The initial and residual concentrations of the metal ions in the filtrate were measured by inductively coupled plasma atomic emission spectrometry (ICPS-8100, Shimadzu, Japan). The pH values of the solution were measured with a pH meter (F-52, Horiba, Japan) before and after the adsorption experiment. The amount of adsorbed metal ions was calculated from the difference in metal concentration between the initial solution and the filtrate. The amount of the metal adsorbed on the adsorbent [q (mmol/g-adsorbent)] was calculated using the following equation:

$$q = \frac{C_i - C_f}{M} \times V \quad (1)$$

where C_i and C_f are the metal concentrations (mmol/dm³) before and after adsorption, V is the volume of the test solution (L), and M is the dry mass of the adsorbent (g).

3. Results and Discussion

3.1 Characteristics of Chitosan–Cellulose Hydrogel Beads

Figure 1 shows photo images of the chitosan–cellulose gel beads before and after copper adsorption. The shapes were almost spherical, and the mean diameter of the beads was ca 4 mm. After Cu adsorption, the colour of the beads uniformly changed to blue, suggesting that copper was adsorbed on the chitosan–cellulose hydrogel beads. The average pore sizes and the specific surface areas of the cellulose beads and the chitosan–cellulose beads are listed in Table 1 with the hydration rates of the beads. The hydration rate of the chitosan–cellulose hydrogel beads exceeded that of cellulose. This result corresponds to a previous work, where adding cellulose in the chitosan reduced the water content [2].

Table 1. Characteristics of gel beads

	Specific surface area (m²/g)	Pore size (nm)	Hydration rate (%)
Cellulose 4 wt%	44.77	17.23	86.3
Cellulose 4 wt% + Chitosan 2 wt%	7.05	26.34	90.1

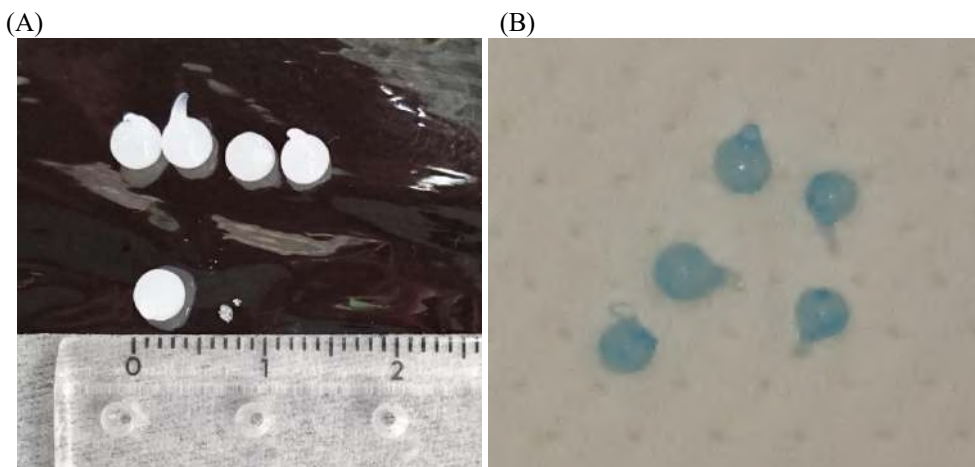


Figure 1. Images of chitosan–cellulose gel beads before (A) and after (B) copper adsorption.

3.2 Durability of Chitosan–Cellulose Hydrogel Beads

The chitosan–cellulose hydrogel beads, the cellulose beads, and the chitosan flakes were tested for durability in the acidic and basic solutions. Table 2 lists the ratio of the weights of the beads or flakes after being placed in water, 0.1 mol/dm³ acetic acid, 0.1 mol/dm³ hydrochloric acid, 0.1 mol/dm³ sulfuric acid, and 0.1 mol/dm³ sodium hydroxide solutions for 24 h to the initial weights of the beads. After 24 h, chitosan was completely dissolved in the acetic acid and hydrochloric acid solutions and the shapes of the cellulose–chitosan gel beads were maintained in all the tested solutions. The cellulose–chitosan gel beads that were formed by blending chitosan and cellulose were dissolved in an acetic acid solution [2], and the gels that were regenerated from [Bmim][Cl] were stable in the HCl aqueous solution with pH=1 [3]. The present gels regenerated from [Emim][Ac] were stable even in the acidic acid and basic solutions. This suggests that the interaction of cellulose and chitosan in the gel beads regenerated from the ionic liquid solution was critical for the durability.

Table 2. Durability of gel beads and flakes

	Water	Acetic acid	HCl	H ₂ SO ₄	NaOH
Cellulose gel beads	1.00	0.98	1.00	1.00	0.68
Chitosan flakes	1.00	0.00	0.00	0.32	0.99
Cellulose–chitosan beads	1.00	1.00	0.99	0.94	0.93

3.3 Adsorption of Metallic Ions on Chitosan-Cellulose Hydrogel Beads

Figure 2 shows the effect of pH on Cu adsorption on the chitosan–cellulose and cellulose gel beads, as well as chitosan flakes. As described above, chitosan flakes were dissolved in the acidic solution (pH=3 and 4). The Cu adsorption was attributed to chitosan [1]. The adsorption capacities of the chitosan–cellulose gel beads and the chitosan flakes increased with pH because of the protonation of the amino groups on chitosan at a lower pH [2,3].

The adsorption ability of the chitosan–cellulose hydrogels for metals from the aqueous solution were examined. We observed no appreciable adsorption of Fe³⁺, Mn²⁺, and Co²⁺

DURABILITY OF CHITOSAN/CELLULOSE HYDROGEL BEADS REGENERATED FROM AN IONIC LIQUID IN ACIDIC AND BASIC MEDIA AND THEIR METAL ADSORPTIVE CHARACTERISTICS

from the buffer solution and Pt^{4+} , Au^{3+} , and Pd^{2+} from the hydrochloric acid solution. However, an adsorption affinity to Cu^{2+} , Zn^{2+} , and Ni^{2+} was exhibited. **Figure 3** shows the adsorption isotherms of these metals. The data were analysed by the Langmuir isotherm. The parameters, the maximum amount of adsorption (q_{max}), and a constant of the Langmuir model (K) were determined by a non-linear regression program included in the Sigmaplot 14 software. Solid lines in **Figure 3** were calculated by these parameters. The calculated lines agree well with the experimental results. The obtained parameters are listed in **Table 3**. The order of the q_{max} values was $\text{Cu}^{2+} > \text{Zn}^{2+} > \text{Ni}^{2+}$ and obeyed the Irving-Williams series, which refers to the stabilities between metal cations and ligands.

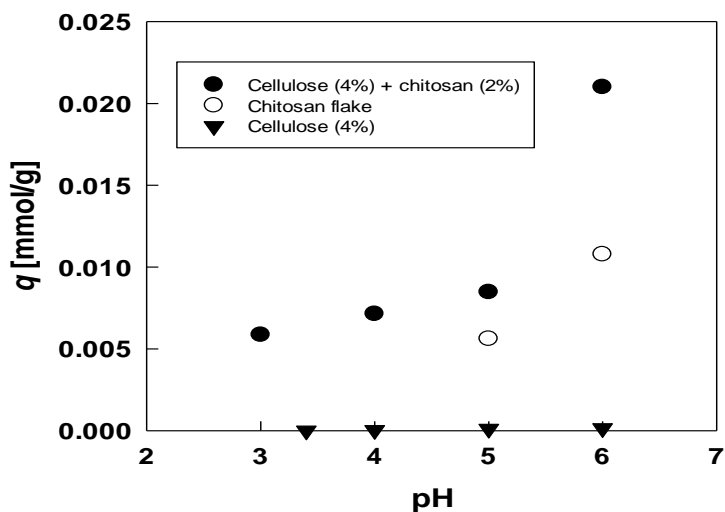


Figure 2. Effect of pH on adsorption of Cu^{2+} on cellulose, cellulose (4%)–chitosan (2%) hydrogel beads, and chitosan flakes (initial Cu^{2+} concentration of 1.0 mmol/dm^3)

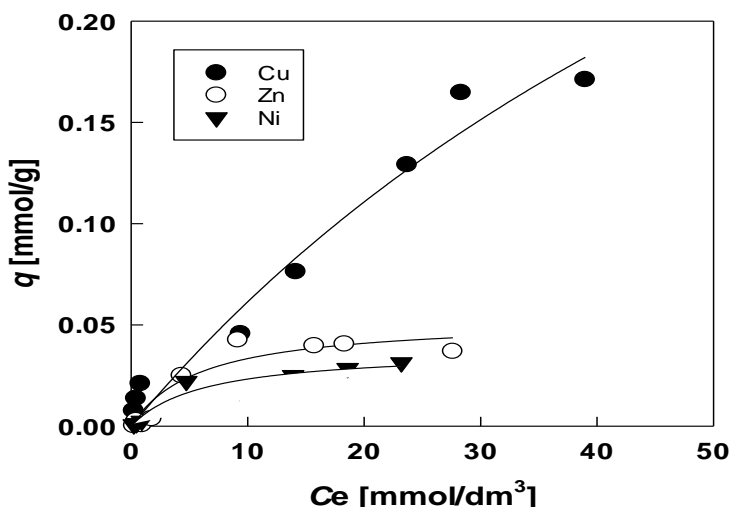


Figure 3. Adsorption isotherm of metallic ions on cellulose (4%)–chitosan (2%) hydrogel beads

Table 3. Langmuir parameters

	$10^2 q_{\max}$ (mmol/g)	$10^2 K$ (dm ³ /mmol)
Cu	56.7±3.2	1.21±0.92
Zn	5.28±0.92	17.1±9.1
Ni	3.76±0.65	16.2±8.5

4. Conclusion

Chitosan–cellulose gel beads were regenerated from an ionic liquid ([Emim][Ac]) and used as an adsorbent for metal removal. The prepared cellulose–chitosan gel beads had higher stability in the acidic and basic aqueous solutions than cellulose or chitosan. The adsorption of Cu on the chitosan–cellulose gel beads increased with pH, suggesting that the amino groups on chitosan were concerned with adsorption. The adsorption isotherm of the metal ions was well described by the Langmuir model, and the adsorption ability of the metal ions obeyed the Irving-Williams series. The chitosan–cellulose gel regenerated from [Emim][Ac] had high chemical stability and excellent metal adsorption ability.

5. Acknowledgments

This work was supported by JSPS KAKENHI Grant Number 16H04556 and the MEXT-Supported Program for the Strategic Research Foundation at Private Universities.

6. References

- [1] Varma, A. J., Deshpande, S. V., Kennedy, J. F.;(2004) Metal complexation by chitosan and its derivatives: a review. *Carbohydrate Polymers* 55, 77-93; DOI: 10.1016/j.carbopol.2003.08.005
- [2] Li, N., Bai, R.; (2005) Copper adsorption on chitosan-cellulose hydrogel beads: behaviors and mechanisms. *Separation and Purification Technology* 42, 237-247; DOI: 10.1016/j.seppur.2004.08.002
- [3] Sun, X., Peng, B., Ji, Y., Chen, J., Li, D.; (2009) Chitosan (Chitin)/cellulose composite biosorbents prepared using ionic liquid for heavy metal ions adsorption. *AIChE Journal* 55, 2062-2069; DOI: 10.1002/aic.11797
- [4] Tran, C. J., Duri, S., Delneri, A., Franko, M.; (2013) Chitosan-cellulose composite materials: preparation, characterization and application for removal microcystin. *Journal of Hazardous Materials* 252-253. 355-366; DOI: 10.1016/j.hazmat.2013.02.046
- [5] Liu, Z., H. Wang, Liu, C., Jiang, Y., Yu, G., Mu, X, Wang, X.; (2012) Magnetic cellulose-chitosan hydrogels prepared from ionic liquids as reusable adsorbent for removal of heavy metals. *Chemical Communications* 48, 7350-7352; DOI: 10.1039/c2cc17795a
- [6] Peng, S., Meng, H., Ouyang, Y., Chang, J.; (2014) Nonporous magnetic cellulose-chitosan composite microspheres: preparation, characterization, and application for Cu(II) adsorption. *Industrial and Engineering Chemistry Research* 53, 2106-2113; DOI: 10.1021/ie402855t
- [7] Li, M., Wang Z., Li, B.; (2016) Adsorption behavior of congo red by cellulose/chitosan hydrogel beads regenerated from ionic liquid. *Desalination and Water Treatment* 57, 16970-16980; DOI: 10.1080/19443994.2015.1082945

Article

Manipulating Living Cells to Construct a 3D Single-Cell Assembly without an Artificial Scaffold

Aoi Yoshida ^{1,†}, Shoto Tsuji ^{1,†}, Hiroaki Taniguchi ^{2,†}, Takahiro Kenmotsu ¹, Koichiro Sadakane ^{1,*} and Kenichi Yoshikawa ^{1,*}

¹ Faculty of Life and Medical Sciences, Doshisha University, Kyoto 610-0394, Japan;

aoi.yoshida342@gmail.com (A.Y.); t.shoto.bmun1109@gmail.com (S.T.); tkenmots@mail.doshisha.ac.jp (T.K.)

² The Institute of Genetics and Animal Breeding, Polish Academy of Sciences, Postepu 36A, Jastrzebiec, 05-552 Magdalenka, Poland; h.taniguchi@ighz.pl

* Correspondence: ksadakan@mail.doshisha.ac.jp (K.S.); keyoshik@mail.doshisha.ac.jp (K.Y.); Tel.: +81-774-65-6127 (K.S.); +81-774-65-6243 (K.Y.)

† These authors contributed equally to this work.

Received: 30 June 2017; Accepted: 25 July 2017; Published: 30 July 2017

Abstract: Artificial scaffolds such as synthetic gels or chemically-modified glass surfaces that have often been used to achieve cell adhesion are xenobiotic and may harm cells. To enhance the value of cell studies in the fields of regenerative medicine and tissue engineering, it is becoming increasingly important to create a cell-friendly technique to promote cell–cell contact. In the present study, we developed a novel method for constructing stable cellular assemblies by using optical tweezers in a solution of a natural hydrophilic polymer, dextran. In this method, a target cell is transferred to another target cell to make cell–cell contact by optical tweezers in a culture medium containing dextran. When originally non-cohesive cells are held in contact with each other for a few minutes under laser trapping, stable cell–cell adhesion is accomplished. This method for creating cellular assemblies in the presence of a natural hydrophilic polymer may serve as a novel next-generation 3D single-cell assembly system with future applications in the growing field of regenerative medicine.

Keywords: 3D cellular assembly; optical tweezers; crowding effect; depletion effect; remote control

1. Introduction

Stem-cell-based tissue engineering has emerged as a promising approach for the treatment of intractable diseases [1,2]. To enhance the value of cell studies in the fields of regenerative medicine and tissue engineering, it is becoming increasingly important to create a cell-friendly technique for three-dimensional (3D) cellular assembly [3]. The development of an efficient, minimally-invasive cellular system capable of 3D assembly within an in vitro or in vivo micro environment has been challenging. We recently reported a novel system that could generate a single-cell-based 3D assembly of cells using polyethylene glycol (PEG) by establishing stable cell–cell contact even after the cell assembly was transferred to a PEG-free solution [4]. While synthetic polymers and hydrogels, including PEG, have defined chemical structures and stable physicochemical properties [5–7], they are foreign material to cells [8]. It has been reported that PEG promotes cell–cell fusion, and that it has non-negligible effects on the structure and function of living cells in a culture medium [9,10]. Recent trials aimed at producing cellular scaffolds using natural polymers including gelatin, chitosan, dextran, alginate and collagen have been gaining significant momentum [11–16]. However, while these natural polymers have also been used to promote cellular adhesion within these cell structures in a non-selective manner, further improvements in hydrogel biocompatibility and adaptability for handling 3D cellular assembly systems are needed.

Dextrans are polysaccharides that contain a linear backbone of α -linked D-glucopyranosyl repeating units [17]. Several studies have implicated dextrans in 3D cellular assembly [18,19]. In this regard, cross-linking glycidyl methacrylate derivatized dextran and dithiothreitol under physiological conditions allows 3D encapsulation of rat bone marrow mesenchymal stem cells (BM-MSCs) and NIH/3T3 fibroblasts; while maintaining high viability [20]. Although it has been proposed that dextran can be used for 3D cellular assembly in a less toxic environment, nearly all of the studies of dextran-induced 3D cellular assembly reported thus far have used a 3D mass cell culture system [21,22]. We and others have recently developed an efficient procedure for constructing cellular assemblies by arranging desired cells at desired positions using optical tweezers in a PEG solution [4,23]. The aim of the present study was to modify the aforementioned PEG protocol to establish a 3D single-cell-based manipulation system that uses a less invasive method of cellular assembly involving optical tweezers and dextran as a natural polymer. This dextran-based method may serve as a novel next-generation 3D single-cell assembling system with future applications in the growing field of regenerative medicine.

2. Materials and Methods

2.1. Cell Culture

NAMRU mouse mammary gland epithelial cells (NMuMG cells) were cultured in Dulbecco's modified Eagle's medium (DMEM) (Wako Pure Chem. Inc., Osaka, Japan) supplemented with 10% fetal bovine serum (FBS) (Cell Culture Biosci., Nichirei Biosci. Inc., Tokyo, Japan), 40 $\mu\text{g}/\text{mL}$ streptomycin, and 40 units/mL penicillin (Life Tech. Corp., Carlsbad, CA, USA). Neuro2A cells were cultured in Dulbecco's modified Eagle's medium supplemented with 10% FBS (Atlas Biological, Fort Collins, CO, USA), 1% non-essential amino acids, 100 U/mL penicillin and 10 $\mu\text{g}/\text{mL}$ streptomycin (Wako Pure Chem. Inc., Osaka, Japan). The cells were incubated at 37 °C in a humidified atmosphere of 5% CO_2 . Sub-confluent cells were harvested with trypsin (0.25% Trypsin- EDTA (1X)) (Life Tech. Corp., Carlsbad, CA, USA) and cryopreserved with CELLBANKER1 (Nippon Zenyaku Kogyo, Koriyama, Japan). For preparation of the polymer solution, we used dextran (DEX) (200,000; molecular biology-grade, Wako Pure Chem. Inc., Osaka, Japan). We prepared DMEM solution containing 10–50 mg/mL of DEX.

2.2. Single-Beam Optical Tweezers

Optical trapping with single laser beam was carried out using an inverted microscope (TE-300, Nikon) equipped with a Charge Coupled Device (CCD) camera (WAT-120N, Watec Co., Ltd., Tsuruoka, Japan). A 1064 nm Continuous Wave (CW) laser beam (Spectra Physics, Santa Clara, CA, USA) was introduced into the microscope, and focused into the sample through an oil-immersed objective lens (100 \times , N.A. = 1.3). The laser power at the focal point was set between 42 and 84 mW. All experiments were carried out at room temperature, i.e., 25 °C.

2.3. Double-Beam Optical Tweezers

Optical trapping with a double laser beam was carried out using a commercial optical tweezer instrument (NanoTracker 2, JPK Instruments, Berlin, Germany), which is constructed on an inverted microscope (IX71, Olympus, Tokyo, Japan) equipped with a CCD camera (DFK 31AF03, The Imaging Source, Taipei, Taiwan). A 1064 nm CW laser beam was split into two beams by a polarization beam splitter, and both beams were focused into the sample through a water-immersed objective lens (60 \times , N.A. = 1.2) for independent trapping. One of these focal points can be moved by using a piezo-mirror. The laser power at each focal point was set between 40 and 130 mW. All experiments were carried out at room temperature, i.e., 25 °C.

2.4. Viscosity Measurement

The kinetic viscosities of the dextran and polyethylene glycol were measured using a vibrational viscometer (SV-10, A&D Company, Tokyo, Japan) at room temperature (between 19 and 23 °C). The measurement time for each mixture was 60 s.

2.5. Cell Viability Assay

The NMuMG cells were cultured in a 6-well dish (Thermo Fisher Scientific, Waltham, MA, USA) and treated with 10–40 mg/mL of DEX. After 24 h of culture, cell viability was verified by trypan blue staining.

3. Results

Figure 1 shows the relationship between the concentration of DEX C_{dex} and kinetic viscosity ν in a water-based dextran solution. C_{dex} denotes the concentration of dextran in solution and ν represents kinetic viscosity. ν increases linearly as C_{dex} increases. Since the slope changes at 50 mg/mL C_{dex} , the overlap concentration C^* was deduced to be ca. 50 mg/mL. This value was 2.5 times greater than that of a water-based PEG (50 K) mixture, 20 mg/mL [4].

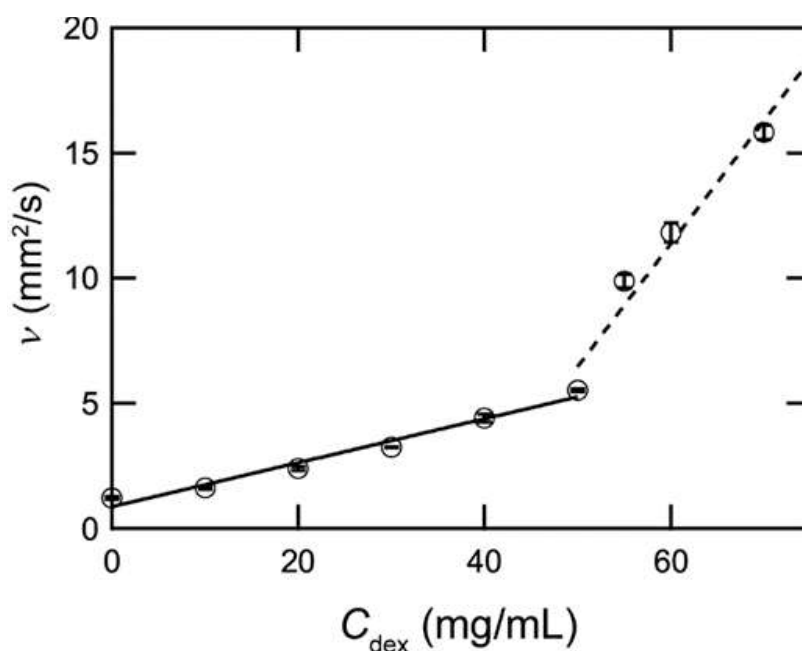


Figure 1. Relationship between C_{dex} and ν in a water-based dextran solution. The solid and dashed lines represent the linear regression between a C_{dex} ranging from 0–50 and 50–70 mg/mL, respectively. Error bars represent the standard error of the mean calculated from three independent measurements.

To determine the cytotoxic effect of dextran, we adapted a trypan blue exclusion method to identify the proportion of viable cells. As a result, 40 mg/mL of dextran-containing medium was associated with a NMuMG cell viability similar to that of cells cultured in a medium without dextran (Figure 2). This suggests that, even after treatment with laser tweezers, cellular activity in the presence of dextran is maintained, without cytotoxicity.

Figure 3 examines the optical-tweezer-dependent mechanism of cell–cell contact. In this experiment, we applied single-beam optical tweezers. Figure 3A,B show cell adherence induced with optical tweezers for 5 and 300 s, respectively. As shown, 5 s of forced contact was insufficient to induce cell adherence. On the other hand, as reported previously, 300 s of forced contact produced stable cell–cell contact. This suggests that 300 s are required to produce cell adherence and in turn

establish 3D cellular assembly. Figure 3C demonstrates the stability of cell–cell contact represented by the percentage of surviving cellular pairs following the indicated actions (approach or contact).

Figure 4 demonstrates the formation of various cell morphologies. Here, we applied double-beam optical tweezers.

Figure 5 confirms the formation of various cell morphologies from Neuro2A mouse brain neuroblastoma cells. In this experiment, we applied single-beam optical tweezers. Neuro2A cells were manipulated with optical tweezers to form various cellular structures. Since undifferentiated Neuro2A cells are used in models of neuronal differentiation [24], 3D assembly of these cells may be useful for modelling neuronal differentiation in 3D cell structures. This system may serve to demonstrate the relationship between 3D cell positioning of undifferentiated neuronal stem cells and neurogenesis.

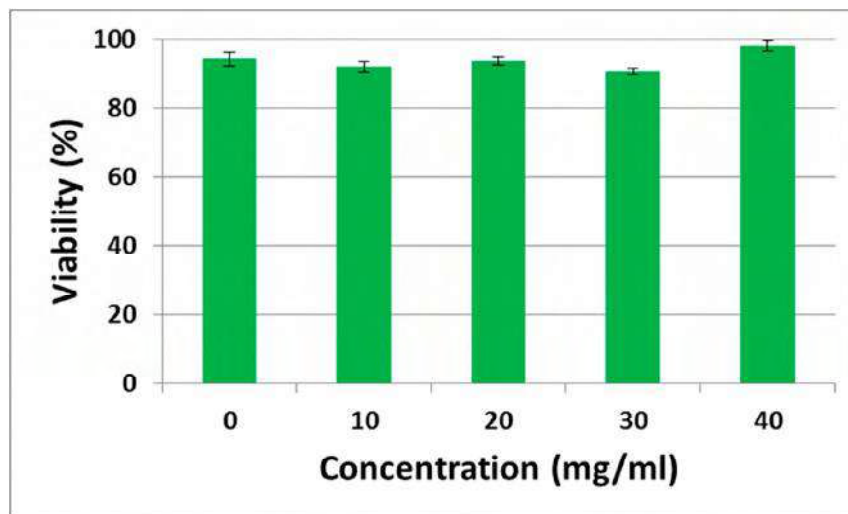


Figure 2. Viability of NMuMG cells. These cells were treated with various concentrations of dextran ranging from 0 to 40 mg/mL. Error bars represent the standard error of the mean calculated from three independent measurements.

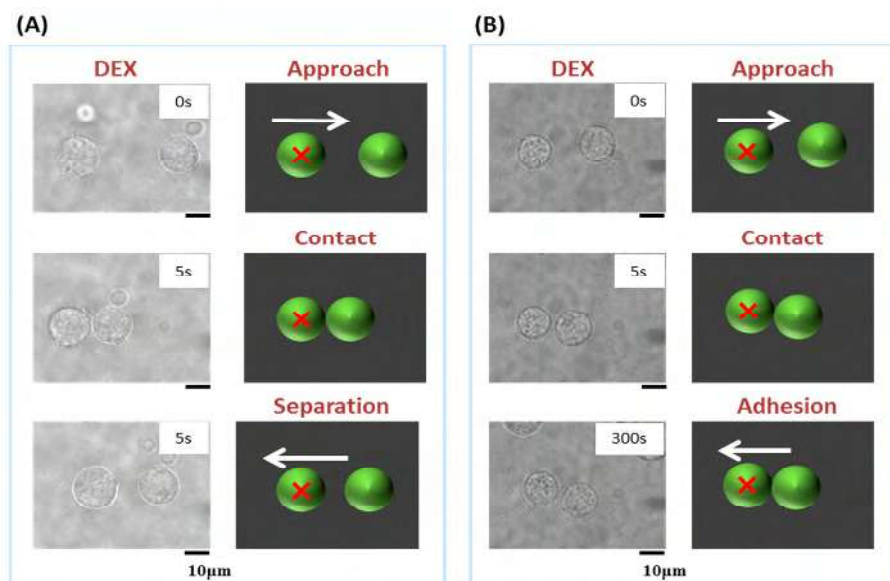


Figure 3. Cont.

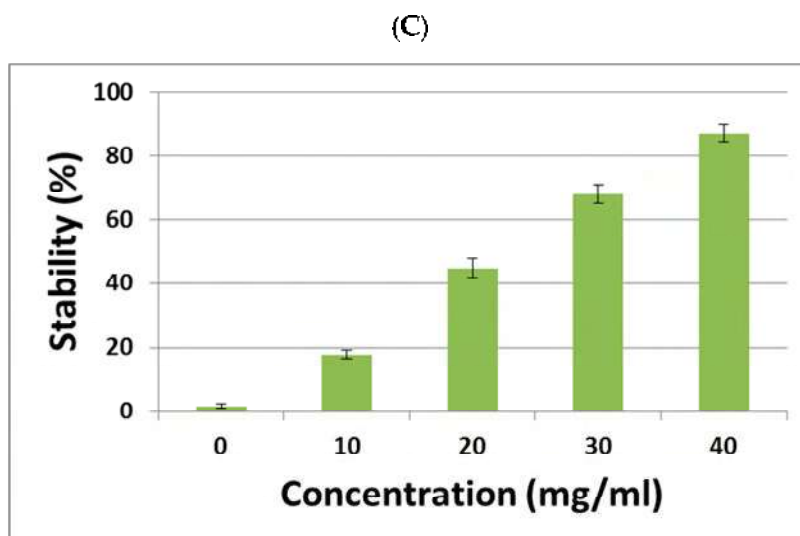


Figure 3. Laser manipulation of a pair of epithelial cells (NMuMG); (A) 5 s or (B) 300 s in the presence of dextran (40 mg/mL): Spatio-temporal diagram illustrating the process of manipulation (Approach, Contact or Separation (A) or Adhesion (B)). (C) The probability that stable cell–cell contact is maintained through optical transportation for the distance of ca. 5 mm, i.e., the percentage of experimental runs to obtain the result as exemplified in (B), where the result as in (A) was counted as a failure. Error bars represent the standard error of the mean calculated from three independent measurements.

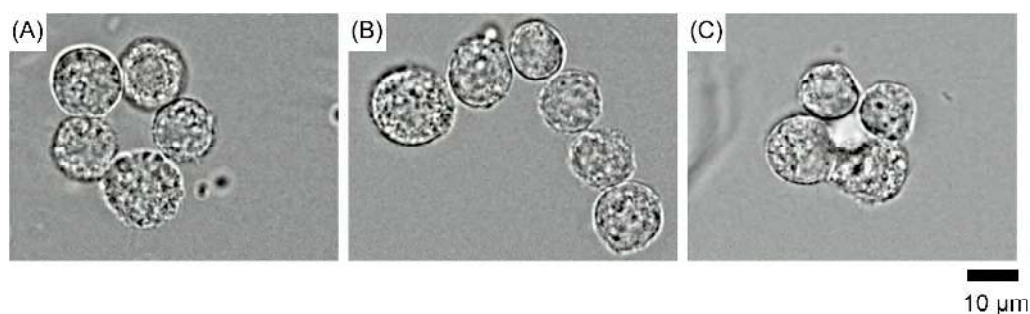


Figure 4. Assemblies of epithelial cells (NMuMG) of various shapes in a medium with DEX (40 mg/mL): the shape of a donut (A), letter 'L' (B), and tetragonal pyramid as an example of 3D cluster (C).

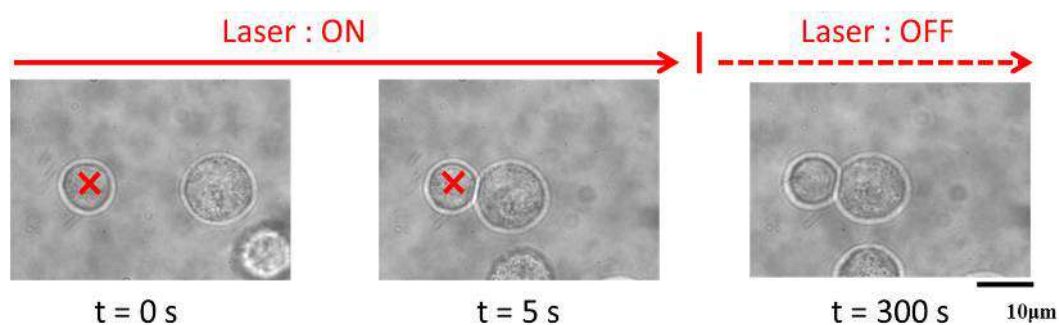


Figure 5. Stable cellular assembly of Neuro2A cells in a dextran (50 mg/mL) medium using optical laser tweezers. The focal point of the laser is marked by the red 'x'.

4. Discussion

The present study successfully extends our recent results on the use of solvable polymers for 3D single-cell-based manipulation. This system adapts an invasive cell assembly method involving

optical tweezers and dextran. This dextran-based method is expected to serve as a next-generation 3D single-cell assembly system with future applications in cell biology and regenerative medicine. The results of the present study suggest further advancement of the present method for the formation of stable 3D cellular assemblies through the use of various kinds of solvable polymers, including proteins, polysaccharides, polynucleic acids, etc.

It is widely considered that cell adhesion may be engendered using the congestion or crowding effect [4], which has been attributable to the effect of higher osmotic pressure. Here, it is noted that the effect exerted by a polymer “crowding” solution on living cells is much different from the simple osmotic pressure caused by the addition of small solute molecules. With an increase in osmotic pressure due to the presence of small solutes, cells tend to shrink. However, such osmotic pressure does not directly switch cell–cell interaction from repulsive to attractive. Cell aggregation is a secondary effect caused by an increase in osmotic pressure. In contrast, a solution crowded with macromolecules or large polymer chains causes a so-called depletion effect [4,25,26]. The attractive interaction as a result of the depletion effect by polymer crowding occurs at a length scale on the order of the size of the polymer chain, for example on a scale represented by R_g for the radius of gyration or R_H for the hydrodynamic radius. In contrast, as for the osmotic effect of polymers, the increase in osmotic pressure is roughly proportional to the contour length or full-stretch length of the polymer chain, which is proportional to the volume as the product of the contour length and the cross-sectional area of the polymer, being much smaller than the volume occupied by the polymer chain. Thus, in general, the depletion effect is much more significant for polymer chains with a large contour length of more than several tens of nm. The attractive interactions between facing cells due to the entropic depletion force causes flat contact between a pair of cells by creating a gap with the size of the polymer, accompanied by slight deformation of the curvature of the facing side of the membrane on the order of the energy of thermal fluctuation. The occurrence of such a flat gap contributes to the formation of stable cellular contact, by allowing the 2D random walk of individual membrane components, such as membrane proteins and sugar lipids, so as to form attractive contact pairs upon encountering membrane surfaces. The stabilization energy between the facing membranes per unit area due to depletion interaction, ε_a , is expressed with approximation as [4],

$$\begin{aligned} \varepsilon_a &= -\pi_P(2d - x) & \text{when } x \leq 2d \\ \varepsilon_a &= 0 & \text{when } x > 2d, \end{aligned} \quad (1)$$

where π_P is the depletion pressure due to the coexisting polymer such as DEX polymer; d is the diameter of the polymer in a random coil confirmation; and x is the distance between the facing membranes. Thus, the attractive force per surface area due to the depletion effect can be described as,

$$\begin{aligned} P_{dep} &\approx -\frac{\partial \varepsilon_a}{\partial x} = -\pi_P & \text{when } x \leq 2d \\ P_{dep} &\approx 0 & \text{when } x > 2d. \end{aligned} \quad (2)$$

Meanwhile, the repulsive interactions between a pair of cells floating in solution, such as electric interactions [27], short-range hydration repulsion force [28], and membrane duration [29,30], are inherent properties of a cell membrane [31]. The following relationship has been proposed for repulsive interaction between facing membranes [27]. The positive pressure P_{rep} can be represented as,

$$P_{rep} = P_{rep}^0 \exp\left(-\frac{x}{L}\right), \quad (3)$$

where P_{rep}^0 is a positive variable that depends on the ionic strength of the medium and the surface potential at the extreme of $x = 0$; and L is the characteristic length on the order of 1 nm for a conventional medium for cell culture.

Based on the above arguments regarding the interactions between facing membranes, the net pressure P_{net} is the sum of the depletion and repulsive interactions: $P_{net} = P_{dep} + P_{rep}$ [4]. With regard

to the experimental conditions for DEX (200 k), the size of the DEX polymer chain in solution, d , is regarded as 15–20 nm [32]. We reported that the transmembrane distance is $x = 10 - 15\text{nm}$ in the balance between attractive and repulsive contributions in solutions containing PEG as a crowding polymer [4]. Under similar treatment, we deduced that the width of the gap between facing cells in the present work is of a similar order of magnitude, i.e., $x = 10 - 15\text{nm}$. Thus, when cell–cell contact is achieved in the presence of a crowding polymer, there remains a void space with a width comparable to the size of the polymer between the facing membranes of the adjacent cells. As we discussed in our recent article, the existence of this void space between facing membranes provides the opportunity for the facing membranes to switch repulsive interaction to attractive interaction during cell–cell contact due to dielectric attraction under a focused laser. As a result, stable cell–cell contact could be achieved even after the removal of the coexisting polymer [4]. With regard to the generation of attractive interaction between neighboring cells, a crowding solution environment causes DNA condensation and compaction through the occurrence of the attractive interaction between negatively charged DNA segments [33]. The essential mechanism of attraction is similar to that in our observation of the formation of stable cell–cell contact in PEG solution [4]. Altogether, the overall findings suggest that repulsive single cells can be easily attracted to each other in a medium which contains water soluble polymers such as dextran and PEG, through the depletion effect. This effect facilitates us to construct 3D single cell structures and is, therefore, useful for further applications.

In this study, stable cellular adhesion of NMuMG cells was achieved at concentrations even lower than the overlap concentration C^* . The fact that the polymer solution formed stable cell–cell contact below C^* is of value because the viscosity of the solution is essentially the same as that of the usual cell culture medium. Under such low viscosity, transportation of individual cells by laser does not encounter any difficulty. While PEG is a synthetic polymer, we have demonstrated for the first time that a natural polymer (dextran) can precipitate cell adhesion and facilitate 3D cellular assembly. In related studies on the use of DEX solution for cell manipulation, Takayama et al. have examined cell printing on a solid substrate. With the use of a dextran solution, they successfully localized cell aggregates at desired positions [34,35]. They reported that the gene expression profile of cells that differentiated after treatment with dextran solution was almost the same as that of cells in the usual medium. In this study, we noted that 10–40 mg/mL of dextran did not have any cytotoxic effect on NMuMG cells. Moreover, since natural compounds like dextran are relatively safe and therefore easily added to the cell culture medium, our dextran-based method may be able to achieve relatively less invasive 3D single-cell assembly.

Cell–cell contact influences the ability of progenitor cells to differentiate [36,37]. Moreover, embryonic stem cells are occasionally cultured as 3D aggregates, known as embryoid bodies. This enhances the differentiation of several cell types. Similarly, neurogenesis can be triggered using sphere-cultured P19 mouse carcinoma cells [38]. Therefore, how these cells are reconstituted in a 3D structure is quite important for proper differentiation. In this regard, our dextran-based 3D cell assembly technique may enable users to control 3D-structure assembly in the hope of achieving novel advances in regenerative medicine.

Cell therapy has received great attention in the field of neuroscience. In the near future, these therapies may be used to treat neurodegenerative diseases such as Parkinson's disease. In this regard, we were able to make single cell–cell contact using Neuro2A cells. Since neuronal circuits are well organized, it is important to precisely manage the position of neuronal cells and their progenitors. Our 3D single-cell assembly method together with DEX should help to facilitate the reconstitution of damaged neuronal networks. To this end, our approach, which involves the use of optical tweezers, may contribute to the regeneration of well-functioning neuronal systems. Since neuronal systems are composed of many cell types, our next challenge will be to produce lasting cell–cell adhesion between these various cells. Moreover, although we optimized the conditions required for fine control of the position of neuronal progenitor cells in this study, a functional analysis was not performed. Therefore, it will be important to further evaluate our findings using long-term cell culture methods and various

functional assays (e.g., single cell transcriptome analysis). To develop functional organoids, which has recently been used as the scientific term to indicate 3D organ-like structures composed of specific cell types or progenitor cells [39,40], it is important to establish an experimental methodology to construct 3D cellular assembly of a large number of cells (above the order of one hundred) with various morphologies. In this regard, we would like to propose the future extension of our study with the hierarchical construction of small cell assemblies (on the order of ten) into a larger assembly with specific shape where each small cell assembly exhibits suitable positioning to generate the specific function as an organoid.

Concluding the present article, we would like to stress the difference between the crowding effect or depletion effect due to macromolecules and the effect of osmotic pressure. The depletion effect induces attractive interaction between neighboring cells through the effect of the exclusion volume by macromolecules on the scale of R^3 , where R is the radius of a polymer chain as represented by R_g or R_H . In contrast, the osmotic effect scales with the exclusion volume along the polymer chain, which is much smaller than the scale of R^3 for the depletion volume of macromolecules. Additionally, depletion interaction induces attractive interaction between neighboring cells as a primary, direct effect. The present study indicated that depletion interaction is promising for the formation of stable cell–cell contact. We have shown that the natural macromolecule DEX is useful for this purpose, similar to the synthetic polymer PEG. Although there is a large difference in conformational characteristics between DEX and PEG, they result in similar cell–cell attraction, suggesting that the depletion effect can generally be applicable for the construction of stable 3D cellular assemblies. Further extension of this study is expected to contribute to future developments in cellular biology and regenerative medicine. Lastly, we would like to stress that most eukaryotic cells maintain their lives surrounded by crowding body fluids.

Acknowledgments: The authors thank Hashimoto and Ohta at Doshisha University for generous assistance with the experimental setup. This work was supported by KAKENHI (15H02121, 15K05400, 25103012, 50587441) and by the MEXT-Supported Program for the Strategic Research Foundation at Private Universities.

Author Contributions: Hiroaki Taniguchi, Koichiro Sadakane, and Kenichi Yoshikawa conceived and designed the experiments; Aoi Yoshida and Shoto Tsuji performed the experiments; Aoi Yoshida, Shoto Tsuji, and Koichiro Sadakane analyzed the data, and Hiroaki Taniguchi, Koichiro Sadakane, Takahiro Kenmotsu, and Kenichi Yoshikawa wrote the paper.

Conflicts of Interest: The authors declare no conflict of interest.

References

1. Lane, S.W.; Williams, D.A.; Watt, F.M. Modulating the Stem Cell Niche for Tissue Regeneration. *Nat. Biotechnol.* **2014**, *32*, 795–803. [[CrossRef](#)] [[PubMed](#)]
2. Li, M.; Guo, K.; Ikehara, S. Intractable Diseases Treated with Intra-Bone Marrow-Bone Marrow Transplantation. *Front. Cell Dev. Biol.* **2014**, *2*, 48. [[CrossRef](#)] [[PubMed](#)]
3. Chen, Y.W.; Huang, S.X.; de Carvalho, A.L.R.T.; Ho, S.H.; Islam, M.N.; Volpi, S.; Notarangelo, L.D.; Ciancanelli, M.; Casanova, J.L.; Bhattacharya, J.; et al. A Three-Dimensional Model of Human Lung Development and Disease from Pluripotent Stem Cells. *Nat. Cell Biol.* **2017**, *19*, 542–549. [[CrossRef](#)] [[PubMed](#)]
4. Hashimoto, S.; Yoshida, A.; Ohta, T.; Taniguchi, H.; Sadakane, K.; Yoshikawa, K. Formation of Stable Cell-Cell Contact without a Solid/Gel Scaffold: Non-invasive Manipulation by Laser under Depletion Interaction with a Polymer. *Chem. Phys. Lett.* **2016**, *655*, 11–16. [[CrossRef](#)]
5. Tanaka, M.; Sackmann, E. Polymer-Supported Membranes as Models of the Cell Surface. *Nature* **2005**, *437*, 656–663. [[CrossRef](#)] [[PubMed](#)]
6. Tang, Y.; Liu, L.; Li, J.; Yu, L.; Wang, L.; Shi, J.; Chen, Y. Induction and Differentiation of Human Induced Pluripotent Stem Cells into Functional Cardiomyocytes on a Compartmented Monolayer of Gelatin Nanofibers. *Nanoscale* **2016**, *8*, 14530–14540. [[CrossRef](#)] [[PubMed](#)]

7. Masuda, S.; Yanase, Y.; Usukura, E.; Ryuzaki, S.; Wang, P.; Okamoto, K.; Kuboki, T.; Kidoaki, S.; Tamada, K. High-Resolution Imaging of a Cell-Attached Nanointerface using a Gold-Nanoparticle Two-Dimensional Sheet. *Sci. Rep.* **2017**, *7*, 3720. [[CrossRef](#)] [[PubMed](#)]
8. Li, W.A.; Lu, B.Y.; Gu, L.; Choi, Y.; Kim, J.; Mooney, D.J. The Effect of Surface Modification of Mesoporous Silica Micro-Rod Scaffold on Immune Cell Activation and Infiltration. *Biomaterials* **2016**, *83*, 249–256. [[CrossRef](#)] [[PubMed](#)]
9. Gietz, R.D.; Schiestl, R.H.; Willems, A.R.; Woods, R.A. Studies on the Transformation of Intact Yeast Cells by the LiAc/SS-DNA/PEG Procedure. *Yeast* **1995**, *11*, 355–360. [[CrossRef](#)] [[PubMed](#)]
10. Robinson, J.M.; Roos, D.S.; Davidson, R.L.; Kamovsky, M.J. Membrane Alterations and Other Morphological Features Associated with Polyethylene Glycol-Induced Cell Fusion. *J. Cell Sci.* **1979**, *40*, 63–75. [[PubMed](#)]
11. Dhandayuthapani, B.; Krishnan, U.M.; Sethuraman, S. Fabrication and Characterization of Chitosan–Gelatin Blend Nanofibers for Skin Tissue Engineering. *J. Biomed. Mater. Res. B* **2010**, *94*, 264–272. [[CrossRef](#)] [[PubMed](#)]
12. Huang, Y.; Onyeri, S.; Siewe, M.; Moshfeghian, A.; Madihally, S.V. In Vitro Characterization of Chitosan-Gelatin Scaffolds for Tissue Engineering. *Biomaterials* **2005**, *26*, 7616–7627. [[CrossRef](#)] [[PubMed](#)]
13. Liu, Y.; Chan-Park, M.B. Hydrogel Based on Interpenetrating Polymer Networks of Dextran and Gelatin for Vascular Tissue Engineering. *Biomaterials* **2009**, *30*, 196–207. [[CrossRef](#)] [[PubMed](#)]
14. Rosellini, E.; Cristallini, C.; Barbani, N.; Vozzi, G.; Giusti, P. Preparation and Characterization of alginate/gelatin Blend Films for Cardiac Tissue Engineering. *J. Biomed. Mater. Res. A* **2009**, *91*, 447–453. [[CrossRef](#)] [[PubMed](#)]
15. Sakai, S.; Hashimoto, I.; Kawakami, K. Synthesis of an Agarose-Gelatin Conjugate for use as a Tissue Engineering Scaffold. *J. Biosci. Bioeng.* **2007**, *103*, 22–26. [[CrossRef](#)] [[PubMed](#)]
16. Tan, H.; Wu, J.; Lao, L.; Gao, C. Gelatin/chitosan/hyaluronan Scaffold Integrated with PLGA Microspheres for Cartilage Tissue Engineering. *Acta Biomater.* **2009**, *5*, 328–337. [[CrossRef](#)] [[PubMed](#)]
17. Banerjee, A.; Bandopadhyay, R. Use of Dextran Nanoparticle: A Paradigm Shift in Bacterial Exopolysaccharide Based Biomedical Applications. *Int. J. Biol. Macromol.* **2016**, *87*, 295–301. [[CrossRef](#)] [[PubMed](#)]
18. Lee, V.K.; Kim, D.Y.; Ngo, H.; Lee, Y.; Seo, L.; Yoo, S.S.; Vincent, P.A.; Dai, G. Creating Perfused Functional Vascular Channels using 3D Bio-Printing Technology. *Biomaterials* **2014**, *35*, 8092–8102. [[CrossRef](#)] [[PubMed](#)]
19. Liu, Y.; Rayatpisheh, S.; Chew, S.Y.; Chan-Park, M.B. Impact of Endothelial Cells on 3D Cultured Smooth Muscle Cells in a Biomimetic Hydrogel. *ACS Appl. Mater. Interfaces* **2012**, *4*, 1378–1387. [[CrossRef](#)] [[PubMed](#)]
20. Liu, Z.Q.; Wei, Z.; Zhu, X.L.; Huang, G.Y.; Xu, F.; Yang, J.H.; Osada, Y.; Zrinyi, M.; Li, J.H.; Chen, Y.M. Dextran-Based Hydrogel Formed by Thiol-Michael Addition Reaction for 3D Cell Encapsulation. *Colloids Surf. B* **2015**, *128*, 140–148. [[CrossRef](#)] [[PubMed](#)]
21. Aloysious, N.; Nair, P.D. Enhanced Survival and Function of Islet-Like Clusters Differentiated from Adipose Stem Cells on a Three-Dimensional Natural Polymeric Scaffold: An in Vitro Study. *Tissue Eng. A* **2014**, *20*, 1508–1522. [[CrossRef](#)] [[PubMed](#)]
22. McKee, C.; Perez-Cruet, M.; Chavez, F.; Chaudhry, G.R. Simplified Three-Dimensional Culture System for Long-Term Expansion of Embryonic Stem Cells. *World J. Stem Cells* **2015**, *7*, 1064–1077. [[PubMed](#)]
23. Kirkham, G.R.; Britchford, E.; Upton, T.; Ware, J.; Gibson, G.M.; Devaud, Y.; Ehrbar, M.; Padgett, M.; Allen, S.; BATTERY, L.D.; et al. Precision Assembly of Complex Cellular Microenvironments using Holographic Optical Tweezers. *Sci. Rep.* **2015**, *5*, 8577. [[CrossRef](#)] [[PubMed](#)]
24. Tremblay, R.G.; Sikorska, M.; Sandhu, J.K.; Lanthier, P.; Ribocco-Lutkiewicz, M.; Bani-Yaghoub, M. Differentiation of Mouse Neuro 2A Cells into Dopamine Neurons. *J. Neurosci. Methods* **2010**, *186*, 60–67. [[CrossRef](#)] [[PubMed](#)]
25. Asakura, S.; Oosawa, F. On Interaction between Two Bodies Immersed in a Solution of Macromolecules. *J. Chem. Phys.* **1954**, *22*, 1255–1256. [[CrossRef](#)]
26. Roth, R.; Gotzelmann, B.; Dietrich, S. Depletion Forces Near Curved Surface. *Am. Phys. Soc.* **1998**, *82*, 448–451. [[CrossRef](#)]
27. Hiemenz, P.C.; Rajagopalan, R. *Principles of Colloid and Surface Chemistry*; Marcel Dekker, Inc.: New York, NY, USA, 1997.
28. LeNeveu, D.M.; Rand, R.P.; Parsegian, V.A. Measurement of Forces between Lecithin Bilayers. *Nature* **1976**, *259*, 601–603. [[CrossRef](#)] [[PubMed](#)]

29. Chen, L.; Jia, N.; Gao, L.; Fang, W.; Golubovic, L. Effects of Antimicrobial Peptide Revealed by Simulations: Translocation, Pore Formation, Membrane Corrugation and Euler Buckling. *Int. J. Mol. Sci.* **2013**, *14*, 7932–7958. [[CrossRef](#)] [[PubMed](#)]
30. Sackmann, E.; Smith, S.A. Physics of Cell Adhesion: Some Lessons from Cell Mimetic Systems. *Soft Matter* **2014**, *10*, 1644–1659. [[CrossRef](#)] [[PubMed](#)]
31. Ohki, S. *Cell and Model Membrane Interactions*; Springer: New York, NY, USA, 1991.
32. Neul, B.; Meiselman, H.J. Depletion Interactions in Polymer Solutions Promote Red Blood Cell Adhesion to Albumin-Coated Surfaces. *Biochim. Biophys. Acta* **2006**, *1760*, 1772–1779.
33. Vasilevskaya, V.V.; Khokhlov, A.R.; Matsuzawa, Y.; Yoshikawa, K. Collapse of Single DNA Molecule in Poly(Ethylene Glycol) Solutions. *J. Chem. Phys.* **1995**, *102*, 6595–6602. [[CrossRef](#)]
34. Han, C.; Takayama, S.; Park, J. Formation and Manipulation of Cell Spheroids using a Density Adjusted PEG/DEX Aqueous Two Phase System. *Sci. Rep.* **2015**, *5*, 11891. [[CrossRef](#)] [[PubMed](#)]
35. Tavana, H.; Mosadegh, B.; Takayama, S. Polymeric Aqueous Biphasic Systems for Non-Contact Cell Printing on Cells: Engineering Heterocellular Embryonic Stem Cell Niches. *Adv. Mater.* **2010**, *22*, 2628–2631. [[CrossRef](#)] [[PubMed](#)]
36. Liu, Y.; Li, H.; Yan, S.; Wei, J.; Li, X. Hepatocyte Cocultures with Endothelial Cells and Fibroblasts on Micropatterned Fibrous Mats to Promote Liver-Specific Functions and Capillary Formation Capabilities. *Biomacromolecules* **2014**, *15*, 1044–1054. [[CrossRef](#)] [[PubMed](#)]
37. Ottone, C.; Krusche, B.; Whitby, A.; Clements, M.; Quadrato, G.; Pitulescu, M.E.; Adams, R.H.; Parrinello, S. Direct Cell-Cell Contact with the Vascular Niche Maintains Quiescent Neural Stem Cells. *Nat. Cell Biol.* **2014**, *16*, 1045–1056. [[CrossRef](#)] [[PubMed](#)]
38. Kim, B.S.; Lee, C.H.; Chang, G.E.; Cheong, E.; Shin, I. A Potent and Selective Small Molecule Inhibitor of Sirtuin 1 Promotes Differentiation of Pluripotent P19 Cells into Functional Neurons. *Sci. Rep.* **2016**, *6*, 34324. [[CrossRef](#)] [[PubMed](#)]
39. Clevers, H. Modeling Development and Disease with Organoids. *Cell* **2016**, *165*, 1586–1597. [[CrossRef](#)] [[PubMed](#)]
40. Fatehullah, A.; Tan, S.H.; Barker, N. Organoids as an in vitro Model of Human Development and Disease. *Nat. Cell Biol.* **2016**, *18*, 246–254. [[CrossRef](#)] [[PubMed](#)]



Sol–Gel Coexisting Phase of Polymer Microgels Triggers Spontaneous Buckling

Keisuke Koyanagi,[†] Kazue Kudo,[‡] and Miho Yanagisawa^{*,†,§,||}

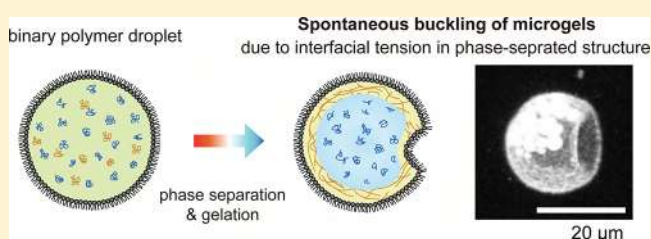
[†]Department of Applied Physics, Tokyo University of Agriculture and Technology, Naka-cho 2-24-16, Koganei, Tokyo 184-8588, Japan

[‡]Department of Computer Science, Ochanomizu University, Otsuka 2-1-1, Bunkyo, Tokyo 112-8610, Japan

[§]Department of Basic Science and ^{||}Komaba Institute for Science, The University of Tokyo, Komaba 3-8-1, Meguro, Tokyo 153-8902, Japan

S Supporting Information

ABSTRACT: Mechanical buckling is a ubiquitous phenomenon of elastic bodies like core–shell microgels. Although conventional theory predicts that sufficiently high pressure is the primary factor inducing the buckling of core–shell microgels, they often buckle spontaneously without applying pressure. We explored such spontaneous buckling of microgels by introducing interfacial tension between the gel phase of the shell and sol phase of the core. Thus, we found that the core–shell microgels in a sol–gel coexisting phase with a certain shell thickness ratio exhibit spontaneous buckling. According to our theoretical analysis, spontaneous buckling occurs due to the balance between the gel elasticity E and interfacial tension γ when the characteristic length γ/E is comparable to the microgel size R . Moreover, we found that the ratio between γ/E and R determines the buckling condition of the shell thickness ratio. Our findings establish an important framework for applying spontaneous buckling to the shape control of elastic bodies.



INTRODUCTION

Wrinkling in elastic bodies such as fruits, vegetables, biological tissues, and polymer gels is known to be related to the buckling phenomenon caused by mechanical instability on the surface.^{1–3} The buckling phenomenon attracts much attention for numerous applications such as tunable surface fabrication,^{4–7} optics,^{8–10} bioengineering,¹¹ stretchable electronics,^{12,13} and mechanical measurements.¹⁴

Compared to stress-driven buckling (constrained swelling in response to environmental stimuli), pressure-driven buckling exhibits a simpler mechanism: buckling occurs when the external pressure exceeds a critical pressure P_c . In the case of a spherical shell with an outer radius R and a shell thickness h , the value of P_c is described by using two parameters: (i) the shell thickness ratio, h/R , and (ii) the Young's modulus of the shell, E , as follows:^{15–17}

$$P_c = \frac{2E}{\sqrt{3(1-\mu^2)}} \left(\frac{h}{R - \frac{h}{2}} \right)^2 \quad (1)$$

where μ is Poisson's ratio of the elastic shell.

Although elastic bodies show buckling under a sufficiently large pressure, the critical pressure at which buckling occurs is often lower than the theoretical value. In the case of spherical shells of polymer gels (core–shell microgels), one of the reasons is the inhomogeneity of the elastic shells. The influence of spatially varying thickness h and elasticity E on the buckling

mechanism of the shell has been investigated experimentally¹⁸ and theoretically.¹⁹ Another reason is inhomogeneity in the internal structure of the elastic bodies. Spherical microgels prepared from emulsion polymerization often buckle spontaneously without applying pressure.^{20–23} Sacanna et al. explained that spontaneous buckling might occur when the remaining polymer polymerizes inside previously cross-linked spherical shells.^{20,21} This indicates that the inhomogeneous internal structure of microgels in the sol–gel coexisting phase plays an important role in the spontaneous buckling. However, how the sol–gel coexisting phase in elastic bodies causes the buckling is still elusive.

Here, we aimed to elucidate the underlying mechanism by which the inhomogeneous internal structure of polymer gels in a sol–gel coexisting phase causes spontaneous buckling without applying pressure. For this purpose, we used core–shell microgels prepared from phase separation solutions of poly(ethylene glycol) (PEG) and gelatin confined within lipid droplets.²⁴ The gelatin/PEG system enabled us to regulate the sol–gel coexisting phase by changing the quenching rate because both phase separation with complete wetting of gelatin on the lipid membrane and gelation of the gelatin proceed with a decrease in temperature.^{24–26} We demonstrated that the interfacial tension between the gel phase of the shell and sol

Received: November 6, 2018

Revised: December 18, 2018

Published: January 14, 2019

phase of the core is responsible for the spontaneous buckling of the core–shell microgels. Our theoretical analysis reveals that spontaneous buckling occurs due to the balance between the gel elasticity and interfacial tension when the characteristic length is comparable to the microgel size. Our findings provide new insights into the mechanism by which the inhomogeneous internal structure of elastic bodies causes buckling during polymerization^{20–23,27,28} and phase separation.^{29,30}

EXPERIMENTAL SECTION

Materials. 1,2-Dioleoyl-*sn*-glycero-3-phosphoethanolamine (PE) was purchased from Wako Pure Chemical Industries (Osaka, Japan). Mineral oil was purchased from Nacalai Tesque (Kyoto, Japan), while alkali-treated gelatin was supplied by Merck (Darmstadt, Germany). The average molecular weight determined by gel permeation chromatography was 69000. Poly(ethylene glycol) (molecular weight 1000; PEG 1k) was purchased from Sigma-Aldrich. Thioflavin T (ThT; Wako) and fluorescein isothiocyanate isomer I (FITC; Sigma-Aldrich Japan; Tokyo, Japan) were used as a fluorescent dye for the gelatin-rich gel phase. All the materials were used without further purification.

Preparation of Core–Shell Microgels. For preparing core–shell microgels, we confined a gelatin/PEG solution inside lipid droplets in oil. The gelatin/PEG solution underwent phase separation and gelation with a decrease in temperature (Figure 1a). The droplets were coated

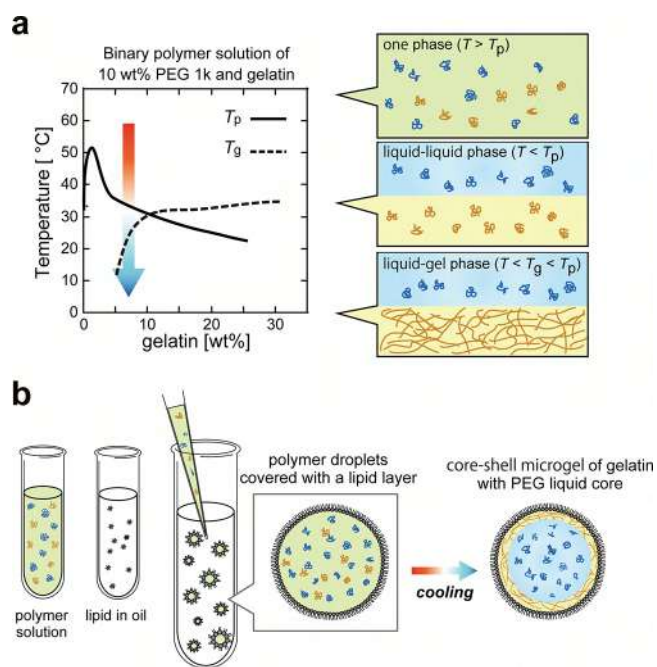


Figure 1. (a) Schematic illustrations of (left) phase diagram of 10 wt % PEG 1k and various concentrations of gelatin and of (right) three different phases appeared with a decrease in temperature along the arrow. The solid and dashed lines indicate the phase separation point T_p and the gelation point T_g , respectively. (b) Preparation of core–shell microgels. Above T_p , the gelatin/PEG solution was entrapped in lipid-coated droplets via pipetting. After the cooling, the gelatin/PEG droplets transit to core–shell microgel of gelatin with PEG liquid core.

with a lipid layer in an oil phase. First, dry films of the lipid PE formed at the bottom of a glass tube. The mineral oil was added to the lipid films followed by 90 min of sonication. The final concentration of the lipid/oil solution was ~ 1 mM. The gelatin and PEG 1k were dissolved in water at 70 °C (above the gelation temperature T_g and phase separation temperature T_p ; Figure 1a) for 1 h. To prepare droplets, a binary polymer solution of 10 wt % PEG 1k and 9 wt % gelatin was added to the lipid/oil solution at 70 °C and emulsified via pipetting. We placed

an aliquot containing the droplets on a silicone-coated cover glass to prevent the droplets from sticking to the glass plate. Owing to the temperature quenching below T_p and T_g , the gelatin/PEG droplets transitioned to core–shell microgels, as reported previously²⁴ (Figure 1b).

Fluorescence Observation of Microgels. The microgels were observed by fluorescence microscopy (Olympus IX81; Olympus) and confocal laser scanning fluorescence microscopy (CLSM) (Olympus IX83 with FV1200). Fluorescent images of fluorescein-tagged gelatin and thioflavin (ThT), which were excited by a mercury lamp or laser at 488 nm, were obtained using fluorescence filter sets (U-FBNA and U-MNIBA3; from 510 to 550 nm). The sample was cooled from 70 to 4 °C (below T_g) at a rate of ~ 0.01 –40 °C/min using a Peltier-type cooling heating stage (10021, Linkam; Scientific Instruments, Ltd., UK). The pinhole size was fixed to be 1 μ m. The obtained images were analyzed by “National Institutes of Health ImageJ” software.

RESULTS AND DISCUSSION

Buckling of Core–Shell Microgels in Sol–Gel Coexisting Phase. To regulate the inhomogeneous internal structure of microgels in the coexisting sol–gel phase, we prepared core–shell microgels from gelatin/PEG droplets. The gelatin/PEG solution simultaneously caused phase separation and gelation with a decrease in temperature (Figure 1a). For 10 wt % PEG 1k and 9 wt % gelatin solutions, the phase separation temperature T_p was slightly higher than the gelation temperature T_g . Upon temperature quenching, the one-phase gelatin/PEG solution first separated into two liquid phases below T_p , following which the gelatin-rich phase turned into a gel phase below T_g .³¹ The higher quenching rate prevented coarsening from the earlier stage of phase separation upon gelation. By changing the quenching rate for the gelatin/PEG solution with $T_p > T_g$, we regulated the inhomogeneity derived from the coexisting sol–gel phase.

The gelatin/PEG solution in one phase (at above T_p) was confined inside the droplets covered with a lipid layer of phosphatidylethanolamine (PE) (Figure 1b). The radius of the obtained droplets was in the range 5–50 μ m. Given that gelatin has a high affinity for a PE membrane compared to PEG, the gelatin-rich phase localized near the droplet PE surface and finally formed a spherical shell of gelatin gel with the PEG solution at the core, as reported previously.²⁴

To modify the inner structure of the core–shell microgels, we increased the temperature quenching rate from 70 to 4 °C (from above T_p to below T_g) to 0.1 to 50 °C/min. Under a certain quenching rate, the gelatin/PEG microgels underwent a sudden buckling transition without applying pressure (Movie S1). Figure 2a (left) shows a differential interference contrast (DIC) image of a buckling microgel. The buckling microgels quickly recovered the initial spherical shape upon temperature increase above T_g (Figure 2a (right) and Movie S2). When the temperature quenched below T_g , the microgels buckled again (Movie S1 shows the second buckling). This means that the observed buckling is a reversible phenomenon caused by the temperature change across T_g . The reversible buckling is due to the inner coexisting phase of the microgel which reversibly changes with temperature shift. The overall size of the buckling microgels was similar to the initial size of spherical droplets at above T_p . Hereinafter, the outer radii (R) of the droplet in the liquid phase and the microgel in the sol–gel phase are identical. Such buckling of microgels and volume change by temperature quenching were not observed for homogeneous microgels of gelatin without PEG (Figure S1).

By visualizing the inhomogeneous inner structure of the microgels,³² we obtained cross-sectional images and three-

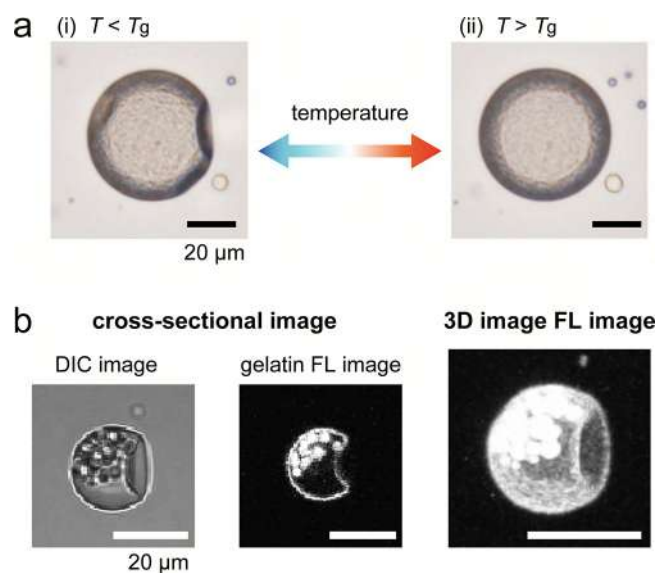


Figure 2. (a) Reversible buckling phenomena by changing temperature across the phase separation temperature and the gelation temperature T_g ($<T_p$). (b) An example of buckling microgels is shown as the DIC image (left), confocal cross-sectional fluorescence (FL) image of the gelatin-rich phase (center), and the 3D FL image (right).

dimensional (3D) images of the buckling microgels with a fluorescent dye for the gelatin-rich phase, namely Thioflavin T (ThT) (Figure 2b). We confirmed that the ThT was localized and visualized in the gelatin-rich phase, like FITC-conjugated gelatin (Figure S2). The gelatin-rich phase formed core–shell microgels with the PEG solution at the core. Given that the thickness of the shell was spatially uniform, this buckling was not caused by the stress concentration on the thin part of the inhomogeneous shell. The most possible trigger for spontaneous buckling is the inhomogeneous inner structure in the sol–gel coexisting phase upon gelatin during phase separation.

Inhomogeneous Inner Structure of Buckling Microgels. To clarify the relation between the quenching rate and internal structure of the buckling microgels, the fluorescence images of the microgels were compared for several conditions associated with different quenching rates. When the quenching rate is low enough to complete phase separation into two liquid phases before gelation, a thick shell capsule is obtained, as depicted in Figure 3a (low quenching rate, 0.1 $^{\circ}\text{C}/\text{min}$). Under this condition, the shell thickness is $2 \mu\text{m} < h < 7 \mu\text{m}$ for droplets with $5 \mu\text{m} < R < 50 \mu\text{m}$, which corresponds to the h value estimated from the volume fraction of the gelatin-rich phase (30–45 vol %). With an increase in the quenching rate up to 30 $^{\circ}\text{C}/\text{min}$ (moderate quenching rate, Figure 3b), we observed spontaneous buckling of microgels. The shells of the buckling microgels were thinner than those of microgels for the low quenching rate because the gelation prevented coarsening from the initial stage of phase separation. Resultant domains of the gelatin-rich phase formed isolated domains inside the gelatin capsules without coalescence with the capsule wall. For a high quenching rate (50 $^{\circ}\text{C}/\text{min}$), the shell was much thinner, as shown in Figure 3c ($h \ll 0.8 \mu\text{m}$). In the fast quenching condition, buckling was not observed, as was the case with the slow quenching condition. These results clearly show that the spontaneous buckling condition of the shell thickness has an adequate value.

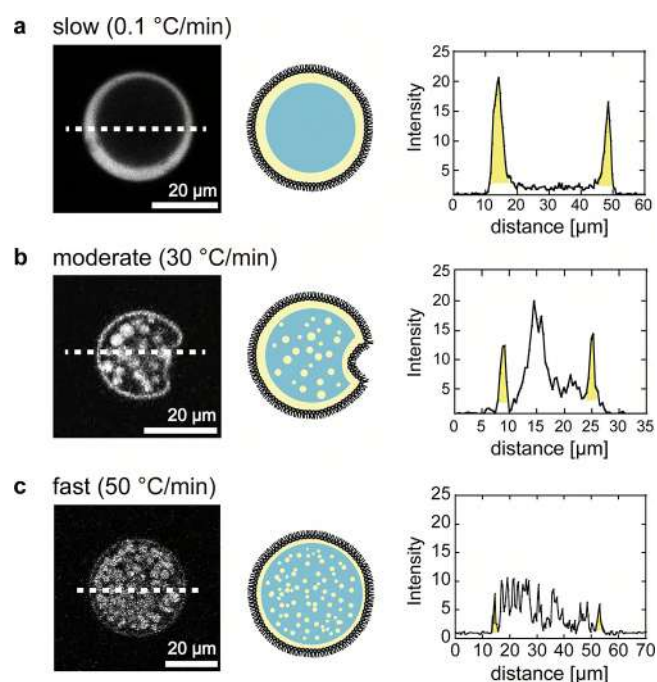


Figure 3. Quench rate dependence of buckling of core–shell microgels and the shell thickness. An example of gelatin/PEG microgels is shown as confocal cross-sectional fluorescence (FL) image of gelatin-rich phase (left) and the schematic image (center). The gelatin-rich gel phase and PEG-rich liquid phase are shown in white (yellow) and black (blue), respectively. (right) Intensity profiles along the dotted lines in the FL images. The yellow regions correspond to the shell of gelatin gel.

To clarify the spontaneous buckling condition of the shell thickness h , the h of microgels with and without buckling is plotted against the microgel size R in Figure 4a. The quenching rate is 30 $^{\circ}\text{C}/\text{min}$ (moderate quenching rate). It clearly demonstrates that buckling is not observed for core–shell

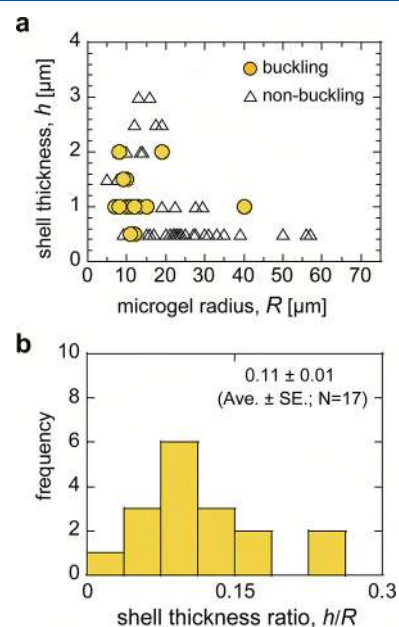


Figure 4. (a) Microgel size R dependence of shell thickness h for buckling core–shell microgels (closed yellow circles) and for nonbuckling core–shell microgels (triangles). (b) Histogram of shell thickness ratio, h/R , for buckling core–shell microgels.

microgels with large shell thickness ($h > 2.5 \mu\text{m}$) and with small shell thickness ($h \ll 1 \mu\text{m}$). Only microgels with medium shell thickness (average \pm SE = 1.2 ± 0.2 ; $N = 17$) exhibit buckling. Moreover, small microgels ($R = 12.5 \pm 1.9 \mu\text{m}$; $R_{\text{min}} = 7 \mu\text{m}$) seem more likely to buckle than large microgels ($R \gg 20 \mu\text{m}$), and the reduced volume of such buckling microgels is increased up to 40 vol % (Figure S3). Compared to localized buckling with the large reduced volume, the presence of slight buckling at the surface is difficult to judge, especially for small microgels. This may be the reason that buckling and nonbuckling microgels seem to coexist under the same shell thickness and microgel radius conditions. The histogram of the shell thickness ratio h/R has a peak, as shown in Figure 4b (0.11 ± 0.01 (average \pm SE)). In the conventional buckling theory (eq 1), pressure-induced buckling under a constant pressure is observed for spherical shells with a smaller shell thickness ratio than a certain value. Therefore, the existence of a lower limit for h/R constitutes a unique condition for the spontaneous buckling of microgels in the sol–gel coexisting phase.

Mechanism of Spontaneous Buckling for Core–Shell Microgels. To explain the observed spontaneous buckling without applying pressure, we calculated the force balance for core–shell microgels with a liquid core. The extended critical pressure P should be composed of two factors: gel elasticity P_c (eq 1) and interfacial tension P_{int} as illustrated in Figure 5a.

$$P = P_c - P_{\text{int}} = \frac{2E}{\sqrt{3(1-\mu^2)}} \left(\frac{h}{R - \frac{h}{2}} \right)^2 - \frac{2\gamma}{R - h} \quad (2)$$

where E , μ , and γ are the Young's modulus of the shell in the gel phase, Poisson's ratio of the elastic shell, and interfacial tension between gel phase at the skin shell (gelatin-rich phase) and sol phase at the core (PEG-rich phase), respectively. These values of P_c and $-P_{\text{int}}$ are plotted against the shell thickness ratio h/R in

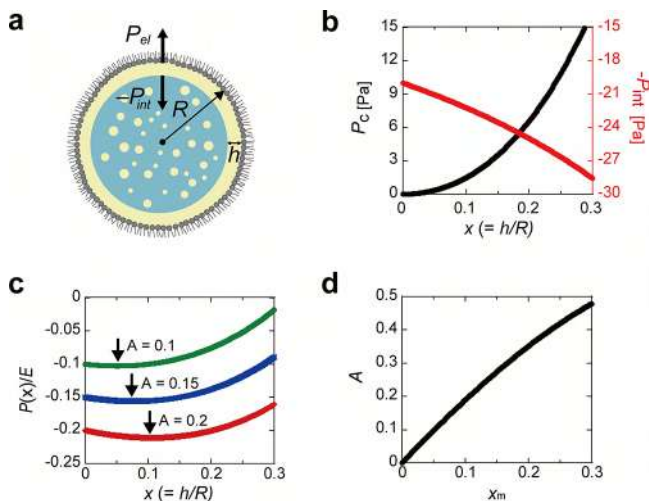


Figure 5. (a) Schematic illustration of force balance between elastic pressure P_c and interfacial tension pressure $-P_{\text{int}}$. R and h denote the outer radius of the core–shell microgel and shell thickness of the gel capsule (yellow). (b) Values of P_c and $-P_{\text{int}}$ are plotted against the shell thickness ratio h/R . The values of E , γ , R , and μ are 100 Pa, 100 $\mu\text{N/m}$, 10 μm , and 0.5, respectively. (c) Normalized extended critical pressure $P(x)/E$ ($= (P_c - P_{\text{int}})/E$) with various A ($= 2\gamma/ER$) is plotted against the shell thickness ratio, x ($= h/R$). The arrows denote the minimum points. (d) The relation between the A and the x value at the minimum point, x_m .

Figure 5b, where E , μ , R , and γ are fixed to 100 Pa, 0.5, 10 μm , and 100 $\mu\text{N/m}$, respectively.^{26,32} With an increase in h/R , the P_c increases as well, whereas $-P_{\text{int}}$ decreases, because the surface area at the phase interface becomes smaller. Therefore, the extended critical pressure P ($= P_c - P_{\text{int}}$) becomes a downward-convex function of h/R depending on the values of E and γ .

In our experimental results, the core–shell microgels show spontaneous buckling when h/R reaches a certain value ($h/R = 0.11 \pm 0.01$; see Figure 4b). We interpret this in terms of the extended critical pressure P of a downward-convex function reaching a minimum at a certain h/R value ($h/R = 0.11$) and the core–shell microgels having that h/R value tending to buckle more easily than microgels having smaller and larger values of h/R .

To derive the condition of P with a minimum point, we rewrite eq 2 as a function of h/R ($\equiv x$) as follows:

$$\frac{P(x)}{E} = \frac{2}{\sqrt{3(1-\mu^2)}} \left(\frac{x}{1 - \frac{x}{2}} \right)^2 - \frac{A}{1-x} \quad (3)$$

$$A \equiv \frac{2\gamma}{ER} \quad (4)$$

We plot $P(x)/E$ for various A in Figure 5c. Depending on the value of A , the minimum point of $P(x)$ changes, and its x value increases with A . The relation between the parameter A and x value at the minimum point, x_m , is derived from eq 3 as follows:

$$A = \frac{2}{\sqrt{3(1-\mu^2)}} \frac{x_m(1-x_m)^2}{\left(1 - \frac{x_m}{2}\right)^3} \quad (5)$$

Thus, the parameter A has a positive correlation with the shell thickness ratio x_m . The value of A is plotted against x_m under the experimental condition ($x < 0.3$) in Figure 5d. It shows that the value of A should be smaller than 0.5 for $P(x)$ to have a minimum point.

We assume that the ratio γ/E is independent of the microgel size R because the confined polymer composition is independent of the confined size R . Figure 5d shows that the value of A ($= 2\gamma/ER$), which is a decreasing function of R , increases with increasing x_m at the minimum point of $P(x)$. Therefore, we expect that a larger buckling microgel has a smaller shell thickness ratio; i.e., h/R at the minimum point is a decreasing function of R . To verify this, we plot them as shown in Figure 6 (closed circles; by using the data in Figure 4a) and fit the data with eq 6, rewriting eq 5 to R :

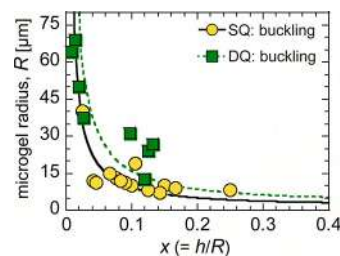


Figure 6. Relation between the size R of buckling microgels and the shell thickness ratio h/R for single quenching (SQ; circles) and double quenching with 10–30 min incubation time at T_p (DQ; squares). The solid and dashed lines are the fitting lines of eq 6 for SQ and DQ, respectively.

$$R = \frac{\gamma \sqrt{3(1 - \mu^2)}}{E} \frac{\left(1 - \frac{x_m}{2}\right)^3}{x_m(1 - x_m)^2} \quad (6)$$

Figure 6 clearly demonstrates that the relation between h/R and R of the buckling microgels satisfies the theoretically obtained relation of eq 6. After fitting with μ fixed at 0.5, we found that the characteristic length γ/E is $\sim 0.6 \mu\text{m}$.

Furthermore, Figure 5d suggests that the h/R of buckling microgels increases when increasing γ/E for fixed R conditions because $A (= 2\gamma/ER)$ is an increasing function of h/R . To change the value of γ/E , we performed double-quenching experiments where the sample was incubated for 10–30 min at the phase separation point T_p before the second quenching below the gelation point T_g occurred. As phase separation proceeded with an incubation process above T_g , we expected that the value of γ/E became greater than that of the single quenching experiment. This is because the interfacial tension γ increases until the progress of phase separation is inhibited by gelation. As plotted in Figure 6 (closed square), the h/R of buckling microgels with similar R for the double quenching was greater than that for single quenching. The fitting-derived γ/E was found to be $>1.5 \mu\text{m}$ (dashed line in Figure 6), which is larger than that of single quenching ($\sim 0.6 \mu\text{m}$), as we expected. Accordingly, the minimum R for satisfying $A (= 2\gamma/ER) < 0.5$ (Figure 5d) increases with an increase of γ/E . In fact, the minimum R of buckling microgels for double quenching ($12.5 \mu\text{m}$) is larger than that of single quenching ($7 \mu\text{m}$). These tendencies support our theoretical model.

This spontaneous buckling resulting from the balance between the gel elasticity E and interfacial tension γ brings a new insight into the shape change of various elastic bodies with an inhomogeneous inner structure in the sol–gel coexisting phase, for example, microgels during polymerization (sol–gel transition)^{20–23,27,28} and phase separation.^{29,30} The buckling condition of the shell thickness ratio depending on the size of the elastic bodies and the characteristic size of γ/E derived from both experimental and theoretical analysis make it possible to apply spontaneous buckling for the morphological regulation of elastic bodies.

To focus on the condition of spontaneous buckling occurrence, we ignored the influence of core elasticity derived from the isolated domain of gelatin gel in the PEG solution. However, the core elasticity also becomes important, like shell elasticity and interfacial tension, in discussing the shape of buckling microgels (buckling mode). Compared to large microgels, small microgels tend to show a localized buckling with a large reduced volume (Figure 4a and Figure S3). It has been reported that as the elasticity ratio between the shell and core increases, the buckling depth increases and localized buckling tends to occur.^{2,3,33} For small microgels where phase separation completes faster,²⁴ the core elasticity might be effectively reduced and finally lead to localized buckling. For a comprehensive understanding of the buckling pattern that is beyond the scope here, it will be necessary to consider the mechanical properties of the core depending on the microgel size.

CONCLUSION

We explored the influence of the inhomogeneous inner structure of microgels in a sol–gel coexisting phase on buckling by using core–shell microgels of a polymer solution that exhibits phase separation and gelation with a decrease in temperature. By

preventing phase separation with gelation upon temperature quenching, we varied the shell thickness ratio h/R of the core–shell microgels. We found that the microgels with a certain h/R ratio spontaneously buckle without applying pressure. To explain this buckling condition of h/R , we analyzed the extended critical pressure for buckling by taking into account the gel elasticity E and interfacial tension between the sol–gel coexisting phase γ . The extended critical pressure is a downward-convex function with respect to the h/R ratio, which implies that the microgel having a certain h/R ratio at which the critical pressure reaches a minimum tends to buckle spontaneously. Moreover, the buckling condition of h/R depends on the ratio between the characteristic length γ/E and microgel radius R . The derived condition of spontaneous buckling contributes to establishing a method for microgel shape control through the inner structure in a sol–gel coexisting phase (e.g., emulsion polymerization).

ASSOCIATED CONTENT

Supporting Information

The Supporting Information is available free of charge on the ACS Publications website at DOI: 10.1021/acs.langmuir.8b03751.

Microscopic image of homogeneous microgels of gelatin (Figure S1), fluorescence image of microgels with different fluorescence localized in the gelatin-rich phase (Figure S2), and morphological analyses of buckling microgels (Figure S3) (PDF)

Buckling of microgels upon temperature decrease (Movie S1) (AVI)

Shape change of buckling microgels upon temperature increase (Movie S2) (AVI)

AUTHOR INFORMATION

Corresponding Author

*E-mail myanagisawa@g.ecc.u-tokyo.ac.jp (M.Y.).

ORCID

Miho Yanagisawa: 0000-0001-7872-8286

Notes

The authors declare no competing financial interest.

ACKNOWLEDGMENTS

We thank Prof. Masayuki Tokita (Kyushu University), Mr. Sinpei Nigorikawa (Kyushu University), and Mr. Atsushi Sakai (Tokyo University of Agriculture and Technology) for their experimental support in microgel preparation and Prof. Kei Fujiwara (Keio University) for critical reading of the manuscript. This work was supported by JSPS KAKENHI (M.Y.; No. 15KT0081, No. 16H01443, and No. 17H00769).

REFERENCES

- (1) Chen, X.; Yin, J. Buckling patterns of thin films on curved compliant substrates with applications to morphogenesis and three-dimensional micro-fabrication. *Soft Matter* **2010**, *6* (22), 5667–5680.
- (2) Yin, J.; Cao, Z.; Li, C.; Sheinman, I.; Chen, X. Stress-driven buckling patterns in spheroidal core/shell structures. *Proc. Natl. Acad. Sci. U. S. A.* **2008**, *105* (49), 19132–19135.
- (3) Li, B.; Cao, Y. P.; Feng, X. Q.; Gao, H. J. Mechanics of morphological instabilities and surface wrinkling in soft materials: a review. *Soft Matter* **2012**, *8* (21), 5728–5745.

- (4) Shim, J.; Perdiguero, C.; Chen, E. R.; Bertoldi, K.; Reis, P. M. Buckling-induced encapsulation of structured elastic shells under pressure. *Proc. Natl. Acad. Sci. U. S. A.* **2012**, *109* (16), 5978–5983.
- (5) Singamaneni, S.; Tsukruk, V. V. Buckling instabilities in periodic composite polymeric materials. *Soft Matter* **2010**, *6* (22), 5681–5692.
- (6) Mei, H.; Huang, R.; Chung, J. Y.; Stafford, C. M.; Yu, H.-H. Buckling modes of elastic thin films on elastic substrates. *Appl. Phys. Lett.* **2007**, *90* (15), 151902.
- (7) Mei, Y. F.; Kiravittaya, S.; Harazim, S.; Schmidt, O. G. Principles and applications of micro and nanoscale wrinkles. *Mater. Sci. Eng., R* **2010**, *70* (3–6), 209–224.
- (8) Gao, L.; Zhang, Y. H.; Zhang, H.; Doshay, S.; Xie, X.; Luo, H. Y.; Shah, D.; Shi, Y.; Xu, S. Y.; Fang, H.; Fan, J. A.; Nordlander, P.; Huang, Y. G.; Rogers, J. A. Optics and Nonlinear Buckling Mechanics in Large-Area, Highly Stretchable Arrays of Plasmonic Nano structures. *ACS Nano* **2015**, *9* (6), 5968–5975.
- (9) Chan, E. P.; Crosby, A. J. Fabricating microlens arrays by surface wrinkling. *Adv. Mater.* **2006**, *18* (24), 3238–3242.
- (10) Chandra, D.; Yang, S.; Lin, P.-C. Strain responsive concave and convex microlens arrays. *Appl. Phys. Lett.* **2007**, *91* (25), 251912.
- (11) Tallinen, T.; Chung, J. Y.; Rousseau, F.; Girard, N.; Lefevre, J.; Mahadevan, L. On the growth and form of cortical convolutions. *Nat. Phys.* **2016**, *12* (6), 588–593.
- (12) Kim, D. H.; Rogers, J. A. Stretchable Electronics: Materials Strategies and Devices. *Adv. Mater.* **2008**, *20* (24), 4887–4892.
- (13) Khang, D. Y.; Rogers, J. A.; Lee, H. H. Mechanical Buckling: Mechanics, Metrology, and Stretchable Electronics. *Adv. Funct. Mater.* **2009**, *19* (10), 1526–1536.
- (14) Chung, J. Y.; Nolte, A. J.; Stafford, C. M. Surface Wrinkling: A Versatile Platform for Measuring Thin-Film Properties. *Adv. Mater.* **2011**, *23* (3), 349–368.
- (15) Van der Heijden, A. M. *WT Koiter's Elastic Stability of Solids and Structures*; Cambridge University Press: Cambridge, England, 2008.
- (16) Pan, B. B.; Cui, W. C. An overview of buckling and ultimate strength of spherical pressure hull under external pressure. *Mar Struct* **2010**, *23* (3), 227–240.
- (17) Hutchinson, J. W. Imperfection sensitivity of externally pressurized spherical shells. *J. Appl. Mech.* **1967**, *34* (1), 49–55.
- (18) Datta, S. S.; Kim, S. H.; Paulose, J.; Abbaspourrad, A.; Nelson, D. R.; Weitz, D. A. Delayed buckling and guided folding of inhomogeneous capsules. *Phys. Rev. Lett.* **2012**, *109* (13), 134302.
- (19) Vernizzi, G.; Sknepnek, R.; Olvera de la Cruz, M. Platonic and Archimedean geometries in multicomponent elastic membranes. *Proc. Natl. Acad. Sci. U. S. A.* **2011**, *108* (11), 4292–6.
- (20) Sacanna, S.; Irvine, W. T. M.; Chaikin, P. M.; Pine, D. J. Lock and key colloids. *Nature* **2010**, *464* (7288), 575–578.
- (21) Sacanna, S.; Pine, D. J. Shape-anisotropic colloids: Building blocks for complex assemblies. *Curr. Opin. Colloid Interface Sci.* **2011**, *16* (2), 96–105.
- (22) Shen, H. F.; Du, X. L.; Ren, X. L.; Xie, Y. H.; Sheng, X. X.; Zhang, X. Y. Morphology control of anisotropic nonspherical functional polymeric particles by one-pot dispersion polymerization. *React. Funct. Polym.* **2017**, *112*, 53–59.
- (23) Yanagisawa, M.; Watanabe, C.; Fujiwara, K. Single Micrometer-Sized Gels: Unique Mechanics and Characters for Applications. *Gels* **2018**, *4* (2), 29.
- (24) Yanagisawa, M.; Nigorikawa, S.; Sakaue, T.; Fujiwara, K.; Tokita, M. Multiple patterns of polymer gels in microspheres due to the interplay among phase separation, wetting, and gelation. *Proc. Natl. Acad. Sci. U. S. A.* **2014**, *111* (45), 15894–9.
- (25) Yamashita, Y.; Yanagisawa, M.; Tokita, M. Sol-gel transition and phase separation in ternary system of gelatin-water-poly(ethylene glycol) oligomer. *J. Mol. Liq.* **2014**, *200*, 47–51.
- (26) Yanagisawa, M.; Yamashita, Y.; Mukai, S.-A.; Annaka, M.; Tokita, M. Phase separation in binary polymer solution: Gelatin/poly(ethylene glycol) system. *J. Mol. Liq.* **2014**, *200*, 2–6.
- (27) Salmon, A. R.; Parker, R. M.; Groombridge, A. S.; Maestro, A.; Coulston, R. J.; Hegemann, J.; Kierfeld, J.; Scherman, O. A.; Abell, C. Microcapsule Buckling Triggered by Compression-Induced Interfacial Phase Change. *Langmuir* **2016**, *32*, 10987.
- (28) Park, S. H.; Kim, J.; Lee, W. E.; Byun, D. J.; Kim, M. H. One-Step Synthesis of Hollow Dimpled Polystyrene Microparticles by Dispersion Polymerization. *Langmuir* **2017**, *33* (9), 2275–2282.
- (29) Bahadur, J.; Sen, D.; Mazumder, S.; Paul, B.; Bhatt, H.; Singh, S. G. Control of buckling in colloidal droplets during evaporation-induced assembly of nanoparticles. *Langmuir* **2012**, *28* (3), 1914–23.
- (30) Pathak, B.; Basu, S. Phenomenology and control of buckling dynamics in multicomponent colloidal droplets. *J. Appl. Phys.* **2015**, *117* (24), 244901.
- (31) Yamashita, Y.; Yanagisawa, M.; Tokita, M. Dynamics of Spinodal Decomposition in a Ternary Gelling System. *Gels* **2018**, *4* (2), 26.
- (32) Sakai, A.; Murayama, Y.; Fujiwara, K.; Fujisawa, T.; Sasaki, S.; Kidoaki, S.; Yanagisawa, M. Increasing Elasticity through Changes in the Secondary Structure of Gelatin by Gelation in a Microsized Lipid Space. *ACS Cent. Sci.* **2018**, *4* (4), 477–483.
- (33) Lagrange, R.; López Jiménez, F.; Terwagne, D.; Brojan, M.; Reis, P. M. From wrinkling to global buckling of a ring on a curved substrate. *J. Mech. Phys. Solids* **2016**, *89*, 77–95.

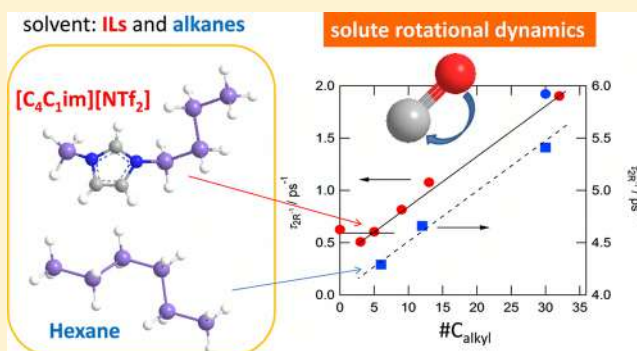
Polarity and Nonpolarity of Ionic Liquids Viewed from the Rotational Dynamics of Carbon Monoxide

Y. Yasaka* and Y. Kimura*

Department of Molecular Chemistry and Biochemistry, Faculty of Science and Engineering, Doshisha University, Kyotanabe, Kyoto 610-0321, Japan

S Supporting Information

ABSTRACT: The rotational dynamics of carbon monoxide (CO) in a molten salt, ionic liquids (ILs), and alkanes were investigated by ^{17}O NMR T_1 measurements using labeled C^{17}O . The molten salt and the studied ILs have the bis(trifluoromethanesulfonyl)imide anion ($[\text{NTf}_2]^-$) in common. In hexane near room temperature, the rotational relaxation times are close to the values predicted from the slip boundary condition in the Stokes–Einstein–Debye (SED) theory. However, in contradiction to the theoretical prediction, the rotational relaxation times decrease as the value of η/T increases, where η and T are the viscosity and absolute temperature, respectively. In other alkanes and ILs used in this study, the rotational relaxation times are much faster than those predicted by SED, and show a unique dependence on the number of alkyl carbons. For the same value of η/T , the CO rotational relaxation times in ILs composed of short-alkyl-chain-length imidazolium cations (1-ethyl-3-methylimidazolium and 1-butyl-3-methylimidazolium) are close to those for a molten salt ($\text{Cs}[\text{NTf}_2]$). On the other hand, the rotational relaxation times in ILs composed of long-chain-length imidazolium (1-methyl-3-octylimidazolium) and phosphonium (tributylmethylphosphonium and tetraoctylphosphonium) cations are much shorter than the SED predictions. This deviation from theory increases as the alkyl chain length increases. We also found that the rotational relaxation times in dodecane and squalane are similar to those in ILs with a similar number of alkyl carbons. These results are discussed in terms of heterogeneous solvation and in comparison with the translational diffusion of CO in ILs.



1. INTRODUCTION

From the early stages of research on ionic liquids (ILs), molecular dynamics of solutes dissolved in ILs has been extensively studied.^{1,2} Solute dynamics is strongly influenced by molecular interactions, and thus can serve as a microscopic probe into a liquid's structure. The strong Coulomb forces between charged species (cation–anion, etc.) or charged and dipolar species (cation–solute, etc.) generally make the dynamics of molecules in ILs slow and complex due to the correlated motions of interacting species. In addition, the cations and anions of ILs may carry noncharged “tails” (e.g., the butyl chain in 1-butyl-3-methylimidazolium ($[\text{C}_4\text{C}_1\text{im}]^+$) cation). These groups introduce an additional uniqueness into the liquid structure of ILs. X-ray analysis, neutron scattering studies, and computer simulations have revealed that the charged head groups and noncharged tails tend to aggregate separately. It has been proposed that ILs with longer tails form a segregated structure.^{3–7} Recently, attention has been paid to how this kind of heterogeneity contributes to the solvation environment and the molecular dynamics of solutes in ILs.

The rotational dynamics of solutes can be investigated by time-resolved fluorescence anisotropy measurements,^{8–25} as

well as by magnetic resonance measurements such as NMR^{26–28} and electron paramagnetic resonance (EPR).^{29,30} Each of these methods targets different types of solutes. By studying solutes that are different in size and polarity, a wide range of time/space domains of an IL structure can be investigated. Standard fluorescent probes are ~ 1 nm in size, and rotate on the sub-ns to several ns time frame. The rotation of nonfluorescent smaller molecules is much faster (on the order of a few ps) and, hence, can be studied using NMR spin–lattice relaxation measurements. The rotational relaxation time, τ_R , is often discussed on the basis of hydrodynamic theory, represented by the Stokes–Einstein–Debye (SED) equation shown in eq 1

$$\tau_R = \frac{\eta f V C}{k_B T} \quad (1)$$

where η is the viscosity of the solvent, V is the van der Waals volume of the solute, C is the boundary condition parameter, which has a value between 0 and 1, k_B is the Boltzmann

Received: October 6, 2015

Revised: November 18, 2015

Published: November 19, 2015

constant, T is the absolute temperature, and f is the shape parameter introduced to account for the nonspherical solute molecule. The parameters V and f are determined by the geometry of the solute molecule, whereas the theory gives only the lower ($C = C_{\text{slip}}$; slip conditions) and upper limit ($C = 1$; stick conditions) for C . It is common to attribute the magnitude of C to the strength of the solute–solvent interaction. For small-sized nonpolar solute molecules, τ_R observed is sometimes faster than predictions from the slip boundary condition, termed superslip.^{15,19} In contrast, for charged solutes, C may be larger than 1 (superstick conditions) for some systems.^{15,25} The rotational relaxation times lie between the values of the stick and the slip boundary conditions for a number of dipolar molecules.^{10,17,19,21} In recent studies, deviations from SED theory for some fluorescent solutes in ILs have been interpreted by considering the heterogeneous structure of ILs. For example, Samanta et al. measured τ_R for three different probe molecules, 4-aminopyridine (4AP), 6-propionyl-2-dimethylaminonaphthalene (PRODAN), and anthracene, in *N*-alkyl-*N*-methylmorpholinium ILs with different alkyl chain lengths.¹⁹ The τ_R 's of these three probe molecules lie on different boundary conditions, indicating that the effect of microheterogeneity of solvation becomes evident at different magnitudes depending on the solute molecules studied.

All of these preceding works indicate that rotational dynamics sharply reflects the local environment caused by heterogeneous solvation. To the best of our knowledge from the viewpoint of rotational dynamics, however, testing has not been done to determine whether the IL environment is polar or nonpolar in comparison with conventional liquid solvents. In this work, we present our studies of the rotational dynamics of carbon monoxide (CO) in ILs, which is a nearly nonpolar molecule, using ¹⁷O NMR. Due to its small size, CO can more sharply reflect the local molecular environments in which it is solvated than standard fluorescent probes. The dipole moment of CO is small (0.122 D),³¹ and the dispersion force between CO and other molecules is expected to be small, as is represented by the Lennard-Jones attractive parameter (ϵ/k_B) for CO (91.7 K).³² In the segregated picture of the IL structure, the volume occupied by the “tail” domain increases as the length (number of carbons) of the alkyl chains attached on the cation increases. At a certain point, the nonpolar domain of the IL is large enough to look like a liquid alkane. In this case, we would like to learn how CO is solvated, and how the liquid structure of the IL changes, by measuring the τ_R of CO as a function of the number of alkyl carbons ($\#C_{\text{alkyl}}$) in the liquid alkane. More specifically, we determine τ_R in ILs comprised of standard imidazolium cations, such as 1-ethyl-3-methylimidazolium ($[C_2C_1\text{im}]$, $\#C_{\text{alkyl}} = 3$), 1-butyl-3-methylimidazolium ($[C_4C_1\text{im}]$, $\#C_{\text{alkyl}} = 5$), and 1-methyl-3-octylimidazolium ($[C_8C_1\text{im}]$, $\#C_{\text{alkyl}} = 9$). We also evaluate tetraalkylphosphonium cations with shorter ($\#C_{\text{alkyl}} = 13$) and longer ($\#C_{\text{alkyl}} = 32$) alkyl chains by using common anionic species of bis(trifluoromethanesulfonyl)imide ($[\text{NTf}_2]^-$). One molten inorganic salt, $\text{Cs}[\text{NTf}_2]$, is chosen as an example of the “polar” limit for ILs. These results will be compared with those for alkanes with different alkyl chain lengths (hexane (C_6H_{14}), dodecane ($C_{12}H_{26}$), and squalane ($C_{30}H_{62}$)). To anticipate our results, there is a threshold for the number of carbons making up a nonpolar environment around CO. As the number of cation alkyl carbon increases, the rotational dynamics of CO resembles that of alkanes having a similar number of carbons.

2. EXPERIMENTAL SECTION

2.1. Materials. $[C_2C_1\text{im}][\text{NTf}_2]$ (>99.99%), $[C_4C_1\text{im}][\text{NTf}_2]$ (>99.99%), and $[P_{4441}][\text{NTf}_2]$ (>99.98%) were purchased from Kanto Kagaku. $[C_8C_1\text{im}][\text{NTf}_2]$ (>99%) was purchased from Iolitec. $\text{Cs}[\text{NTf}_2]$ was synthesized in our lab by metathesis of $\text{Li}[\text{NTf}_2]$ (Tokyo Kasei) and CsCl (Cooper Chemical Company) in water. $[P_{888}][\text{NTf}_2]$ was synthesized according to a procedure described previously.³³ The purity of $[P_{888}][\text{NTf}_2]$ (>99%) was confirmed by NMR. The ILs were dried under a vacuum at 100 °C for 1 day before use. All ILs were handled in a glovebox. ¹⁷O-Labeled water (40% isotopic purity) was obtained from Chembridge Isotope Laboratory. Sodium hydride (60% in mineral oil), tetrahydrofuran (THF), chloral hydrate, and phosphorus(V) oxide (P_2O_5) were obtained from Nacalai and used without purification. Hexane (>99%, Nacalai), dodecane (>99%, Nacalai), and squalane (>99%, Aldrich) were used as received. Viscosities of $[P_{4441}][\text{NTf}_2]$, $[P_{888}][\text{NTf}_2]$, and $\text{Cs}[\text{NTf}_2]$ at elevated temperatures (up to 180 °C) were measured using an Electro Magnetically Spinning (EMS) Viscometer (EMS-1000, Kyoto Electronics Manufacturing Co. Ltd.).

2.2. Sample Preparation of ¹⁷O-Enriched CO. ¹⁷O-Enriched CO was prepared by thermal decomposition of ¹⁷O-enriched sodium formate in a sealed quartz tube containing an aliquot of studied liquid (IL or alkane), as shown in Figure 1.

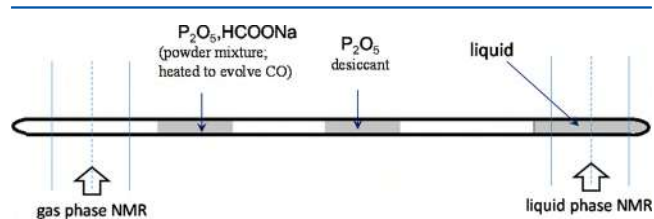
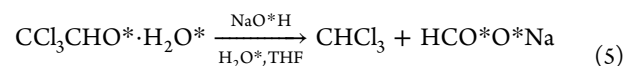
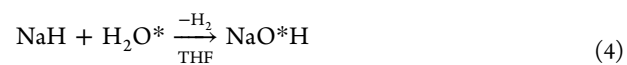
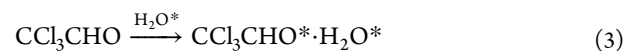
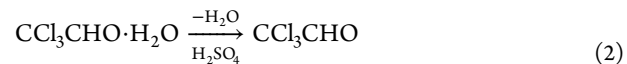


Figure 1. Schematic illustration of the sample tube. The quartz tube is 40 cm long and 2.3 mm in inner diameter. The tube contains liquid sample, phosphorus oxide (as a desiccant), and a powder mixture of ¹⁷O-enriched sodium formate and phosphorus oxide for the preparation of ¹⁷O-enriched carbon monoxide. Each component is separated by glass wool (not shown). Both ends of the tube are measured by NMR.

¹⁷O-Enriched sodium formate was synthesized according to eqs 2–5.



In eqs 2–5, asterisks denote an ¹⁷O isotopic label. In eq 2, chloral hydrate was distilled from sulfuric acid at 115 °C and ambient pressure to obtain anhydrous chloral (75% purity, contaminated mainly by chloral hydrate). The latter was then turned back into chloral hydrate in eq 3 by treatment with ¹⁷O-labeled water. The ¹⁷O (40%)-labeled chloral hydrate was then reacted at room temperature with ¹⁷O-labeled sodium hydroxide, which was prepared according to eq 4 from sodium hydride and ¹⁷O-labeled water. In this manner, we obtained

^{17}O -labeled sodium formate as a precipitate from THF solution (see eq 5). The ^{17}O isotopic purity of sodium formate was determined to be 25% by ^1H and ^{17}O NMR.

Approximately 60 mg of ^{17}O -enriched sodium formate, powdered and dried, was mixed with 50–100 mg of P_2O_5 in a drybox, and loaded into a quartz tube (2.3 mm i.d., 4.0 mm o.d., and 40 cm long), as shown in Figure 1. This powder mixture was placed >8 cm away from one end of the tube and sandwiched by glass wool. An aliquot of the liquid (IL or alkane) was placed at the opposite end of the quartz tube. The liquid occupied 4 cm of the tube so that high-resolution NMR signals could be obtained. Between the powder mixture and the IL solvent, 0.1 g of P_2O_5 was placed as a desiccant.

After the quartz tube was sealed at both ends, the left part of the tube was heated at 250 °C for 10 min to synthesize ^{17}O -labeled CO. The evolution of gaseous CO and its isotopic purity were confirmed by ^{13}C and ^{17}O NMR measurement at the (empty) left end of the sample tube. The ^{17}O NMR signal for gaseous C^{17}O was observed at 350.4 ppm (Figure 2, upper

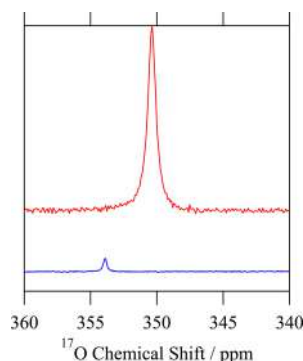


Figure 2. ^{17}O NMR signal of C^{17}O in $[\text{P}_{888}][\text{NTf}_2]$ at 294 K. The upper trace shows the spectrum in the gaseous phase and the lower trace in $[\text{P}_{888}][\text{NTf}_2]$.

trace) using D_2O as an external reference, which is consistent with the literature value.³⁴ The ^{17}O isotopic purity was about 15%, which is lower than that of the precursor (sodium formate). This is presumably due to reactive oxygen exchange between sodium formate and P_2O_5 . The partial pressure of C^{17}O was typically 0.2 MPa, and the total pressure of CO (C^{16}O and C^{17}O) was 2 MPa. The gaseous CO thus prepared was allowed to dissolve in the liquid phase by keeping the sample at 100 °C for 24 h except for hexane (room temperature) and $\text{Cs}[\text{NTf}_2]$ (180 °C). The ^{17}O NMR signal for C^{17}O in $[\text{P}_{888}][\text{NTf}_2]$ was observed at 353.9 ppm using D_2O as an external reference (Figure 2, lower trace). The concentration of C^{17}O was 6 mM. The Ostwald constant (the gas phase concentration divided by the liquid phase concentration) was about 10. The Ostwald constants and the liquid phase concentrations of CO in each liquid studied are summarized in Table SI in the Supporting Information.

2.3. T_1 Measurements. The T_1 of the ^{17}O nucleus for C^{17}O dissolved in ILs and alkanes was measured using a JEOL ECA300 (8.4 T) equipped with a standard 5 mm probe (THSAT). The inversion–recovery method (π - t_d - $\pi/2$ pulse sequence) was applied using 16 delay times of t_d . The number of scans was varied (500–10000 for each t_d) depending on the CO concentration and temperature. At low temperatures, the CO signal was broad and, hence, a higher number of scans

showed an acceptable signal-to-noise ratio (~ 20). A typical example of the inversion recovery data is shown in Figure 3.

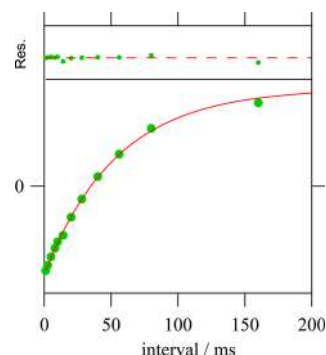


Figure 3. ^{17}O NMR inversion recovery data for C^{17}O in $[\text{P}_{888}][\text{NTf}_2]$ at 313 K.

T_1 measurements were carried out in the temperature range 183–413 K. T_1 measurements at different temperatures were done successively for each sample. The sample temperature was equilibrated for at least 60 min before scans were started. The CO concentration was checked during the scan to make sure it did not change in the middle of a scan. A change in CO concentration may occur during a scan because changing the sample temperature forces the CO dissolution equilibrium to rebalance. This rebalancing may take a significant amount of time due to the thickness of the liquid phase region and the slow diffusion that occurs in ILs. Any increase/decrease of CO concentration while the scans are running for inversion recovery experiments would likely distort the inversion recovery curve. We compared the CO concentration in $[\text{P}_{888}][\text{NTf}_2]$ at 20 °C before and after heating the sample at 80 °C for 9 h. As expected from the lower gas solubility at high temperatures, the CO concentration after heating was slightly lower ($\sim 5\%$) than before heating. This level of error was acceptable, since we are interested in the solvent effect on T_1 , which is much larger in magnitude.

To determine T_1 , the inversion recovery data with respect to the delay time, t_d , were fitted using eq 6

$$f(t_d) = A\{1 - (2 - B)\exp(-t_d/T_1)\} \quad (6)$$

where A is a constant dependent on the signal intensity and B is a small (0.05–0.15) empirical correction factor for the imperfectness of the pulse. The fit typically gives a standard deviation of $\pm 3\%$ for T_1 . The values of T_1 thus obtained are summarized in Table SII in the Supporting Information.

3. RESULTS AND DISCUSSION

3.1. Analysis. The main relaxation mechanism for the ^{17}O nucleus is quadrupolar relaxation. T_1 is expressed in eq 7,³⁴ under the extreme narrowing condition, i.e., $\tau_{2R}\omega_0 \ll 1$,

$$\frac{1}{T_1} = \frac{3\pi^2}{10} \frac{2I + 3}{I^2(2I - 1)} \left(\frac{e^2Qq}{h}\right)^2 \tau_{2R} \quad (7)$$

where ω_0 is the Larmor frequency (40.7 MHz or 2.55×10^8 rad s^{-1} at a magnetic field strength of 8.4 T), I is the nuclear spin (5/2 for ^{17}O), and e^2Qq/h is the quadrupolar coupling constant (QCC). Here we denote the rotational relaxation time as τ_{2R} following the convention and indicating that the time constant is obtained by the integral of the orientational

correlation function of the second order Legendre polynomial. In the following, we will use τ_{2R} instead of τ_R , which are the same meaning in the present paper. The QCC value (4.34 MHz) for CO was adopted using a literature value.³⁵ As shown below, τ_{2R} for CO in the ILs studied in this work is ≤ 10 ps. This validates our adoption of the extreme narrowing condition.

The τ_{2R} values of CO versus temperature for various ILs are plotted in Figure 4. The numerical values for the data in Figure

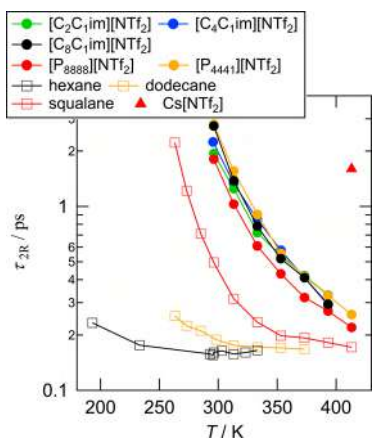


Figure 4. τ_{2R} of $C^{17}O$ in various solvents at different temperatures.

4 are tabulated in the Supporting Information (Table SIII). For all of the ILs studied here, the τ_{2R} values change by an order of magnitude within the temperature range studied (295–413 K). This large temperature effect is related to a change in viscosity. Thus, in section 3.2, we analyze the τ_{2R} values in relation to the Stokes–Einstein–Debye (SED) model. It is to be noted that the τ_{2R} value in hexane shows a weak inverse temperature dependence above room temperature.

3.2. Correlation of the Rotational Relaxation Time with Viscosity (Hydrodynamic Theory). The standard way to estimate rotational relaxation time is to use the SED equation (eq 1). In order to use this equation, the van der Waals volume of CO was estimated using the atomic increment method, and was found to be 27 \AA^3 .³⁶ The CO molecule was modeled as an ellipsoid. The long axis ($2b$) and the short axis ($2a$) were calculated to reproduce the volume and surface area of CO derived from the van der Waals spheres of the C and O atoms. In the latter calculation, the radii of C and O were assumed to be 1.72 and 1.50 \AA , respectively, and the bond length 1.10 \AA . The values of a and b were calculated to be 1.65 and 2.34 \AA , respectively. From these values, the shape factor, f , and the slip boundary condition, C_{slip} , were calculated to be 1.18 and 0.086, respectively.^{37–39}

Figure 5 shows the plot of τ_{2R} versus η/T . The viscosities of conventional liquids are taken from the literature.^{40,41} The viscosities of imidazolium-cation-based ILs are calculated from empirical equations.^{2,42} Although the data range of the reference is limited to 353 K, we applied the equation up to 393 K. Viscosities of $[P_{4441}][NTf_2]$, $[P_{8888}][NTf_2]$, and $Cs[NTf_2]$ were measured by us in the present study (see Table SIV in the Supporting Information), since high-temperature data were not available. The viscosity data were fit to the empirical equation shown in eq 8

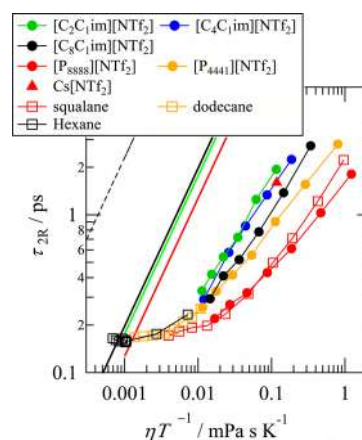


Figure 5. τ_{2R} of $C^{17}O$ in various solvents against η/T . The black broken line represents the prediction from the SED relation with the stick boundary condition, and the black solid line represents that with the slip boundary condition. The green and red lines represent the predictions from the GW theory for the corresponding ILs of the same color notations.

$$\eta = \eta_0 \exp\left(\frac{B}{T - T_0}\right) \quad (8)$$

where η_0 , B , and T_0 are the fitting parameters. Best fit parameters are given in Table 1. The viscosities of $[P_{4441}][NTf_2]$ and $[P_{8888}][NTf_2]$ at room temperature are in agreement with literature values.³³

Table 1. Parameters of the Viscosities Obtained by the Fit to eq 8

	η_0 (mPa s)	B (K)	T_0 (K)
$[P_{4441}][NTf_2]$	0.0680	1038	168.9
$[P_{8888}][NTf_2]$	0.0325	1484	137.0

As shown in Figure 5, the rotational relaxation time, τ_{2R} , for CO in hexane near room temperature was found to be very close to the prediction of SED theory using the slip boundary condition. For all other solvents, τ_{2R} was more or less below the prediction (superslip). In squalane and $[P_{8888}][NTf_2]$, the deviation from theory is especially large. As for the temperature dependence of τ_{2R} , hexane is extraordinary in that τ_{2R} slightly decreases with increasing η/T (from 60 to 20 $^\circ\text{C}$) and then increases (from 0 to -80 $^\circ\text{C}$), which is not expected from the theory. For other solvents, the values increase with increasing η/T , as predicted by the theory. The functional form with respect to η/T is not linear, however. As was done in previous papers,³³ we made the correlation of τ_{2R} with η/T in ILs using eq 9

$$\tau_{2R} = \tau_{2R}^0 \left(\frac{\eta \text{ (mPa s)}}{T \text{ (K)}}\right)^P \quad (9)$$

where τ_{2R}^0 and P are constants depending on the solvent ILs. Best-fit parameters are given in Table 2, and the fitting curves are shown in Figure S1 in the Supporting Information. The values of the exponent decrease as the size of the solvent molecules increases. The values of the exponent are similar to those reported for the translational diffusion of CO (0.64) except for the phosphonium-cation-based ILs.³³

Table 2. Parameters Obtained by the Fit of τ_{2R} to eq 9

	$[\text{C}_2\text{C}_1\text{im}][\text{NTf}_2]$	$[\text{C}_4\text{C}_1\text{im}][\text{NTf}_2]$	$[\text{C}_8\text{C}_1\text{im}][\text{NTf}_2]$	$[\text{P}_{4441}][\text{NTf}_2]$	$[\text{P}_{8888}][\text{NTf}_2]$
τ_{2R}^0 (ps)	10.20	7.96	5.40	3.11	1.49
P	0.77	0.73	0.69	0.57	0.49

The superslip behavior of a nonpolar solute is often attributed to the ratio of the van der Waals volumes of the solvent and solute. In fact, CO is a small diatomic molecule and the solvent species are bulky in our systems. According to the Gierer–Wirtz (GW) quasi-hydrodynamic model, the boundary condition parameter C_{GW} is given by eq 10^{19,43}

$$C_{\text{GW}} = \sigma_0 C_0 \quad (10)$$

where σ_0 is the sticking factor given by eq 11

$$\sigma_0 = \left[1 + 6 \left(\frac{V_S}{V_P} \right)^{1/3} C_0 \right]^{-1} \quad (11)$$

and where C_0 is given by eq 12.

$$C_0 = \left\{ \frac{6 \left(\frac{V_S}{V_P} \right)^{1/3}}{\left[1 + 2 \left(\frac{V_S}{V_P} \right)^{1/3} \right]^4} + \frac{1}{\left[1 + 4 \left(\frac{V_S}{V_P} \right)^{1/3} \right]^3} \right\} \quad (12)$$

In these equations, V_S and V_P are the van der Waals volumes of the solvent and solute, respectively. V_S is the sum of the cation and anion volumes.¹⁹ The van der Waals volumes of the solvent cation and anion were calculated by the atom increment method and taken from the literature.^{36,44,45} The values of C_{GW} were calculated to be 0.077 and 0.055 for $[\text{C}_2\text{C}_1\text{im}][\text{NTf}_2]$ (the smallest IL in this study) and $[\text{P}_{8888}][\text{NTf}_2]$ (the largest one), respectively. As shown in Figure 5, the correction to the hydrodynamic theory using the GW model was too small to account for the rotational dynamics of CO in ILs. The failure of hydrodynamic theory suggests that friction acting on the rotational motion of CO is separate from the forces between the solvent ions, which brings about the high viscosity.

3.3. Effect of Alkyl Carbons on the CO Rotational Relaxation. The importance of the nonhydrodynamic effect on CO dynamics in ILs reminds us about the segregated picture of the liquid structure of ionic liquids, which was first proposed by computer simulation^{46,47} and later verified by experiment.^{3–7} In this segregated picture, the longer alkyl chains on the cation enhance formation of a nonpolar domain. In this domain, molecular dynamics is believed to be controlled by “microviscosity”, an effective viscosity that is consistent with experimentally observed dynamics (but is not the bulk viscosity). Thus, in this section, we focus on the effect of alkyl chain length on CO dynamics. We studied three imidazolium and two phosphonium ILs that have the $[\text{NTf}_2]^-$ anion in common. In addition, we studied molten $\text{Cs}[\text{NTf}_2]$ just above its melting point (140 °C). In this salt, no alkyl carbon exists.

Surprisingly, two imidazolium ILs that have shorter alkyl chains ($[\text{C}_2\text{C}_1\text{im}][\text{NTf}_2]$ and $[\text{C}_4\text{C}_1\text{im}][\text{NTf}_2]$) and $\text{Cs}[\text{NTf}_2]$ showed similar τ_{2R} 's (see Figure 5). Apparently, these liquids provide similar solvation environments for CO. The ionic radius of Cs^+ is 1.81 Å,⁴⁸ while that of $[\text{C}_2\text{C}_1\text{im}]^+$ is 3.0 Å, as estimated from the van der Waals volume. This difference in ionic radius, in fact, brings about different viscosities at the

same temperature ($\text{Cs}[\text{NTf}_2]$ is more viscous). However, when scaled by η/T , both liquids look very similar with respect to CO rotational dynamics.

On the other hand, the effect of alkyl chain length emerges for ILs that have more alkyl carbons. The imidazolium and phosphonium cations have a different number of alkyl chains, so we count all the carbons in two alkyl chains (in the case of imidazolium ILs) or four (in the case of phosphonium ILs). This count is denoted by $\#C_{\text{alkyl}}$, the number of alkyl carbons in ILs. Note that ring carbons in imidazolium cations are not counted. As the $\#C_{\text{alkyl}}$ increases from $[\text{C}_4\text{C}_1\text{im}]^+$ (5) to $[\text{C}_8\text{C}_1\text{im}]^+$ (9), $[\text{P}_{4441}]^+$ (13), and $[\text{P}_{8888}]^+$ (32), the τ_{2R} at a fixed η/T decreases (faster rotation) in the same order.

In Figure 6, we plot the rotational relaxation rate, τ_{2R}^{-1} , as a function of the number of alkyl carbons in the solvent. Note

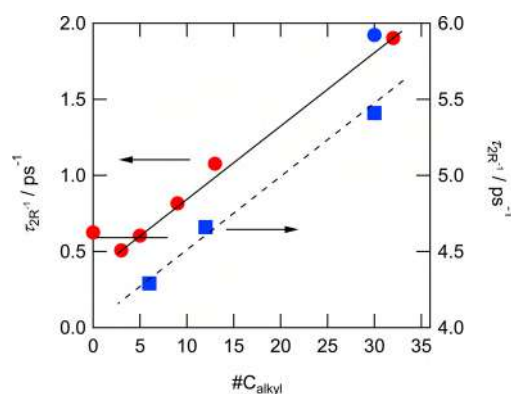


Figure 6. Comparison of the rotational relaxation rate at the same values of η/T . The circles are the results at $\eta/T = 0.118 \text{ mPa s K}^{-1}$, and the squares are those at $0.00724 \text{ mPa s K}^{-1}$. Red symbols are those in ILs, and blue ones are those in alkanes. The lines are drawn to guide the eye.

that the comparison is made at a constant $\eta/T = 0.118 \text{ mPa s K}^{-1}$ (where τ_{2R} for $\text{Cs}[\text{NTf}_2]$ is available). Data for hexane and dodecane at this η/T were not measured due to freezing. From Figure 6, the CO rotational relaxation rate begins to rise in ILs that have ~ 5 alkyl carbons. It seems that, under this threshold, the alkyl carbons do not play a role in the solvation of CO. Then, τ_{2R}^{-1} monotonously increases as the number of alkyl carbons increases, as if the CO molecules can count the number of alkyl carbons in the ILs. Apparently, the type of cation (imidazolium or phosphonium) does not matter.

At this point, our data are not what we expect from the segregated picture. If CO molecules are preferentially solvated in the nonpolar domain formed by the alkyl carbons when $\#C_{\text{alkyl}} \geq 5$, we expect that its dynamics would be nearly invariable, whether the nonpolar domain is small (but not too small) or large in volume. What we actually observed is that CO rotates faster as the nonpolar domain becomes larger.

To interpret these results, we paid attention to CO rotational dynamics in alkanes. If nonpolar domains made up of alkyl carbons exist in ILs, the environment should resemble that in liquid alkanes. Thus, we compared the CO rotational relaxation times in hexane (C_6H_{14}), dodecane ($\text{C}_{12}\text{H}_{26}$), and squalane

(C₃₀H₆₂). As seen from Figure 6 (lower trend line), the alkyl chain length in fact influences the CO rotational dynamics (the comparison is made at $\eta/T = 0.00724 \text{ mPa s K}^{-1}$ corresponding to the lowest temperature of hexane). As the number of carbons increases, CO rotates faster in liquid *alkanes*.

In Figure 5, the τ_{2R} values in ILs and alkanes are plotted together. Remarkably, the data points for [P₈₈₈][NTf₂] (#C_{alkyl} = 32) and squalane (#C_{alkyl} = 30) overlap. The plots of [P₄₄₁][NTf₂] (#C_{alkyl} = 13) and dodecane (#C_{alkyl} = 12) are also about to overlap (due to freezing, data for dodecane are missing in the larger η/T region). These results suggest that the solvation environment of CO is very similar in ILs and alkanes if they have a similar number of alkyl carbons. An interesting question follows: Does this similarity hold only between phosphonium cations and alkanes, or does it also hold for imidazolium cations and alkanes? Although we do not have a clear answer to this question, the linear relation in Figure 6 (including [C₈C₁im][NTf₂], [P₄₄₁][NTf₂], and [P₈₈₈][NTf₂]) suggests that the type of cation is unimportant.

In addition to rotational dynamics, ¹⁷O chemical shift (δ) of CO reflects intermolecular interactions in the solvent. The observed δ for the liquids studied was in the range from 351 ([C₂C₁im][NTf₂]) to 355 ppm (squalane); see Table S1. When compared within the same group (i.e., imidazolium ILs, phosphonium ILs, alkanes), the chemical shift showed positive correlation to the number of alkyl carbons. For ILs, this may be interpreted by the charge shielding of the cation center by the alkyl chains. Alkanes tend to have slightly larger δ than ILs that have a similar number of carbons probably because they do not have electro-withdrawing atoms. However, detailed interpretations require rigorous classical and ab initio computations.

The superslip behavior of the rotational dynamics of nonpolar solutes in alkanes has already been reported by several groups.^{49,50} Tiffon and Ancian have studied the rotational dynamics of acetonitrile in *n*-alkanes from #C_{alkyl} = 6 to 16.⁴⁹ According to their results, the plot of the rotational relaxation time against η/T was almost linear and has a common intercept, although the slope decreases with increasing #C_{alkyl}. The slope was smaller than the prediction of the slip boundary condition in SED theory, although GW theory did not explain the experimental results. Similar to the latter work, the deviation from SED theory for the slip boundary condition is more evident in our work with increasing #C_{alkyl}.⁴⁹ However, the rotational relaxation time in alkanes is not a linear function of η/T in our case, and the dependence of the rotational relaxation time on η/T becomes lower at lower values of η/T (high temperature or low viscosity). Further, the rotational relaxation time of CO in different solvents seems to merge to the same value near $\eta/T = 0.001$, and the slope becomes inverted around $\eta/T = 0.001 \text{ mPa s K}^{-1}$ for hexane.

The inversion of the viscosity (or solvent density) dependence of τ_{2R} has been reported for several molecular liquids under supercritical conditions. For example, the τ_{2R} value of water determined by NMR shows inversion of the density dependence in a very low density region.⁵¹ Similar behavior has been reported for the rotational dynamics of CO₂ under supercritical conditions.^{52,53} The τ_{2R} value shows a shallow minimum around the critical density of carbon dioxide.

These phenomena are ascribed to a change in the functional form of the rotational correlation function as demonstrated by MD simulations.⁵⁴ As the rotational dynamics changes from a diffusive motion to free rotational motion, the functional form of the rotational correlation function changes from an

exponential decay to a nonexponential decay, which shows a minimum after the first initial decay and then approaches an asymptotic value. Therefore, the integral of the rotational correlation function increases in the lower density region.

The free-rotor correlation time (τ_{FR}) of CO is given by eq 13^{55,56} assuming rotation with the mean angular velocity, $(kT/I)^{1/2}$,

$$\tau_{FR} \approx (2\pi/9)(I/kT)^{1/2} \quad (13)$$

where I is the moment of inertia. Using the value of the rotational constant for CO (57635 MHz) in the gaseous phase,⁵⁷ τ_{FR} ranges from 0.163 ps (193 K) to 0.112 ps (413 K). These values are close to τ_{2R} in alkanes, suggesting a rotational dynamics approach to nondiffusive, free-rotational motion in alkanes at low viscosity. We consider, therefore, that the inversion of the η/T dependence of τ_{2R} is caused by a change of the rotational relaxation mechanism. Further details should be pursued in the future with the aid of computer simulations.

3.4. Comparison between Rotational Dynamics and Translational Dynamics. Translational and rotational dynamics are linearly correlated under the hydrodynamic model, since dynamics (translational and rotational diffusion coefficients) are dependent on the temperature and solvent viscosity in the form of η/T . Unexpectedly, we noticed a nearly linear relationship between the translational and rotational dynamics of CO in ILs despite the fact that the hydrodynamic model is not strictly obeyed for either dynamics mode.

In a previous paper,³³ we measured the diffusion coefficients of CO (D_{CO}) for the same ILs studied here. A linearity between D_{CO} and η/T was not found for any of these systems. Instead, D_{CO} was well correlated by a fractional power of T/η . D_{CO} in [C₂C₁im][NTf₂] and [C₄C₁im][NTf₂] can be regressed using almost the same function of T/η . These two ILs show similar D_{CO} values when compared with the same T/η value. However, [P₄₄₁][NTf₂] and [P₈₈₈][NTf₂] give significantly larger D_{CO} values than the two imidazolium ILs when compared with a fixed T/η value. This situation is very similar to what we encountered for the rotational dynamics of CO. To make it more clear, we normalized all the τ_{2R} data by an arbitrary chosen reference value, τ_{2R}^0 , which is the τ_{2R} in [C₂C₁im][NTf₂] at 298 K. Similarly, we normalized D_{CO} with respect to the diffusion coefficient (D_{CO}^0) of CO in [C₂C₁im][NTf₂] at 298 K and 0.1 MPa. In this way, we can compare the translation and rotational dynamics in one plot. Figure 7 shows the plot of D_{CO}/D_{CO}^0 and τ_{2R}^0/τ_{2R} versus T/η . Surprisingly good overlap between the translational diffusion and rotational diffusion is obtained for [C₂C₁im][NTf₂] and [C₄C₁im][NTf₂]. Two phosphonium ILs also show fair coincidence, but hexane (295 K) does not. The exceptional behavior found in hexane may be ascribed to its relaxation mechanism, as mentioned in section 3.3. That is, the rotational correlation of CO in hexane at room temperature is approaching free-rotor diffusion. On the other hand, the velocity correlation function, of which the integration gives the translational diffusion coefficient,⁵⁸ still shows a diffusive decay as is usual in other liquids.

Until now, direct comparisons between rotational and translational dynamics have rarely been carried out in ILs. Guo et al. studied the rotational and translational dynamics of rhodamine 6G (R6G) in *N*-butyl-*N*-methylpyrrolidinium bis(trifluoromethanesulfonyl)imide ([P₁₃][NTf₂]).¹⁷ R6G is a relatively large charged molecule, and its rotational relaxation time was found to lie between the slip and stick boundary conditions of SED theory (near stick rotational behavior). The

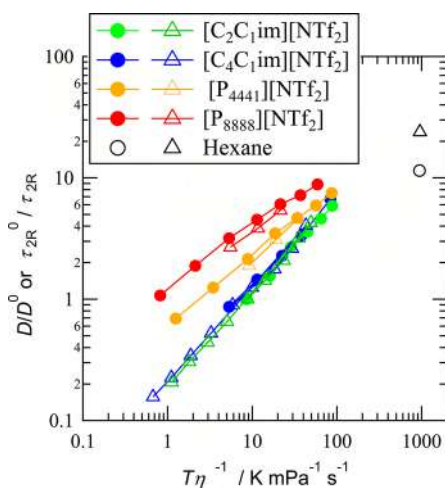


Figure 7. Comparison of the translational diffusion coefficient and the rotational relaxation rate. The ratios to the value in $[C_2C_1im][NTf_2]$ at 298 K are plotted against T/η . Triangles are the ratios of the translational diffusion coefficients, and circles are the ratios of the rotational relaxation rates.

rotational relaxation time obeyed the power law of η/T , and its exponent was 0.66. On the other hand, the translational diffusion coefficients of R6G are linearly dependent on T/η , as predicted by SED theory. The Coulomb interaction between the positively charged R6G and $[NTf_2]^-$ anion was thought to be the reason for the near-stick boundary condition of rotational dynamics.

The present situation is quite different from the case of R6G. As discussed in section 3.3, CO molecules may prefer to stay in the nonpolar region of ILs and rotate within the time scale of solvent reorientation. On the other hand, the time scale of translational diffusion is longer. During the measuring time of the transient grating signal, due to CO diffusion (sub ms), the CO molecules travel over μm -scale distances. Therefore, CO molecules have chances to exist in different solvation states.

Very recently, Araque et al. ran MD simulations to determine the different diffusivities between a small charged molecule and a small nonpolar molecule in 1-butyl-1-methylpyrrolidinium $[NTf_2]^-$.⁵⁹ According to their results, small nonpolar molecules probe both locally “stiff” (mostly charged) regions and locally “soft” (mostly nonpolar) regions. The faster diffusion of the small nonpolar solute molecules is attributed to the contribution of the lower friction of the nonpolar region, although the small nonpolar solute molecules remain in stiff regions for quite a long time. The similarity between the translational and rotational dynamics results obtained here suggests that a similar explanation may hold for the rotational dynamics of CO for shorter alkyl chain ILs. That is, the contribution from the nonpolar region dominates the rotational dynamics of CO, while CO stays in locally stiff and locally soft regions. As the number of alkyl chains increases, the probability of finding CO in locally soft regions is expected to increase, which results in further deviation from the hydrodynamic theory.

4. CONCLUSION

We determined the rotational relaxation time of the CO molecule in ILs and alkanes by measuring the T_1 value from ^{17}O NMR experiments using ^{17}O -labeled CO. The rotational relaxation time of CO is generally much faster than predicted

by the hydrodynamic theory. Viewing the η/T dependence of rotational dynamics, $[C_2C_1im]^+$ and $[C_4C_1im]^+$ resemble Cs^+ , $[P_{4441}]^+$ resembles dodecane, and $[P_{8888}]^+$ resembles squalane. We found a good linear relationship between the rotational relaxation rate and the number of alkyl carbon atoms in cations with more than five carbons, as if CO can count the number of alkyl carbons. The dependence of the rotational relaxation rate on η/T is also found to be quite similar to that of the translational diffusion coefficient. From these results, we conclude that CO molecules are preferentially located in the nonpolar part of ILs, when nonpolar regions exist, in space and in time. A more systematic investigation using ILs with different numbers of alkyl chains will be needed in the future to demonstrate the universality of our results.

■ ASSOCIATED CONTENT

Supporting Information

The Supporting Information is available free of charge on the ACS Publications website at DOI: 10.1021/acs.jpcc.5b09745.

Tables of the concentrations of CO in the liquid and gaseous phases of the prepared samples, T_1 for CO in ILs and alkanes, τ_R for CO in ILs and alkanes, the temperature dependence of the viscosity of $[P_{4441}][NTf_2]$, $[P_{8888}][NTf_2]$, and $\text{Cs}[NTf_2]$, parameters of the viscosity fitting functions, parameters of the fitting functions for τ_{2R} , and a plot of τ_{2R} versus η/T , with fitting lines (PDF)

■ AUTHOR INFORMATION

Corresponding Authors

*E-mail: yyasaka@mail.doshisha.ac.jp. Phone: +81-774-65-6562.

*E-mail: yokimura@mail.doshisha.ac.jp. Phone: +81-774-65-6561. Fax: +81-774-65-6801.

Notes

The authors declare no competing financial interest.

■ ACKNOWLEDGMENTS

We are very grateful to Mr. Masanori Yasuda and Ms. Sanae Kanji (Kyoto Electronics Manufacturing CO. LTD.) for the measurement of viscosity at high temperature using an EMS viscometer. We also thank Mr. S. Hashimoto (Doshisha University) for the synthesis of ^{17}O -enriched sodium formate and Prof. M. Ueno (Doshisha University) for useful discussions. This work was partially supported by the MEXT-Supported Program for the Strategic Research Foundation at Private Universities 2015–2019.

■ REFERENCES

- (1) Wasserscheid, P.; Welton, T. Outlook. In *Ionic Liquids in Synthesis*; Wiley-VCH Verlag GmbH & Co. KGaA: 2008; pp 689–704.
- (2) Nishikawa, K.; Ouchi, Y.; Ito, T.; Ohno, H.; Watanabe, M. *Science of Ionic Liquid*; Maruzen: Tokyo, 2012.
- (3) Xiao, D.; Hines, L. G.; Li, S.; Bartsch, R. A.; Quitevis, E. L.; Russina, O.; Triolo, A. Effect of Cation Symmetry and Alkyl Chain Length on the Structure and Intermolecular Dynamics of 1,3-Dialkylimidazolium Bis(Trifluoromethanesulfonyl)Amide Ionic Liquids. *J. Phys. Chem. B* **2009**, *113*, 6426–33.
- (4) Triolo, A.; Russina, O.; Bleif, H. J.; Di Cola, E. Nanoscale Segregation in Room Temperature Ionic Liquids. *J. Phys. Chem. B* **2007**, *111*, 4641–4.

- (5) Yamamuro, O.; Yamada, T.; Kofu, M.; Nakakoshi, M.; Nagao, M. Hierarchical Structure and Dynamics of an Ionic Liquid 1-Octyl-3-Methylimidazolium Chloride. *J. Chem. Phys.* **2011**, *135*, 054508.
- (6) Kofu, M.; Nagao, M.; Ueki, T.; Kitazawa, Y.; Nakamura, Y.; Sawamura, S.; Watanabe, M.; Yamamuro, O. Heterogeneous Slow Dynamics of Imidazolium-Based Ionic Liquids Studied by Neutron Spin Echo. *J. Phys. Chem. B* **2013**, *117*, 2773–2781.
- (7) Triolo, A.; Russina, O.; Fazio, B.; Appetecchi, G. B.; Carewska, M.; Passerini, S. Nanoscale Organization in Piperidinium-Based Room Temperature Ionic Liquids. *J. Chem. Phys.* **2009**, *130*, 164521.
- (8) Mali, K. S.; Dutt, G. B.; Mukherjee, T. Do Organic Solutes Experience Specific Interactions with Ionic Liquids? *J. Chem. Phys.* **2005**, *123*, 174504.
- (9) Paul, A.; Samanta, A. Solute Rotation and Solvation Dynamics in an Alcohol-Functionalized Room Temperature Ionic Liquid. *J. Phys. Chem. B* **2007**, *111*, 4724–31.
- (10) Ingram, J. A.; Moog, R. S.; Ito, N.; Biswas, R.; Maroncelli, M. Solute Rotation and Solvation Dynamics in a Room-Temperature Ionic Liquid. *J. Phys. Chem. B* **2003**, *107*, 5926–5932.
- (11) Ito, N.; Arzhantsev, S.; Heitz, M.; Maroncelli, M. Solvation Dynamics and Rotation of Coumarin 153 in Alkylphosphonium Ionic Liquids. *J. Phys. Chem. B* **2004**, *108*, 5771–5777.
- (12) Paul, A.; Samanta, A. Effect of Nonpolar Solvents on the Solute Rotation and Solvation Dynamics in an Imidazolium Ionic Liquid. *J. Phys. Chem. B* **2008**, *112*, 947–53.
- (13) Mali, K. S.; Dutt, G. B.; Mukherjee, T. Rotational Diffusion of a Nonpolar and a Dipolar Solute in 1-Butyl-3-Methylimidazolium Hexafluorophosphate and Glycerol: Interplay of Size Effects and Specific Interactions. *J. Chem. Phys.* **2008**, *128*, 054504.
- (14) Dutt, G. B. Influence of Specific Interactions on the Rotational Dynamics of Charged and Neutral Solutes in Ionic Liquids Containing Tris(Pentafluoroethyl)trifluorophosphate (Fap) Anion. *J. Phys. Chem. B* **2010**, *114*, 8971–8977.
- (15) Fruchey, K.; Fayer, M. D. Dynamics in Organic Ionic Liquids in Distinct Regions Using Charged and Uncharged Orientational Relaxation Probes. *J. Phys. Chem. B* **2010**, *114*, 2840–5.
- (16) Sarkar, S.; Pramanik, R.; Ghatak, C.; Setua, P.; Sarkar, N. Probing the Interaction of 1-Ethyl-3-Methylimidazolium Ethyl Sulfate ([Emim][Etso4]) with Alcohols and Water by Solvent and Rotational Relaxation. *J. Phys. Chem. B* **2010**, *114*, 2779–89.
- (17) Guo, J.; Han, K. S.; Mahurin, S. M.; Baker, G. A.; Hillesheim, P. C.; Dai, S.; Hagaman, E. W.; Shaw, R. W. Rotational and Translational Dynamics of Rhodamine 6g in a Pyrrolidinium Ionic Liquid: A Combined Time-Resolved Fluorescence Anisotropy Decay and Nmr Study. *J. Phys. Chem. B* **2012**, *116*, 7883–90.
- (18) Kumar Das, S.; Das, S.; Sarkar, M. Studies on the Solvation Dynamics of Coumarin 153 in 1-Ethyl-3-Methylimidazolium Alkylsulfate Ionic Liquids: Dependence on Alkyl Chain Length. *ChemPhys:Chem* **2012**, *13*, 2761–2768.
- (19) Khara, D. C.; Kumar, J. P.; Mondal, N.; Samanta, A. Effect of the Alkyl Chain Length on the Rotational Dynamics of Nonpolar and Dipolar Solutes in a Series of N-Alkyl-N-Methylmorpholinium Ionic Liquids. *J. Phys. Chem. B* **2013**, *117*, 5156–64.
- (20) Barra, K. M.; Sabatini, R. P.; McAtee, Z. P.; Heitz, M. P. Solvation and Rotation Dynamics in the Trihexyl(Tetradecyl)-Phosphonium Chloride Ionic Liquid/Methanol Cosolvent System. *J. Phys. Chem. B* **2014**, *118*, 12979–92.
- (21) Guo, J.; Mahurin, S. M.; Baker, G. A.; Hillesheim, P. C.; Dai, S.; Shaw, R. W. Influence of Solute Charge and Pyrrolidinium Ionic Liquid Alkyl Chain Length on Probe Rotational Reorientation Dynamics. *J. Phys. Chem. B* **2014**, *118*, 1088–96.
- (22) Kometani, N.; Tai, A. High Pressure Study of Rotational Dynamics of Perylene and Sodium 8-Methoxypyrene-1,3,6-Trisulfonate in Imidazolium-Based Ionic Liquids. *J. Solution Chem.* **2014**, *43*, 1529–1538.
- (23) Prabhu, S. R.; Dutt, G. B. Rotational Dynamics of Imidazolium-Based Ionic Liquids: Do the Nature of the Anion and the Length of the Alkyl Chain Influence the Dynamics? *J. Phys. Chem. B* **2014**, *118*, 13244–51.
- (24) Sahu, P. K.; Das, S. K.; Sarkar, M. Fluorescence Response of a Dipolar Organic Solute in a Dicationic Ionic Liquid (II): Is the Behavior of Dicationic II Different from That of Usual Monocationic II? *Phys. Chem. Chem. Phys.* **2014**, *16*, 12918–12928.
- (25) Sahu, P. K.; Das, S. K.; Sarkar, M. Toward Understanding Solute-Solvent Interaction in Room-Temperature Mono- and Dicationic Ionic Liquids: A Combined Fluorescence Spectroscopy and Mass Spectrometry Analysis. *J. Phys. Chem. B* **2014**, *118*, 1907–15.
- (26) Yasaka, Y.; Wakai, C.; Matubayasi, N.; Nakahara, M. Rotational Dynamics of Water and Benzene Controlled by Anion Field in Ionic Liquids: 1-Butyl-3-Methylimidazolium Chloride and Hexafluorophosphate. *J. Chem. Phys.* **2007**, *127*, 104506.
- (27) Kimura, H.; Yasaka, Y.; Nakahara, M.; Matubayasi, N. Nuclear Magnetic Resonance Study on Rotational Dynamics of Water and Benzene in a Series of Ionic Liquids: Anion and Cation Effects. *J. Chem. Phys.* **2012**, *137*, 194503.
- (28) Yasaka, Y.; Klein, M. L.; Nakahara, M.; Matubayasi, N. Rotational Dynamics of Benzene and Water in an Ionic Liquid Explored Via Molecular Dynamics Simulations and Nmr T1 Measurements. *J. Chem. Phys.* **2012**, *136*, 074508.
- (29) Miyake, Y.; Hidemori, T.; Akai, N.; Kawai, A.; Shibuya, K.; Koguchi, S.; Kitazume, T. Epr Study of Rotational Diffusion in Viscous Ionic Liquids: Analysis by a Fractional Stokes–Einstein–Debye Law. *Chem. Lett.* **2009**, *38*, 124–125.
- (30) Miyake, Y.; Akai, N.; Shibuya, K.; Kawai, A. Solute Size-Dependent Rotational Diffusion of Nitroxide Radicals in Ionic Liquids as Studied by Epr Spectroscopy. *Chem. Lett.* **2013**, *42*, 1429–1431.
- (31) Scuseria, G. E.; Miller, M. D.; Jensen, F.; Geertsen, J. The Dipole Moment of Carbon Monoxide. *J. Chem. Phys.* **1991**, *94*, 6660–6663.
- (32) Reid, R. C.; Prausnitz, J. M.; Poling, B. E. *The Properties of Gases and Liquids*, 4th ed.; McGraw-Hill Book, Co.: Singapore, 1988.
- (33) Kimura, Y.; Kida, Y.; Matsushita, Y.; Yasaka, Y.; Ueno, M.; Takahashi, K. Universality of Viscosity Dependence of Translational Diffusion Coefficients of Carbon Monoxide, Diphenylacetylene, and Diphenylcyclopropanone in Ionic Liquids under Various Conditions. *J. Phys. Chem. B* **2015**, *119*, 8096–103.
- (34) Gerthoff, I. P. Oxygen-17 Nmr Spectroscopy: Basic Principles and Applications. Part II. *Prog. Nucl. Magn. Reson. Spectrosc.* **2010**, *57*, 1–110.
- (35) Frerking, M. A.; Langer, W. D. A Measurement of the Hyperfine Structure of C¹⁷O. *J. Chem. Phys.* **1981**, *74*, 6990–6991.
- (36) Bondi, A. Van Der Waals Volumes and Radii. *J. Phys. Chem.* **1964**, *68*, 441–451.
- (37) Hu, C.-M.; Zwanzig, R. Rotational Friction Coefficients for Spheroids with the Slipping Boundary Condition. *J. Chem. Phys.* **1974**, *60*, 4354–4357.
- (38) Fleming, G. R. *Chemical Applications of Ultrafast Spectroscopy*; Oxford University Press: New York, 1986.
- (39) Perrin, P. R. Mouvement Brownien D'un Ellipsoïde (I). Dipersion Dielectrique Pour Des Molecules Ellipsoidales. *J. Phys. Radium* **1934**, *5*, 497–511.
- (40) Viswanath, D. S.; Ghosh, T. K.; Prasad, D. H. L.; Dutt, N. V. K.; Rani, K. *Viscosity of Liquids*; Springer: The Netherlands, 2007.
- (41) Comuña, M. J. P.; Paredes, X.; Gaciño, F. M.; Fernández, J.; Bazile, J. P.; Boned, C.; Daridon, J. L.; Galliero, G.; Pauly, J.; Harris, K. R.; Assael, M. J.; Mylona, S. K. Reference Correlation of the Viscosity of Squalane from 273 to 373 K at 0.1 MPa. *J. Phys. Chem. Ref. Data* **2013**, *42*, 033101.
- (42) Tokuda, H.; Hayamizu, K.; Ishii, K.; Susan, M. A.; Watanabe, M. Physicochemical Properties and Structures of Room Temperature Ionic Liquids. 2. Variation of Alkyl Chain Length in Imidazolium Cation. *J. Phys. Chem. B* **2005**, *109*, 6103–10.
- (43) Gierer, V. A.; Wirtz, K. Molekulare Theorie Der Mikrorreibung. *Z. Naturforsch., A: Phys. Sci.* **1953**, *8a*, 832–538.
- (44) Kaintz, A.; Baker, G.; Benesi, A.; Maroncelli, M. Solute Diffusion in Ionic Liquids, Nmr Measurements and Comparisons to Conventional Solvents. *J. Phys. Chem. B* **2013**, *117*, 11697–708.

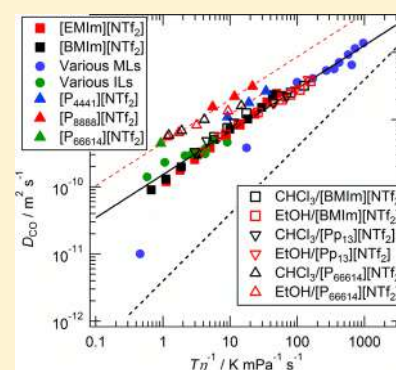
- (45) Kaintz, A.; Baker, G.; Benesi, A.; Maroncelli, M. Correction to "Solute Diffusion in Ionic Liquids, Nmr Measurements and Comparisons to Conventional Solvents. *J. Phys. Chem. B* **2014**, *118*, 5615–5615.
- (46) Wang, Y.; Voth, G. A. Unique spatial heterogeneity in ionic liquids. *J. Am. Chem. Soc.* **2005**, *127*, 12192–12193.
- (47) Canongia Lopes, J. N.; Padua, A. A. Nanostructural organization in ionic liquids. *J. Phys. Chem. B* **2006**, *110*, 3330–3335.
- (48) *Kagaku Binran*; The Chemical Society of Japan, Maruzen: Tokyo, Japan, 2004.
- (49) Tiffon, B.; Ancian, B. ^{14}N nuclear magnetic resonance study of the rotation of acetonitrile in n-alkanes. *J. Chem. Phys.* **1982**, *76*, 1212–1216.
- (50) Jiang, Y.; Blanchard, G. J. Rotational Diffusion Dynamics of Perylene in N-Alkanes. Observation of a Solvent Length-Dependent Change of Boundary Condition. *J. Phys. Chem.* **1994**, *98*, 6436–6440.
- (51) Matubayasi, N.; Nakao, N.; Nakahara, M. Structural Study of Supercritical Water. III. Rotational Dynamics. *J. Chem. Phys.* **2001**, *114*, 4107.
- (52) Holz, M.; Haselmeier, R.; Dyson, A. J.; Huber, H. On the Density Dependence of the Rotational Dynamics of Carbon Dioxide and Its 17o Quadrupole Coupling Constant. *Phys. Chem. Chem. Phys.* **2000**, *2*, 1717–1720.
- (53) Umecky, T.; Kanakubo, M.; Ikushima, Y. Experimental Determination of Reorientational Correlation Time of CO_2 over a Wide Range of Density and Temperature. *J. Phys. Chem. B* **2003**, *107*, 12003–12008.
- (54) Adams, J. E.; Siavosh-Haghighi, A. Rotational Relaxation in Supercritical CO_2 . *J. Phys. Chem. B* **2002**, *106*, 7973–7980.
- (55) Bartoli, F. J.; Litovitz, T. A. Raman Scattering: Orientational Motions in Liquids. *J. Chem. Phys.* **1972**, *56*, 413–425.
- (56) Alms, G. R.; Bauer, D. R.; Brauman, J. I.; Pecora, R. Depolarized Rayleigh Scattering and Orientational Relaxation of Molecules in Solution. I. Benzene, Toluene, and para-xylene. *J. Chem. Phys.* **1973**, *58*, 5570–5578.
- (57) Varberg, T. D.; Evenson, K. M. Accurate Far-Infrared Rotational Frequencies of Carbon Monoxide. *Astrophys. J.* **1992**, *385*, 763–765.
- (58) Hansen, J. P., McDonald, I. R. *Theory of Simple Liquid*, 2nd ed.; Academic Press: London, 1986.
- (59) Araque, J. C.; Yadav, S. K.; Shadeck, M.; Maroncelli, M.; Margulis, C. J. How Is Diffusion of Neutral and Charged Tracers Related to the Structure and Dynamics of a Room-Temperature Ionic Liquid? Large Deviations from Stokes-Einstein Behavior Explained. *J. Phys. Chem. B* **2015**, *119*, 7015–29.

Universality of Viscosity Dependence of Translational Diffusion Coefficients of Carbon Monoxide, Diphenylacetylene, and Diphenylcyclopropenone in Ionic Liquids under Various Conditions

Y. Kimura,^{*,†,‡} Y. Kida,[‡] Y. Matsushita,[§] Y. Yasaka,[†] M. Ueno,[†] and K. Takahashi[§][†]Department of Molecular Chemistry and Biochemistry, Faculty of Science and Engineering and [‡]Department of Applied Chemistry, Graduate School of Science and Engineering, Doshisha University, Kyotanabe 610-0321, Japan[§]Institute of Science and Engineering, Kanazawa University, Kakuma-machi, Kanazawa, 920-1192, Japan

Supporting Information

ABSTRACT: Translational diffusion coefficients of diphenylcyclopropenone (DPCP), diphenylacetylene (DPA), and carbon monoxide (CO) in 1-butyl-3-methylimidazolium bis(trifluoromethanesulfonyl)imide ([BMIm][NTf₂]) and 1-ethyl-3-methylimidazolium bis(trifluoromethanesulfonyl)imide ([EMIm][NTf₂]) were determined by the transient grating (TG) spectroscopy under pressure from 0.1 to 200 MPa at 298 K and from 298 to 373 K under 0.1 MPa. Diffusion coefficients of these molecules at high temperatures in tributylmethylphosphonium bis(trifluoromethanesulfonyl)imide ([P₄₄₄₁][NTf₂]), and tetraoctylphosphonium bis(trifluoromethanesulfonyl)imide ([P₈₈₈₈][NTf₂]), and also in the mixtures of [BMIm][NTf₂], *N*-methyl-*N*-propylpiperidinium bis(trifluoromethanesulfonyl)imide ([P₁₃][NTf₂]), and trihexyltetradecylphosphonium bis(trifluoromethanesulfonyl)imide ([P₆₆₆₁₄][NTf₂]) with ethanol or chloroform have been determined. Diffusion coefficients except in ILs of phosphonium cations were well scaled by the power law of T/η , i.e., $(T/\eta)^P$, where T and η are the absolute temperature and the viscosity, irrespective of the solvent species, pressure and temperature, and the compositions of mixtures. The values of the exponent P were smaller for the smaller size of the molecules. On the other hand, the diffusion coefficients in ILs of phosphonium cations with longer alkyl chains were larger than the values expected from the correlation obtained by other ILs and conventional liquids. The deviation becomes larger with increasing the number of carbon atoms of alkyl-chain of cation, and with decreasing the molecular size of diffusing molecules. The molecular size dependence of the diffusion coefficient was correlated by the ratio of the volume of the solute to that of the solvent as demonstrated by the preceding work (Kaintz et al., *J. Phys. Chem. B* **2013**, *117*, 11697). Diffusion coefficients have been well correlated with the power laws of both T/η and the relative volume of the solute to the solvent.



1. INTRODUCTION

Translational mobility of a molecule dissolved in ionic liquids (ILs) has attracted much attention of a lot of chemists due to its importance for application, and numerous researches have been performed on the mobility of ions and neutral molecules dissolved in ILs by using various kinds of methods such as conductivity, pulse-field gradient (PFG) NMR, transient grating spectroscopy, and so on.^{1,2} Watanabe's group has compared the mobility of ion estimated from the conductivity with the translational diffusion coefficient derived from the PFG-NMR method, and discussed the iconicity of ionic liquids by taking the ratio of them.³⁻⁷ They considered that the ratio represents the correlated motion between cations and anions and that the ionic liquid has high iconicity if the ratio is close to 1. Through these works it has been found that the diffusion coefficients of the solvent ion are almost proportional to the reciprocal viscosity (η^{-1} , η the viscosity of the solvent) as is expected by the Stokes-Einstein (SE) relationship, although the proportional constant is not exactly the same as the molecular radius estimated by the van der Waals volume. For

neutral solute molecules in ionic liquids, several interesting properties have been revealed until now. Diffusion coefficients of small neutral molecules such as gases (oxygen, carbon monoxide, carbon dioxide, and so on) are much larger than expected from the SE predictions by an order of magnitude.⁸⁻¹³ The diffusion coefficients of nonpolar solute molecules are generally not proportional to η^{-1} , but rather expressed by η^P , where P is the constant dependent on the molecular size of the solute. Recently Kaintz et al. reported a detailed collection of the translational diffusion coefficients in various kinds of ILs together with new data measured by PFG-NMR.^{14,15} They evaluated the ratio of the diffusion coefficient determined experimentally to that estimated from the SE relation, and showed a good correlation of the ratio to the relative volume of the solute molecule to that of the solvent ions.

Received: March 26, 2015

Revised: May 10, 2015

Published: June 10, 2015

In this paper, we have investigated the pressure and temperature dependence of the translational diffusion of nonpolar solute molecules (tracer diffusion) in imidazolium-based ionic liquids; 1-butyl-3-methylimidazolium bis(trifluoromethanesulfonyl)imide ([BMIm][NTf₂]) and 1-ethyl-3-methylimidazolium bis(trifluoromethanesulfonyl)imide ([EMIm][NTf₂]) by using the transient grating spectroscopy. One of the authors previously investigated the translational diffusion coefficients of the molecules associated with the photodissociation of diphenylcyclopropanone (DPCP) in various kinds of ILs.¹³ DPCP is photodissociated into carbon monoxide (CO) and diphenylacetylene (DPA) by UV light. By using the transient grating spectroscopy, the diffusion coefficients of these three chemical species were determined simultaneously. Since the molecular size of CO is quite different from those of DPA and DPCP, the reaction system is suitable for the investigation of the molecular size effect on the translational diffusion. It has been reported that the diffusion coefficients of CO were much larger than those predicted by SE relation, and the deviation from the SE prediction became smaller for DPA and DPCP.¹³ In this work, we use a high-pressure optical cell designed for the TG measurement, and report the translational diffusion coefficients of CO, DPA, and DPCP under pressure up to 200 MPa. We have also measured the temperature effect on the diffusion coefficients up to 373 K for the same system under ambient pressure. By the combination of pressure and temperature variations, we can change the value of T/η (T the absolute temperature), which is a key factor affecting the diffusion, by 2 orders of magnitude. There are several reports on the temperature dependence of the diffusion coefficients on neutral molecules in ILs, and it has been reported that the activation energy of the diffusion coefficient is not exactly the same as that of $1/\eta$.¹⁴ However, the pressure effect on the translational diffusion has scarcely been reported,¹⁶ although there are several reports on thermodynamic data such as density and viscosity under pressure.^{17–21} It is an interesting issue how the effects of pressure and temperature will appear in the different sizes of solute molecules.

In parallel with the study on the pressure and the temperature effects in the imidazolium cation-based ionic liquids, we have performed a study on the solvent molecular size effect on the solute diffusion coefficient using phosphonium cation-based ILs with longer alkyl chains and the mixtures of the ILs with conventional liquid solvents. As mentioned, it has been known that molecules in ILs with longer alkyl chains such as trihexyltetradecylphosphonium bis(trifluoromethanesulfonyl)imide ([P₆₆₆₁₄][NTf₂]) diffuse much faster than expected from the SE relationship.^{11,13} The report by Kaintz et al. indicated that the relative volume of the solvent ions to that of the solute is the determining factor.¹⁴ In order to pursue this issue and compare the results with the imidazolium-cation cases, we have measured the DPCP system in two different phosphonium cation-based ILs (tributylmethylphosphonium bis(trifluoromethanesulfonyl)imide ([P₄₄₄₁][NTf₂]) and tetraoctylphosphonium bis(trifluoromethanesulfonyl)imide ([P₈₈₈][NTf₂])), and in the mixture of several ILs with conventional liquid solvents. We chose three ILs of different cations as [BMIm]⁺, *N*-methyl-*N*-propylpiperidinium ([Pp13]⁺), and [P₆₆₆₁₄]⁺. By using the mixture, the relative size of the solvent molecules can be continuously varied. For the better understanding of the size effect of the diffusion coefficient, the effects of temperature and

pressure should be taken into account separately, although we found that the molecular size dependence is well explained by the correlation found in the previous work.¹⁴

2. EXPERIMENTAL SECTION

2.1. Materials. DPCP was purchased from *Nacalai Tesque* or *Aldrich* and used without further purification. Bromocresolpurple (BCP) and methanol were purchased from *Nacalai Tesque* and used without further purification. [P₄₄₄₁][NTf₂] (>99.98%, product of *Nippon Chemical Industrial Co.*), [Pp13][NTf₂] (>98%, product of *Merck*), [P₆₆₆₁₄][NTf₂] (>98%, product of *Cytec*), ethanol (>99.5%), and chloroform (>99.5%) were purchased from *Kanto Kagaku*. For the measurements of the high pressure or the high temperature solutions, specially prepared high purity grade of [EMIm][NTf₂] and [BMIm][NTf₂] (>99.99%), supplied from *Kanto Kagaku* were used for the measurements. For the measurements of the mixture solution, products of *Merck* (>98%) were used. [P₈₈₈][NTf₂] were synthesized as is described in the Supporting Information. The purity of [P₈₈₈][NTf₂] (>99%) was confirmed by NMR. All ILs were transparent at 355 nm (the excitation wavelength of the laser). For the measurements under high pressure or high temperature, ILs were evacuated under 0.4 Pa overnight at about 50 °C. The concentrations of DPCP were typically 30 mM, and the solutions were evacuated for more than 2 h before use. The solution was kept in a drybox under argon atmosphere. The ILs used for the measurements of the mixtures contained somewhat large amount of water (<1%), and the overnight evacuation resulted in typically 350 ppm water contamination. Dehydrated grade of ethanol and chloroform were used for experiments, and the solutions of different molar fraction of ILs and ethanol or chloroform were prepared by measuring the weight. These mixtures were used for the TG measurement and the viscosity measurement.

2.2. Transient Grating Measurement. The experimental setup for the transient grating measurements is described elsewhere.^{13,22} Briefly the third harmonic output from a pulsed Nd:YAG laser (*Continuum Surelite II*, *Continuum Minilight*, or *LOTIS TII LS-2136D*) was used for the excitation pulse. The pulse was divided into two pulses by a beam splitter and simultaneously introduced into the sample cell with a certain angle (θ) which produced the transient grating in the sample. Photodissociation reaction of DPCP occurred in the bright fringe of the optical grating, which produced the population grating of CO, DPA, and DPCP. These population gratings produced the refractive index modulation in the sample solution, which was detected by the diffraction of probe beam (the CW output of a He–Ne laser) introduced into the sample solution with a Bragg diffraction angle. The diffracted light was detected by a photomultiplier, and transferred into an oscilloscope (*Tektronix DPO7104*, *Agilent DSO-X 2014A*, or *Tektronix 2024B*). The decay of the signal, which represents the translational diffusions of the molecules across the grating fringe, was transferred into the PC and analyzed as will be described later.

For the measurement under high pressure, a specially designed high pressure optical cell was used, which was manufactured by *Syn-Corporation*. A schematic illustration of the high pressure cell is given in Figure S1, Supporting Information. The cell has two optical windows made of sapphire, and contains the inner cell between the optical windows. The inner cell is made of quartz, and the optical path length of the inner cell is 2 mm. The inner cell has a cap seal

made of Kalrez tube, and the external pressure is applied to the sample of the inner cell by shrinking the tube due to the hydrostatic pressure applied to the cell. The temperature of the cell is controlled by the thermostated water running through the cell. The hydrostatic pressure is applied to the cell via water by a screw pump (Nova Swiss Type 550.0301.1) connected by 1/16 in. tube. The pressure of the system is measured by a strain gage (Kyowa Electronic Instruments Co PG-2TH). Although the cell is designed for the use up to 400 MPa, all experiments were performed up to 200 MPa due to the limitation of the pressure gage.

For the measurement under high temperature, a quartz cell of 2 mm path length with sample solution was placed in the temperature-controlled cell made of a brass block, which is reported elsewhere.^{23,24} The temperature of the cell was controlled by cartridge heaters immersed into the brass block and a PID regulator. For the measurements of the TG signal in mixture solvents, the solution was kept in a quartz cell of 1 cm path length, and the measurements were performed at room temperature (typically 23 °C).

The experiments were performed as follows. At first, the TG signal of the solution of BCP in methanol or ethanol was measured under the certain crossing angle of the excitation pulses at room temperature. Then the TG signals of the DPCP solution of IL under high pressure or high temperature were measured successively under the same angle of the excitation pulse. We have performed this series of experiments at different angles of the excitation pulses (at least five different angles). The repetition rate of the laser was adjusted from 5 to 0.01 Hz depending on the pressure and/or temperature (i.e., viscosity). If the repetition rate was too fast, the photoproducts were accumulated at the spot of the laser, and the signal-to-noise ratio became worse. Because of this reason, the TG measurements in [P₄₄₄₁][NTf₂] and [P₈₈₈][NTf₂] were limited above 60 °C. Above 100 °C, it was impossible to apply the TG measurement due to the thermal decomposition of DPCP.

The viscosities of [P₄₄₄₁][NTf₂] and [P₈₈₈][NTf₂] at high temperatures, and of the mixtures of ILs with ethanol or chloroform were measured by a viscometer of the cone plate type (Brookfield DVII+ Pro).

3. RESULTS AND DISCUSSION

3.1. Analysis. Typical TG signals of DPCP in [EMIm]-[NTf₂] under different pressures are shown in Figure 1. The time profile of the TG signal under high pressure is similar to those reported for the results under ambient condition.¹³ After

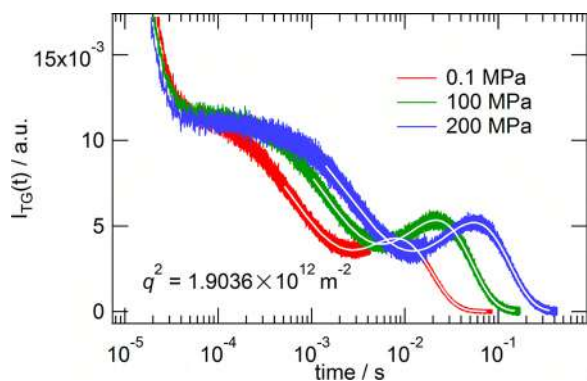


Figure 1. Typical TG signals of DPCP in [EMIm][NTf₂] under different pressures (0.1, 100, 200 MPa) at 298.2 K.

the initial very fast decay of the thermal grating signal, there are three components of the exponentials due to the translational diffusion of CO, DPA and DPCP, respectively. By applying the pressure, the signal decay becomes slow. The time profile of the TG signal due to the molecular diffusions is well simulated by the following equation:¹³

$$I_{\text{TG}}(t) = \{a_{\text{CO}} \exp(-k_{\text{CO}}t) + a_{\text{DPA}} \exp(-k_{\text{DPA}}t) - a_{\text{DPCP}} \exp(-k_{\text{DPCP}}t)\}^2 \quad (1)$$

where

$$k_i = D_i q^2 \quad (2)$$

Here a_i , D_i , and q are the constant depending on the peak-null difference of the refractive index of the molecular species i , the translational diffusion coefficient of molecular species (tracer diffusion coefficient) i , and the grating lattice vector defined by

$$q = \frac{4\pi \sin(\theta/2)}{\lambda_p} \quad (3)$$

where θ and λ_p are the crossing angle and the wavelength of the excitation pulse, respectively. In the signal fitting, we have assumed the ratio $a_{\text{DPCP}}/a_{\text{DPA}}$ is equal to 1.15 as was done in the previous paper.¹³ The simulated curves are shown by the solid lines in the figure, which reproduce the experimental results well.

In order to determine the diffusion coefficient of each species, the TG signals were measured at different crossing angle θ , i.e., different q . Then the decay rate of each component k_i was plotted against q^2 as is shown in Figures 2(a) and (b). The value of q was determined by the decay of the thermal grating signal (k_{th}) obtained for the solution of BCP measured at the same optical geometry, using the relation

$$k_{\text{th}} = D_{\text{th}} q^2 \quad (4)$$

Here D_{th} is the thermal diffusivity given by $\lambda/C_p\rho$ where λ is the thermal conductivity, C_p the isobaric heat capacity, and ρ the density, respectively. The data in the figure are well fit by a straight line passing through the origin, and from the slope of the plot we determined the diffusion coefficient at each experimental condition. The results are summarized in Tables S1 to S10. The results of [BMIm][NTf₂] coincide with the values reported previously within experimental errors.¹³

3.2. Correlation of Diffusion Coefficients with Viscosities. According to the SE relationship, the diffusion coefficients are given by

$$D_i = \frac{k_{\text{B}}T}{C\pi\eta R_i} \quad (5)$$

where R_i is the radius of the molecular species i , k_{B} the Boltzmann constant, and C the constant depending on the boundary condition of the molecular surface (4 for slip and 6 for stick), respectively. Therefore, we have checked the correlation of the diffusion coefficients with T/η of the solvent. The viscosity of the solvent at high temperature was calculated by the empirical equations given in refs 3 and 4. The viscosity under high pressure was calculated by the empirical equations given in refs 17 and 25. In ref 17, the experimental data of the viscosity of [EMIm][NTf₂] are given up to 122 MPa, and in ref 25, the data for [BMIm][NTf₂] are given up to 150 MPa. We simply used the same equations (eq 11 in ref 17 and eq 8 in ref 25) to calculate the viscosity under higher pressure which is not

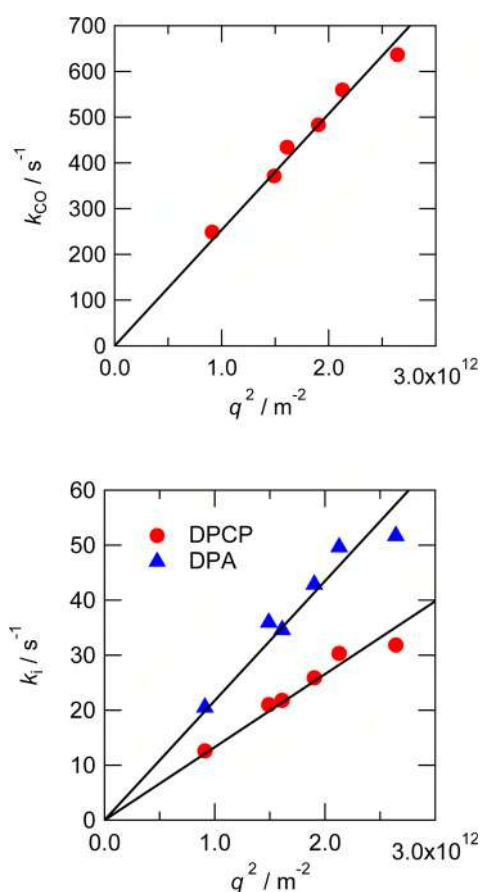


Figure 2. Typical examples of q^2 -plot. [EMIm][NTf₂] at 100 MPa and 298.2 K.

guaranteed by the original papers, since these equations represent the pressure dependence of the viscosity fairly well. Since we could not find the temperature dependence of the viscosity of [P₄₄₄₁][NTf₂] and [P₈₈₈₈][NTf₂], the viscosities at high temperatures were measured by viscometer. The results are given in Tables S11 and S12. The temperature dependence of viscosity was simulated by the following equation

$$\eta = \eta_0 \exp\left(\frac{B}{T - T_0}\right) \quad (6)$$

where η_0 , B , and T_0 are the parameters determined by the fit. The parameters obtained by the fit are listed in Table S13. The viscosity at each temperature was calculated by eq 6. The viscosity of [P₄₄₄₁][NTf₂] at 25 °C was reported to be 207 mPa s,²⁶ which is close to the value calculated by the equation determined here (201 mPa s). The viscosities of the mixture of ILs with conventional liquids were also measured by viscometer, of which the values are listed in Tables S5–S10. In the cases of the mixture solutions, we measured the viscosity of the solution of DPCP dissolved in the mixture, which was used for the TG measurements.

Figures 3–5 show the plot of the diffusion coefficients against T/η . In the plot, both scales are presented in logarithmic. The black broken lines in the figures represent the prediction from the SE relation. In the calculation, we assumed the stick boundary condition ($C = 6$ in eq 5) and used the Stokes radius calculated from the van der Waals volume (CO 1.86 Å, DPA 3.50 Å, and DPCP 3.54 Å).²⁷ Interestingly, pressure and temperature dependences of the diffusion

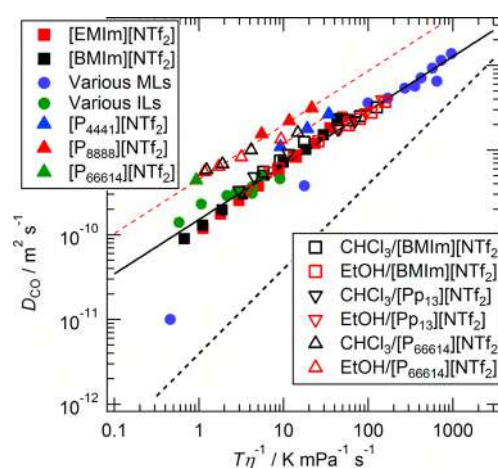


Figure 3. Plot of diffusion coefficients of CO in various liquids against T/η : (red ■) under high pressures and high temperatures in [EMIm][NTf₂]; (■) under high pressures and high temperatures in [BMIm][NTf₂]; (blue ●) in various molecular liquids;¹³ (green ●) in various ILs;¹³ (blue ▲) in [P₄₄₄₁][NTf₂] at high temperatures; (red ▲) in [P₈₈₈₈][NTf₂] at high temperatures; (green ▲) in [P₆₆₆₁₄][NTf₂]; (□) in the mixtures of [BMIm][NTf₂] with chloroform; (red □) in the mixtures of [BMIm][NTf₂] with ethanol; (▽) in the mixtures of [P₁₃][NTf₂] with chloroform; (red ▽) in the mixtures of [P₁₃][NTf₂] with ethanol; (△) in the mixtures of [P₆₆₆₁₄][NTf₂] with chloroform; (red △) in the mixtures of [P₆₆₆₁₄][NTf₂] with ethanol. The black broken line represents the prediction from SE relation. The black solid line represents the fit to eq 7. The two red broken lines are the fits to eq 7 of the data in [P₄₄₄₁][NTf₂] and in [P₈₈₈₈][NTf₂], respectively.

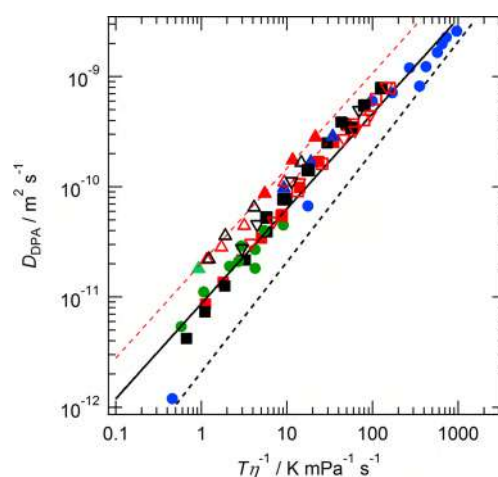


Figure 4. Plot of diffusion coefficients of DPA in various liquids against T/η . The legends of the symbols are the same as those in Figure 3. The black broken line represents the prediction from SE relation. The black solid line represents the fit to eq 7. The red broken lines are the fits to eq 7 of the data in [P₄₄₄₁][NTf₂] and in [P₈₈₈₈][NTf₂], respectively.

coefficients are well scaled by the function of T/η irrespective of the temperature, the pressure, the molecular species, and the compositions of mixtures, with a few exceptions. The exceptions are strongly hydrogen-bonding solvents such as ethylene glycol and glycerol (two blue closed circles at the highest and the second highest viscosities), and ILs with long alkyl chains such as [P₄₄₄₁][NTf₂], [P₈₈₈₈][NTf₂], and [P₆₆₆₁₄][NTf₂] (closed triangles).

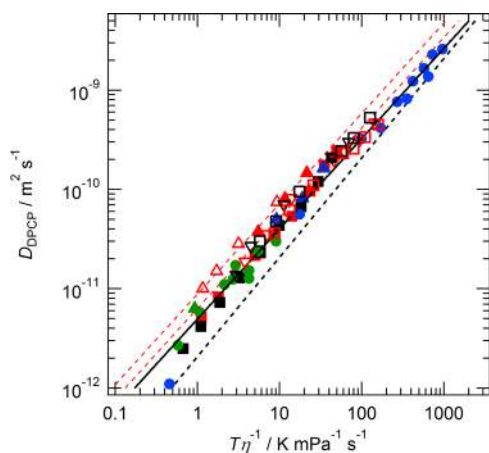


Figure 5. Plot of diffusion coefficients of DPCP in various liquids against T/η . The legends of the symbols are the same as those in Figure 3. The black broken line represents the prediction from SE relation. The black solid line represents the fit to eq 7. The red broken lines are the fits to eq 7 of the data in $[P_{4441}][NTf_2]$ and in $[P_{8888}][NTf_2]$, respectively.

The deviations of the tracer diffusion coefficients from the SE relationship have often been reported, and various empirical equations have been proposed.^{28,29} Among them, fractional power of the reciprocal viscosity has been tested from the very early stage of the study on the diffusion coefficients.³⁰ The applicability of the functional form has been tested recently for various kinds of fluids including ionic liquids, and it has been shown that the fractional power works well except for protic solvents.³¹ In the present case, we have made the correlation of the diffusion coefficients with T/η by the following formula, as was done previously¹³

$$D_i \text{ (m}^2\text{s}^{-1}\text{)} = D_i^0 \left(\frac{T \text{ (K)}}{\eta \text{ (mPa s)}} \right)^P \quad (7)$$

where D_i^0 and P are the constants depending on the molecular species. In the fitting, we omit the data in ethylene glycol, glycerol, $[P_{4441}][NTf_2]$, $[P_{8888}][NTf_2]$, $[P_{66614}][NTf_2]$, and the mixtures of $[P_{66614}][NTf_2]$ with conventional liquids. Best fit curves are given by the solid black lines in the figures. All results lie on a single fitting curve quite well as shown in the figures. The correlation is somewhat worse for DPA in conventional liquids. In conventional liquids such as alkanes, the TG signals due to DPA and DPCP were not well separated and a single exponential decay due to these two species were detected, because the diffusion coefficients of these species are close to each other in nonpolar solvents.^{32,33} This may be the reason for some discrepancy. The optimized values of P are 0.64, 0.86, and 0.91, and those of D^0 are 1.51×10^{-10} , 8.67×10^{-12} , and 4.93×10^{-12} for CO, DPA, and DPCP, respectively. The parameter P decreases with decreasing the molecular size of the solute, indicating that the deviation from the SE relation becomes more evident. This tendency is similar to those reported previously.^{28,34} Evans et al. have shown a very good linear correlation of the exponent P with the solute reciprocal radius in various conventional aprotic solvents.³⁴ The correlation has been tested for the solute diffusion in a wider range of the viscosity of the solvent using supercritical fluids as solvents.³⁵ The value of P for CO (0.64) obtained here is close to the value of CO_2 (0.54) or xenon (0.70) in various liquids and supercritical fluids.

It is quite interesting that a single correlation as eq 7 holds over the wide range of T/η (nearly 3 orders of magnitude), irrespective of the temperature, the pressure, the molecular species, and the compositions of mixtures. Recently various kinds of high pressure phase transition of ILs have been reported above GPa range, and the high pressure phase is reported to be unique only under high pressure, which is different from the phases observed in the temperature variation.^{36–41} High pressure phase changes are generally confirmed more than 0.5 GPa, although higher frequency shifts of the C–H stretching vibrations of cations are evident from ambient pressure to 0.3 GPa in the cases of $[BMIm]^+$ and $[EMIm]^+$.^{38,41} The fact that the pressure and the temperature effects are connected smoothly in this study suggests that a phase transition unlikely occurs by 0.2 GPa. Since the molecules used here are weakly polar (CO and DPCP), and have π -electrons (DPA and DPCP), there may be some specific interaction between solute and solvent. For example, the carbonyl group of DPCP shows a spectroscopic sign of strong hydrogen bondings with the solvent.^{42–44} However, these differences in the solute–solvent interactions do not appear within the logarithmic scale of three orders of difference. The difference of each datum from the correlation line may reflect the individual interaction between the solute and the solvent.

3.3. Correlation of Diffusion Coefficients with Molecular Volumes. Now the question is what is the origin for the deviations of ILs with longer alkyl chains, ethylene glycol and glycerol. Ethylene glycol and glycerol are poly ols and they are strongly hydrogen-bonding solvents. The network of the hydrogen-bonding is considered to be the origin of the higher viscosity of the solvent. The deviation from the correlation predicted by eq 7 in the case of the self-diffusion of alcohols is reported in ref 31. The mechanism of the solute diffusion in these liquids may be different from that in ILs, and we will not discuss these solvents further in this paper. As shown in Figures 3–5, the diffusion coefficients of solute molecules in phosphonium-cation-based ionic liquids are relatively larger than those in other liquids. The deviation is more evident for the smaller solute molecule such as CO. However, the dependence on T/η is quite similar to that obtained for other liquids. The red-broken lines in each figure show the fits to eq 7 of the diffusion coefficients in $[P_{4441}][NTf_2]$ and $[P_{8888}][NTf_2]$, respectively, by fixing the value of P to those determined by other liquids. The fit works well for all solutes studied here. Interestingly, the diffusion coefficients in $[P_{66614}][NTf_2]$ lie on the fitting line for $[P_{8888}][NTf_2]$ for all solutes. The results of the mixture of $[P_{66614}][NTf_2]$ with conventional liquids approach to the line of the general correlation with increasing the composition of the latter.

In order to explain the specialty observed for the smaller solute molecule, Kaintz et al. proposed the relative van der Waals volume of the solute (V_U) to that of the solvent (V_V) as an key factor.¹⁴ They evaluated the ratio of the friction for the translational diffusion (ζ_{obs}) experimentally determined ($\zeta_{obs} = k_B T/D$) to that determined from the SE relation ($\zeta_{SE} = k_B T/D_{SE}$, where D_{SE} is the diffusion coefficient estimated from eq 5 with stick boundary condition) and made the correlation of ζ_{obs}/ζ_{SE} with V_U/V_V by the following equation^{14,15}

$$\zeta_{obs}/\zeta_{SE} = \{1 + a(V_U/V_V)^{-b}\}^{-1} \quad (8)$$

where a and b are parameters determined by the fitting. By using the collections of the diffusion coefficients (distinct 323 solute/solvent pairs), they obtained $a = 1.93$ and $b = 1.88$.

Figure 6 shows the plot of $\zeta_{\text{obs}}/\zeta_{\text{SE}}$ against V_U/V_V for all data presented in Figures 3 to 5. Here the values of V_V for ILs are

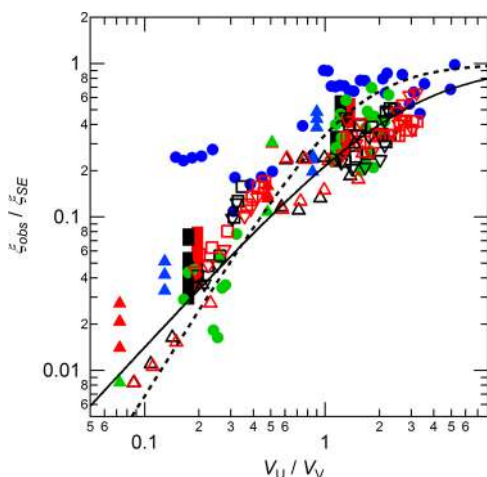


Figure 6. Correlation of the friction ratio with the volume ratio of the solute to the solvent. The legends of the symbols are the same as those in Figure 3. The black broken line represents the prediction from the literature.¹⁴ The black solid line represents the fit to eq 8

the average values of the cation and the anion as in the previous report.¹⁴ For the mixture of an IL with a conventional liquid solvent, the values of V_V are calculated by $(1 - F_x)V_{V(\text{IL})} + F_x V_{V(x)}$, where F_x , $V_{V(x)}$, and $V_{V(\text{IL})}$ are the mole fraction of the conventional liquid (ethanol or chloroform), the van der Waals volume of the conventional liquid and that of the IL, respectively. The van der Waals volumes of the solute are taken from ref 27 (CO 27 Å³, DPA 179 Å³, and DPCP 186 Å³). The black broken line in the figure shows the fitting curve given by the previous work.¹⁴ As shown in the figure, our results almost follow the fitting curve, especially the results for the CO diffusion in the mixed solvent of ILs with conventional liquids (data from 0.07 to 0.5 of V_U/V_V). These results strongly indicate that the relative molecular size of the solvent to the solute is important factor in determining the translational diffusion. The solid line in the figure is the best fit curve of our data to eq 8 ($a = 3.66$ and $b = 1.28$). We also made a plot of the similar correlation considering only the van der Waals volume of the cation in the case of ILs. The plot is shown in Figure S2, where the fitting quality to eq 8 is slightly better ($a = 3.17$ and $b = 1.19$). Therefore, we consider that the existence of the large molecule (cation) in the solution is the key to understand the smaller friction for the smaller molecule.

ILs with longer alkyl chains are said to have a segregated structure according to studies on X-ray scattering and neutron scattering.^{45–49} The contrast of charged-part and nonpolar part of the cation molecule is considered to be the origin of the segregated structure of ILs, although the detail of the structure is still under debate. It has been suggested that the domain structure is related to the heterogeneous solvation of solute molecule dissolved in ILs.^{44,50–52} In relation to the diffusional motion, Patra and Samanta have found that the diffusion coefficient of the solute molecule is affected by the heterogeneity of the solvation by using the fluorescence correlation spectroscopy.⁵³ The general trend of the relative volume dependence of the relative friction shown in Figure 6 indicates that the heterogeneous structure of ILs may not strongly contribute the diffusional motion of the solute

molecule dissolved in ILs, as suggested by Kaintz et al.¹⁴ If the heterogeneous structure of ILs is a dominant factor, the dilution of [P₆₆₆₁₄][NTf₂] with conventional liquid solvents may result in the different correlation with the case of pure ILs. To address this issue further, more detailed investigation using phosphonium or ammonium cation based ILs with different alkyl-chain lengths will be desirable together with the studies of conventional liquid solvents with longer alkyl chains.

Figure 6 indicates that the relative volume is not the only determining factor of the friction. As expected from the good correlation to eq 7, the magnitude of T/η also strongly affects the deviation from the SE prediction. A series of the pressure or the temperature dependence of the same IL cannot be totally explained by the relative volume model. The deviation from the SE prediction is more pronounced for the smaller molecule and for the solvent with smaller value of T/η . In order to take both effects into consideration, we tested the following functional form to simulate all data presented here:

$$D_{\text{calc}} (\text{m}^2 \text{s}^{-1}) = A \left(\frac{T (\text{K})}{\eta (\text{mPa s})} \right)^\alpha \left(\frac{V_U}{V_V} \right)^\beta \quad (9)$$

where A , α , and β are the constants determined by the fitting. The best fit parameters are $A = 1.16 \times 10^{-11}$, $\alpha = 0.95$, and $\beta = -1.17$, respectively. Figure 7 shows the plot of the calculated

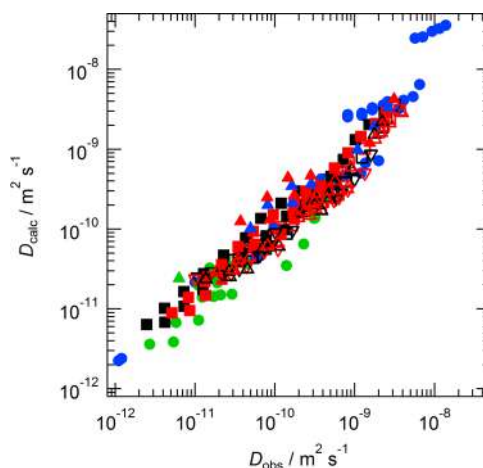


Figure 7. Correlation of calculated diffusion coefficients by eq 9 against observed diffusion coefficients.

values of the diffusion coefficients D_{calc} against the observed values D_{obs} . The model function works fairly well to simulate the diffusion coefficients although the quality of the fitting is somewhat worse than that of the fitting of each solute molecule separately (Figures 3–5). It is to be noted that α is close to 1, indicating that the correction of the relative volume size leads to the better correlation with the hydrodynamic prediction ($\alpha = 1$). On the other hand, the effect of the size of the solute molecule ($\beta = -1.17$) is more enhanced in this model than in the hydrodynamic theory ($\beta = -1/3$).

4. CONCLUSION

Translational diffusion coefficients (tracer diffusion coefficients) of CO, DPA, and DPCP have been determined under various conditions of ILs. It has been revealed that the diffusion coefficients are well scaled by the power law of T/η over nearly 3 orders of magnitude, irrespective of the pressure, temper-

ature, and the compositions of ILs. The exponent of the power law was smaller for the smaller solute, indicating a significant deviation from the SE prediction. It has also been revealed that the diffusion coefficients in ILs with longer alkyl-chains do not obey the same power law, and show much larger values. By taking the relative volume of the solute to that of the solvent into consideration, the different behavior of the solute in ILs with longer alkyl chain is explained as was done previously.¹⁴ The result of the mixture of ILs with conventional liquid solvents suggests that the heterogeneous structure of ILs may not contribute the faster diffusion of the smaller solute in ILs with longer alkyl chains. For the detailed study on the translation diffusion in the domain structure; however, more examples with different alkyl chain lengths and mechanistic study using molecular dynamics simulations will be desirable in the future.

■ ASSOCIATED CONTENT

■ Supporting Information

Synthetic method used for [P₈₈₈][NTf₂], tables of diffusion coefficients in [BMIm][NTf₂] and [EMIm][NTf₂] at different pressures and temperatures, in [P₄₄₁][NTf₂] and [P₈₈₈]-[NTf₂] at different temperatures, in the mixtures of [BMIm]-[NTf₂], [Pp₁₃][NTf₂], and [P₆₆₁₄][NTf₂] with chloroform or ethanol together with the values of the viscosity, tables of viscosity of [P₄₄₁][NTf₂] and [P₈₈₈][NTf₂] at different temperatures, table of the optimized parameters of the temperature dependence of the viscosity of [P₄₄₁][NTf₂] and [P₈₈₈][NTf₂], the schematic illustration of the high pressure optical cell, and correlation of the friction ratio with the volume ratio of the solute to the solvent. The Supporting Information is available free of charge on the ACS Publications website at DOI: 10.1021/acs.jpcc.5b02898.

■ AUTHOR INFORMATION

Corresponding Author

*(Y.Kim.) E-mail: yokimura@mail.doshisha.ac.jp. Telephone: +81-774-65-6561. Fax: +81-774-65-6801.

Notes

The authors declare no competing financial interest.

■ ACKNOWLEDGMENTS

This work was supported by JSPS KAKENHI Grant Number 23350006.

■ REFERENCES

- (1) Wassercheid, P.; Welton, T. *Ionic Liquids in Synthesis*, Second, Completely Revised and Enlarged ed.; Wiley-VCH: Weinheim, Germany, 2008.
- (2) Nishikawa, K.; Ouchi, Y.; Ito, T.; Ohno, H.; Watanabe, M. *Science of Ionic Liquid*; Maruzen: Tokyo, 2012.
- (3) Noda, A.; Hayamizu, K.; Watanabe, M. Pulsed-Gradient Spin-Echo ¹H and ¹⁹F NMR Ionic Diffusion Coefficient, Viscosity, and Ionic Conductivity of Non-Chloroaluminate Room-Temperature Ionic Liquids. *J. Phys. Chem. B* **2001**, *105*, 4603–4610.
- (4) Tokuda, H.; Hayamizu, K.; Ishii, K.; Susan, M. A. B. H.; Watanabe, M. Physicochemical Properties and Structures of Room Temperature Ionic Liquids. 1. Variation of Anionic Species. *J. Phys. Chem. B* **2004**, *108*, 16593–16600.
- (5) Tokuda, H.; Ishii, K.; Susan, M. A.; Tsuzuki, S.; Hayamizu, K.; Watanabe, M. Physicochemical Properties and Structures of Room-Temperature Ionic Liquids. 3. Variation of Cationic Structures. *J. Phys. Chem. B* **2006**, *110*, 2833–9.

- (6) Tokuda, H.; Tsuzuki, S.; Susan, M. A.; Hayamizu, K.; Watanabe, M. How Ionic Are Room-Temperature Ionic Liquids? An Indicator of the Physicochemical Properties. *J. Phys. Chem. B* **2006**, *110*, 19593–600.
- (7) Ueno, K.; Tokuda, H.; Watanabe, M. Ionicity in Ionic Liquids: Correlation with Ionic Structure and Physicochemical Properties. *Phys. Chem. Chem. Phys.* **2010**, *12*, 1649–1658.
- (8) Shiflett, M. B.; Yokozeki, A. Solubilities and Diffusivities of Carbon Dioxide in Ionic Liquids: [Bmim][PF₆] and [Bmim][BF₄]. *Ind. Eng. Chem. Res.* **2005**, *44*, 4453–4464.
- (9) Morgan, D.; Ferguson, L.; Scovazzo, P. Diffusivities of Gases in Room-Temperature Ionic Liquids: Data and Correlations Obtained Using a Lag-Time Technique. *Ind. Eng. Chem. Res.* **2005**, *44*, 4815–4823.
- (10) Camper, D.; Becker, C.; Koval, C.; Noble, R. Diffusion and Solubility Measurements in Room Temperature Ionic Liquids. *Ind. Eng. Chem. Res.* **2006**, *45*, 445–450.
- (11) Ferguson, L.; Scovazzo, P. Solubility, Diffusivity, and Permeability of Gases in Phosphonium-Based Room Temperature Ionic Liquids: Data and Correlations. *Ind. Eng. Chem. Res.* **2007**, *46*, 1369–1374.
- (12) Hou, Y.; Baltus, R. E. Experimental Measurement of the Solubility and Diffusivity of CO₂ in Room-Temperature Ionic Liquids Using a Transient Thin-Liquid-Film Method. *Ind. Eng. Chem. Res.* **2007**, *46*, 8166–8175.
- (13) Nishiyama, Y.; Fukuda, M.; Terazima, M.; Kimura, Y. Study of the Translational Diffusion of the Benzophenone Ketyl Radical in Comparison with Stable Molecules in Room Temperature Ionic Liquids by Transient Grating Spectroscopy. *J. Chem. Phys.* **2008**, *128*, 164514.
- (14) Kaintz, A.; Baker, G.; Benesi, A.; Maroncelli, M. Solute Diffusion in Ionic Liquids, NMR Measurements and Comparisons to Conventional Solvents. *J. Phys. Chem. B* **2013**, *117*, 11697–708.
- (15) Kaintz, A.; Baker, G.; Benesi, A.; Maroncelli, M. Correction to “Solute Diffusion in Ionic Liquids, NMR Measurements and Comparisons to Conventional Solvents. *J. Phys. Chem. B* **2014**, *118*, 5615–5615.
- (16) Kanakubo, M.; Harris, K. R.; Tsuchihashi, N.; Ibuki, K.; Ueno, M. Effect of Pressure on Transport Properties of the Ionic Liquid 1-Butyl-3-Methylimidazolium Hexafluorophosphate. *J. Phys. Chem. B* **2007**, *111*, 2062–9.
- (17) Ahoosini, A.; Scurto, A. Viscosity of Imidazolium-Based Ionic Liquids at Elevated Pressures: Cation and Anion Effects. *Int. J. Thermophys.* **2008**, *29*, 1222–1243.
- (18) Harris, K. R.; Woolf, L. A.; Kanakubo, M. Temperature and Pressure Dependence of the Viscosity of the Ionic Liquid 1-Butyl-3-Methylimidazolium Hexafluorophosphate. *J. Chem. Eng. Data* **2005**, *50*, 1777–1782.
- (19) Tomida, D.; Kenmochi, S.; Tsukada, T.; Qiao, K.; Yokoyama, C. Thermal Conductivities of [Bmim][PF₆], [Hmim][PF₆], and [Omim][PF₆] from 294 to 335 K at Pressures up to 20 mpa. *Int. J. Thermophys.* **2007**, *28*, 1147–1160.
- (20) Tomida, D.; Kumagai, A.; Kenmochi, S.; Qiao, K.; Yokoyama, C. Viscosity of 1-Hexyl-3-Methylimidazolium Hexafluorophosphate and 1-Octyl-3-Methylimidazolium Hexafluorophosphate at High Pressure. *J. Chem. Eng. Data* **2007**, *52*, 577–579.
- (21) Atilhan, M.; Jacquemin, J.; Rooney, D.; Khraisheh, M.; Aparicio, S. Viscous Behavior of Imidazolium-Based Ionic Liquids. *Ind. Eng. Chem. Res.* **2013**, *52*, 16774–16785.
- (22) Demizu, M.; Harada, M.; Saijo, K.; Terazima, M.; Kimura, Y. Transport Properties and Solvation Structure of Mixtures of Carbon Dioxide and Room-Temperature Ionic Liquids. *Bull. Chem. Soc. Jpn.* **2011**, *84*, 70–78.
- (23) Fujisawa, T.; Terazima, M.; Kimura, Y. Solvent Effects on the Local Structure of P-Nitroaniline in Supercritical Water and Supercritical Alcohols. *J. Phys. Chem. A* **2008**, *112*, 5515–26.
- (24) Osawa, K.; Hamamoto, T.; Fujisawa, T.; Terazima, M.; Sato, H.; Kimura, Y. Raman Spectroscopic Study on the Solvation of P-

- Aminobenzonitrile in Supercritical Water and Methanol. *J. Phys. Chem. A* **2009**, *113*, 3143–54.
- (25) Harris, K. R.; Kanakubo, M.; Woolf, L. A. Temperature and Pressure Dependence of the Viscosity of the Ionic Liquids 1-Hexyl-3-Methylimidazolium Hexafluorophosphate and 1-Butyl-3-Methylimidazolium Bis(Trifluoromethylsulfonyl)Imide. *J. Chem. Eng. Data* **2007**, *52*, 1080–1085.
- (26) sunashima, K.; Sugiyama, M. Physical and Electrochemical Properties of Room Temperature Ionic Liquids Based on Quaternary Phosphonium Cations. *Electrochemistry* **2007**, *75*, 734–736.
- (27) Bondi, A. Van Der Waals Volumes and Radii. *J. Phys. Chem.* **1964**, *68*, 441–451.
- (28) Tyrrell, H. J. V.; Harris, K. R. *Diffusion in Liquids*; Butterworth-Heinemann: New York, 1984; pp 322–339.
- (29) Reid, R. C.; Prausnitz, J. M.; Poling, B. E. *The Properties of Gases and Liquids*, 4th ed.; McGraw-Hill Book, Co.: Singapore, 1988; p 577.
- (30) Arnold, H. J. Studies in Diffusion. II. A Kinetic Theory of Diffusion in Liquid Systems. *J. Am. Chem. Soc.* **1930**, *52*, 3937–3955.
- (31) Harris, K. R. The Fractional Stokes-Einstein Equation: Application to Lennard-Jones, Molecular, and Ionic Liquids. *J. Chem. Phys.* **2009**, *131*, 054503.
- (32) Terazima, M.; Hara, T.; Hirota, N. Reaction Volume and Enthalpy Changes in Photochemical Reaction Detected by the Transient Grating Method; Photodissociation of Diphenylcyclopropenone. *Chem. Phys. Lett.* **1995**, *246*, 577–582.
- (33) Hara, T.; Hirota, N.; Terazima, M. New Application of the Transient Grating Method to a Photochemical Reaction: The Enthalpy, Reaction Volume Change, and Partial Molar Volume Measurements. *J. Phys. Chem.* **1996**, *100*, 10194–10200.
- (34) Fennell Evans, D.; Tominaga, T.; Chan, C. Diffusion of Symmetrical and Spherical Solutes in Protic, Aprotic, and Hydrocarbon Solvents. *J. Soln. Chem.* **1979**, *8*, 461–478.
- (35) Funazukuri, T.; Kong, C. Y.; Kagei, S. Predictive Correlation of Binary Diffusion and Self-Diffusion Coefficients under Supercritical and Liquid Conditions. *J. Supercrit. Fluids* **2008**, *46*, 280–284.
- (36) Chang, H.-C.; Jiang, J.-C.; Tsai, W.-C.; Chen, G.-C.; Lin, S. H. Hydrogen Bond Stabilization in 1,3-Dimethylimidazolium Methyl Sulfate and 1-Butyl-3-Methylimidazolium Hexafluorophosphate Probed by High Pressure: The Role of Charge-Enhanced C–H...O Interactions in the Room-Temperature Ionic Liquid. *J. Phys. Chem. B* **2006**, *110*, 3302–3307.
- (37) Su, L.; Li, M.; Zhu, X.; Wang, Z.; Chen, Z.; Li, F.; Zhou, Q.; Hong, S. In Situ Crystallization of Low-Melting Ionic Liquid [Bmim][PF₆] under High Pressure up to 2 GPa. *J. Phys. Chem. B* **2010**, *114*, 5061–5065.
- (38) Chang, H.-C.; Chang, S.-C.; Hung, T.-C.; Jiang, J.-C.; Kuo, J.-L.; Lin, S. H. A High-Pressure Study of the Effects of TiO₂nanoparticles on the Structural Organization of Ionic Liquids. *J. Phys. Chem. C* **2011**, *115*, 23778–23783.
- (39) Su, L.; et al. In Situ Observation of Multiple Phase Transitions in Low-Melting Ionic Liquid [Bmim][BF₄] under High Pressure up to 30 GPa. *J. Phys. Chem. B* **2012**, *116*, 2216–22.
- (40) Yoshimura, Y.; Abe, H.; Imai, Y.; Takekiyo, T.; Hamaya, N. Decompression-Induced Crystal Polymorphism in a Room-Temperature Ionic Liquid, *N,N*-Diethyl-*N*-Methyl-*N*-(2-Methoxyethyl) Ammonium Tetrafluoroborate. *J. Phys. Chem. B* **2013**, *117*, 3264–9.
- (41) Chang, H.-C.; Hung, T.-C.; Wang, H.-S.; Chen, T.-Y. Local Structures of Ionic Liquids in the Presence of Gold under High Pressures. *AIP Adv.* **2013**, *3*, 032147.
- (42) Almeida, L. C. J.; Santos, P. S. The Anomalous Solvent Effect in the Vibrational Spectrum of 2,3-Diphenyl-Cycloprop-2-Enone: An Experimental and Theoretical Investigation. *Spectrochim. Acta, Part A: Mol. Biomol. Spectrosc.* **2002**, *58*, 3139–3148.
- (43) Kimura, Y.; Fukuda, M.; Fujisawa, T.; Terazima, M. Acceptor Number of Room Temperature Ionic Liquid Determined by the Raman Spectrum of Diphenylcyclopropenone. *Chem. Lett.* **2005**, *34*, 338–339.
- (44) Fujisawa, T.; Fukuda, M.; Terazima, M.; Kimura, Y. Raman Spectroscopic Study on Solvation of Diphenylcyclopropenone and Phenol Blue in Room Temperature Ionic Liquids. *J. Phys. Chem. A* **2006**, *110*, 6164–72.
- (45) Xiao, D.; Hines, L. G.; Li, S.; Bartsch, R. A.; Quitevis, E. L.; Russina, O.; Triolo, A. Effect of Cation Symmetry and Alkyl Chain Length on the Structure and Intermolecular Dynamics of 1,3-Dialkylimidazolium Bis(Trifluoromethanesulfonyl)Amide Ionic Liquids. *J. Phys. Chem. B* **2009**, *113*, 6426–33.
- (46) Triolo, A.; Russina, O.; Bleif, H. J.; Di Cola, E. Nanoscale Segregation in Room Temperature Ionic Liquids. *J. Phys. Chem. B* **2007**, *111*, 4641–4.
- (47) Yamamuro, O.; Yamada, T.; Kofu, M.; Nakakoshi, M.; Nagao, M. Hierarchical Structure and Dynamics of an Ionic Liquid 1-Octyl-3-Methylimidazolium Chloride. *J. Chem. Phys.* **2011**, *135*, 054508.
- (48) Kofu, M.; Nagao, M.; Ueki, T.; Kitazawa, Y.; Nakamura, Y.; Sawamura, S.; Watanabe, M.; Yamamuro, O. Heterogeneous Slow Dynamics of Imidazolium-Based Ionic Liquids Studied by Neutron Spin Echo. *J. Phys. Chem. B* **2013**, *117*, 2773–2781.
- (49) Triolo, A.; Russina, O.; Fazio, B.; Appetecchi, G. B.; Carewska, M.; Passerini, S. Nanoscale Organization in Piperidinium-Based Room Temperature Ionic Liquids. *J. Chem. Phys.* **2009**, *130*, 164521.
- (50) Mandal, P. K.; Sarkar, M.; Samanta, A. Excitation-Wavelength-Dependent Fluorescence Behavior of Some Dipolar Molecules in Room-Temperature Ionic Liquids. *J. Phys. Chem. A* **2004**, *108*, 9048–9053.
- (51) Jin, H.; Li, X.; Maroncelli, M. Heterogeneous Solute Dynamics in Room Temperature Ionic Liquids. *J. Phys. Chem. B* **2007**, *111*, 13473–8.
- (52) Kimura, Y.; Hamamoto, T.; Terazima, M. Raman Spectroscopic Study on the Solvation of *N,N*-Dimethyl-*p*-Nitroaniline in Room-Temperature Ionic Liquids. *J. Phys. Chem. A* **2007**, *111*, 7081–9.
- (53) Patra, S.; Samanta, A. Microheterogeneity of Some Imidazolium Ionic Liquids as Revealed by Fluorescence Correlation Spectroscopy and Lifetime Studies. *J. Phys. Chem. B* **2012**, *116*, 12275–12283.



Spectral microscopic imaging of heterocysts and vegetative cells in two filamentous cyanobacteria based on spontaneous Raman scattering and photoluminescence by 976 nm excitation



Kouto Tamamizu, Shigeichi Kumazaki*

Department of Chemistry, Graduate School of Science, Kyoto University, Kyoto 606-8502, Japan

ARTICLE INFO

Keywords:

Heterocystous cyanobacteria
Raman scattering microscopy
Anabaena variabilis
Rivularia
Photosystems
Thylakoid membranes

ABSTRACT

Photosynthetic pigment-protein complexes are highly concentrated in thylakoid membranes of chloroplasts and cyanobacteria that emit strong autofluorescence (mainly 600–800 nm). In Raman scattering microscopy that enables imaging of pigment concentrations of thylakoid membranes, near infrared laser excitation at 1064 nm or visible laser excitation at 488–532 nm has been often employed in order to avoid the autofluorescence. Here we explored a new approach to Raman imaging of thylakoid membranes by using excitation wavelength of 976 nm. Two types of differentiated cells, heterocysts and vegetative cells, in two diazotrophic filamentous cyanobacteria, *Anabaena variabilis*, and *Rivularia* M-261, were characterized. Relative Raman scattering intensities of phycobilisomes of the heterocyst in comparison with the nearest vegetative cells of *Rivularia* remained at a significantly higher level than those of *A. variabilis*. It was also found that the 976 nm excitation induces photoluminescence around 1017–1175 nm from the two cyanobacteria, green alga (*Parachlorella kessleri*) and plant (*Arabidopsis thaliana*). We propose that this photoluminescence can be used as an index of concentration of chlorophyll *a* that has relatively small Raman scattering cross-sections. The *Rivularia* heterocysts that we analyzed were clearly classified into at least two subgroups based on the Chl*a*-associated photoluminescence and carotenoid Raman bands, indicating two physiologically distinct states in the development or aging of the terminal heterocyst.

1. Introduction

The thylakoid membranes (TM) in chloroplasts of plants and algae or in cyanobacterial cells are highly enriched in the pigment-protein complexes containing photosynthetic pigments, majority of which are working for absorbing light and transferring electronic excitation energy to the reaction centers that drives the primary charge separations for the oxygenic photosynthesis [1,2]. Although the conversions from the fluorescent electronic excited states to the stable charge separated states are highly efficient (> 80%), the high concentration of the pigments enables one to study the photochemical events in the TM in live cells by observing autofluorescence from the photosynthetic pigments, especially chlorophyll *a* (Chl*a*) by various fluorescence microscopic techniques [3–7].

In fluorescence microscopy, the signal at a spatial point is generally given by the product of molecular concentration and fluorescence quantum yield. With an image of fluorescence intensity alone, the two quantities are inseparable. Fluorescence lifetime imaging microscopy

(FLIM) can in principle indicate the two quantities separately as images of amplitude and (average) decay time constant of time-dependent fluorescence [3,8–11], but the former is still often distorted by position-dependence and wavelength dependence of reabsorption/scattering/reflection between the focus point of interest and microscope objective. The reabsorption effects are particularly serious for Chl*a* fluorescence because of its small Stokes shift [12,13]. On the other hand, spontaneous Raman scattering signal is proportional to the concentration of molecules [14]. It also suffers from reabsorption effects, but the Raman scattering signal can be tuned to wavelength regions with a high transmission like near infrared region by changing the excitation wavelength. One significant merit of Raman scattering for the imaging of TM is that non- or weakly fluorescent carotenoids are very sensitively detected and differentiated with highly characteristic fingerprints of molecular vibrational spectra [15–21]. Carotenoid molecules in TM play important roles in both light-harvesting and protective energy dissipation under strong light conditions [22–24].

Avoidance of autofluorescence around 600–800 nm region from

* Corresponding author.

E-mail address: kumazaki@kuchem.kyoto-u.ac.jp (S. Kumazaki).

<https://doi.org/10.1016/j.bbatio.2018.11.012>

Received 4 June 2018; Received in revised form 30 October 2018; Accepted 7 November 2018

Available online 08 November 2018

0005-2728/ © 2018 Elsevier B.V. All rights reserved.

TMs can be commonly achieved by shorter or longer excitation wavelengths. The relatively short wavelength excitation should be favorable for resonance enhancements of the Raman scattering and resultant selectivities of target molecules [14,17]. One drawback of the resonance effects is excessive excitation that may result in disturbance of visible-light-induced physiological phenomena and/or damages in viability of cells [25,26]. Optical absorption of Chla-based TM, especially by the absorption of photosystem I (PSI), seem to be extended up to at least 740 nm [27]. Recent studies have shown that excitations of PSI and photosystem II (PSII), both of which are the most essential Chla-containing pigment-protein complexes in TM for the oxygenic photosynthesis, seem to be possible at least up to 840 and 820 nm, respectively [28–32]. Some previous works using spontaneous Raman scattering microscopy have reported bleaching effects of chloroplasts and cyanobacteria by 785 nm laser [33,34]. Plants, algae and cyanobacteria or their symbiotic forms in lichens have been, thus, often studied by 1064 nm laser excitation, by which autofluorescence is minimized [33,35–37]. Relatively high transmission and low scattering of the near infrared light through plant tissues full of photosynthetic pigments should be advantageous for imaging of deep tissues [38].

In this study, we have aimed at extending the range of possible excitation wavelengths for Raman (micro)spectroscopy by choosing a near-infrared (NIR) excitation at 976 nm. Excitation at 976 nm has several advantages over the one at 1064 nm. First, non-resonant Raman scattering cross-sections with excitation wavelength at 976 nm is about 40–50% greater than those at 1064 nm by the high frequency effects for the Stokes Raman scattering between 1000 and 2000 cm^{-1} [39]. Second, typical array detector or camera for the wavelength range of 0.9–1.6 μm is InGaAs sensors [40], with which Raman bands of higher vibrational frequencies can be obtained by 976 nm than by 1064 nm, especially when the quantum yield of the detector at the long-wavelength edge drops by cooling of the detector. One possible drawback of the 976 nm excitation is relatively high absorption by water in comparison with 1064 nm [41]. However, use of 976 nm beam certainly provides an additional degree of freedom in the design of microscope optics. For example, two beams of 976 and 1064 nm may be simultaneously used for different purposes like optical trapping of cells [42], inducing genes in cells by local heating [43], as well as Raman scatterings.

When some filamentous cyanobacteria sense a shortage of fixed nitrogen, approximately 1 in 10 to 20 vegetative cells differentiates into a heterocyst, in which oxygenic photosynthesis is suppressed through (at least partial) degradation of oxygen-evolving PSII while nitrogenase, nitrogen-fixing enzyme sensitive to oxygen, becomes operative [44–47]. On the other hand, the other cells, vegetative cells, continue oxygenic photosynthesis. The TMs in vegetative cells thus contain both PSI and PSII, while those in heterocysts contain predominantly PSI. The PSI in the heterocysts produce ATP by cyclic electron transport, because nitrogen fixation demands a large amount of ATP [31,45]. These drastic differences between heterocysts and vegetative cells have been frequently studied by fluorescence microscopy [4,31,48–51]. To the best of our knowledge, however, investigations on heterocyst-forming cyanobacteria by Raman scattering spectral microscopy have been relatively limited [52,53]. Here, we have successfully estimated the differences in amounts and/or concentrations of photosynthetic pigments between heterocysts and nearest vegetative cells in two genetically and morphologically distinct cyanobacteria, *Anabaena variabilis* and *Rivularia M-261* [54]. It was unexpectedly found that 976 nm laser light actually induces a significant luminescence attributable to Chla not only from the cyanobacterial cells but also from chloroplasts in a green alga and plant. Correlations between the Chla-associated photoluminescence and Raman bands of carotenoids or phycobilins helped us understand the differences in pigment compositions between the two cyanobacteria and multiple physiological phases of *Rivularia* heterocysts.

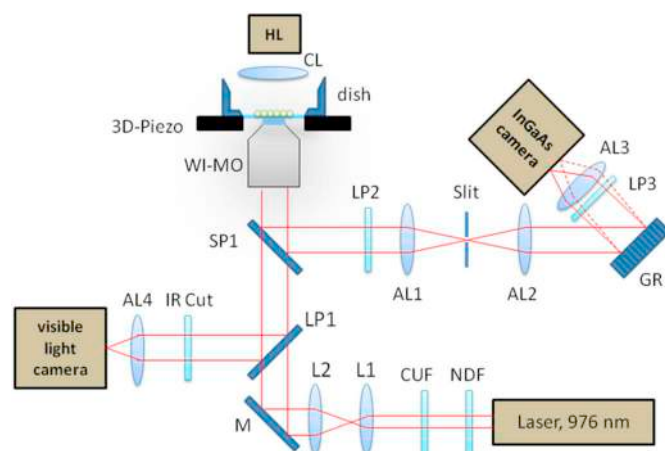


Fig. 1. Schematic diagram of the Raman microspectrometer. WI-MO: water-immersion microscope objective, AL1–AL3: achromatic lenses for the near infrared light, AL4: achromatic lens for the visible light, LP1: long-pass mirror with an edge wavelength of 900 nm, LP2 and LP3: long-pass filters with an edge wavelength at 980 nm, SP1: short-pass mirror with an edge wavelength of 1000 nm, M: mirror, GR: grating, CUF: narrow band transmission filter (laser clean up filter), NDF: neutral density filter, IR Cut: IR-absorbing filter, HL: halogen lamp, CL: condenser lens, L1 and L2: pair of lenses for a telescope, 3D-piezo: piezo actuator stage to move the sample positions, dish: glass-bottomed dish.

2. Experimental

2.1. Raman microspectroscopy based on 976 nm excitation

A schematic diagram of our deep NIR multichannel Raman microspectrometer is shown in Fig. 1. When samples were illuminated by a halogen lamp, the transmitted light through the short-pass dichroic mirror (SP1, edge wavelength (λ_{edge}) \approx 1000 nm) was focused on a color CMOS camera (SILICON VIDEO 9M001, EPIX, Illinois, USA) after reflection by a long-pass dichroic mirror (LP1, $\lambda_{\text{edge}} \approx$ 900 nm) for a bright-field imaging in the visible region. A narrow-band diode laser (center wavelength of 976 nm, frequency band width $<$ 1 MHz, I0976SA0200B-THTK, Innovative photonics solutions) was used as the excitation source for the Raman scattering. The 976 nm laser beam, after transmission through a spectral clean-up (CUF) and neutral density filters (NDF), was first magnified by a telescope and focused onto a sample with a water-immersion microscope objective lens with a magnification of $\times 60$ and numerical aperture of 1.27 (Nikon, CFI PlanApo IR60XWI). Raman scattering signals were collected by the same objective lens. The short-pass mirror (SP1) reflected the signals toward a home-made achromatic-lens-based imaging polychromator with a focal length of 250 mm and 1:1 magnification. The entrance slit of the polychromator was set to be 0.12 mm width. The blaze wavelength of the grating was 1000 nm or 1200 nm and the number of grooves was 300/mm (Thorlabs GR50-0310 or Photon Design, Tokyo, Japan). An electrically cooled InGaAs camera (-80°C , 640×512 pixels, pixel size = $20 \times 20 \mu\text{m}$, DMDIR-640, Photon Design, Tokyo) was fixed at the exit port of the polychromator. Residual laser light was rejected by two long-pass filters (LP2 and LP3, $\lambda_{\text{edge}} \approx$ 980 nm) that were located outside and inside the polychromator. The laser power at the sample position was most typically 10–14 mW unless otherwise specified. In the imaging measurement, the sample was horizontally and/or vertically translated by a piezoelectric stage (PK3L150-100UA, Nanocontrol, Tokyo) with a typical step of 0.4 μm and 1.0 μm , respectively. At each spatial point, one Raman scattering spectrum was obtained with an exposure time of 2.0 s.

2.2. Cyanobacterial cells, unicellular green alga and plant leaf

A filamentous cyanobacterium, *Anabaena variabilis* (*A. variabilis* strain NIES-2095), was purchased from the microbial culture collection at the National Institute of Environmental Studies in Tsukuba, Japan. The filamentous cells were grown photoautotrophically under fixed-nitrogen-depleted conditions in a nitrogen-free BG-11 liquid medium [55] for 5 to 76 days at 29 °C with a 15-h-light/9-h-dark photoperiod. The medium was prepared by removing NaNO₃ and replacing ferric ammonium citrate with ferric citrate in the BG-11 formulation. The flux density of photosynthetic photon at the sample position in the incubator was about 20 μmol photons m⁻² s⁻¹.

Rivularia sp. IAM M-261 was obtained from the culture collection of Institute of Molecular and Cellular Biosciences, the University of Tokyo (IAM Collection), which has been transferred to Microbial Culture Collection at the National Institute for Environmental Studies (NIES Collection Tsukuba, Ibaraki, Japan). *Rivularia* filaments were grown on agar media based on the nitrogen-free BG-11 at about 20 μmol photons m⁻² s⁻¹ without any dark period for 9 to 23 days. Both *A. variabilis* and *Rivularia* cells were precultured in the fixed-nitrogen-free BG11 media for longer than 14 days and inoculated to fixed-nitrogen-free BG11 media that were maintained for the above-mentioned durations until the microscopic observations.

Unicellular green alga, *Parachlorella kessleri* (*P. kessleri*), was purchased from the IAM culture collection as IAM C-531 (now maintained as NIES-2160). The cells were grown photoautotrophically in 40 cm³ of BG-11 liquid medium (including fixed nitrogen) in the same incubator as *A. variabilis*. The preparation for the microscopic observation was also the same as used for *A. variabilis* cells. *Arabidopsis thaliana* plants were grown in soil in chambers at 21–23 °C under a 12-h-light/12-h-dark photoperiod using fluorescent lamps (about 100 μmol m⁻² s⁻¹).

For the Raman microscopic imaging of *A. variabilis* and chloroplasts of green alga (*P. kessleri*), the cell suspensions were transferred to glass-bottomed dishes (Matsunami, D111505). The upper surface of the glass was coated with poly-L-Lysine to immobilize the cells before addition of the cell suspensions. About 10 min after the cell suspension was added, a block of solidified growth-medium-based agarose was put on the adsorbed cells to fix the cells better. In the case of *Rivularia*, a piece of agar block was transferred from the agar plates to the cover-glass-bottomed dishes for observing cells on the agar surface.

For microscopic imaging of *A. thaliana* chloroplasts, one green leaf was sandwiched by a cover glass (No.1, Matsunami) and optical window with a thickness of 1.0 mm. A home-made aluminum sample holder was used to fix the leaf and two glass plates with a help of Teflon spacers. The internal space of the sample holder was filled with tap water. Microscopic observations of chloroplasts in mesophyll cells of *A. thaliana* leaf were conducted from the adaxial surface.

2.3. Reference pigments and pigment-protein complex

Raman scattering spectra of representative photosynthetic pigments and pigment-protein complexes were obtained by using powders of β-carotene (Nacalai tesque, 07312-81), C-phycocyanin (from *Spirulina*, Sigma-Aldrich, P2172), and Chla (Wako Pure Chemical Industries, 034-21361). These were used as received by placing them between cover and slide glass plates, in the same sample holder as used for the *A. thaliana* leaf.

3. Results

3.1. Raman scattering spectral imaging of *Anabaena variabilis* cells

The bright field image of some filaments of *A. variabilis* grown in the fixed-nitrogen-depleted medium typically showed a terminal heterocyst that was located at the end of the filament (designated as het in Fig. 2A or S1B). The heterocyst was connected to vegetative cells (in the order

of het, veg1, veg2, veg3, as in Fig. 2A). The heterocyst was characterized by a higher optical transmission than the vegetative cells, because of a decrease in the amount of photosynthetic pigments, especially phycobilisome [31,49,54,56]. The total intensity of the Raman scatterings and/or photoluminescence signals integrated over all detected wavelength range (1017–1175 nm) was calculated in each pixel and shown as a monochromatic image (Fig. 2B). It should be noted that the heterocyst and vegetative cells were comparable in the brightness of the total Raman scattering and photoluminescence signals. This is in contrast to conventional fluorescence images of heterocysts and neighboring vegetative cells of filamentous cyanobacteria (including *A. variabilis*), in which fluorescence of heterocyst is far weaker than that of vegetative cells [10,31,49,54].

Raman scattering signals of individual single cells were extracted semiautomatically in an analogous way that was previously described for fluorescence spectral microscopy (Fig. 2C) [54]. The average Raman spectra of heterocysts and vegetative cells that were obtained from 31 *A. variabilis* filaments, each containing one heterocyst (only one filament contained intercalary heterocyst, see Fig. S1), are shown in Fig. 3. The Raman band assignments were mainly based on the Raman spectra of the powders of β-carotene, C-phycocyanin (phycobilin-protein complex) and Chla (Fig. 4A–D) obtained with the same setup, which seemed to be consistent with several references (Table S1) [33,57–59]. The phycobilin bands that were clearly visible in vegetative cells were almost totally absent in the heterocysts (Figs. 2F and 3). The carotenoid bands were slightly decreased in the heterocysts in comparison with the vegetative cells (Figs. 2E and 3). The Raman scattering spectra of both the heterocysts and vegetative cells were superimposed on a broad photoluminescence spectrum (Fig. 3). The spectral features of het, veg1 and veg2 were thus consistent with the selective images of individual Raman bands and photoluminescence (Fig. 2D–F). Although at least three Raman bands were ascribed to Chla in the average spectra of the 31 cells (Fig. 3), the signal-to-noise ratios of the single Raman bands were insufficient to produce Chla selective image with a reasonable contrast.

3.2. Raman scattering spectral imaging of *Rivularia* cells

Analogous analysis was also performed on Raman/photoluminescence spectra of 34 *Rivularia* filaments. Only major differences between *A. variabilis* and *Rivularia* are described here. In terms of relative signals of the heterocysts in comparison with the nearby vegetative cells, photoluminescence signals in *Rivularia* heterocysts were on average weaker than those of *A. variabilis* (Tables 1, 2, Figs. 2D, J, 3, S2). Phycobilin Raman signals in *Rivularia* heterocysts were stronger than those of *A. variabilis* (Tables 1, 2, Figs. 2F, L, 3, S2). The latter feature is consistent with our previous study with microscopic absorption spectroscopy showing that there remains a substantial amount of phycocyanin in the *Rivularia* heterocysts, while mature heterocysts of *A. variabilis* are virtually free from phycobilisomes [54].

3.3. Photoluminescence of the cyanobacterial cells excited by 976 nm is attributable to chlorophyll a

The Raman spectrum of β-carotene was virtually free from any broad luminescence component (Fig. 4A). C-phycocyanin is a subunit of phycobilisome that works as extra light-harvesting antenna mainly for PSII but also for PSI [60,61]. Although C-phycocyanin containing phycobilins as light-harvesting chromophores showed some broad photoluminescence superimposed on the narrow banded Raman signals, the intensity ratio of luminescence to Raman of C-phycocyanin seemed to be far lower than that of Chla (Fig. 4B, C). Moreover, phycobilin contribution to the photoluminescence of the *A. variabilis* cell can be estimated as follows. After magnification of the heterocyst spectrum by 1.59 in Fig. 3, the normalized spectrum becomes very similar to that of veg1, except in the wavelength regions in which

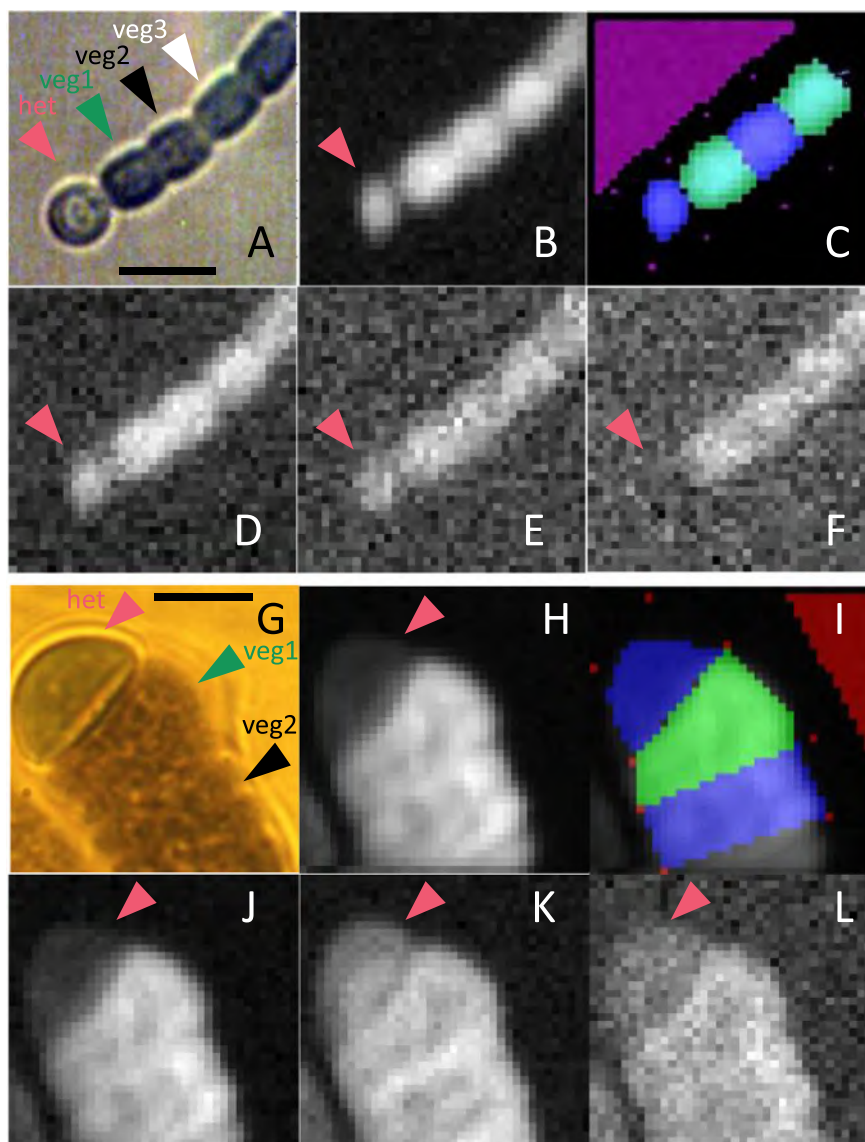


Fig. 2. Typical microscopic images of a filament of *A. variabilis* (A–F) and *Rivularia* cells (G–L). (A, G) Bright field image of a filament with a heterocyst at the terminus. The colors of these images are artificial due to applications of auto-contrast and auto-level functions of a software (XnView) and yellowish illumination of the halogen lamp, while the darkness of the pixels reflects absorption, reflection, and scattering at some visible wavelengths of the cells. The magenta arrow head indicates a heterocyst, and the vegetative cells marked by the three arrow heads of green, black and white are designated veg1, veg2 and veg3, respectively. Scale bar = 5 μm in both (A) and (G), which is also applicable to the other panels. (B, H) Image of the total intensity of Raman scattering and photoluminescence signals integrated over all the detected wavelength range. (C, I) Map of selected areas of individual cells for spectral analysis. Blue and green regions alternately show selected regions of individual cells. The triangular area in purple (in C) or red (in I) shows a cell-free background region. Four magenta points surrounding individual cells were given by visual inspections, and they worked as reference points to locate cell junctions. (D, J) Image of the photoluminescence detected in the Raman shift range between 1707 and 1736 cm^{-1} (between 1171 and 1175 nm in wavelength). (E, K) Image of a carotenoid Raman band between 1513 and 1528 cm^{-1} . (F, L) Image of a phycobilin Raman band between 1618 and 1633 cm^{-1} . For both (E, F) and (K, L), photoluminescence signals were subtracted (see Fig. S3).

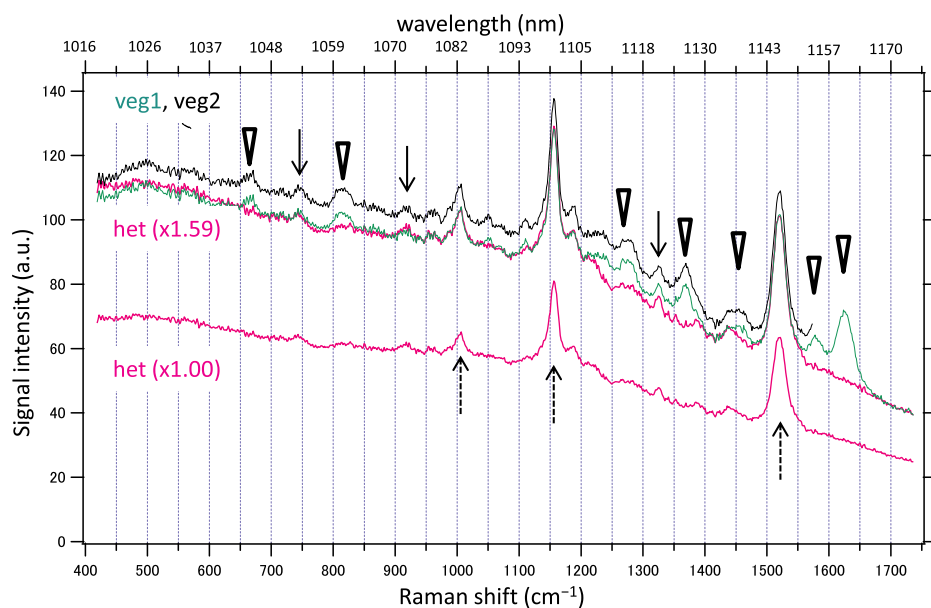
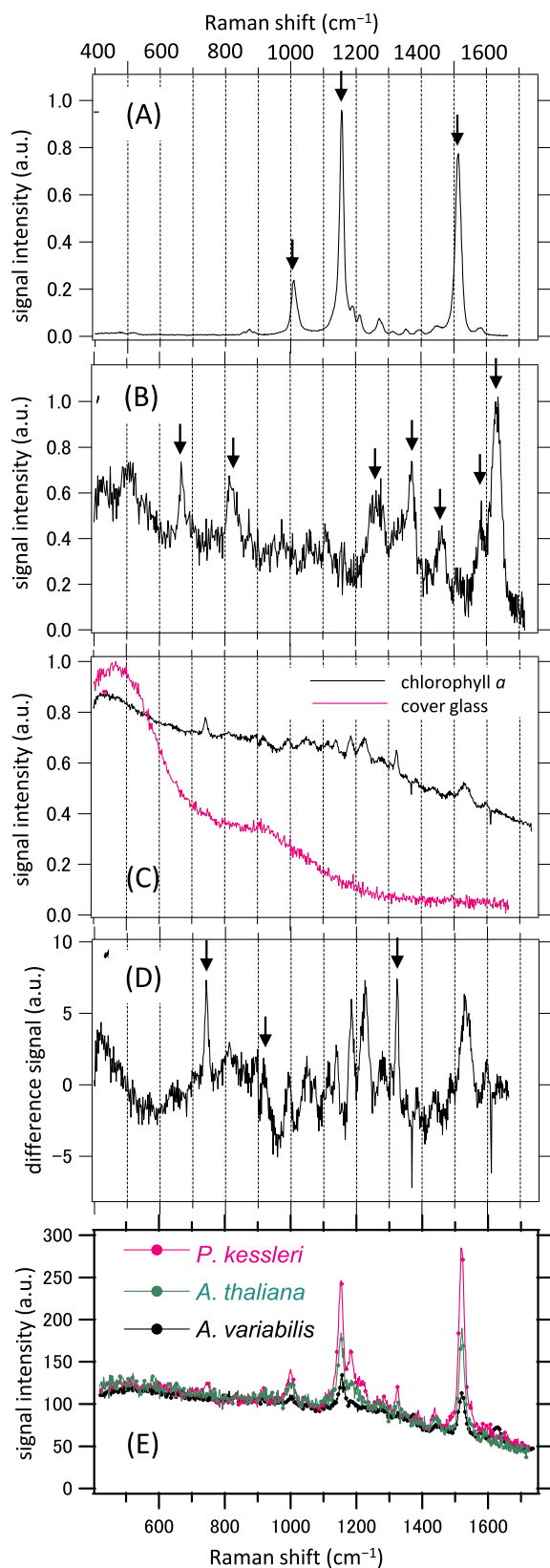


Fig. 3. Cell-type specific average single-cell spectra of *A. variabilis* cells in which Raman scattering and photoluminescence signals are present. The intensities of the spectra are based on the “whole-cell-integrated intensities” in the Tables 1 and S2, which are functions of cell sizes. The two plots in magenta represent average spectra of heterocysts, among which one spectrum (het ($\times 1.59$)) is magnified by 1.59 times from the other spectrum (het ($\times 1.00$)) preserving the original intensities. The plot in green (veg1) represents the vegetative cell that is directly adjacent to the heterocysts. The plot in black (veg2) indicates the vegetative cell that is directly adjacent to veg1 but not to heterocyst (see Fig. 2A). Upward arrows with broken lines, downward arrows with solid lines and downward triangular arrow heads indicate Raman bands attributable to carotenoids, Chla and phycobilin molecules, respectively. See Table 1 for cell-by-cell variations of signal intensities.



C-phycoerythrin Raman bands are prominent (cf. Fig. 4B). Given the nearly total disappearance of phycobilins Raman bands in the transition from the vegetative cells to the heterocysts, this situation indicates that photoluminescence of phycobilisome does not contribute to the

Fig. 4. Raman scattering and photoluminescence spectra of powders of photosynthetic pigments, cover glass, cyanobacterial cells and chloroplasts of green alga and plant that were obtained with excitation at 976 nm. (A) β -Carotene, (B) C-phycoerythrin, (C) Chla and cover glass. In (D), the same spectrum of Chla in (C) is shown after a broad photoluminescence spectrum was subtracted. The luminescence spectrum contained in the Chla spectrum in (C) was approximated by a seventh-degree univariate polynomial fitted to the whole Chla spectrum in (C). The Raman bands marked by arrows in (A), (B) and (D) indicate those that are marked by the arrows or arrow heads in the cell-type specific spectra in Fig. 3. (E) Comparison of the average Raman and photoluminescence spectra of *Parachlorella kessleri* cells (two cells) in magenta, two chloroplasts inside a mesophyll cell in a leaf of *Arabidopsis thaliana* in green and vegetative cells in five filaments of *A. variabilis* in black. The three spectra were arbitrarily magnified so that the broad photoluminescence components overlap with each other.

observed broad photoluminescence of the *A. variabilis* cells. Overall, the whole situation is best represented by the idea that photoluminescence in both the vegetative cells and heterocysts of *A. variabilis* is exclusively attributable to Chla.

It should be here noted that some photoluminescence was also observed when the 976 nm laser focus was near the cover glass (plot in magenta, Fig. 4C) [62,63], which probably indicates impurities, defects, and/or doped elements in the glass [64]. The spectral shape of the cover glass luminescence was clearly different from those of Chla and cyanobacterial cells (Figs. 3, 4C). Its contribution to the Raman scattering/photoluminescence spectra of the reference chemicals and cells was always subtracted before analysis (see caption of Fig. S3).

3.4. Single cell amount and average intracellular concentration of photosynthetic pigments in the neighboring cells

The intensities of the Raman bands of β -carotene and phycobilins as well as the photoluminescence attributable to Chla were estimated from the Raman spectra of single cells or single pixels in the way described in the caption of Fig. S3. The axial spatial resolution of our Raman microscopy setup was well approximated by a Gaussian function with a full width at half maximum of 3.7 μm (Fig. S4), which was comparable to the thickness of the *A. variabilis* cells ($\approx 2\text{--}4 \mu\text{m}$, Figs. 2A–F and S1). It is thus concluded that the Raman signal intensity of an *A. variabilis* image per single pixel (corresponding to I_{sig} in Table 1) is largely proportional to the integrated amount of pigments along the depth axis (z axis, which is perpendicular to the plane of the images in Fig. 2A–F). The integration of the signals in the whole two-dimensional area (S_{cell}) of an *A. variabilis* cell (as in the case of the spectra in Fig. 3 and corresponding to $I_{\text{sig}} \times S_{\text{cell}}$ in Table 1), thus, reflects the whole single-cell amount of the pigments. Average concentration of a pigment inside the *A. variabilis* cell is approximately proportional to the average signal intensity per single pixel divided by the thickness of the cell (corresponding to $I_{\text{sig}} \times (S_{\text{cell}})^{-1/2}$ in Table 1), as far as we neglect the heterogeneous distribution of TM in the *A. variabilis* cell. The above-mentioned three quantities reflecting integrated amounts or concentrations of photosynthetic pigments in the specified cell types (heterocyst and veg1, see Fig. 2A) are summarized in Table 1, after they were normalized by the corresponding quantities in veg2 (see Fig. 2A and Table S2 for veg3).

Among the three connected cells designated as het, veg1, veg2, and veg3 (Fig. 2A), the *A. variabilis* heterocyst showed the least amount of photosynthetic pigments (Tables 1 and S2). Relative amount of phycobilins in heterocyst on average was only 6% of veg2 cell. Because of the signal-to-noise ratio and unavoidable arbitrariness in the subtraction of photoluminescence background, we regard this 6% as an upper limit of the phycobilin amount on average (Fig. S3). The nearly complete disappearance of phycobilin was in good agreement with our own previous study on *A. variabilis*, in which heterocysts and its neighboring vegetative cells were analyzed by microscopic absorption spectroscopy

Table 1

Ratio of Raman band and luminescence intensities of specified cell types to the corresponding values of veg2 (vegetative cell) in the same *A. variabilis* filament, for which at least three consecutive cells, one heterocyst and two vegetative cells (het, veg1, and veg2) were imaged by our spectro-microscope (e.g., Fig. 2A). Number of analyzed filaments was 31 including the 21 filaments analyzed in the Supplemental Table S2. See the captions of Figs. 2 and S3 for the selected Raman shift or wavelength regions. According to paired *t*-tests with the corresponding values of the veg2 cell in the same filament, statistical significance is indicated by the following symbols. *: $p < 0.05$, **: $p < 0.01$, ***: $p < 0.005$, ****: $p < 0.001$, #: $p < 0.0005$, ##: $p < 0.0001$. Even smaller *p* values are not distinguished.

Component	Cell type	Whole-cell integrated intensity (\pm s.e.), $I_{\text{sig}} \times S_{\text{cell}}$	Average intensity per single pixel in the region occupied by TM (\pm s.e.) I_{sig}	Average intensity per unit volume occupied by TM (\pm s.e.) $I_{\text{sig}} \times (S_{\text{cell}})^{-1/2}$	Average cross-section of TM-occupied region in the image (\pm s.e.) S_{cell}
Luminescence	het	0.584## (\pm 0.066)	0.733## (\pm 0.046)	0.878* (\pm 0.045)	0.733# (\pm 0.058)
	veg1	0.936 (\pm 0.054)	0.940* (\pm 0.023)	0.964 (\pm 0.023)	0.984 (\pm 0.046)
Carotenoid	het	0.599## (\pm 0.051)	0.826## (\pm 0.026)	1.073 (\pm 0.081)	
	veg1	0.915 (\pm 0.052)	0.922*** (\pm 0.022)	0.950 (\pm 0.026)	
Phycobilin	het	0.063## (\pm 0.009)	0.090## (\pm 0.013)	0.095## (\pm 0.014)	
	veg1	0.896* (\pm 0.049)	0.903## (\pm 0.016)	0.929*** (\pm 0.021)	

[54]. Although a small portion of PSII may remain in the heterocysts [4,10,31,47], degradation of PSII during the heterocyst differentiation of *A. variabilis* seems to be accompanied by nearly complete degradation of its light-harvesting phycobilisomes containing phycobilins. Statistically significant differences were found between veg1 and veg2 (Tables 1 and S2) of *A. variabilis*. The differences between veg2 and veg3 were less significant than those between veg1 and veg2. To the best of our knowledge, such gradients in the properties of TM of vegetative cells near heterocysts have not been reported previously for *Anabaena* and genetically similar *Nostoc* [65].

In the case of *Rivularia* cells, the thickness (dimension perpendicular to filament axis) near the heterocyst terminal was typically 7–10 μm (Figs. 2G, S1), which was longer than the above-mentioned full width at half maximum of the axial point-spread function (3.7 μm). Given the imaging at only a single depth under these conditions, only “whole-TM-cross-section-integrated intensity” and “average intensity per single pixel in the region occupied by TM” were given as in Table 2.

3.5. Correlations among pigments in the same cell

Correlation among intracellular pigment concentrations were analyzed on the basis of average intensities per single pixel in the TM-occupied regions of single cells (Fig. 5, c.f. Fig. S5). In the case of the vegetative cells of both *A. variabilis* and *Rivularia*, moderate to high correlations ($r \approx 0.4$ –0.8) were found in all three combinations. This must reflect a certain level of stability in ratios among PSI, PSII and phycobilisome in the vegetative cells under our growth conditions as

well as those of photosynthetic pigments in the individual pigment-protein complexes of PSI, PSII (see also Tables S3, S4).

In the heterocysts of *A. variabilis*, low or almost no correlation was found among all three combinations ($-0.22 < r < 0.11$ in Fig. 5A–C). The low correlations associated with phycobilins are understandable, because most phycobilisomes are degraded in matured *A. variabilis* heterocyst [54]. Remaining phycobilisomes in the heterocysts of *A. variabilis*, if any, are probably not forming stable complex with PSI. On the other hand, the low correlation between Chla-associated photoluminescence and carotenoid in the *A. variabilis* heterocyst ($r = -0.003$) cannot be explained by only the changes in the stoichiometry of PSII and PSI between vegetative cells and heterocysts (Tables S3, S4). It is noteworthy that a high correlation coefficient was found if these signals were plotted on the basis of whole-cell integrated intensities (Fig. S5A). The correlation plots in Fig. 5 are thus substantially free from effects coming from cell sizes.

Compared to *A. variabilis* heterocyst, substantially higher correlations in all three combinations were found in the case of *Rivularia* heterocyst ($0.470 \leq r \leq 0.793$ in Fig. 5D–F). These are at least in part explained by the PSI-phycocyanin complex previously found in the *Rivularia* heterocysts [54,61]. It is to be noted that there seem to be at least two distinct subgroups of *Rivularia* heterocysts in terms of the ratio of the photoluminescence to carotenoid signals (Fig. 5D). One subgroup of heterocysts was aligned near the line in which Chla/carotenoid ratio in the vegetative cells are conserved (the diagonal line, $y = x$ in the Fig. 5D), while the other was aligned near the line in which luminescence/carotenoid ratio is about 0.35 (magenta line with a relatively low

Table 2

Ratio of Raman band and luminescence intensities of specified cell types to the corresponding values of veg2 (vegetative cell) in the same *Rivularia* filament. The definitions of signals and symbols are the same as in Table 1, unless otherwise mentioned. Total number of analyzed filaments was 34, and they were classified into two subgroups of A ($N = 16$) and B ($N = 18$) according to photoluminescence/carotenoid Raman intensity ratio (see Figs. 5D, S2, S7). See Fig. 2G in the main text for the notations of het, veg1, and veg2.

Component	Cell type	Subgroup	Whole-TM-cross-section-integrated intensity ($I_{\text{sig}} \times S_{\text{cell}}$)	Average intensity per single pixel in the region occupied by TM (I_{sig})	Average cross-section of TM-occupied region in the image (S_{cell})
Luminescence	het	all ⁽¹⁾	0.277 (\pm 0.034)##	0.452 (\pm 0.044)##[# ⁽³⁾]	0.609 (\pm 0.050)##
		A ⁽²⁾	0.408 (\pm 0.048)## ⁽²⁾	0.665 (\pm 0.052)## ⁽²⁾	0.653 (\pm 0.077)
		B ⁽²⁾	0.161 (\pm 0.029)## ⁽²⁾	0.262 (\pm 0.019)## ⁽²⁾	0.569 (\pm 0.061)
Carotenoid	veg1	all ⁽¹⁾	1.05 (\pm 0.090)	0.923 (\pm 0.018)#	1.12 (\pm 0.082)
		all ⁽¹⁾	0.440 (\pm 0.041)##	0.731 (\pm 0.032)##[# ⁽³⁾]	
		A ⁽²⁾	0.448 (\pm 0.051)	0.728 (\pm 0.048)	
Phycobilin	het	B ⁽²⁾	0.433 (\pm 0.064)	0.732 (\pm 0.044)	
		veg1	1.06 (\pm 0.086)	0.946 (\pm 0.015)***	
		all ⁽¹⁾	0.311 (\pm 0.034)##	0.528 (\pm 0.041)##[# ⁽³⁾]	
	veg1	A ⁽²⁾	0.358 (\pm 0.053)	0.622 (\pm 0.077) ^{*(2)}	
		B ⁽²⁾	0.270 (\pm 0.044)	0.446 (\pm 0.027) ^{*(2)}	
		all ⁽¹⁾	1.05 (\pm 0.082)	0.938 (\pm 0.018)*	

Notes: (1) When all *Rivularia* filaments are concerned, statistically significant differences between het and veg2, or between veg1 and veg2, are shown in the same way as in the case of *A. variabilis* (Tables 1 and S2).

(2) The statistical significance associated with the subgroups A or B were given by *t*-tests between the heterocysts of the subgroups A and B.

(3) The symbols in the bracket, like [#], indicate statistically significant differences in the heterocyst between *Rivularia* and *A. variabilis*.

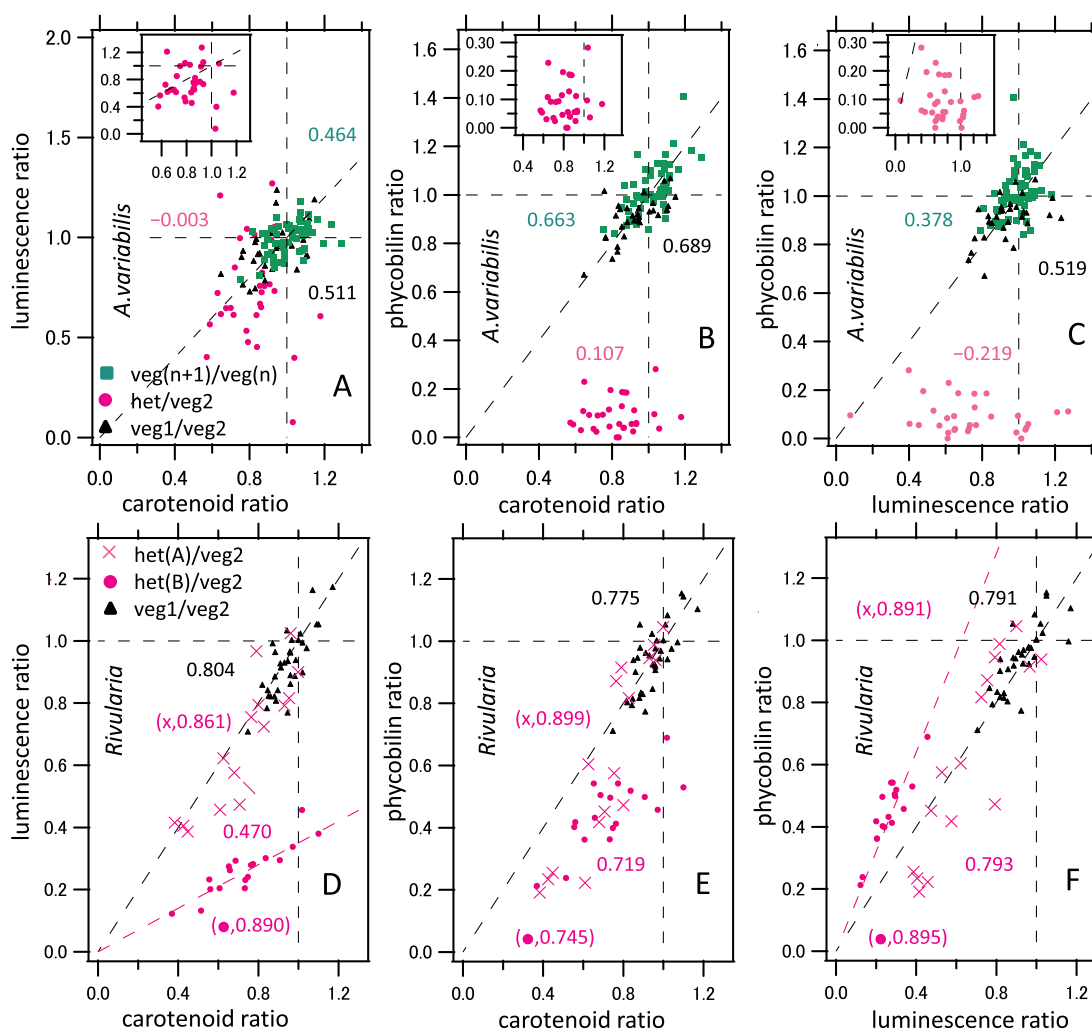


Fig. 5. Correlation plots between pigments in the same cell of *A. variabilis* (A–C) and *Rivularia* (D–F). All plotted relative intensities are based on the “average intensities per pixel (in the region occupied by TM)” as shown in Tables 1 and 2. See the captions of Fig. 2 or S3 for the selected Raman shift or wavelength regions. The quantities of the heterocysts and veg1 cells are normalized by those in veg2 in the same filament. Only in the case of *A. variabilis*, pairs of neighboring vegetative cells designated as veg(n + 1) and veg(n) were analyzed, in which the two cells were far from heterocysts in relatively long filaments grown under the fixed-nitrogen-deprived conditions. The inserted graph in (A–C) shows the plot for het/veg2 in an approximately square frame. In (D–F), *Rivularia* heterocysts were classified into two subgroups A and B (het(A)/veg2 and het(B)/veg2), according to the ratio of Chla-associated photoluminescence and carotenoid Raman intensity (see Section 3.5 and Fig. S7). In all panels, numbers in the graphs are correlation coefficients. In (D–F), correlation coefficients for the subgroups A and B are shown separately by the numbers in brackets. Broken lines in black or magenta are reference lines indicating $y = 1$ (horizontal), $x = 1$ (vertical), $y = x$ (approximately or rigorously diagonal), $y = 0.35x$ (magenta, in D) and $y = 1.6x$ (magenta in F).

gradient, $y = 0.35x$ in the Fig. 5D). Based on the luminescence/carotenoid signal ratio, *Rivularia* heterocysts were classified into two subgroups A and B, in which heterocysts of the subgroup A were located above $y = 0.6x$ and those of the subgroup B were located below $y = 0.5x$ in the Fig. 5D (see also Fig. S7). The two subgroups of heterocysts are also well separated in the phycobilin Raman/Chla-associated photoluminescence correlation plot (Fig. 5F). Differences in the average values of the two subgroups are summarized in Table 2, and representative average single-cell spectra are shown in Fig. S2.

3.6. Laser power dependence of the photoluminescence

The excitation mechanism leading to the photoluminescence of the cyanobacterial cells was also investigated through laser power dependence of the signal amplitude in the case of *A. variabilis* (Table S6). Contribution ratios of apparently one-photon and two-photon excitations at 13.5 mW was estimated to be between 77:23 and 53:47 in five spectral regions that were relatively free from obvious Raman components. It is noteworthy that one-photon excitation at 976 nm is not

negligible at all.

3.7. Photoluminescence of chloroplasts of plant and green alga induced by the 976 nm continuous wave excitation

The TMs in the chloroplasts of plants and eukaryotic green algae are also highly enriched in Chla [12]. The generality of the broad photoluminescence attributed to Chla in the above section was also tested by applying the same spectromicroscopic setup to the chloroplasts in unicellular green alga (*Parachlorella kessleri*) and in leaves of a model plant (*Arabidopsis thaliana*). The spectral shapes of the broad photoluminescence of the plant and green alga were very similar to that of cyanobacterium *A. variabilis* (Fig. 4E). In the cases of the plant and green alga, the ratios of the integrated intensities of the carotenoid Raman bands at around 1520 cm^{-1} to the photoluminescence background at the same wavelength region are estimated to be 2.6 and 4.2 times greater than that of cyanobacterial vegetative cell, respectively. See Text S1 for possible interpretations of this ratio.

4. Discussion

4.1. Comparison with previous absorption spectral microscopy

Microscopic absorption spectra of heterocysts and neighboring vegetative cells in the two cyanobacteria, *A. variabilis* and *Rivularia*, were previously analyzed [54]. The relative photoluminescence intensities of *A. variabilis* heterocyst in comparison with veg2 in this work are very similar to the corresponding values of the microscopic absorbance attributed to Chla that were given by the spectral decomposition of single-cell absorption spectra in the previous work (Tables 1, S7). This leads us to propose that the intensity of the spectrally broad photoluminescence induced by the 976 nm continuous wave laser is fairly proportional to the concentration of Chla.

It should be noted here that possible sensitization of the Chla photoluminescence by phycobilins in the phycobilisome of vegetative cells in *A. variabilis* is excluded by the above-mentioned high correlation between the Chla absorbance and the photoluminescence. Possible sensitization of the Chla photoluminescence by Chlb and/or carotenoids in the cyanobacterium, green alga and plant is discussed in the Supplemental Text S1.

On the other hand, the average decrease of Chla absorption from the veg2 to heterocyst in *Rivularia* filaments in the previous microscopic absorption microspectroscopy ($\approx 28\%$) was comparable to that in the photoluminescence intensity of the heterocyst subgroup A in this work ($\approx 34\%$), which is, however, far milder than that in the subgroup B ($\approx 74\%$) (Tables 2, S8) [54]. Given the presence of at least two subgroups of *Rivularia* heterocysts with clearly different spectral characters (Figs. 5D, S7), it is possible that the samplings of heterocysts in the previous absorption microscopy and this work may have been somehow differently biased.

4.2. Mechanisms and implications of photoluminescence from chlorophyll a in the thylakoid membrane

Linear portion of the photoluminescence in terms of the laser power dependence (Table S6) is possibly attributable to spin-forbidden but actually very weakly allowed transitions between S_0 and T_1 . Phosphorescence spectrum of Chla in mature pea leaves at 77 K has been reported to have a main peak around 980–990 nm and a vibronic progression peaking around 1100 nm [66]. On the other hand, it is also possible that long-wavelength tail (vibronic progression) of the fluorescence bands ($S_1 \rightarrow S_0$, main bands are peaking around 670–730 nm depending on the spectral forms of Chla in cyanobacteria) give substantial contributions to the detected photoluminescence (1017–1175 nm) in our study [63]. The nonlinear portion of the detected photoluminescence (Table S6) can be attributable to the fluorescence of Chla, because the high intensity of the focused 976 nm laser may induce two-photon direct excitation of some photosynthetic pigments and/or multistep excitations consisting of heating effects by the laser (generation of vibrationally excited states in S_0 (hot S_0)) and single-photon excitation (hot $S_0 \rightarrow S_1$). The heating can be caused by absorption of the 976 nm photon at least in part by the water in the case of the cyanobacterial cells [41], but there is no water in the Chla powder (Fig. 4C). In the case of the powder of Chla, lattice vibrations of the powder as well as combinations and/or overtones of molecular vibrations of the individual Chla may contribute to absorption of 976 nm and rise of the local (vibrational) temperature.

The clear photoluminescence from matured *A. variabilis* heterocysts (Table 1, Figs. 2D, 3, 5A) readily supports an idea that PSI is a strong emitter of this photoluminescence under our experimental conditions. Some discussion on relative contributions of PSI and PSII to the photoluminescence is given in the Supplemental Text S1.

4.3. Side effects of the 976 nm excitation

The photoluminescence of Chla implies two possible disadvantages of using the 976 nm laser for imaging of TM, as discussed in Section 4.2. One is the possible production of harmful triplet excited states of Chla leading to generation of singlet oxygen (1O_2) [67]. The other is the heating of water molecules, which should be certainly more substantial than those at 1064 nm [41]. We may have to avoid using the 976 nm excitation laser for repetitive examinations of physiological phenomena of photosynthetic organisms, although long-term observations of organisms after the 976 nm excitation remains to be performed. When the laser power at the sample position was 20 mW or even higher, we sometimes found bleaching of photosynthetic pigments of *A. variabilis* cells and/or obvious changes of the cell shapes. On the other hand, pinpoint production of triplet states of pigments and/or singlet oxygen may be useful for analyzing possible roles of signaling by such molecular species as well as protection mechanisms of the photosynthetic systems against harmful chemicals [68].

4.4. Properties of the heterocysts of *Rivularia* and *Anabaena variabilis*

Rivularia filaments were subcultured from a densely populated agar medium to a freshly prepared one, which seemed to stimulate development of hormogonia (relatively short motile filaments for the dispersal and relocation of the microorganism) from parental filaments (Fig. S1) [69]. Even though the *Rivularia* filaments had been subcultured over several agar media that did not originally contain fixed nitrogen, hormogonia did not have obvious heterocysts. Hormogonia are generally thought to consist of undifferentiated cells [70]. It is thus possible that the terminal cells at the heterocyst position of *Rivularia* analyzed in this study were situated at various transition stages from a transient terminal vegetative cell to a matured heterocyst. Among the two subgroups of *Rivularia* heterocysts (Table 2, Figs. 5D–F, S7), the signal ratios of photoluminescence/carotenoid of the subgroup A are similar to those of nearby vegetative cells. It is thus likely that the heterocysts in the subgroup B are more matured ones and that those in the subgroup A are relatively young heterocysts. The signal ratios of phycobilins/photoluminescence of the subgroup B (postulated mature heterocysts) are higher than those of subgroup A (postulated young heterocysts). This trend is contrary to the one in *A. variabilis*, in which phycobilins/photoluminescence ratio is clearly lower in heterocysts than in vegetative cells (Fig. 5C). This situation probably reflects two factors: (i) a high portion of PSI in the *Rivularia* heterocysts is bound to phycocyanin [54], and (ii) Chla contents in the heterocyst subgroup B (matured heterocyst) were on average lower than those in the subgroup A (young heterocyst) (Table 2, Fig. S3). Based on our proposal that Chla concentration, as measured by microscopic absorbance per unit depth [54], is approximately proportional to the Chla-associated photoluminescence (Table S6), differences between heterocysts and vegetative cells of the *Rivularia* leads to the idea that the heterocysts in the subgroup A observed here are similar to those analyzed in our previous study (Table S8) [54]. Although the heterocysts in the subgroup A seem to be relatively young in comparison with the subgroup B, their absorption and fluorescence features including PSII/PSI fluorescence intensity ratio may be sufficiently distinct from those of vegetative cells [54]. It is noteworthy that so many young heterocysts (16 among 34) were clearly separated from matured heterocysts by the spectroscopic indices, which suggests a relatively long lifetime of the young stage of the heterocysts and swift drastic change in the intracellular pigments at certain maturation/aging stages.

The low ratios of Chla-associated photoluminescence to carotenoid in the subgroup B of *Rivularia* heterocyst (postulated matured heterocysts) in comparison with the vegetative cells ($\sim 0.35:1$, Fig. 5D) are not simply explained by the decrease of PSII/PSI ratio from the vegetative cells to the heterocysts, because Chla: carotenoid number ratio of PSI (96:22 $\approx 4.36:1$) is higher than that of and PSII (35:11 $\approx 3.18:1$)

(Tables S3, S4). The observed low ratio ($\sim 0.35:1$) is actually even lower than the lower limit ($0.729:1 \approx 3.18/4.36:1$) given by a virtual conversion from 100% PSI in vegetative cells to 100% PSII in heterocysts, although these ratios are totally unrealistic for the two cell types (Table S8). It is thus likely that the ratio of carotenoids other than those bound in PSI or PSII have increased from vegetative cells to heterocysts of the subgroup B in the *Rivularia* filaments. Changes in carotenoid compositions of two heterocystous cyanobacteria (*Anabaena* sp. PCC7120 and *Calothrix* sp. 336/3) upon deprivation of exogenous combined nitrogen were reported [71]. Total β -carotene (including both trans and cis forms) was decreased from 37.6–42.5% to 27.4–31.5% while some of the other carotenoids (echinenone in both the species, zeaxanthin in only *Calothrix*) were increased. Although heterocysts and vegetative cells were not separately analyzed in the reference [71], these results may lead to the idea that the carotenoids not bound to PSI or PSII in the subgroup B of *Rivularia* heterocysts may be echinenone and/or zeaxanthin [72]. The frequency of the C=C stretching vibration (around 1520 cm^{-1}) of echinenone has been reported to be down shifted by about 5 cm^{-1} in comparison with β -carotene and zeaxanthin [73–75]. However, we did not detect clear change in the frequency between vegetative cells and heterocysts in both *A. variabilis* and *Rivularia* (Figs. 3, S2), suggesting that there is no strong localization of echinenone in the heterocysts. In spite of an elevated rate of respiration, thick cell wall and substantial decrease of PSII in the heterocysts, diffusion of O_2 through the terminal pore into the heterocysts and concomitant production of reactive oxygen species may be unavoidable [76]. The carotenoids in the *Rivularia* heterocyst other than those bound in PSI or small amount of PSII may be effective as a singlet oxygen quencher [77].

In view of the relatively high correlations between photoluminescence and carotenoid signals of the *Rivularia* heterocyst subgroups, the negligibly small correlation coefficient in the corresponding plot of *A. variabilis* heterocyst is remarkable (Fig. 5A, D). Some carotenoids not bound to PSI or small amount of PSII may accumulate at least a portion of *A. variabilis* heterocysts (see also Section 3.5). It is also suggested that the ratio of total intracellular carotenoid to PSI in the heterocyst is more tightly regulated in *Rivularia* than in *A. variabilis*.

4.5. Implications for physiological status of vegetative cells in filamentous cyanobacteria

Some heterocystous cyanobacteria consist of vegetative cells with varied shapes and sizes, as in the case of *Rivularia* filaments (Fig. S1) [54,69,78]. In contrast, autofluorescence spectra as well as their sizes of vegetative cells of *Anabaena* and *Nostoc* are mostly very similar to each other [31,49,54,79]. For example, as far as we employed autofluorescence spectral microscopy and absorption spectral microscopy to analyze the individual vegetative cells near the heterocyst in *A. variabilis*, we were not able to detect convincing spectral differences between veg1 and veg2 (Table S6) [31,54]. On the other hand, some works reported at least transient appearance of abnormal vegetative cells [4,80]. Overall, our results and some previous studies indicate that transient and/or steady differences in the properties of thylakoid membranes between apparently similar vegetative cells are induced under some conditions.

All *A. variabilis* heterocysts we analyzed seemed to be already matured, because amounts of phycobilins in the heterocysts were on average only 6% of the average vegetative cell (Table 1, Fig. 5B, Table S2) [31]. PSI in some of the heterocysts may be decreased by aging of the heterocysts, because heterocyst is a terminally differentiated state (no possibility of division) and its lifetime is finite. The veg1 cell should be the candidate for the next terminal heterocyst cell, in which decrease of PSII-related photosynthetic pigments is expected if it is time for the terminal heterocyst to be replaced. Due possibly to the lack of synchronization in the culture and relatively long incubation time from the inoculation to the microscopic measurements (5–74 days for *A.*

variabilis), we did not find correlation between the incubation time and the quantities of photosynthetic pigments in the heterocysts or veg1 cells (Fig. S6). More systematic tracking of the maturation or aging process of heterocysts is necessary to understand the physiological meaning of the special status of veg1 cell.

The mechanisms for the formation of the semiregularly spaced heterocyst positions among vegetative cells have been extensively studied [46,81]. Although many genes are involved in the differentiation process [82], the essential pattern formation and maintenance has been successfully reproduced by computer simulations considering several key genes and factors [83,84]. However, subtle differences between vegetative cells have not been paid much attention. The special status of the vegetative cells nearest to heterocysts (veg1) that we found (Table 1) may reflect a delicate balance among inhibitions of heterocyst differentiation in the vegetative cells, exchange of metabolites and signaling molecules between heterocysts and vegetative cells, aging of the heterocyst and cell division cycles in the vegetative cells [50,85].

5. Conclusions

The photoluminescence of Chla (around 1017–1175 nm) in *A. variabilis* cells induced by the continuous wave laser at 976 nm seems to be fairly proportional to the concentration of Chla. The photoluminescence spectrum was found to be almost common among the two cyanobacteria (*A. variabilis* and *Rivularia*), green alga and plant. Our analysis of the Raman bands of carotenoids, phycobilins and photoluminescence of Chla supports the view that the phycobilisomes remain substantially in the *Rivularia* heterocysts, but only almost negligibly in *A. variabilis* heterocysts. At least two distinct physiological states of the terminal heterocyst in *Rivularia* filaments were distinguished by the correlations between the Raman bands of carotenoids and Chla-associated photoluminescence, in which one state seems to be matured heterocyst and the other is relatively young heterocyst. The photoluminescence we observed by the continuous wave excitation at 976 nm is not something to be subtracted and neglected, but signals useful for analysis of chloroplasts and cyanobacteria on a single-cell basis. Some special roles of carotenoids other than those bound to PSI or small amount of PSII in both *A. variabilis* and *Rivularia* heterocysts are suggested through the photoluminescence/carotenoid correlations.

Transparency document

The Transparency document associated with this article can be found, in online version.

Acknowledgements

We thank Profs. Masahide Terazima (Kyoto Univ.), Haruo Inoue (Tokyo Metropolitan Univ.), Takashi Shiina (Kyoto Prefectural Univ.), Yoshifumi Kimura (Doshisha Univ.) and Hirozo Oh-Oka (Osaka Univ.) for valuable advice, Prof. Masanori Izumi (Tohoku Univ.) for providing *A. thaliana*. We also thank Dr. Shuho Nozue (King Abdullah Univ.) and Prof. Mitsunori Katayama (Nihon University) for their valuable contributions to our previous study that were highly relevant to this work.

Funding

This work was supported in part by the Japan Science and Technology Agency (the Precursory Research for Embryonic Science and Technology, “Chemical conversion of light energy”, to S.K.), MEXT-Supported Program for the Strategic Research Foundation at Private Universities (2015–2018, no. S1511025 partly to S.K.) and Molecular Science for Supra functional Systems (Area No.477, 19056012 to S.K.), JSPS KAKENHI (17H03968 partly to S.K. and 18K06153 partly to S.K.), the Murata Science Foundation (to S.K.), the Kyoto University Foundation (to S.K.) and Imaging Science Project of the Center for

Novel Science Initiatives (CNSI), National Institutes of Natural Sciences (NINS) (no. IS281001 to S.K.).

Appendix A. Supplementary data

Supplementary data to this article can be found online at <https://doi.org/10.1016/j.bbabi.2018.11.012>.

References

- [1] B. Ke, *Photosynthesis Photobiochemistry and Photobiophysics*, Springer Science & Business Media, 2001.
- [2] R.E. Blankenship, *Molecular Mechanisms of Photosynthesis*, John Wiley & Sons, 2014.
- [3] K. Harter, A.J. Meixner, F. Schleifenbaum, *Spectro-microscopy of living plant cells*, *Mol. Plant* 5 (2012) 14–26.
- [4] N. Ferimazova, K. Felcmanova, E. Setlikova, H. Kupper, I. Maldener, G. Hauska, B. Sediva, O. Prasil, Regulation of photosynthesis during heterocyst differentiation in *Anabaena* sp strain PCC 7120 investigated in vivo at single-cell level by chlorophyll fluorescence kinetic microscopy, *Photosynth. Res.* 116 (2013) 79–91.
- [5] K. Omasa, A. Konishi, H. Tamura, F. Hosoi, 3D confocal laser scanning microscopy for the analysis of chlorophyll fluorescence parameters of chloroplasts in intact leaf tissues, *Plant Cell Physiol.* 50 (2009) 90–105.
- [6] S. Kumazaki, M. Hasegawa, M. Ghoneim, Y. Shimizu, K. Okamoto, M. Nishiyama, H. Oh-oka, M. Terazima, A line-scanning semi-confocal multi-photon fluorescence microscope with a simultaneous broadband spectral acquisition and its application to the study of the thylakoid membrane of a cyanobacterium *Anabaena* PCC7120, *J. Microsc.* (Oxford) 228 (2007) 240–254.
- [7] *Chlorophyll a Fluorescence: A Signature of Photosynthesis*, Springer Netherlands, 2004.
- [8] M.A. Amin, S. Nandi, P. Mondal, T. Mahata, S. Ghosh, K. Bhattacharyya, Physical chemistry in a single live cell: confocal microscopy, *Phys. Chem. Chem. Phys.* 19 (2017) 12620–12627.
- [9] C.A. Bücherl, A. Bader, A.H. Westphal, S.P. Laptanok, J.W. Borst, FRET-FLIM applications in plant systems, *Protoplasma* 251 (2014) 383–394.
- [10] S. Nozue, A. Mukuno, Y. Tsuda, T. Shiina, M. Terazima, S. Kumazaki, Characterization of thylakoid membrane in a heterocystous cyanobacterium and green alga with dual-detector fluorescence lifetime imaging microscopy with a systematic change of incident laser power, *Biochim. Biophys. Acta, Bioenerg.* 1857 (2016) 46–59.
- [11] I. Iermak, J. Vink, A.N. Bader, E. Wientjes, H. van Amerongen, Visualizing heterogeneity of photosynthetic properties of plant leaves with two-photon fluorescence lifetime imaging microscopy, *Biochim. Biophys. Acta, Bioenerg.* 1857 (2016) 1473–1478.
- [12] Govindjee, Chlorophyll a fluorescence: a bit of basics and history, in: C. Papageorgiou, Govindjee (Eds.), *Chlorophyll a Fluorescence a Signature of Photosynthesis*, Springer, Netherland, 2004, pp. 1–42.
- [13] E. Kim, T.K. Ahn, S. Kumazaki, Changes in antenna sizes of photosystems during state transitions in granal and stroma-exposed thylakoid membrane of intact chloroplasts in *Arabidopsis* mesophyll protoplasts, *Plant Cell Physiol.* 56 (2015) 759–768.
- [14] H.-O. Hamaguchi, Developments of Raman spectroscopy in the past 40 years: from a molecule to a living cell, *Curr. Sci.* 97 (2009) 186–191.
- [15] H. Kandori, H. Sasabe, M. Mimuro, Direct determination of a lifetime of the S2 state of beta-carotene by femtosecond time-resolved fluorescence spectroscopy, *J. Am. Chem. Soc.* 116 (1994) 2671–2672.
- [16] H. Hashimoto, K. Yanagi, M. Yoshizawa, D. Polli, G. Cerullo, G. Lanzani, S. De Silvestri, A.T. Gardiner, R.J. Cogdell, The very early events following photo-excitation of carotenoids, *Arch. Biochem. Biophys.* 430 (2004) 61–69.
- [17] B. Robert, Resonance Raman studies in photosynthesis—chlorophyll and carotenoid molecules, *Biophysical Techniques in Photosynthesis*, Springer, 1996, pp. 161–176.
- [18] W.F.J. Vermaas, J.A. Timlin, H.D.T. Jones, M.B. Sinclair, L.T. Nieman, S.W. Hamad, D.K. Melgaard, D.M. Haaland, In vivo hyperspectral confocal fluorescence imaging to determine pigment localization and distribution in cyanobacterial cells, *Proc. Natl. Acad. Sci. U. S. A.* 105 (2008) 4050–4055.
- [19] M. Baranska, M. Roman, H. Schulz, R. Baranski, Recent advances in Raman analysis of plants: alkaloids, carotenoids, and polyacetylenes, *Curr. Anal. Chem.* 9 (2013) 108–127.
- [20] X. Wei, D. Jie, J.J. Cuello, D.J. Johnson, Z. Qiu, Y. He, Microalgal detection by Raman microspectroscopy, *TRAC Trends Anal. Chem.* 53 (2014) 33–40.
- [21] P. Vitek, C. Ascaso, O. Artieda, M.C. Casero, J. Wierzbosch, Discovery of carotenoid red-shift in endolithic cyanobacteria from the Atacama Desert, *Sci. Rep.* 7 (2017) 11116.
- [22] B. DemmigAdams, A.M. Gilmore, W.W. Adams, Carotenoids 3. In vivo functions of carotenoids in higher plants, *FASEB J.* 10 (1996) 403–412.
- [23] C.I. Cazzonelli, Carotenoids in nature: insights from plants and beyond, *Funct. Plant Biol.* 38 (2011) 833–847.
- [24] A.V. Ruban, Nonphotochemical chlorophyll fluorescence quenching: mechanism and effectiveness in protecting plants from photodamage, *Plant Physiol.* 170 (2016) 1903–1916.
- [25] S.-G. Kong, M. Wada, Recent advances in understanding the molecular mechanism of chloroplast photorelocation movement, *Biochim. Biophys. Acta, Bioenerg.* 1837 (2014) 522–530.
- [26] Y. Huang, C. Beal, W. Cai, R. Ruoff, E. Terentjev, Micro-Raman spectroscopy of algae: composition analysis and fluorescence background behavior, *Biotechnol. Bioeng.* 105 (2010) 889–898.
- [27] B. Gobets, R. van Grondelle, Energy transfer and trapping in photosystem I, *BBA-Bioenergetics* 1507 (2001) 80–99.
- [28] A. Thapper, F. Mamedov, F. Mokvist, L. Hammarstrom, S. Styring, Defining the far-red limit of photosystem II in spinach, *Plant Cell* 21 (2009) 2391–2401.
- [29] M. Hasegawa, T. Shiina, M. Terazima, S. Kumazaki, Selective excitation of photosystems in chloroplasts inside plant leaves observed by near-infrared laser-based fluorescence spectral microscopy, *Plant Cell Physiol.* 51 (2010) 225–238.
- [30] M. Hasegawa, T. Yoshida, M. Yabuta, M. Terazima, S. Kumazaki, Anti-stokes fluorescence spectra of chloroplasts in *Parachlorella kessleri* and maize at room temperature as characterized by near-infrared continuous-wave laser fluorescence microscopy and absorption microscopy, *J. Phys. Chem. B* 115 (2011) 4184–4194.
- [31] S. Kumazaki, M. Akari, M. Hasegawa, Transformation of thylakoid membranes during differentiation from vegetative cell into heterocyst visualized by microscopic spectral imaging, *Plant Physiol.* 161 (2013) 1321–1333.
- [32] F. Mokvist, F. Mamedov, S. Styring, Defining the far-red limit of photosystem I the primary charge separation is functional to 840 nm, *J. Biol. Chem.* 289 (2014) 24630–24639.
- [33] M. Ando, M. Sugiura, H. Hayashi, H.-o. Hamaguchi, 1064 nm deep near-infrared (NIR) excited Raman microspectroscopy for studying photolabile organisms, *Appl. Spectrosc.* 65 (2011) 488–492.
- [34] H. Wu, J.V. Volponi, A.E. Oliver, A.N. Parikh, B.A. Simmons, S. Singh, In vivo lipidomics using single-cell Raman spectroscopy, *Proc. Natl. Acad. Sci. U. S. A.* 108 (2011) 3809–3814.
- [35] B. Schrader, H. Klump, K. Schenzel, H. Schulz, Non-destructive NIR FT Raman analysis of plants, *J. Mol. Struct.* 509 (1999) 201–212.
- [36] H.G. Edwards, E.M. Newton, D.L. Dickensheets, D.D. Wynn-Williams, Raman spectroscopic detection of biomolecular markers from Antarctic materials: evaluation for putative Martian habitats, *Spectrochim. Acta A Mol. Biomol. Spectrosc.* 59 (2003) 2277–2290.
- [37] R. Baranski, M. Baranska, H. Schulz, Changes in carotenoid content and distribution in living plant tissue can be observed and mapped in situ using NIR-FT-Raman spectroscopy, *Planta* 222 (2005) 448–457.
- [38] D.M. Gates, H.J. Keegan, J.C. Schleiter, V.R. Weidner, Spectral properties of plants, *Appl. Opt.* 4 (1965) 11–20.
- [39] R. Loudon, *The Quantum Theory of Light*, Oxford University Press, 2000.
- [40] S. York, InGaAs SWIR cameras open new opportunities, *Photonics Spectra*, 48 2014, pp. 55–58.
- [41] K.F. Palmer, D. Williams, Optical properties of water in the near infrared*, *J. Opt. Soc. Am.* 64 (1974) 1107–1110.
- [42] Z. Pilát, J. Ježek, M. Šerý, M. Trtílek, L. Nedbal, P. Zemánek, Optical trapping of microalgae at 735–1064 nm: photodamage assessment, *J. Photochem. Photobiol. B Biol.* 121 (2013) 27–31.
- [43] Y. Kamei, M. Suzuki, K. Watanabe, K. Fujimori, T. Kawasaki, T. Deguchi, Y. Yoneda, T. Todo, S. Takagi, T. Funatsu, Infrared laser-mediated gene induction in targeted single cells in vivo, *Nat. Methods* 6 (2009) 79.
- [44] R. Haselkorn, Heterocysts, *Annu. Rev. Plant Physiol. Plant Mol. Biol.* 29 (1978) 319–344.
- [45] C. Wolk, A. Ernst, J. Elhai, Heterocyst metabolism and development, in: B. D (Ed.), *The Molecular Biology of Cyanobacteria*, Kluwer Academic Publisher, Netherland, 1994, pp. 769–823.
- [46] A. Herrero, J. Stavans, E. Flores, The multicellular nature of filamentous heterocyst-forming cyanobacteria, *FEMS Microbiol. Rev.* 40 (2016) 831–854.
- [47] A. Magnuson, T. Cardona, Thylakoid membrane function in heterocysts, *Biochim. Biophys. Acta, Bioenerg.* 1857 (2016) 309–319.
- [48] L. Ying, X. Huang, B. Huang, J. Xie, J. Zhao, X.S. Zhao, Fluorescence emission and absorption spectra of single *Anabaena* sp. strain PCC7120 cells, *Photochem. Photobiol.* 76 (2002) 310–313.
- [49] K. Sugiura, S. Itoh, Single-cell confocal spectrometry of a filamentous cyanobacterium *Nostoc* at room and cryogenic temperature. Diversity and differentiation of pigment systems in 311 cells, *Plant Cell Physiol.* 53 (2012) 1492–1506.
- [50] M. Toyoshima, N.V. Sasaki, M. Fujiwara, S. Ehira, M. Ohmori, N. Sato, Early candidacy for differentiation into heterocysts in the filamentous cyanobacterium *Anabaena* sp. PCC 7120, *Arch. Microbiol.* 192 (2010) 23–31.
- [51] S. Ke, R. Haselkorn, Fluorescence spectroscopy study of heterocyst differentiation in *Anabaena* PCC 7120 filaments, *Microbiology* 159 (2013) 253–258.
- [52] J. Ishihara, M. Tachikawa, A. Mochizuki, Y. Sako, H. Iwasaki, S. Morita, Raman imaging of the diverse states of the filamentous cyanobacteria, *Nano-Bio Sensing, Imaging and Spectroscopy*, International Society for Optics and Photonics, 2013(pp. 88790V-88790V-88794).
- [53] A. Dementjev, J. Kostkevicene, Applying the method of coherent anti-stokes Raman microscopy for imaging of carotenoids in microalgae and cyanobacteria, *J. Raman Spectrosc.* 44 (2013) 973–979.
- [54] S. Nozue, M. Katayama, M. Terazima, S. Kumazaki, Comparative study of thylakoid membranes in terminal heterocysts and vegetative cells from two cyanobacteria, *Rivularia* M-261 and *Anabaena variabilis*, by fluorescence and absorption spectral microscopy, *Biochim. Biophys. Acta, Bioenerg.* 1858 (2017) 742–749.
- [55] R.Y. Stanier, R. Kunisawa, M. Mandel, G. Cohenbaz, Purification and properties of unicellular blue-green algae (order Chroococcales), *Bacteriol. Rev.* 35 (1971) 171.
- [56] J.C. Meeks, J. Elhai, Regulation of cellular differentiation in filamentous cyanobacteria in free-living and plant-associated symbiotic growth states, *Microbiol. Mol. Biol. Rev.* 66 (2002) 94–121.
- [57] S.F. Parker, S.M. Tavender, N.M. Dixon, H. Herman, K.P.J. Williams, W.F. Maddams, Raman spectrum of beta-carotene using laser lines from green

- (514.5 nm) to near-infrared (1064 nm): implications for the characterization of conjugated polyenes, *Appl. Spectrosc.* 53 (1999) 86–91.
- [58] C. Kneip, A. Parbel, H. Foerstendorf, H. Scheer, F. Siebert, P. Hildebrandt, Fourier transform near-infrared resonance Raman spectroscopic study of the α -subunit of phycoerythrocyanin and phycocyanin from the cyanobacterium *Mastigocladus laminosus*, *J. Raman Spectrosc.* 29 (1998) 939–944.
- [59] H. Sato, K. Okada, K. Uehara, Y. Ozaki, Near-infrared Fourier-transform Raman study of chlorophyll *a* in solutions, *Photochem. Photobiol.* 61 (1995) 175–182.
- [60] W.A. Sidler, Phycobilisome and phycobiliprotein structures, *The Molecular Biology of Cyanobacteria*, Springer, 1994, pp. 139–216.
- [61] M. Watanabe, D.A. Semchonok, M.T. Webber-Birungi, S. Ehira, K. Kondo, R. Narikawa, M. Ohmori, E.J. Boekema, M. Ikeuchi, Attachment of phycobilisomes in an antenna–photosystem I supercomplex of cyanobacteria, *Proc. Natl. Acad. Sci.* 111 (2014) 2512–2517.
- [62] M. Donahue, H. Huang, C. Brouillette, W. Smith, S. Farquharson, Detecting explosives by portable Raman analyzers: a comparison of 785-, 976-, 1064-, and 1550-nm (retina-safe) laser excitation, *Spectroscopy* (2011), <http://www.spectroscopyonline.com/detecting-explosives-portable-raman-analyzers-comparison-785-976-1064-and-1550-nm-retina-safe-laser?id=&pageID=1&sk=&date=>.
- [63] D.A. Hartzler, D.M. Niedzwiedzki, D.A. Bryant, R.E. Blankenship, Y. Pushkar, S. Sayikhin, Triplet excited state energies and phosphorescence spectra of (bacterio) chlorophylls, *J. Phys. Chem. B* 118 (2014) 7221–7232.
- [64] G.C. Righini, M. Ferrari, Photoluminescence of rare-earth-doped glasses, *Riv. Nuovo Cimento* 28 (2005) 1–53.
- [65] M. Howard-Azzeh, L. Shamseer, H.E. Schellhorn, R.S. Gupta, Phylogenetic analysis and molecular signatures defining a monophyletic clade of heterocystous cyanobacteria and identifying its closest relatives, *Photosynth. Res.* 122 (2014) 171–185.
- [66] A. Krasnovsky, Y.V. Kovalev, Spectral and kinetic parameters of phosphorescence of triplet chlorophyll *a* in the photosynthetic apparatus of plants, *Biochem. Mosc.* 79 (2014) 349–361.
- [67] A. Telfer, Singlet oxygen production by PSII under light stress: mechanism, detection and the protective role of beta-carotene, *Plant Cell Physiol.* 55 (2014) 1216–1223.
- [68] C. Triantaphylidès, M. Havaux, Singlet oxygen in plants: production, detoxification and signaling, *Trends Plant Sci.* 14 (2009) 219–228.
- [69] B.A. Whitton, P. Mateo, Rivulariaceae, in: B.A. Whitton (Ed.), *Ecology of Cyanobacteria II: Their Diversity in Space and Time*, Springer Science + Business Media, 2012.
- [70] D.G. Adams, P.S. Duggan, Heterocyst and akinete differentiation in cyanobacteria, *New Phytol.* 144 (1999) 3–33.
- [71] S. Kosourov, G. Murukesan, J. Jokela, Y. Allahverdiyeva, Carotenoid biosynthesis in *Calothrix* sp. 336/3: composition of carotenoids on full medium, during diazotrophic growth and after long-term H₂ photoproduction, *Plant Cell Physiol.* 57 (2016) 2269–2282.
- [72] P. Fromme, P. Jordan, N. Krauß, Structure of photosystem I, *Biochim. Biophys. Acta, Bioenerg.* 1507 (2001) 5–31.
- [73] E. Kish, M.M.M. Pinto, D. Kirilovsky, R. Spezia, B. Robert, Echinone vibrational properties: from solvents to the orange carotenoid protein, *Biochim. Biophys. Acta, Bioenerg.* 1847 (2015) 1044–1054.
- [74] L.F. Maia, R.F. Fernandes, G. Lobo-Hajdu, L.F. de Oliveira, Conjugated polyenes as chemical probes of life signature: use of Raman spectroscopy to differentiate polyenic pigments, *Phil. Trans. R. Soc. A* 372 (2014) 20140200.
- [75] J. Jehlička, H.G. Edwards, K. Osterrothová, J. Novotná, L. Nedbalová, J. Kopecký, I. Němec, A. Oren, Potential and limits of Raman spectroscopy for carotenoid detection in microorganisms: implications for astrobiology, *Phil. Trans. R. Soc. A* 372 (2014) 20140199.
- [76] A.E. Walsby, Cyanobacterial heterocysts: terminal pores proposed as sites of gas exchange, *Trends Microbiol.* 15 (2007) 340–349.
- [77] R. Edge, D. McGarvey, T. Truscott, The carotenoids as anti-oxidants—a review, *J. Photochem. Photobiol. B Biol.* 41 (1997) 189–200.
- [78] Á.M. Plominsky, J. Larsson, B. Bergman, N. Delherbe, I. Osses, M. Vásquez, Dinitrogen fixation is restricted to the terminal heterocysts in the invasive cyanobacterium *Cylindrospermopsis raciborskii* CS-505, *PLoS One* 8 (2013) e51682.
- [79] S. Ke, V. Bindokas, R. Haselkorn, *Anabaena* cell ageing monitored with confocal fluorescence spectroscopy, *Microbiology* 161 (2015) 84–88.
- [80] T. Cardona, N. Battchikova, Á. Agervald, P. Zhang, E. Nagel, E.-M. Aro, S. Styring, P. Lindblad, A. Magnuson, Isolation and characterization of thylakoid membranes from the filamentous cyanobacterium *Nostoc punctiforme*, *Physiol. Plant.* 131 (2007) 622–634.
- [81] L. Corrales-Guerrero, V. Mariscal, D.J. Nurnberg, J. Elhai, C.W. Mullineaux, E. Flores, A. Herrero, Subcellular localization and clues for the function of the HetN factor influencing heterocyst distribution in *Anabaena* sp strain PCC 7120, *J. Bacteriol.* 196 (2014) 3452–3460.
- [82] S. Ehira, Transcriptional regulation of heterocyst differentiation in *Anabaena* sp. strain PCC 7120, *Russ. J. Plant Physiol.* 60 (2013).
- [83] A. Torres-Sánchez, J. Gómez-Gardeñes, F. Falo, An integrative approach for modeling and simulation of heterocyst pattern formation in cyanobacteria filaments, *PLoS Comput. Biol.* 11 (2015) e1004129.
- [84] J. Muñoz-García, S. Ares, Formation and maintenance of nitrogen-fixing cell patterns in filamentous cyanobacteria, *Proc. Natl. Acad. Sci.* 113 (2016) 6218–6223.
- [85] C.W. Mullineaux, V. Mariscal, A. Nenninger, H. Khanum, A. Herrero, E. Flores, D.G. Adams, Mechanism of intercellular molecular exchange in heterocyst-forming cyanobacteria, *EMBO J.* 27 (2008) 1299–1308.

Excited-State Proton Transfer of Cyanonaphthols in Protic Ionic Liquids: Appearance of a New Fluorescent Species

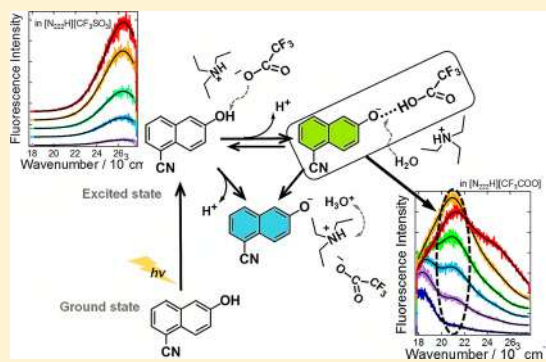
Kaori Fujii,[†] Yoshiro Yasaka,[‡] Masakatsu Ueno,[‡] Yoshinari Koyanagi,[§] Sora Kasuga,[§] Yoshihiro Matano,^{||} and Yoshifumi Kimura^{*,†,‡,§}

[†]Department of Applied Chemistry, Graduate School of Science and Engineering and [‡]Department of Molecular Chemistry and Biochemistry, Faculty of Science and Engineering, Doshisha University, Kyotanabe, Kyoto 610-0321, Japan

[§]Department of Fundamental Sciences, Graduate School of Science and Technology and ^{||}Department of Chemistry, Faculty of Science, Niigata University, Nishi-ku, Niigata 950-2181, Japan

Supporting Information

ABSTRACT: Excited-state proton transfer (ESPT) of 5-cyano-2-naphthol (5CN2) and 5,8-dicyano-2-naphthol (DCN2) in three different protic ionic liquids (PILs), triethylammonium trifluoromethanesulfonate ($[N_{222}H][CF_3SO_3]$), triethylammonium methanesulfonate ($[N_{222}H][CH_3SO_3]$), and triethylammonium trifluoroacetate ($[N_{222}H][CF_3COO]$), was studied by time-resolved fluorescence. In $[N_{222}H][CF_3SO_3]$, both 5CN2 and DCN2 showed fluorescence only from ROH* (normal form of substituted naphthol in the excited states), indicating that no ESPT occurred in $[N_{222}H][CF_3SO_3]$. For 5CN2 in $[N_{222}H][CH_3SO_3]$, fluorescence bands from ROH* and RO^{-*} (anionic form of substituted naphthol in the excited states) were observed, indicating that 5CN2 could dissociate proton to surrounding solvents and form RO^{-*}. More interestingly, 5CN2 in $[N_{222}H][CF_3COO]$ and DCN2 in $[N_{222}H][CH_3SO_3]$ and $[N_{222}H][CF_3COO]$ showed an anomalous fluorescence band around 470 nm (5CN2) or around 520 nm (DCN2) which has not been reported previously. The kinetics of each fluorescent component of 5CN2 and DCN2 was analyzed on the basis of the time profile of fluorescence intensity. Plausible ESPT schemes of 5CN2 and DCN2 were discussed on the basis of the kinetics and the basicity of anion in PILs.



1. INTRODUCTION

Recently, ionic liquids (ILs) have attracted many scientists in a broad range of fields because of their unique physicochemical characteristics.^{1–7} Although ILs are salts composed of anions and cations, they are liquids in room temperature mainly due to the bulky and asymmetric structure of the cations. By changing the pairs of anions and cations, a variety of ILs that have special functionality can be synthesized. Among various kinds of ILs, protic ionic liquids (PILs), which are easily synthesized by simple Brønsted acid–base reactions,⁸ have active protons in the cations. Because of the protons in the cations and the basicity of the anions, PILs can undergo proton transfer (PT) in solutions with solute molecules dissolved in them. Until now, numerous research studies on the physicochemical properties^{5,9–14} and dynamics of PILs have been conducted by computational methods,^{15–19} thermal analysis,²⁰ and spectroscopies such as NMR spectroscopy^{21–23} and Raman spectroscopy.^{24,25} Among these studies, the basicity of the anions can be expected to have a large impact on the behavior of PILs, especially on the PT reactions that occur in them. However, there are few studies which focus on the real-time analysis of PT dynamics in PILs. In this study, we aim to investigate PT dynamics in three different PILs by probing the fluorescence dynamics of photoacids dissolved in them.

2-Naphthol is known as a photoacid whose acidity is enhanced in the excited state.²⁶ Substituted compounds of 2-naphthol with an electron withdrawing group at the C5 and/or C8 site show large enhancement of acidity.^{27,28} For example, the values of pK_a^* (pK_a in the excited states) of 5-cyano-2-naphthol (5CN2) and 5,8-dicyano-2-naphthol (DCN2) are reported to be -0.75 and -4.5 , respectively, while that of 2-naphthol is 2.8 .^{29,31} Because of the remarkable enhancement of the acidity, they can undergo excited-state proton transfer (ESPT) not only in water but also in solvents that show lower acceptor number such as alcohols, DMSO, and so on.³⁰ Since cyano-substituted 2-naphthols show dual fluorescence from the normal form (ROH*) at shorter wavelength and the anionic form (RO^{-*}) at longer wavelength, it is possible to clarify the kinetics of PT by monitoring the fluorescence dynamics.^{27–39} For example, Huppert et al. studied the ESPT dynamics of four cyano-substituted 2-naphthols in H₂O and D₂O by time-resolved fluorescence measurement²⁷ and found that the dissociation rate constant of 5CN2 in H₂O is extremely fast, 0.07 ps^{-1} . Since ESPT dynamics highly reflects the surrounding

Received: April 18, 2017

Revised: May 21, 2017

Published: June 8, 2017

environments, effects of the temperature, the pressure, and the degree of hydrogen bond on the ESPT have been reported by many researchers.^{32–39} For example, Kimura et al. studied the ESPT of 5CN2 in sub- and supercritical water^{32,33} and found that the PT rate of 5CN2 to water correlated with the number of solvent–solvent hydrogen bond.

Although unique proton transfer kinetic is discussed in PILs,^{17,40,41} the number of studies on real-time dynamics of PT in ILs or PILs is limited. For example, Samanta et al. studied the PT dynamics of 7-hydroxyquinoline in the mixture of ILs with alcohols and discussed the specific configuration between solute and solvent.⁴² Kimura et al. studied the intramolecular PT dynamics in various ILs and discussed the effect of the heterogeneity of ILs.⁴³ Recently, Manna et al. investigated the intramolecular proton transfer of 1,8-dihydroxyanthraquinone in PILs and observed the solvent-viscosity-dependent backward intramolecular proton transfer.⁴⁴ According to these studies, it is expected that there should be an anomalous dynamics of solute molecules specific to PILs. At present, we have investigated the ESPT dynamics of 5CN2 and DCN2 in three PILs which are composed of triethylammonium ($N_{222}H^+$) and three different anions, trifluoromethanesulfonate ($CF_3SO_3^-$), methanesulfonate ($CH_3SO_3^-$), and trifluoroacetate (CF_3COO^-), by measuring steady-state and time-resolved fluorescence spectra. Since the pK_a values of conjugate acids of anions in aqueous solution are -12 (CF_3SO_3H), -2 (CH_3SO_3H), and 0.23 (CF_3COOH),⁴⁵ we expected that the dynamics of photoacids should be different; that is, an appearance of RO^-* may depend on the basicity of the anions. In this study, we have found that the pK_a value of conjugate acid of anion in aqueous solution is a good standard for the occurrence of PT. More interestingly, when the acidity of 5CN2 or DCN2 is larger than that of the conjugate acid of anion, an anomalous fluorescence band that is different from both ROH^* and RO^-* has appeared. The analysis of the fluorescence dynamics has revealed that this anomalous band is due to the intermediate species which may be composed of RO^-* with solvent anion.

2. EXPERIMENTAL SECTION

2.1. Materials. Figure 1 shows the structures of PILs and photoacids we used. 5-Cyano-2-naphthol (5CN2) and 5,8-

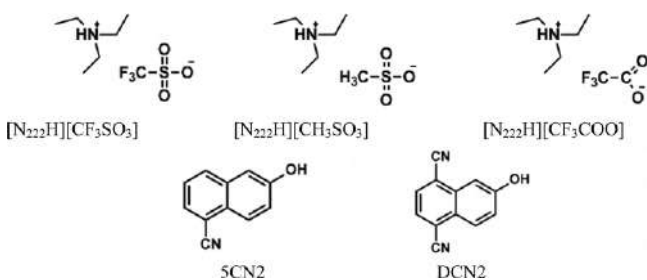


Figure 1. Structures of protic ionic liquids and cyano-substituted 2-naphthols we used.

dicyano-2-naphthol (DCN2) were synthesized according to refs 26 and 46–48. Reaction schemes are shown in the Supporting Information (Schemes S1 and S2). The crude products of 5CN2 and DCN2 were purified by sublimation and reprecipitation, respectively. All PILs were synthesized in our laboratory. Triethylamine, trifluoromethanesulfonic acid, methanesulfonic acid, and trifluoroacetic acid (guaranteed grade)

were purchased from Nakalai Tesque. Triethylamine was purified by distillation before use. To prepare the PILs, the corresponding acid was added dropwise to 1.1 equiv of triethylamine at 0 °C under Ar atmosphere. The ice bath was removed and the reaction mixture was stirred at room temperature for 3 h (in the case of $[N_{222}H][CF_3SO_3]$), overnight (in the case of $[N_{222}H][CH_3SO_3]$), or 8 h (in the case of $[N_{222}H][CF_3COO]$). In the cases of $[N_{222}H][CH_3SO_3]$ and $[N_{222}H][CF_3COO]$, crude products were purified by recrystallization from 1,2-dimethoxyethane at 213 K. The recrystallized samples were treated under vacuum at room temperature for 24 h to remove the residual solvent. Since $[N_{222}H][CF_3SO_3]$ was yellowish, it was treated by charcoal and successfully decolorized. The purities of these ionic liquids were confirmed by 1H and ^{13}C NMR spectroscopies. In the case of $[N_{222}H][CF_3SO_3]$, the purity was also checked by the fluorescence spectrum, and we confirmed that fluorescence from $[N_{222}H][CF_3SO_3]$ was negligible.

Before spectroscopic measurements, $[N_{222}H][CH_3SO_3]$ and $[N_{222}H][CF_3COO]$ were evacuated at room temperature, and $[N_{222}H][CF_3SO_3]$ was evacuated at 333 K. The level of water contamination was confirmed to be below 300 ppm by Karl Fischer titration. Values of water content of each sample are summarized in the Supporting Information (Table S1). After drying the PILs, a certain amount of 5CN2 or DCN2 was dissolved in each PIL in a glovebox, and the solution was enclosed in a 1 mm path length quartz cell used for the measurement.

2.2. Absorption and Fluorescence Measurements.

Absorption and fluorescence spectra were measured at room temperature by standard spectrometers (Shimadzu UV-2500PC and JASCO, FP-6500), respectively. For time-resolved fluorescence measurement, we used the same setups as described elsewhere.⁴⁹ Briefly, an excitation light of 800 nm from an amplified Ti:sapphire laser (Spectra Physics, Spitfire Xp) was converted to 340 nm (for 5CN2 measurements) or 370 nm (for DCN2 measurements) by an optical parametric amplifier (OPA; Spectra Physics, TOPAS-800C) and a BBO crystal. Fluorescence from a sample solution was detected by a streak camera (Hamamatsu, C4334) attached to a spectrometer (Princeton Instruments, Acton SP2150). A typical system response time was ca. 30 ps, which was enough to discuss the dynamics in this study. The color sensitivity and the time shift were corrected as was done previously.⁵⁰ All spectral measurements were conducted at 295 K.

3. RESULTS

3.1. Steady State Absorption and Fluorescence Spectra.

Figure 2 shows absorption spectra of (a) 5CN2 and (b) DCN2 in PILs. The spectral shapes of 5CN2 in three PILs were almost the same and were identical to those of ROH (the nondissociated form in the electronic ground state) reported previously.^{29,32} In the case of DCN2, the same can be said; that is, the spectral shapes in different PILs were almost the same. Therefore, we conclude that 5CN2 and DCN2 do not undergo PT in PILs in the ground states. The absorption peak positions of 5CN2 and DCN2 in $[N_{222}H][CH_3SO_3]$ and $[N_{222}H][CF_3COO]$ were relatively red-shifted to those in $[N_{222}H][CF_3SO_3]$ (see Table 1).

Figure 3 shows the steady-state fluorescence spectra of (a) 5CN2 and (b) DCN2 in PILs. As mentioned in the Introduction, the band around 360 nm of 5CN2 is the fluorescence from ROH^* and the band around 530 nm is the

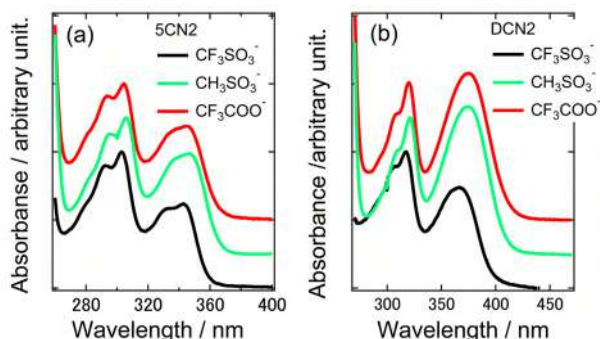


Figure 2. Absorption spectra of (a) 5CN2 and (b) DCN2. Each spectrum is normalized by the peak intensity around 300 nm and shown with an arbitrary vertical offset.

Table 1. Peak Positions of the Absorption (ν^{abs}) and of the Steady-State Fluorescence Spectrum ($\nu_{\text{p,ROH}^*}$, $\nu_{\text{p,Y}^*}$, $\nu_{\text{p,RO}^{-*}}$) of 5CN2 and DCN2^a

	ν^{abs}	$\nu_{\text{p,ROH}^*}$	$\nu_{\text{p,Y}^*}$	$\nu_{\text{p,RO}^{-*}}$	$\Delta\nu$
5CN2					
CF_3SO_3^-	29.15	25.98	—	—	3.17
CH_3SO_3^-	28.78	24.91	—	18.43	3.88
CF_3COO^-	28.92	24.50	20.80	18.16	4.42
DCN2					
CF_3SO_3^-	27.17	22.68	—	—	4.49
CH_3SO_3^-	26.60	21.21	18.50	16.31	5.39
CF_3COO^-	26.55	21.30	18.44	16.64	5.25

^a ν^{abs} is the absorption peak position of the lowest transition energy. $\Delta\nu$ is the Stokes shift calculated from $\Delta\nu = \nu^{\text{abs}} - \nu_{\text{p,ROH}^*}$ (unit 10^3 cm^{-1}).

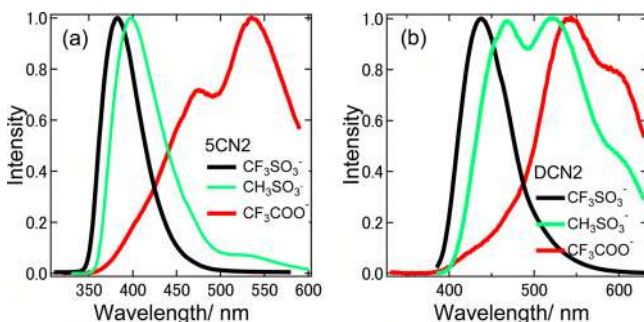


Figure 3. Steady-state fluorescence spectra of (a) 5CN2 and (b) DCN2. Each spectrum is normalized at the peak position of the maximum intensity.

fluorescence from RO^{-*} . For 5CN2, except in $[\text{N}_{222}\text{H}][\text{CF}_3\text{COO}]$, fluorescence from ROH^* was dominant. In $[\text{N}_{222}\text{H}][\text{CH}_3\text{SO}_3]$, weak fluorescence from RO^{-*} appeared, which indicates the occurrence of ESPT of 5CN2 in $[\text{N}_{222}\text{H}][\text{CH}_3\text{SO}_3]$. On the other hand, the fluorescence spectrum in $[\text{N}_{222}\text{H}][\text{CF}_3\text{COO}]$ was quite different from those in other PILs. The fluorescence from ROH^* almost disappeared and two bands appeared around 470 and 530 nm. The intensity of the band at the shorter wavelength decreased with an addition of water to the solution, while that of the longer wavelength increased with an addition of water (see Figure S1a). Considering the peak position,^{30–32} the band around 530 nm should be assigned to the fluorescence from RO^{-*} , while the band around 470 nm implies the presence of an unknown species. Hereafter we denote the fluorescent

species around 470 nm as Y^{-*} and expect it to be negatively charged since the fluorescence peak position is close to that of RO^{-*} .

For DCN2 in $[\text{N}_{222}\text{H}][\text{CF}_3\text{SO}_3]$, the fluorescence from ROH^* was dominant and no other species was observed. However, in $[\text{N}_{222}\text{H}][\text{CH}_3\text{SO}_3]$ and $[\text{N}_{222}\text{H}][\text{CF}_3\text{COO}]$, the fluorescence bands from Y^{-*} (around 520 nm) and RO^{-*} (around 600 nm) were apparent. Especially in $[\text{N}_{222}\text{H}][\text{CF}_3\text{COO}]$, the intensity of Y^{-*} was very strong and decreased with an addition of water as in the case of 5CN2 (see Figure S1b).

In order to obtain the fluorescence peak position of each component, the fluorescence spectra in Figure 3 were simulated by a sum of log-normal functions as follows:

$$I_{\text{fl}}(\nu) = \sum h_i \begin{cases} \exp[-\ln(2)\{\ln(1 + \alpha_i)/\gamma_i\}^2] & \alpha_i > -1 \\ 0 & \alpha_i \leq -1 \end{cases} \quad (1)$$

where $I_{\text{fl}}(\nu)$ is the fluorescence intensity as a function of wavenumber ν , $\alpha_i = 2\gamma_i(\nu - \nu_{\text{pi}})/\Delta_i$, h_i is the scaling factor, ν_{pi} is the peak position of the spectrum, γ_i is the asymmetric factor, and Δ_i is the bandwidth parameter. The suffix, i , denotes the chemical species. Typical examples of the spectral decomposition are shown in Figure S2. In the case of 5CN2 and DCN2 in $[\text{N}_{222}\text{H}][\text{CF}_3\text{COO}]$, since the intensity of ROH^* was too small, it was difficult to decompose the spectrum into three species. Therefore, we fixed the peak position of ROH^* to the value obtained by the analysis of the time-resolved spectrum of these species. Since the fluorescence from ROH^* was apparent in earlier delay time (~ 1 ns) after the photoexcitation (Figures 4c and 5b), the peak value of ROH^* was unambiguously determined as will be discussed in section 3.2. Table 1 summarizes peak positions of fluorescence bands together with the absorption peak positions of the lowest transition energy. In Table 1, the fluorescence Stokes shift for ROH^* ($\Delta\nu$) is also

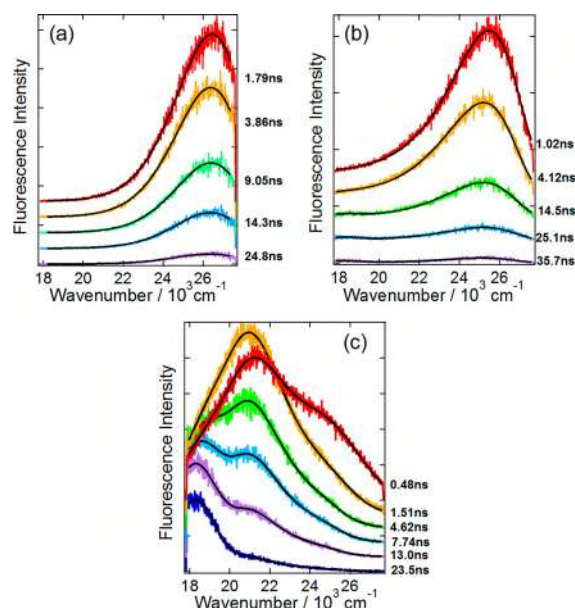


Figure 4. Time-resolved fluorescence spectra of 5CN2 in (a) $[\text{N}_{222}\text{H}][\text{CF}_3\text{SO}_3]$, (b) $[\text{N}_{222}\text{H}][\text{CH}_3\text{SO}_3]$, and (c) $[\text{N}_{222}\text{H}][\text{CF}_3\text{COO}]$. Each spectrum at different delay is shown with a different offset.

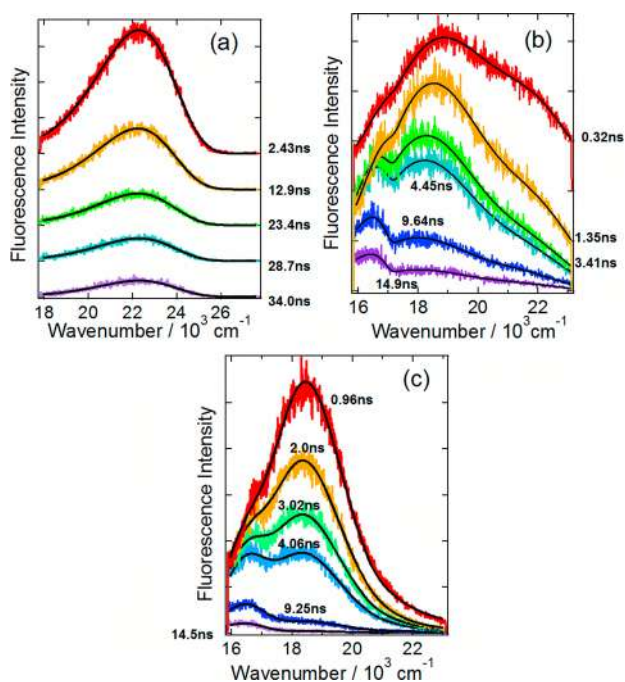


Figure 5. Time-resolved fluorescence spectra of DCN2 in (a) $[N_{222}H][CF_3SO_3]$, (b) $[N_{222}H][CH_3SO_3]$, and (c) $[N_{222}H][CF_3COO]$. Each spectrum at different delay is shown with a different offset.

calculated. With increasing the basicity of the anion, the Stokes shift increases in the case of 5CN2. Although in the case of DCN2 the value is not necessarily in the order of the basicity of anion, the values in $[N_{222}H][CH_3SO_3]$ and $[N_{222}H][CF_3COO]$ are larger than that in $[N_{222}H][CF_3SO_3]$. This indicates that the anion with larger basicity more strongly interacts in the excited state, probably with the hydroxyl group of cyanonaphthols.

3.2. Time-Resolved Fluorescence Spectra. Figure 4 shows time-resolved fluorescence spectra of 5CN2 in PILs. The horizontal scale of each part of Figure 4 is in wavenumbers, and the fluorescence at higher wavenumbers corresponds to that from ROH* (around 25 000 cm^{-1}). It is apparent that time-resolved spectra significantly depend on the solvent anion species. In the case of 5CN2 in $[N_{222}H][CF_3SO_3]$ (Figure 4a), only the fluorescence from ROH* was observed and no other species was apparent even if time passed by. This indicates that 5CN2 did not undergo ESPT in $[N_{222}H][CF_3SO_3]$, probably because the acidity of CF_3SO_3H ($pK_a = -12$) is larger than that of 5CN2 ($pK_a^* = -0.75$), and ROH* is not able to give protons to the surrounding solvent. In $[N_{222}H][CH_3SO_3]$ (Figure 4b), as expected from the steady-state spectrum in Figure 3a, fluorescence from RO* gradually increased over several nanoseconds after excitation, although the intensity of RO* was quite small. More interestingly, time-resolved fluorescence in $[N_{222}H][CF_3COO]$ showed the appearance and disappearance of a newly found species. Upon excitation, not only a fluorescence band from ROH* but also a new fluorescence band around 21 000 cm^{-1} emerged within 0.5 ns. Then this new fluorescence component Y* disappeared and the fluorescence from RO* increased by ~ 10 ns.

For DCN2 as shown in Figure 5, almost the same story can be true for the solution of $[N_{222}H][CF_3SO_3]$, where only the fluorescence from ROH* was observed. However, in $[N_{222}H][CF_3COO]$

and $[N_{222}H][CH_3SO_3]$, the contribution from Y* dramatically changed the time-resolved fluorescence spectra.

In order to extract the time profile of each component, the time dependent fluorescence spectrum was simulated by a sum of log-normal functions as was done for the steady state fluorescence spectrum (eq 1). In the case of time-resolved data, the parameters in the equation are expected to depend on the delay time after the photoexcitation. However, for the case where three fluorescence components exist, we have assumed that some parameters do not depend on the delay time since the number of the fitting parameters is too large. Fitting procedures for each combination of solute and solvent are as follows. For both 5CN2 and DCN2 in $[N_{222}H][CF_3SO_3]$ where only the fluorescence from ROH* was observed, the time dependent spectrum was once simulated by a single log-normal function assuming that all parameters were time dependent. Then the spectrum at each delay time was resimulated by fixing the parameters of γ and Δ to the averaged values over all the spectral data simulated. For 5CN2 in $[N_{222}H][CH_3SO_3]$ in which ROH* and RO* appeared, two log-normal functions were used to simulate the spectrum. Since the contribution of RO* was quite small, the parameters of ν_{pi} , Δ_i , and γ_i of RO* were fixed to the values determined at the longer delay time after the photoexcitation, where the fluorescence from RO* was dominant. Here the parameters of Δ_i and γ_i of ROH* were also fixed to the values determined in the earlier delay time neglecting the contributions of RO*. For 5CN2 in $[N_{222}H][CF_3COO]$ and DCN2 in $[N_{222}H][CH_3SO_3]$ and $[N_{222}H][CF_3COO]$, where three components are expected, three log-normal functions were used to simulate the spectrum. Since the rise of Y* and the decay of ROH* were very fast, we first determined the parameters related to these species by fitting the spectrum at earlier delay time (~ 1 ns) where fluorescence bands from ROH* and Y* were dominant. Then the spectrum at the longest delay time, where fluorescence bands from Y* and RO* were dominant, was simulated by using the parameters Δ_i and γ_i of ROH* determined in the earlier delay time. Finally, all time-dependent data were fitted by assuming that parameters of each species were time-independent except for the peak position of Y* and intensities of all species. The black solid lines in Figures 4 and 5 are the results of fitting, and the spectral simulation worked quite well in each case.

Time profiles of fluorescence intensities of species ROH*, Y*, and RO* evaluated by the integral of each fluorescence component are shown in Figures 6 and 7. The time profile of

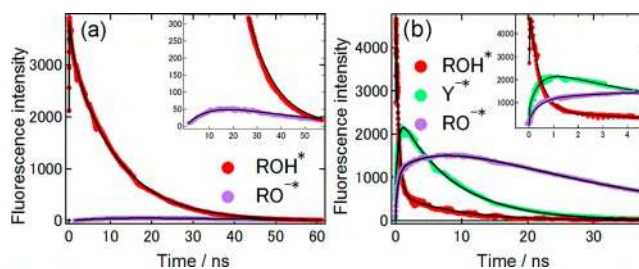


Figure 6. Time profiles of fluorescence intensity of 5CN2 in (a) $[N_{222}H][CH_3SO_3]$ and (b) $[N_{222}H][CF_3COO]$. Solid line is a fitting curve to a multiexponential function convoluted with an instrumental response function. Inset graph represents the fluorescence decay in early delay time.

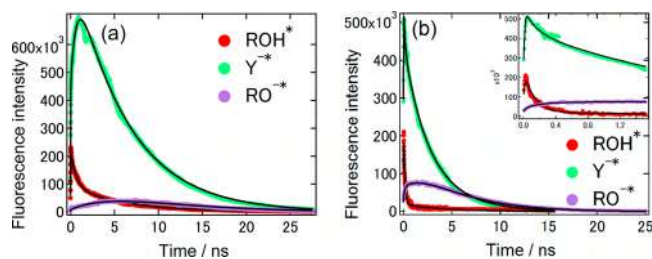


Figure 7. Time profile of fluorescence intensity of DCN2 in (a) $[N_{222}H][CH_3SO_3]$ and (b) $[N_{222}H][CF_3COO]$. Solid line is a fitting curve to a multiexponential function convoluted with an instrumental response function. Inset graph represents the fluorescence decay in early delay time.

each component was generally simulated by a multiexponential function (at most three exponents) as follows:

$$I_X(t) = A_1 e^{-k_1 t} + A_2 e^{-k_2 t} + A_3 e^{-k_3 t} \quad (2)$$

where $I_X(t)$ means the time profile of the integrated fluorescence intensity of molecular species X. Here X represents ROH^* , Y^{-*} , or RO^{-*} . In the cases of 5CN2 and DCN2 in $[N_{222}H][CF_3SO_3]$, the integrated intensity of ROH^* was simulated by a single exponential decay (not shown in Figures 6 and 7). In the case of 5CN2 in $[N_{222}H][CH_3SO_3]$, as shown in Figure 6a, ROH^* showed a double exponential decay with a small contribution of the very fast component, and a large contribution of the slower component (see Table 2). On the other hand, RO^{-*} kinetics showed an exponential rise and decay (see inset graph in Figure 6a). Since the time constant of the rise of RO^{-*} was similar to that of the slow decay of ROH^* , we fit these two profiles by linking this time constant. The results of the fittings are shown by the solid lines in Figure 6a. The fitting almost captures the time profile of each species, although a slight deviation is noticed in the longer time region of ROH^* . In the cases of 5CN2 in $[N_{222}H][CF_3COO]$ and DCN2 in $[N_{222}H][CH_3SO_3]$ and $[N_{222}H][CF_3COO]$ (Figures 6b and 7), the fastest decay constant of ROH^* seems to be equal to the rise time constant of Y^{-*} , and the decay time of Y^{-*} to be equal to the rise time constant of RO^{-*} . Considering these factors, we fit these profiles to eq 2 by linking the three time constants. The parameters obtained by the fitting are summarized in Tables 2 (5CN2) and 3 (DCN2).

4. DISCUSSION

4.1. Modeling of Reaction Kinetics. In this section, we discuss the reaction scheme of each case from the observed fluorescence kinetics in section 3. Scheme 1a shows a standard PT reaction of 5CN2 as reported previously.³² In the present work, the reaction of 5CN2 in $[N_{222}H][CH_3SO_3]$ corresponds

to this case, although the chemical species of the proton acceptor is not clear at present. According to Scheme 1a, the time profile of the concentration of each species is given as follows by assuming that $k_d, k_p[H^+] \gg k_0, k'_0$:³²

$$[ROH^*] = [ROH^*]_0 \frac{k_d}{k_1} \left\{ \exp(-k_1 t) + \frac{k_p[H^+]}{k_d} \exp(-k_s t) \right\} \quad (3)$$

$$[RO^{-*}] = [ROH^*]_0 \frac{k_d}{k_1} \{-\exp(-k_1 t) + \exp(-k_s t)\} \quad (4)$$

where

$$k_1 = k_p[H^+] + k_d \quad (5)$$

$$k_s = \frac{k'_0 k_d + k_0 k_p[H^+]}{k_d + k_p[H^+]} \quad (6)$$

The equation of RO^{-*} (eq 4) successfully describes the experimentally observed fluorescence intensity where the rise and decay amplitudes are the same. The observed rise component corresponds to the PT rate (0.09 ns^{-1}) in $[N_{222}H][CH_3SO_3]$, which is quite slow in comparison with that in the aqueous system (0.07 ps^{-1}).²⁷ On the other hand, there are some discrepancies in the experimentally observed fluorescence intensity dynamics of ROH^* from eq 3. In experimental observation, as is shown in Figure 6a, a very fast decay component (1.36 ns^{-1}) was observed for ROH^* . We are not sure of the origin of this component, which may be related to the solvent relaxation process specific to PILs. In addition, the slowest decay component (0.03 ns^{-1}) corresponding to the decay kinesis of RO^{-*} was absent in the kinetics of ROH^* . This may be ascribed to the small contribution of the backward PT, and to the difficulty of the spectral separation of very weak intensities by log-normal functions.

For the cases where three species exist, we consider Scheme 1b as the most general one. According to Scheme 1b, rate equations are given as follows:

$$\begin{aligned} \frac{d}{dt}[ROH^*] &= -(k_{d1} + k_0 + k_{d3})[ROH^*] \\ &+ k_{p1}[H^+][Y^{-*}] + k_{p3}[H^+][RO^{-*}] \end{aligned} \quad (7)$$

$$\begin{aligned} \frac{d}{dt}[Y^{-*}] &= k_{d1}[ROH^*] - (k_{p1}[H^+] + k_{d2} + k_{0Y})[Y^{-*}] \\ &+ k_{p2}[RO^{-*}] \end{aligned} \quad (8)$$

Table 2. Rate Constants of ESPT of 5CN2 Determined by Multiexponential Fitting of the Time Profile of Fluorescence Intensity of Each Species^a

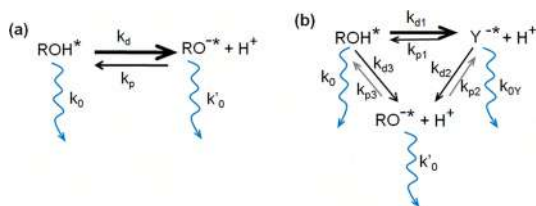
anion	species	A_1	A_2	A_3	k_1/ns^{-1}	k_2/ns^{-1}	k_3/ns^{-1}
$CF_3SO_3^-$	ROH^*	1			0.13		
	RO^{-*}	0	-0.26	0.26			
$CH_3SO_3^-$	ROH^*	1	6.28	0	1.36	0.09	0.03
	Y^{-*}	-0.41	0.54	0.04			
	RO^{-*}	-0.22	-0.34	0.59			
CF_3COO^-	ROH^*	1	0.15	0	2.40	0.14	0.03
	Y^{-*}	-0.41	0.54	0.04			
	RO^{-*}	-0.22	-0.34	0.59			

^aThe amplitude parameters are normalized by the value of the fastest component of ROH^* .

Table 3. Rate Constants of ESPT of DCN2 Determined by Multiexponential Fitting of the Time Profile of Fluorescence Intensity of Each Species^a

anion	species	A ₁	A ₂	A ₃	k ₁ /ns ⁻¹	k ₂ /ns ⁻¹	k ₃ /ns ⁻¹
CF ₃ SO ₃ ⁻	ROH*	1			0.09		
CH ₃ SO ₃ ⁻	ROH*	1	0.71	0	1.60	0.16 ₃	0.15 ₈
	Y ^{-*}	-3.68	7.12	0.00			
	RO ^{-*}	0	-22.8	22.9			
CF ₃ COO ⁻	ROH*	1	0	0.09	7.12	0.41	0.22
	Y ^{-*}	0.51	1.66	0.46			
	RO ^{-*}	-0.13	-0.72	1.04			

^aThe amplitude parameters are normalized by the value of the fastest component of ROH*.

Scheme 1. ESPT Schemes of (a) 5CN2 in [N₂₂₂H][CH₃SO₃] and (b) 5CN2 in [N₂₂₂H][CF₃COO], DCN2 in [N₂₂₂H][CH₃SO₃], and DCN2 in [N₂₂₂H][CF₃COO]

$$\frac{d}{dt}[\text{RO}^{-*}] = k_{d3}[\text{ROH}^*] + k_{d2}[\text{Y}^{-*}] - (k_{p3}[\text{H}^+] + k_{p2} + k'_0)[\text{RO}^{-*}] \quad (9)$$

The general solutions of these equations are quite complicated and useless. We have made some simplifications to extract the essential parts of the reaction. First, we have neglected the backward reactions from RO^{-*} ($k_{p3} = k_{p2} = 0$). Since the appearance of RO^{-*} from Y^{-*} or ROH* was fast, we have neglected the decay process of Y^{-*} and ROH* except for the reaction paths to RO^{-*}; i.e. k_0 and k_{0Y} were neglected. Further, we have assumed that the concentration of proton ($[\text{H}^+]$) is time-independent, that the initial concentrations of Y^{-*} and RO^{-*} are zero, and that $k_{d1} \gg k_{d2}$, k_{d3} , $k_{p1} \gg k'_0$. Based on these assumptions, eqs 7, 8, and 9 are approximately solved to give the following answers:

$$[\text{ROH}^*] = [\text{ROH}^*]_0 \frac{1}{k_{d1} + k_{p1}[\text{H}^+]} \{k_{p1}[\text{H}^+] \exp(-k_{d2}t) + k_{d1} \exp(-k_m t)\} \quad (10)$$

$$[\text{Y}^{-*}] = [\text{ROH}^*]_0 \frac{k_{d1}}{k_{d1} + k_{p1}[\text{H}^+]} \{ \exp(-k_{d2}t) - \exp(-k_m t) \} \quad (11)$$

$$[\text{RO}^{-*}] = [\text{ROH}^*]_0 \{ P \exp(-k'_0 t) + Q \exp(-k_{d2}t) + R \exp(-k_m t) \} \quad (12)$$

where

$$k_m = k_{d1} + k_{d3} + k_{p1}[\text{H}^+] \quad (13)$$

$$P = -Q - R \quad (14)$$

$$Q = \frac{k_{d3}k_{p1}[\text{H}^+] + k_{d1}k_{d2}}{(k_{d1} + k_{p1}[\text{H}^+])(k'_0 - k_{d2})} \quad (15)$$

$$R = \frac{k_{d1}(k_{d3} - k_{d2})}{(k_{d1} + k_{p1}[\text{H}^+])(k'_0 - k_m)} \quad (16)$$

The fitting result for 5CN2 in [N₂₂₂H][CF₃COO] seems to correspond to the model case calculated here, although there are some discrepancies of the coefficients. In this case, the fastest rate constant corresponds to k_m ($=2.40 \text{ ns}^{-1}$), and the second fastest rate constant corresponds to k_{d2} ($=0.14 \text{ ns}^{-1}$). For other cases, similar correspondence should be applicable, although the discrepancies from the model are more apparent.

4.2. Assignment of the New Component. From the analysis of the kinetics, Y^{-*} is considered to be a reaction intermediate. Furthermore, the stability of Y^{-*} is strongly affected by water contaminated in PILs. As is mentioned in the Introduction, the pK_a* values of 5CN2 and DCN2 in aqueous solution have been reported to be -0.75 and -4.5, respectively.^{29,31} The pK_a values of conjugate acids of the anions used here are -12 (CF₃SO₃H), -2 (CH₃SO₃H), and 0.23 (CF₃COOH).⁴⁵ If this acidity holds in PILs, CF₃COO⁻ can be a proton acceptor from 5CN2, and CH₃SO₃⁻ and CF₃COO⁻ can be proton acceptors from DCN2. These cases for the prediction of the occurrence of PT correspond to the experimental cases where Y^{-*} is observed. Therefore, we consider that Y^{-*} is the species which results from the direct PT from the solute to the solvent anion, and the complex RO^{-*} with the protonated anion. The complex is temporally solvated and stabilized by the surrounding cation. Then the question is, what is the origin of the fluorescence band assigned to RO^{-*}? Since the species generally appeared after the formation of Y^{-*}, we consider this species is RO^{-*} which has no specific interaction with a protonated conjugate acid. The species may be derived from the dissociation of the complex Y^{-*} or from the direct PT of ROH* to H₂O contaminated in PIL. As mentioned in the discussion of the steady-state fluorescence, the intensity of Y^{-*} decreased and that of RO^{-*} increased with an addition of water. The spectral position of RO^{-*} is close to that in aqueous solutions. All these facts support the idea.

Since the proton transfer reaction is a short-ranged one, the formation of the encounter complex can be rate limiting. If the formation of the encounter complex is diffusion controlled, the rate coefficient k_D (s⁻¹) can be estimated to be⁵¹

$$k_D = \frac{2}{3} \frac{k_B T}{\eta} [\text{M}] \quad (17)$$

where k_B is the Boltzmann constant, T is the absolute temperature, η is the viscosity of the solvent, and $[\text{M}]$ is the concentration of the proton acceptor. If the proton acceptor is the anion, the value of k_D is estimated to be on the order of

10^{-1} ns^{-1} , considering that the concentration of anion in $[\text{N}_{222}\text{H}][\text{CH}_3\text{SO}_3]$ is about 5 M and that the viscosity of $[\text{N}_{222}\text{H}][\text{CH}_3\text{SO}_3]$ at room temperature is 100 mPa s.⁸ The value is close to k_1 estimated from the time profile of the fluorescence, indicating the validity of assignment of the species Y^* .

Before concluding the paper, we mention the proton transfer dynamics observed for 5CN2 in $[\text{N}_{222}\text{H}][\text{CH}_3\text{SO}_3]$. According to the discussion in the previous paragraph, CH_3SO_3^- is not the proton acceptor from 5CN2. Therefore, water contained in the PIL should be the proton acceptor in this case. By roughly estimating the water concentration (7.4 mol m^{-3}) and the viscosity of the PILs (100 mPa s),⁸ the value of k_D is estimated to be $1.2 \times 10^{-4} \text{ ns}^{-1}$. This value is about 10^4 times slower than the experimental value k_{d1} . A plausible explanation for this is as follows. When the concentration of water is low, a water molecule locates between the anion and the cation of a PIL due to the existence of the preferred interaction sites for water in PILs.^{8,52} The large difference between the theoretical and experimental values may reflect such heterogeneously located water molecules. Currently we are analyzing the effect of water on the reactivity of anion PILs in more detail by changing the concentration of water, of which the results will appear in the future.

5. CONCLUSIONS

In this study, we investigated the ESPT dynamics of 5CN2 and DCN2 in three different PILs by steady-state and time-resolved fluorescence measurements. To sum up briefly, the occurrence of PT of these photoacids in PILs was simply explained by the basicity of the anions in the aqueous solution. In $[\text{N}_{222}\text{H}][\text{CF}_3\text{SO}_3]$ fluorescence from RO^* was not observed for both 5CN2 and DCN2, indicating that ESPT did not occur in $[\text{N}_{222}\text{H}][\text{CF}_3\text{SO}_3]$. For 5CN2 in $[\text{N}_{222}\text{H}][\text{CH}_3\text{SO}_3]$, we confirmed the fluorescence from RO^* by the steady-state and time-resolved fluorescence measurements. Most interestingly, in the case of 5CN2 in $[\text{N}_{222}\text{H}][\text{CF}_3\text{COO}]$ and DCN2 in $[\text{N}_{222}\text{H}][\text{CH}_3\text{SO}_3]$ and $[\text{N}_{222}\text{H}][\text{CF}_3\text{COO}]$, a new fluorescence component (Y^*) around 470 nm (5CN2) and 520 nm (DCN2) was observed. According to the analysis of the time-dependent fluorescence spectra, we proposed plausible reaction schemes in each case. From these schemes and the rate coefficients, it was suggested that Y^* was generated by proton dissociation of ROH^* to the anion, and the complex RO^* with the protonated anion. The kinetics of Y^* depended on the acidity of PILs and solute molecules.

■ ASSOCIATED CONTENT

Supporting Information

The Supporting Information is available free of charge on the ACS Publications website at DOI: 10.1021/acs.jpcc.7b03658.

Amount of water in PILs, syntheses of 5CN2 and DCN2, steady-state fluorescence spectra of 5CN2 and DCN2 in three PILs with a certain amount of water, and spectral decomposition of steady-state fluorescence spectrum of 5CN2 and DCN2 in $[\text{N}_{222}\text{H}][\text{CF}_3\text{COO}]$ (PDF)

■ AUTHOR INFORMATION

Corresponding Author

*E-mail: yokimura@mail.doshisha.ac.jp. Tel.: +81-774-65-6561. Fax: +81-774-65-6801.

ORCID

Yoshifumi Kimura: 0000-0002-2248-9973

Notes

The authors declare no competing financial interest.

■ ACKNOWLEDGMENTS

This work is supported by the MEXT-Supported Program for the Strategic Research Foundation at Private Universities 2015–2019 (S1511025).

■ REFERENCES

- (1) Tokuda, H.; Hayamizu, K.; Ishii, K.; Susan, M. A. B. H.; Watanabe, M. Physicochemical Properties and Structures of Room Temperature Ionic Liquids. 1. Variation of Anionic Species. *J. Phys. Chem. B* **2004**, *108*, 16593–16600.
- (2) Ab Rani, M. A.; Brant, A.; Crowhurst, L.; Dolan, A.; Lui, M.; Hassan, N. H.; Hallett, J. P.; Hunt, P. A.; Niedermeyer, H.; Perez-Arlandis, J. M.; et al. Understanding the Polarity of Ionic Liquids. *Phys. Chem. Chem. Phys.* **2011**, *13*, 16831–16840.
- (3) Giammanco, C. H.; Kramer, P. L.; Fayer, M. D. Ionic Liquid versus Li+ Aqueous Solutions: Water Dynamics near Bistriflimide Anions. *J. Phys. Chem. B* **2016**, *120*, 9997–10009.
- (4) Majhi, D.; Pabbathi, A.; Sarkar, M. Probing the Aggregation Behavior of Neat Imidazolium-Based Alkyl Sulfate (Alkyl = Ethyl, Butyl, Hexyl, and Octyl) Ionic Liquids through Time Resolved Fluorescence Anisotropy and NMR and Fluorescence Correlation Spectroscopy Study. *J. Phys. Chem. B* **2016**, *120*, 193–205.
- (5) Fumino, K.; Reimann, S.; Ludwig, R. Probing Molecular Interaction in Ionic Liquids by Low Frequency Spectroscopy: Coulomb Energy, Hydrogen Bonding and Dispersion Forces. *Phys. Chem. Chem. Phys.* **2014**, *16*, 21903–21929.
- (6) Tsuge, S.; Uno, K.; Hanasaki, T.; Takekiyo, T.; Abe, H.; Yoshimura, Y. Structural and Conformational Properties of the Quaternary Ammonium Ionic Liquid N,N-Diethyl-N-Methyl-N-(2-Methoxyethyl) Ammonium Iodide. *J. Mol. Struct.* **2014**, *1060*, 208–214.
- (7) Endo, T.; Kato, T.; Nishikawa, K. Effects of Methylation at the 2 Position of the Cation Ring on Phase Behaviors and Conformational Structures of Imidazolium-Based Ionic Liquids. *J. Phys. Chem. B* **2010**, *114*, 9201–9208.
- (8) Greaves, T. L.; Drummond, C. J. Protic Ionic Liquids: Evolving Structure–Property Relationships and Expanding Applications. *Chem. Rev.* **2015**, *115*, 11379–11448.
- (9) Belieres, J.-P.; Angell, C. A. Protic Ionic Liquids: Preparation, Characterization, and Proton Free Energy Level Representation. *J. Phys. Chem. B* **2007**, *111*, 4926–4937.
- (10) Er, H.; Wang, H. Properties of Protic Ionic Liquids Composed of N-Alkyl (=Hexyl, Octyl and 2-Ethylhexyl) Ethylenediaminum Cations with Trifluoromethanesulfonate and Trifluoroacetate Anion. *J. Mol. Liq.* **2016**, *220*, 649–656.
- (11) Thawarkar, S.; Khupse, N. D.; Kumar, A. Solvent-Mediated Molar Conductivity of Protic Ionic Liquids. *Phys. Chem. Chem. Phys.* **2015**, *17*, 475–482.
- (12) Shmukler, L. E.; Gruzdev, M. S.; Kudryakova, N. O.; Fadeeva, Yu. A.; Kolker, A. M.; Safonova, L. P. Thermal Behavior and Electrochemistry of Protic Ionic Liquids Based on Triethylamine with Different Acids. *RSC Adv.* **2016**, *6*, 109664–109671.
- (13) Vogl, T.; Goodrich, P.; Jacquemin, J.; Passerini, S.; Balducci, A. The Influence of Cation Structure on the Chemical–Physical Properties of Protic Ionic Liquids. *J. Phys. Chem. C* **2016**, *120*, 8525–8533.
- (14) Fumino, K.; Fossog, V.; Wittler, K.; Hempelmann, R.; Ludwig, R. Dissecting Anion–Cation Interaction Energies in Protic Ionic Liquids. *Angew. Chem., Int. Ed.* **2013**, *52*, 2368–2372.
- (15) Zentel, T.; Kühn, O. A network Approach to Unravel Correlated Ion Pair Dynamics in Protic Ionic Liquids. The Case of Triethylammonium Nitrate. *J. Mol. Liq.* **2017**, *226*, 56–62.

- (16) Docampo-Álvarez, B.; Gómez-González, V.; Méndez-Morales, T.; Carrete, J.; Rodríguez, J. R.; Cabeza, Ó.; Gallego, L. J.; Varela, L. M. Mixtures of Protic Ionic Liquids and Molecular Cosolvents: A Molecular Dynamics Simulation. *J. Chem. Phys.* **2014**, *140*, 214502.
- (17) Sun, X.; Cao, B.; Zhou, X.; Liu, S.; Zhu, X.; Fu, H. Theoretical and Experimental Studies on Proton Transfer in Acetate-Based Protic Ionic Liquids. *J. Mol. Liq.* **2016**, *221*, 254–261.
- (18) Watanabe, H.; Doi, H.; Saito, S.; Matsugami, M.; Fujii, K.; Kanzaki, R.; Kameda, Y.; Umebayashi, Y. Hydrogen Bond in Imidazolium Based Protic and Aprotic Ionic Liquids. *J. Mol. Liq.* **2016**, *217*, 35–42.
- (19) Huang, Y.; Zhou, G.; Li, Y.; Yang, Z.; Shi, M.; Wang, X.; Chen, X.; Zhang, F.; Li, W. Molecular Dynamics Simulations of Temperature-Dependent Structures and Dynamics of Ethylammonium Nitrate Protic Ionic Liquid: The Role of Hydrogen Bond. *Chem. Phys.* **2016**, *472*, 105–111.
- (20) Murphy, T.; Varela, L. M.; Webber, G. B.; Warr, G. G.; Atkin, R. Nanostructure–Thermal Conductivity Relationships in Protic Ionic Liquids. *J. Phys. Chem. B* **2014**, *118*, 12017–12024.
- (21) Yaghini, N.; Garaga, M. N.; Martinelli, A. Transport Properties, Local Coordination, and Thermal Stability of the Water/Diethylmethylammonium Methanesulfonate Binary System. *Fuel Cells* **2016**, *16* (1), 46–54.
- (22) Davidowski, S. K.; Thompson, F.; Huang, W.; Hasani, M.; Amin, S. A.; Angell, C. A.; Yarger, J. L. NMR Characterization of Ionicity and Transport Properties for a Series of Diethylmethylamine Based Protic Ionic Liquids. *J. Phys. Chem. B* **2016**, *120*, 4279–4285.
- (23) Hasani, M.; Yarger, J. L.; Angell, C. A. On the Use of a Protic Ionic Liquid with a Novel Cation to Study Anion Basicity. *Chem. - Eur. J.* **2016**, *22*, 13312–13319.
- (24) Martinelli, A. Conformational Changes and Phase Behaviour in the Protic Ionic Liquid 1-Ethylimidazolium Bis-(trifluoromethylsulfonyl)imide in the Bulk and Nano-Confined State. *Eur. J. Inorg. Chem.* **2015**, *2015*, 1300–1308.
- (25) Watanabe, H.; Doi, H.; Saito, S.; Sadakane, K.; Fujii, K.; Kanzaki, R.; Kameda, Y.; Umebayashi, Y. Raman Spectroscopic Speciation Analyses and Liquid Structures by High-Energy X-ray Total Scattering and Molecular Dynamics Simulations for N-methylimidazolium-Based Protic Ionic Liquids. *Bull. Chem. Soc. Jpn.* **2016**, *89*, 965–972.
- (26) Tolbert, L. M.; Haubrich, J. E. Photoexcited Proton Transfer from Enhanced Photoacids. *J. Am. Chem. Soc.* **1994**, *116*, 10593–10600.
- (27) Huppert, D.; Tolbert, L. M.; Linares-Samaniego, S. Ultrafast Excited-State Proton Transfer from Cyano-Substituted 2-Naphthols. *J. Phys. Chem. A* **1997**, *101*, 4602–4605.
- (28) Agmon, N.; Rettig, W.; Groth, C. Electronic Determinants of Photoacidity in Cyanonaphthols. *J. Am. Chem. Soc.* **2002**, *124*, 1089–1096.
- (29) Nunes, R. M. D.; Arnaut, L. G.; Solntsev, K. M.; Tolbert, L. M.; Formosinho, S. J. Excited-State Proton Transfer in Gas-Expanded Liquids: The Roles of Pressure and Composition in Supercritical CO₂/Methanol Mixtures. *J. Am. Chem. Soc.* **2005**, *127*, 11890–11891.
- (30) Solntsev, K. M.; Huppert, D.; Agmon, N. Photochemistry of “Super”-Photoacids. Solvent Effects. *J. Phys. Chem. A* **1999**, *103*, 6984–6997.
- (31) Solntsev, K. M.; Huppert, D.; Agmon, N.; Tolbert, L. M. Photochemistry of “Super” Photoacids. 2. Excited-State Proton Transfer in Methanol/Water Mixtures. *J. Phys. Chem. A* **2000**, *104*, 4658–4669.
- (32) Kobayashi, I.; Terazima, M.; Kimura, Y. Study of the Excited-State Proton-Transfer Reaction of 5-Cyano-2-naphthol in Sub- and Supercritical Water. *J. Phys. Chem. B* **2012**, *116*, 1043–1052.
- (33) Kobayashi, I.; Terazima, M.; Kimura, Y. Correction to “Study of the Excited State Proton Transfer Reaction of 5-Cyano-2-naphthol in Sub- and Supercritical Water. *J. Phys. Chem. B* **2012**, *116*, 7604–7604.
- (34) Ryan, E. T.; Xiang, T.; Johnston, K. P.; Fox, M. A. Excited-State Proton Transfer Reactions in Subcritical and Supercritical Water. *J. Phys. Chem.* **1996**, *100*, 9395–9402.
- (35) Cohen, B.; Huppert, D. Evidence for a Continuous Transition from Nonadiabatic to Adiabatic Proton Transfer Dynamics in Protic Liquids. *J. Phys. Chem. A* **2001**, *105*, 2980–2988.
- (36) Cohen, B.; Leiderman, P.; Huppert, D. Effect of Temperature and Pressure on Proton Transfer Rate from a Photoacid to Ethanol Solution. *J. Lumin.* **2003**, *102–103*, 676–681.
- (37) Genosar, L.; Leiderman, P.; Koifman, N.; Huppert, D. Effect of Pressure on the Proton-Transfer Rate from a Photoacid to a Solvent. 2. DCN2 in Propanol. *J. Phys. Chem. A* **2004**, *108*, 309–319.
- (38) Genosar, L.; Lasitza, T.; Gepshtein, R.; Leiderman, P.; Koifman, N.; Huppert, D. Effect of Pressure on the Proton Transfer Rate from a Photoacid to a Solvent. 4. Photoacids in Methanol. *J. Phys. Chem. A* **2005**, *109*, 4852–4861.
- (39) Gould, E.-A.; Popov, A. V.; Tolbert, L. M.; Presiado, I.; Erez, Y.; Huppert, D.; Solntsev, K. M. Excited-State Proton Transfer in N-methyl-6-hydroxyquinolinium salts: Solvent and Temperature Effects. *Phys. Chem. Chem. Phys.* **2012**, *14*, 8964–8973.
- (40) Noda, A.; Susan, M. A. B. H.; Kudo, K.; Mitsushima, S.; Hayamizu, K.; Watanabe, M. Brønsted Acid-Base Ionic Liquids as Proton-Conducting Nonaqueous Electrolytes. *J. Phys. Chem. B* **2003**, *107*, 4024–4033.
- (41) Stoimenovski, J.; Izgorodina, E. I.; MacFarlane, D. R. Ionicity and Proton Transfer in Protic Ionic Liquids. *Phys. Chem. Chem. Phys.* **2010**, *12*, 10341–10347.
- (42) Bhattacharya, B.; Samanta, A. Excited-State Proton-Transfer Dynamics of 7-Hydroxyquinoline in Room Temperature Ionic Liquids. *J. Phys. Chem. B* **2008**, *112*, 10101–10106.
- (43) Kimura, Y.; Fukuda, M.; Suda, K.; Terazima, M. Excited State Intramolecular Proton Transfer Reaction of 4'-N, N-Diethylamino-3-hydroxyflavone and Solvation Dynamics in Room Temperature Ionic Liquids Studied by Optical Kerr Gate Fluorescence Measurement. *J. Phys. Chem. B* **2010**, *114*, 11847–11858.
- (44) Manna, A.; Sayed, M.; Kumar, A.; Pal, H. Atypical Energetic and Kinetic Course of Excited-State Intramolecular Proton Transfer (ESIPT) in Room-Temperature Protic Ionic Liquids. *J. Phys. Chem. B* **2014**, *118*, 2487–2498.
- (45) Kano, K. *Theory of Organic Reaction*; Sankyo Publishing: Tokyo, 2006.
- (46) Aravinda Reddy, P.; Babul Reddy, A.; Ramachandra Reddy, G.; Subbarami Reddy, N. Suzuki-Miyaura Cross-Coupling Reaction of Naphthyl Triflate with Indole Boronic Acids Catalyzed by a Recyclable Polymer-Supported N-Heterocyclic Carbene-Palladium Complex Catalyst: Synthesis of Naphthalene-Linked Bis-Heterocycles. *J. Heterocyclic Chem.* **2013**, *50*, 1451–1456.
- (47) Jacobs, S. A.; Harvey, R. G. Synthesis of a conjugated nitrile from a benzylic ketone via a cyanotrimethylsilane adduct: 3,4-dihydro-6-methoxynaphthalene-1-carbonitrile. *J. Org. Chem.* **1983**, *48*, 5134–5135.
- (48) Gingrich, D. E.; Lisko, J. G.; Curry, M. A.; Cheng, M.; Quail, M.; Lu, L.; Wan, W.; Albom, M. S.; Angeles, T. S.; Aimone, L. D.; et al. Discovery of an Orally Efficacious Inhibitor of Anaplastic Lymphoma Kinase. *J. Med. Chem.* **2012**, *55*, 4580–4593.
- (49) Kimura, Y.; Suda, K.; Shibuya, M.; Yasaka, Y.; Ueno, M. Excitation Wavelength Dependence of the Solvation Dynamics of 4-N, N-Diethylamino-3-methoxyflavon in Ionic Liquids. *Bull. Chem. Soc. Jpn.* **2015**, *88*, 939–945.
- (50) Gardecki, J. A.; Maroncelli, M. Set of Secondary Emission Standards for Calibration of the Spectral Responsivity in Emission Spectroscopy. *Appl. Spectrosc.* **1998**, *52*, 1179–1189.
- (51) See, e.g.: Rice, S. A. *Comprehensive Chemical Kinetics: Diffusion Limited Reaction*; Bamford, C. H., Tipper, C. F. H., Compton, R. G., Eds.; Elsevier Science: Amsterdam, Netherlands, 1985.
- (52) Yaghini, N.; Nordstierna, L.; Martinelli, A. Effect of Water on the Transport Properties of Protic and Aprotic Imidazolium Ionic Liquids- an Analysis of Self-Diffusivity, Conductivity, and Proton Exchange Mechanism. *Phys. Chem. Chem. Phys.* **2014**, *16*, 9266–9275.

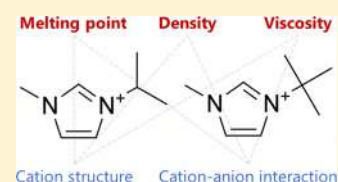
Structure–Property Relationship for 1-Isopropyl-3-methylimidazolium- and 1-*tert*-Butyl-3-methylimidazolium-Based Ionic Liquids: Thermal Properties, Densities, Viscosities, and Quantum Chemical Calculations

Takatsugu Endo,*^{ORCID} Kei Sakaguchi, Kazuki Higashihara, and Yoshifumi Kimura^{ORCID}

Department of Molecular Chemistry and Biochemistry, Faculty of Science and Engineering, Doshisha University, 1-3 Tatara Miyakodani, Kyotanabe-City, Kyoto 610-0394, Japan

Supporting Information

ABSTRACT: We systematically analyzed the thermal phase behaviors (phase change and thermal decomposition temperatures), densities, and viscosities of 1-isopropyl-3-methylimidazolium ($[iC_3mim]^+$)- and 1-*tert*-butyl-3-methylimidazolium ($[tC_4mim]^+$)-based ionic liquids (ILs) with $[I]^-$, $[PF_6]^-$, bis(fluorosulfonyl)imide, bis(trifluoromethylsulfonyl)imide, and bis(pentafluoroethylsulfonyl)imide counterions. The results were compared to those for ILs based on the corresponding linear alkyl imidazolium cations (1-methyl-3-propylimidazolium and 1-butyl-3-methylimidazolium). Our results revealed that the melting points of the branched ILs are always higher than those of the linear ILs. The densities of $[tC_4mim]X$ are higher than those of the linear ILs, which is somewhat counterintuitive when considering previously reported molecular liquid data. Using the van der Waals volume data estimated in this work, the fractional free volumes of the ILs were estimated. This revealed that the linear and branched ILs have largely similar void space values in the liquid state. The viscosities of $[tC_4mim]X$ are higher than those of the linear ILs, while those of $[iC_3mim]X$ are comparable. To better understand the structure–property relationship for the branched ILs, density functional theory calculations were performed for the ions in the gas phase. The structure–property relationship of the branched ILs is discussed in terms of bulkiness, conformational entropy, structural symmetry, and cation–anion interaction changes.



1. INTRODUCTION

Ionic liquids (ILs) can be defined as salts that are liquids around room temperature, even though there are still arguments on the definition of ILs.¹ Owing to their ionic nature, ILs can show some characteristic properties that are not normally observable in molecular liquids,² e.g., negligible vapor pressure and flammability, high thermal/chemical/electrochemical stability, and unique solubility (e.g., immiscibility with water). Furthermore, the high tunability of their physicochemical properties is an outstanding characteristic of ILs. A vast number of ILs can be formed by appropriately selecting the ion structures and cation/anion combinations, e.g., ions with large size and high flexibility.³ Owing to this high tunability, ILs are becoming a potential candidate for electrolytes,⁴ lubricants,⁵ biomass processing agents,⁶ drug delivery vehicles,⁷ protein storage media,⁸ among others.

Changing the length of the linear alkyl side chain in the IL cation is synthetically facile and significantly alters its physicochemical properties. This is the most common method for tuning the properties of ILs, and numerous examples of ILs with different alkyl chain lengths and positions have been reported. It is known that, except methyl group, the melting point of ILs presents a V-shape profile,^{9,10} while the viscosity decreases monotonically.¹¹ An intriguing feature of the presence of long alkyl chains is that it induces structural change at the nanolevel.^{2,12} In such ILs (e.g., 1-alkyl-3-methylimidazolium-

based ILs), nanostructural phase separation can occur between the polar (localized charge, dominated by Coulombic interaction) and nonpolar (alkyl chain, dominated by van der Waals interaction) domains, significantly influencing physicochemical properties.

However, adding hydrocarbon units is not limited to linear moieties; branching alkyl side chains is another option. Although synthesizing ILs with such functional groups provides an alternative strategy for achieving desired properties, studies published on branched ILs are currently far fewer compared to those on linear ILs. As a rare example, Quitevis's group presented a systematic work on the physical properties and molecular level features of an imidazolium-based IL with an isopropyl-terminated alkyl chain, i.e., a 1-(iso-alkyl)-3-methylimidazolium cation paired with a bis(trifluoromethylsulfonyl)imide anion ($[NTf_2]^-$).^{13–16} They found that by the branching melting point and viscosity monotonically increased, except for 1-(2-methylpropyl)-3-methylimidazolium-based IL. The origin of the exception was later explored with molecular dynamics simulations.

Herein, we focus on branching at the α -carbon of the alkyl group in the cation, i.e., cations having an isopropyl group (1-

Received: August 10, 2019

Accepted: November 14, 2019

Published: November 27, 2019

isopropyl-3-methylimidazolium ($[iC_3mim]^+$) or a *tert*-butyl group (1-*tert*-butyl-3-methylimidazolium ($[tC_4mim]^+$)), with different counterions (Figure 1). Branching at the α -position is a

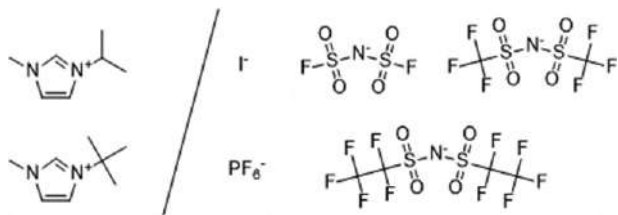


Figure 1. Structures of the target cations and anions considered in this study.

rational idea because it can start with the shortest alkyl chain length (i.e., ethyl) compared to the other position. However, very few fundamental physical property data have been reported for such systems, particularly those featuring the *tert*-butyl group, as summarized in Table 1.

Five common anions were chosen, i.e., iodide ($[I]^-$), hexafluorophosphate ($[PF_6]^-$), bis(fluorosulfonyl)imide ($[NTf_2]^-$), $[NTf_2]^-$, and bis(pentafluoroethylsulfonyl)imide ($[NPF_2]^-$). The thermal properties (thermal phase behavior including melting crystallization and glass transition, and thermal decomposition temperatures), densities, and viscosities of the ILs, as fundamental physical properties were measured, and the values were compared to those of ILs with the corresponding linear alkyl chains, i.e., 1-methyl-3-propylimidazolium ($[C_3mim]X$)- and 1-butyl-3-methylimidazolium ($[C_4mim]X$)-based ILs. The physical property data for the linear chain ILs were mostly taken from the NIST ionic liquids database.¹⁷ Since the physical properties of $[C_3mim][Nf_2]$ were largely unknown, this IL was also synthesized and its properties were measured in this work. To help rationalize the differences in these properties, density functional theory (DFT) calculations for the IL ions were also performed.

2. EXPERIMENTAL SECTION

2.1. Synthesis, Characterization, and Sample Handling. The synthesis of $[iC_3mim]X$ followed previously reported representative procedures.² $[iC_3mim][I]$ was first obtained from 1-methylimidazole and 2-iodopropane. Subsequently, $[iC_3mim][PF_6]$, $[iC_3mim][Nf_2]$, $[iC_3mim][NTf_2]$, and $[iC_3mim][NPF_2]$ were produced from $[iC_3mim][I]$ by ion exchange. $[C_3mim][Nf_2]$ was synthesized by a similar procedure using 1-bromopropane. To prepare $[tC_4mim]X$, 1-*tert*-butyli-

midazole was first synthesized according to a previously reported procedure.²² $[tC_4mim][I]$ was prepared from 1-*tert*-butylimidazole and iodomethane, and other $[tC_4mim]X$ species were synthesized via ion exchange in the same way as $[iC_3mim]X$. The synthetic details are described in the Supporting Information. After ion exchange, all of the ILs passed the $AgNO_3$ test, revealing that residual $[I]^-$ was below 3×10^{-3} mol L^{-1} .²³ If the ILs were colored, they were treated with activated charcoal. All ILs obtained here were colorless liquids or crystals at room temperature.

The ILs were vacuum-dried (less than 1 Pa) for more than 1 day with heating, and they were handled in a glovebox where the dew point was 193–203 K. The ILs were characterized by 1H , ^{13}C , ^{19}F , and ^{31}P NMR using a JEOL JNM-ECA300W (Figure S1). The water content was measured by 1H NMR. The IL was dissolved in dried dimethyl sulfoxide- d_6 , and the solution was analyzed by 1H NMR at room temperature with a relaxation time of 60 s and eight accumulations. The H_2O peak originating from the pure solvent was subtracted. The water content of the ILs was confirmed by NMR measurement, which was below 100 ppm (under the detection limit of our NMR measurements). For several samples, we also confirmed the results by Karl Fischer titration (see the Supporting Information for details). The purities of the ILs are summarized in Table 2. The details of the NMR characterization are shown in the Supporting Information.

2.2. Physical Property Measurements. Differential scanning calorimetry (DSC) measurements, which provide temperature and enthalpy/entropy changes during thermal phase change (e.g., melting), were performed with a DSC7020 (Hitachi High-Tech Science). Calibrations were conducted with indium, and uncertainty was estimated from distilled water. Approximately 5 mg of the IL was sealed in an aluminum pan. All of the measurements were started from the liquid state, and then, the sample was cooled to 123 K and reheated to beyond the melting point at a scan rate of 10 K min^{-1} . Thermogravimetry/differential thermal analysis (TG/DTA) measurements to monitor thermal decomposition behavior of the ILs were conducted by an STA7200 (Hitachi High-Tech Science). The temperature was calibrated with indium and tin, and its uncertainty was estimated with cellulose. The IL (5–10 mg) was placed in an open aluminum cell, and the cell was heated from room temperature to 823 K at 10 K min^{-1} under N_2 .

Density measurements were performed with an oscillation-type density meter (DA-500, Kyoto Electronics Manufacturing) in the range 293–353 K. Calibration was performed with dry air

Table 1. Physical Properties of Interest for the Target ILs Considered in This Study

	thermal phase behavior	thermal decomposition temperature	density	viscosity
$[iC_3mim][I]$	reported, ^{18,19} this work	reported, ¹⁹ this work	— ^a	— ^a
$[iC_3mim][PF_6]$	reported, ¹⁹ this work	reported, ¹⁹ this work	— ^a	— ^a
$[iC_3mim][Nf_2]$	this work	this work	this work	this work
$[iC_3mim][NTf_2]$	reported, ^{14,19} this work	reported, ^{14,19} this work	reported, ¹⁴ this work	reported, ¹⁴ this work
$[iC_3mim][NPF_2]$	this work	this work	this work	this work
$[tC_4mim][I]$	this work	this work	— ^a	— ^a
$[tC_4mim][PF_6]$	reported, ^{20,21} this work	this work	— ^a	— ^a
$[tC_4mim][Nf_2]$	this work	this work	— ^a	this work
$[tC_4mim][NTf_2]$	this work	this work	this work	this work
$[tC_4mim][NPF_2]$	this work	this work	this work	this work

^aData not available due to the IL being solid at the temperature at which the property is measured.

Table 2. Specification of Chemicals

ionic liquid	abbreviation	CAS reg. no.	NMR purity	purification method
1-isopropyl-3-methylimidazolium iodide	[iC ₃ mim][I]	119171-19-6	¹ H: 99.9%	washing; recrystallizing; vacuum drying
1-isopropyl-3-methylimidazolium hexafluorophosphate	[iC ₃ mim][PF ₆]	216300-13-9	¹ H: 99.9%; ¹⁹ F: >99.9%	washing; recrystallizing; vacuum drying
1-isopropyl-3-methylimidazolium bis(fluorosulfonyl)imide	[iC ₃ mim][NF ₂]	936744-90-0	¹ H: >99.9%; ¹⁹ F: 97.9%	washing; recrystallizing; decolorizing with activated charcoal; vacuum drying
1-isopropyl-3-methylimidazolium bis(trifluoromethylsulfonyl)imide	[iC ₃ mim][NTf ₂]	216299-73-9	¹ H: 99.9%; ¹⁹ F: 99.0%	washing; vacuum drying
1-isopropyl-3-methylimidazolium bis(pentafluoroethylsulfonyl)imide	[iC ₃ mim][NPf ₂]		¹ H: 99.3%; F: >99.0%	washing; vacuum drying
1-tert-butyl-3-methylimidazolium iodide	[tC ₄ mim][I]	905726-42-3	¹ H: >99.9%	washing; recrystallizing; vacuum drying
1-tert-butyl-3-methylimidazolium hexafluorophosphate	[tC ₄ mim][PF ₆]	340154-48-5	¹ H: 99.9%; ¹⁹ F: > 99.9%	washing; recrystallizing; vacuum drying
1-tert-butyl-3-methylimidazolium bis(fluorosulfonyl)imide	[tC ₄ mim][NF ₂]		¹ H: >99.9%; ¹⁹ F: > 96.7%	washing; recrystallizing; decolorizing with activated charcoal; vacuum drying
1-tert-butyl-3-methylimidazolium bis(trifluoromethylsulfonyl)imide	[tC ₄ mim][NTf ₂]	950578-92-4	¹ H: >99.9%; ¹⁹ F: 99.0%	washing; vacuum drying
1-tert-butyl-3-methylimidazolium bis(pentafluoroethylsulfonyl)imide	[tC ₄ mim][NPf ₂]		¹ H: 99.9%; ¹⁹ F: 99.0%	washing; vacuum drying
1-methyl-3-propylimidazolium bis(fluorosulfonyl)imide	[C ₃ mim][NF ₂]	873667-96-0	¹ H: 99.9%; ¹⁹ F: 96.9%	washing; vacuum drying

Table 3. Measured Thermal Properties of the ILs at Atmospheric Pressure (100.9 kPa)^{a,b}

	T _m (K)	Δ _{fus} H (kJ mol ⁻¹)	Δ _{fus} S (J K ⁻¹ mol ⁻¹)	T _g (K)	T _c (K)	T _d (K)
[iC ₃ mim][I]	383.4	16.3	42.5		285.2	568.1
[iC ₃ mim][PF ₆]	374.0	15.7	42.0		285.4	637.3
[iC ₃ mim][NF ₂]	269.2	14.3	53.3		241.4	599.7
[iC ₃ mim][NTf ₂]	283.5	24.2	85.4		247.4	674.1
[iC ₃ mim][NPf ₂]				197.4		674.4
[tC ₄ mim][I]	432.7	15.2	35.1		354.0	520.9
[tC ₄ mim][PF ₆]	421.0	23.1	55.0		404.9	535.0
[tC ₄ mim][NF ₂]	326.6	17.4	53.2		294.0	540.9
[tC ₄ mim][NTf ₂]	280.4	22.9	81.7		235.9	532.6
[tC ₄ mim][NPf ₂]	294.3	16.7	56.6	215.1	272.5	533.6

^aΔ_{fus}S was obtained from eq 3 (vide infra). Melting point (T_m), crystallization point (T_c), and glass transition temperature (T_g) were taken from the onset temperature from the DSC traces. T_d was taken as onset temperature from the thermogravimetric curve. ^bStandard uncertainties are u(T_m) = u(T_g) = u(T_c) = 0.8 K; u(Δ_{fus}H) = 0.4 kJ mol⁻¹; u(Δ_{fus}S) = 1.2 J K⁻¹ mol⁻¹; and u(T_d) = 0.5 K.

and degassed distilled water. The obtained values were also calibrated with respect to viscosity.

The viscosity was measured with two different cone-plate type viscometers. A Brookfield DV-II+Pro (temperature calibration, a calibrated thermocouple) was used for the 293–313 K range, and a Brookfield CAP2000+ (temperature calibration, an IL²⁴) was used for the 323–353 K range. The uncertainty in viscosity value for both viscometers was estimated with several oils.

2.3. DFT Calculations. All of the DFT calculations were performed with the Gaussian09 software package.²⁵ Basis sets of 6-311++G(d,p) based on Becke's three-parameter hybrid method²⁶ with LYP correlation (B3LYP) were used.^{27,28} Optimized structures were confirmed to produce no imaginary frequencies. Partial atomic charges were derived for the optimized geometries with the CHelpG algorithm.²⁹ The interaction energies between cations and anions were estimated by the supermolecule approach without the basis set superposition error correction. The ion pair structures modeled here (displayed in Figure S2) were taken from a previous report.³⁰ Ion volume was calculated with the Gaussian09 program that employs Monte Carlo integration. In the calculation, the "volume = tight" keyword, which increases the density of points

for more accurate integration, was applied, and the calculations for the ion volume estimation were repeated 1000 times. The obtained histogram was fitted with a Gaussian function, and the peak position was used as ion volume. To convert the ion volume to van der Waals volume, the procedure reported by Parsons and Ninham was used,³¹ which is simply to multiply the obtained ion volume by 0.7236.

3. RESULTS

3.1. Physical Properties. **3.1.1. Thermal Properties.** Table 3 lists thermal properties of [iC₃mim]X and [tC₄mim]X such as melting point (T_m), fusion enthalpy and entropy (Δ_{fus}H and Δ_{fus}S), glass transition temperature (T_g), crystallization temperature (T_c), and thermal decomposition temperature (T_d). The DSC and TG/DTA curves are shown in the Supporting Information (Figures S3 and S4). The melting points of [iC₃mim][I], [iC₃mim][PF₆], and [iC₃mim][NTf₂] are somewhat lower (1–5 K) than the previously reported data by Ngo et al.,¹⁹ possibly due to the differences in the analytical procedure and apparatus employed. On the other hand, the agreement of the melting point and the fusion enthalpy of [iC₃mim][NTf₂] between this work and the work by Xue et al.¹⁴ (T_m = 282.1 K

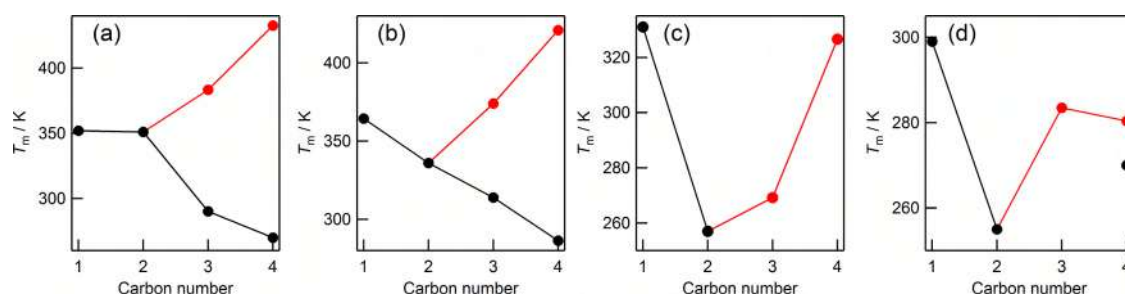


Figure 2. Comparison of melting points (T_m) between the branched (red) and linear (black) ILs. The anions in the ILs are (a) $[I]^-$,^{35–38} (b) $[PF_6]^-$,³⁹ (c) $[Nf_2]^-$,^{40,41} and (d) $[NTf_2]^-$.⁴² The data for $[NPF_2]^-$ -based ILs are not shown because most of them do not exhibit T_m .

Table 4. Density (ρ , kg m^{-3}) Values of the ILs at Various Temperatures at Atmospheric Pressure (100.9 kPa)^a

	293.15 K	298.15 K	303.15 K	313.15 K	323.15 K	333.15 K	343.15 K	353.15 K
$[iC_3\text{mim}][Nf_2]$	1399.4	1394.9	1390.6	1382.1	1373.2	1364.8	1356.3	1347.8
$[iC_3\text{mim}][NTf_2]$	1481.9	1476.8	1472.0	1462.5	1452.4	1442.9	1433.4	1423.7
$[iC_3\text{mim}][NPF_2]$	1556.7	1551.3	1546.0	1535.5	1524.6	1514.0	1503.5	1492.8
$[tC_4\text{mim}][NTf_2]$	1451.5	1446.6	1442.0	1432.8	1423.1	1413.8	1404.5	1395.0
$[tC_4\text{mim}][NPF_2]$	1530.8	1525.2	1519.9	1509.6	1498.9	1488.6	1478.4	1467.8
$[C_3\text{mim}][Nf_2]$	1399.4	1395.1	1390.6	1381.8	1373.1	1364.5	1355.8	1347.2

^aStandard uncertainties are $u(T) = 0.01$ K; $u(\rho) = 0.1$ kg m^{-3} ; and $u(p) = 0.5$ kPa.

and $\Delta_{\text{fus}}H = 23.9$ kJ mol^{-1}) is relatively good. These comparisons are graphically displayed in Figure S5.

Most of the ILs (except $[iC_3\text{mim}][NPF_2]$ and $[tC_4\text{mim}][NPF_2]$) crystallized upon cooling, as regular molecular liquids do. This is somewhat different from the results for the linear chain ILs, where $[C_3\text{mim}]X$ and $[C_4\text{mim}]X$ are sometimes noncrystallized ILs or show cold crystallization (crystallizing on heating).^{32,33} $[iC_3\text{mim}][NPF_2]$ shows a glass transition temperature of 197.4 K. If the empirical $T_g/T_m = 2/3$ rule was applied, T_m of this IL was estimated to be ca. 296 K, which is probable considering T_m of the other ILs reported here (Table 3). Some of the ILs have complex DSC curves consisting of solid–solid phase changes, i.e., $[iC_3\text{mim}][Nf_2]$ and $[tC_4\text{mim}][I]$. However, the discussion of such behavior is beyond the scope of this paper.

Melting point is the most important property for ILs because it determines whether a salt is an IL or not. As shown in Table 3, the ILs having anions with a smaller size and higher symmetry (Sym) (i.e., $[I]^-$ and $[PF_6]^-$) show higher melting points than the others, which is consistent with the linear-chain ILs.^{19,34} To highlight the change in melting point upon branching, Figure 2 displays T_m against the number of carbon atoms in the alkyl chain. For carbon numbers 1–4, the melting point typically decreases with the increasing carbon number for linear chains.^{19,34} This is also the case in Figure 2, with the exception of the NTf_2 -paired ILs, where T_m for $[C_4\text{mim}][NTf_2]$ is higher than that of $[C_2\text{mim}][NTf_2]$. Conversely, for the branched species, the melting point increases with the increasing carbon number except for the NTf_2 -paired ILs, where T_m for $[tC_4\text{mim}][NTf_2]$ is slightly lower than that for $[iC_3\text{mim}][NTf_2]$. Thus, we concluded that the melting points of the branched ILs are higher than those of the linear ILs.

Table 3 also includes thermal decomposition temperatures (T_d) estimated from the TG/DTA curves (Figure S4). Concerning anion structure, T_d follows the order $[NTf_2]^- \approx [NPF_2]^- > [PF_6]^- > [Nf_2]^- > [I]^-$ for $[iC_3\text{mim}]X$, which is the same order as that for the linear ILs.^{19,43} T_d values for $[iC_3\text{mim}]X$ are comparable or slightly lower than those for $[C_3\text{mim}]X$.^{14,19} Meanwhile, the T_d values for $[tC_4\text{mim}]X$ are largely independent of anion species and significantly lower than

those of $[C_4\text{mim}]X$.⁴⁴ For example, the reported T_d values are 538 K for $[C_4\text{mim}][I]$, 622 K for $[C_4\text{mim}][PF_6]$, and 682–723 K for $[C_4\text{mim}][NTf_2]$.⁴⁴ This suggests that thermal decomposition starts from the cation for $[tC_4\text{mim}]X$. There are several thermal decomposition mechanisms proposed for imidazolium-based ILs.^{2,44} One major pathway is breaking of the N–C(α) bond that connects the imidazolium ring and the alkyl chain. In this scenario, the well-established high stability of the *tert*-butyl carbocation is considered to be responsible for the low T_d value for $[tC_4\text{mim}]X$.

3.1.2. Density. Temperature-dependent density (ρ) data for the five branched ILs that are liquids at room temperature, i.e., $[iC_3\text{mim}][Nf_2]$, $[iC_3\text{mim}][NTf_2]$, $[iC_3\text{mim}][NPF_2]$, $[tC_4\text{mim}][NTf_2]$, and $[tC_4\text{mim}][NPF_2]$, are summarized in Table 4 and plotted in Figure 3a. The densities of $[tC_4\text{mim}][Nf_2]$ and the branched ILs containing $[I]^-$ and $[PF_6]^-$ were not measured because they are solids at room temperature and thus not suitable for our density measurement apparatus. As shown in the figure, the previously reported density values for $[iC_3\text{mim}][NTf_2]$ ¹⁴ (gray squares) are in excellent agreement with those in the present study (red squares). The deviations are below 0.1% in the whole temperature range (Figure S6). The densities of $[tC_4\text{mim}]X$ are always lower than those of $[iC_3\text{mim}]X$. When the anion becomes heavier (as from Nf_2 to NPF_2 via NTf_2), the density increases, as expected. Figure 3b–e shows a comparison between the branched and linear ILs. The difference in densities between $[C_3\text{mim}]X$ and $[iC_3\text{mim}]X$ is slight, while the density of $[tC_4\text{mim}]X$ is clearly higher than that of $[C_4\text{mim}]X$.

3.1.3. Viscosity. Figure 4a shows temperature-dependent viscosity (η) data for the six branched ILs, i.e., $[iC_3\text{mim}][Nf_2]$, $[iC_3\text{mim}][NTf_2]$, $[iC_3\text{mim}][NPF_2]$, $[tC_4\text{mim}][Nf_2]$, $[tC_4\text{mim}][NTf_2]$, and $[tC_4\text{mim}][NPF_2]$ and the Vogel–Fulcher–Tammann (VFT) fits of the branched ILs. The numerical data are summarized in Table 5. The VFT equation is expressed as follows

$$\eta = \eta_0 \exp\left(\frac{B}{T - T_0}\right) \quad (1)$$

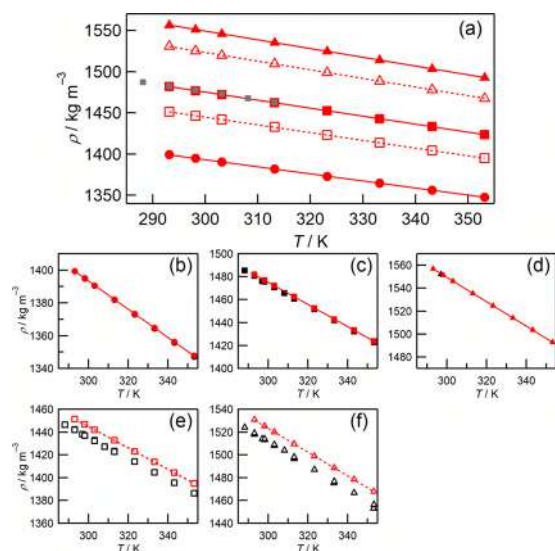


Figure 3. Density data versus temperature for (a) $[iC_3mim][Nf_2]$ (filled red circles), $[iC_3mim][NTf_2]$ (filled red squares), $[iC_3mim][NPF_6]$ (filled red triangles), $[tC_4mim][NTf_2]$ (open red squares), and $[tC_4mim][NPF_6]$ (open red triangles). Lines are linear fits (see Table S1). Filled gray squares represent reported density data for $[iC_3mim][NTf_2]$.¹⁴ (b–e) Comparison with the linear ILs (black symbols): (b) $[C_3mim][Nf_2]/[iC_3mim][Nf_2]$, (c) $[C_3mim][NTf_2]/[iC_3mim][NTf_2]$,^{14,32,45–47} (d) $[C_3mim][NPF_6]/[iC_3mim][NPF_6]$, (e) $[C_4mim][NTf_2]/[tC_4mim][NTf_2]$,^{14,32,45–47} (f) $[C_4mim][NPF_6]/[tC_4mim][NPF_6]$.^{32,42,48–50}

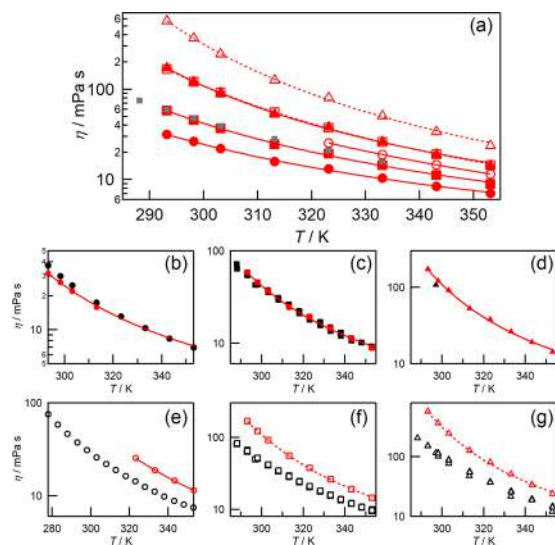


Figure 4. Viscosity data versus temperature for (a) $[iC_3mim][Nf_2]$ (filled red circles), $[iC_3mim][NTf_2]$ (filled red squares), $[iC_3mim][NPF_6]$ (filled red triangles), $[tC_4mim][Nf_2]$ (open red circles), $[tC_4mim][NTf_2]$ (open red squares), and $[tC_4mim][NPF_6]$ (open red triangles). It should be noted that the values of $[iC_3mim][NPF_6]$ and $[tC_4mim][NTf_2]$ are severely overlapped. Filled gray squares represent reported viscosity data for $[iC_3mim][NTf_2]$.¹⁴ Displayed curves are VFT fits (see Table S2). (b–g) Comparison with the linear ILs (black symbols): (b) $[C_3mim][Nf_2]/[iC_3mim][Nf_2]$, (c) $[C_3mim][NTf_2]/[iC_3mim][NTf_2]$,^{14,32,51–53} (d) $[C_3mim][NPF_6]/[iC_3mim][NPF_6]$, (e) $[C_4mim][Nf_2]/[tC_4mim][Nf_2]$,⁵⁴ (f) $[C_4mim][NTf_2]/[tC_4mim][NTf_2]$,^{51,55–59} (g) $[C_4mim][NPF_6]/[tC_4mim][NPF_6]$.^{32,42,48–50}

where η_0 , B , and T_0 are the VFT parameters. The fitted values are summarized in Table S2. The viscosity of $[iC_3mim][NTf_2]$ was

previously reported¹⁴ and is also plotted in the figure (gray squares). The agreement is good, particularly at low temperatures. For example, the reported value at 293.15 K was 59 mPa s, which is almost the same as 58.3 mPa s in this study. At 333.15 K, the reported and present values were 16 and 14.5 mPa s, respectively. Considering uncertainty (2 mPa s for the literature and 0.04 η in this work), the deviation is within the experimental error. The relative percent deviations are also displayed in Figure S7, where the maximum deviation is ca. 10%. The viscosity of $[tC_4mim]X$ (filled symbols) is significantly higher than that of $[iC_3mim]X$ (open symbols), where the same anion is used. When fixing the cation structure, the viscosity follows the trend $NPf_2 > NTf_2 > Nf_2$, which is the same for the linear-chain ILs.^{32,43} In Figure 3b–e, the viscosities of the branched ILs are compared with those of the corresponding linear ILs. The viscosities of $[iC_3mim]X$ are comparable to those of $[C_3mim]X$, while significant differences are observed for $[C_4mim]X$ and $[tC_4mim]X$. $[tC_4mim]X$ has approximately twice the viscosity of the corresponding $[C_4mim]X$.

3.2. DFT Calculation Results. 3.2.1. Cation Structure.

Since alkyl groups are normally flexible, several stable conformers are possible. To investigate and compare the branched cation structures with the linear cation structures, the potential energy surface (PES) while rotating the alkyl group along the N–C(α) bond was investigated, as shown in Figure 5. Stable structures derived from the PESs are summarized in Figure 6. The PESs of $[C_2mim]^+$,⁶⁰ $[C_4mim]^+$,⁶¹ and $[iC_3mim]^+$ ¹⁸ are consistent with the previous results. The PESs for the ILs with linear alkyl chains are similar. The most stable structures (nonplanar for $[C_2mim]^+$, trans for $[C_3mim]^+$, and trans–trans (TT) for $[C_4mim]^+$) are located at a dihedral angle of ca. 105°. The rotational activation energies for 0 and 180° are estimated to be ca. 2–3 and 5–6 kJ mol^{−1}, respectively. There is a local minimum at 0°, and the corresponding structure (planar) has a reflectional symmetry. Even though the presence of this metastable structure is computational method/level-dependent, it has been experimentally observed with Raman spectroscopy for $[C_2mim]^+$.⁶⁰

The PESs of the branched ILs are different from those of the linear ILs. The most stable structure is located at 0° with a reflectional symmetry (Sym). $[iC_3mim]^+$ has a relatively high rotational barrier (7 kJ mol^{−1}) and the local minimum has a dihedral angle of 150° (Asym), which is also observable by Raman spectroscopy.¹⁸ Conversely, the rotational barrier for $[tC_4mim]^+$ is rather low (3 kJ mol^{−1}). Since the structures with dihedral angles of 0 and 120° are identical, a possible local minimum is only seen at 60° (or 180°). However, such a structure produces one imaginary frequency, indicating that it is energetically unstable. It should be noted that the stability of this structure is computational method/level-dependent (when calculated at B3LYP/6-311+G(d,p) level, the structure produce no imaginary frequency); hence, it may be experimentally observable.

An important difference between the linear and branched ILs, which is not apparent in Figure 5, is that when carbons are added linearly to the side chain, there are other conformational isomers present, which is not the case for the branched chains. It is known that additional conformers for 2 and 8–9 exist for $[C_3mim]^+$ (gauche and gauche') and $[C_4mim]^+$ (the combination of planar, trans, gauche, and gauche'), respectively.⁶² Except for the planar form, which is metastable, all of the conformers for the ILs with linear chains have the lowest symmetry (C_1). However, for $[iC_3mim]^+$, the C_s symmetry conformation (Sym)

Table 5. Viscosity (η , mPa s) Value of the ILs at Various Temperatures at Atmospheric Pressure (100.9 kPa)^a

	293.2 K	298.2 K	303.2 K	313.2 K	323.2 K	333.2 K	343.2 K	353.2 K
[iC ₃ mim][Nf ₂]	31.6	26.4	22.0	15.9	13.1	10.4	8.4	7.0
[iC ₃ mim][NTf ₂]	58.3	45.5	36.9	24.5	19.3	14.5	11.2	8.9
[iC ₃ mim][NPF ₂]	172.6	121.4	91.7	53.0	38.0	26.4	19.1	14.4
[tC ₄ mim][Nf ₂]					25.5	18.9	14.6	11.5
[tC ₄ mim][NTf ₂]	167.3	121.4	91.5	55.6	37.5	26.2	19.0	14.5
[tC ₄ mim][NPF ₂]	571.1	367.2	246.7	126.1	80.9	50.7	33.9	23.8
[C ₃ mim][Nf ₂]	37.1	29.9	24.8	17.4	13.2	10.4	8.4	6.9

^aStandard uncertainties are $u(T) = 0.1$ K for 293.2–313.2 K; $u(T) = 0.1$ K for 323.2–353.2 K; $u(\eta) = 0.04\eta$ for 293.2–313.2 K; $u(\eta) = 0.04\eta$ for 323.2–353.2 K; and $u(p) = 0.5$ kPa.

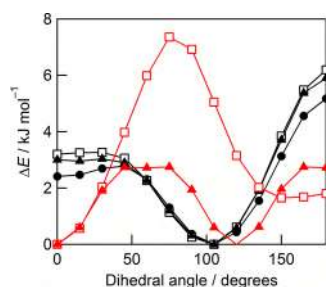


Figure 5. Potential energy surfaces as a function of the C(2)–N(1 or 3)–C(α)–C(β) dihedral angle for [C₂mim]⁺ (filled black circles), [C₃mim]⁺ (open black squares), [C₄mim]⁺ (filled black triangles), and [tC₄mim]⁺ (filled red triangles) and as a function of the C(2)–N(1)–C(α)–H dihedral angle for [iC₃mim]⁺ (open red squares).

is the most stable, and [tC₄mim]⁺ can take only the Sym form. In other words, the population of the symmetric form becomes low when increasing the number of carbons linearly, whereas the opposite is the case for ILs with branched chains. From a thermodynamic viewpoint, these conformational and structural symmetrical differences can be represented by conformational entropy (S_c)

$$S_c = -R \sum_i p_i \ln(p_i) \quad (2)$$

where R is the gas constant and p_i is the probability of conformer i in the cation as estimated from the Gibbs energy difference of the conformers. Figure 7 shows the differences in S_c between the linear and branched ILs. As expected, S_c increases with the increasing hydrocarbon units in the linear ILs. S_c for [C₂mim]⁺ and [iC₃mim]⁺ are comparable, while [tC₄mim]⁺ produces a conformational entropy of 0 J K⁻¹ mol⁻¹. Unlike [C₂mim]⁺, [iC₃mim]⁺ takes the symmetrical form as the most stable conformer, which should result in a low S_c . However, the energy difference among the conformers is small for [iC₃mim]⁺, which increases S_c . Consequently, S_c for [iC₃mim]⁺ is very similar to

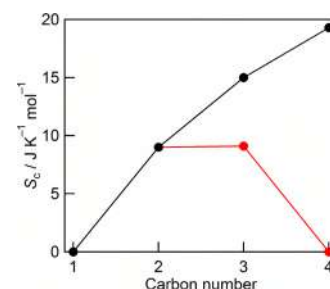


Figure 7. Conformational entropy (S_c) versus carbon number in the alkyl group. Black and red symbols represent ILs with linear and branched alkyl chains, respectively. The value of [C₄mim]⁺ was taken from the literature.⁶³

that for [C₂mim]⁺. The differences in conformational and symmetrical behaviors between the linear and branched ILs affect physical properties and will be discussed in later sections.

3.2.2. Cation–Anion Interaction. The interaction energy between a cation and an anion dominates the physical properties of the corresponding IL and is affected by the type of structure in the side chain. There are several experimental^{15,64} and computational^{13,65} demonstrations that branching changes the cation–anion interaction. However, no systematic study has been performed for the current system. Figure 8a–e shows the calculated interaction energies for cations and anions in the gas phase. As is consistent with the previous results, the 1:1 interaction energy decreases with the increasing alkyl chain length in the linear form.⁶⁶ As the alkyl chain becomes longer, the decrease in the interaction energy becomes smaller. The interaction energies for the ILs with branched chains are always lower than those for the ILs with linear chains. The gap in energy is wider for a carbon number of 4 than that for 3. Isopropyl and *tert*-butyl groups have relatively high electron-donating abilities. This results in delocalized cation charge, and consequently, the interaction energies in ILs that are governed by Coulombic interactions may be weakened. To validate this idea, the partial

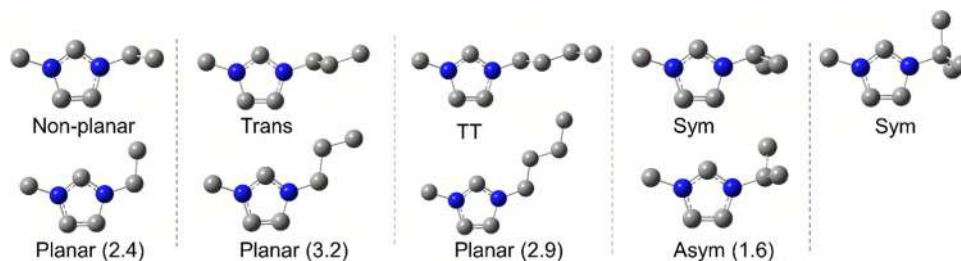


Figure 6. Most stable (top) and metastable (bottom) cation structures obtained from Figure 5. TT stands for the trans–trans conformation. Energy differences between the metastable and the most stable structures are shown in parentheses (in kJ mol⁻¹). For further details, see Table S3.

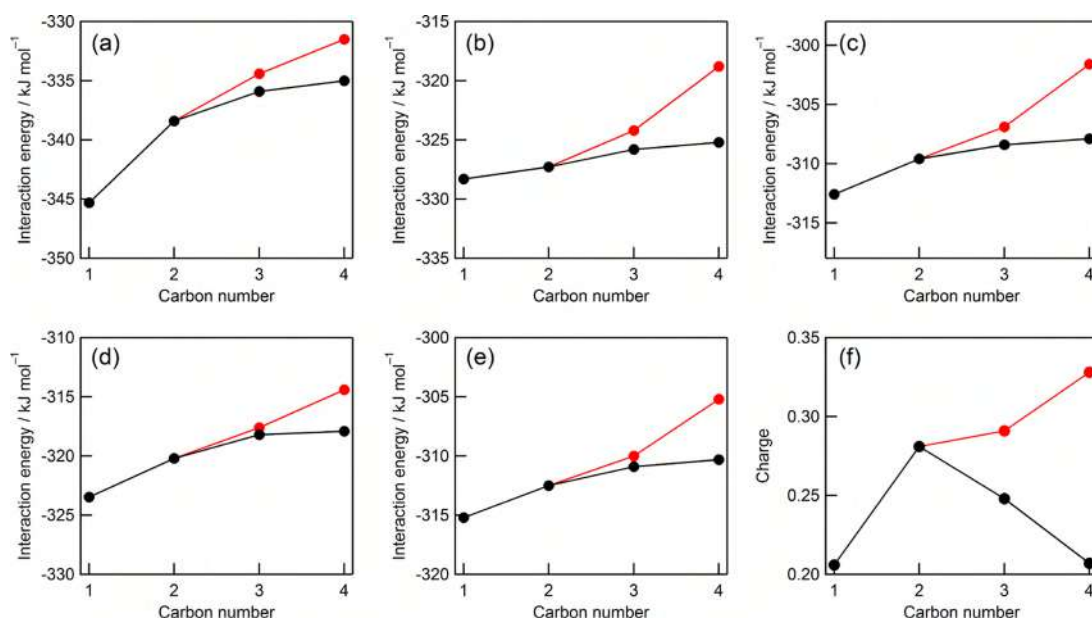


Figure 8. (a–e) Interaction energies of the branched ILs (red) and the linear ILs (black). ILs containing (a) $[I]^-$, (b) $[PF_6]^-$, (c) $[Nf_2]^-$, (d) $[NTf_2]^-$, and (e) $[NPF_2]^-$. (f) Sums of the positive charges on the carbon and hydrogen atoms in the alkyl groups for the branched ILs (red) and the linear ILs (black).

charges on the alkyl groups were calculated for the most stable conformers and are displayed in Figure 8f. The positive charges in the branched groups are higher than those in the linear groups, and the gap widens for $[C_4mim]^+/[tC_4mim]^+$, which supports the above-mentioned idea. It should be noted that the high positive charge delocalization in the branched ILs stabilizes them, i.e., $[iC_3mim]^+$ and $[tC_4mim]^+$ are more energetically stable than the corresponding linear cations (Table S3). The positive charge in the linear alkyl groups decreases from $[C_2mim]^+$ to $[C_4mim]^+$. This indicates that charge delocalization is not the only factor that determines the interaction energy. The bulkiness of the alkyl group in the cation, which pushes the anion away, would also contribute to decreasing the interaction energy.

3.2.3. Ion Volume. Volume is a fundamental property of a molecule or an ion, and van der Waals volume (V_{vdw}), which is the volume that other molecules cannot access, was estimated here to further investigate the experimental density values (vide infra). The Bondi method⁶⁷ or its analogue is commonly used for V_{vdw} estimation. This is based on the assumption that atoms are spherical with an invariable empirical radius. The volume is calculated using the additivity rule for individual atoms and/or atomic groups. To overcome these assumptions, V_{vdw} for $[iC_3mim]^+$, $[tC_4mim]^+$, $[Nf_2]^-$, and $[NPF_2]^-$ were calculated with DFT calculations, while V_{vdw} for $[C_3mim]^+$, $[C_4mim]^+$, and $[NTf_2]^-$ were taken from our previous work,⁶⁶ which employed the same method. Table 6 lists the V_{vdw} values of the ions of interest. The V_{vdw} values for the branched ILs are slightly lower than those of the linear ILs, and the gap is wider for $[C_4mim]^+/[tC_4mim]^+$ than for $[C_3mim]^+/[iC_3mim]^+$. It should be noted that, in general, branching also slightly decreases the V_{vdw} for molecular liquids.^{68–70}

4. DISCUSSION

4.1. Melting Point. Generally speaking, the effect of alkyl chain branching on the melting point of a molecule is not straightforward. The melting points of alkanes tend to decrease

Table 6. Estimated van der Waals Volumes of the IL Ions

	V_{vdw} (Å ³)
$[C_3mim]^{+a}$	131.1 ± 0.2
$[iC_3mim]^+$	129.9 ± 0.2
$[C_4mim]^{+a}$	147.6 ± 0.2
$[tC_4mim]^+$	145.3 ± 0.2
$[Nf_2]^-$	101.5 ± 0.2
$[NTf_2]^{-a}$	150.5 ± 0.2
$[NPF_2]^-$	198.1 ± 0.4

^aFrom the literature.⁶⁶

upon branching, while the melting points of 2-propyl alcohol and *tert*-butyl alcohol are higher than those of the corresponding linear alcohols.⁷¹ The melting points of several ILs containing branched cations have been reported. Depending on the position of the branching, cation structure, and type of paired anion, T_m can either increase or decrease.^{14,64,72–75} For example, 1-(iso-alkyl)-3-methylimidazolium-based ILs tend to show higher T_m values than the corresponding linear ILs,¹⁴ while the opposite trend is observed for dicationic ILs.⁷⁵ This indicates that branching involves several competing factors that influence T_m .

Despite this complexity, the T_m values of the branched ILs studied here are always higher than those of the linear ILs, as shown in Figure 2. This suggests that there is an underlying mechanism that determines the high T_m values of $[iC_3mim]X$ and $[tC_4mim]X$. According to thermodynamic relationships, T_m is related to $\Delta_{fus}H$ and $\Delta_{fus}S$ as follows

$$T_m = \frac{\Delta_{fus}H}{\Delta_{fus}S} \quad (3)$$

Table 7 summarizes the available $\Delta_{fus}H$ and $\Delta_{fus}S$ data for the linear ILs, i.e., $[C_4mim][I]$, $[C_3mim][PF_6]$, $[C_4mim][PF_6]$, and $[C_4mim]NTf_2$. Care must be taken when discussing $\Delta_{fus}H$ and $\Delta_{fus}S$ because they are highly sensitive to individual crystalline structure, polymorphism, experimental and analytical proce-

Table 7. Reported $\Delta_{\text{fus}}H$ and $\Delta_{\text{fus}}S$ Values for Linear ILs^a

	$\Delta_{\text{fus}}H$ (kJ mol ⁻¹)	$\Delta_{\text{fus}}S$ (J K ⁻¹ mol ⁻¹)
[C ₃ mim][PF ₆] ^{39,77}	16.8 ± 0.1	53.6 ± 0.1
[C ₄ mim][I] ³³	18.99 ± 0.02	65.06 ± 0.05
[C ₄ mim][PF ₆] ^{55,78–81}	20.7 ± 1.2	73.3 ± 3.8
[C ₄ mim][NTf ₂] ^{11,14,79,82–84}	22.9 ± 1.5	85.1 ± 5.7

^aIf there were multiple data available, an average value is presented. In [C₄mim][PF₆], where several polymorphic crystals are known,⁷⁶ the value for the most stable (called γ phase) is given.

dures, and sample purity. However, there is one common feature when comparing $\Delta_{\text{fus}}H$ and $\Delta_{\text{fus}}S$ between the linear and branched ILs (Tables 3 and 7). The branched ILs have lower $\Delta_{\text{fus}}S$ values than the linear ILs, which results in higher T_m values for the branched ILs. For [C₄mim][I]/[tC₄mim][I], [C₃mim]-[PF₆]/[iC₃mim][PF₆], and [C₄mim][NTf₂]/[tC₄mim][NTf₂], the dominant contribution of $\Delta_{\text{fus}}S$ is apparent because $\Delta_{\text{fus}}H$ is the same ([C₄mim][NTf₂]/[tC₄mim][NTf₂]) or lower in the branched ILs ([C₄mim][I]/[tC₄mim][I] and [C₃mim][PF₆]/[iC₃mim][PF₆]), which makes T_m for the branched ILs the same or lower. For [C₄mim][PF₆]/[tC₄mim][PF₆], $\Delta_{\text{fus}}H$ is higher and $\Delta_{\text{fus}}S$ is lower in [tC₄mim][PF₆], both of which lead to the higher T_m value for [tC₄mim][PF₆]. However, the difference in $\Delta_{\text{fus}}H$ increases T_m by 1.16-fold (23.1/20.7), while the difference in $\Delta_{\text{fus}}S$ increases T_m by 1.33-fold (73.3/55.0), the latter of which is more prominent. Although $\Delta_{\text{fus}}S$ is not a parameter that can be straightforwardly related to molecular structure, the lower S_c value for the branched IL (Figure 7) partially contributes to the low $\Delta_{\text{fus}}S$ value for [iC₃mim]X and [tC₄mim]X.

4.2. Density and Fractional Free Volume. The branched ILs, particularly [tC₄mim]X, have higher densities than the linear ILs, which is not the case for molecular liquids,^{71,85} where branching normally decreases density due to bulkiness inhibiting efficient packing. The densities of ILs can either increase or decrease upon branching,^{14,64,73,75,86} depending on the IL structure. This indicates that additional competing factors affect the densities of branched ILs.

To gain insight into the molecular level from the density data, fractional free volume (FFV), i.e., void fraction per unit volume, is a meaningful parameter. FFV also provides insight into the packing efficiency in the condensed phase. FFV is conventionally defined as⁸⁷

$$\text{FFV} = \frac{V_m - 1.3V_{\text{vdw}}}{V_m} \quad (4)$$

where V_m is the molar volume and V_{vdw} is the van der Waals volume. Conventionally, $1.3V_{\text{vdw}}$ is considered as the specific

volume of a molecule (or ion) at 0 K. V_m can be estimated from density, and V_{vdw} is taken from Table 6.

Figure 9 compares FFV values between the branched and linear ILs. In linear ILs, increases in anion size and cation alkyl chain length are both known to increase FFV.⁶⁶ This is the case for the current system. For the branched ILs, the values seem to be largely the same as those for the linear ILs. These results contradict those for molecular liquids, where a lower density and smaller V_{vdw} produce larger FFV values in branched substances (vide supra). The interaction energies between cations and anions estimated here also indicate that FFV should be larger in branched ILs. Thus, there are other factors that drive packing in the ions in the branched system despite their bulkiness and the weak 1:1 interaction. One plausible explanation involves the molecular symmetry. The branched cations prefer symmetrical forms, unlike the linear cations (Figure 6), which prompts efficient packing of ions in the liquid state. Another factor may be the absence of nonpolarity in the alkyl groups. Since alkyl groups that are governed by weak van der Waals interactions tend to possess large free volumes in the liquid state, lengthening the alkyl chain in the imidazolium cation increases the FFV of the ILs.^{66,88–91} However, probably due to the large positive charge in the branched groups (Figure 8a), they do not create large free volumes as the linear nonpolar alkyl groups do. These factors compete with the bulkiness and the weak interactions for the branched group and consequently provide similar FFVs to the linear ILs.

4.3. Viscosity. Although the viscosities of [iC₃mim]X are comparable to those of [C₃mim]X, the viscosities of [tC₄mim]X are roughly twice those of the linear ILs. In addition to the FFV data discussed above, which suggest high viscosity in the branched ILs, there are two competing factors involved in the viscosity of branched ILs, i.e., bulkiness and interaction energy, according to previous works on the viscosity of branched molecules.^{13,14,64,73–75,85,92–97} The viscosity increase upon alkyl chain branching has been observed in other ILs^{14,64,73–75,92} and some molecular liquids.⁸⁵ These behaviors are normally interpreted as being due to the bulkiness of branched chains. A detailed explanation has been proposed by Davis et al. by means of molecular dynamics simulations on alkanes.⁹³ In this simulation, when the strain rate was increased, a linear alkane elongated and became a prolate ellipsoid, while a branched one flattened and became an oblate ellipsoid.

Another important parameter affecting the viscosity of branched ILs is the interaction energy, as demonstrated in the classical Eyring equation.⁹⁸ Several authors have discussed the relationship between the viscosity and interaction energy of an ion pair in the gas phase for ILs.^{94,95} If this is the case as shown in Figure 8, the viscosity is lowered by branching. In the Eyring equation, the activation energy for viscosity is associated with

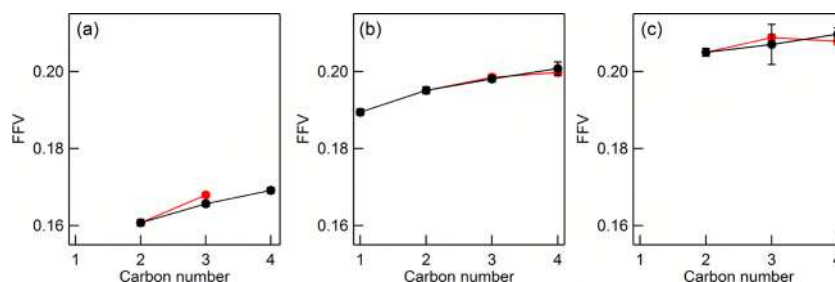


Figure 9. Comparison of FFV values between branched ILs (red) and linear ILs (black). ILs containing (a) [Nf₂]⁻, (b) [NTf₂]⁻, and (c) [NPF₂]⁻.

the vaporization energy; hence, the cohesive energy would be a more proper parameter than the interaction energy for an ion pair. Both experimental and computational studies have demonstrated that the cohesive energies of linear ILs increase with the increasing chain length.^{96,97} This is a result of the overcompensation of strengthening van der Waals interactions among alkyl chains despite the decrease in Coulombic interactions. Conversely, Zhang et al. performed molecular dynamics simulations and concluded that the total energy per atom in $[iC_3mim][NTf_2]$ is lower than that in $[C_3mim][NTf_2]$.¹³ This is caused by the charge delocalization in $[iC_3mim]^+$, which is consistent with the results shown in Figure 8f. Verevkin's group reported the vaporization enthalpies of $[C_3mim][NTf_2]$ ⁹⁹ and $[iC_3mim][NTf_2]$.¹⁰⁰ They concluded that the vaporization enthalpy of the branched IL at 298.15 K is comparable to that of the linear IL within the experimental error.

Combining these factors, our hypothesis is that differences in packing, bulkiness, and interaction energy upon branching are weak and balanced, which results in the comparable viscosities observed between $[iC_3mim]X$ and $[C_3mim]X$. Conversely, the viscosity of $[tC_4mim]X$ is higher than that of $[C_4mim]X$ because the former is well packed in the liquid state and has higher bulkiness that dominates the weak interaction energy. Since the cohesive energy of $[tC_4mim]X$ has not yet been estimated, additional experimental/computational approaches are necessary to interpret the significantly higher viscosity of $[tC_4mim]X$ than that of $[C_4mim]X$.

5. SUMMARY

We systematically measured the thermal properties, densities, and viscosities of $[iC_3mim]^+$ - and $[tC_4mim]^+$ -based ILs containing $[I]^-$, $[PF_6]^-$, $[Nf_2]^-$, $[NTf_2]^-$, and $[NPF_2]^-$ anions. DFT calculations for the gas phase were performed to better understand the structure–property relationship. To highlight the characteristic features of the branching effect, the results were compared to those for linear ILs, i.e., $[C_3mim]X$ and $[C_4mim]X$.

- (1) T_m for the branched ILs is always higher than that of the corresponding linear ILs, and unlike the linear ILs, T_m tends to increase upon increasing the carbon number in the branched alkyl group. It was suggested that the higher T_m for the branched ILs stems from the lower $\Delta_{fus}S$ values. A low S_c , which was revealed by DFT calculations, would partially contribute to lowering the entropy in the liquid state.
- (2) Compared to those of $[C_4mim]X$, the densities of $[tC_4mim]X$ are higher, while $[C_3mim]X$ and $[iC_3mim]X$ have comparable densities. Combined with the V_{vdw} data, FFV was estimated, and it was found that the values are similar for the linear and branched ILs. It was expected that the low cation–anion interaction and the bulkiness of the branched alkyl group could lead to a large free volume. Therefore, competing factors seem to be involved. One such factor may be the higher symmetries of the cation structures for $[iC_3mim]^+$ and $[tC_4mim]^+$ than those for the linear cations, with the most stable structures possessing the C_s symmetry. Another interpretation is based on the fact that $[iC_3mim]^+$ and $[tC_4mim]^+$ have relatively high positive charges on the alkyl side chain. This erases its “alkane” nature, which leads to a large free volume.

- (3) The viscosities of $[iC_3mim]X$ are comparable to those of $[C_3mim]X$, while the viscosities of $[tC_4mim]X$ are twice those of $[C_4mim]X$. The well-packed nature in the liquid state (based on FFV value) and bulkiness of the *tert*-butyl group in $[tC_4mim]^+$ are thought to be responsible for the higher viscosities. Since the interactions between cations and anions are weaker in the branched ILs, such well-packed nature and bulkiness may dominate the interaction effect.

■ ASSOCIATED CONTENT

Supporting Information

The Supporting Information is available free of charge at <https://pubs.acs.org/doi/10.1021/acs.jced.9b00776>.

Synthetic details, NMR characterizations, coefficients for the fits of density and viscosity, calculated energies of the cations, optimized ion pair structures, and DSC and TG/DTA curves (PDF)

■ AUTHOR INFORMATION

Corresponding Author

*E-mail: taendo@mail.doshisha.ac.jp.

ORCID

Takatsugu Endo: 0000-0002-7272-0715

Yoshifumi Kimura: 0000-0002-2248-9973

Notes

The authors declare no competing financial interest.

■ ACKNOWLEDGMENTS

The work was partially supported by the MEXT-Supported Program for the Strategic Research Foundation at Private Universities 2015–2019 (S1511025), by JSPS KAKENHI (Grant Number JP19K05393), and by grants-in-aid from the Harris Science Research Institute of Doshisha University.

■ REFERENCES

- (1) MacFarlane, D. R.; Chong, A. L.; Forsyth, M.; Kar, M.; Vijayaraghavan, R.; Somers, A.; Pringle, J. M. New dimensions in salt–solvent mixtures: a 4th evolution of ionic liquids. *Faraday Discuss.* **2018**, *206*, 9–28.
- (2) MacFarlane, D. R.; Kar, M.; Pringle, J. M. *Fundamentals of Ionic Liquids: From Chemistry to Applications*; Wiley-VCH, 2017.
- (3) Seddon, K. R. In *Ionic Liquids: Designer Solvents?* Boghosian, S., Dracopoulos, V., Kontoyannis, C. G., Voyiatzis, G. A., Eds.; Institute of Chemical Engineering and High Temperature Chemical Processes: Patras, 1999.
- (4) Watanabe, M.; Dokko, K.; Ueno, K.; Thomas, M. L. From ionic liquids to solvate ionic liquids: Challenges and opportunities for next generation battery electrolytes. *Bull. Chem. Soc. Jpn.* **2018**, *91*, 1660–1682.
- (5) Lhermerout, R.; Diederichs, C.; Perkin, S. Are ionic liquids good boundary lubricants? A molecular perspective. *Lubricants* **2018**, No. 6.
- (6) Halder, P.; Kundu, S.; Patel, S.; Setiawan, A.; Atkin, R.; Parthasarthy, R.; Paz-Ferreiro, J.; Surapaneni, A.; Shah, K. Progress on the pre-treatment of lignocellulosic biomass employing ionic liquids. *Renewable Sustainable Energy Rev.* **2019**, *105*, 268–292.
- (7) Chen, J.; Xie, F.; Li, X.; Chen, L. Ionic liquids for the preparation of biopolymer materials for drug/gene delivery: A review. *Green Chem.* **2018**, *20*, 4169–4200.
- (8) Patel, R.; Kumari, M.; Khan, A. B. Recent Advances in the Applications of Ionic Liquids in Protein Stability and Activity: A Review. *Appl. Biochem. Biotechnol.* **2014**, *172*, 3701–3720.

- (9) Holbrey, J. D.; Seddon, K. R. The phase behaviour of 1-alkyl-3-methylimidazolium tetrafluoroborates; ionic liquids and ionic liquid crystals. *J. Chem. Soc., Dalton Trans.* **1999**, 2133–2140.
- (10) Rodrigues, A. S. M. C.; Santos, L. M. N. B. F. Nanostructuring Effect on the Thermal Behavior of Ionic Liquids. *ChemPhysChem* **2016**, *17*, 1512–1517.
- (11) Tokuda, H.; Hayamizu, K.; Ishii, K.; Susan, M. A. B. H.; Watanabe, M. Physicochemical properties and structures of room temperature ionic liquids. 2. Variation of alkyl chain length in imidazolium cation. *J. Phys. Chem. B* **2005**, *109*, 6103–6110.
- (12) Russina, O.; Lo Celso, F.; Plechkova, N. V.; Triolo, A. Emerging Evidences of Mesoscopic-Scale Complexity in Neat Ionic Liquids and Their Mixtures. *J. Phys. Chem. Lett.* **2017**, *8*, 1197–1204.
- (13) Zhang, Y.; Xue, L.; Khabaz, F.; Doerfler, R.; Quitevis, E. L.; Khare, R.; Maginn, E. J. Molecular Topology and Local Dynamics Govern the Viscosity of Imidazolium-Based Ionic Liquids. *J. Phys. Chem. B* **2015**, *119*, 14934–14944.
- (14) Xue, L.; Gurung, E.; Tamas, G.; Koh, Y. P.; Shadeck, M.; Simon, S. L.; Maroncelli, M.; Quitevis, E. L. Effect of Alkyl Chain Branching on Physicochemical Properties of Imidazolium-Based Ionic Liquids. *J. Chem. Eng. Data* **2016**, *61*, 1078–1091.
- (15) Xue, L.; Bardak, F.; Tamas, G.; Quitevis, E. L. Comparative study of the intermolecular dynamics of imidazolium-based ionic liquids with linear and branched alkyl chains: OHD-RIKES measurements. *Phys. Chem. Chem. Phys.* **2017**, *19*, 4661–4672.
- (16) Khabaz, F.; Zhang, Y.; Xue, L.; Quitevis, E. L.; Maginn, E. J.; Khare, R. Temperature Dependence of Volumetric and Dynamic Properties of Imidazolium-Based Ionic Liquids. *J. Phys. Chem. B* **2018**, *122*, 2414–2424.
- (17) Dong, Q.; Muzny, C. D.; Kazakov, A.; Diky, V.; Magee, J. W.; Widegren, J. A.; Chirico, R. D.; Marsh, K. N.; Frenkel, M. ILThermo: A free-access web database for thermodynamic properties of ionic liquids. *J. Chem. Eng. Data* **2007**, *52*, 1151–1159.
- (18) Endo, T.; Nishikawa, K. Isomer populations in liquids for 1-isopropyl-3-methylimidazolium bromide and its iodide and their conformational changes accompanying the crystallizing and melting processes. *J. Phys. Chem. A* **2008**, *112*, 7543–7550.
- (19) Ngo, H. L.; Lecompte, K.; Hargens, L.; McEwen, A. B. Thermal properties of imidazolium ionic liquids. *Thermochim. Acta* **2000**, *357*–358, 97–102.
- (20) Swartling, D.; Ray, L.; Compton, S.; Ensor, D. Preliminary Investigation Into Modification of Ionic Liquids to Improve Extraction Parameters. *SAAS Bull. Biochem. Biotechnol.* **2000**, *13*, 1–7.
- (21) Carmichael, A. J.; Hardacre, C.; Holbrey, J. D.; Seddon, K. R.; Nieuwenhuyzen, M. *Structure and Bonding in Ionic Liquids*; Electrochemical Society: Pennington, NJ, 1999; Vol. 99-41.
- (22) Cowley, R. E.; Bontchev, R. P.; Duesler, E. N.; Smith, J. M. Removing the Sting from the Tail: Reversible Protonation of Scorpionate Ligands in Cobalt(II) Tris(carbene)borate Complexes. *Inorg. Chem.* **2006**, *45*, 9771–9779.
- (23) Thomazeau, C.; Olivier-Bourbigou, H.; Magna, L.; Luts, S.; Gilbert, B. Determination of an Acidic Scale in Room Temperature Ionic Liquids. *J. Am. Chem. Soc.* **2003**, *125*, 5264–5265.
- (24) Yasaka, Y.; Kimura, Y. Polarity and Nonpolarity of Ionic Liquids Viewed from the Rotational Dynamics of Carbon Monoxide. *J. Phys. Chem. B* **2015**, *119*, 15493–15501.
- (25) Frisch, M. J.; Trucks, G. W.; Schlegel, H. B.; Scuseria, G. E.; Robb, M. A.; Cheeseman, J. R.; Scalmani, G.; Barone, V.; Mennucci, B.; Petersson, G. A.; Nakatsuji, H.; Caricato, M.; Li, X.; Hratchian, H. P.; Izmaylov, A. F.; Bloino, J.; Zheng, G.; Sonnenberg, J. L.; Hada, M.; Ehara, M.; Toyota, K.; Fukuda, R.; Hasegawa, J.; Ishida, M.; Nakajima, T.; Honda, Y.; Kitao, O.; Nakai, H.; Vreven, T.; Montgomery, J. A., Jr.; Peralta, J. E.; Ogliaro, F.; Bearpark, M.; Heyd, J. J.; Brothers, E.; Kudin, K. N.; Staroverov, V. N.; Keith, T.; Kobayashi, R.; Normand, J.; Raghavachari, K.; Rendell, A.; Burant, J. C.; Iyengar, S. S.; Tomasi, J.; Cossi, M.; Rega, N.; Millam, J. M.; Klene, M.; Knox, J. E.; Cross, J. B.; Bakken, V.; Adamo, C.; Jaramillo, J.; Gomperts, R.; Stratmann, R. E.; Yazyev, O.; Austin, A. J.; Cammi, R.; Pomelli, C.; Ochterski, J. W.; Martin, R. L.; Morokuma, K.; Zakrzewski, V. G.; Voth, G. A.; Salvador, P.; Dannenberg, J. J.; Dapprich, S.; Daniels, A. D.; Farkas, O.; Foresman, J. B.; Ortiz, J. V.; Cioslowski, J.; Fox, D. J. *Gaussian 09*; Gaussian, Inc.: Wallingford, CT, 2010.
- (26) Becke, A. D. Density-functional thermochemistry. III. The role of exact exchange. *J. Chem. Phys.* **1993**, *98*, 5648–5652.
- (27) Miehlich, B.; Savin, A.; Stoll, H.; Preuss, H. Results obtained with the correlation energy density functionals of Becke and Lee, Yang and Parr. *Chem. Phys. Lett.* **1989**, *157*, 200–206.
- (28) Lee, C.; Yang, W.; Parr, R. G. Development of the Colle-Salvetti correlation-energy formula into a functional of the electron density. *Phys. Rev. B* **1988**, *37*, 785–789.
- (29) Breneman, C. M.; Wiberg, K. B. Determining atom-centered monopoles from molecular electrostatic potentials. The need for high sampling density in formamide conformational analysis. *J. Comput. Chem.* **1990**, *11*, 361–373.
- (30) Marekha, B. A.; Kalugin, O. N.; Idrissi, A. Non-covalent interactions in ionic liquid ion pairs and ion pair dimers: a quantum chemical calculation analysis. *Phys. Chem. Chem. Phys.* **2015**, *17*, 16846–16857.
- (31) Parsons, D. F.; Ninham, B. W. Ab Initio Molar Volumes and Gaussian Radii. *J. Phys. Chem. A* **2009**, *113*, 1141–1150.
- (32) Shirota, H.; Mandai, T.; Fukazawa, H.; Kato, T. Comparison between dicationic and monocationic ionic liquids: Liquid density, thermal properties, surface tension, and shear viscosity. *J. Chem. Eng. Data* **2011**, *56*, 2453–2459.
- (33) Paulechka, Y. U.; Blokhin, A. V. Low-temperature heat capacity and derived thermodynamic properties for 1-methyl-3-propylimidazolium bromide and 1-butyl-3-methylimidazolium iodide. *J. Chem. Thermodyn.* **2014**, *79*, 94–99.
- (34) López-Martin, I.; Burello, E.; Davey, P. N.; Seddon, K. R.; Rothenberg, G. Anion and cation effects on imidazolium salt melting points: a descriptor modelling study. *ChemPhysChem* **2007**, *8*, 690–695.
- (35) Vlahakis, J. Z.; Lazar, C.; Crandall, I. E.; Szarek, W. A. Anti-Plasmodium activity of imidazolium and triazolium salts. *Bioorg. Med. Chem.* **2010**, *18*, 6184–6196.
- (36) Every, H.; Bishop, A. G.; MacFarlane, D. R.; Orädd, G.; Forsyth, M. Room temperature fast-ion conduction in imidazolium halide salts. *J. Mater. Chem.* **2001**, *11*, 3031–3036.
- (37) Wachter, P.; Schreiner, C.; Schweiger, H.-G.; Gores, H. J. Determination of phase transition points of ionic liquids by combination of thermal analysis and conductivity measurements at very low heating and cooling rates. *J. Chem. Thermodyn.* **2010**, *42*, 900–903.
- (38) Nakakoshi, M.; Shiro, M.; Fujimoto, T.; Machinami, T.; Seki, H.; Tashiro, M.; Nishikawa, K. Crystal Structure of 1-Butyl-3-methylimidazolium Iodide. *Chem. Lett.* **2006**, *35*, 1400–1401.
- (39) Endo, T.; Masu, H.; Fujii, K.; Morita, T.; Seki, H.; Sen, S.; Nishikawa, K. Determination of missing crystal structures in the 1-alkyl-3-methylimidazolium hexafluorophosphate series: Implications on structure – property relationships. *Cryst. Growth Des.* **2013**, *13*, 5383–5390.
- (40) Fujii, K.; Mukai, T.; Nishikawa, K. Crystal Structure of 1,3-Dimethylimidazolium Bis(fluorosulfonyl)amide: Unexpectedly High Melting Point Arising from Polydentate Hydrogen Bonding. *Chem. Lett.* **2014**, *43*, 405–407.
- (41) Kerner, M.; Plylahan, N.; Scheers, J.; Johansson, P. Ionic liquid based lithium battery electrolytes: fundamental benefits of utilising both TFSI and FSI anions? *Phys. Chem. Chem. Phys.* **2015**, *17*, 19569–19581.
- (42) Tokuda, H.; Tsuzuki, S.; Susan, M. A. B. H.; Hayamizu, K.; Watanabe, M. How ionic are room-temperature ionic liquids? An indicator of the physicochemical properties. *J. Phys. Chem. B* **2006**, *110*, 19593–19600.
- (43) Tsunashima, K.; Kawabata, A.; Matsumiya, M.; Kodama, S.; Enomoto, R.; Sugiya, M.; Kunugi, Y. Low viscous and highly conductive phosphonium ionic liquids based on bis(fluorosulfonyl)amide anion as potential electrolytes. *Electrochem. Commun.* **2011**, *13*, 178–181.

- (44) Maton, C.; De Vos, N.; Stevens, C. V. Ionic liquid thermal stabilities: Decomposition mechanisms and analysis tools. *Chem. Soc. Rev.* **2013**, *42*, 5963–5977.
- (45) Tariq, M.; Serro, A. P.; Mata, J. L.; Saramago, B.; Esperança, J. M. S. S.; Canongia Lopes, J. N.; Rebelo, L. P. N. High-temperature surface tension and density measurements of 1-alkyl-3-methylimidazolium bistriflamide ionic liquids. *Fluid Phase Equilib.* **2010**, *294*, 131–138.
- (46) Rocha, M. A. A.; Neves, C. M. S. S.; Freire, M. G.; Russina, O.; Triolo, A.; Coutinho, J. A. P.; Santos, L. M. N. B. F. Alkylimidazolium Based Ionic Liquids: Impact of Cation Symmetry on Their Nanoscale Structural Organization. *J. Phys. Chem. B* **2013**, *117*, 10889–10897.
- (47) Skowronek, J.; Dzida, M.; Zorebski, E.; Chorażewski, M.; Jezak, S.; Żarska, M.; Zorębski, M.; Goodrich, P.; Jacquemin, J. High Pressure Speed of Sound and Related Thermodynamic Properties of 1-Alkyl-3-methylimidazolium Bis(trifluoromethyl)sulfonylimides (from 1-Propyl- to 1-Hexyl-). *J. Chem. Eng. Data* **2016**, *61*, 3794–3805.
- (48) Nazet, A.; Sokolov, S.; Sonnleitner, T.; Makino, T.; Kanakubo, M.; Buchner, R. Densities, Viscosities, and Conductivities of the Imidazolium Ionic Liquids [Emim][Ac], [Emim][FAP], [Bmim][BETI], [Bmim][FSI], [Hmim][TFSI], and [Omim][TFSI]. *J. Chem. Eng. Data* **2015**, *60*, 2400–2411.
- (49) Liu, H.; Maginn, E.; Visser, A. E.; Bridges, N. J.; Fox, E. B. Thermal and Transport Properties of Six Ionic Liquids: An Experimental and Molecular Dynamics Study. *Ind. Eng. Chem. Res.* **2012**, *51*, 7242–7254.
- (50) Morgan, D.; Ferguson, L.; Scovazzo, P. Diffusivities of Gases in Room-Temperature Ionic Liquids: Data and Correlations Obtained Using a Lag-Time Technique. *Ind. Eng. Chem. Res.* **2005**, *44*, 4815–4823.
- (51) Tariq, M.; Carvalho, P. J.; Coutinho, J. A. P.; Marrucho, I. M.; Lopes, J. N. C.; Rebelo, L. P. N. Viscosity of (C2-C14) 1-alkyl-3-methylimidazolium bis(trifluoromethylsulfonyl)amide ionic liquids in an extended temperature range. *Fluid Phase Equilib.* **2011**, *301*, 22–32.
- (52) Gómez, E.; Calvar, N.; Macedo, E. A.; Domínguez, A. Effect of the temperature on the physical properties of pure 1-propyl 3-methylimidazolium bis(trifluoromethylsulfonyl)imide and characterization of its binary mixtures with alcohols. *J. Chem. Thermodyn.* **2012**, *45*, 9–15.
- (53) Papović, S.; Vranješ, M.; Gadžurić, S. A comprehensive study of { γ -butyrolactone + 1-methyl-3-propylimidazolium bis(trifluoromethylsulfonyl)imide} binary mixtures. *J. Chem. Thermodyn.* **2015**, *91*, 360–368.
- (54) Kakinuma, S.; Ishida, T.; Shirota, H. Femtosecond Raman-Induced Kerr Effect Study of Temperature-Dependent Intermolecular Dynamics in Imidazolium-Based Ionic Liquids: Effects of Anion Species and Cation Alkyl Groups. *J. Phys. Chem. B* **2017**, *121*, 250–264.
- (55) Nemoto, F.; Kofu, M.; Yamamuro, O. Thermal and structural studies of imidazolium-based ionic liquids with and without liquid-crystalline phases: The origin of nanostructure. *J. Phys. Chem. B* **2015**, *119*, 5028–5034.
- (56) Harris, K. R.; Kanakubo, M.; Woolf, L. A. Temperature and Pressure Dependence of the Viscosity of the Ionic Liquids 1-Hexyl-3-methylimidazolium Hexafluorophosphate and 1-Butyl-3-methylimidazolium Bis. *J. Chem. Eng. Data* **2007**, *52*, 1080–1085.
- (57) Atilhan, M.; Jacquemin, J.; Rooney, D.; Khraisheh, M.; Aparicio, S. Viscous Behavior of Imidazolium-Based Ionic Liquids. *Ind. Eng. Chem. Res.* **2013**, *52*, 16774–16785.
- (58) Almeida, H. F. D.; Canongia Lopes, J. N.; Rebelo, L. P. N.; Coutinho, J. A. P.; Freire, M. G.; Marrucho, I. M. Densities and Viscosities of Mixtures of Two Ionic Liquids Containing a Common Cation. *J. Chem. Eng. Data* **2016**, *61*, 2828–2843.
- (59) Salgado, J.; Regueira, T.; Lugo, L.; Vijande, J.; Fernández, J.; García, J. Density and viscosity of three (2,2,2-trifluoroethanol+1-butyl-3-methylimidazolium) ionic liquid binary systems. *J. Chem. Thermodyn.* **2014**, *70*, 101–110.
- (60) Umebayashi, Y.; Fujimori, T.; Sukizaki, T.; Asada, M.; Fujii, K.; Kanzaki, R.; Ishiguro, S.-I. Evidence of conformational equilibrium of 1-ethyl-3-methylimidazolium in its ionic liquid salts: Raman spectroscopic study and quantum chemical calculations. *J. Phys. Chem. A* **2005**, *109*, 8976–8982.
- (61) Tsuzuki, S.; Arai, A. A.; Nishikawa, K. Conformational analysis of 1-butyl-3-methylimidazolium by CCSD(T) level ab initio calculations: effects of neighboring anions. *J. Phys. Chem. B* **2008**, *112*, 7739–7747.
- (62) Turner, E. A.; Pye, C. C.; Singer, R. D. Use of ab initio calculations toward the rational design of room temperature ionic liquids. *J. Phys. Chem. A* **2003**, *107*, 2277–2288.
- (63) Endo, T.; Hoshino, S.; Shimizu, Y.; Fujii, K.; Nishikawa, K. Comprehensive Conformational and Rotational Analyses of the Butyl Group in Cyclic Cations: DFT Calculations for Imidazolium, Pyridinium, Pyrrolidinium, and Piperidinium. *J. Phys. Chem. B* **2016**, *120*, 10336–10349.
- (64) Lartey, M.; Meyer-Ilse, J.; Watkins, J. D.; Roth, E. A.; Bowser, S.; Kusuma, V. A.; Damodaran, K.; Zhou, X.; Haranczyk, M.; Albenze, E.; Luecke, D. R.; Hopkinson, D.; Kortright, J. B.; Nulwala, H. B. Branched isomeric 1,2,3-triazolium-based ionic liquids: New insight into structure-property relationships. *Phys. Chem. Chem. Phys.* **2015**, *17*, 29834–29843.
- (65) Verma, P. L.; Gejji, S. P. Electronic structure, spectral characteristics and physicochemical properties of linear, branched and cyclic alkyl group substituted 1-alkyl-3-butylimidazolium cation based ionic liquids. *J. Mol. Liq.* **2018**, *251*, 394–406.
- (66) Endo, T.; Nishisaka, Y.; Kin, Y.; Kimura, Y. Systematic estimation and interpretation of fractional free volume in 1-alkyl-3-methylimidazolium-based ionic liquids. *Fluid Phase Equilib.* **2019**, *498*, 144–150.
- (67) Bondi, A. Van der Waals volumes and radii. *J. Phys. Chem. A* **1964**, *68*, 441–451.
- (68) Zhao, Y. H.; Abraham, M. H.; Zissimos, A. M. Fast calculation of van der Waals volume as a sum of atomic and bond contributions and its application to drug compounds. *J. Org. Chem.* **2003**, *68*, 7368–7373.
- (69) Ciubotariu, D.; Medeleanu, M.; Vlaia, V.; Olariu, T.; Ciubotariu, C.; Dragos, D.; Corina, S. Molecular van der Waals space and topological indices from the distance matrix. *Molecules* **2004**, *9*, 1053–1078.
- (70) Meyer, A. Y. Molecular mechanics and molecular shape. Part 1. Van der Waals descriptors of simple molecules. *J. Chem. Soc., Perkin Trans. 2* **1985**, 1161–1169.
- (71) Linstrom, P. J.; Mallard, W. G., Eds. *NIST Chemistry WebBook*, NIST Standard Reference Database; National Institute of Standards and Technology: Gaithersburg, MD.
- (72) Quek, S. K.; Lyapkalo, I. M.; Huynh, H. V. Synthesis and properties of N,N'-dialkylimidazolium bis(nonafluorobutane-1-sulfonyl)imides: A new subfamily of ionic liquids. *Tetrahedron* **2006**, *62*, 3137–3145.
- (73) Yoshida, Y.; Baba, O.; Larriba, C.; Saito, G. Imidazolium-based ionic liquids formed with dicyanamide anion: influence of cationic structure on ionic conductivity. *J. Phys. Chem. B* **2007**, *111*, 12204–12210.
- (74) Higashi, T.; Ueda, T.; Mochida, T. Effects of substituent branching and chirality on the physical properties of ionic liquids based on cationic ruthenium sandwich complexes. *Phys. Chem. Chem. Phys.* **2016**, *18*, 10041–10048.
- (75) Talebi, M.; Patil, R. A.; Armstrong, D. W. Physicochemical properties of branched-chain dicationic ionic liquids. *J. Mol. Liq.* **2018**, *256*, 247–255.
- (76) Endo, T.; Fujii, K.; Nishikawa, K. Crystal polymorphism of 1-butyl-3-methylimidazolium hexafluorophosphate: Phase diagram, structure, and dynamics. *Aust. J. Chem.* **2019**, *72*, 11–20.
- (77) Neves, C. M. S. S.; Batista, M. L. S.; Cláudio, A. F. M.; Santos, L. M. N. B. F.; Marrucho, I. M.; Freire, M. G.; Coutinho, J. A. P. Thermophysical properties and water saturation of [PF6]-based ionic liquids. *J. Chem. Eng. Data* **2010**, *55*, 5065–5073.
- (78) Kabo, G. J.; Blokhin, A. V.; Paulechka, Y. U.; Kabo, A. G.; Shymanovich, M. P.; Magee, J. W. Thermodynamic Properties of 1-Butyl-3-methylimidazolium Hexafluorophosphate in the Condensed State. *J. Chem. Eng. Data* **2004**, *49*, 453–461.
- (79) Troncoso, J.; Cerdeirín, C. A.; Sanmamed, Y. A.; Romani, L.; Rebelo, L. P. N. Thermodynamic Properties of Imidazolium-Based

Ionic Liquids: Densities, Heat Capacities, and Enthalpies of Fusion of [bmim][PF₆] and [bmim][NTf₂]. *J. Chem. Eng. Data* **2006**, *51*, 1856–1859.

(80) Zhang, Z. H.; Cui, T.; Zhang, J. L.; Xiong, H.; Li, G. P.; Sun, L. X.; Xu, F.; Cao, Z.; Li, F.; Zhao, J. J. Thermodynamic investigation of room temperature ionic liquid: the heat capacity and thermodynamic functions of BMIPF₆. *J. Therm. Anal. Calorim.* **2010**, *101*, 1143–1148.

(81) Endo, T.; Nishikawa, K. Thermal phase behavior of 1-butyl-3-methylimidazolium hexafluorophosphate: Simultaneous measurements of the melting of two polymorphic crystals by Raman spectroscopy and calorimetry. *Chem. Phys. Lett.* **2013**, *584*, 79–82.

(82) Blokhin, A. V.; Paulechka, Y. U.; Strechan, A. A.; Kabo, G. J. Physicochemical properties, structure, and conformations of 1-Butyl-3-methylimidazolium bis(trifluoromethanesulfonyl)imide [C₄mim]-NTf₂ ionic liquid. *J. Phys. Chem. B* **2008**, *112*, 4357–4364.

(83) Jin, H.; O'Hare, B.; Dong, J.; Arzhantsev, S.; Baker, G.; Wishart, J. F.; Benesi, A. J.; Maroncelli, M. Physical properties of ionic liquids consisting of the 1-butyl-3-methylimidazolium cation with various anions and the bis(trifluoromethylsulfonyl)imide anion with various cations. *J. Phys. Chem. B* **2008**, *112*, 81–92.

(84) Shimizu, Y.; Ohte, Y.; Yamamura, Y.; Saito, K. Effects of Thermal History on Thermal Anomaly in Solid of Ionic Liquid Compound, [C₄mim][Tf₂N]. *Chem. Lett.* **2007**, *36*, 1484–1485.

(85) Lide, D. R. *CRC Handbook of Chemistry and Physics*. CRC Press: Boca Raton, FL, 2005.

(86) Rotrekl, J.; Storch, J.; Kloužek, J.; Vrbka, P.; Husson, P.; Andresová, A.; Bendová, M.; Wagner, Z. Thermal properties of 1-alkyl-3-methylimidazolium bis(trifluoromethylsulfonyl)imide ionic liquids with linear, branched and cyclic alkyl substituents. *Fluid Phase Equilib.* **2017**, *443*, 32–43.

(87) Choudalakis, G.; Gotsis, A. D. Free volume and mass transport in polymer nanocomposites. *Curr. Opin. Colloid Interface Sci.* **2012**, *17*, 132–140.

(88) Cheng, H.; Zhang, J.; Qi, Z. Effects of interaction with sulphur compounds and free volume in imidazolium-based ionic liquid on desulphurisation: a molecular dynamics study. *Mol. Simul.* **2018**, *44*, 55–62.

(89) Shannon, M. S.; Tedstone, J. M.; Danielsen, S. P. O.; Hindman, M. S.; Irvin, A. C.; Bara, J. E. Free Volume as the Basis of Gas Solubility and Selectivity in Imidazolium-Based Ionic Liquids. *Ind. Eng. Chem. Res.* **2012**, *51*, 5565–5576.

(90) Jeffrey Horne, W.; Shannon, M. S.; Bara, J. E. Correlating fractional free volume to CO₂ selectivity in [Rmim][Tf₂N] ionic liquids. *J. Chem. Thermodyn.* **2014**, *77*, 190–196.

(91) Dai, C.; Lei, Z.; Chen, B. Gas solubility in long-chain imidazolium-based ionic liquids. *AIChE J.* **2017**, *63*, 1792–1798.

(92) Andresova, A.; Storch, J.; Traïkia, M.; Wagner, Z.; Bendova, M.; Husson, P. Branched and cyclic alkyl groups in imidazolium-based ionic liquids: Molecular organization and physico-chemical properties. *Fluid Phase Equilib.* **2014**, *371*, 41–49.

(93) Daivis, P. J.; Evans, D. J.; Morriss, G. P. Computer simulation study of the comparative rheology of branched and linear alkanes. *J. Chem. Phys.* **1992**, *97*, 616–627.

(94) Shirota, H.; Wishart, J. F.; Castner, E. W. Intermolecular interactions and dynamics of room temperature ionic liquids that have silyl- and siloxy-substituted imidazolium cations. *J. Phys. Chem. B* **2007**, *111*, 4819–4829.

(95) Tsuzuki, S.; Hayamizu, K.; Seki, S. Origin of the low-viscosity of [emim][(FSO₂)₂N] ionic liquid and its lithium salt mixture: Experimental and theoretical study of self-diffusion coefficients, conductivities, and intermolecular interactions. *J. Phys. Chem. B* **2010**, *114*, 16329–16336.

(96) Santos, L. M. N. B. F.; Lopes, J. N. C.; Coutinho, J. A. P.; Esperança, J. M. S. S.; Gomes, L. R.; Marrucho, I. M.; Rebelo, L. P. N. Ionic liquids: First direct determination of their cohesive energy. *J. Am. Chem. Soc.* **2007**, *129*, 284–285.

(97) Shimizu, K.; Tariq, M.; Gomes, M. F. C.; Rebelo, L. P. N.; Lopes, J. N. C. Assessing the dispersive and electrostatic components of the

cohesive energy of ionic liquids using molecular dynamics simulations and molar refraction data. *J. Phys. Chem. B* **2010**, *114*, 5831–5834.

(98) Glasstone, S.; Laidler, K. J.; Eyring, H. *The Theory of Rate Processes. The Kinetics of Chemical Reactions, Viscosity, Diffusion and Electrochemical Phenomena*; McGraw-Hill: New York, 1941; 611 p.

(99) Verevkin, S. P.; Zaitsau, D. H.; Emel'Yanenko, V. N.; Yermalayeu, A. V.; Schick, C.; Liu, H.; Maginn, E. J.; Bulut, S.; Krossing, I.; Kalb, R. Making Sense of Enthalpy of Vaporization Trends for Ionic Liquids: New Experimental and Simulation Data Show a Simple Linear Relationship and Help Reconcile Previous Data. *J. Phys. Chem. B* **2013**, *117*, 6473–6486.

(100) Zaitsau, D. H.; Varfolomeev, M. A.; Verevkin, S. P.; Stanton, A. D.; Hindman, M. S.; Bara, J. E. Structure-property relationships in ionic liquids: Influence of branched and cyclic groups on vaporization enthalpies of imidazolium-based ILs. *J. Chem. Thermodyn.* **2016**, *93*, 151–156.



Characterization of thylakoid membrane in a heterocystous cyanobacterium and green alga with dual-detector fluorescence lifetime imaging microscopy with a systematic change of incident laser power



Shuho Nozue^a, Akira Mukuno^a, Yumi Tsuda^a, Takashi Shiina^b, Masahide Terazima^a, Shigeichi Kumazaki^{a,*}

^a Department of Chemistry, Graduate School of Science, Kyoto University, Kyoto 606-8502, Japan

^b Graduate School of Life and Environmental Sciences, Kyoto Prefectural University, Sakyo-ku, Kyoto 606-8522, Japan

ARTICLE INFO

Article history:

Received 3 June 2015

Received in revised form 29 September 2015

Accepted 11 October 2015

Available online 22 October 2015

Keywords:

Photosystem II

Photosystem I

Chlorophyll fluorescence

Fluorescence lifetime imaging microscopy

Heterocystous cyanobacteria

Green algae

ABSTRACT

Fluorescence Lifetime Imaging Microscopy (FLIM) has been applied to plants, algae and cyanobacteria, in which excitation laser conditions affect the chlorophyll fluorescence lifetime due to several mechanisms. However, the dependence of FLIM data on input laser power has not been quantitatively explained by absolute excitation probabilities under actual imaging conditions. In an effort to distinguish between photosystem I and photosystem II (PSI and PSII) in microscopic images, we have obtained dependence of FLIM data on input laser power from a filamentous cyanobacterium *Anabaena variabilis* and single cellular green alga *Parachlorella kessleri*. Nitrogen-fixing cells in *A. variabilis*, heterocysts, are mostly visualized as cells in which short-lived fluorescence (≤ 0.1 ns) characteristic of PSI is predominant. The other cells in *A. variabilis* (vegetative cells) and *P. kessleri* cells show a transition in the status of PSII from an open state with the maximal charge separation rate at a weak excitation limit to a closed state in which charge separation is temporarily prohibited by previous excitation(s) at a relatively high laser power. This transition is successfully reproduced by a computer simulation with a high fidelity to the actual imaging conditions. More details in the fluorescence from heterocysts were examined to assess possible functions of PSII in the anaerobic environment inside the heterocysts for the nitrogen-fixing enzyme, nitrogenase. Photochemically active PSII:PSI ratio in heterocysts is tentatively estimated to be typically below our detection limit or at most about 5% in limited heterocysts in comparison with that in vegetative cells.

© 2015 Elsevier B.V. All rights reserved.

1. Introduction

All chemical energy in the biosphere on Earth is mostly attributable to photosynthesis, the primary step of which is a conversion from a solar photon to transmembrane charge separation in chloroplasts of plants and algae or some photosynthetic prokaryotes including cyanobacteria. Although most of the absorbed photons by photosynthetic pigments are used to drive the charge separation and subsequent synthesis of energy-rich chemicals, some minor portion of photons are reemitted as

autofluorescence or dissipated as heat. Autofluorescence of photosynthetic pigments, especially that of chlorophyll *a* (Chl_a), has been thus widely and extensively monitored as an index of photosynthetic reactions in oxygenic photosynthetic organisms [1,2]. Microscopic fluorescence images of Chl_a is also useful for understanding the structures and photochemical functions of thylakoid membrane in chloroplasts of plants and cyanobacterial cells under physiological conditions [3–5]. Fluorescence spectral acquisition in microscopic imaging has also been successful to obtain images of important photosynthetic molecular components like photosystem I (PSI), photosystem II (PSII), and light-harvesting molecules [4,6–12]. However, fluorescence intensity suffers from attenuation due to absorption, refraction and scattering during transmission through the samples between focus plane of interest and microscope objective. This leads to deformation of fluorescence spectra, because the attenuation of signals is dependent on fluorescence wavelength [11].

Fluorescence lifetime (FL) measurement function has been recently implemented in laser scanning confocal fluorescence microscopy in order to obtain an image with fluorescence decay parameters in all pixels (Fluorescence Lifetime Imaging Microscopy, FLIM) [4,13]. Time constants of fluorescence decay are robust parameters against

Abbreviations: APC, allophycocyanin, light-harvesting subunit of phycobilisome; CF, chlorophyll fluorescence; CFL, chlorophyll fluorescence lifetime; Chl_a, Chl_b, chlorophyll a, chlorophyll b; CP26, CP29, light-harvesting complex of photosystem II; FL, fluorescence lifetime; FLIM, Fluorescence Lifetime Imaging Microscopy; FWHM, full width at half maximum; IRF, instrument-response function; LHCl, light-harvesting complex of photosystem I; LHClI, light-harvesting complex of photosystem II; NPQ, nonphotochemical quenching; PAM, Pulse-amplitude-modulation fluorometry; PBS, phycobilisome; PC, phycocyanin, light-harvesting subunit of phycobilisome; PEC, phycoerythrocyanin, light-harvesting subunit of phycobilisome; PSI, PSII, photosystem I, photosystem II; Q_A, electron acceptor quinone in photosystem II.

* Corresponding author at: Department of Chemistry, Graduate School of Science, Kyoto University, Kyoto 606-8502, Japan.

E-mail address: kumazaki@kuchem.kyoto-u.ac.jp (S. Kumazaki).

attenuation, because they are just determined by the nature of distribution of the delay time between absorption of excitation photon and emission of fluorescence photon. The nature of the distribution is unchanged by the attenuation of the number of fluorescence photons, as far as attenuation is in a linear regime, under which propagation and transmission of the fluorescence does not depend on the fluorescence intensity.

Fluorescence decay on a picosecond to nanosecond time scale of thylakoid membrane reflects the time scales of energy conversion and/or dissipation from photons to chemical energy and/or heat. It is thus expected that FLIM can be used to a wide range of studies on thylakoid membrane in plants, algae and cyanobacteria. There are already a substantial number of applications of FLIM to study many aspects of thylakoid membrane in vivo by visible short pulses [14–17]. Two-photon excitation has also been tested in the application of FLIM to chloroplasts [18–21]. However, there still remain several uncertainties in the potential and limitations in the FLIM measurements. First, excitation power dependence of the FLIM data has not been sufficiently documented. There are hundreds of photosynthetic pigments that can exchange electronic excitation energy. It is thus possible that annihilations between multiple excited pigments (singlet–singlet, singlet–triplet etc.) can lead to an abnormally fast decay of fluorescence [18,22,23,24]. It is also well known that strong pulse and/or continued illumination on the same sample region can temporarily convert substantial portion of reaction centers of PSII into charge-separated state that cannot perform primary charge separation (closed PSII). The closed PSII shows a longer fluorescence lifetime (about 0.7–2 ns) than PSII that is ready for the primary charge separation (about 0.17–0.4 ns, open PSII) [15,18,21,25–29,30,31]. The effects of annihilation and the open-closed status of PSII to the actual FLIM images can be predicted only if scanning parameters of the excitation laser, absorption cross section of PSII and transition rate from closed PSII to open PSII are all properly considered. Second, contribution of PSI to the chlorophyll fluorescence (CF) at physiological temperature has not been sufficiently characterized. PSI fluorescence is most conventionally measured at cryogenic temperatures, because fluorescence quantum yield from PSI and/or its closely associated antenna like light-harvesting complex I (LHCI) in chloroplasts are relatively enhanced in comparison with that of PSII [1]. However, PSI fluorescence at physiological temperatures is not negligible [26,32,33]. The lifetime of PSI fluorescence (about 0.025–0.12 ns) is generally reported to be independent of excitation light intensity and shorter than that of PSII [26,28,34–36]. It is then likely that the image of PSII/PSI ratio in various chloroplasts/cells can be potentially obtained if dependence of fluorescence lifetimes on laser power is obtained. It is thus desirable to accumulate examples of FLIM measurements on various types of thylakoid membranes with different ratios of PSI/PSII.

Based on the above background, we have conducted FLIM measurements of an algal chloroplast and cyanobacterial cells with systematically varied excitation laser power. Our FLIM system has two channels of rigorously simultaneous fluorescence detection, largely corresponding to PSII and PSI. As a first test, we have avoided multicellular organisms in which it is difficult to estimate excitation power reaching a target focal plane. We have selected a filamentous diazotroph, *Anabaena variabilis* (*A. variabilis*), which contains differentiated cell, heterocyst. It is well known that the PSII content in matured heterocyst is far lower than that of vegetative cells in the same filament [9,10,37]. It is thus expected that FL of PSI-rich thylakoid membrane in the heterocyst can be obtained and compared with that of vegetative cells having substantial PSII in addition to PSI. As a second example, a unicellular green alga, *Parachlorella kessleri* (*P. kessleri*) was selected, because it lacks motility and has chlorophyll-based light-harvesting complexes [38,39]. Our available excitation wavelength was 404 nm, at which chlorophyll-based light-harvesting systems show far greater absorption cross section than phycobilin-based antenna, phycobilisome (PBS), of cyanobacteria. It is then likely that multiple excitation effects in the single PSI and/or PSII units are more sensitively observed in the *P. kessleri*

than in *A. variabilis*. In addition, we have composed a numerical simulation that almost fully reflects all relevant parameters: absorption cross section of PSII and its associated light-harvesting complexes, decay time constants of closed PSII (recovery time constant of open PSII) and laser-scanning parameters in the actually employed FLIM conditions. The simulation can largely reproduce experimental sensitivity of the FL to the absolute laser power. As an application example of our methodology, possible indication of functional PSII in the PSI-rich heterocyst was examined in detail. There have been reports on the presence of transcripts and proteins of PSII reaction centers in isolated heterocysts [40–42]. PSII activity in heterocysts in filaments in vivo was also reported by single cell variable fluorescence intensity [5]. These observations raised a question of how oxygen-sensitive nitrogenase for the nitrogen-fixation is compatible with the function of PSII in the heterocysts. Our methodology will hopefully add one more experimental observation on this interesting issue on a single cell basis in intact filaments.

2. Experimental

A. variabilis cells (strain NIES-2095) were purchased from the microbial culture collection at the National Institute of Environmental Studies (Tsukuba, Ibaraki, Japan). The cell filaments were grown photoautotrophically in nitrogen-free BG-11 medium (removing NaNO₃ and replacing ferric ammonium citrate with ferric citrate in the BG-11 formulation [43]) for 3, 24, or 90 days at 29 °C under a 15-h light/9-h dark photoperiod after an inoculation. The same nitrogen-free BG-11 medium was also used before the inoculation. The photosynthetic photon flux density at the sample position in an incubator was about 20 μmol photons m⁻² s⁻¹. A cell suspension after a suitable dilution was transferred to glass-bottom dish (D111505, Matsunami, Osaka, Japan). One piece of agar was put on the cell suspension in order to immobilize cells at the surface of the cover glass. All microspectroscopic measurements were started after 15–20 min of dark adaptation period on the microscope stage (Table S1).

P. kessleri cells were purchased from the IAM culture collection as IAM C-531 (now maintained as NIES-2160 in the microbial culture collection, at the National Institute of Environmental Studies, Tsukuba, Ibaraki, Japan). The cells used for measurement were grown photoautotrophically in 40 cm³ of BG-11 incubation medium in the same incubator as *A. variabilis* for 15 or 29 days after an inoculation. The preparation for the microscopic observation was also the same as used for *A. variabilis* cells. All microspectroscopic measurements were started after 15–20 min of dark adaptation period on the microscope stage (Table S1).

Autofluorescence images and lifetimes of the cells were obtained by a laser-scanning confocal imaging system (DCS-120, Becker & Hickl GmbH) with time-correlated single photon counting (TCSPC) boards (SPC-152, Becker & Hickl GmbH). The glass-bottom dish containing cells was mounted on an inverted microscope (IX-71, Olympus), with which the confocal scanner (DCS-120) was coupled. Photosynthetic pigments were excited by the second harmonic beam (404 nm) of a mode-locked Ti:Sapphire oscillator (Coherent) with a repetition rate of 75.5 MHz. Two detection channels with band-pass filters (673–698 nm and 703–740 nm) were simultaneously used to see mainly CF, which largely corresponds to PSII and PSI. The wavelength regions were optically selected by combinations of a long-wavelength-passing beam splitter (with an edge wavelength at 700 nm) and two band-pass filters. Residual laser light was rejected by long-wavelength-passing filter with an edge wavelength at about 500 nm. The obtained datasets of FL images were analyzed using image analysis software (SPCImage, Becker & Hickl GmbH), and some kinetic traces of selected regions were fitted by Igor Pro (version 6, e.g., Figs. S1–S5). Images at different depth positions were obtained by using a piezo actuator for changing the focus of an oil-immersion microscope objective (Olympus UPLSAPO, 100XO, NA = 1.40). The excitation intensity of the laser was

automatically controlled by a filter wheel with neutral density filters of different transmissions. A laser power of 20 nW at the sample position was confirmed by a power meter (PD-300-SH & NOVA, Ophir), and weaker laser powers were achieved by the filters of known transmission at 404 nm. Confocal pinhole sizes for the two fluorescence bands were manually changed between FLIM acquisitions at different laser powers (Table S1), by which the maximal probability of detection of fluorescence photons per single excitation pulse was limited to at most 3×10^{-3} at the brightest spot in fluorescence images. It is thus to be noted that fluorescence counts at different laser powers cannot be directly compared. (Figs. S2–S5). The instrument-response function (IRF) was 0.08 ± 0.015 ns at 689 nm and 0.10 ± 0.015 ns at 716 nm in full width at half maximum (FWHM). One test on time-resolution is shown in Fig. S1. The curve with a time constant of 0.084 ns obtained

in the constraint-free fitting is clearly better than that in the constrained fitting with a fixed time constant of 0.050 ns. As far as our data analysis is based on data with a comparable s/n or better, the distinguishability of the time constant is at worst about 0.03 ns (30 ps).

3. Results

3.1. Fluorescence lifetime imaging

FLIM measurements at varied laser intensities of *A. variabilis* were performed on 22 filaments of cells (or trichomes) including a total of about 190 vegetative cells and 22 heterocysts. One set of data is shown in Fig. 1. The cells in the image panels are all vegetative cells except one heterocyst indicated by white (Figs. 1(a)–(o)) or black (Figs. 1(a)–(o))

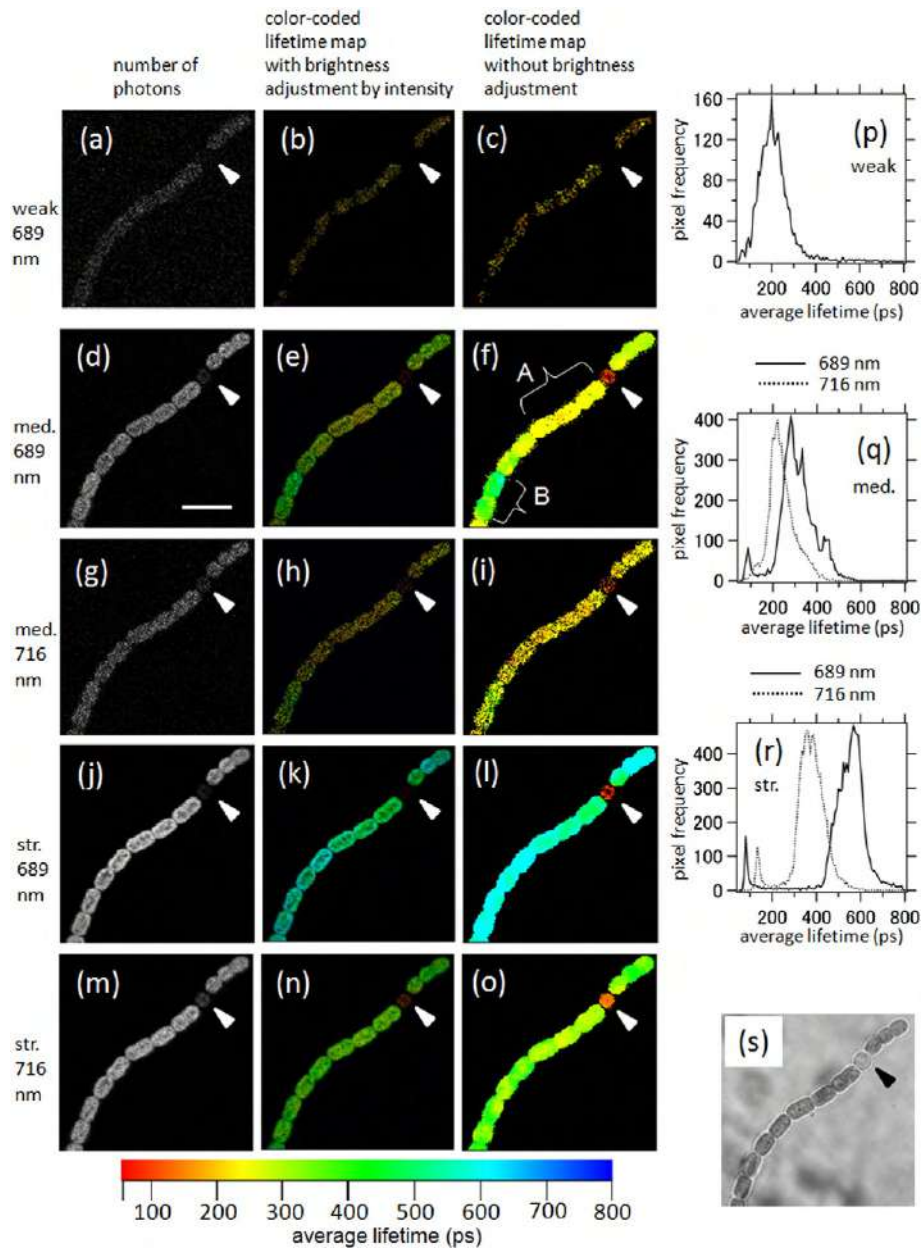


Fig. 1. Characteristics of average fluorescent lifetime images *A. variabilis* at different laser powers and detection wavelengths in the FLIM measurements. Excitation laser power at the sample position was 0.08 nW (weak), 1.1 nW (med.) and 20 nW (str.) in (a–c), (d–i) and (j–o), respectively. The laser powers and detection wavelength (centered at 689 nm or 716 nm) are shown on the left. (a), (d), (g), (j), (m): Photon count-based fluorescent images. (b), (e), (h), (k), (n): Corresponding average fluorescent lifetime images with intensity-dependent brightness adjustment. (c), (f), (i), (l), (o): Corresponding average fluorescent lifetime images without the brightness adjustment. (p), (q), (r): Distributions of average fluorescence lifetime at the three different laser intensities. (s): Bright-field image of the same area. Scale bar in (d) is equal to 10 μ m and applicable to all the image panels. The effective spatial resolution in the color-coded average FL images is about 1.94 μ m due to the binning of 11×11 pixels.

(Fig. 1(s)) arrow heads. Three levels of excitation laser power, 0.08, 1.1 and 20 nW at the sample position were employed in this order (Table S1) in one set of experiments on 6 filaments containing 6 heterocysts that were 90 days after inoculation (Tables S2,S3). Five levels of excitation laser power, 0.08, 0.30, 1.1, 5.3 and 20 nW at the sample position were also analogously employed in this order in the other two independent sets of experiments on filaments harvested 3 and 24 days after inoculation (7 and 9 filaments containing 7 and 9 heterocysts, respectively)(Tables S2, S3). In order to check damage or any long-lived actinic effects of previous laser scans on the sample, a FLIM measurement with the lowest power at 0.08 nW was always repeated after the measurement at the highest laser power (Fig. S2,S3, Table S1). Average FL at each pixel, $\langle \tau \rangle$, was calculated according to the following formulae,

$$F(t) \approx \int_{-\infty}^{+\infty} IRF(s) \left\{ \begin{array}{l} A_0 + A_1 \exp\left[-\frac{(t-s)}{\tau_1}\right] + A_2 \exp\left[-\frac{(t-s)}{\tau_2}\right], \quad t \geq s \\ 0, \quad t < s \end{array} \right\} ds, \quad (1)$$

$$\langle \tau \rangle = (A_1 \tau_1 + A_2 \tau_2) / (A_1 + A_2), \quad \tau_1 < \tau_2, \quad (2)$$

where temporal profile of fluorescence intensity at the pixel, $F(t)$, was fitted by convolution of a sum of two exponential functions with the instrument-response function, $IRF(s)$, (as Eq. (1)). The fitting yielded exponential decay time constants, τ_1 and τ_2 , and their amplitudes, A_1 and A_2 , in addition to a non-decaying component, A_0 . Our measurement time window was only between minus 0.3 ns and plus 2.7 ns, and the pulse-to-pulse interval in the excitation laser was 13.24 ns. The amplitude of A_0 thus suggests a long-lived fluorescence with an approximate lifetime between 2 and 13 ns. A_0 was always set to be zero in the SPC image analysis program. When fluorescence decay profiles were later extracted from certain specified areas of cells, amplitude of A_0 were set to be non-negative and they were typically 0–1% or at most 2–3% in a very few cases with a relatively poor s/n, which does not affect our following discussion (Tables 1–3 and S2–S4). In using the SPCimage analysis program for *A. variabilis*, a binning of pixels was performed in which photon data in 11×11 raw pixels (square region of about $1.94 \times 1.94 \mu\text{m}$) were all included to obtain a fluorescence decay profile

at the center pixel. This binning was employed at all the laser power levels, which enabled us to obtain the color-coded images of average FL of cells even at the weakest laser power employed. However, it caused degradation of apparent spatial resolution in the average FL map. As the laser power is increased, the lifetimes in the whole filament except the heterocyst are elongated. At the weakest laser power of 0.08 nW, the most frequent average FL obtained at 689 nm is around 200 ps (Fig. 1(p)). The average FL at 689 nm given by the middle (1.1 nW) and strongest laser power (20 nW) are 300 and 570 ps, respectively (Fig. 1(q) and (r)). This elongation of average FL is evident in all the vegetative cells in both the two detection channels (689 and 716 nm). The FL of the heterocysts does not show obvious elongation. It is to be noted that contribution of the heterocyst to the lifetime histogram is recognized as a small peak around 0.08–0.09 ns and 0.12–0.13 ns in the cases of 689 nm and 716 nm, respectively (Fig. 1(q) and (r)).

Multi-exponential nature of the fluorescence decay is not visualized in the map of average FL like Fig. 1. Photon counting data, which are photon counts versus arrival times, were separately collected from the vegetative cells and heterocyst, which gave fluorescence decay traces (Fig. 2(a)–(c), S2–S4). Before the curve fitting by Eq. (1), average photon counts in the sufficiently negative time region (For example, 5–10 and 3–19 counts per time channel in the 689 and 716 nm wavelength channels, respectively, for the traces shown in Fig. S2) was subtracted. It is thus possible that artificially negative photon counts arise (Figs. 2, S2–S5). These counts at negative times remained in the above-mentioned range even when the laser power was increased by 200 times. It is thus unlikely that the subtracted counts are attributable to short-lived laser-induced transient phenomena in samples (< 10 s). These small signals are thus not considered in this work. All types of fluorescence traces in the two cellular types (heterocysts or vegetative cells), with the two center wavelengths of detection (689 or 716 nm), and with the three or five different laser intensities were fitted by the sum of two decaying exponential components (Eq. (1), Tables 1, 2, Figs. 2, S2–S4). When the two exponential time constants are not separated well due to intrinsic nature of the decay and/or signal-to-noise, single decaying exponential function was used. The judgment was also supported by the reduced chi square values (Figs. S2–S4). Although some reduced chi square values are substantially larger than 1, we focus

Table 1
Parameters yielded by curve fitting of the FLIM data of vegetative cells of *A. variabilis*.

λ_{fl} [nm]	P_{laser} [nW]	τ_1 [ns] (Amplitude in %)	τ_2 [ns] (Amplitude in %)	∞ (Amplitude in %)	Average lifetime [ns]
689 ^a	0.08	0.22 ^a ± 0.01 ^c (97.5 ^a (+2.5 / -1.5) ^c)	1.09 ^a (±0.00 / -0.34) ^c (2.5 ^a ± 2.5) ^c	(0.0 ^a (+1.5/-0.0) ^c)	0.25 ^a (+0.00 / -0.03) ^c
	0.30	0.23(+0.00 / -0.01) (96)	0.88(+0.00 / -0.09) (4)	(0)	0.25
	1.1	0.23(+0.01 / -0.02) (85(+3 / -5))	0.74(+0.03 / -0.12) (15(+5 / -3))	(0)	0.31(+0.03 / -0.04)
	5.3	0.26(+0.00 / -0.02) (67(+5 / -10))	0.80(+0.00 / -0.08) (33(+10 / -5))	(0)	0.43 ± 0.05
	20	0.25 ± 0.02 (62(+8 / -9))	0.75 ± 0.05 (37(+10 / -7))	(0.5 ± 0.5)	0.44(+0.03 / -0.05)
716 ^b	0.08	0.225 ^b ± 0.005 ^c (99.5 ^b ± 0.5 ^c)	n.d.	(0 ^b)	0.225 ^b ± 0.005 ^c
	0.30	0.225 ± 0.005 (100)	n.d.	(0)	0.225 ± 0.005
	1.1	0.23 ± 0.01 (95.5 ± 2.5)	1.13 ± 0.18 (4.5 ± 2.5)	(0)	0.25
	5.3	0.23 (85 ± 3)	0.88 ± 0.05 (15 ± 3)	(0)	0.33 ± 0.03
	20	0.225 ± 0.015 (84 ± 3)	0.85 ± 0.05 (16 ± 3)	(0)	0.34

^a These parameters in the case of fluorescence at 689 nm were given by the curve fitting of the sum of all available data (3 independent experiments) at the same laser excitation power to the double exponential function convoluted with the IRF. See Table S2 for the parameters separately obtained for the three sets of experiments.

^b These parameters in the case of fluorescence at 716 nm are given as the average values obtained by the curve fitting for the two or three independent experiments (See Table S2).

^c All error bars in this table are given so as to cover the differences between the multiple data sets that were acquired independently (See Table S2).

Table 2
Parameters yielded by curve fitting of the FLIM data of heterocysts of *A. variabilis*.

λ_{fl} [nm]	P_{laser} [nW]	τ_1 [ns] (Amplitude in %)	τ_1 [ns] of the subsets ^c (Amplitude in %) upper :w/o lower:w/	τ_2 [ns] (Amplitude in %)	τ_2 [ns] of the subsets ^c (Amplitude in %) upper :w/o lower:w/	∞ (Amplitude in %)	Average lifetime [ns]	Average lifetime of the subsets ^c upper :w/o lower:w/ [ns]
689 ^a	0.08	0.087 ^a ± 0.009 ^b (99 ^a ± 1 ^b)	0.084(99) 0.072(91)	n.d.	n.d. 0.57(8)	(1 ^a ± 1 ^b)	0.087	0.084 0.112
		0.30	0.089 ± 0.005 (99.5 ± 0.5)	0.084 (100)	n.d.	n.d.	(0.5 ± 0.5)	0.089
	1.1	0.080 ± 0.002 (96 ± 2)	0.088(88) 0.078(98)	0.86 ± 0.25 (4 ± 2)	0.69(11) 0.64(2)	(0)	0.112	0.155 0.089
		5.3	0.081 ± 0.002 (96.5 ± 1.5)	0.075(98) 0.088(87)	0.855 ± 0.25 (3.5 ± 1.5)	0.67(2) 0.70(12)	(0)	0.108
	20	0.081 ± 0.003 (94.5 ± 3.5)	0.075(98) 0.085(88)	1.03 ± 0.39 (5 ± 3)	0.70(2) 0.70(11)	(0.5 ± 0.5)	0.129	0.088 0.153
716 ^a	0.30	0.145 ± 0.005 (100)	n.a.	n.d.	n.a.	(0)		
	1.1	0.14 ± 0.01 (100)	n.a.	n.d.	n.a.	(0)		
	5.3	0.14 (100)	n.a.	n.d.	n.a.	(0)		
	20	0.14 ± 0.01 (100)	n.a.	n.d.	n.a.	(0)		

^a These parameters in the two wavelength regions are given as the average values between maximum and minimum obtained by the curve fitting for the three independent experiments (See Table S3).

^b All error bars in this table are given so as to cover the differences between the multiple data sets that were acquired independently (See Table S3).

^c One of the subsets of heterocysts (subset/w) includes 5 heterocysts with a substantial amplitude of long-lived fluorescence (>0.6 ns). The other subset of heterocysts (subset/w/o) includes 17 heterocysts with a relatively small amplitude of long-lived fluorescence (>0.6 ns).

on the approximate description of the whole data by at most two exponential functions, which is mainly for the consistency with the simulation framework (See Sections 3.2 and 4.6). It is to be noted that the short lifetime component of vegetative cell is limited in a very narrow range (0.22–0.26 ns in Table 1), which seems to be independent of the center wavelength of the fluorescence detection and the excitation laser powers employed, even though we did not impose any linkage of parameters (so-called globally common parameters) in the curve fitting between the different fluorescence traces. This lifetime is in good agreement with the most dominant component observed in an ensemble of cells of *A. variabilis* (0.22 ns and 85%) [44]. It is also largely comparable to CFL observed in other cyanobacteria at room temperatures (Table S6) [34,36,45–47]. The average FL of the vegetative cell

gradually increases as the excitation power is raised, which is caused by the increase of the long lifetime component with time constants of 0.74–1.09 ns and 0.85–1.13 ns at the detection wavelengths of 689 and 716 nm, respectively (Fig. 2(a), Table 1, Fig. S2). These behaviors are largely consistent with those reported in another cyanobacterium *Synechococcus* 6301 by raising the level of closed PSII [46].

In the sum of FLIM data of all 22 heterocysts, at least 94% of its fluorescence decays with a time constant of 0.080–0.089 ns and 0.14 ns at 689 and 716 nm, respectively, at all the excitation powers (Table 2, Fig. S2). There is a minor long-lived component with a time constant of 0.86–1.03 ns. Since single-cell fluorescence spectra and photochemical behavior changes during differentiation process [5,9,10,48,49], it is likely that FLIM data from randomly selected heterocyst are

Table 3
Parameters yielded by curve fitting of FLIM data of *P. kessleri*.

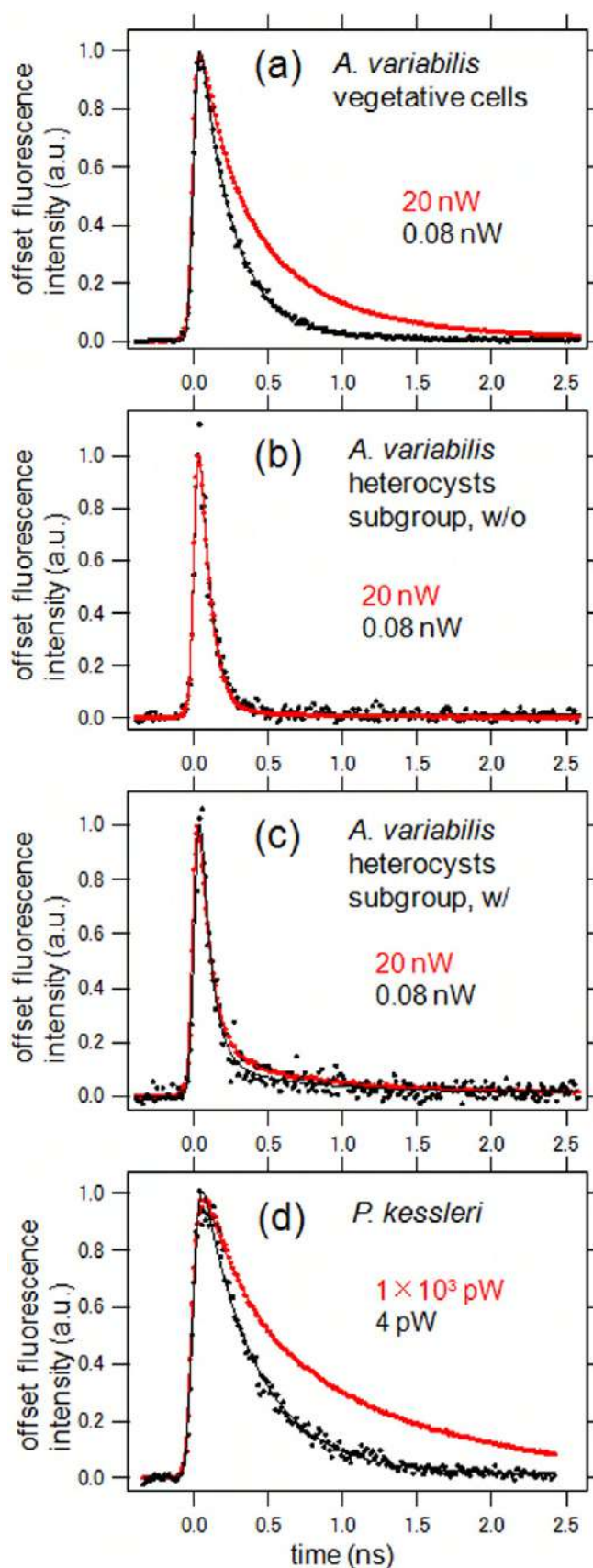
λ_{fl} [nm]	P_{laser} [pW]	τ_1 [ns] (Amplitude in %)	τ_2 [ns] (Amplitude in %)	∞ (Amplitude in %)	Average lifetime [ns]
689 ^a	4	0.32 ^a (+0.08 / -0.04) ^c (88 (+11 / -5) ^c)	0.82 ^a (+0.00 / -0.20) ^c (12(+5 / -12) ^c)	(0(+1 / -0) ^c)	0.38 ^a (+0.02 / -0.02) ^c
		15	0.28 (77)	0.63 (23)	(0)
	55	0.29(+0.00 / -0.00) (75(+1 / -9))	0.70(+0.00 / -0.02) (25(+9 / -1))	(0)	0.39 (+0.03 / -0.01)
		265	0.29 (61)	0.83 (39)	(0)
	1.0 × 10 ³	0.33 ± 0.01 (47 ± 1)	1.24 ± 0.06 (53 ± 1)	(0)	0.81 (±0.04)
716 ^b	15	0.32 ^b (95)	0.87 ^b (5)	(0)	0.34 ^b
	55	0.37 ± 0.03 (100)	n.d.	(0)	0.37
	265	0.36(90)	1.3(10)	(0)	0.45
1.0–1.2 × 10 ³	0.365 ± 0.005 (72)	1.4 ± 0.1 (28)	(0)	0.655 ± 0.025	

^a These parameters in the case of fluorescence at 689 nm were given by the curve fitting of the sum of all available data (2 independent experiments) at the same laser excitation power to the double exponential function convoluted with the IRF. See Table S4 for the parameters separately obtained for the two experiments.

^b These parameters in the case of fluorescence at 716 nm are given as the average values obtained by the curve fitting for the two independent experiments (See Table S4).

^c These error bars are given so as to cover the ranges of the parameters separately obtained for the multiple data sets that were acquired independently (See Table S4).

heterogeneous, which may reflect developmental stage or age of each heterocyst. The 22 heterocysts that we analyzed were classified into two subsets (17 and 5 heterocysts) based on an approximate single-



exponential curve fittings of the 689 nm fluorescence kinetics of individual heterocysts at the highest laser power (20 nW). The lifetimes of 689 nm fluorescence kinetics of the first subset (17 heterocysts) are shorter than those of the second one (5 heterocysts). The former and the latter subsets are designated as subset/w/o (without a substantial long-lived component) and subset/w/ (with a substantial long-lived component). Sum of photon data were separately prepared from the two subsets (Fig. 2(b) and (c), Table 2, Fig. S4). The subset/w/ has a long-lived component even at the weakest laser power (0.57 ns, 8%) that was distinguishable from infinitely long-lived component (with an approximate time constant of 2–13 ns) and the amplitude of the long-lived component was constantly greater than those of the subset/w/o at all power levels (Table 2).

Excitation power dependence of FLIM in the case of *P. kessleri* were obtained for 32 cells at excitation laser powers that were about one order of magnitude weaker than those of *A. variabilis* (Figs. 2(d), 3, S5, Table 3). Example of one data set, in which three cells were imaged at the same time, is shown in Fig. 3. The color-coded average FL image for the *P. kessleri* cells was obtained with a binning of 21×21 raw pixels (square region of about $3.7 \times 3.7 \mu\text{m}$). Three or five levels of excitation laser power, ($4, 55$ and 1.0×10^3 pW or $4, 15, 55, 265$ and 1.0×10^3 pW) at the sample position were employed in this order (Table S1). In order to check damage or any long-lived actinic effects of previous laser scans on the sample, FLIM measurement with the lowest power at 4 pW was repeated after the measurement at the highest laser power (Fig. S5), which have shown essentially the same results as the first ones with the same power. One of the three cells (cell no. 2 in Fig. 3(m)) showed clearly longer average FL than the other two cells (cell no. 1 and 3 in Fig. 3(m)). Such a cell with exceptional lifetime was not included as the target cells of fine analysis on the fluorescence decay profiles. An elongation of the average FL was evident especially between 55 and 265 pW (Tables 3 and S4). The shortest lifetime observed in the case of *P. kessleri* was about 0.28–0.33 ns at 689 nm, which was always longer than that of the vegetative cells of *A. variabilis* (0.22–0.26 ns) (Figs. 1, 2, and Table 1).

3.2. Simulation on open-closed state of PSII under the FLIM imaging conditions

Although it seems to be well established that open and closed PSII show relatively short (0.1–0.4 ns) and long fluorescence lifetimes (0.8–2 ns), [15,21,25,28,29,26,27,31,30] (See also Tables S5 and S6 for more references), how the components appear in fluorescence kinetics under actual FLIM experimental conditions has remained unexplained in a sufficiently quantitative manner. The purpose of the computer simulation described here is to quantitatively support our hypothesis that double exponential decay observed in our FLIM measurements in vegetative cells of *A. variabilis* and *P. kessleri* (Tables 1, 3, S2, S4) is a result of

Fig. 2. Effects of incident excitation laser power on decay profiles of fluorescence centered at 689 nm. Dots represent normalized fluorescence intensities based on photon count data from which average photon counts in the sufficiently negative time region was subtracted. It is thus possible that artificially negative fluorescence intensities arise. (a) Photon count data from all vegetative cells in 22 filaments (about 8–13 cells per filament) of *A. variabilis* at single focal planes were used. (b) Selected 17 heterocysts of *A. variabilis* at two or three focal planes were used. These heterocysts were selected as having relatively low level of long-lived fluorescence at the highest laser power (See Table 2). (c) Selected 5 heterocysts of *A. variabilis* at two or three focal planes were used. These heterocysts were selected as having relatively high level of long-lived fluorescence at the highest laser power (See Table 2). (d) Photon count data from 32 cells of *P. kessleri* at 1–3 focal planes were used. Solid lines represent fitting curves made by convolution of the instrument-response function with a sum of one or two exponential functions. The parameters obtained through the curve fitting are shown in Tables 1–3. The plots in black and red represent data and fitting curves in the cases of weakest and strongest laser power levels, respectively. More examples of fluorescence decay profiles of fluorescence at both 689 and 716 nm at all employed laser power levels are shown in Figs. S2–S5.

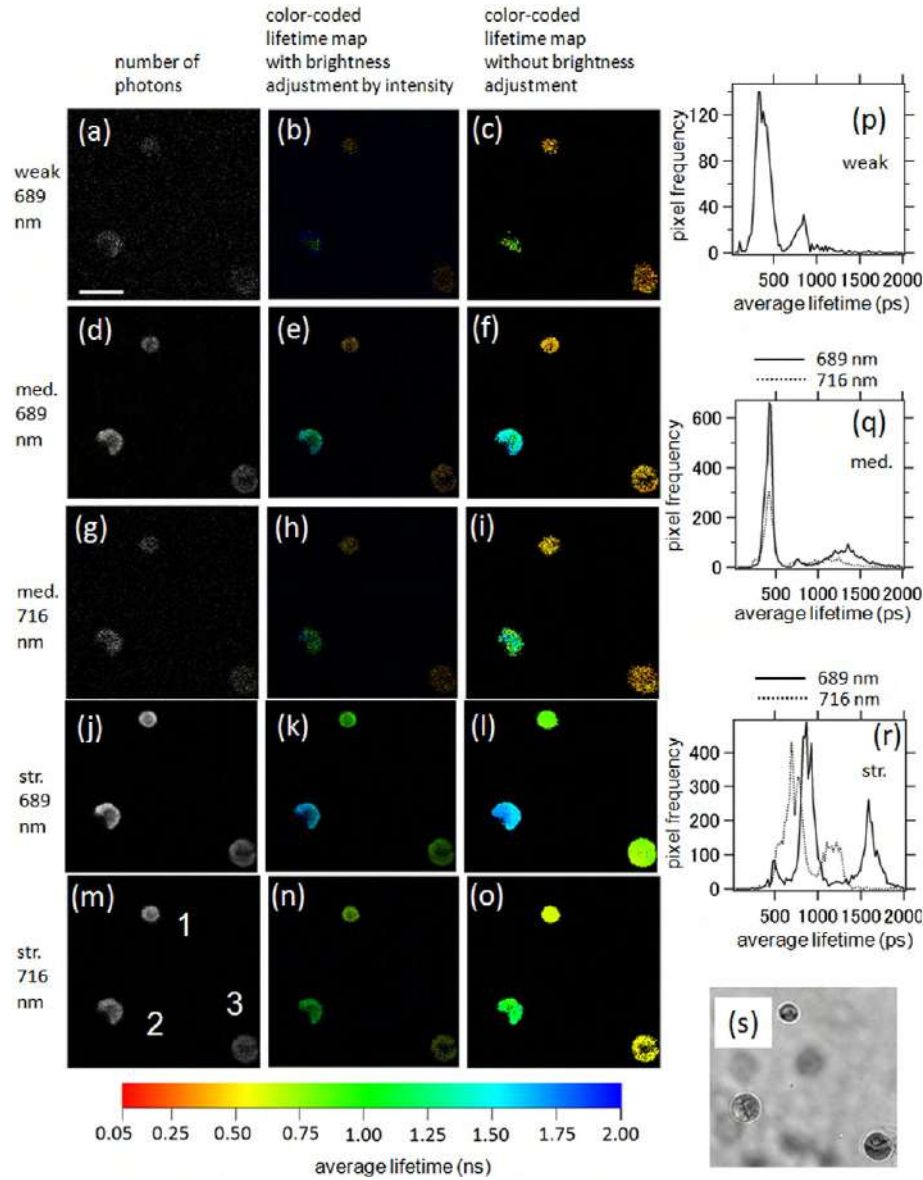


Fig. 3. Characteristics of average fluorescent lifetime images *P. kessleri* at different laser powers and detection wavelengths in the FLIM measurements. Excitation laser power at the sample position was 4 pW (weak), 55 pW (med.) and 1×10^3 pW (str.) in (a–c), (d–i) and (j–o), respectively. The laser powers and detection wavelength (centered at 689 nm or 716 nm) are shown on the left. (a), (d), (g), (j), (m): Photon count-based fluorescent images. (b), (e), (h), (k), (n): Corresponding average fluorescent lifetime images with intensity-dependent brightness. (c), (f), (i), (l), (o): Corresponding average fluorescent lifetime images without the adjustment of brightness. (p), (q), (r): Distributions of average fluorescence lifetime. (s): Bright-field image of the same area. Scale bar in (a) is equal to $10 \mu\text{m}$ and applicable to all the image panels. The effective spatial resolution in the color-coded average FL images is about $3.7 \mu\text{m}$ due to the binning of 21×21 pixels.

observing fluorescence from both open and closed PSII. Only an outline of the simulation is presented below and the details are fully described in Text S1.

The experimentally obtained fluorescence decay is made of fluorescence from many PSII units in the cells, but this situation is equivalently expressed by a single representative PSII unit at the position $(x, y, z) = (0, 0, 0)$ with full description on the probability of open/closed status (Fig. S6 and Text S1). In the simulation, a laser beam focus is moved in a manner of raster scan around the PSII, as in the experiments. Excitation probability of the PSII unit by a single laser pulse is assumed to be given by the single pulse laser energy, a Gaussian laser intensity profile, position of the laser focus, and an effective absorption cross section of PSII at the laser wavelength (404 nm) (Fig. S6 and Text S1). Once the PSII in the open state is optically excited, it is converted into a closed PSII with a probability of the photosynthetic charge separation. The time-dependent populations of open PSII and closed PSII in a unit

volume, $N_{\text{open}}(t_m)$ and $N_{\text{closed}}(t_m)$, or their proportional quantities that are probabilities for the PSII to be open or closed, $p_{\text{open}}(t)$ or $p_{\text{closed}}(t)$, are calculated as follows (Text S1).

$$\begin{aligned} \begin{bmatrix} N_{\text{open}}(t_{m+1}) \\ N_{\text{closed}}(t_{m+1}) \end{bmatrix} &= \begin{bmatrix} N_{\text{PSII}} p_{\text{open}}(t_{m+1}) \\ N_{\text{PSII}} p_{\text{closed}}(t_{m+1}) \end{bmatrix} = N_{\text{PSII}} \begin{bmatrix} p_{\text{open}}(t_{m+1}) \\ 1 - p_{\text{open}}(t_{m+1}) \end{bmatrix} \\ &= N_{\text{PSII}} \begin{bmatrix} 1 - 0.80 p_f(j_y(t_m), j_x(t_m)) \{1 - \exp[-(t_{m+1} - t_m)/\tau_R]\} \\ 0.80 p_f(j_y(t_m), j_x(t_m)) \exp[-(t_{m+1} - t_m)/\tau_R] \end{bmatrix} \\ &\quad \begin{bmatrix} p_{\text{open}}(t_m) \\ 1 - p_{\text{open}}(t_m) \end{bmatrix}, \end{aligned} \quad (3)$$

where t_m and t_{m+1} represent a time in the simulation and its subsequent time, respectively, N_{PSII} the total population of PSII in a unit volume (assumed to be constant), $p_f(j_y(t_m))$ and $j_x(t_m)$ the probability

for the PSII to be excited by the laser pulses between t_m and t_{m+1} , $j_y(t_m)$ and $j_x(t_m)$ are x (horizontal-axis) and y (vertical-axis) interger coordinates with a unit length of 25 nm of the laser beam at the time t_m , respectively, τ_R the time constant for the closed PSII to be converted back into open state. The excitation probability function, p_f in Eq. (3) (and in Eqs. (4)–(5) (*vide infra*)), is set to be two-dimensional Gaussian and non-zero only when $-10 \leq j_y(t_m) \leq +10$ and $-10 \leq j_x(t_m) \leq +10$. This means that PSII is excited only when the laser spot resides in the square of a side length of 500 nm that is centered at PSII (See Supplemental Fig. S6 and Text S1). Closed PSII is set to be generated from the optically excited PSII supercomplex with a probability of 0.80, which is the most typical parameter F_v/F_m of dark-adapted chloroplasts in the pulse-amplitude-modulation fluorometry (PAM) [50–52]. The same yield was also applied to the case of *A. variabilis*, because similar F_v/F_m values are obtained in phycobilisome-lacking and/or PSII-enriched cyanobacterial mutants [53,54]. The numbers of fluorescence photons from open and closed PSII units are proportional to the populations of open PSII and closed PSII before each excitation, respectively. Thus, the experimentally obtained ratios of short-lived and long-lived fluorescence components were compared with the following time-integrated sum of the product between excitation probability and populations of open and closed PSII units at each simulation time, respectively.

$$F_{\text{open,accum}} \propto \sum_{s=1}^{2\text{or}3} \sum_{k=1}^{29} \sum_{i=N_{y1}}^{N_{y2}} \sum_{j=-N_x}^{+N_x} p_f(7i + \{\Delta_{\text{offset}}/25\}, j) N_{\text{PSII}} p_{\text{open}}(t_{j,i,k,s})$$

$$= N_{\text{PSII}} \sum_{s=1}^{2\text{or}3} \sum_{k=1}^{29} \sum_{i=N_{y1}}^{N_{y2}} \sum_{j=-N_x}^{+N_x} p_f(7i + \{\Delta_{\text{offset}}/25\}, j) p_{\text{open}}(t_{j,i,k,s}) \quad (4)$$

$$F_{\text{closed,accum}} \propto \sum_{s=1}^{2\text{or}3} \sum_{k=1}^{29} \sum_{i=N_{y1}}^{N_{y2}} \sum_{j=-N_x}^{+N_x} p_f(7i + \{\Delta_{\text{offset}}/25\}, j) N_{\text{PSII}} \{1 - p_{\text{open}}(t_{j,i,k,s})\}$$

$$= N_{\text{PSII}} \sum_{s=1}^{2\text{or}3} \sum_{k=1}^{29} \sum_{i=N_{y1}}^{N_{y2}} \sum_{j=-N_x}^{+N_x} p_f(7i + \{\Delta_{\text{offset}}/25\}, j) \{1 - p_{\text{open}}(t_{j,i,k,s})\} \quad (5)$$

where the previously used index m and time t_m in Eq. (3) is replaced with a new set of indices j, i, k, s that reflect actual raster scan of the laser. The index j corresponds to different horizontal positions of the laser focus at a constant vertical position, i to different vertical positions of the laser focus in a single focal plane, k to different frames for accumulation in the same focal plane, and s to different focal planes. The integer coordinates, $7i + (\Delta_{\text{offset}}/25)$ and j corresponding to j_y and j_x in the previous notations (Eq. (3)) indicate the relative location of the laser focus with respect to the position of PSII (at the origin). The parameter Δ_{offset} (varied between 0 and 175 nm with a step size of 25 nm for averaging) represents a relative vertical offset in nm between the origin (location of PSII) and one of the horizontal lines that are fastest scan axes of the laser. The actual ranges of j, i, k and s ($-N_x \leq j \leq +N_x$, $N_x = 10$, $N_{y1} \leq i \leq N_{y2}$, $N_{y2} - N_{y1} = 1$ or 2) are given by the finite size of the laser spot (with a diffraction-limited size of 176 nm for the excitation wavelength of 404 nm) and the other actual scanning parameters (See Text S1 for more details). When PSII is located in the exact focal plane, laser focus in the simulation is set to move by 25 nm along the x axis by the single step in the index j ($j \rightarrow j + 1$). The single step in the index i ($i \rightarrow i + 1$) is set to move the laser focus by 176 nm, which gives the rounded integer 7 in the Eqs. (4) and (5) ($176 / 25 = 7$). One should take into account the weights (w_1, w_2, w_3) of the three different time constants, $\tau_{R,1}, \tau_{R,2}, \tau_{R,3}$, for the recovery of open PSII from closed PSII [55,56]. The experimentally obtained dependence of FLIM

on the laser power should be compared with a weighted average as follows (cf. Fig. S8).

$$\langle F_{\text{open,accum}}(P_{\text{laser}}) \rangle = \sum_{i=1}^3 w_i F_{\text{open,accum}}(P_{\text{laser}}, \tau_{R,i})$$

$$\langle F_{\text{closed,accum}}(P_{\text{laser}}) \rangle = \sum_{i=1}^3 w_i F_{\text{closed,accum}}(P_{\text{laser}}, \tau_{R,i}) \quad (6)$$

More details of this simulation is fully described in Text S1.

Relatively long-lived components (>0.6 ns) show greater weights at 689 nm than at 716 nm (Tables 1–3), which is understandable because PSII and PSI show maximum CF intensity near 689 and 716 nm, respectively [8,9,7,11,32,26] and because the FL of only PSII shows an elongation due to increase of the laser power [26,27]. It is thus reasonable that our simulation on PSII is compared with the amplitude ratio of the long-lived components at 0 ps ($A_2/(A_0 + A_1 + A_2)$) in Eq. (2) in the 689 nm CF kinetics (Fig. 4). Contribution of PSI CF is not considered from the beginning in the simulation, but it will be later considered if its contribution is unavoidable, especially in the case of a cyanobacterium *A. variabilis* that is generally more rich in PSI than in green algae (including *P. kessleri*) [57].

One essential parameter in the simulation is the absorption cross section of PSII supercomplex, to which the excitation probability function, p_f in Eqs. (3)–(5), is proportional. The pigments of PS II monomer of *A. variabilis* was assumed to be the same as those in the core of the PSII complex from *Thermosynechococcus vulcanus* [58], in which 35 molecules of Chla, 2 molecules of pheophytin *a* and 11 molecules of β -carotene are contained. Absorption coefficients of these molecules at 404 nm ($6.11 \times 10^5 \text{ cm}^{-1} \text{ mol}^{-1} \text{ dm}^3$, $1.07 \times 10^6 \text{ cm}^{-1} \text{ mol}^{-1} \text{ dm}^3$, and $5.59 \times 10^5 \text{ cm}^{-1} \text{ mol}^{-1} \text{ dm}^3$ for Chla, pheophytin *a* and β -carotene, respectively) were obtained with the help of absorption spectra in several references [59–61]. When only the pigments in the monomer units are considered, the total absorption coefficient of PSII monomer at 404 nm thus amounts to $2.97 \times 10^6 \text{ cm}^{-1} \text{ mol}^{-1} \text{ dm}^3$ (Text S2, Table S7). Cyanobacterial PSII is assumed to be in the state 2 since we have given a dark period of 15–20 min before each set of measurements (Table S1) [62,63,64]. One simulation was thus carried out with a minimal light-harvesting ability for PSII, where there is no PBS transferring energy to PSII. The reopening time constants of PSII in *A. variabilis* (the transition from closed state to open state) were assumed to be the same as those in another cyanobacterium, *Synechocystis* sp. PCC 6803 [55], in which there are three time constants (0.22 ms (68%), 2.9 ms (23%) and 13 s (9%)). The simulation yielded ratios of the accumulated number of excitations of closed PSII to the total accumulated number of excitations of PSII in *A. variabilis* at varied excitation laser power (PSII alone, dashed line in Fig. 4(a)). The possible association of PBS to PSII makes the effective absorption coefficient of PSII even larger, although the energy transfer efficiency from phycocyanin in PBS to PSII was reported to be 78% in a red alga *Porphyridium cruentum* and 86% in a cyanobacterium *Anacystis nidulans*, which was found to be substantially lower than about 100% in the transfer from Chlb to Chla in a green alga *Chlorella pyrenoidosa* [65]. The energy transfer from PBS to PSII lifts the simulation curve to the upper side, which results in an even greater gap between experimental and simulation plots (PSII + full PBS, solid line in Fig. 4(a)). On the other hand, the deviation of the simulation from experimental data can be alleviated if one considers contribution of PSI. Contribution of PBS fluorescence is not considered here, because the excitation wavelength at 404 nm was relatively preferential for Chla and the cyanobacterium was set to be state II (See also Section 4.3 and Table S7). In the modified simulation to better reproduce the experimental plot, the CF from PSI is assumed to contribute to 33% of the total amplitude at the weak excitation limit, and its lifetime (about 0.025–0.12 ns) [26,28,34–36] are safely in the short lifetime range (<0.25 ns) at all excitation laser power levels (PSII alone $\times (2/3)$, dashed and dotted line in Fig. 4(a), cf. Table 1).

In the case of *P. kessleri*, a green alga, the initial state of the thylakoid membrane before each set of FLIM measurements is state 1, because the dark period of 15–20 min was also given (Table S1) [66]. The

organization of PS II supercomplex of *P. kessleri* was assumed to be the same as that proposed in the case of *Chlamydomonas reinhardtii* [67]. When light-harvesting ability per PSII is largest (state 1), there are three trimers of LHCII, one CP26 and one CP29 per PSII monomer in the model PSII complex (Text S2). The total number of pigments per monomer PSII were largely based on a reference [68]. In addition to the above-mentioned absorption coefficients for the pigments common to cyanobacterial PSII, absorption coefficients of the other pigments at 404 nm ($1.45 \times 10^5 \text{ cm}^{-1} \text{ mol}^{-1} \text{ dm}^3$, $4.75 \times 10^5 \text{ cm}^{-1} \text{ mol}^{-1} \text{ dm}^3$, $6.01 \times 10^5 \text{ cm}^{-1} \text{ mol}^{-1} \text{ dm}^3$, and $5.69 \times 10^5 \text{ cm}^{-1} \text{ mol}^{-1} \text{ dm}^3$ for Chl *b*, neoxanthin, violaxanthin, lutein) were obtained with the help of several references reporting their absorption spectra and absorption coefficients at representative peaks (Table S8) [59,60,69–71]. Given the sum of all pigments per PSII monomer (124.5 Chl*a*, 62.5 Chl*b*, 10 neoxanthin, 6.3 violaxanthin, 24.7 lutein, 11 β -carotene, 2 pheophytin molecules), the total absorption coefficient amounts to $1.16 \times 10^7 \text{ cm}^{-1} \text{ mol}^{-1} \text{ dm}^3$, which yields a simulation curve designated as the equivalent number of Chl*a* of 190 (Fig. 4(b)). We also added another simulation curve in the case where effective absorption cross section is twice (380 Chl*a*) [72]. The decay of the closed state of PSII in *P. kessleri*, (reopening of PSII) was assumed to be the same as that in *C. reinhardtii*, in which there are three time constants (0.23 ms (73%), 46 ms (16%) and 7.5 s (11%)) [56]. We also performed an extra FLIM experiments with an excessively strong excitation power, which yielded a decay profile to be fitted by a sum of two exponential functions with time constants of 0.60 ns (33%) and 1.42 ns (67%) (Fig. S6), although the target cells measured for the Fig. S6 on a longer time scale were different from those analyzed as in Tables 3 and S4. This result is also added to the Fig. 4(b and c). The relatively short time constant of 0.60 ns at 6 nW excitation is clearly longer than those at the lower excitation powers (Tables 3 and S4). Possible presence of more than two decay time constants in the CF decay suggests that the open-closed PSII model (two-state model) is not sufficient. Given the current simulation framework and the signal-to-noise ratio, not the amplitude ratio of relatively long-lifetime component, but the average lifetime (Eq. (2)) is tentatively fitted by the simulation results as a compromise (Fig. 4(c)). The average FL at the weak limit and longest FL observed as a slowly-decaying component was averaged with weights of open and closed PSII that

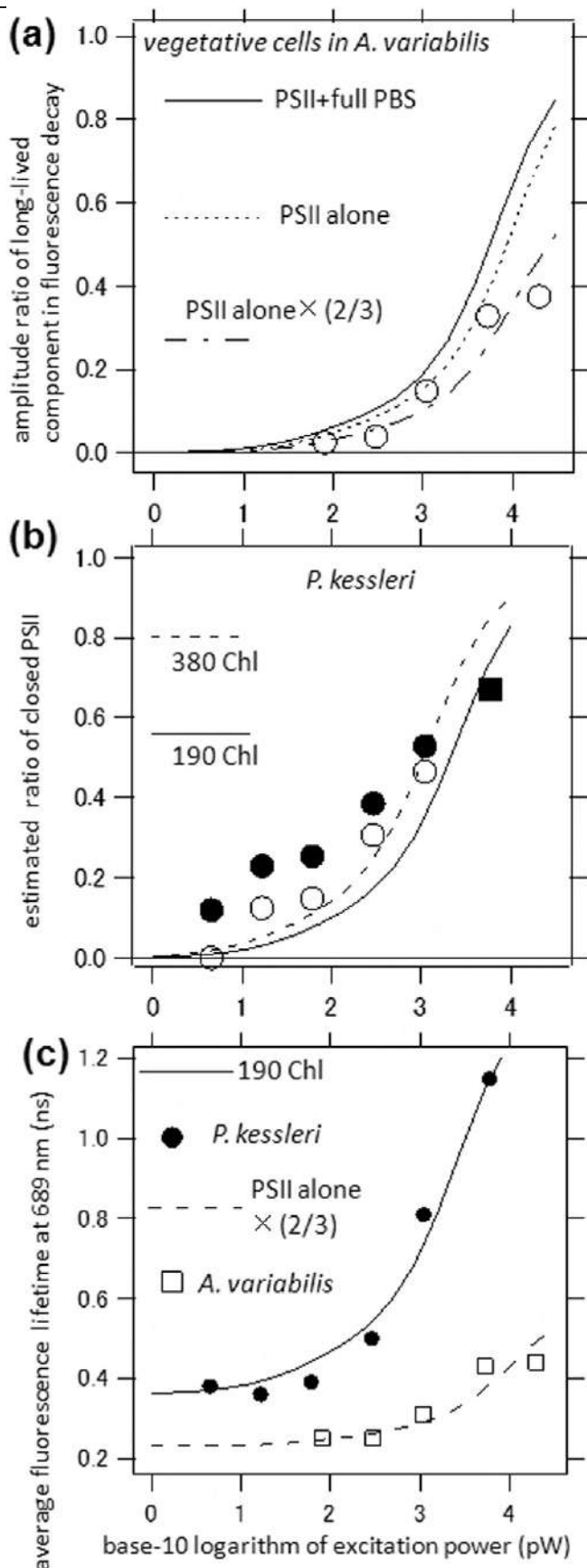


Fig. 4. Comparison between simulation and experimental parameters derived from fluorescence at 689 nm. (a) Amplitude ratios of long-lived fluorescence (>0.6 ns) at 689 nm for vegetative cells of *A. variabilis* (open circles (○), cf. Table 1). Simulated probabilities of detecting fluorescence from its closed PSII in the cases of PSII with fully extended PBS (solid line, PSII + full PBS), PSII without extra antenna (broken line, PSII alone). The dashed and dotted line (---, PSII alone × (2/3)) represent a modified plot that is a simple multiplication of the broken line (---) by a factor of 0.666. This means a situation where PSI and/or PBS fluorescence is always contributing to one third of the total fluorescence at $t = 0$ ps and its fluorescence lifetime is always included in the relatively short lifetime (≤ 0.25 ns). (b) Amplitude ratios of long-lived fluorescence (>0.6 ns) at 689 nm for *P. kessleri* (closed circles (●), cf. Table 3). The data point at 6 nW ($\log_{10}(6000) \sim 3.78$, closed square (■)) was obtained from a separate measurement on different cells described in Supplemental Fig. S7(e). Modified estimation of ratio of closed PSII (○), which are made from the corresponding closed circles at the same excitation power by postulating that there is a relatively long-lived component with a lifetime of 0.60–0.83 ns intrinsically from open PSII with a ratio of 12% in amplitude relative to that of the short-lived component (cf. Table 3). Solid and broken lines are ratios of closed PSII simulated in the cases of PSII having light-harvesting abilities equivalent to 190 and 380 Chl*a* molecules, respectively. (c) Dependence of average lifetime on laser power in the vegetative cells of *A. variabilis* and *P. kessleri* cells. The solid line is given by a formula $0.36 \times (1 - R_{\text{closed}}) + 1.42 \times R_{\text{closed}}$, which is an average fluorescence lifetime in ns given by the weighted sum of those from open and closed PSII in the case of *P. kessleri*. The ratio of closed PSII, R_{closed} , is the same as the simulated curve of solid line in (b). The broken line is given by a formula $0.23 \times (1 - R_{\text{closed}}) + 0.79 \times R_{\text{closed}}$, which is an average fluorescence lifetime in ns given by the weighted sum of those from open and closed PSII in the case of vegetative cells of *A. variabilis*. The ratio of closed PSII in the total fluorescence signal, R_{closed} , is the same as the simulated curve (dashed and dotted line (---)) in (a).

were given by the simulations at varied laser intensities, which nicely reproduces the experimental average FLs.

4. Discussion

4.1. Contribution of PSI fluorescence

Chlorophyll FL (CFL) of PSI (about 0.025–0.12 ns in the previous works) in live cells have been reported by careful decomposition/deconvolution in wild type cells [26,31,35] or from PSII-deficient mutant cells that were grown heterotrophically [34,36,73]. To the best of our knowledge, the CF obtained from single heterocysts of *A. variabilis* in this work is probably a rare example in that CF in wild-type intact cells is almost purely attributable to PSI. However, it should be noted that PSI in heterocyst may be associated with the so-called rod part of PBS (consisting of phycocyanin (PC) and phycoerythrocyanin (PEC)) [9,41,74–76]. The high purity of the PSI (nearly negligible contribution by PSII) in the heterocysts is supported by several features, although possible minor contribution of PSII is also analyzed in the next Section 4.2. First, there is almost no increase of slowly-decaying component in heterocyst by the increase of laser power (Table 2, Figs. 2(b), (c), S3, S4). Even in the selected subset of heterocysts (subset/w) (Table 2), the increase of the long-lived component at 689 nm is from 8% to at most 12% in the amplitude while the corresponding long-lived component in vegetative cells increases in the amplitude from 2.5% to 37% between 0.08 and 20 nW. Second, the CFLs at both 689 and 716 nm in heterocyst are clearly shorter than those in vegetative cells (Table 1). This reflects higher abundance of PSI in heterocyst as CFL of PSI is widely reported to be shorter than that of PSII [18,28,36,77]. Third, the CFL at 689 nm of heterocyst is shorter than that at 716 nm. This is in contrast to the very similar CFL of the short-lived component (0.22–0.26 ns) in the vegetative cells between 689 and 716 nm (Table 1). This feature is consistent with the observation in purified PSI complexes (PSI or PSI-LHCI) or in mutants lacking PSII and its associated antenna system, in which there are one relatively fast decay around the main peak of the Qy band (major spectral forms of Chla in PSI, with fluorescence wavelength <700 nm) and one relatively slow decay of the so-called minor long-wavelength-absorbing form (>700 nm) [36,77]. For example, one of the above-cited time-resolved spectroscopic study reported two main fluorescence decay lifetimes of 15 ps and 50 ps that are attributable to net loss of fluorescence (trapping) in isolated PSI from a cyanobacterium *Spirulina platensis* [77]. In their work, the fast trapping component (15 ps) is centered around 700 nm with an approximate FWHM of 46 nm, whereas the slow component (50 ps) is centered around 730 nm with an approximate FWHM of 57 nm. Although our IRFs (0.08 ns at 689 nm and 0.10 ns at 716 nm in FWHM) and the signal-to-noise ratio are presumably not sufficient to resolve the two trapping components at a single wavelength alone, the relatively slow decay at 716 nm (0.13–0.14 ns) than at 689 nm (0.084–0.096 ns) of the CF in heterocyst is most plausibly attributable to the presence of the two trapping dynamics with different spectra and lifetimes in PSI. This trend would not be easily observed if there was a substantial contribution from PSII to the wavelength region around the main Qy peak (around 689 nm), as the CFL of PSII is generally even slower than the slow trapping component in PSI.

Contribution of PSI in the vegetative cells of *A. variabilis* is noticeable as a decreased amplitude of the long-lived CF due to closed PSII around 716 nm (16% at 20 nW) than that around 689 nm (37% at 20 nW in Table 1). The decreased amplitude of the long-lived component at 716 nm than at 689 nm can be at least in part attributable to higher spectral weight of PSI at 716 nm than at 689 nm. Contribution of PSI in *P. kessleri* was also noticeable in the varied amplitude of the long-lived components (28% at 716 nm vs. 53% at 689 nm with 1.0×10^3 pW in Table 3). These suggest that not only the dependence of FL on laser power but also dual-wavelength detection can be helpful for imaging PSI/PSII.

4.2. Long-lived fluorescence and possible presence of PSII in heterocysts

In one selected subset of heterocysts (subset/w, 5 among 22 heterocysts), a long-lived fluorescence with a lifetime of 0.57–0.74 ns was found with a substantial amplitude larger than 8% at all laser intensities (Table 2, Fig. S4). However, its increase in amplitude by the rise of laser power was only from 8 to at most 12% (Table 2, Fig. S4), which is about one-order of magnitude smaller than that in vegetative cells (from 2.5 to 37%, Table 1). The amplitude of 8% at the weakest excitation should be thus attributed to long-lived fluorescence other than closed PSII. One possibility is that these indicate phycobilisomes or parts of phycobilisomes that are uncoupled from both PSII and PSI [78]. In our random selection of heterocysts, it is impossible to avoid premature heterocysts, which temporarily contain substantial number of uncoupled highly fluorescent phycobilisome [9,49,79]. Given this possibility, the small increase of the long-lived component from 8 to 11–12% in the subset of heterocyst (subset/w) by the rise of laser intensity (Table 2) may also be attributable not to stable presence of functional PSII but to residual but photochemically active PSII that is not yet decomposed during the heterocyst differentiation. It should be noted that the substantial amplitude of the long-lived component was observed only in the minor subset (subset/w): 3 heterocysts in filaments harvested 24 days after the inoculation (total was 9 heterocysts), 2 heterocysts in filaments harvested 90 days after the inoculation (total was 6 heterocysts), and none in filaments harvested 3 days after the inoculation (total was 7 heterocysts). All these inoculations were *not* step-down of the nitrogen, but simply dilutions of cells from cell-rich nitrogen-deficient media to new nitrogen-deficient media. As far as randomly sampled 22 heterocysts in this study are concerned, we tentatively estimated that photochemically active PSII:PSI ratio in heterocysts are estimated to be typically below our detection limit and at most about 5% in limited cases in comparison with that in vegetative cells (See Text S3 for the details of this estimation). This number was given on an assumption that effective light-harvesting abilities of PSII in vegetative cells and heterocysts are the same under the experimental conditions in this work (state II and 404 nm excitation). To further clarify the molecular entity of the long-lived fluorescence, it is thus desirable to carry out a FLIM-based time-lapse observation on heterocyst differentiation, which will be described in our next publications.

4.3. Fluorescence lifetime when PSII is in the open state

Most obvious mission of FLIM should be to obtain absolute values of CFLs in a wide spatial region including three dimensional objects like plant leaves. Straightforward comparison of CFLs between different organisms or different cells is generally meaningful, but only when CFLs to be compared should be obtained at well-defined excitation and preillumination conditions, e.g., at weak excitation limits after dark adaptation that are generally attained at different laser powers for different organisms/tissues, as demonstrated in Fig. 4. The average FL at 689 nm seems to reach a weak limit below 0.30 nW and 55 pW in the cases of *A. variabilis* vegetative cells and *P. kessleri* cells, respectively (Tables 1 and 3, Fig. 4), although double exponential curve fitting did not give constant results due probably to the limited s/n ratio in the relatively weak excitation powers. The average FL with PSII in the open state thus seems to be 0.25 ns and 0.36–0.39 ns in the cases of *A. variabilis* vegetative cells and *P. kessleri* cells, respectively, which are largely consistent with previous reports (Tables S5, S6). Even if the primary charge separation in the isolated core PSII dimer is intrinsically common between *P. kessleri* and *A. variabilis*, the different CFLs between *A. variabilis* and *P. kessleri* at the weak limit (0.25 and 0.36–0.39 ns, respectively) observed in this study can be caused by the difference in the organization of light-harvesting system. With the 404 nm excitation in our PSII models, 63% and 26% of the excitation at 404 nm is estimated to initially reside in the PSII dimer in *A. variabilis* and *P. kessleri*, respectively (Table S7 and S8), when any excitation in the whole PSII supercomplex including associated phycobilisome is set to be 100%. In addition, back

energy transfer from the PSII dimer to light-harvesting systems in the *P. kessleri* (PSII → LHCII, CP26 and CP29) seems to be far more significant than that in *A. variabilis* (PSII → APC, PC, PEC). This is supported by the estimation of number of pigments weighted by the thermal excitation probability in both the core PSII dimer and associated light-harvesting systems (Tables S7 and S8). It should be also noted that PBS tends to be associated with PSI rather than with PSII in the dark-adapted state (state 2 in the case of cyanobacteria) [2,62,63]. It thus seems very reasonable that average FL at the weak limit in *A. variabilis* is shorter than in *P. kessleri* upon the 404 nm excitation. However, it should be certainly noted that contribution of PSI, which has a CFL of largely 0.08–0.09 ns at 689 nm in heterocyst in *A. variabilis* (Table 2), should also make the apparent CFL of vegetative cells around 689 nm shorter than that of pure PSII to some extent. The contribution of PBS to the lifetime of vegetative cells of *A. variabilis* at 689 nm is likely less substantial than that of PSI, since substantial part of PBS is dissociated from PSII by the state II conditions and the excitation wavelength at 404 nm is more preferential for Chla than phycobilin (Table S7).

4.4. Transition from open to closed state of PSII as observed by varied excitation laser power

The transition from open to closed state in the majority of PSII of *A. variabilis* is observed at about one-order of magnitude higher excitation power than that of *P. kessleri*. The recovery dynamics of open PSII from closed PSII in cyanobacteria (0.22 ms (68%), 2.9 ms (23%) and 13 s (9%) in *Synechocystis* sp. PCC 6803 [55]) seems to be largely similar to that in green algae (0.23 ms (73%), 46 ms (16%) and 7.5 s (11%) in *C. reinhardtii* [56]). The difference in the laser power necessary to close most PSII thus seems to be primarily attributable to the difference in the absorption coefficient at 404 nm for PSII. In *P. kessleri*, as one of green algae, PSII possess an antenna system that contains Chla and chlorophyll *b* (Chlb) as main antenna pigments exhibiting strong absorption mainly in the blue-green and red regions [80,81]. For the simulation, we have assumed the same molecular organization of PSII supercomplex as in *C. reinhardtii* [67], the total absorption coefficient per PSII monomer in state 1 (Text S2) is equivalent to about 191 Chla molecules per monomer PSII (Fig. 4(b)). The simulation curve for the light-harvesting ability equivalent to 380 Chla may give a slightly improved fit to the experiment. Absolute absorption cross section of PSII in *Chlorella vulgaris* was reported to be equivalent to 130–400 Chla [72]. It should be also noted that there remains a certain long-lived component (≥ 0.6 ns) even at the weak limit, which is similar to the situations in some references reporting such minor long-lived component (See Table S5 for references) [26,35]. Given this possibility, the estimated ratio of closed PSII based on the amplitude of the long-lived component (closed circles in Fig. 4(b)) may have to be modified. On an assumption that 12% of the amplitude at zero time (the amplitude of the 0.82 ns component at 689 nm, 4 pW in Table 3) is intrinsically given by the open PSII, our experimental data yield another plot for the ratio of closed PSII (open circles) in Fig. 4(b). This modified experimental plot matches well with the simulation. In the case of *A. variabilis*, the experiment was best reproduced by the simulation if all PBS components are dissociated from PSII and if PSI contribute to the short-lived component (≤ 0.23 ns) at 689 nm by about 33% in the amplitude ratio at $t = 0$ ps (the simulation curve: PSII alone $\times (2/3)$ in Fig. 4(a)), as explained in Section 3.2.

The rise in FL with the increase of laser power is sensitively influenced by both the antenna size of PSII and recovery dynamics of open PSII from its closed states (Fig. S8(b)). Although the two factors of antenna size and the recovery rate of open PSII are inseparable in the input-power dependence of FLIM alone, FLIM will be certainly helpful for obtaining a new type of images on antenna size and/or recovery rate of open PSII. For example, about 3–4 cells near the heterocyst cell in *A. variabilis* (part A of the filament in Fig. 1(f)) show an average FL of about 0.25 ns, and about 2 cells in the same filament (part B of the filament in Fig. 1(f)) show an average FL of about 0.4 ns at the same

excitation power. Such a difference is not yet generalized, but it may suggest differently regulated light-harvesting abilities and/or redox conditions of plastoquinone pool affecting electron transfers from QA [53,64]. Properties of individual vegetative cells as well as heterocysts will be analyzed based on FLIM data in our next publications.

4.5. Relevance of FLIM to PAM parameters

Pulse-amplitude-modulation fluorometry (PAM) of CF is probably the most popular chlorophyll fluorometry on photosynthetic organisms [51,52]. There have been extensive reports demonstrating microscopic images for PAM-related parameters from individual chloroplasts and cyanobacterial cells [5,82–85]. FLIM data with varied excitation power also contains information directly related to the PAM. Since the simulation based on open-closed status of PSII in this study largely reproduced the experimental results in terms of ratio of closed PSII included in the FLIM data (Fig. 4), the maximum yield of PSII charge separation under dark-adapted chloroplasts or cyanobacteria in PAM analysis is related to the CFL as follows.

$$\frac{\langle \tau_{open} \rangle^{-1} - \tau_{closed}^{-1}}{\langle \tau_{open} \rangle^{-1}} = \frac{(0.38)^{-1} - (1.42)^{-1}}{(0.38)^{-1}} = 0.73 \quad (6)$$

for *P. kessleri* (cf. Table 3, Text S6, Fig. S7).

$$\frac{\langle \tau_{open} \rangle^{-1} - \tau_{closed}^{-1}}{\langle \tau_{open} \rangle^{-1}} = \frac{(0.25)^{-1} - (0.75)^{-1}}{(0.25)^{-1}} = 0.67 \quad (7)$$

for vegetative cells of *A. variabilis*.

(cf. Table 1, Text S6).

The above $\langle \tau_{open} \rangle$ and τ_{closed} are set to be the average fluorescence lifetime at 689 nm at the weakest laser power and the time constant of the slowly-decaying component at 689 nm at the highest laser power, respectively. In the above estimation, we assume that the average fluorescence lifetime at a sufficiently high laser power to close all PSII should be equal to the CFL of the most long-lived component that we observed. In the case of *P. kessleri*, this value is slightly lower than the typical value of $(F_M - F_0) / F_M = F_V / F_M$ (about 0.8) in dark-adapted state in the PAM fluorometry on green algae including *Chlorella* [62, 86], although the two values should be ideally the same in the simple two-state model (Text S6). Possible activation of protective quenching against excess excitation (so-called nonphotochemical quenching, NPQ) during the scanning laser illumination may decrease the apparent maximum yield of PSII charge separation through shortening of τ_{closed} . However, such a scenario is unlikely in this study, because the average intensity of the excitation laser at 1 nW (strongest laser power in the consecutive FLIM measurements in the case of *P. kessleri* summarized in Table 3) for $45 \times 45 \mu\text{m}$ scanning area is estimated to be about $1.7 \mu\text{mol photons m}^{-2}\text{s}^{-1}$ (Text S4). This is about one or two order of magnitude smaller than that used for actinic light in most PAM measurements to induce NPQ [51,52]. Moreover, consecutive FLIM measurements for a total exposure time of 45 s at even higher excitation laser at 6 nW (the other experimental conditions are unchanged from those used in the results of the main text) did not show noticeable changes in CF decay profile from the first 4.5 s to the last 4.5 s in the case of *P. kessleri* cells (Fig. S7). The above discrepancy in the maximum quantum yield (between 0.73 and about 0.8) may suggest an underestimation of the amplitude of some short-lived component in the fluorescence decay due to our limited time-resolution (FWHM of IRF was 80 ps at 689 nm) and/or s/n. On the other hand, the above value of $(\langle \tau_{open} \rangle^{-1} - \tau_{closed}^{-1}) / \tau_{open}^{-1}$ is higher than typical values of F_V / F_M of dark-adapted cyanobacteria [53,62,64]. This is caused by the contribution of at least PSI and also PBS to the short lifetime component with the FL of about 0.23 ns (See Section 3.2 and Fig. 4(a)). The PSI/PSII ratio in cyanobacteria are generally higher than those in green

algae [57]. It is thus likely that CFL of pure PSII is longer than 0.25 ns in *A. variabilis*. For a direct comparison with actual PAM measurements on cyanobacteria, τ_{closed} in Eq. (7) may have to be replaced with $\langle \tau_{\text{closed}} \rangle$ as follows.

$$\frac{\langle \tau_{\text{open}} \rangle^{-1} - \langle \tau_{\text{closed}} \rangle^{-1}}{\langle \tau_{\text{open}} \rangle^{-1}} = \frac{(0.25)^{-1} - (0.44)^{-1}}{(0.25)^{-1}} = 0.43 \quad (8)$$

for vegetative cells of *A. variabilis*.
(cf. Table 1, Text S6).

$$\frac{\langle \tau_{\text{open}} \rangle^{-1} - \langle \tau_{\text{closed}} \rangle^{-1}}{\langle \tau_{\text{open}} \rangle^{-1}} = \frac{(0.087)^{-1} - (0.129)^{-1}}{(0.087)^{-1}} = 0.33 \quad (9)$$

for all 22 heterocysts of *A. variabilis*.
(cf. Table 2, Text S6).

These are comparable to and largely consistent with the values of F_V/F_M reported for vegetative cells and heterocysts in *Anabaena* sp. strain PCC7120 by time-lapse microscopic PAM (or fluorescence kinetic microscopy, FKM) [5]. The estimation on heterocysts based on our results, however, critically depends on the two subsets, subset/w/o and subset/w, for which the Eq. (9) gives 0.07 and 0.27 based on Table 2, respectively. According to the time-dependent F_V/F_M values after the nitrogen step-down in the reference [5], the value of 0.07 for the subset/w/o corresponds to a late “stress period” (about 30 h after the nitrogen step-down). The value of 0.27 for the subset/w corresponds to an early “stress period” (about 20–25 h after the nitrogen step-down) or “acclimation period” (about 120 h after the nitrogen step-down). In the former case, the relatively minor subset of heterocysts (subset/w having a substantial long-lived fluorescence) is indeed understandable as a transient state during the heterocyst development. However, it should be noted that our estimation is critically dependent on the accuracy of the curve fitting at the weak excitation limit and that we need to increase the number of sampling in order to reach a definite conclusion.

4.6. Limitations of current simulation model and data analysis

Some previous studies have suggested a need to introduce the so-called three-state model of the charge separation assuming open, semi-closed, and closed states, which reflect redox states of at least two sequential electron acceptors (Text S5) [87,88]. Semi-closed state is suggested to show lower fluorescence quantum yield than that in fully closed state [87], which may be consistently observed in this study as the slightly shorter CFLs of the “closed” state at the medium laser powers (0.63–0.82 ns at 4–265 pW in *P. kessleri*) than those at the highest laser power (1.24–1.42 ns at $1.0\text{--}6.0 \times 10^3$ pW in *P. kessleri*) (Table 3, Fig. S5). The need for the three-state model is also supported by the residuals and chi square values of the curve fitting in Figs. S2–S5, which show that the single or double exponential function are sufficient only at weak–medium excitation powers that we employed. The presence of more than two exponential components at the relatively high laser powers should be explained in an improved model in our next publications.

Moreover, even at low laser powers where most PSII are open, the intrinsic fluorescence decay of PSII is generally multiexponential with at least 3–5 lifetimes in both green algae [25,31,35] and cyanobacteria [36,45–47] especially when the decay of CF is observed from many cells by non-FLIM TCSPC with a high s/n (See also Tables S5, S6). The sufficiency of single or double components especially at the relatively weak laser powers in our case is just given by our limited s/n. The relatively low s/n is inevitable as far as we primarily concern imaging in order to resolve individual cells within a short time. Our contribution is thus focusing on the overall reproduction of the experimental results, which are approximately described as sum of at most two exponential functions at all power levels, by the relatively crude but elaborate two-state model for the PSII status. Improvement of the simulation model together

with the more accurate analysis on the experimental results will be carried out in our next studies with more focus on differences between individual cells.

4.7. Comparison with other FLIM studies in terms of open-closed status of PSII and laser power dependence

A brief overview is given to the laser power levels and/or excitation probabilities that are employed in previously reported FLIM-based imaging of chloroplasts and cyanobacteria. In some cases, NPQ processes were mainly studied at light levels that seem to close substantial fraction of PSII [14,16]. In one of the studies [16], the major CFL in avocado plants was about 1.5 ns (probably from closed PSII) and activation of NPQ was observed as appearance of CFL around 0.5 ns. A certain oligomeric state of LHCII was suggested to show a CFL of 0.4 ns when NPQ was induced in *Arabidopsis* leaves [89]. In other cases, average CFL was found to be in the range between 0.15 and 0.5 ns at relatively weak laser power [15,21,36,90]. On the other hand, CF with two-photon excitation has been reported to decrease in lifetime by raising incident laser power [18,19], which has been ascribed to singlet–singlet and/or singlet–triplet annihilation. This is a qualitatively different trend than those reported with visible excitation including this work [34]. Singlet–singlet annihilation can be operative only when a single laser pulse excites multiple pigments in the same or nearby PSII unit(s) among which at least multi-step energy transfer to each other is possible, because typical pulse-to-pulse interval of about 10 ns or longer (13.2 ns in this work) is sufficiently longer than lifetime of fluorescence (lifetime of singlet excited state of Chls). Our estimation of the excitation probability of PSII in *P. kessleri* by a single laser pulse of 1 nW power (at 404 nm, and highest laser power in Table 3) is only about 5×10^{-3} , by which singlet–singlet annihilation should be virtually negligible (Text S5). If prepared concentration of excited PSII at the focus and detection efficiency of CF in the references ([18,19]) are comparable to our conditions, singlet–singlet annihilation can thus be safely excluded. Singlet–triplet annihilation may be operative, since formation of triplet state(s) of Chls and/or carotenoids is certainly enhanced when substantial portion of PSII is closed at high input laser power and their lifetimes are in the range of μs to ms [91–94]. The long-lived triplet states may thus interact with singlet excited state prepared in the subsequent laser pulses, which leads to shortening of fluorescence lifetime. Lifetime shortening in the FLIM by NPQ and singlet–triplet annihilation may be differentiated on a more quantitative basis if one performs a numerical simulation to estimate the transient accumulation of the triplet states during FLIM imaging, as shown in this work.

5. Conclusions

FLIM data of a single cellular green alga *P. kessleri* and nitrogen-fixing filamentous cyanobacterium *A. variabilis* were obtained at varied excitation powers. At weak excitation limits, fluorescence lifetimes of the thylakoid membrane with mostly open PSII can be obtained, although it takes a long total exposure time to obtain a high quality image. The transition in FLIM data from the weak excitation limits to higher powers that close a substantial fraction of PSII can be successfully explained by a numerical model considering the open-closed status of PSII based on absolute laser powers. The difference in FLIM between *P. kessleri* and cyanobacterium *A. variabilis* can be largely explained by the difference in the light-harvesting ability of the PSII supercomplex at the excitation wavelength at 404 nm. The fluorescence decay in nitrogen-fixing heterocysts is largely independent of the excitation power. This reflects a high purity of PSI in the unique heterocyst thylakoid lacking PSII. Among heterocysts that were randomly sampled, photochemically active PSII/PSI ratio in heterocysts is at most about 5% in comparison with that of vegetative cells. Heterogeneous properties of individual heterocysts were found, but accurate determination of their physiological states should await further studies.

A whole plant leaf can be a target of FLIM, but special care should be taken when comparing chloroplasts in deep regions with those close to the surface, because it is in general difficult to estimate absolute laser power reaching deep individual chloroplasts. The dependence of FLIM on laser power is sensitively influenced by at least the antenna size of PSII and recovery rates of open PSII from its closed states. A simulation fully reflecting laser scanning conditions, as shown in this work, will potentially help one to interpret observed features of FLIM images in terms of important parameters of photochemistry in individual chloroplasts, cyanobacterial cells and thylakoid domains.

Funding

This work was supported in part by the Japan Science and Technology Agency (the Precursory Research for Embryonic Science and Technology, “Chemical conversion of light energy”, to S.K.), the Ministry of Education, Culture, Sports, Science and Technology in Japan (MEXT) (grant no. 24,657,036 to T. S. & S.K.), MEXT-Supported Program for the Strategic Research Foundation at Private Universities (2015–2018, no. S1511025 partly to S.K.), the Murata Science Foundation (to S.K.), and Shorai Foundation for Science and Technology (to S.K.).

Disclosures

Dr. Kumazaki reports grants and personal fees from Japan Science and Technology Agency, grants from The Murata Science Foundation, grants from Shorai Foundation for Science and Technology, grants from the Ministry of Education, Culture, Sports, Science and Technology in Japan during the conduct of the study.

Transparency document

The Transparency document associated with this article can be found, in online version.

Acknowledgments

We thank Profs. Haruo Inoue (Tokyo Metropolitan University) for many valuable advice and Mr. Masashi Akari, Mr. S. Fukuda, Mr. K. Tamamizu, Mr. K. Kodama for their contributions at preliminary stages of this work.

Appendix A supplementary data

Supplementary data to this article can be found online at <http://dx.doi.org/10.1016/j.bbabo.2015.10.003>.

References

- [1] Govindjee, Chlorophyll a fluorescence: a bit of basics and history, in: C. Papageorgiou, Govindjee (Eds.), *Chlorophyll a Fluorescence a Signature of Photosynthesis*, Springer, Netherland 2004, pp. 1–42.
- [2] G.C. Papageorgiou, M. Tsimilli-Michael, K. Stamatakis, The fast and slow kinetics of chlorophyll a fluorescence induction in plants, algae and cyanobacteria: a viewpoint, *Photosynth. Res.* 94 (2007) 275–290.
- [3] V. Sarafis, Chloroplasts: a structural approach, *J. Plant Physiol.* 152 (1998) 248–264.
- [4] K. Harter, A.J. Meixner, F. Schleifenbaum, Spectro-microscopy of living plant cells, *Mol. Plant* 5 (2012) 14–26.
- [5] N. Ferimazova, K. Felcmanova, E. Setlikova, H. Kupper, I. Maldener, G. Hauska, B. Sediva, O. Prasil, Regulation of photosynthesis during heterocyst differentiation in *Anabaena* sp strain PCC 7120 investigated in vivo at single-cell level by chlorophyll fluorescence kinetic microscopy, *Photosynth. Res.* 116 (2013) 79–91.
- [6] W.F.J. Vermaas, J.A. Timlin, H.D.T. Jones, M.B. Sinclair, L.T. Nieman, S.W. Hamad, D.K. Melgaard, D.M. Haaland, In vivo hyperspectral confocal fluorescence imaging to determine pigment localization and distribution in cyanobacterial cells, *Proc. Natl. Acad. Sci. U. S. A.* 105 (2008) 4050–4055.
- [7] M. Hasegawa, T. Shiina, M. Terazima, S. Kumazaki, Selective excitation of photosystems in chloroplasts inside plant leaves observed by near-infrared laser-based fluorescence spectral microscopy, *Plant Cell Physiol.* 51 (2010) 225–238.
- [8] M. Hasegawa, T. Yoshida, M. Yabuta, M. Terazima, S. Kumazaki, Anti-stokes fluorescence spectra of chloroplasts in *Parachlorella kessleri* and maize at room temperature as characterized by near-infrared continuous-wave laser fluorescence microscopy and absorption microscopy, *J. Phys. Chem. B* 115 (2011) 4184–4194.
- [9] S. Kumazaki, M. Akari, M. Hasegawa, Transformation of thylakoid membranes during differentiation from vegetative cell into heterocyst visualized by microscopic spectral imaging, *Plant Physiol.* 161 (2013) 1321–1333.
- [10] K. Sugiura, S. Itoh, Single-cell confocal spectrometry of a filamentous cyanobacterium *Nostoc* at room and cryogenic temperature. Diversity and differentiation of pigment systems in 311 cells, *Plant Cell Physiol.* 53 (2012) 1492–1506.
- [11] E. Kim, T.K. Ahn, S. Kumazaki, Changes in antenna sizes of photosystems during state transitions in granal and stroma-exposed thylakoid membrane of intact chloroplasts in *Arabidopsis* mesophyll protoplasts, *Plant Cell Physiol.* 56 (2015) 759–768.
- [12] Y. Shibata, W. Katoh, Y. Tahara, Study of cell-differentiation and assembly of photosynthetic proteins during greening of etiolated *Zea mays* leaves using confocal fluorescence microspectroscopy at liquid-nitrogen temperature, *Biochim. Biophys. Acta Bioenerg.* 1827 (2013) 520–528.
- [13] C.A. Buecherl, A. Bader, A.H. Westphal, S.P. Liptenok, J.W. Borst, FRET–FLIM applications in plant systems, *Protoplasma* 251 (2014) 383–394.
- [14] O. Holub, M.J. Seufferheld, C.G. Govindjee, G.J. Heiss, R.M. Clegg, Fluorescence lifetime imaging microscopy of *Chlamydomonas reinhardtii*: non-photochemical quenching mutants and the effect of photosynthetic inhibitors on the slow chlorophyll fluorescence transient, *J. Microsc. (Oxford)* 226 (2007) 90–120.
- [15] M. Iwai, M. Yokono, N. Inada, J. Minagawa, Live-cell imaging of photosystem II antenna dissociation during state transitions, *Proc. Natl. Acad. Sci. U. S. A.* 107 (2010) 2337–2342.
- [16] S. Matsubara, Y.-C. Chen, R. Caliandro, Govindjee, R.M. Clegg, Photosystem II fluorescence lifetime imaging in avocado leaves: contributions of the lutein-epoxide and violaxanthin cycles to fluorescence quenching, *J. Photochem. Photobiol. B Biol.* 104 (2011) 271–284.
- [17] C. Unlu, B. Drop, R. Croce, H. van Amerongen, State transitions in *Chlamydomonas reinhardtii* strongly modulate the functional size of photosystem II but not of photosystem I, *Proc. Natl. Acad. Sci. U. S. A.* 111 (2014) 3460–3465.
- [18] K. Broess, J.W. Borst, H. van Amerongen, Applying two-photon excitation fluorescence lifetime imaging microscopy to study photosynthesis in plant leaves, *Photosynth. Res.* 100 (2009) 89–96.
- [19] Y. Zeng, Y. Wu, D. Li, W. Zheng, W.X. Wang, J.N.Y. Qu, Two-photon excitation chlorophyll fluorescence lifetime imaging: a rapid and noninvasive method for in vivo assessment of cadmium toxicity in a marine diatom *Thalassiosira weissflogii*, *Planta* 236 (2012) 1653–1663.
- [20] Y. Wu, Y. Zeng, J.A.Y. Qu, W.X. Wang, Mercury effects on *Thalassiosira weissflogii*: applications of two-photon excitation chlorophyll fluorescence lifetime imaging and flow cytometry, *Aquat. Toxicol.* 110 (2012) 133–140.
- [21] A.S. Kristoffersen, O. Svensen, N. Ssebiyonga, S.R. Erga, J.J. Starnes, O. Frette, Chlorophyll a and NADPH fluorescence lifetimes in the microalgae *Haematococcus pluvialis* (Chlorophyceae) under normal and astaxanthin-accumulating conditions, *Appl. Spectrosc.* 66 (2012) 1216–1225.
- [22] T. Kolubayev, N.E. Geacintov, G. Pailletin, J. Breton, Domain sizes in chloroplasts and chlorophyll–protein complexes probed by fluorescence yield quenching induced by singlet–triplet exciton annihilation, *Biochim. Biophys. Acta* 808 (1985) 66–76.
- [23] V. Barzda, V. Gulbinas, R. Kananavicius, V. Cervinskis, H.V. Amerongen, R.V. Grondelle, L. Valkunas, Singlet–singlet annihilation kinetics in aggregates and trimers of LHClI, *Biophys. J.* 80 (2001) 2409–2421.
- [24] V. Barzda, C.J. de Grauw, J. Vroom, F.J. Kleima, R. van Grondelle, H. van Amerongen, H.C. Gerritsen, Fluorescence lifetime heterogeneity in aggregates of LHClI revealed by time-resolved microscopy, *Biophys. J.* 81 (2001) 538–546.
- [25] R.J. Gulotty, L. Mets, R.S. Alberte, G.R. Fleming, Picosecond fluorescence study of photosynthetic mutants of *Chlamydomonas reinhardtii*: origin of the fluorescence decay kinetics of chloroplasts, *Photochem. Photobiol.* 41 (1985) 487–496.
- [26] A.R. Holzwarth, J. Wendler, W. Haehnel, Time-resolved picosecond fluorescence spectra of the antenna chlorophylls in *Chlorella vulgaris*. Resolution of photosystem I fluorescence, *Biochim. Biophys. Acta Bioenerg.* 807 (1985) 155–167.
- [27] I. Moya, M. Hodges, J. Briantais, G. Hervo, Evidence that the variable chlorophyll fluorescence in *Chlamydomonas reinhardtii* is not recombination luminescence, *Photosynth. Res.* 10 (1986) 319–325.
- [28] G.H. Krause, E. Weis, Chlorophyll fluorescence and photosynthesis – the basics, *Annu. Rev. Plant Physiol. Plant Mol. Biol.* 42 (1991) 313–349.
- [29] H.J. Keuper, K. Sauer, Effect of photosystem II reaction center closure on nanosecond fluorescence relaxation kinetics, *Photosynth. Res.* 20 (1989) 85–103.
- [30] K. Amarnath, J. Zaks, S.D. Park, K.K. Niyogi, G.R. Fleming, Fluorescence lifetime snapshots reveal two rapidly reversible mechanisms of photoprotection in live cells of *Chlamydomonas reinhardtii*, *Proc. Natl. Acad. Sci. U. S. A.* 109 (2012) 8405–8410.
- [31] F. Rizzo, G. Zucchelli, R. Jennings, S. Santabarbara, Wavelength dependence of the fluorescence emission under conditions of open and closed Photosystem II reaction centres in the green alga *Chlorella sorokiniana*, *Biochim. Biophys. Acta Bioenerg.* 1837 (2014) 726–733.
- [32] F. Franck, P. Juneau, R. Popovic, Resolution of the photosystem I and photosystem II contributions to chlorophyll fluorescence of intact leaves at room temperature, *Biochim. Biophys. Acta Bioenerg.* 1556 (2002) 239–246.
- [33] N. Moise, I. Moya, Correlation between lifetime heterogeneity and kinetics heterogeneity during chlorophyll fluorescence induction in leaves: 1. Mono-frequency phase and modulation analysis reveals a conformational change of a PSII pigment complex during the IP thermal phase, *Biochim. Biophys. Acta Bioenerg.* 1657 (2004) 33–46.
- [34] L.J. Tian, S. Farooq, H. van Amerongen, Probing the picosecond kinetics of the photosystem II core complex in vivo, *Phys. Chem. Chem. Phys.* 15 (2013) 3146–3154.
- [35] J. Wendler, A.R. Holzwarth, State transitions in the green alga *Scenedesmus obliquus* probed by time-resolved chlorophyll fluorescence spectroscopy and global data analysis, *Biophys. J.* 52 (1987) 717.

- [36] S.B. Krumova, S.P. Laptanok, J.W. Borst, B. Ughy, Z. Gombos, G. Ajlani, H. van Amerongen, Monitoring photosynthesis in individual cells of *synechocystis* sp. PCC 6803 on a picosecond timescale, *Biophys. J.* 99 (2010) 2006–2015.
- [37] R. Haselkorn, *Heterocysts*, *Annu. Rev. Plant Physiol. Plant Mol. Biol.* 29 (1978) 319–344.
- [38] R. Grotjohann, M.S. Rho, W. Kowallik, Influences of blue and red-light on the photosynthetic apparatus of *Chlorella kessleri* – alterations in pigment–protein complexes, *Bot. Acta* 105 (1992) 168–173.
- [39] I. Ikegami, A. Kamiya, Presence of the photoactive reaction-center chlorophyll of PSI (P700) in dark-grown cells of a chlorophyll-deficient mutant of *Chlorella kessleri*, *Plant Cell Physiol.* 39 (1998) 1087–1092.
- [40] S.Y. Ow, T. Cardona, A. Taton, A. Magnuson, P. Lindblad, K. Stensjö, P.C. Wright, Quantitative shotgun proteomics of enriched heterocysts from *nostoc* sp. PCC 7120 using 8-plex isobaric peptide tags, *J. Proteome Res.* 7 (2008) 1615–1628.
- [41] T. Cardona, N. Battchikova, P. Zhang, K. Stensjö, E.M. Aro, P. Lindblad, A. Magnuson, Electron transfer protein complexes in the thylakoid membranes of heterocysts from the cyanobacterium *nostoc punctiforme*, *Biochim. Biophys. Acta* 1787 (2009) 252–263.
- [42] J.-J. Park, S. Lechno-Yossef, C.P. Wolk, C. Vieille, Cell-specific gene expression in *Anabaena variabilis* grown phototrophically, mixotrophically, and heterotrophically, *BMC Genomics* 14 (2013).
- [43] R.Y. Stanier, R. Kunisawa, M. Mandel, G. Cohenbaz, Purification and properties of unicellular blue–green algae (Order Chroococcales), *Bacteriol. Rev.* 35 (1971) 171.
- [44] E. Bittersmann, A. Holzwarth, G. Agel, W. Nultsch, Picosecond time-resolved emission spectra of photoinhibited and photobleached *Anabaena variabilis*, *Photochem. Photobiol.* 47 (1988) 101–105.
- [45] E. Bittersmann, W. Vermaas, Fluorescence lifetime studies of cyanobacterial photosystem II mutants, *Biochim. Biophys. Acta Bioenerg.* 1098 (1991) 105–116.
- [46] C.W. Mullineaux, A.R. Holzwarth, Effect of photosystem II reaction centre closure on fluorescence decay kinetics in a cyanobacterium, *Biochim. Biophys. Acta Bioenerg.* 1183 (1993) 345–351.
- [47] J. Veerman, F.K. Bentley, J.J. Eaton-Rye, C.W. Mullineaux, S. Vasil'ev, D. Bruce, The PsbU subunit of photosystem II stabilizes energy transfer and primary photochemistry in the phycobilisome-photosystem II assembly of *synechocystis* sp. PCC 6803, *Biochemistry* 44 (2005) 16939–16948.
- [48] L. Ying, X. Huang, B. Huang, J. Xie, J. Zhao, X.S. Zhao, <Ying_2002_Anabaena_sp PCC7120_spectral_confocal.pdf>, *Photochem. Photobiol.* 76 (2002) 310–313.
- [49] S. Ke, R. Haselkorn, Fluorescence spectroscopy study of heterocyst differentiation in *Anabaena* PCC 7120 filaments, *Microbiology-SGM* 159 (2013) 253–258.
- [50] S.W. Hogewoning, E. Wientjes, P. Douwstra, G. Trouwborst, W. van Leperen, R. Croce, J. Harbinson, Photosynthetic quantum yield dynamics: from photosystems to leaves, *Plant Cell* 24 (2012) 1921–1935.
- [51] K. Roháček, M. Barták, Technique of the modulated chlorophyll fluorescence: basic concepts, useful parameters, and some applications, *Photosynthetica* 37 (1999) 339–363.
- [52] U. Schreiber, Pulse-amplitude-modulation (PAM) fluorometry and saturation pulse method: an overview, *Chlorophyll a Fluorescence*, Springer 2004, pp. 279–319.
- [53] D. Campbell, V. Hurry, A.K. Clarke, P. Gustafsson, G. Oquist, Chlorophyll fluorescence analysis of cyanobacterial photosynthesis and acclimation, *Microbiol. Mol. Biol. Rev.* 62 (1998) 667.
- [54] K. El Bissati, D. Kirilovsky, Regulation of *psbA* and *psaE* expression by light quality in *Synechocystis* species PCC 6803. A redox control mechanism, *Plant Physiol.* 125 (2001) 1988–2000.
- [55] I. Vass, D. Kirilovsky, A.L. Etienne, UV-B radiation-induced donor- and acceptor-side modifications of photosystem II in the cyanobacterium *synechocystis* sp. PCC 6803, *Biochemistry* 38 (1999) 12786–12794.
- [56] A. Volgusheva, G. Kukarskikh, T. Krendeleva, A. Rubin, F. Mamedov, Hydrogen photoproduction in green algae *Chlamydomonas reinhardtii* under magnesium deprivation, *RSC Adv.* 5 (2015) 5633–5637.
- [57] Y. Hihara, K. Sonoike, Regulation, inhibition and protection of photosystem I, *Regulation of Photosynthesis*, Springer 2001, pp. 507–531.
- [58] Y. Umena, K. Kawakami, J.-R. Shen, N. Kamiya, Crystal structure of oxygen-evolving photosystem II at a resolution of 1.9 Å, *Nature* 473 (2011) 55–60.
- [59] T. Watanabe, A. Hongu, K. Honda, M. Nakazato, M. Konno, S. Saitoh, Preparation of chlorophylls and pheophytins by isocratic liquid-chromatography, *Anal. Chem.* 56 (1984) 251–256.
- [60] E.W. Chappelle, M.S. Kim, J.E. McMurtrey, Ratio analysis of reflectance spectra (rars) – an algorithm for the remote estimation of the concentrations of chlorophyll-a, chlorophyll-b, and carotenoids in soybean leaves, *Remote Sens. Environ.* 39 (1992) 239–247.
- [61] S.L. Ustin, A.A. Gitelson, S. Jacquemoud, M. Schaepman, G.P. Asner, J.A. Gamon, P. Zarco-Tejada, Retrieval of foliar information about plant pigment systems from high resolution spectroscopy, *Remote Sens. Environ.* 113 (2009) S67–S77.
- [62] U. Schreiber, T. Endo, H.L. Mi, K. Asada, Quenching analysis of chlorophyll fluorescence by the saturation pulse method – particular aspects relating to the study of eukaryotic algae and cyanobacteria, *Plant Cell Physiol.* 36 (1995) 873–882.
- [63] S. Joshua, C.W. Mullineaux, Phycobilisome diffusion is required for light-state transitions in cyanobacterial, *Plant Physiol.* 135 (2004) 2112–2119.
- [64] T. Ogawa, T. Harada, H. Ozaki, K. Sonoike, Disruption of the *ndhF1* gene affects Chl fluorescence through state transition in the cyanobacterium *synechocystis* sp. PCC 6803, resulting in apparent high efficiency of photosynthesis, *Plant Cell Physiol.* 54 (2013) 1164–1171.
- [65] G. Tomita, E. Rabinowitch, Excitation energy transfer between pigments in photosynthetic cells, *Biophys. J.* 2 (1962) 483.
- [66] J.F. Allen, Protein-phosphorylation in regulation of photosynthesis, *Biochim. Biophys. Acta* 1098 (1992) 275–335.
- [67] B. Drop, M. Webber-Birungi, S.K.N. Yadav, A. Filipowicz-Szymanska, F. Fusetti, E.J. Boekema, R. Croce, Light-harvesting complex II (LHCII) and its supramolecular organization in *Chlamydomonas reinhardtii*, *Biochim. Biophys. Acta Bioenerg.* 1837 (2014) 63–72.
- [68] S. Caffarri, T. Tibiletti, R.C. Jennings, S. Santabarbara, A comparison between plant photosystem I and photosystem II architecture and functioning, *Curr. Protein Pept. Sci.* 15 (2014) 296–331.
- [69] G. Britton, UV/visible spectroscopy, in: G. Britton, S. Liaaen-Jensen, H. Pfander (Eds.), *Carotenoids: Spectroscopy*, Birkhauser, Basel 1995, pp. 13–62.
- [70] B.H. Davies, H.P. Köst, Carotenoids, in: H.-P. Köst (Ed.), *Handbook of Chromatography: Plant Pigments*, CRC Press, Boca Raton 1988, pp. 1–185.
- [71] H.A. Frank, J.A. Bautista, J.S. Josue, A.J. Young, Mechanism of nonphotochemical quenching in green plants: energies of the lowest excited singlet states of violaxanthin and zeaxanthin, *Biochemistry* 39 (2000) 2831–2837.
- [72] A.C. Ley, D.C. Mauzerall, Absolute absorption cross-sections for photosystem II and the minimum quantum requirement for photosynthesis in *Chlorella vulgaris*, *Biochim. Biophys. Acta Bioenerg.* 680 (1982) 95–106.
- [73] M. Werst, Y. Jia, L. Mets, G.R. Fleming, Energy transfer and trapping in the photosystem I core antenna. A temperature study, *Biophys. J.* 61 (1992) 868.
- [74] R.B. Peterson, E. Dolan, H.E. Calvert, B. Ke, Energy transfer from phycobiliproteins to photosystem I in vegetative cells and heterocysts of *Anabaena variabilis*, *Biochim. Biophys. Acta Bioenerg.* 634 (1981) 237–248.
- [75] M. Watanabe, D.A. Semchonok, M.T. Webber-Birungi, S. Ehira, K. Kondo, R. Narikawa, M. Ohmori, E.J. Boekema, M. Ikeuchi, Attachment of phycobilisomes in an antenna-photosystem I supercomplex of cyanobacteria, *Proc. Natl. Acad. Sci.* 111 (2014) 2512–2517.
- [76] G. Yamanaka, A. Glazer, Phycobiliproteins in *Anabaena* 7119 Heterocysts, *Photosynthetic Prokaryotes: Cell Differentiation and Function*, Elsevier Science Publishing, Amsterdam, 1983 69–90.
- [77] B. Gobets, R. van Grondelle, Energy transfer and trapping in photosystem I, *Biochim. Biophys. Acta Bioenerg.* 1507 (2001) 80–99.
- [78] A.M. Acuña, J.J. Snellenburg, M. Gwizdala, D. Kirilovsky, R. van Grondelle, I.H. van Stokkum, Resolving the contribution of the uncoupled phycobilisomes to cyanobacterial pulse-amplitude modulated (PAM) fluorometry signals, *Photosynth. Res.* (2015) 1–12.
- [79] M. Toyoshima, N.V. Sasaki, M. Fujiwara, S. Ehira, M. Ohmori, N. Sato, Early candidacy for differentiation into heterocysts in the filamentous cyanobacterium *Anabaena* sp. PCC 7120, *Arch. Microbiol.* 192 (2010) 23–31.
- [80] A.B. Juárez, L. Barsanti, V. Passarelli, V. Evangelista, N. Vesentini, V. Conforti, P. Gualtieri, In vivo microspectroscopy monitoring of chromium effects on the photosynthetic and photoreceptive apparatus of *Eudorina unicocca* and *Chlorella kessleri*, *J. Environ. Monit.* 10 (2008) 1313–1318.
- [81] M.M. Saleh, D.N. Matorin, B.K. Zayadan, D.A. Todorenko, E.P. Lukashov, M.M. Gaballah, Differentiation between two strains of microalga *Parachlorella kessleri* using modern spectroscopic method, *Bot. Stud.* 55 (2014) 53.
- [82] B. Osmond, O. Schwartz, B. Gunning, Photoinhibitory printing on leaves, visualised by chlorophyll fluorescence imaging and confocal microscopy, is due to diminished fluorescence from grana, *Aust. J. Plant Physiol.* 26 (1999) 717–724.
- [83] H. Kupper, I. Setlik, M. Trtilek, L. Nedbal, A microscope for two-dimensional measurements of in vivo chlorophyll fluorescence kinetics using pulsed measuring radiation, continuous actinic radiation, and saturating flashes, *Photosynthetica* 38 (2000) 553–570.
- [84] K. Oxborough, Using chlorophyll a fluorescence imaging to monitor photosynthetic performance, *Chlorophyll a Fluorescence*, Springer 2004, pp. 409–428.
- [85] K. Omasa, A. Konishi, H. Tamura, F. Hosoi, 3D confocal laser scanning microscopy for the analysis of chlorophyll fluorescence parameters of chloroplasts in intact leaf tissues, *Plant Cell Physiol.* 50 (2009) 90–105.
- [86] W.I. Gruszecki, K. Wojtowicz, Z. Krupa, K. Strzalka, A direct measurement of the thermal-energy dissipation in the photosynthetic apparatus during induction of fluorescence, *J. Photochem. Photobiol. B Biol.* 22 (1994) 23–27.
- [87] W.J. Vredenberg, A three-state model for energy trapping and chlorophyll fluorescence in photosystem II incorporating radical pair recombination, *Biophys. J.* 79 (2000) 26–38.
- [88] W. Vredenberg, O. Prasil, On the polyphasic quenching kinetics of chlorophyll a fluorescence in algae after light pulses of variable length, *Photosynth. Res.* 117 (2013) 321–337.
- [89] Y. Miloslavina, A. Wehner, P.H. Lambrev, E. Wientjes, M. Reus, G. Garab, R. Croce, A.R. Holzwarth, Far-red fluorescence: a direct spectroscopic marker for LHCII oligomer formation in non-photochemical quenching, *FEBS Lett.* 582 (2008) 3625–3631.
- [90] S.B. Krumova, S.P. Laptanok, L. Kovács, T. Tóth, A. van Hoek, G. Garab, H. van Amerongen, Digalactosyl-diacylglycerol-deficiency lowers the thermal stability of thylakoid membranes, *Photosynth. Res.* 105 (2010) 229–242.
- [91] J. Durrant, L. Giorgi, J. Barber, D. Klug, G. Porter, Characterisation of triplet states in isolated Photosystem II reaction centres: oxygen quenching as a mechanism for photodamage, *Biochim. Biophys. Acta Bioenerg.* 1017 (1990) 167–175.
- [92] A. Telfer, Singlet oxygen production by PSII under light stress: mechanism, detection and the protective role of beta-carotene, *Plant Cell Physiol.* 55 (2014) 1216–1223.
- [93] L. Zhang, T.B. Melo, H. Li, K.R. Naqvi, C. Yang, The inter-monomer interface of the major light-harvesting chlorophyll a/b complexes of photosystem II (LHCII) influences the chlorophyll triplet distribution, *J. Plant Physiol.* 171 (2014) 42–48.
- [94] D.A. Hartzler, D.M. Niedzwiedzki, D.A. Bryant, R.E. Blankenship, Y. Pushkar, S. Sayikhin, Triplet excited state energies and phosphorescence spectra of (bacterio) chlorophylls, *J. Phys. Chem. B* 118 (2014) 7221–7232.

PAPER



CrossMark
click for updates

Cite this: *Mol. Syst. Des. Eng.*, 2016, 1, 208

Received 28th December 2015,
Accepted 4th May 2016

DOI: 10.1039/c5me00012b

rsc.li/molecular-engineering

A molecular assembly that crawls on a solid substrate with a metabolic-like process†

Masato Nakada, Yukihiro Fujikami, Masaharu Kawaguchi,
Daigo Yamamoto and Akihisa Shioi*

A vesicular aggregate filled with lipid molecules exhibited crawling motion over a glass surface as a result of chemical reactions. The vesicular aggregate was composed of didodecyltrimethylammonium bromide (DDAB) and sodium oleate with calcium ions. The crawling motion was induced by the chemical reaction between DDAB and iodide ions, and it caused discharge of the inner lipids. This was responsible for the size reduction of the aggregate. However, it engulfed the neighboring smaller vesicles, which were taken up into the vesicular aggregate in the dehydrated state and became a constituent of the aggregate. The size of the vesicular aggregate recovered and could translate in a sustainable manner. This is probably the first example of an amphiphilic molecular assembly that exhibits crawling motion as a result of chemical reactions without size reduction. This may be regarded as the cell-like behavior of an abiotic molecular assembly with a metabolic-like process.

Design, System, Application

The development of chemical systems that mimic the behavior of living matter results in the determination of characteristics that impart a semblance of life. A chemical reaction driven vesicle can be designed with metabolic-like characteristics, taking in surrounding material to reconstruct its body and obtain energy for motion. Here, amphiphilic molecular aggregates exhibit crawling motion on a glass surface, sustained by “eating” the other aggregates and discharging waste. This biomimetic motion is achieved by cheap simple chemicals, showing that it is possible to discover intriguing effects in apparently simple systems. The chemical reactions that form precipitates are controlled by the coexisting lipids. This process drives the aggregates. The vesicle internal structure is optimised by altering the chemical constituents to give the dense packing of lipids that enables long distance sustainable motion. This scenario may be general irrespective of the used chemicals, and hence self-healing, self-duplication and communication functions may be achieved based on this study. The system may be developed for self-patterning and drug delivery: we may be able to control the aggregate motion along a line composed of eaten objects, and then, the waste may draw a micropattern. If biocompatible chemicals can be used, the aggregates may become a scavenger that removes lipid aggregates on the wall of blood vessels.

Introduction

Living organisms maintain their lives as open and dynamic systems. Their dynamic features are maintained by metabolism. Organisms derive nutrition from and release waste to the surroundings. Through metabolism, living organisms replace old parts of the body with new ones. This process serves numerous biological functions. Because the metabolic process is associated with the self-healing and self-duplication of living organisms,¹ the study of active soft mat-

ter² exhibiting metabolic-like behavior may lead to the design of colloidal systems with these characteristics.

Such colloidal systems will be possible only if they are open systems under a non-equilibrium state. Thus, a study of self-moving colloids under a strongly non-equilibrium state may provide a basis for the design of these systems. Until now, liquid droplets and catalytic particles have been employed in numerous studies of self-moving colloids. The results showed that some characteristics contained in biological motions, such as vectorial motion in an isotropic field^{3,4} and chemotaxis,^{5,6} can be mimicked by colloidal objects. The energy of self-motion is provided by chemical reactions⁷ and adsorption/desorption processes.⁸ These characteristics are inherent in biological motion.¹ However, these colloidal systems do not contain metabolic-like processes, except in some rare cases.⁹ Here, a metabolic-like process refers to the spontaneous replacement of an old part of the body with a new

Department of Chemical Engineering & Materials Science, Doshisha University,
1-3 Tatara Miyakodani, Kyotanabe, Kyoto 610-0321, Japan.

E-mail: ashioi@mail.doshisha.ac.jp

† Electronic supplementary information (ESI) available: Fluorescence confocal microscopy images of vesicles; tabulated dynamic aggregate behaviors; movies of the molecular assemblies, crawling motion of the vesicular aggregates, absorption of smaller vesicles, and film formation. See DOI: 10.1039/c5me00012b

one. This situation is the same for a study of self-moving vesicles (liposomes) that are formed with a bilayer membrane and used for cytomimetic research. A vesicle with self-propulsion that contained the protein ActA, which polymerizes actin filaments, was reported.¹⁰ The compression force caused by polymerization drove the vesicle. This study was inspired by the motion mechanism of *Listeria monocytogenes*¹¹ and provides an example of vesicle propulsion without a decrease in its size. Recently, the authors' group has reported the cyclic motion of a vesicle under a pH gradient without size reduction.¹² On the other hand, in many cases, vesicles that exhibit spontaneous motion or deformation decrease in size because chemical reactions and physical stimuli for vesicle motion cause damage to the vesicle.¹³

Self-moving colloids with metabolic-like characteristics have not been fully investigated. To provide this characteristic to an abiotic colloid, vesicles would be most appropriate because they are formed by amphiphilic molecules that can coexist in a solution where the vesicles move. If a vesicle takes the surrounding amphiphiles to reconstruct its body and obtain the energy for motion, it may possess self-healing, self-duplication and communication functions. The self-duplication and communication functions of vesicles (liposomes) have been studied.¹⁴ The constituents of the vesicle with self-duplication are dissolved in the vesicular solution and transformed into the membrane constituent by chemical reactions. These studies focused on the self-duplication process and were interesting from the viewpoints of the origins of life.¹⁵ The addition of biomimetic motion for the ingestion of a constituent may be the subject of future studies where the mechanism for many active biological functions will be revealed. The formation of a vesicle driven by chemical reaction that possesses metabolic-like characteristics may become the basis for this purpose.

The authors' group reported a self-moving vesicle with size reduction.¹⁶ In that study, the vesicle composed of the cationic surfactant didodecyldimethylammonium bromide (DDAB) migrated in water *via* ion exchange with iodide ions. The motion was accompanied by size reduction of the vesicle because DDAB and iodide ions formed a precipitate that was eliminated from the vesicle membrane. In the present study, sodium oleate and calcium ions were mixed with a DDAB based vesicle. The mixture formed an aggregate with a complicated inner structure. This vesicular aggregate (VA) was adsorbed on a glass surface. During the diffusion of iodide ions, the VA moved over the glass surface, leaving behind a thin film on the glass surface. This film was the reaction product of the inner lipid molecules. As a result, the inner lipids were discharged from the VA. This resulted in the size reduction of the VA. However, the VA took other smaller vesicles into the body and recovered its size. Without this size recovery, VA could not show sustainable self-motion. A VA with these characteristics may be regarded as a model molecular assembly that exhibits cell like behavior with a metabolic-like process. The sustained translational motion may be applied to an active transport carrier of useful chemicals and parti-

cles, for patterning in materials design and smart delivery in microchannels.

Experimental

Chemicals

Sodium oleate (>97%) and didodecyldimethylammonium bromide (>98%) were purchased from Tokyo Chemical Industry Co., Ltd. The other chemicals used were of reagent grade and obtained from Wako Pure Chemical Industries, Ltd. All chemicals were used without further purification.

Vesicle preparation

The drying–rehydration method was used for vesicle preparation.¹⁷ Sodium oleate and DDAB were dissolved in acetone with sonication. Calcium chloride and a fluorescent probe (perylene) were also added to the solution. The resulting solution was poured into a glass vial, and the acetone was evaporated under nitrogen gas and then completely under vacuum. After evaporation, a thin film remained on the wall of the vial. A bicine buffer solution (pH \approx 8.4) was then poured into the vial and maintained at 50°C for 1 h. The concentration of bicine was 70 mM, and its pH was adjusted to the desired value using a small amount of NaOH. The vesicle suspension was obtained by gentle shaking of the solution. The concentrations of each solute were 3.2 mM (DDAB), 2.3 mM (sodium oleate), and 10 mM (CaCl₂) in the vesicle suspension. These concentrations were chosen because the motion of VA was observed with sufficient reproducibility. A trace amount of perylene was used.

Vesicle observation

The vesicle suspension was poured into a hole-slide glass and covered with a cover glass. As shown in Fig. 1, a small gap was formed beside the cover glass, and an aqueous solution containing 40 mM KI (without bicine) was diffused from the gap into the vesicle suspension. The volume ratio of the KI solution to the vesicle suspension was approximately 1:3, and the final KI concentration after complete diffusion was estimated to be 10 mM. After the convection disappeared, the vesicles were observed by fluorescence microscopy (Olympus

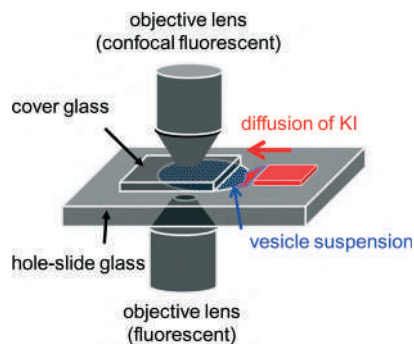


Fig. 1 Experimental setup. Two types of objective lens were selected depending on the purpose.

IX-71). An Olympus BX-51 confocal microscope was also used. Image analysis was performed using Move-tr/2D (Library Co., Ltd.), ImageJ (Wayne Rasband, NIH), and Movie Ruler ver. 2 (Photoron Ltd.). All experiments were performed at room temperature, which was controlled by an air conditioner within approximately 18–25 °C.

Results and discussion

Structure of the vesicular assembly

Fig. 2 shows fluorescence confocal microscopy images of the amphiphilic molecular assemblies formed by the present experiment. Three cross sections at different depths are shown. Perylene, a hydrophobic molecule, was used as the fluorescence probe. Fluorescence microscopy showed that the molecular assemblies can be classified into two types, as shown in Fig. 2a and b.

Fig. 2a shows the first type. Tiny vesicles appear to be packed, but the structure is complicated and obscure. This type of structure will be discussed later and is denoted as VA (vesicular aggregate). The second type shown in Fig. 2b is an onion-like vesicle. A multi-membrane structure can be observed, which is denoted as OV. A much simpler vesicle that was composed of a single water pool surrounded by an amphiphilic molecular layer was also observed.

To examine the structure of VA, water was added to the solution. In this experiment, the water permeates into the aggregate. Fig. 3 shows confocal fluorescence microscopy images of a VA during water permeation. Fig. 3a shows the time course of a VA that swells due to water permeation. The images at $t = 11.0$ and 43.0 s were taken by fluorescence confocal microscopy, whereas at $t = 29.2$ s, weak incident light was introduced into the fluorescence microscope to clarify the image. Immediately after the addition of water ($t = 0$), fluorescence was emitted uniformly from the VA ($t = 11.0$). As the water permeated, the volume increased, and the fluorescence

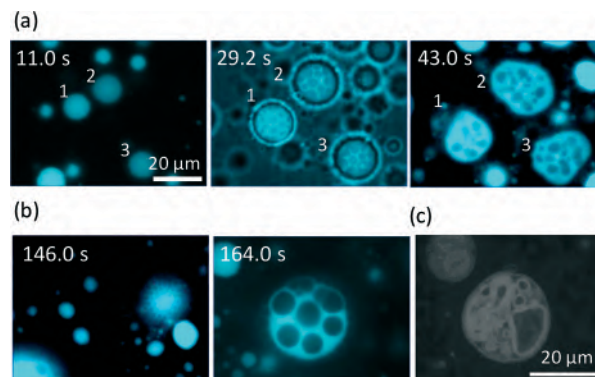


Fig. 3 Fluorescence microscopy images of a VA that swells due to water permeation. The time after water injection is shown. (a) Time dependency of a swelling VA. Weak incident light was introduced for the observation at 29.2 s. The outer ring is a halo as a result of this operation. The same vesicle is indicated by the same number. (b) The other two examples of VA swollen by water. (a, b) $[\text{DDAB}]/[\text{oleate}] = 1.4 (=3.2/2.3)$. (c) Fluorescence microscopy image of a VA at $[\text{DDAB}]/[\text{oleate}] = 2.0$. Water did not permeate.

was concentrated on the restricted portions ($t = 43.0$). The non-fluorescent part is considered to be the water pool. The image at $t = 43.0$ s indicates that a VA swollen by water is comprised of numerous small water pools surrounded by amphiphilic molecules. Other examples of swollen VAs are shown in Fig. 3b. In these results, the water pools were rather uniform and spherical. These results indicate that a VA before water addition is composed of dehydrated molecular assemblies. The dehydrated vesicles packed tightly in a VA is one possible interpretation. Fig. 3c exemplifies a vesicle formed in $[\text{DDAB}]/[\text{oleate}] = 2$ without Ca^{2+} (*i.e.* more DDAB-rich compared to the standard conditions for sample preparation). Numerous smaller vesicles aggregated under these conditions. This suggests that an aggregate with nearly homogeneous fluorescence in the presence of Ca^{2+} may be composed of densely packed dehydrated vesicles. However, reconstruction of an inner structure may occur by water addition, and the fluorescent part that surrounds the internal water compartments was too thick to be a bilayer structure. The inner structure before water addition may be more complicated such as a cubic phase. The three dimensional view of the VA, which was constructed from the cross sectional images, showed that VAs are adsorbed under the cover glass (on the glass surface) (see ESI† Movie S1).

The populations of the two types of vesicles (VA and OV) depend on the compositions of the vesicular solution. When DDAB, oleate and Ca^{2+} coexist, most of the molecular assemblies are the VA type. Confocal fluorescence microscopy of a VA with perylene showed almost uniform emission from them, as shown in Fig. 2a and 3a (11.0 s). This indicates the dense packing of lipid molecules. When DDAB molecules are the only constituent of the vesicles, they form simple vesicles.¹⁸ The addition of Ca^{2+} transforms the simple vesicles into a more complicated structure, as shown in Fig. S1a,† where the vesicles appear to be intermediate between OV and

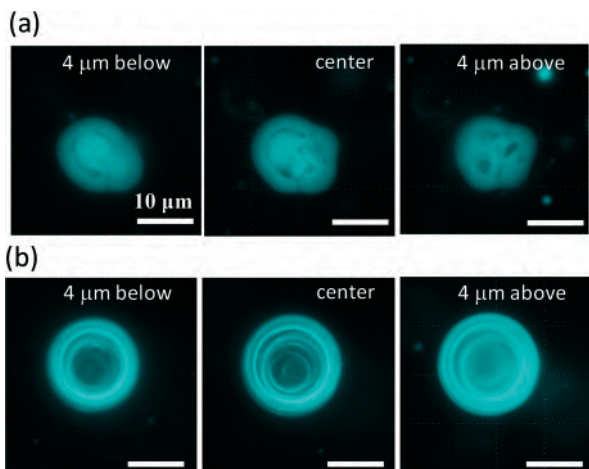


Fig. 2 Two types of molecular assemblies in an aqueous solution containing DDAB, sodium oleate and CaCl_2 . The structure shown in (a) is denoted as VA and that in (b) is denoted as OV. Three cross sections are shown for each structure.

VA: spherical shells can be seen, but the inner structure is complicated. When oleate was added to DDAB without Ca^{2+} , numerous OV type vesicles appeared (see Fig. S1b†). According to these results, the mixture of DDAB and oleate formed numerous VAs in the presence of Ca^{2+} , but OVs may contain less Ca^{2+} . Ca^{2+} and oleate generally form a precipitate in water. We did not see any macroscopic precipitates in the DDAB–oleate solution with Ca^{2+} at the present chemical concentrations. Thus, the Ca^{2+} and oleate compounds dissolved in the solution with the help of DDAB, resulting in the formation of VAs. Mixtures of single-tailed anionic and cationic surfactants often precipitate in water. However, they can form vesicles at appropriate mixing ratios.¹⁹ The stability of the present VAs may be discussed in a similar manner to that of the spontaneous vesicles.

Crawl motion of the vesicular aggregate

When KI diffuses toward the VAs, they deform and crawl as they are adsorbed on the glass surface. OVs do not exhibit any long distance motion, and they sometimes collapse at their places. This suggests that the dense packing of lipid molecules inside a VA is essential for sustainable motion under KI diffusion. Fig. 4 shows the fluorescence microscopy image of the crawl motion of a VA (see ESI† Movie S2). The VA with a red mark in Fig. 4 exhibits translational motions and absorbs the surrounding smaller vesicles, some of which are indicated by the white arrows. Fig. 5a and b show the moving distance of the center and the area occupied by the moving VA. Two types of experimental results are shown. The first one is when the VA absorbs smaller vesicles for its motion (Fig. 5a), and the second one is when it does not (Fig. 5b). The former type of motion is observed when numerous smaller vesicles surround the VA. In this case, the area of the VA remains relatively constant, as shown in Fig. 5a. The

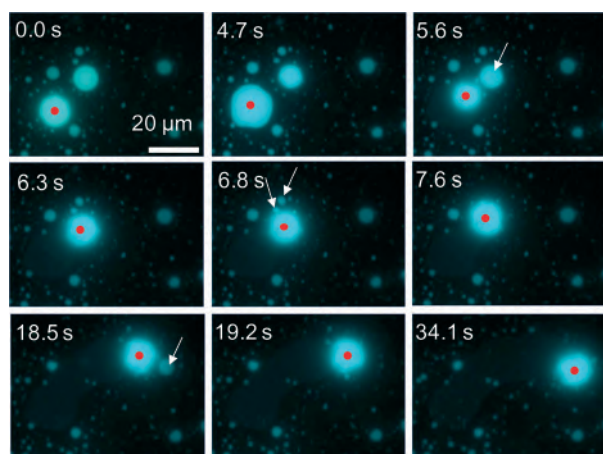


Fig. 4 Consecutive snapshots of a VA crawling over a glass surface. The flame is fixed. The crawling VA is indicated by the red mark. The white arrows indicate some vesicles absorbed by the VA. A KI solution was injected at 0.0 s, and the adsorption state of the VA changed at 4.7 s.

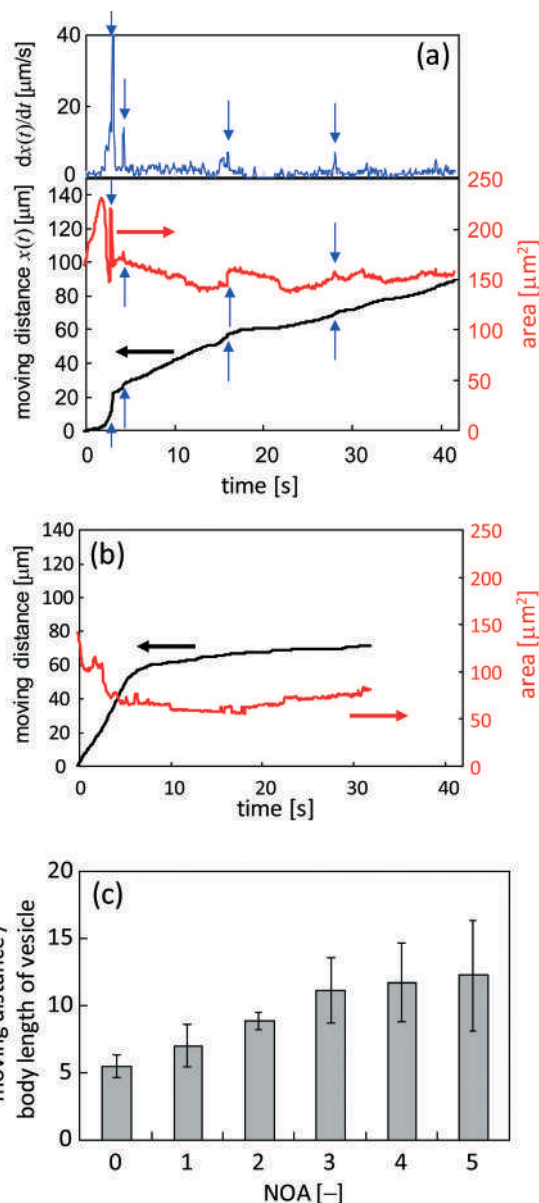


Fig. 5 Characteristics of the crawling motion of the VA. (a) The moving distance and area of the VA that absorbs the surrounding smaller vesicles. The upper panel shows the velocity. (b) The moving distance and area of the VA that is not surrounded by smaller vesicles. (c) The moving distance that is scaled by the body length of the VA is shown against the number of absorptions that were clearly observed.

initial increase in area results from a change in the adsorbed state of the VA onto the glass. The volume of the VA is probably constant, but the area projected onto the glass increases. In contrast, the VA that does not absorb the surrounding vesicles collapses monotonically.

The moving distance of the VA that absorbs the surrounding vesicles increases monotonically over a period of more than 40 s, while the motion of the VA without absorption stops within a few seconds. The gradual increase after approximately 6 s, as shown in Fig. 5b, is the result of vibrational fluctuations without translation. The time when the

observable absorption events occurred is indicated by the blue arrows in Fig. 5a. The VA size was recovered by absorption. The speed of VA motion, which is shown in the upper panel of Fig. 5a, became faster at each absorption. This suggests that absorption provides not only the constituent of the VA body but also the motility of the VA. The same experiments were performed, and the relationship between the mean moving distance and the number of observable absorptions (NOA) was determined. The moving distance from the start position to the final one is shown. (The VA no longer moves at the final position.) The result is shown in Fig. 5c. The ordinate shows the moving distance that is scaled by the body length of the VA. When the NOA is less than three, the distance increases linearly with increasing NOA. However, the rate of the increase decreases when the NOA exceeds four.

Fig. 6 shows snapshots of a moving VA that absorbs a smaller vesicle. They are indicated by a red arrow and a white arrow in Fig. 6a (see ESI† S3 (slideshow)). The structure of the smaller one appears to be much simpler than that of the VA. This shows that the smaller one is almost a simple vesicle in structure. Immediately after their contact, the VA forms a tip and absorbs the smaller vesicle through the tip. Fig. 6a-f and ESI† S3 show that the size of the smaller vesicle decreases drastically as a result of the absorption. This suggests that the water contained in the smaller vesicle is drained rapidly during absorption, and the resulting dehydrated vesicle becomes part of the VA.

Fig. 7 shows the trajectory of seven VAs that exhibit long distance motion. KI diffuses from left to right. The VA tends to go down along the gradient of the KI concentration, even though randomness is included in each trajectory. For this tendency, a moving VA may be able to meet smaller vesicles that have not reacted with KI. If a VA went up along the gradient, the smaller vesicles that the VA could encounter would be exposed to the concentrated KI solution. In this case, the

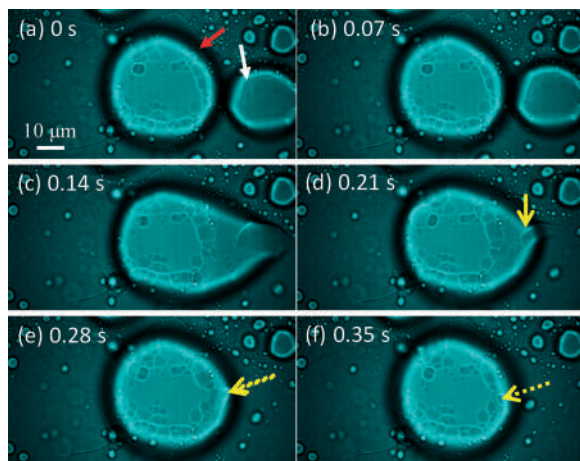


Fig. 6 Consecutive snapshots of a VA (red arrow) absorbing a smaller vesicle (white arrow). Weak incident light is introduced into the fluorescence microscope. The yellow arrow indicates the smaller vesicle after absorption, which collapses by absorption.

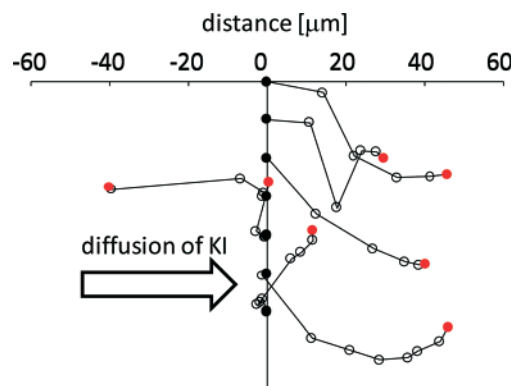


Fig. 7 Trajectory of the VA motion. Seven VAs were selected. Each start point is indicated by a black circle arranged in a line. The final position is indicated by a red circle. A white circle is drawn every 5 s. KI diffuses from left to right.

smaller vesicles would already have reacted and cannot provide the motility of the VA. Therefore, this weak chemotactic nature may be required so that the VA meets fresh smaller vesicles. However, because randomness is included in the trajectory, the probability of the VA colliding with fresh vesicles decreases with time. Hence, the VA cannot maintain its motility. Therefore, the total traveling distance shown in Fig. 5c does not increase as much when NOA is larger than 3.

Fig. 8a shows the film that is formed by VA motion (see ESI† Movie S4). The fluorescence of perylene is emitted from

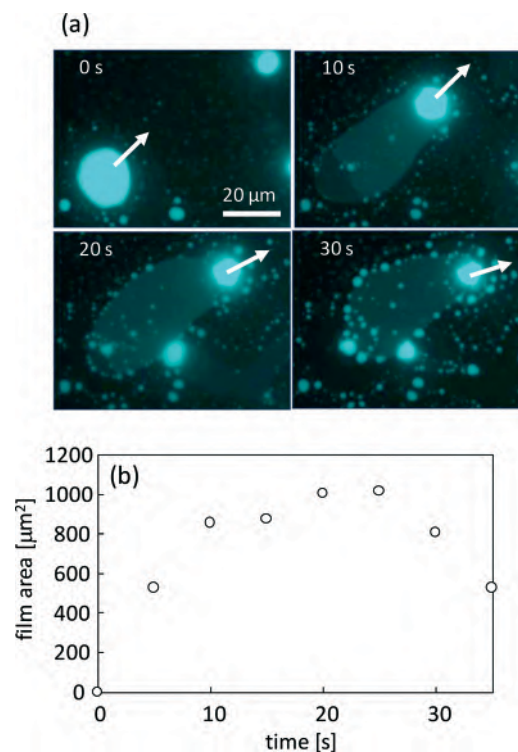


Fig. 8 Film formation behind the VA when it crawls over the glass surface. (a) Consecutive snapshots. The moving direction in each image is indicated by a white arrow. (b) The time course of the area of the film shown in (a).

the film spread over the surface, and the VA moves leaving the film behind. For this characteristic, once the formed film surrounds the VA, it no longer moves. After film formation, numerous small aggregates form at the periphery of the film, as shown in Fig. 8a (30 s). Fig. 8b shows the time dependency of the film area. The area increases with the exclusion of DDAB and oleate molecules from the VA but decreases shortly through the transformation into the aggregates. After this transformation, the glass surface is free from the film and may be able to serve as a place for VA motion. The film and the resulting aggregates are the waste of the VA, which is the reaction product with KI.

Fig. 9 shows that the film is formed from smaller vesicles contained in the VA. An inner smaller vesicle appears to be a simple vesicle, where a simple vesicle means that it has a single water pool surrounded by an amphiphilic membrane. The inner vesicle and the film are connected to each other; the conjunction points are indicated by the yellow arrows. The direction of VA motion is indicated by the black arrow. This result shows that the film formed behind the moving VA is generated by the collapse of vesicles contained in the VA. This collapse generates the motility of the VA. The inner vesicle may have been present as a dehydrated vesicle before the addition of the KI solution or may be formed by water permeation after the addition.

When two VAs collide, they behave as a prey–predator system. One VA absorbs the other, through which the VA achieves motility. The relationship appears to be determined by the relative size of the VA. The larger VA filled with inner lipid molecules plays the role of the predator. The larger VA absorbs smaller vesicles to obtain a part of the body and its motility. The VA with complicated inner structures formed in the presence of Ca^{2+} . Thus, the concentration of Ca^{2+} is probably lower in the simpler vesicle (prey). We may consider that a Ca-rich aggregate could move to engulf Ca-poor aggregates. Based on this postulate, the Ca^{2+} concentration in the VAs would decrease by eating the simpler vesicles. This may ex-

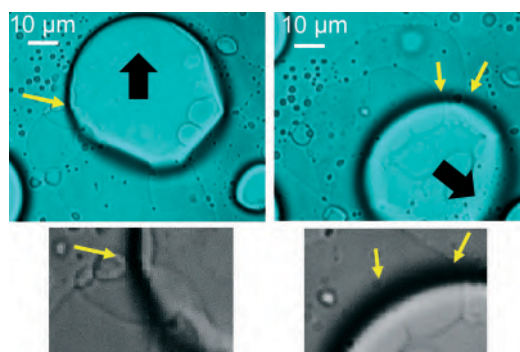


Fig. 9 Film formation from the vesicles contained in a moving VA. Weak incident light was introduced to the fluorescence microscope. The black arrow indicates the moving direction of the VA. The yellow arrow indicates the junction of the boundaries of the inner vesicle and the film. The images shown in the lower panels are enhanced so that the junction points can be seen.

plain why the motion of the VA stops after several collisions with simpler vesicles.

The chemical conditions required for the prey–predator behavior were examined by changing the cation species, concentrations, and pH. At least four aggregates were selected to observe the response to the addition of KI. Here, the aggregate refers to an object with homogeneous fluorescence. The concentrations of DDAB, oleate, and Ca^{2+} were double their standard concentrations because a larger number of aggregates were required for these experiments. However, the KI concentration was fixed at 40 mM. These results are summarized in the table in the ESI.† A pH above 8.0 was required to induce the prey–predator behavior. This suggests that the dissociation of oleic acid to form oleate is necessary. When the Ca^{2+} concentration was above 40 mM, the aggregate translation was less common. The oleate anion and Ca^{2+} formed a water-insoluble compound. The higher Ca^{2+} concentration typically formed precipitates to eliminate oleate molecules from the VAs. When the Ca^{2+} concentration was less than 10 mM, the prey–predator behavior was less common because most of the aggregates were OV-type. When the Ca^{2+} concentration was approximately 20 mM, the Ca^{2+} and oleate compounds did not precipitate in the presence of DDAB. Moreover, most of the aggregates were VA-type. This indicates that the compound was dissolved in the VA membranes. DDAB molecules prevented precipitation of the calcium salt of oleate, and the complicated inner structure formed. The 20 mM Ca^{2+} concentration corresponded to 10 mM under the standard experimental conditions.

Additional experiments were performed using Mg^{2+} , Sr^{2+} , and Co^{2+} instead of Ca^{2+} . The motion observed for Mg^{2+} was almost identical to that of Ca^{2+} . In contrast, aggregates containing Sr^{2+} and Co^{2+} did not show the prey–predator behavior but showed a similar response to the Ca^{2+} -free experiments of the original system. This suggests that the solubility of $\text{M}(\text{RCOO})_2$ in the DDAB membrane was strongly affected by the cation type (M^{2+}).

The mixing ratio of DDAB and oleate changed in the presence of 10 mM Ca^{2+} . Most of the aggregates were similar to the OV type when less oleate was used (oleate: 1.5 mM, DDAB: 4.1 mM, Fig. S2a†). This indicates that OV-type aggregates formed in the absence of oleate or Ca^{2+} . Thus, the complicated inner structure of the VA was formed by the interaction of Ca^{2+} and oleate in the presence of DDAB. After KI diffusion, the chemical reaction proceeded and the OVs were transformed into simple vesicles (Fig. S2b†). The inner vesicles collapsed due to the reaction and appeared to be adsorbed on the outer membrane. There were fewer aggregates when less DDAB was used (oleate: 3.3 mM, DDAB: 2.3 mM). An irregular change in the aggregates was observed due to KI diffusion, but a meaningful observation was difficult. However, this result suggests that the major constituents of VA and OV are DDAB molecules, and the main chemical reaction for the VA motion is that of DDAB and KI.

A vesicle composed of DDAB migrates three dimensionally in water when KI is added.¹⁶ The vesicle moved in a KI-

containing solution three dimensionally as its size decreased monotonically. DDAB and KI formed a precipitate by ion exchange between Br^- and I^- . The precipitate formation proceeded at the outer surface of a vesicle. The precipitates gathered at a single point on the vesicle surface. This point was chosen occasionally. Once the precipitation point had been selected, all precipitates gathered at the point. This point was positioned at the tail of the moving vesicle. The gathering of the precipitates caused surface flow of the precipitates toward the tail of a vesicle. This surface flow induced solvent flow around the vesicle, and the vesicle propelled itself by momentum conservation. In the present system, the reaction of DDA^+ and I^- is considered to form a film on the glass surface in the presence of oleate and Ca^{2+} . The film formation may play a similar role to precipitate formation in the previous system.¹⁶

In this discussion, the decrease in the solubility of DDA^+ plays an essential role in the crawling motion. In general, the solubility of DDA^+ in water decreases with increasing ionic strength. This suggests that the same crawling motion may occur under concentrated KBr, which was actually observed (ESI† Movie S5). When concentrated KBr (1 M) is injected, the VAs exhibit crawling motion. However, this was not observed when the concentration was 40 mM, which was used for the KI diffusion experiment. Iodide ions decrease the solubility of DDA^+ more effectively than Br^- .

Elucidation of the mechanism of crawling motion would be difficult without understanding the detailed chemistry of the VA and the film. In the ESI† however, we attempted to propose a possible mechanism for vesicle crawling based on the assumption that VA is composed of numerous dehydrated vesicles.

Summary and perspective

A vesicular aggregate (VA) composed of didodecyltrimethylammonium bromide (DDAB) and oleate exhibited translational motion by a chemical reaction with KI. The reaction generated the driving force for motion and decreased the size of the VA. However, the VA recovered its size by absorbing the surrounding small and simpler vesicles that had not reacted. The VA showed sustainable motion as a result of this ‘eating’ behavior. The VA had a complicated inner structure containing lipid molecules. The chemical reaction between I^- and DDA^+ inside the VA formed a film that spread over the glass surface. This film formation drove the VA. The VA then absorbed smaller vesicles to obtain its motility. Water that had been contained in the smaller vesicle was excluded by this absorption process. As a result, the dehydrated smaller vesicle became a constituent of the moving VA. This is probably the first example of an abiotic molecular assembly crawling over a solid substrate *via* ‘eating’ and waste discharge.

In the future, movement of vesicle-type aggregates can be exploited by means of a kind of chemical control. If the aggregate is placed on the solid surface where the smaller ones are placed in line, the aggregate moves along the line, leaving the film behind it. The onset of this motion is controlled by

a chemical trigger (*e.g.* KI). This may be used for self-patterning; the film may form the pattern. As another possibility, the vesicle-type aggregate may be used as a scavenger that removes lipid aggregates on the solid surface. A similar system has already been reported with a liquid droplet.²⁰ If a similar system can be realized with biocompatible chemicals, it may be applied to clean the wall of blood vessels. The present study may become a basis for further intriguing ideas.

Acknowledgements

The authors thank Mr. Shohei Siraishi for help in the experiments with the calcium-free system in the early stage of this study. A.S. gratefully acknowledges the financial support from JSPS KAKENHI (Grant Numbers 16H04189 and 25630351) and the MEXT-Supported Program for the Strategic Research Foundation at Private Universities.

Notes and references

- 1 R. Phillips, J. Kondev and J. Theriot, *Physical Biology of the Cell*, Garland Science, Taylor & Francis Group, LLC, 2009.
- 2 F. C. MacKintosh and M. E. Cates, *Soft Matter*, 2011, 7, 3050.
- 3 Y. Sumino, N. Magome, T. Hamada and K. Yoshikawa, *Phys. Rev. Lett.*, 2006, 94, 068301.
- 4 D. Yamamoto, T. Takada, M. Tachibana, Y. Iijima, A. Shioi and K. Yoshikawa, *Nanoscale*, 2015, 7, 13186.
- 5 I. Lagzi, S. Soh, P. J. Wesson, K. P. Browne and B. A. Grzybowski, *J. Am. Chem. Soc.*, 2010, 132, 1198.
- 6 Y. Hong, N. M. K. Blackman, N. D. Kopp, A. Sen and D. Velegol, *Phys. Rev. Lett.*, 2007, 99, 178103.
- 7 W. F. Paxton, K. C. Kistler, C. C. Olmeda, A. Sen, S. K. St. Angelo, Y. Cao, T. E. Mallouk, P. E. Lammert and V. H. Crespi, *J. Am. Chem. Soc.*, 2004, 126, 13424.
- 8 A. Shioi, K. Katano and Y. Onodera, *J. Colloid Interface Sci.*, 2003, 266, 415.
- 9 T. Banno and T. Toyota, *Langmuir*, 2015, 31, 6943; M. M. Hanczyc, T. Toyota, T. Ikegami, N. Packard and T. Sugawara, *J. Am. Chem. Soc.*, 2007, 129, 9386; P. L. Luisi, M. Allegretti, T. P. de Souza, F. Steiniger, A. Fahr and P. Stano, *ChemBioChem*, 2010, 11, 1989.
- 10 P. A. Giardini, D. A. Fletcher and J. A. Theriot, *Proc. Natl. Acad. Sci. U. S. A.*, 2003, 100, 6493.
- 11 F. Gerbal, P. Chaikin, Y. Rabin and J. Prost, *Biophys. J.*, 2000, 79, 2259.
- 12 E. Nawa, D. Yamamoto and A. Shioi, *Soft Matter*, 2013, 9, 7832; E. Nawa, D. Yamamoto and A. Shioi, *Bull. Chem. Soc. Jpn.*, 2015, 88, 1536; E. Nawa, D. Sakashita, K. Owaki, D. Yamamoto and A. Shioi, *Colloids Interface Sci. Commun.*, 2015, 8, 10.
- 13 F. Brochard-Wyart, P. G. de Gennes and O. Sandre, *Phys. A*, 2000, 278, 32; F. Nomura, M. Nagata, T. Inaba, H. Hiramatsu, H. Hotani and K. Takiguchi, *Proc. Natl. Acad. Sci. U. S. A.*, 2001, 98, 2340; T. Hamada, Y. Hirabayashi, T. Ohta and M. Takagi, *Phys. Rev. E: Stat., Nonlinear, Soft Matter Phys.*, 2009, 80, 051921.
- 14 I. Chen and P. Walde, *Cold Spring Harbor Perspect. Biol.*, 2010, 2, a002170; K. Kurihara, M. Tamura, K. Shohda, T.

- Toyota, K. Suzuki and T. Sugawara, *Nat. Chem.*, 2011, 3, 775;
- P. Carrara, P. Stano and P. L. Luisi, *ChemBioChem*, 2012, 13, 1497;
- K. Kurihara, Y. Okura, M. Matsuo, T. Toyota, K. Suzuki and T. Sugawara, *Nat. Commun.*, 2015, 6, 8352.
- 15 P. L. Luisi, *The Emergence of Life – From Chemical Origins to Synthetic Biology*, Cambridge University Press, 2006.
- 16 T. Miura, H. Oosawa, M. Sakai, Y. Syundou, T. Ban and A. Shioi, *Langmuir*, 2010, 26, 1610.
- 17 S. Manley and V. D. Gordon, *Current Protocols in Cell Biology*, 2008, vol. 40, p. 24.3.
- 18 F. M. Menger and K. D. Gabrielson, *Angew. Chem., Int. Ed. Engl.*, 1995, 34, 2091.
- 19 E. W. Kaler, A. K. Murthy, B. E. Rodriguez and J. A. Zasadzinski, *Science*, 1989, 245, 1371.
- 20 Y. Goto, M. Kanda, D. Yamamoto and A. Shioi, *Sci. Rep.*, 2015, 5, 14348.

ARTICLE

Received 9 Feb 2015 | Accepted 15 Apr 2015 | Published 22 May 2015

DOI: 10.1038/ncomms8189

OPEN

The evolution of spatial ordering of oil drops fast spreading on a water surface

Daigo Yamamoto¹, Chika Nakajima¹, Akihisa Shioi¹, Marie Pierre Krafft² & Kenichi Yoshikawa³

The design of dynamically self-assembled systems is of high interest in science and technology. Here, we report a unique cascade in the self-ordering of droplets accompanied by a dewetting transition. The dynamic self-emergent droplets are observed when a thin liquid layer of an immiscible fluorocarbon oil (perfluorooctyl bromide, PFOB) is placed on a water surface. Due to the gradual evaporation of PFOB, a circular PFOB-free domain appears as a result of a local dewetting transition. A circular pearling structure is generated at the rim with the growth of the dewetting hole. As the next stage, linear arrays of droplets are generated in a radial manner from the centre of the hole. These one-dimensional arrangements then evolve into two-dimensional hexagonal arrays of microdroplets through collective rhythmical shrinking/expanding motions. The emergence of such dynamic patterns is discussed in terms of the nonlinear kinetics of the dewetting transition under thermodynamically dissipative conditions.

¹Department of Chemical Engineering and Materials Science, Doshisha University, Kyoto 610-0321, Japan. ²Fluorinated Soft Matter Group, Institut Charles Sadron (CNRS), University of Strasbourg, 23 rue du Loess, Strasbourg 67034, France. ³Laboratory of Life Physics, Faculty of Life and Medical Sciences, Doshisha University, Kyoto 610-0394, Japan. Correspondence and requests for materials should be addressed to D.Y. (email: dyamamot@mail.doshisha.ac.jp.) or to M.P.K. (email: krafft@unistra.fr.).

The dynamic self-assembly of locally interacting individual entities to form patterns with higher-level structures and complexity plays a fundamental role in nature, science and technology^{1–3}. In both living and non-living systems, spatiotemporal patterns are frequently mediated through various types of interfaces under thermodynamically open conditions. Collective motion, which is ubiquitous in ensembles of both primitive organisms and evolved animals, offers fascinating examples of spatiotemporal patterns, such as those formed by, for example, colonies of bacteria⁴, schools of fish⁵, flocks of birds⁶, ungulate herds and even human crowds⁷, in which individuals can behave in synchrony. Simple abiotic synthetic systems that are capable of autonomous coherent motion are useful for unveiling the underlying mechanisms of biological collective motion. Since the earliest reports of the ‘camphor dance’^{8,9}, the autonomous motion of solid or solid-like particles has attracted interest in associated phenomena, including micromotors such as catalytic particles^{10,11}, AgCl particles¹², self-oscillating responsive polymer gels¹³, nematic liquid crystal phases¹⁴ and magnetic disks¹⁵. With regard to liquid systems, droplets of partially water-soluble alcohols¹⁶, aniline¹⁷ and dichloromethane¹⁸, when dissolved at the surface of water, have been shown to display complex shapes and self-motility. None of these systems, however, exhibit coordinated droplet dynamics, which could lead to synchronous collective movement of the ensemble. Fluorocarbons offer a combination of unique properties, including quasi-insolubility in water, rapid spreading on water surfaces, low surface tension and high volatility with respect to molecular weight, which makes them effective building blocks for the design of self-assembling systems.

We describe here a series of hitherto unreported phenomena that occur over time during the dewetting of thin films of a liquid fluorocarbon (perfluorooctyl bromide (PFOB), C₈F₁₇Br) spread on water. These phenomena include the spontaneous formation of similarly sized and regularly spaced humps at the fluorocarbon’s dewetting front, the chain ejection of linear arrangements of microdroplets from these humps and the transition from these one-dimensional (1D) arrangements to two-dimensional (2D) hexagonal arrays through a shrinking/expanding rhythmical behaviour. These events are made possible by the distinctive properties of the selected fluorocarbon, which is essentially insoluble in water, yet highly volatile and fast spreading. The observed unique time-dependant dynamic coherent translational motion that leads to regular ordering of the droplets is interpreted solely on the basis of a dissipative effect due to evaporation of the fluorocarbon.

Results

A series of dynamical events of a fluorocarbon droplet. When a droplet of the selected liquid but volatile fluorocarbon, PFOB, is

deposited on the surface of deionized water, it spreads immediately over the entire surface due to its positive spreading coefficient (+2.7 mN m⁻¹)¹⁹. Surprisingly, the thin layer (film) of PFOB then spontaneously undergoes a series of dynamical events that occur in a cascade that culminates with the collective translation of ensembles of microdroplets (Figs 1 and 2; Supplementary Movie 1). Chronologically, these events involve (I) the formation of circular PFOB-free domains (water holes) in the PFOB film caused by its dewetting; (II) the progressive upheaval of the rim of these holes (which is the three-phase circular contact line) to form regularly distributed humps of PFOB; (III) the rhythmical cascade ejection of microdroplets from these humps, creating radial 1D alignments; (IV) the collective translational motion of the microdroplet ensemble resulting in the formation of regular 2D hexagonal patterns.

To the best of our knowledge, this is the first report of spontaneous transformation from a 1D array to a 2D array of microdroplets through coherent motion. This dynamic behaviour strongly differs from previously reported static orderings, such as the formation of hexagonal patterns of crystallized polymer aggregates, generated by a stick–slip sequence of the contact line during dewetting of the polymer solution on a solid substrate²⁰, or the hexagonal lattices of monodisperse crystalline nanodomains formed by (perfluoroalkyl)alkanes on water and solid substrates^{21–23}.

Formation of liquid fluorocarbon humps around water holes.

At the very initial stage of the experiment, the existence of a thin film of PFOB covering the entire surface of water demonstrates that the spreading coefficient of PFOB is indeed positive (Fig. 2b). During the thinning process caused by the evaporation of PFOB, the film of PFOB becomes unstable when it becomes thinner than a critical thickness, which induces a dewetting transition. A circular water hole is then spontaneously generated within the film (Figs 1 and 2c). Note that the surface of the hole is not pure water, but rather is covered by PFOB molecules (nanolayer) as described later. The formation of holes in a thin oil film, as well as fragmentation, fingering, pulsation and/or autonomous motions, is well known when organic solvents such as 1-butanol and 3-octanol¹⁶, aniline¹⁷ or dichloromethane¹⁸ are spread on water. These phenomena are interpreted in terms of dewetting instability²⁴. The behaviour of our system is original. As the hole grows, the rim of the PFOB film starts upheaving, resulting in the formation of PFOB humps that are regularly distributed along the periphery of the hole. To the best of our knowledge, the generation of regularly spaced humps in receding organic solvent fronts has not been observed previously. Actually, we verified that a film of a volatile hydrocarbon solvent, cyclohexane, exhibits a monotonous evaporation process, with the formation of water holes that grow without the formation of ordered humps until the

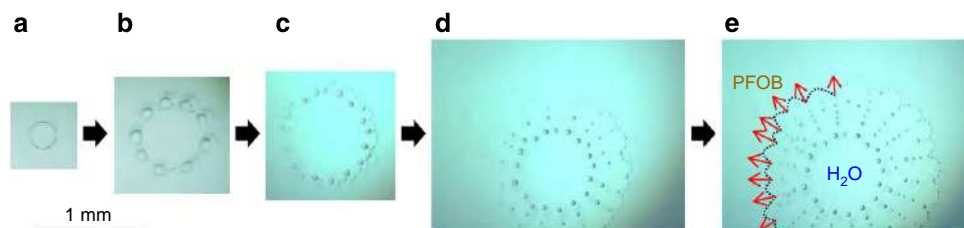


Figure 1 | Generation of droplets pearling accompanied by a dewetting transition. (a) A thin film of PFOB floating on a water surface yields water holes decorated with pearling humps caused by the dewetting transition of the film, accompanied by the slow evaporation of PFOB. (b) A critical point is reached when, during the growth of the hole, the PFOB rim acquires a smaller curvature than that of the humps. (c) This triggers a rhythmical chain ejection of microdroplets from the humps. (d,e) After the first ejection, humps that are smaller than the initial humps are created and ejected repetitively. The black dotted line and red arrows represent the contact line between PFOB and water, and the direction in which the contact line recedes, which also indicates the direction of the growing hole of water. Note that the images (a,b) and (c–e) were obtained from different holes, due to technical reasons.

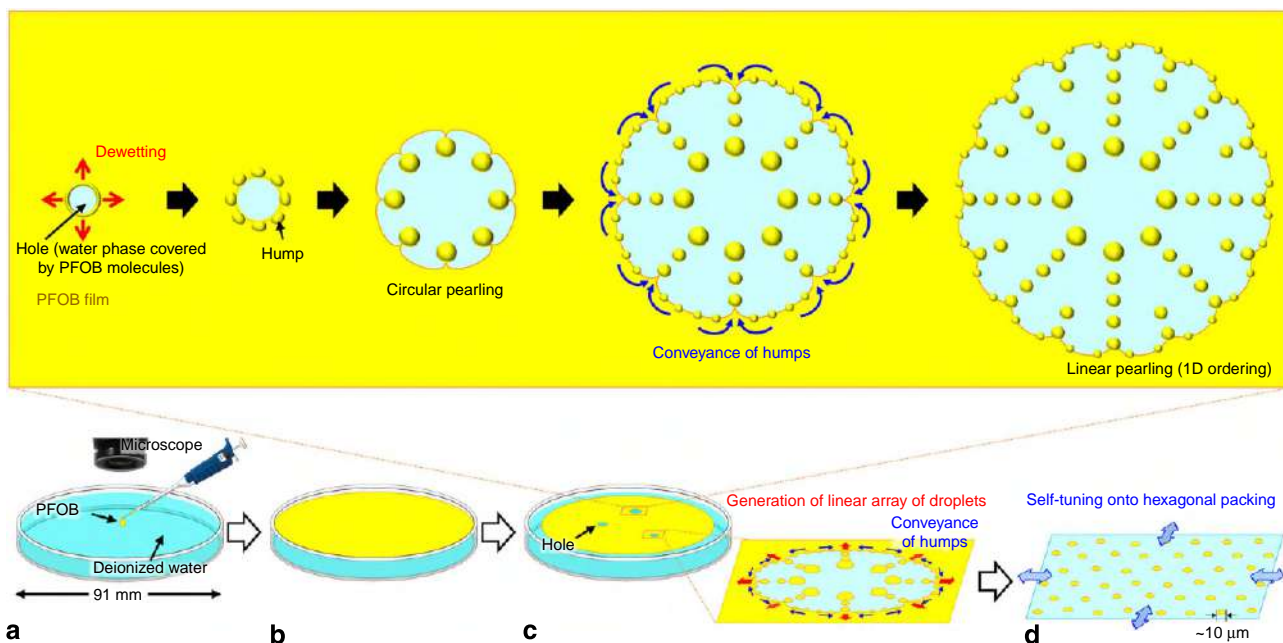


Figure 2 | Spontaneous dynamic behaviour of PFOB spread on water. (a) PFOB is pipetted onto a water surface. (b) Immediately after contact with water, it spreads to form a thin film. On the basis of the injection volume ($8\ \mu\text{l}$) and the surface area of water ($\sim 65\ \text{cm}^2$), the thickness of the film can be estimated to be $1\ \mu\text{m}$. (c,d) As the PFOB gradually evaporates, the system exhibits characteristic pearling phenomena consisting of four successive non-equilibrium events; event I: a water hole is generated through the evaporation of PFOB molecules and the dewetting transition; event II: fluorocarbon humps are formed on the rim of the water holes, which causes circular pearling of the droplet array; event III: appearance of a linear pearling (1D array), where droplets are generated periodically; event IV: (d) a regular hexagonal 2D structure is formed over the entire water surface by rhythmical shrinking and expanding motion, and remains for a relatively long time as a stable pattern. Finally, the arranged droplets disappear within 20 s due to evaporation.

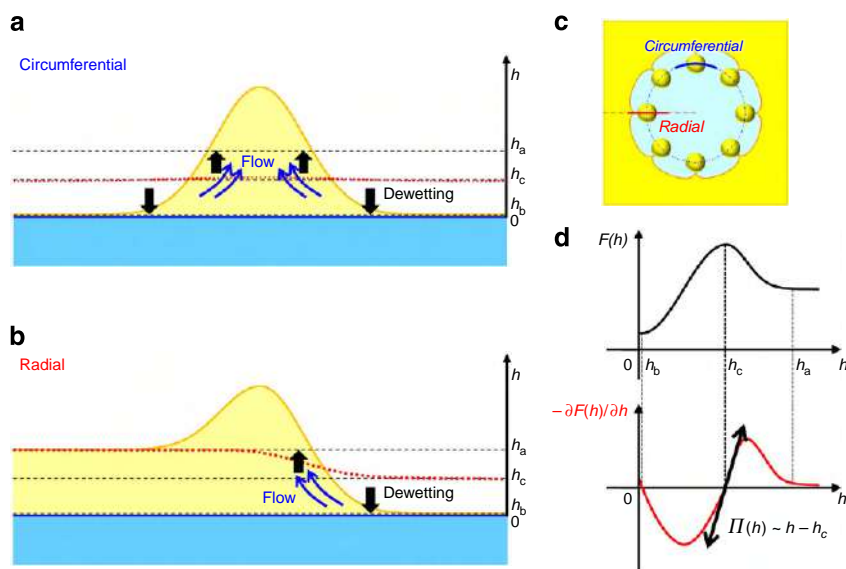


Figure 3 | Scheme of the dewetting transition leading to pearling instability. The dewetting transition first causes circular pearling and then linear pearling. (a,b) Schematic representations of the side view along the circular and radial lines in a hole, which correspond to the blue and red lines in the top view (c), respectively. $F(h)$ is the free energy of a PFOB film per unit surface area as a function of film thickness h , and the film thickness exhibits bistability with a maximum at $h = h_c$ (d)²⁴. If we begin the experiment with the entire surface covered by a sufficiently thick PFOB film, $h > h_a$, thinning of the film due to gradual evaporation causes instability and, accompanied by the dewetting transition, a hole appears and grows. Depending on the time development of the hole, the dewetting transition generates circular and linear pearling, as depicted in the figure. A more detailed explanation of the pearling instability in these experiments is given in Supplementary Note 1.

film disappears (Supplementary Movie 2). The formation of these humps at the rim is attributable to the bistability of the PFOB film height h on the water surface. It can be described as a pearling instability (Fig. 3). The occurrence of the dewetting transition implies that the local free energy $F(h)$ of the film exhibits a

maximum at the film's critical height h_c . By considering the intrinsic property of the dewetting transition, one can expect that the disjoining pressure $\Pi(h) = -\frac{\partial F}{\partial h}$ is positive or negative when h is above or below h_c , respectively. Thus, we can expect that the kinetics of the change in height can be given in a first-order

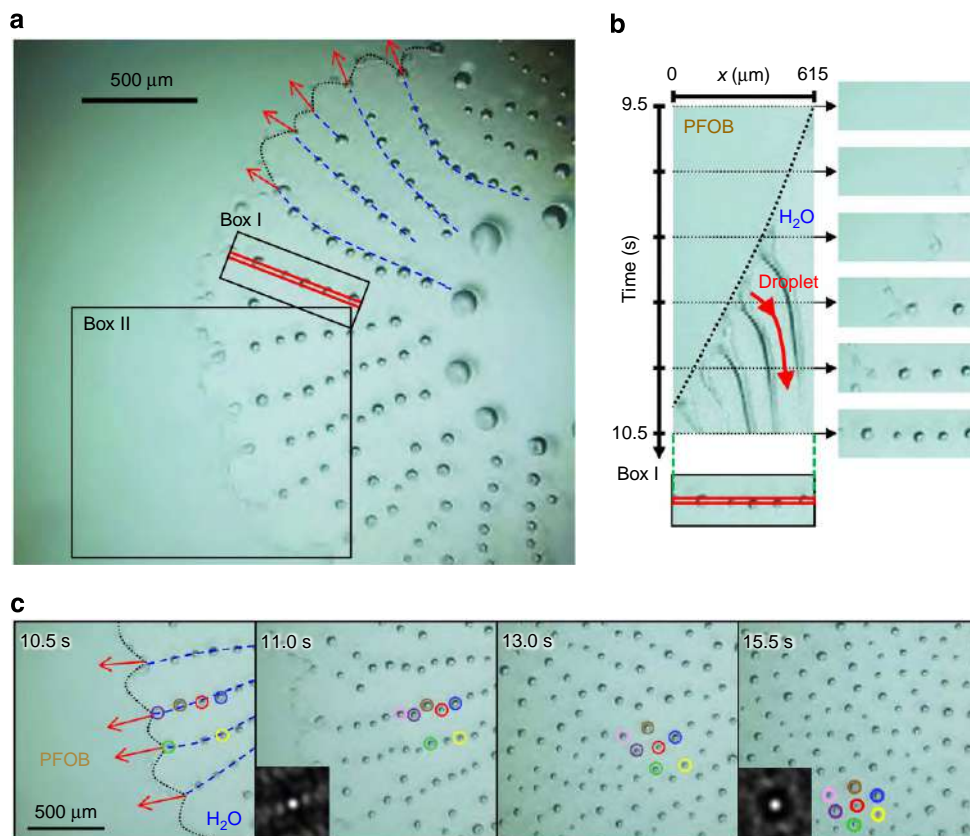


Figure 4 | Transformation from 1D linear pearling to 2D hexagonal regularity. (a) Linear alignments of numerous regularly spaced droplets are produced by repetitive ejection. The contact line between PFOB and water (black dotted line) is a cycloid-like curve. Blue dashed lines represent typical trajectories of the projection points of the contact line. Red arrows show the direction in which the PFOB/water surface recedes. This demonstrates that microdroplets are ejected from projection points of the contact line to form 1D arrays. (b) Spatiotemporal diagram of 1D linear pearling is prepared along a red diagonal line in box I. (c) Spontaneous transformation from 1D linear pearling to a 2D hexagonal regular lattice in box II. To clarify the nature of the changes over time, the droplets are assigned different colours, indicating rearrangement from 1D to 2D hexagonal. Insets in snapshots at 11.0 and 15.5 s show the 2D Fourier transforms of the pattern. Times displayed on the figures represent the elapsed times after the injection of a PFOB droplet.

approximation as $\frac{\partial h}{\partial t} \sim -\frac{\partial F}{\partial h} \sim (h - h_c)$. Here, the term $-\frac{\partial F}{\partial h}$ corresponds to the disjoining pressure $\Pi(h)$. Thus, near the critical height, the disjoining pressure exhibits symmetry with respect to h as follows: $\Pi(h) \sim (h - h_c)$. Along the dewetting line, the thin film exhibits a severe instability attributable to the bimodality of the free energy depending on the depth of the film, that is, positive/negative disjoining pressure. Therefore, the disjoining pressure symmetry leads to the formation of humps (for a detailed theoretical interpretation, see Supplementary Note 1).

1D alignments through periodical ejection of microdroplets.

The spatio-periodically arranged humps generated through pearling instability evolve to emit radial linear strings of microdroplets (Figs 1 and 2c). This behaviour is believed to occur as follows: as a consequence of hump formation, portions of the rim located in the vicinity of a hump acquire a highly negative curvature and tend to show an increase in height by attracting fluorocarbon oil molecules, thus further contributing to the instability of the film. This growing instability causes the repetitive, radial ejection of microdroplets from the humps, resulting in a time- and spatio-periodical 1D repeating pattern. Such 1D ejection of microdroplets to form a dendritic pattern is a unique phenomenon, and is different from all previous examples of the ejection of droplets, such as from drops of fatty alcohols deposited on water or of dichloromethane on solutions of

cetyltrimethylammonium bromide^{16,18}. In the latter case, the daughter droplets that are ejected radially from the mother drop disappear in less than 1 s due to rapid evaporation (vapour pressure: 47 kPa for CH_2Cl_2 versus 0.59 kPa for PFOB at 20 °C¹⁹) and the dissolution of CH_2Cl_2 in water. A seminal difference with our system is that the CH_2Cl_2 droplets radiate outwards from the periphery of the mother droplet onto a practically infinite water surface, while the fluorocarbon droplets propagate within a finite water hole that is confined by the fluorocarbon film. Therefore, our system uniquely provides self-confined conditions that allow the interactions between droplets to operate and generate close-packed patterns as described below.

As the microdroplets are continuously ejected in the cascade, the humps surging at the rim and the ejected droplets become slightly smaller than those observed during the initial ejection period (Fig. 4). Figure 4b shows a spatiotemporal diagram of the repetitive microdroplet ejection pattern that propagates on a water hole. The time interval between two subsequent ejections is about 0.2 s, and the ejected droplets are aligned at almost identical spatial intervals. During repetitive ejection, the droplets move away from the contact line: the speed of their vectorial motion is maximal ($\sim 0.5 \text{ mm s}^{-1}$) just after ejection and decreases afterwards. This means that a repulsive force is at work between the droplets and the rim of the PFOB film. This repulsive force cannot arise from Marangoni flow^{25,26}, because of the extremely low solubility of PFOB in water ($\sim 5 \times 10^{-9} \text{ mol l}^{-1}$)¹⁹. Actually, the surface tension of water saturated with PFOB

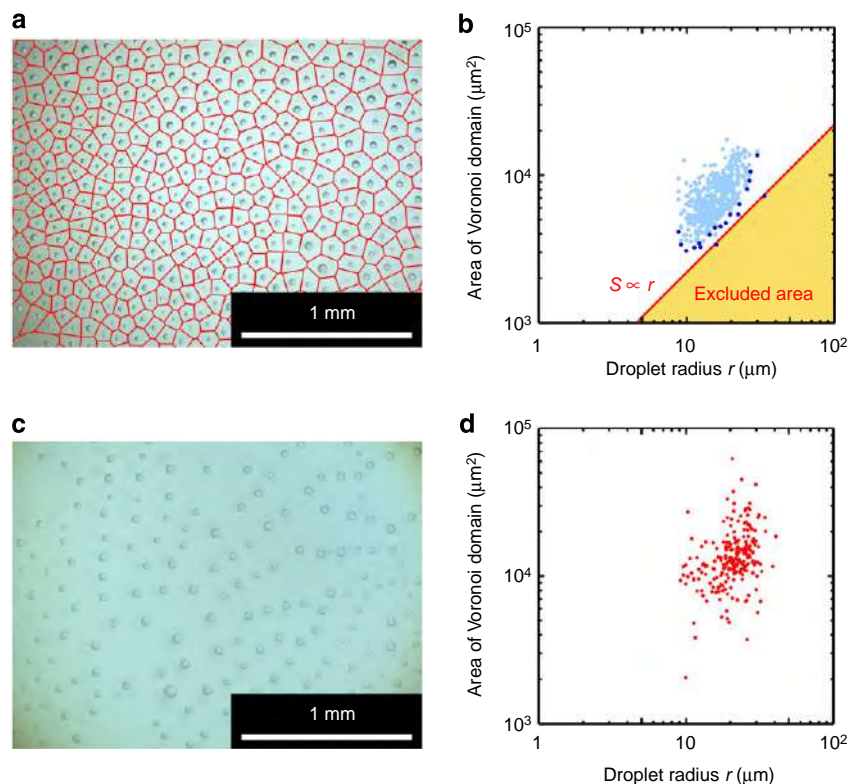


Figure 5 | Rates of surface-spreading and evaporation of the fluorocarbon. (a) A Voronoi diagram of an example of a shrinking hexagonal pattern; seed points are set to be the centre of gravity of each droplet. (b) The relationship between droplet radius r and surface area of Voronoi domains S_{Vor} , as obtained from a. Dark-blue circles show data points that have the minimum S_{Vor} in the particular range of droplet radius (interval of log-scaled radius: $\Delta(\log_{10} r) = 1/30$). (c,d) Results of a control experiment where evaporation rate is reduced by covering a Petri dish with a glass plate.

(measured after the deposition of a PFOB droplet at the bottom of a water-filled cell) is essentially identical ($\sim 72 \text{ mN m}^{-1}$) to the surface tension of pure water at 25°C . Thus, we consider that the repulsive force is attributable to the outward 2D flow caused by dewetting transition together with gradual evaporation. The detailed mechanism is described in the next section.

Collective motion of microdroplets generating 2D ordering.

Our fluorocarbon oil/water system offers the remarkable capacity to spontaneously confine a population of droplets with a long lifetime in a closed space. As shown in Fig. 4c, the microdroplets that are initially aligned in a 1D pattern (10.5–13.0 s) rearrange to form a regular 2D hexagonal pattern (13.0–15.5 s). Insets in snapshots at 11.0 and 15.5 s show images of the 2D Fourier transforms of the pattern, demonstrating that the linear and hexagonal pattern is not local. The extent of the hexagonal ordering may appear modest on the figures because they are snapshots on a dynamic behaviour. Supplementary Movie 1 shows clearly that the droplets self-organize into a hexagonal ordering under large dynamical fluctuations, revealing that the self-organization is accompanied by rhythmical shrinking and expanding translational movements reminiscent of those of flocks of birds (Supplementary Fig. 1). Remarkably, contact between droplets and subsequent coalescence have never been observed to occur during their lifetime. This suggests that each droplet has an excluded area around itself that induces mutual repulsion. The existence of this excluded area is more easily appreciated at a lower temperature (10°C). Each droplet shows rapid translational movement ($\sim 8 \text{ mm s}^{-1}$, corresponding to ~ 200 body lengths per sec) (Supplementary Movie 3). When two droplets get close to each other ($\sim 100 \mu\text{m}$ distance, only 3 body lengths), they start

repelling each other. As a result, the direction of translational motion undergoes a rapid change, despite the droplet's high speed, to avoid collision.

The mechanism that underlies the generation of the regular 2D hexagonal pattern is understood to be as follows: instead of being dissolved in water, the PFOB molecules contained in a droplet actually spread to form a fluid nanolayer floating on the water surface around the droplet. Simultaneously, this nanolayer evaporates slowly into air. As a result, the nanolayer spreads over a certain area that has a characteristic length scale. This scale is determined by the balance between the supply of PFOB molecules coming from the droplet and their evaporation from the nanolayer. Such evaporation maintains a flow in the nanolayer that is directed outwards. This type of repulsion, due to the intrinsic nature of dewetting transition, is also at work between droplets and the rim of the film, which drives the periodical ejection. Collision between the flows of the nanolayers issued from two neighbouring droplets will transform the kinetic energy per unit volume into pressure. This pressure would cause the observed repulsive force arising between droplets. Actually, when we covered the Petri dish with a glass plate just after having spread PFOB to reduce evaporation rate, the ordering of droplets became more irregular than that without the plate (Fig. 5a,c). This demonstrates that the driving forces for the formation of the dynamic pattern are not of thermodynamic origin (such as depletion force, for example), as they cannot operate in the absence of evaporation-generated motion, but are rather driven by nonlinear kinetics of the dewetting transition and evaporation under thermodynamically dissipative conditions. The rates of surface-spreading and evaporation of the fluorocarbon around a certain droplet can be evaluated as follows: the flow rate supplied by a droplet onto the surface is proportional to the length of a

contact line between the PFOB layer and the water surface ($\propto 2\pi r$, where r is the radius of the droplet), while the rate of evaporation is proportional to the surface area of the nanolayer ($\propto S$, where S is the area of the nanolayer). Considering a quasi-steady state where both rates are balanced, the area of the nanolayer is proportional to the radius of the droplet ($S \propto r$). It is technically difficult to precisely evaluate the excluded area generated by a droplet. Nevertheless, we estimated this area based on a Voronoi diagram (Fig. 5a). The relationship between the radii of the droplets and the area of their individual Voronoi domains is shown in Fig. 5b. The red line in Fig. 5b demonstrates that the minimum size (marked by dark-blue circles) of the Voronoi domain linearly correlates with the droplet radius. This threshold value is thought to correspond to the excluded area of the nanolayer, while the threshold value when we covered the Petri dish is equivocal (Fig. 5d). This correlation supports the validity of our proposed mechanism based on evaporation-induced flow within the nanolayer ($S \propto r$).

Discussion

We describe a new synthetic system for the spontaneous creation and dynamic self-assembly of fluorocarbon droplets on water. This ensemble of droplets undergoes a transformation in a confined space between 1D arrays of microdroplets and 2D hexagonal arrays through periodical collective motion. This results in the formation of a hexagonal pattern that shows a unique collective cyclic shrinking and expanding behaviour, reminiscent of a flock of birds. These dynamics can be attributed to repulsive force between the droplets. An evaporation-induced surface flow, which is a quasi-2D flow of a PFOB nanolayer on the surface of water, may account for this phenomenon. This simple synthetic system that exhibits spatiotemporal behaviour appears to mimic collective behaviours found in nature and may serve as a model for the study of dynamically assembled systems. Furthermore, liquid fluorocarbons are generally immiscible with most organic solvents. Their characteristics are expected to provide new strategies for the design of systems of hybrid particles composed of mutually immiscible liquids that are expected to show novel non-equilibrium behaviour.

Methods

Chemicals. PFOB, $C_8F_{17}Br$, was obtained from Alliance Pharmaceutical Corp. (San Diego, CA) and thoroughly purified by repeated distillations and alumina column treatment.

Observation of the dynamic behaviour of a PFOB droplet. A droplet of PFOB (8 μ l) was deposited on the surface of deionized water (30 ml) in a Petri dish with a diameter of 91 mm (Fig. 2a). PFOB floats on water, even though PFOB is more dense (1.9 $g\ ml^{-1}$) than water, because the high interfacial tension overcomes the growth of Rayleigh–Taylor instability. The behaviour of droplets was monitored at room temperature (20–25 °C) using an optical microscope (VX-6,000/5,000, Keyence Corp.) equipped with a universal zoom lens (VH-Z20UW, Keyence Corp.).

References

- Fialkowski, M. *et al.* Principles and implementations of dissipative (dynamic) self-assembly. *J. Phys. Chem. B* **110**, 2482–2496 (2006).
- Lehn, J.-M. Toward self-organization and complex matter. *Science* **295**, 2400–2403 (2002).
- Whitesides, G. M. & Grzybowski, B. Self-assembly at all scales. *Science* **295**, 2418–2421 (2002).
- Zhang, H. P., Be'er, A., Florin, E. L. & Swinney, H. L. Collective motion and density fluctuations in bacterial colonies. *Proc. Natl Acad. Sci. USA* **107**, 13626–13630 (2010).
- Parrish, J. K., Viscido, S. V. & Grünbaum, D. Self-organized fish schools: an examination of emergent properties. *Biol. Bull.* **202**, 296–305 (2002).
- Hemelrijk, C. K. & Hildenbrandt, H. Some causes of the variable shape of flocks of birds. *PLoS ONE* **6**, e22479 (2011).
- Couzin, I. D. & Krause, J. Self-organization and collective behavior in vertebrates. *Adv. Study Behav.* **32**, 1–75 (2003).
- Rayleigh, L. Measurements of the amount of oil necessary in order to check the motions of camphor upon water. *Proc. R. Soc. Lond.* **47**, 364–367 (1889).
- Pockels, A. Surface tension. *Nature* **43**, 437–439 (1891).
- Paxton, W. F. *et al.* Catalytic nanomotors: autonomous movement of striped nanorods. *J. Am. Chem. Soc.* **126**, 13424–13431 (2004).
- Yamamoto, D. & Shioi, A. Self-propelled nano/micromotors with a chemical reaction: underlying physics and strategies of motion control. *KONA Powder Part. J.* **32**, 2–22 (2015).
- Ibele, M., Mallouk, T. E. & Sen, A. Schooling behavior of light-powered autonomous micromotors in water. *Angew. Chem. Int. Ed.* **48**, 3308–3312 (2009).
- Yoshida, R. Self-oscillating gels driven by the Belousov-Zhabotinsky reaction as novel smart materials. *Adv. Mater.* **22**, 3463–3483 (2010).
- Narayan, V., Ramaswamy, S. & Menon, N. Long-lived giant number fluctuations in a swarming granular nematic. *Science* **317**, 105–108 (2007).
- Grzybowski, B. A., Stone, H. A. & Whitesides, G. M. Dynamic self-assembly of magnetized, millimetre-sized objects rotating at a liquid-air interface. *Nature* **405**, 1033–1036 (2000).
- Bates, C. M., Stevens, F., Langford, S. C. & Dickinson, J. T. Motion and dissolution of drops of sparingly soluble alcohols on water. *Langmuir* **24**, 7193–7199 (2008).
- Chen, Y. J., Nagamine, Y. & Yoshikawa, K. Self-propelled motion of a droplet induced by Marangoni-driven spreading. *Phys. Rev. E* **80**, 016303 (2009).
- Pimienta, V., Brost, M., Kovalchuk, N., Bresch, S. & Steinbock, O. Complex shapes and dynamics of dissolving drops of dichloromethane. *Angew. Chem. Int. Ed.* **50**, 10728–10731 (2011).
- Riess, J. G. Oxygen carriers ("blood substitutes") - raison d'être, chemistry, and some physiology. *Chem. Rev.* **101**, 2797–2919 (2001).
- Karthaas, O., Gräsjö, L., Maruyama, N. & Shimomura, M. Formation of ordered mesoscopic polymer arrays by dewetting. *Chaos* **9**, 308–314 (1999).
- Krafft, M. P. & Riess, J. G. Chemistry, physical chemistry, and uses of molecular fluorocarbon-hydrocarbon diblocks, triblocks, and related compounds-unique "apolar" components for self-assembled colloid and interface engineering. *Chem. Rev.* **109**, 1714–1792 (2009).
- Krafft, M. P. Large organized surface domains self-assembled from nonpolar amphiphiles. *Acc. Chem. Res.* **45**, 514–524 (2012).
- Krafft, M. P. & Riess, J. G. Perfluorocarbons: life sciences and biomedical uses. *J. Polym. Sci. A Polym. Chem.* **45**, 1185–1198 (2007).
- de Gennes, P. G. Wetting: statics and dynamics. *Rev. Mod. Phys.* **57**, 827–863 (1985).
- Ikura, Y. S., Tenno, R., Kitahata, H., Suematsu, N. J. & Nakata, S. Suppression and regeneration of camphor-driven Marangoni flow with the addition of sodium dodecyl sulfate. *J. Phys. Chem. B* **116**, 992–996 (2012).
- Antoine, C. & Pimienta, V. Mass-spring model of a self-pulsating drop. *Langmuir* **29**, 14935–14946 (2013).

Acknowledgements

We thank Dr Yong-Jun Chen (Shaoxing University) for useful suggestions concerning Supplementary Note 1. M.P.K. acknowledges the Japan Society for the Promotion of Science for a research grant. This study was partially supported by Grants-in-Aid, KAKENHI (23240044; 25103012; 25610111).

Author contributions

A.S., M.P.K. and K.Y. conceived this research. C.N. performed the main experiments. D.Y. analysed the data. D.Y. and M.P.K. wrote the paper. A.S. and K.Y. edited the paper. All authors discussed the results and commented on the manuscript.

Additional information

Supplementary Information accompanies this paper at <http://www.nature.com/naturecommunications>

Competing financial interests: The authors declare no competing financial interests.

Reprints and permission information is available online at <http://npg.nature.com/reprintsandpermissions/>

How to cite this article: Yamamoto, D. *et al.* The evolution of spatial ordering of oil drops fast spreading on a water surface. *Nat. Commun.* **6**:7189 doi: 10.1038/ncomms8189 (2015).



This work is licensed under a Creative Commons Attribution 4.0 International License. The images or other third party material in this article are included in the article's Creative Commons license, unless indicated otherwise in the credit line; if the material is not included under the Creative Commons license, users will need to obtain permission from the license holder to reproduce the material. To view a copy of this license, visit <http://creativecommons.org/licenses/by/4.0/>

Branched-Chain Polyamine Found in Hyperthermophiles Induces Unique Temperature-Dependent Structural Changes in Genome-Size DNA

Takashi Nishio,^[a] Yuko Yoshikawa,^[a] Wakao Fukuda,^[b] Naoki Umezawa,^[c] Tsunehiko Higuchi,^[c] Shinsuke Fujiwara,^[b] Tadayuki Imanaka,^[d] and Kenichi Yoshikawa*^[a]

A pentavalent branched-chain polyamine, N^4 -bis(aminopropyl)spermidine 3(3)(3)4, is a unique polycation found in the hyperthermophilic archaeon *Thermococcus kodakarensis*, which grows at temperatures between 60 and 100 °C. We studied the effects of this branched-chain polyamine on DNA structure at different temperatures up to 80 °C. Atomic force microscopic observation revealed that 3(3)(3)4 induces a mesh-like structure on a large DNA (166 kbp) at 24 °C. With an increase in

temperature, DNA molecules tend to unwind, and multiple nano-loops with a diameter of 10–50 nm are generated along the DNA strand at 80 °C. These results were compared to those obtained with linear-chain polyamines, homocaldopentamine 3334 and spermidine, the former of which is a structural isomer of 3(3)(3)4. These specific effects are expected to neatly concern with its role on high-temperature preference in hyperthermophiles.

1. Introduction

Polyamines are found in all living organisms, where they play important roles in many cellular processes including cell growth and proliferation.^[1–3] The most commonly occurring natural polyamines are putrescine [2+], spermidine [3+] and spermine [4+], all of which have a linear chain structure. Linear analogues of these polyamines, such as norspermidine [3+], norspermine [4+], thermospermine [4+] and homocaldopentamine [5+], which differ with regard to the length and arrangement of CH₂ spacers and valency, are also found in various organisms.^[4,5] It is known that polyamines induce DNA condensation/compaction because of their polycationic nature at physiological pH.^[6] A number of *in vitro* studies have investigated the physicochemical mechanism of polyamine-induced DNA condensation/compaction.^[7–25] These *in vitro* studies shed some light on the manner of packing of DNA in living systems.^[26,27]

Recently, it was reported that a hyperthermophilic archaeon microorganism, *Thermococcus kodakarensis*, synthesizes a unique branched-chain polyamine N^4 -bis(aminopropyl)spermidine 3(3)(3)4 that has not been found in other microorganisms.^[28,29] *T. kodakarensis* grows at temperatures between 60 and 100 °C, with an optimum growth temperature of 85 °C.^[30] Interestingly, synthesis of the branched-chain polyamine 3(3)(3)4 increases with an increase in the growth temperature.^[28] Therefore, this branched-chain polyamine may be a key molecule for survival in high-temperature environments.^[28]

We previously investigated the effects of branched- and linear-chain polyamines on the higher-order structure of genome-size DNA at room temperature by the use of fluorescence microscopy and atomic force microscopy (AFM).^[31] We found that branched-chain polyamines tend to induce a meshwork assembly of randomly oriented DNA fibers, whereas linear-chain polyamines cause a parallel alignment between DNA segments.^[31] Circular dichroism (CD) measurements revealed that branched-chain polyamines induce the A-like form in the secondary structure of DNA, while linear-chain polyamines have only a minimal effect.^[31]

Here we extended this work by focusing on the temperature-dependence of the interactions of polyamines with DNA. We evaluated the temperature-dependent effect of a pentavalent branched-chain polyamine, 3(3)(3)4, on DNA structure. The results were compared to those obtained with linear-chain polyamines, spermidine SPD and homocaldopentamine 3334 which is a structural isomer of 3(3)(3)4. Their chemical structures are shown in Scheme 1. We used a genome-size DNA, T4 GT7 DNA (166 kbp), to monitor the change in conformation by AFM observation. It has been shown that the size or length of DNA molecules is a critical determinant governing their overall morphological features.^[32–36] Teif reported that long enough DNA molecules can collapse into compact globules with various shapes such as a toroid or rod,

[a] T. Nishio, Dr. Y. Yoshikawa, Prof. K. Yoshikawa
Faculty of Life and Medical Sciences, Doshisha University, Kyotanabe 610-0394, (Japan)

E-mail: keyoshik@mail.doshisha.ac.jp

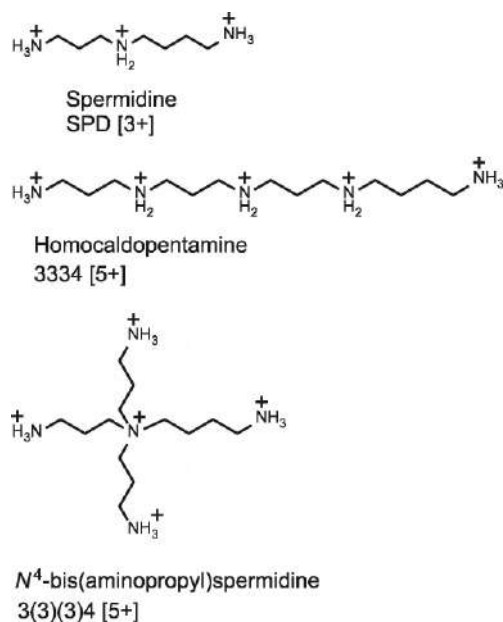
[b] Dr. W. Fukuda, Prof. S. Fujiwara
School of Science and Technology, Kwansai-gakuin University, Sanda 669-1337, (Japan)

[c] Dr. N. Umezawa, Prof. T. Higuchi
Graduate School of Pharmaceutical Sciences, Nagoya City University, Nagoya 467-8603, (Japan)

[d] Prof. T. Imanaka
Research Organization of Science and Technology, Ritsumeikan University, Kusatsu 525-8577, (Japan)

Supporting information for this article is available on the WWW under <https://doi.org/10.1002/cphc.201800396>

© 2018 The Authors. Published by Wiley-VCH Verlag GmbH & Co. KGaA. This is an open access article under the terms of the Creative Commons Attribution Non-Commercial License, which permits use, distribution and reproduction in any medium, provided the original work is properly cited and is not used for commercial purposes.



Scheme 1. Chemical formulas of linear- and branched-chain polyamines examined in the present study.

while DNA fragments shorter than the persistence length do not form such ordered structures.^[34]

2. Results and Discussion

2.1. AFM Observation of the Higher-Order Structure of DNA at Room Temperature

Figure 1 shows typical AFM images of T4 GT7 DNA in the presence of linear- or branched-chain polyamines on a mica surface at 24 °C. The mica surface was not pretreated with any polycations such as magnesium or SPD before the application of a droplet of sample. In this experiment, we adopted 200 μM SPD, 5 μM 3334 and 3 μM 3(3)(3)4 as the polyamine concentrations based on the results obtained through a single molecule observation by fluorescence microscopy (see Supporting Information). The average long-axis length of DNA was ca. 0.4 μm for all polyamines (Figure S1 in the Supporting Information). We have confirmed that the degree of shrinking on the higher-order structure of DNA molecules are essentially the same under the conditions of 200 μM SPD, 5 μM 3334 and 3 μM 3(3)(3)4. Figure 1a shows an elongated conformation of DNA in the presence of a low concentration of SPD (10 μM) as a control observation. In the presence of a linear-chain polyamine, SPD (200 μM) or 3334 (5 μM), DNA molecules with multiple loops tend to crossover at the same point and produce flower-like structures (Figures 1b–1e). Similar DNA conformations induced by SPD were reported by Fang and Hoh.^[37] On the other hand, in the presence of 3 μM 3(3)(3)4, a mesh-like structure with a number of crossings or bridges appears. In other words, DNA segments are aligned parallel to each other in the presence of a linear-chain polyamine but are randomly-

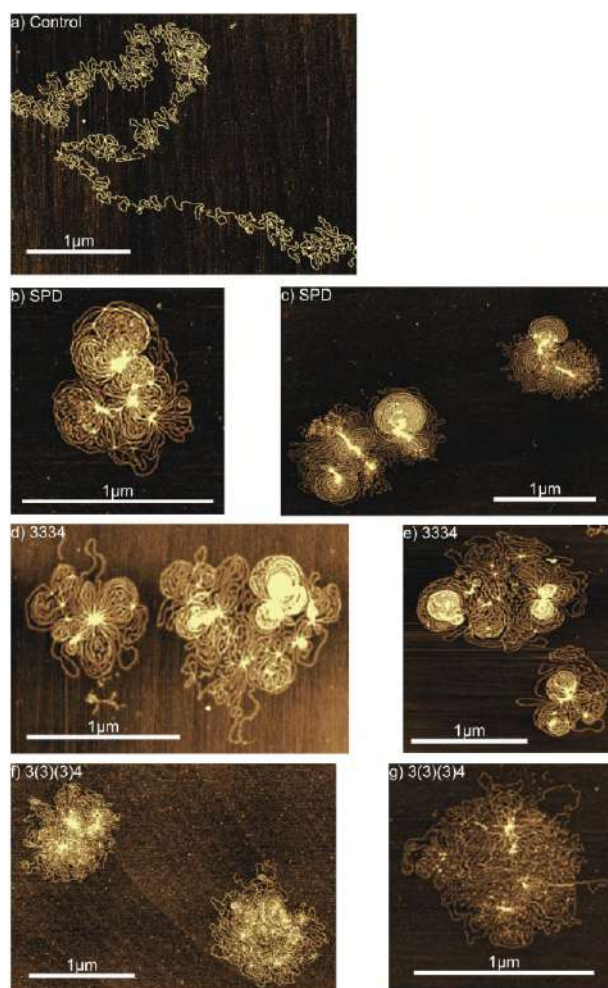


Figure 1. AFM images of T4 DNA in the presence of polyamines at 24 °C: (a) control image at a low concentration, 10 μM SPD; (b) and (c) 200 μM SPD; (d) and (e) 5 μM 3334; (f) and (g) 3 μM 3(3)(3)4. Scale bar: 1 μm. The DNA concentration is 0.5 μM in nucleotide units.

oriented in the presence of a branched-chain polyamine. This difference between linear- and branched-chain polyamines is in good agreement with our previous result.^[31] To compare the frequency of crossings in the presence of linear- and branched-chain polyamines, we calculated the number of crossings per 1 μm, ξ , from AFM images based on the method of analysis depicted in Table 1. We counted the number of crossings N for the total length L of DNA for the region where the density of DNA segments is not so high and is similar among AFM images with different polyamines. The number of crossings per 1 μm is thus obtained as $\xi = N/L$. From the data shown in Table 1, the degree of crossing for 3(3)(3)4 is more than twice those for SPD and 3334.

2.2. Temperature-Dependent Changes in the Higher-Order Structure of DNA Observed by AFM

Figure 2 shows AFM images of DNA in the presence of polyamines on a mica surface at 50 °C; DNA molecules tend to

Table 1. Degree of entanglement ξ , for a DNA chain evaluated from AFM images, where ξ represents the number of crossings per 1 μm of DNA chain as depicted schematically in the lower part.

Polyamine	$\xi[\mu\text{m}^{-1}]$	$L/S[\mu\text{m}^{-1}]$
SPD	5.8 ± 0.2	62.7 ± 2.2
3334	5.7 ± 0.4	59.4 ± 5.8
3(3)(3)4	11.5 ± 0.3	63.7 ± 4.0

ξ : number of crossings per 1 μm N : number of crossings,
 L : total length [μm], S : area [μm^2]

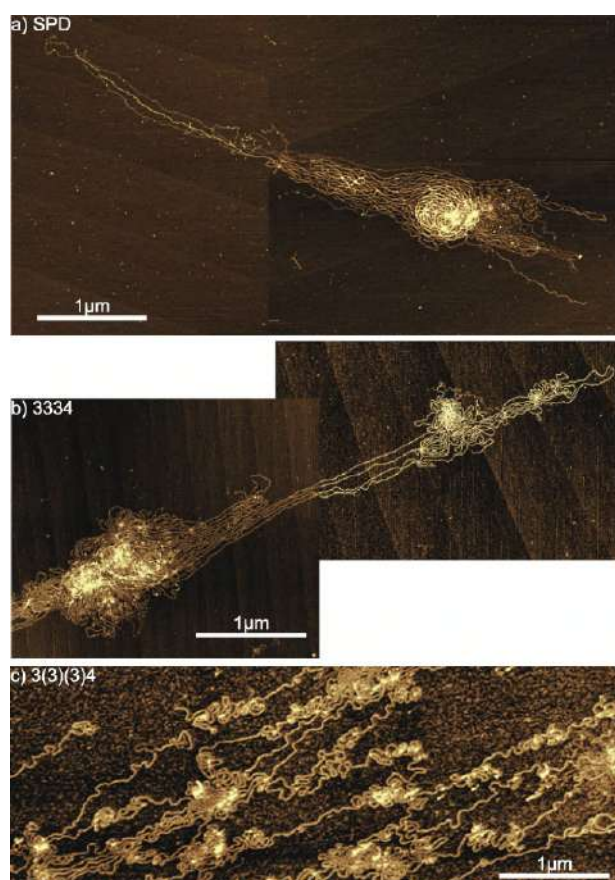
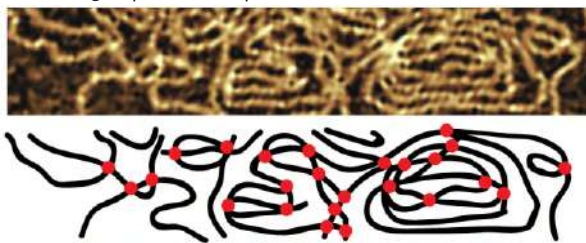


Figure 2. AFM images of T4 DNA in the presence of polyamines at 50 °C: (a) 200 μM SPD; (b) 5 μM 3334; (c) 3 μM 3(3)(3)4.

unwind with increasing temperature. As the temperature rose to 80 °C, there was a marked difference between DNA structures induced by linear- and branched-chain polyamines (Figures 3–5). Especially, the unwounded parts in 3(3)(3)4-induced structure are noted (Figures 5b and 5c). The high-magnification AFM image in Figure 5d clearly indicates that multiple nano-loop structures with diameters of 10–50 nm are

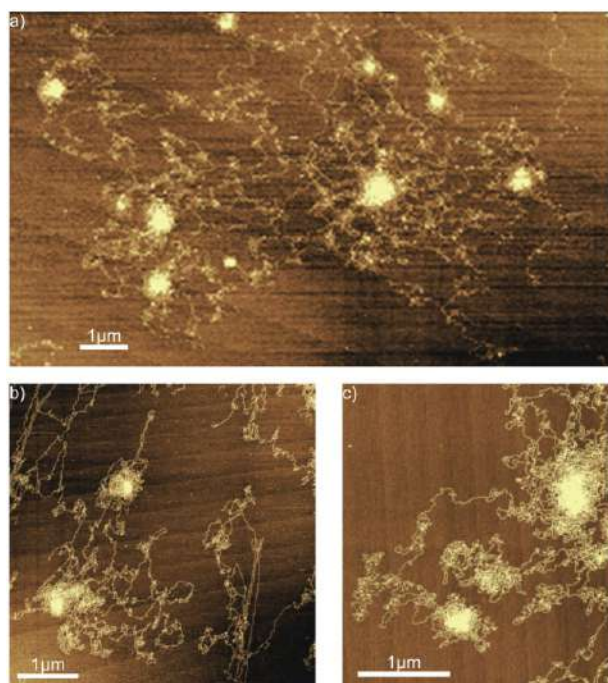


Figure 3. AFM images of T4 DNA in the presence of 200 μM SPD at 80 °C: (a) wide scan image; (b) and (c) enlarged images.

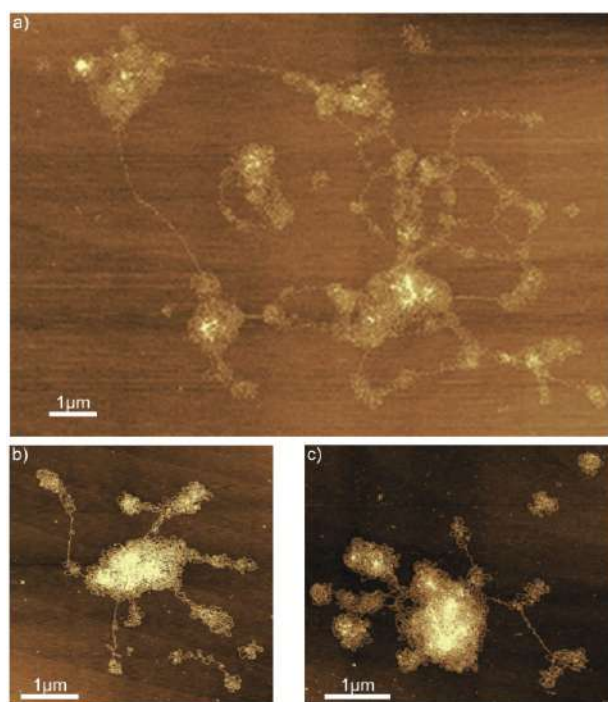


Figure 4. AFM images of T4 DNA in the presence of 5 μM 3334 at 80 °C: (a) wide scan image; (b) and (c) enlarged images.

formed along the DNA strand in the presence of 3(3)(3)4. Such structural features at 80 °C generated by 3(3)(3)4 may be related to its ability to enhance the thermal stability of DNA. The observed nano-looping conformation is similar in size to the inner diameter of a toroid in the tightly folded state of DNA,

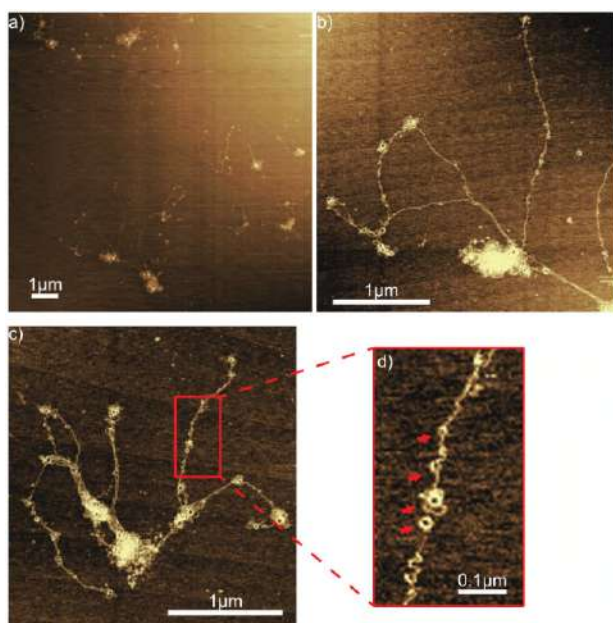


Figure 5. AFM images of T4 DNA in the presence of 3 μM 3(3)(3)4 at 80 $^{\circ}\text{C}$: (a) wide scan image; (b) and (c) enlarged images; (d) magnified image of the red square in (c), where arrows indicate the appearance of nano-loops.

where the outer diameter is 50–80 nm.^[32–36] Here, we will roughly estimate the energy cost for the formation of such a nano-loop structure. It has been well established that the persistence length, L_p , of double-stranded DNA is around 50 nm.^[38] Under the Hooke's law, the bending elastic constant, B , has the following relationship with L_p .^[39]

$$B = k_B T L_p \quad (1)$$

where k_B is Boltzmann constant and T is absolute temperature. Thus, the energy cost, ΔE , to form a loop with diameter D is given as in Eq. (2).

$$\Delta E = 2\pi B/D = 2\pi k_B T L_p/D \quad (2)$$

From this relationship, the energy cost to form a loop of $D = 10$ nm (with ca. 100 bp DNA or with ca. 200 phosphate groups) is estimated to be $10\pi k_B T$ (≈ 80 kJ/mol). It is considered that stabilization energy caused by the binding of a single polyamine to phosphate groups is in the order of 10 kJ/mol or more. Thus, an energy cost of $10\pi k_B T$ to form a 10 nm loop is regarded to be within the range of stabilization energy that can be afforded through the binding of plural number of branched-chain polyamine to the nano-loop.

2.3. Effect of Temperature on the Secondary Structure of DNA as Evaluated by CD Measurements

Figure 6 shows the effect of temperature on CD spectra of calf thymus DNA in the presence of linear- and branched-chain polyamines. The CD spectra with different polyamine concentrations were given in the Supporting Information (Figure S2).

Without polyamine, the CD signals at 240 nm and 275 nm decreased with an increase in temperature to 80 $^{\circ}\text{C}$, indicating the occurrence of a helix-coil transition (Figure 6a). In the presence of the linear-chain polyamine, SPD, the profiles of CD spectra remained essentially the same from 20 $^{\circ}\text{C}$ to 80 $^{\circ}\text{C}$, indicating that the secondary structure retains the B-form even at 80 $^{\circ}\text{C}$. (Figure 6b). This is due to the protective effect of polyamines against the thermal helix-coil transition. The linear-chain polyamine, 3334, was also associated with minimal changes in the CD spectra (Figure 6c). On the other hand, the branched-chain polyamine, 3(3)(3)4, induced a transition from B-form to A-like form DNA characterized by a higher intensity of the positive band at 275 nm over a wide range of temperatures (Figure 6d).^[40] To better understand the changes in the CD spectrum induced by an increase in temperature, we calculated the difference in ellipticities at 275 nm, $\Delta\theta$, between ellipticities obtained in the absence of polyamine, θ_0 and those obtained in the presence of polyamines, θ_r , as defined by the following equation:

$$\Delta\theta = (\theta_r - \theta_0) \quad (3)$$

The change in $\Delta\theta$ at 275 nm depending on the temperature is depicted in Figure 6e, which shows a marked change in CD with the addition of 3(3)(3)4 even at 20 $^{\circ}\text{C}$. The value $\Delta\theta$ tends to increase slightly with an increase of temperature in the presence of 3(3)(3)4. In contrast, the minimal effect of the linear polyamines, SPD and 3334, indicates that the secondary structure retains the B-form even under high temperatures. It was reported that a virus that infects a hyperthermophile, which lives at 80 $^{\circ}\text{C}$ and pH 3, encapsidates A-form DNA.^[41,42] Whelan et al. suggested that the A-form is prevalent in cells under stress based on observations of live bacteria by FTIR spectroscopy.^[43] At present, the mechanisms underlying the change from the B-form to A-like form of DNA induced by the branched-chain polyamine 3(3)(3)4 remain unclear, but the preference for the A-like form over the B-form at higher temperatures suggests that the A-like form is associated with thermal resistance.

3. Conclusions

Past studies showed the effect of various polyamines on thermal stability of DNA oligonucleotides.^[44,45] Here we used a large genome-size DNA (166 kbp) and showed that the branched-chain polyamine induces a unique temperature-dependent structural change. To the best of our knowledge, this is the first report to investigate the effect of polyamines on the higher-order structure of large DNA with increasing temperature up to 80 $^{\circ}\text{C}$. In addition, the branched-chain polyamine induces the secondary structural change from B-form to A-like form that is more marked at higher temperatures. These effects are specific to the branched-chain polyamine and are clearly different from the effects of linear-chain polyamines. These findings in the present study will provide additional insights not only on thermo-adaptation but also on understanding the

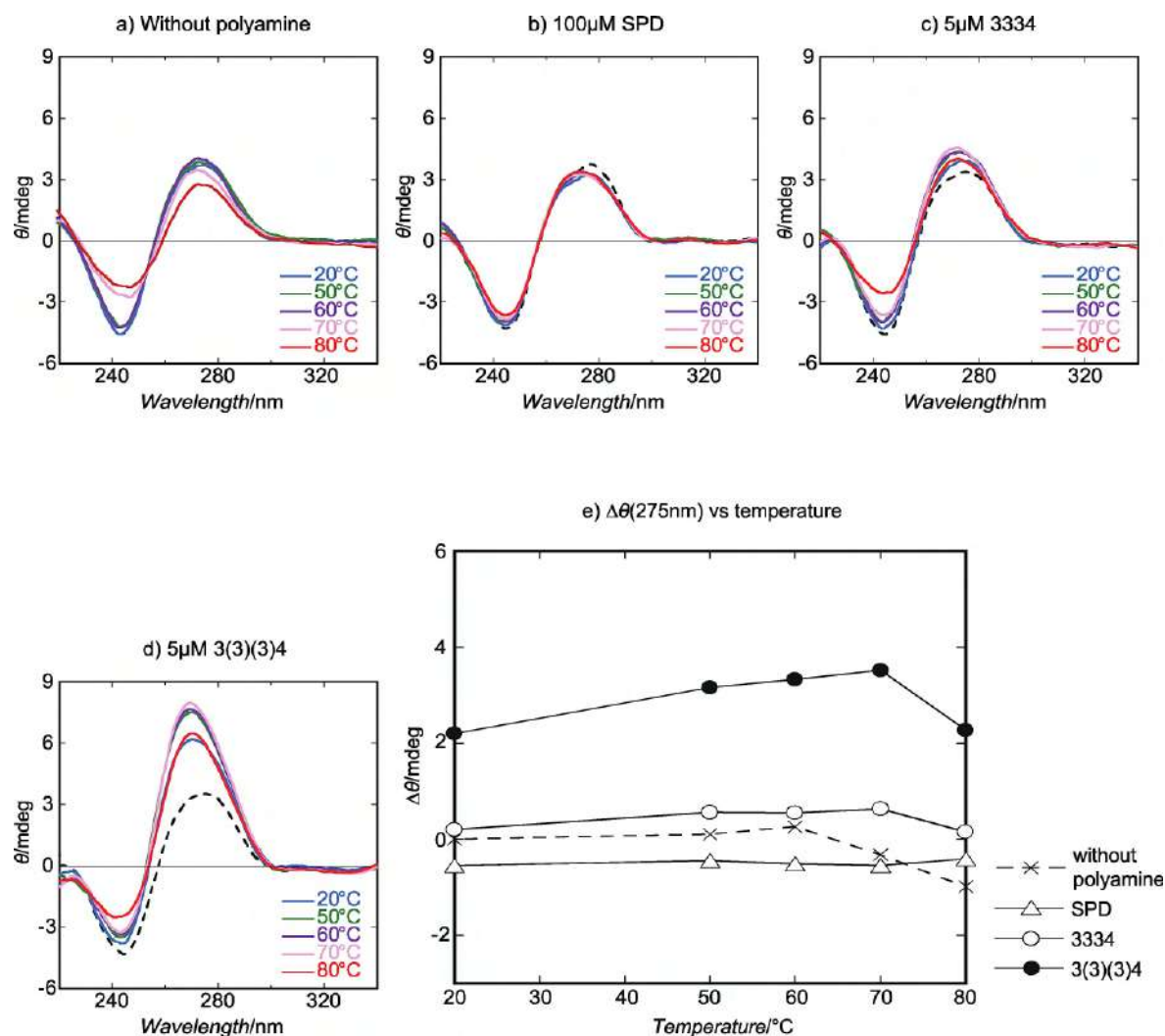


Figure 6. CD spectra of calf thymus (CT) DNA at different temperatures in the presence of polyamines. The black broken line in (b), (c) and (d) indicates the CD spectrum at 20 °C in the absence of polyamine. The concentration of CT DNA is 30 μM in nucleotide units.

mechanism how hyperthermophiles maintain their genetic activity under high temperature environments.

Experimental Section

Materials

Spermidine SPD was purchased from Nacalai Tesque (Kyoto, Japan). Homocaldopentamine 3334 and *N*⁴-bis(aminopropyl)spermidine 3(3)(3)4 were synthesized according to a previous report.^[31] Calf Thymus DNA (CT DNA: 8–15 kbp) was purchased from Wako Pure Chemical Industries (Osaka, Japan). T4 GT7 phage DNA was purchased from Nippon Gene (Toyama, Japan). Other chemicals were analytical grade and obtained from Nacalai Tesque.

AFM Observations

AFM measurements were performed with an SPM-9700 (Shimadzu, Kyoto, Japan). For the preparation of sample specimens, 0.5 μM T4 DNA was dissolved in 1 mM Tris-HCl buffer solution at pH 7.5. Polyamines were then added to the solution. The resulting DNA

solution was incubated at the target temperature for 3 min. Freshly cleaved mica was also incubated at the same target temperature. The DNA solution was then transferred onto the mica surface and was stood for 10 min at room temperature (24 °C). Subsequently, the sample was rinsed with ultra-pure water, dried with nitrogen gas and imaged by AFM. All measurements were performed in air using the tapping mode. The cantilever, OMCL-AC200TS-C2 (Olympus, Tokyo, Japan), was 200 μm long with a spring constant of 9–20 N/m. The scanning rate was 0.4 Hz and images were captured using the height mode in a 512 × 512 pixel format. The obtained images were plane-fitted and flattened by the computer program supplied with the imaging module.

CD Measurements

CD spectra of CT DNA upon heating were measured in the presence of each polyamine in 1 mM Tris-HCl buffer (pH 7.5) on a J-720W spectropolarimeter (JASCO, Tokyo, Japan). The DNA concentration was 30 μM in nucleotide units for all of the CD measurements. The cell path length was 1 cm. Data were collected every 1 nm between 220 and 340 nm at a scan rate of 100 nm/min, and were accumulated 3 times.

Acknowledgements

This work was supported by JSPS KAKENHI Grant Number 15H02121 and 25103012.

Conflict of Interest

The authors declare no conflict of interest.

Keywords: higher-order structure of DNA · branched polyamine · archaea · high temperature · nano-loop

- [1] C. W. Tabor, H. Tabor, *Annu. Rev. Biochem.* **1984**, *53*, 749–790.
- [2] L. Miller-Fleming, V. Olin-Sandoval, K. Campbell, M. Ralsler, *J. Mol. Biol.* **2015**, *427*, 3389–3406.
- [3] A. O. Gevrekci *World J. Microbiol. Biotechnol.* **2017**, *33*, 204.
- [4] N. Nishibori, M. Niitsu, S. Fujihara, T. Sagara, S. Nishio, I. Imai, *FEMS Microbiol. Lett.* **2009**, *298*, 74–78.
- [5] S. Finger, C. Schwieger, A. Arouri, A. Kerth, A. Blume, *Biol. Chem.* **2014**, *395*, 769–778.
- [6] A. M. Katz, I. S. Tolokh, S. A. Pabit, N. Baker, A. V. Onufriev, L. Pollack, *Biophys. J.* **2017**, *112*, 22–30.
- [7] E. C. Ong, C. Snell, G. D. Fasman, *Biochemistry.* **1976**, *15*, 468–477.
- [8] T. H. Eickbush, D. K. Watson, E. N. Moudrianakis, *Cell.* **1976**, *9*, 785–792.
- [9] D. K. Chatteraj, L. C. Gosule, A. Schellman, *J. Mol. Biol.* **1978**, *121*, 327–337.
- [10] R. E. Dickerson, H. R. Drew, *J. Mol. Biol.* **1981**, *149*, 761–786.
- [11] S. A. Allison, J. C. Herr, J. M. Schurr, *Biopolymers.* **1981**, *20*, 469–488.
- [12] B. G. Feuerstein, N. Pattabiraman, L. J. Marton, *Proc. Natl. Acad. Sci. USA.* **1986**, *83*, 5948–5952.
- [13] K. S. Srivenugopal, D. E. Wemmer, D. R. Morris, *Nucleic Acids Res.* **1987**, *15*, 2563–2580.
- [14] T. Thomas, R. P. Messner, *J. Mol. Biol.* **1988**, *201*, 463–467.
- [15] S. Jain, G. Zon, M. Sundaralingam, *Biochemistry.* **1989**, *28*, 2360–2364.
- [16] R. Gessner, C. A. Frederick, G. Quigley, A. Rich, A. Wang, *J. Biol. Chem.* **1989**, *264*, 7921–7935.
- [17] P. G. Arscott, A. Z. Li, V. A. Bloomfield, *Biopolymers.* **1990**, *30*, 619–630.
- [18] V. A. Bloomfield, *Biopolymers.* **1991**, *31*, 1471–1481.
- [19] T. Thomas, T. Thomas, *Biochemistry.* **1993**, *32*, 14068–14074.
- [20] L. W. Tari, A. S. Secco, *Nucleic Acids Res.* **1995**, *23*, 2065–2073.
- [21] V. S. Trubetskoy, A. Loomis, P. M. Slattum, J. E. Hagstrom, V. G. Budker, J. A. Wolff, *Bioconjugate Chem.* **1999**, *10*, 624–628.
- [22] R. Golan, L. I. Pietrasanta, W. Hsieh, H. G. Hansma, *Biochemistry.* **1999**, *38*, 14069–14076.
- [23] H. Deng, V. A. Bloomfield, J. M. Benevides, G. J. T. Jr, *Nucleic Acids Res.* **2000**, *28*, 3379–3385.
- [24] V. Vijayanathan, T. Thomas, A. Shirahata, T. J. Thomas, *Biochemistry.* **2001**, *40*, 13644–13651.
- [25] A. Venancio-Marques, A. Bergen, C. Rossi-Gendron, S. Rudiuk, D. Baigl, *ACS Nano* **2014**, *8*, 3654–3663.
- [26] R. Everaers, H. Schiessel, *J. Phys. Condens. Matter* **2015**, *27*, 060301/1–2.
- [27] T. Nozaki, R. Imai, M. Tanbo, R. Nagashima, S. Tamura, T. Tani, Y. Joti, M. Tomita, K. Hibino, M. T. Kanemaki, K. S. Wendt, Y. Okada, T. Nagai, K. Maeshima, *Mol. Cell* **2017**, *67*, 282–293.
- [28] K. Okada, R. Hidese, W. Fukuda, M. Niitsu, K. Takao, Y. Horai, N. Umezawa, T. Higuchi, T. Oshima, Y. Yoshikawa, T. Imanaka, S. Fujiwara, *J. Bacteriol.* **2014**, *196*, 1866–1876.
- [29] R. Hidese, K. H. Im, M. Kobayashi, M. Niitsu, T. Furuchi, S. Fujiwara, *Biosci. Biotechnol. Biochem.* **2017**, *81*, 1845–1849.
- [30] H. Atomi, T. Fukui, T. Kanai, M. Morikawa, T. Imanaka, *Archaea.* **2004**, *1*, 263–267.
- [31] A. Muramatsu, Y. Shimizu, Y. Yoshikawa, W. Fukuda, N. Umezawa, Y. Horai, T. Higuchi, S. Fujiwara, T. Imanaka, K. Yoshikawa, *J. Chem. Phys.* **2016**, *145*, 235103.
- [32] K. Yoshikawa, Y. Yoshikawa, *Compaction and Condensation of DNA*, In: R. I. Mahato, S. W. Kim (eds.) *Pharmaceutical Perspectives of Nucleic Acid-Based Therapy*, **2004**, Chap. 8, pp. 137–163.
- [33] B. I. Kankia, V. Buckin, V. A. Bloomfield, *Nucleic Acids Res.* **2001**, *29*, 2795–2801.
- [34] V. B. Teif, *Biophys. J.* **2005**, *89*, 2574–2587.
- [35] A. C. Toma, M. de Frutos, F. Livolant, E. Raspaud, *Biomacromolecules.* **2009**, *10*, 2129–2134.
- [36] Y. Yoshikawa, Y. Suzuki, K. Yamada, W. Fukuda, K. Yoshikawa, K. Takeyasu, T. Imanaka, *J. Chem. Phys.* **2011**, *135*, 225101.
- [37] Y. Fang, J. H. Hoh, *J. Am. Chem. Soc.* **1998**, *120*, 8903–8909.
- [38] G. S. Manning, *Biophys. J.* **2006**, *91*, 3607–3616.
- [39] A. Y. Grosberg, A. R. Khokhlov, *Statistical Physics of Macromolecules*, AIP Press, New York **1994**.
- [40] V. I. Ivanov, L. E. Minchenkova, A. K. Schyolkina, A. I. Poletayev, *Biopolymers.* **1973**, *12*, 89–110.
- [41] F. Di Maio, X. Yu, E. Rensen, M. Krupovic, D. Prangishvili, E. H. Egelman, *Science.* **2015**, *348*, 914–917.
- [42] B. R. Wood, *Chem. Soc. Rev.* **2016**, *45*, 1999–1999.
- [43] D. R. Whelan, T. J. Hiscox, J. I. Rood, K. R. Bambery, D. McNaughton, B. R. Wood, *J. R. Soc. Interface* **2014**, *11*, 20140454.
- [44] M. H. Hou, S. B. Lin, J. M. Yuann, W. C. Lin, A. H. Wang, L. Kan Ls *Nucleic Acids Res.* **2001**, *29*, 5121–5128.
- [45] Y. Terui, M. Ohnuma, K. Hiraga, E. Kawashima, T. Oshima, *Biochem. J.* **2005**, *388*, 427–433.

Manuscript received: April 28, 2018
Accepted Article published: June 21, 2018
Version of record online: July 10, 2018

VIP Very Important Paper



Specific Spatial Localization of Actin and DNA in a Water/Water Microdroplet: Self-Emergence of a Cell-Like Structure

Naoki Nakatani,^[a] Hiroki Sakuta,^[a] Masahito Hayashi,^[b, d] Shunsuke Tanaka,^[b] Kingo Takiguchi,^{*,[b]} Kanta Tsumoto,^{*,[c]} and Kenichi Yoshikawa^[a]

The effect of binary hydrophilic polymers on a pair of representative bio-macromolecules in a living cell has been examined. The results showed that these bio-macromolecules exhibited specific localization in cell-sized droplets that were spontaneously formed through water/water microphase segregation under crowding conditions with coexisting polymers. In these experiments, a simple binary polymer system with poly(ethylene glycol) (PEG) and dextran (DEX) was used. Under the conditions of microphase segregation, DNA was entrapped within cell-sized droplets rich in DEX. Similarly, F-actin, linearly polymerized actin, was entrapped specifically within microdroplets rich in DEX, whereas G-actin, a monomeric actin, was distributed evenly inside and outside these droplets. This study has been extended to a system with both F-actin and DNA, and it was found that DNA molecules were localized separately from aligned F-actin proteins to create microdomains inside microdroplets, reflecting the self-emergence of a cellular morphology similar to a stage of cell division.

Living cells keep a highly crowded cellular cytoplasm with 30–40 wt/wt% of cellular materials, such as DNA, RNA, and a rich variety of proteins.^[1] Macromolecular assemblies, such as polynucleotides and cytoskeletons, are dynamically arranged in a self-organized manner during the cell life cycle to contribute to various biological functions, including cell motility, morpho-

genesis, and division, as well as the spatial arrangement and migration of organelles. It is generally considered that the systematic localization of cytoskeletal networks and the manner of polymerization is controlled by regulatory factors determined by genetic material. Various actin-binding proteins have been found to play a role in actin network systems, through polymerization/depolymerization, resulting in the constitution of either a backbone structure or skeleton inside cells.^[2]

Recently, it has been suggested that the crowded cellular environment plays a fundamental role in the construction of subcellular organelles and granules, as well as in the cellular morphology, that is, liquid droplets (cytoplasmic bodies) consisting of RNA and proteins,^[3] assembly of the bacterial cytoskeleton protein FtsZ,^[4] and cytoskeletal networks.^[5] Interestingly, it is becoming clear that these systems lack specific regulatory factors, which suggests that subcellular structures are generated spontaneously under nonspecific environmental factors in a self-organized manner under the crowded conditions of the cytoplasm. Studies to unveil the fundamental mechanism of intracellular self-organization under certain environments are expected to shed light on the fundamental unsolved problem of life: how can individual cells undergo appropriate differentiation in the right location under the same genetic information?

Herein, we report the characteristic behavior of DNA and/or actin in a simple binary hydrophilic polymer system, poly(ethylene glycol) (PEG)/dextran (DEX), as a simple model of a cytoplasmic solution or intracellular fluid crowded with polymeric molecules. If the two polymers were mixed at certain concentrations, cell-sized water/water (w/w) microdroplets (referred to herein as cell-sized aqueous/aqueous microdroplets, CAMDs), with diameters ranging from 10 to 100 μm , emerged and were sustained for more than several hours (Figure S1 and Table S1 in the Supporting Information).^[6] The interior and exterior of CAMDs were occupied by DEX and PEG solutions, respectively. PEG is a flexible polymer and DEX is a branched polymer with a stiff backbone, and thus, they constitute a binary aqueous two-phase system (ATPS), which exhibits liquid–liquid phase separation (LLPS).^[7] Because the CAMDs apparently provide cell-like crowded microenvironments, we have tried to examine whether microcompartmentalization has exotic effects on the behavior of fundamental bio-macromolecules, such as DNA and actins.

Figure 1 shows confocal laser scanning microscopic images of CAMDs in the presence of DNA molecules. Figure 1A reveals that fluorescence-labeled short single-stranded DNAs (11-mers)

[a] N. Nakatani, H. Sakuta, Prof. Dr. K. Yoshikawa
Graduate School of Life and Medical Sciences, Doshisha University
Tataramiyakodani 1–3, Kyotanabe, Kyoto 610-0394 (Japan)

[b] Dr. M. Hayashi, S. Tanaka, Dr. K. Takiguchi
Graduate School of Science, Nagoya University
Furo-cho, Chikusa-ku, Nagoya, Aichi 464-8602 (Japan)
E-mail: j46037a@cc.nagoya-u.ac.jp

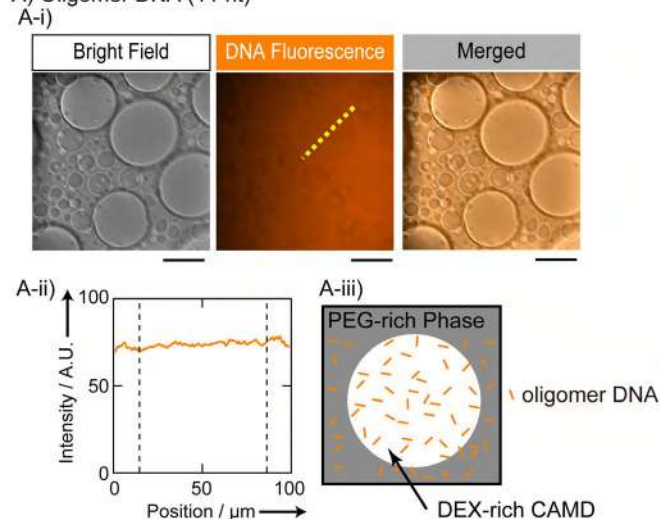
[c] Dr. K. Tsumoto
Division of Chemistry for Materials, Graduate School of Engineering
Mie University
Kurimamachiya-cho 1577, Tsu, Mie 514-8507 (Japan)
E-mail: tsumoto@chem.mie-u.ac.jp

[d] Dr. M. Hayashi
Laboratory for Molecular Biophysics, RIKEN, Center for Brain Science
Hirosawa 2–1, Wako, Saitama 351-0198 (Japan)

Supporting information and the ORCID identification numbers for the authors of this article can be found under: <https://doi.org/10.1002/cbic.201800066>.

© 2018 The Authors. Published by Wiley-VCH Verlag GmbH & Co. KGaA. This is an open access article under the terms of the Creative Commons Attribution Non-Commercial License, which permits use, distribution and reproduction in any medium, provided the original work is properly cited and is not used for commercial purposes.

A) Oligomer DNA (11 nt)



B) λ DNA (49 kbp)

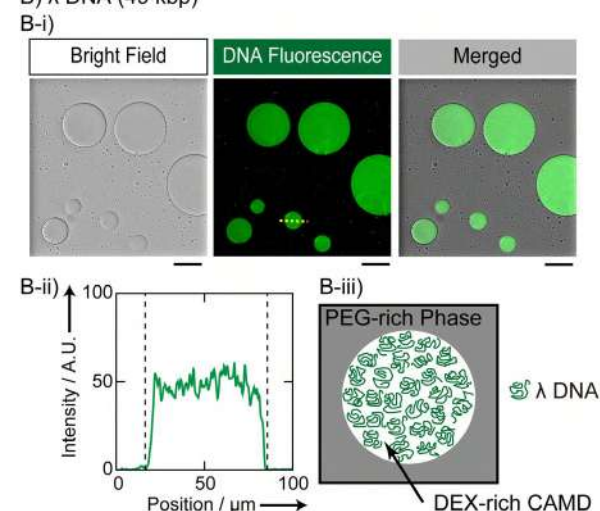


Figure 1. DNA localization in CAMDs in the presence of 5.0 wt% PEG and 5.0 wt% DEX observed by a confocal laser scanning microscope (CLSM). A) Single-stranded DNAs (undecamers, 21 μm in nucleotide units) were distributed homogeneously inside and outside DEX-rich CAMDs. Oligomer DNAs had been labeled with 3'-TAMRA. B) Long double-stranded λ -DNAs (49 kbp, 38.5 μm in nt units) were observed only for DEX-rich CAMDs, and were specifically localized inside the droplets. λ -DNA was labeled with Gel-Green. Fluorescence profiles along the dashed lines in the DNA fluorescence images (middle panels in A-i and B-i) are shown in A-ii and B-ii, and schematic representations are depicted to illustrate how both DNA molecules are located in the PEG/DEX phases (A-iii and B-iii). Scale bars: 50 (A-i) and 100 μm (B-i). (See Tables S2 and S3 for detailed information regarding the conditions.)

are distributed evenly inside and outside of CAMDs. In contrast, long DNAs (λ -DNA, 49 kbp) are distributed homogeneously inside DEX-rich CAMDs (Figure 1B). Thus, it is evident that CAMDs can entrap long DNA chains in a selective manner. Such selective entrapment of long DNA is attributable to the difference in the manner of packing of crowding polymers between PEG and DEX, that is, nanosized void space exists in the DEX-rich phase because of its stiff backbone and branched conformation, whereas the PEG-rich phase is fully occupied with flexible chains.^[8] For double-stranded DNA with a diame-

ter of about 2 nm, the persistence length is known to be around 170 bp, corresponding to about 50 nm. Thus, λ -DNA behaves as a semiflexible polymer chain. It has been reported that such long DNA molecules are compressed to form a compact state and/or align in a liquid-crystalline-like condensate under crowded conditions with a flexible polymer, such as PEG.^[9] In contrast, it is expected that a semiflexible DNA chain can penetrate into the nanosized void space under crowded conditions with DEX. On the other hand, short oligomeric single-stranded DNA has no preference for a phase rich in either PEG or DEX because it is so small.

Figure 2 shows the distributions of actin molecules in solutions with CAMDs. Using a confocal laser scanning microscope (CLSM), we observed that an actin monomer, G-actin, was delocalized evenly outside and inside the droplets (Figure 2A). In contrast, a polymerized actin, F-actin, was distributed homogeneously inside DEX-rich CAMDs (Figure 2B). Here, actins were induced to polymerize through the addition of potassium chloride, and their lengths were between 1 and 30 μm . Figure 2C shows the specific localization of the bundled state of F-actin (bundled F-actin), which was caused by the addition of magnesium ions.^[10] In contrast to F-actin in a dispersed state, as in Figure 2B, F-actin bundles tend to be located at the interface between the PEG- and DEX-rich phases. If much higher concentrations of MgCl_2 were added, F-actins formed a cluster of

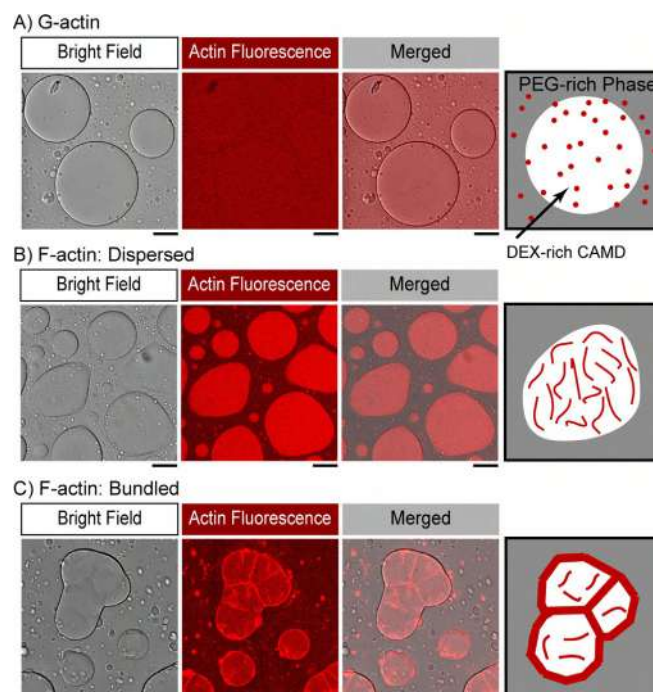


Figure 2. Actin is localized in CAMDs depending on the state of actin polymerization. All CLSM images were acquired with PEG/DEX (5.0 wt% each) and an actin concentration of 9.0 μM with 1.0 mol% Alexa Fluor 546-labeled actin. A) G-actins were distributed homogeneously inside and outside of DEX-rich CAMDs. B) Polymerized F-actins, generated by the addition of 40 mM KCl, were entrapped in DEX-rich CAMDs. C) Bundled F-actins, generated by the addition of 2.0 mM MgCl_2 , were located at the surface of DEX-rich CAMDs, and simultaneously F-actins existed inside the droplets. Scale bar: 50 μm . (See Tables S4, S5, and S6 for detailed information regarding each condition.)

large bundles that appeared to form a cytoskeletal network, and the cluster was entrapped near the periphery of DEX-rich CAMDs (Figure S2). Interestingly, such bundled F-actin caused deformation of the interface, which was not observed for experiments with G-actin and was less frequently observed with F-actin in a dispersed state. Actin plays important roles in cell motility and morphological development,^[11] and can transform giant liposomes, which are considered to be artificial membrane vesicles, through its interaction with the surface of lipid bilayers.^[12] The present observation of the deformation of the interface of CAMDs implies that actin, by nature, plays a role in the development of the morphology of interfaces of soft matter by modulating tension through its accumulation on the surface.

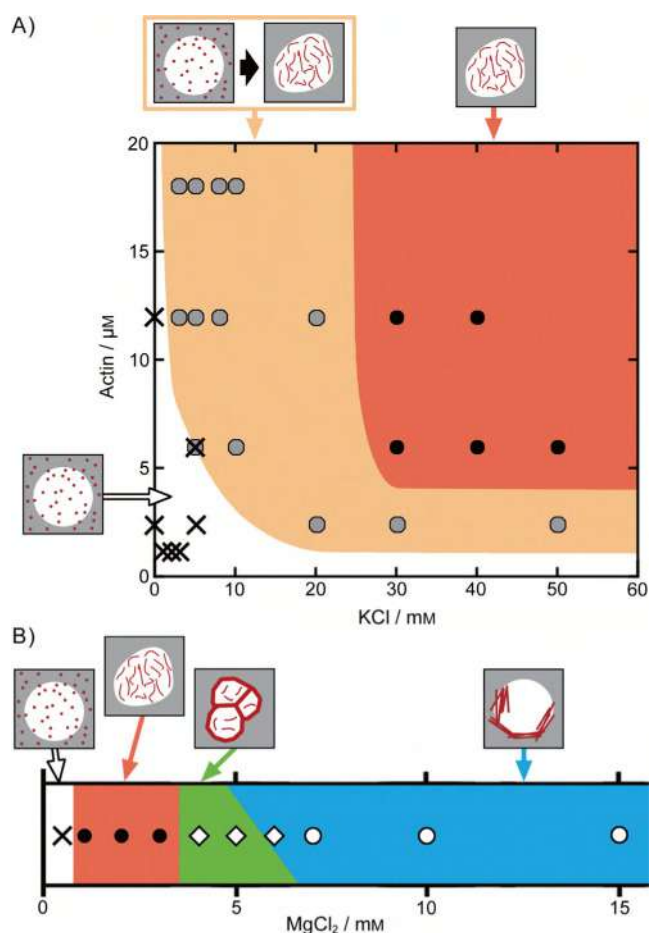


Figure 3. Phase diagrams for the localization and morphological state of actin, depending on the concentrations of A) actin and KCl, and B) $MgCl_2$. In B), the concentration of actin was fixed at $6.0 \mu\text{M}$. Crosses indicate the parameter area for even distribution inside and outside CAMDs (as shown in Figure 2A). The black and gray circles in A) show the localization of dispersed F-actin inside CAMDs (as in Figure 2B). The conditions indicated by closed circles caused actin localization soon after sample preparation, whereas under the conditions indicated by gray-filled circles, several tens of minutes were required for actin localization and the reproducibility of the results was relatively low. The open diamonds show the localization of bundled F-actin at the interface, which causes deformation of the droplets (as in Figure 2C). The open circles indicate the clustering of bundled F-actin inside CAMDs (as shown in Figure S2).

Based on the systematic observation by microscopy, we deduced a phase diagram for the changes in the distribution and polymerization state of actins in CAMDs with different concentrations of KCl and $MgCl_2$ (Figure 3). It has been well established that, in bulk in vitro solution, actin polymerizes into filaments in the presence of KCl (30 mM or more) or $MgCl_2$ (a few mM or more), and F-actins form bundles by paracrystal formation in the presence of 10 mM or more of $MgCl_2$.^[10] In our experiments with the crowded solution of PEG/DEX, interestingly, the threshold concentration of KCl to induce actin polymerization decreased by about one order of magnitude (Figure 3A), and the threshold concentration of $MgCl_2$ to cause bundling of F-actin decreased to about one-third (Figure 3B). This is attributable to a cooperative effect between the restricted localization of actin into the DEX-rich CAMDs, as a result of its polymerization and facilitation of polymerization by accumulation due to restricted localization.

Based on the above-mentioned observations of specific localization and/or morphological changes of DNA or actin, we conducted an experiment in which long DNA and F-actin coexisted within the solution of PEG/DEX with CAMDs. Figure 4 exemplifies the results for the condition in which F-actin is dispersed inside DEX-rich CAMDs, as in Figure 2B, and long double-stranded λ -DNA is entrapped therein, as in Figure 1B. We found that the entrapped DNA and F-actin assembled in a separate manner inside the droplet, that is, segregation between pair of different biopolymers was caused spontaneously. Observation by polarization microscopy, as in the lower-right panel in Figure 4, indicates that F-actin was assembled in parallel with some ordered (nematic) alignment. As a result, long DNAs might be located separately to form discrete domains within CAMDs in a self-organized manner. We sometimes ob-

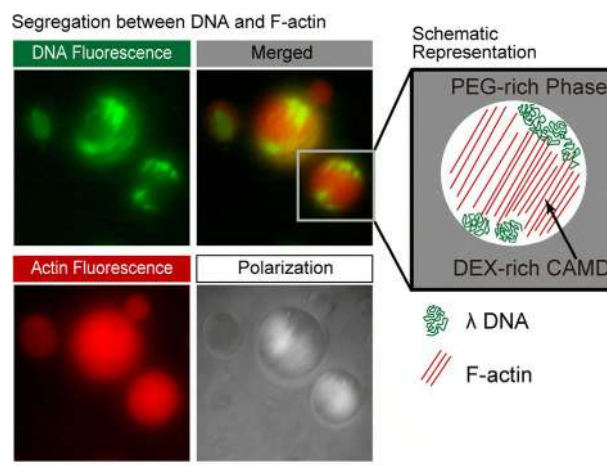


Figure 4. Specific localization of long DNA (λ -DNA) and F-actin in DEX-rich CAMDs. Fluorescence microscopic images of DNA (GelGreen), actin (Alexa Fluor 546), and those merged are shown, together with observations by polarization microscopy (four panels on the left). Images were acquired under conditions of $120 \mu\text{M}$ λ -DNA, $10 \mu\text{M}$ actin, and 4.0mM KCl. F-actins were observed to be in a nematic liquid-crystal state in the center of DEX-rich CAMDs, and DNA molecules appeared to be segregated from the center. In other words, long DNAs are compressed by the aligned F-actin region, as illustrated schematically (right). Scale bar: $100 \mu\text{m}$. (See Table S8 for detailed information regarding the conditions.)

served that entrapped DNAs and actins failed to be segregated in the CAMDs; this suggested that the phenomenon may occur within only a certain range of conditions and further investigation is awaited on the regime at which the microstructures emerge. Actin has also been found in the cell nucleus, and its physiological significance and role are still enigmatic, despite vigorous research.^[13] The nuclear actins have been argued in the context of maintenance of LLPS structures occurring in nuclei of actual cells.^[14] The result observed herein would help to clarify these hypotheses. Even without DEX or PEG, long DNA and F-actin can show phase separation.^[15] However, in order to induce the local phase separation of DNA and F-actin in the bulk solution, the concentration of F-actin has to be at least about tenfold higher than that in the present result; otherwise, DNA and F-actin should be confined to a space with a diameter comparable to that of the F-actin length.

In summary, in the presence of binary polymers (PEG/DEX), 1) both semiflexible long DNAs (λ -DNAs) and F-actin proteins were spontaneously localized within CAMDs, in contrast to the observations with short DNAs and G-actin proteins, which were distributed evenly both inside and outside of the droplets; 2) actin proteins exhibited various localizations in CAMDs if they had different polymerization states (monomer, fiber, and bundle), depending on the salt concentrations without proteinaceous regulatory factors; and 3) long DNAs and F-actin, if they coexisted in the same CAMDs, exhibited microsegregation to form domains. To our surprise, despite the simplicity of the system, PEG/DEX CAMDs, or self-emergent microcompartments under crowding, could exhibit primitive protocell-like morphologies based on the nature of the biopolymers: first, actin proteins can deform the surfaces of CAMDs as they act on cell membranes; second, the bipolar localization of long DNAs, possibly due to the exclusion of aligned F-actins, may also imply a primitive function of cytoskeletal proteins to generate intracellular structures. Because macromolecular crowding regulates biochemical activities,^[16] such confined microcompartments under macromolecular crowding are expected to change both the physicochemical properties and localization of entrapped proteins,^[17] and biological functions, such as enzymatic activities.^[18] Herein, we found that polymerization and bundling of actin in CAMDs were induced at much lower cation concentrations than that in typical aqueous medium in the absence of a crowding polymer. In the discipline of biochemistry, it is usually assumed that specific key-lock interactions determine the structure and function of living cells. However, the present results suggest that nonspecific environmental factors under confined crowding conditions may also play a decisive role in living things.

On the other hand, it should be noted that the localization of DNA, that is, entrapment of long double-stranded DNA and almost homogeneous distribution of single-stranded DNA, could be a specific case with the PEG/DEX CAMDs that we adopted herein. For instance, single-stranded RNA and/or DNA can be entrapped inside microdroplets if the droplets are composed of proteins that possess some affinity to the polynucleotides.^[14,19] The manner of localization of DNA and proteins

would be dependent on which components mainly constitute CAMDs. Because PEG and DEX possess no particular affinity to single- or double-stranded DNA, the localization observed herein could only be determined due to structural characteristics of these polymers. Moreover, it is known that the distribution of biopolymers, such as DNA, is affected by species and concentrations of coexisting salt in the bulk ATPs.^[7] Although we indicate concentrations in bulk solutions in Figures 2–4, at present, it remains unclear how salts such as $MgCl_2$ and KCl would be distributed over microsystems of the CAMDs in relation to actin localization. In addition to adenosine triphosphate (ATP), it is necessary to investigate local concentrations of such small polyelectrolytes in the CAMDs; meanwhile, ATP is smaller than the oligomeric single-stranded DNA used here, and the polymerization activity of actin was not changed, even during long-term observations; this implies that ATP is distributed almost uniformly therein.

Actual cells contain highly complicated macromolecular systems, and this motivated us to simplify these systems to realize an artificial cell model.^[20] A PEG/DEX LLPS that can provide microdroplets, such as CAMDs, has recently gained attention because of its active^[21] and morphological^[22] behavior and usefulness in cell biotechnology.^[23] The present results of coexisting DNA/actin suggest that CAMDs are compartments that develop interactions among bio-macromolecules, and thus, are useful for artificial cell studies. In other words, herein we showed that microdroplets caused by simple depletion effects served a simple real-world model of a cellular system. These systems are generated under markedly different physicochemical interactions from that of coacervates, that is, aggregation products among macromolecules.^[24] Recently, it was found that nuclei could express LLPS with multiphase structures.^[14] Actually, biological macromolecules could interact both attractively and exclusively inside such microcompartments in a complicated manner. CAMDs can provide cell models in which attraction to crowd molecules is avoided, and it is expected that the result of the present study may help to open up new horizons on the significant role of phase separation in the formation of organelles.^[5,6,25]

Experimental Section

Polymers: We used a PEG/DEX ATPs. PEG 6000 was purchased from Wako Pure Chemical Industries (Osaka, Japan), with an average molecular weight (MW) of 7300–9300 Da. DEX was also purchased from Wako Pure Chemical Industries, with an average MW of 180 000 to 210 000 Da. These two polymers were dissolved in nuclease-free water (Milli-Q, 18.2 M Ω cm) to prepare 20 wt% stock solutions. For use as a tracer for PEG-rich domains, methoxyl PEG fluorescein (mPEG-Fluorescein) was purchased from Nanocs Inc. (New York, NY), with an average MW of 10 kDa, an excitation wavelength (λ_{ex}) of 490 nm, and an emission wavelength (λ_{em}) of 520 nm. The mPEG-Fluorescein was dissolved in nuclease-free water to give a 10 wt% stock solution.

DNA: Single-stranded oligomer DNA was purchased from Hokkaido System Science (Sapporo, Japan). The 3'-labeled single-stranded oligomer DNA had the following properties: 11-mer (ATG CTG ATC GC), MW = 3953.84 Da, 3'-carboxytetramethylrhodamine (3'-TAMRA;

$\lambda_{\text{ex}}=542$ nm, $\lambda_{\text{em}}=568$ nm). It was dissolved in nuclease-free water at 100 μM . λ -DNA with a MW of 31.5 MDa (48502 bp) was purchased from Nippon Gene Co., Ltd. (Tokyo, Japan). It was dissolved at a concentration of 0.25 g L^{-1} (nucleotide concentration of 770 μM). To label λ -DNA, GelGreen, as a fluorescent dye ($\lambda_{\text{ex}}=500$ nm, $\lambda_{\text{em}}=530$ nm), was purchased from Biotium Inc. (Fremont, CA). It was dissolved in nuclease-free water as a 0.5 mM stock solution.

Actin: Monomeric actin (globular actin, G-actin) was prepared from acetone powder obtained from chicken breast muscle.^[26] To obtain filamentous actin (F-actin), G-actin was polymerized in G-buffer (1 mM NaHCO_3 , pH 8.0, 0.2 mM CaCl_2 , 0.2 mM ATP) containing salt (potassium chloride or magnesium chloride). Whole actin (1.0 mol%) was labeled with Alexa Fluor 546 C5 maleimide ($\lambda_{\text{ex}}=537$ nm, $\lambda_{\text{em}}=556$ nm; Thermo Fisher Scientific, Inc., Waltham, MA), against actin monomer, as reported previously.^[27] Experiments with actin were performed in G-buffer with or without salt.

Other materials: The antioxidant 2-mercaptoethanol (2ME) was purchased from Wako Pure Chemical Industries. The buffer solution tris(hydroxymethyl)aminomethane-HCl (Tris-HCl 1 M, pH 7.5) was purchased from Nippon Gene, and diluted with nuclease-free water to obtain 200 mM stock solutions. Potassium chloride and magnesium chloride were purchased from Wako Pure Chemical Industries and dissolved in nuclease-free water at 1.0 M as stock solutions.

Microscopy: Images were obtained with a CLSM or an epifluorescent microscope. The CLSM was a Nikon A1 (Nikon Corp., Tokyo, Japan) instrument equipped with a 10 \times objective. The acquired images were analyzed by using a NIS Elements Viewer (Nikon). For phase contrast and polarized epifluorescent microscopic images, we used a BX60 microscope with a 40 \times objective (NA=0.75, Olympus, Tokyo, Japan). The BX60 microscope was equipped with a charge-coupled device (CCD) camera (WAT-910HX; Watec Co., Ltd., Yamagata, Japan). The obtained images were analyzed by using ImageJ software (Rasband, W.S., ImageJ, US National Institutes of Health, Bethesda, Maryland, USA, <http://imagej.nih.gov/ij/>, 1997–2016).

Procedures: We first prepared stock solutions as described above, and then mixed them in each microtube, as shown in the Supporting Information (experimental solution details), prior to microscopic observations.

Acknowledgements

This work was supported, in part, by JSPS KAKENHI grants no. JP15H02121 and JP16K07293, and by MEXT KAKENHI grants no. JP25103012 and JP24104004. H.S. received support as Research Fellow of the Japan Society for the Promotion of Science.

Conflict of Interest

The authors declare no conflict of interest.

Keywords: DNA • liquids • microdroplets • phase separation • synthetic biology

- [1] a) S. B. Zimmerman, A. P. Minton, *Annu. Rev. Biophys. Biomol. Struct.* **1993**, *22*, 27–65; b) R. J. Ellis, *Curr. Opin. Struct. Biol.* **2001**, *11*, 114–119.
- [2] T. D. Pollard, J. A. Cooper, *Science* **2009**, *326*, 1208–1212.
- [3] a) W. M. Aumiller, Jr., C. D. Keating, *Adv. Colloid Interface Sci.* **2017**, *239*, 75–87; b) F. C. Nielsen, H. T. Hansen, J. Christiansen, *BioEssays* **2016**, *38*, 674–681.
- [4] B. Monterroso, S. Zorrilla, M. Sobrinos-Sanguino, C. D. Keating, G. Rivas, *Sci. Rep.* **2016**, *6*, 35140.
- [5] E. M. Courchaine, A. Lu, K. M. Neugebauer, *EMBO J.* **2016**, *35*, 1603–1612.
- [6] A. A. Hyman, C. A. Weber, F. Jülicher, *Annu. Rev. Cell Dev. Biol.* **2014**, *30*, 39–58.
- [7] P.-Å. Albertsson, *Partition of Cell Particles and Macromolecules*, 2nd ed., Wiley, New York, **1971**.
- [8] N. Biswas, M. Ichikawa, A. Datta, Y. T. Sato, M. Yanagisawa, K. Yoshikawa, *Chem. Phys. Lett.* **2012**, *539–540*, 157–162.
- [9] a) L. S. Lerman, *Proc. Natl. Acad. Sci. USA* **1971**, *68*, 1886–1890; b) V. A. Bloomfield, *Curr. Opin. Struct. Biol.* **1996**, *6*, 334–341; c) V. V. Vasilevskaya, A. R. Khokhlov, Y. Matsuzawa, K. Yoshikawa, *J. Chem. Phys.* **1995**, *102*, 6595–6602; d) M. Kojima, K. Kubo, K. Yoshikawa, *J. Chem. Phys.* **2006**, *124*, 024902.
- [10] a) M. Kasai, S. Asakura, F. Oosawa, *Biochim. Biophys. Acta* **1962**, *57*, 13–21; b) J. Hanson, *Proc. R. Soc. London Ser. B* **1973**, *183*, 39–58.
- [11] L. Blanchoin, R. Boujemaa-Paterski, C. Sykes, J. Plastino, *Physiol. Rev.* **2014**, *94*, 235–263.
- [12] M. Honda, K. Takiguchi, S. Ishikawa, H. Hotani, *J. Mol. Biol.* **1999**, *287*, 293–300.
- [13] S. Misu, M. Takebayashi, K. Miyamoto, *Front. Genet.* **2017**, *8*, 27.
- [14] M. Feric, N. Vaidya, T. S. Harmon, D. M. Mitrea, L. Zhu, T. M. Richardson, R. W. Kriwacki, R. V. Pappu, C. P. Brangwynne, *Cell* **2016**, *165*, 1686–1697.
- [15] M. Negishi, T. Sakaue, K. Takiguchi, K. Yoshikawa, *Phys. Rev. E* **2010**, *81*, 051921.
- [16] S.-i. Nakano, D. Miyoshi, N. Sugimoto, *Chem. Rev.* **2014**, *114*, 2733–2758.
- [17] a) M. Hase, K. Yoshikawa, *J. Chem. Phys.* **2006**, *124*, 104903; b) A. Kato, E. Shindo, T. Sakaue, A. Tsuji, K. Yoshikawa, *Biophys. J.* **2009**, *97*, 1678–1686.
- [18] A. Kato, M. Yanagisawa, Y. T. Sato, K. Fujiwara, K. Yoshikawa, *Sci. Rep.* **2012**, *2*, 283.
- [19] T. J. Nott, T. D. Craggs, A. J. Baldwin, *Nat. Chem.* **2016**, *8*, 569–575.
- [20] a) C. Chiarabelli, P. Stano, P. L. Luisi, *Curr. Opin. Biotechnol.* **2009**, *20*, 492–497; b) K. Suzuki, M. Miyazaki, J. Takagi, T. Itabashi, S. i. Ishiwata, *Proc. Natl. Acad. Sci. USA* **2017**, *114*, 2922–2927.
- [21] T. Ban, T. Fukuyama, S. Makino, E. Nawa, Y. Nagatsu, *Langmuir* **2016**, *32*, 2574–2581.
- [22] H. Yuan, Q. Ma, Y. Song, M. Y. H. Tang, Y. K. Chan, H. C. Shum, *Macromol. Chem. Phys.* **2017**, *218*, 1600422.
- [23] C. Han, S. Takayama, J. Park, *Sci. Rep.* **2015**, *5*, 11891.
- [24] a) K. A. Black, D. Priftis, S. L. Perry, J. Yip, W. Y. Byun, M. Tirrell, *ACS Macro Lett.* **2014**, *3*, 1088–1091; b) S. Lindhoud, M. M. A. E. Claessens, *Soft Matter* **2016**, *12*, 408–413.
- [25] a) S. C. Weber, C. P. Brangwynne, *Cell* **2012**, *149*, 1188–1191; b) D. M. Mitrea, R. W. Kriwacki, *Cell Commun. Signaling* **2016**, *14*, 1; c) C. P. Brangwynne, P. Tompa, R. V. Pappu, *Nat. Phys.* **2015**, *11*, 899–904.
- [26] J. A. Spudich, S. Watt, *J. Biol. Chem.* **1971**, *246*, 4866–4871.
- [27] I. Fujiwara, S. Takahashi, H. Tadakuma, T. Funatsu, S. i. Ishiwata, *Nat. Cell Biol.* **2002**, *4*, 666–673.

Manuscript received: February 3, 2018

Accepted manuscript online: April 19, 2018

Version of record online: June 1, 2018